Universidade de Évora - Instituto de Investigação e Formação Avançada

Programa de Doutoramento em Ciências da Terra e do Espaço

Área de especialização | Processos Geológicos

Tese de Doutoramento

Metallogenic evolution of gold and iron deposits from the Ossa-Morena Zone (SW Iberia) - Constraining ore deposition conditions and vectoring future mineral exploration

Miguel Cardoso Maia

Orientador(es) | Fernando Manuel Pereira de Noronha

Jose Mirao

Pedro Miguel Nogueira

Évora 2022

Universidade de Évora - Instituto de Investigação e Formação Avançada

Programa de Doutoramento em Ciências da Terra e do Espaço

Área de especialização | Processos Geológicos

Tese de Doutoramento

Metallogenic evolution of gold and iron deposits from the Ossa-Morena Zone (SW Iberia) - Constraining ore deposition conditions and vectoring future mineral exploration

Miguel Cardoso Maia

Orientador(es) | Fernando Manuel Pereira de Noronha

Jose Mirao

Pedro Miguel Nogueira

Évora 2022

A tese de doutoramento foi objeto de apreciação e discussão pública pelo seguinte júri nomeado pelo Diretor do Instituto de Investigação e Formação Avançada:

Presidente	Rui Paulo Salgado (Universidade de Évora)
Vogais	António Mateus (Universidade de Lisboa - Faculdade de Ciências) Fernando Manuel Pereira de Noronha (Universidade do Porto - Faculdade de Ciências) (Orientador) Jorge Manuel Pedro (Universidade de Évora) Maria Alexandra de Mascarenhas Guedes (Universidade do Porto - Faculdade de Ciências) Mercedes Fuertes-Fuentes (Universidad de Oviedo) Mário Abel Gonçalves (Universidade de Lisboa - Faculdade de Ciências)

Évora 2022

“… there is no necessary connection between the size of an object and the value of a fact, and that, though the objects I have described are minute, the conclusions to be derived from the facts are great.”

Sorby, 1858

Acknowledgments

Personal

The most personally and scientifically defiant stage of my life (until now) comes to an end, and such achievement could not have been made without the help of many people that I would now like to acknowledge.

First, I must warmly thank my Supervisor, Pedro Nogueira, who over the last 5+ years has become a close friend that has accompanied me through the task of completing this PhD project and with whom I have shared many discussions, frustrations, achievements, tennis matches (most of them I lost), laughs and good moments. Pedro has welcomed me in Évora in 2017, and as a fellow “Portuense” he has provided me an environment that has always kept me close to home. I honestly believe that, besides the Supervision task, without this friendship this PhD would have been a much more tumultuous path. I, of course, extend this message to Dália, which has welcomed me in the “family” and had the patience to, most certainly, hear Pedro complain about the work frustrations that I have caused.

To Professor Fernando Noronha a special acknowledge must be made. Has I have already confessed to him; he is responsible for me having enrolled a Bsc in Geology at the Faculty of Sciences of the University of Porto. During the last year of high school, Professor Fernando Noronha did a science communication conference at my high school, that opened my mind to the real impact that Geology, and in particular mineral resources, have in our daily life. Since that moment he has “made” another metallogeny geek, and Professor Fernando Noronha has supervised my scientific work from my bachelor final project to my MsC Thesis and finally this PhD project. I thank him for his resilience in continuing to accompany this scientific work, for his valuable guidance and scientific discussions and for his contribution to the great advances of understanding the processes behind ore deposits formation in Portugal.

The thanks to the supervision team would not be complete without an enormous acknowledgement to Professor José Mirão, that has provided me the tools (particularly the analytical ones) to perform the tasks that were initially delineated for this PhD project. His

contribution to this PhD project has greatly improved the quality of the work and without him none of this would be possible.

A PhD is a work of many people! Without the scientific partnerships this work would not be possible, and for this I deeply thank Mercedes Fuertes-Fuente and Antonia Cepedal for welcoming me in Oviedo for a scientific stay and for the valuable discussions that greatly improved this work. To Pedro Barrulas from the HERCULES Laboratory for the incredible patience and expertise shared during many sessions at the HERCULES LA-ICP-MS Laboratory. To Alexandre Araújo and Jorge Pedro for the innumerable field trips through the puzzling Ossa-Morena Zone which were key for me to understand its complex geology. A final thanks to Sandra Velez for the many months shared in the Geoscience Lab while preparing thin, thick, and cross sections with whom I've shared many frustrations during this task.

The PhD is a mentally challenging path, which many times puts us in a position of almost losing our minds specially though a global pandemic, therefore maintaining a good balance between your work and your personal life is not always easy but it would be much more difficult without friends and family.

Being 400km away from your hometown necessarily distances yourself from family and long-time friends, and for this the "Évora friends" had a major role in maintaining my mental health, by sharing the good moments and the frustrations of a PhD life.

To Sandro Vicente, Diogo São Pedro, Noel Moreira, José Roseiro, Pedro Pereira, and Marcelo Silva, thank you for the unvaluable fellowship and friendship, for the many hours spent inside the same room, the many field trips, conferences, the many scientific discussions, the many beers and "caracóis". Thank you for putting up with my bad humour in the morning and my stubbornness, you guys are incredible! I acknowledge how difficult that must have been… To José Roseiro a special thanks for sharing the turmoil of a PhD and partnering up scientifically so that this work could be a little bit better. Thank you for your generosity in sharing knowledge and opinions, and for reading the numerous versions of manuscripts and conference abstracts. I am sure your future as a geologist will be brilliant, wish you nothing but the best. To Noel, thank you for your friendship, the many field trips and field assistance

that helped me getting a little bit closer to understanding a little bit more of Ossa-Morena geology.

But of course, the long-time friends were also always there to lighten up my visits to Porto and to share frustrations, achievements, and many, many, many laughs. Thank you Zé F., Jóni, Duarte, Filipe V., Diogo, Filipe P., and I'm sorry for the many events that I have missed.

To the ones who have provided me the solid basis of educations, the tools to deal with obstacles and guidance, to my mom and dad – to whom this thesis is dedicated. The sacrifices you´ve made will never be forgotten, I'm sorry for the absence during the last 5 years and thank you for your resilience, advice and love.

"…nunca percas um bom amigo conta com a mãe e conta comigo, mas cuida de ti acredita isso basta." – *Diabo na Cruz*

To Sara, thank you for the incredible patience to keep up with my frustrations, my (sometimes unbearable) stubbornness but also, and fortunately most times, sharing the successes and joys. Your emotional maturity and love have been crucial to keep me in the right direction. Words are not enough to thank you.

Funding and Host Institution acknowledgements

The PhD project to which this thesis is dedicated was developed under the aegis of the Universidade de Évora and the Instituto de Investigação e Formação Avançada, in the Earth and Space Sciences PhD program with a specialization in Geological Processes.

The main funding for this PhD was attributed by the Fundação para a Ciência e Tecnologia through the PhD grant with the reference SFRH/BD/145049/2019.

Analytical funding was additionally acquired through an application for the Student Research Grant annually attributed by the Society for Economic Geologist to most innovative post-graduation research projects. This funding was granted in the year 2019 by the Hugh McKinstry Fund through the Society for Economic Geologist Foundation.

Additional funding was also provided by the host institutions of this PhD project, the Institute of Earth Sciences – Évora Pole, through the projects UIDB/04683/2020 and UIDP/04683/2020 as well as the HERCULES Laboratory, through the and UIDB/04449/2020 project.

Metallogenic evolution of gold and iron deposits from the Ossa-Morena Zone (SW Iberia) - Constraining ore deposition conditions and vectoring future mineral exploration

Abstract

This PhD thesis is the product of a research project that aimed to constrain the metallogenic conditions behind the formation of gold and iron ore deposits in the Ossa-Morena Zone, particularly in the Montemor-o-Novo - Ficalho metallogenic belt. An additional goal of providing a proposal for the use of mining heritage as a tool for formal and informal educational activities was set during the PhD works, therefore contributing not only for the valorisation of the mineral resources from the Alentejo region, but also providing a product that can be used by local communities and other stakeholders as an economic activity (e.g. geotourism).

Three key areas were selected for this thesis, from the NW to the SE of the Ossa-Morena Zone: i) Montemor-o-Novo area which comprises a set of iron deposits of probable Cambrian age that were mined during the late 19th century and early 20th century. These iron deposits, although currently subeconomic, were selected for this study since the model attributed to their genesis is debatable and magnetite chemistry could help in their classification and discrimination. This area is also characterised by numerous gold prospects and deposits, referred as the Escoural gold district, that was disclosed during the last decades by several mineral exploration projects, with orebodies being mostly intersected by drill cores. The Monfurado deposit/prospect, part of the Escoural gold district was selected for this PhD project, due to its proximity to a large iron orebody (mainly magnetite) which was also mined in early times (Monges iron mine); ii) the second area is the ancient Alvito iron mine, which comprises a set of open pits mined during the 19th century. The orebodies are mainly composed of magnetite and corresponds to an exoskarn formed in a carbonate unit by means of the interaction of magmatic-hydrothermal fluids inputted by the emplacement of a Gabbro-Diorite Complex. This area was selected due to the lack of recent studies focusing on the characterisation of the ores and the recent identification of Ni-Cu mineralisation in the surrounding Beja Igneous Complex. iii) The third area, to the southeast of the Montemor-o-Novo-Ficalho belt, corresponds to the Azenhas-Orada iron deposits, a skarn deposit with magnetite hosted by an extremely metasomatized amphibolite. This area was selected because this skarn system contrasts with that of Alvito, with the skarn formation being previously attributed to a reactional skarn promoted by the thrust-fault imbrication of metavolcanic units over carbonate rocks. Furthermore, LA-ICP-MS trace element analysis of

magnetite and isotopic inspection could contribute to understanding the mechanisms behind its formation.

As stated, the Escoural gold district was the target for the constraint of the mechanisms behind the concentration and deposition, and the chosen gold deposit was Monfurado. The paragenetic, geochemistry and fluid inclusion studies were performed in samples from six drill cores and two distinct types of gold mineralisation were found, where: Type i corresponds to massive sulfide horizons in which gold is hosted in arsenopyrite and pyrite or, seldomly, gold particles hosted in an arsenopyrite-rich layer. In this type arsenopyrite geothermometer indicates a temperature between 188ºC and 372ºC and sulfidation processes are responsible for the redox destabilisation of the gold-transporting fluid, therefore imposing gold deposition. Type ii corresponds to quartz-chlorite-pyrite veins crosscutting acid metavolcanic rocks with rhyolite-rhyodacite affinities, in which gold is found filling fractures in pyrite, sometimes accompanied by Bi-Te phases. Primary fluid inclusions were studied in quartz samples to estimate the conditions and fluid composition responsible for gold transport in this type. Secondary H_2O-NaCl fluid inclusions (Lw_2) were found, with mean salinities of 6.0 eq. w(NaCl) and mean homogenization temperature of 226ºC, with corresponding pressures of 3.0 MPa. Chlorite geothermometer results are in the range of 229 ºC and 309 ºC, agreeing with the fluid inclusion homogenization temperatures for Lw_2 fluids.

Sulfur isotope signatures of sulfides from the mineral assemblages (pyrite, pyrrhotite, arsenopyrite) revealed values within the narrow range of 8.5 ‰ and 10.6 ‰, suggesting a similar sulfur source for both mineralisation types. All the gathered data suggests that gold possibly derives from the devolatilization of the Escoural formation (Série Negra) and was transported by reduced fluids through anisotropies created by the Montemor-o-Novo Shear Zone. When these fluids interacted with the magnetite-rich carbonate rocks from the Monfurado Formation sulfidation of magnetite to pyrrhotite occurred, forcing a change to the redox condition of the fluids and forcing the precipitation of gold in the massive sulfide layers of Type i mineralization.

In situ LA-ICP-MS trace element analysis of magnetite allowed the textural and chemical characterisation of the ores from the Montemor-o-Novo Iron Complex (MIC) and from the Alvito and Azenhas-Orada skarn deposits. This thesis contributes to the clarification of the processes of formation of iron deposits in the metallogenic belt of Montemor-o-Novo – Ficalho with emphasis on the iron deposits whose classification is the subject of debate, such as those of the MIC and Azenhas-Orada.

Results show that the magnetite from the MIC deposits has trace element contents that clearly distinguish them from the magnetites from the studied skarns. Magnetites from the MIC deposits display concentration of temperature sensitive elements, such as Ti, V, Al, Ga, Sn, Cr and high field strength elements, extremely lower than those found in the magnetites from

skarns. MIC magnetites usually display trace element concentrations and variations consistent with those formed under low-temperature hydrothermal regimes. In contrast, the Alvito and Azenhas-Orada skarn magnetites are much more closely related to high-temperature hydrothermal fluids.

The magnetites from the studied deposits are not only distinguishable by the individual analysis of trace element concentrations but also by the discriminant diagrams, such as the Al + Mn vs Ti + V and Ti vs Ni/Cr, as well as by the proposed discrimination diagram of Co vs Zn. Furthermore, the application of machine learning algorithms to the classification of LA-ICP-MS trace element data of magnetite, by the means of Random Forest, proved to be a powerful and precise method for the classification of ore deposits. The results from the Random Forest classified 100% of the magnetite from the MIC as VMS and 65 % of magnetite from the Alvito and Azenhas-Orada deposit and Skarn.

The oxygen isotope signatures are aligned to the processes behind the formation of magnetite, as well as with the post-deposition modifications imposed by orogenic metamorphism in the case of the MIC magnetites.

Evolução metalogénica de depósitos de ouro e ferro da Zona de Ossa-Morena (SO Ibérico) – Caracterização das condições de deposição e definição de vetores para a prospeção mineral

Resumo Alargado

A tese de doutoramento doravante apresentada é o produto de um projeto que pretende compreender as condições metalogénicas envolvidas na génese de depósitos de ouro e ferro da Zona de Ossa-Morena, focando-se no sector metalogénico de Montemor-o-Novo - Ficalho. Como objetivo adicional foi apresentada uma proposta do uso do património mineiro enquanto ferramenta para atividades educacionais formais e informais contribuindo não só para a valorização dos recursos minerais do Alentejo, mas também para promover o uso do património geológico enquanto produto económico (e.g. geoturismo) que possa ser usado pelas comunidades locais e outros agentes.

Três localizações chave foram selecionadas como alvos de estudo neste projeto de doutoramento: i) a área de Montemor-o-Novo que compreende um conjunto de depósitos de ferro de idade provável Câmbrica, e que foram alvo de exploração durante o final do século XIX e o início do século XX. Estes depósitos, embora que atualmente sejam sub-económicos, foram selecionados para este estudo uma vez que os modelos metalogénicos atribuídos para a sua génese são discutíveis, sendo que a análise química de magnetites pode contribuir para a sua classificação e discriminação. A área de Montemor-o-Novo é também caracterizada pelas numerosas ocorrências e depósitos de ouro, aqui referidas como os depósitos de ouro do Escoural, que foram identificados no decorrer das últimas décadas por vários projetos de prospeção mineral, tendo os corpos mineralizados sido intersectados por sondagens de prospeção.

O depósito de Monfurado, parte dos depósitos de ouro do Escoural, foi selecionado como alvo preferencial para este projeto de doutoramento uma vez a sua proximidade do depósito de ferro (magnetite) dos Monges. ii) A segunda área escolhida para este projeto corresponde à antiga mina de ferro do Alvito que compreende um conjunto de explorações a céu aberto cuja atividade decorreu durante o século XIX. Os corpos mineralizados são constituídos principalmente por magnetite e correspondem a exoskarns desenvolvidos em unidades carbonatadas provocado pela interação entre fluídos magmático-hidrotermais introduzidos no sistema através da instalação de um Complexo Gabro-Diorítico. Esta área foi selecionada devido à larga falta de estudos recentes focados na caracterização do minério, bem como devido à recente identificação de mineralizações de Ni-Cu nas unidades adjacentes do Complexo Ígneo de Beja. iii) A terceira área, a sudeste do Sector de Montemor-o-Novo,

corresponde ao complexo de depósitos do tipo skarn Azenhas-Orada, nos quais a magnetite é hospedada por anfibolitos intensamente metassomatizados. Esta área foi selecionada uma vez que este depósito skarn contrasta com aquele encontrado em Alvito, tendo a génese dos depósitos das Azenhas-Orada sido atribuída anteriormente a um sistema skarn reacional promovido pela imbricação tectónica de unidades metavulcânicas sobre rochas carbonatadas. Alés disso, a análise in-situ de elementos traço em magnetites aliada à análise isotópica pode contribuir para a identificação dos mecanismos associados à formação dos depósitos selecionados.

Como já referido, os depósitos de ouro do Escoural foram alvo de estudo por forma a constranger os mecanismos de concentração e deposição de ouro no caso do depósito de ouro de Monfurado. Os estudos paragenéticos, geoquímicos e de inclusões fluídas foram realizados em amostras recolhidos em seis sondagens de prospeção tendo sido identificados dois tipos de mineralização de ouro, nomeadamente: O Tipo i corresponde a horizontes maciços de sulfuretos nos quais o ouro de encontra hospedado em cristais de arsenopirite e pirite, assim como foram observadas partículas de ouro livre em níveis ricos em arsenopirite. Neste tipo de mineralização o geotermómetro da arsenopyrite indica temperaturas na ordem dos 188ºC e os 372ºC, e os processos de sulfidização foram identificados como sendo responsáveis pela destabilização das condições redox do fluído transportador do ouro, o que provocou a sua deposição. O segundo tipo, Tipo ii, corresponde a veios de quartzo-clorite-pyrite que cortam rochas ácidas metavulcânicas, com afinidade geoquímica a reólitos e riodacitos, nos quais as partículas de ouro são observadas como preenchimento de micro fracturas em pirite, por vezes acompanhados por fases de Bi-Te. As inclusões fluídas estudadas tiveram um papel preponderante para a estimativa das temperaturas e composição dos fluídos responsáveis pelo transporte do ouro na mineralização Tipo ii. Foram identificadas inclusões fluídas secundárias aquo-salinas (H_2O-NaCl) com salinidade média de 6.0 eq. w(NaCl) e temperatures de homogeneização médias de 226ºC, com pressões estimadas na ordem dos 3.0 MPa. O geotermómetro da clorite revelou resultados na ordem dos 229ºC aos 309ºC, coerentes com os resultados obtidos através do estudo de inclusões fluídas.

A assinatura de isótopos de enxofre dos sulfuretos encontrados na paragénese da mineralização de ouro (pirite, pirrotite, arsenopirite) revelaram valores na ordem dos 8.5 ‰ e 10.6 ‰, o que revela fraca variação. Estes resultados indicam que muito embora tenham sido identificados dois tipos de mineralização de ouro a fonte do enxofre poderá ser a mesma.

Em suma, os resultados obtidos na análise do depósito de ouro de Monfurado sugerem que o ouro possivelmente foi remobilizado das unidades metassedimentares da Formação do Escoural (Série Negra) e transportado através de fluídos metamórficos reduzidos através de anisotropias geradas pela atividade da Zona de Cisalhamento de Montemor-o-Novo. Quando estes fluídos entraram em contacto com as unidades carbonatadas ricas em magnetite

geraram-se processos de sulfidização que provocaram a alteração da magnetite em pirrotite, forçando uma alteração às condições redox do fluído, imponto a precipitação do ouro.

As análises *in-situ* de elementos traço com recurso ao LA-ICP-MS permitiu a caracterização química e textural dos minérios de ferro dos depósitos de Montemor-o-Novo (MIC), e dos depósitos skarn do Alvito e Azenhas-Orada. O trabalho apresentado contribuí para clarificar os processos envoltos na génese dos depósitos de ferro do sector Montemor-o-Novo – Ficalho, com ênfase nos depósitos de ferro de Montemor-o-Novo e Azenhas-Orada, cujos modelos são debatíveis.

Os resultados demonstram que a magnetite dos depósitos de ferro de Montemor-o-Novo apresentam conteúdos em elementos traço que as discriminam claramente das magnetites dos depósitos do tipo skarn estudados. Estas magnetites apresentam concentrações baixas em elementos traço indicadores de ambientes de baixa temperatura, tais como Ti, V, Al, Ga, Sn, Cr e HFSE (high field strength elements), quando comparadas com as magnetites dos depósitos skarn. As magnetites do complexo de depósitos de ferro de Montemor-o-Novo (MIC) apresentam, usualmente, concentrações e variações em elementos traço consistentes com as encontradas em magnetites formadas sob condições hidrotermais de baixa temperatura enquanto as magnetites dos depósitos do Alvito e Azenhas-Orada apresentam características químicas que as colocam mais próximas de ambientes hidrotermais de alta temperatura.

As magnetites dos depósitos estudados não só são distinguidas pela análise individual da concentração em elementos traço, mas também pelos diagramas discriminatórios propostas pela literatura, tais como os diagramas Al + Mn vs Ti + V e Ti vs Ni/Cr, assim como pelo diagrama Co vs Zn proposto nos trabalhos inerentes a esta tese. Adicionalmente, a aplicação de algoritmos de *machine learning*, nomeadamente *Random Forest*, provou ser um método preciso para a classificação de depósitos minerais usando as análises químicas da magnetite como base para essa classificação. O algoritmo Random Forest classificou 100% das magnetites dos depósitos de Montemor-o-Movo como estando associadas a depósitos do tipo VMS, enquanto no caso das magnetites do Alvito e Azenhas-Orada 65% foram classificadas como skarn.

As assinaturas em isótopos de oxigénio das magnetites analisadas estão alinhadas com os processos envolvidos na génese destas mesmas magnetites, assim como com as modificações após a sua deposição introduzidas pelo metamorfismo regional no caso das magnetites dos depósitos de ferro de Montemor-o-Novo.

Table of contents

List of figures

List of tables

Preface

This thesis is the outcome of a PhD project supported by the Fundação para a Ciência e Tecnologia, through a PhD grant under the reference SFRH/BD/145049/2019. The initial phases of this PhD project were supported by a research project from the University of Évora, entitled “ZOM-3D Metallogenic Modelling of Ossa-Morena Zone: Valorisation of the Alentejo Mineral Resources” (ref: ALT20-03-0145- FEDER-000028), which facilitated the access to sampling and laboratory preparation of samples

The specialisation of this PhD is on “Geological Processes”. It is an extremely vast theme, therefore I would like to disclose that this is an “Economic Geology and Mineral Exploration” PhD thesis devoted to the use of a multitude of analytical techniques for the definition of vectors for future mineral exploration in the SW of Iberia, particularly dedicated to understand the metallogenic processes involved with the formation of iron and gold deposits in the Ossa-Morena Zone.

It is usually perceived that getting a PhD is “…knowing more and more, about less and less… up until eventually knowing everything about nothing.”. I tend to agree with this misperception of a PhD project and therefore I have tried hard to apply diverse methodologies, develop competences transversal to many fields of knowledge, and produce research that broadens within different disciplines of geology to contradict such statements.

Foreword on thesis outline

This thesis includes five research papers which were co-authored by different researchers with whom scientific partnerships were kept during the PhD project.

This thesis is organised by chapters, which begin with an introduction to the scientific problem, drawn in the early phases of the research and followed by individual chapters that correspond to the research papers submitted, accepted, and published during the timeframe of the PhD project. Each chapter contains its own reference list so that the original form of the articles is respected. A concluding chapter provides a complete overview of the successful and unsuccessful approaches and proposes future research directions.

Additionally, the supplementary material with the raw data that resulted from this thesis is provided in the appendices section and for this reason, the references for supplementary material of the research papers were modified to meet these criteria, therefore they do not correspond to the supplementary referencing of the original publication.

The following research articles are mentioned according to the date of publication, acceptance, or submission and not according to their appearance in this thesis.

The first research paper is entitled “In situ LA-ICP-MS trace element analysis of magnetite as a vector towards mineral exploration: A comparative case study of Fe-skarn deposits from SW Iberia (Ossa-Morena Zone)” is already published in the **Journal of Geochemical Exploration**, v. 234, Article Number 106941. https://doi.org/10.1016/j.gexplo.2021.106941
This work is co-authored by Pedro Barrulas (PhD in Chemistry), a researcher from the HERCULES Laboratory that is responsible for the LA-ICP-MS equipment and has supported all the trace element analysis of magnetite during this work. The remaining co-authors are Pedro Nogueira, José Mirão, and Fernando Noronha which are the advisor and co-advisors of this PhD Thesis.

The second paper is entitled “New insights on the Escoural Orogenic gold district (Ossa-Morena Zone, SW Iberia): Geochemistry, fluid inclusions and stable isotope constraints from the Monfurado gold prospect” is already published in **Ore Geology Reviews**, v. 142, Article Number 104736. https://doi.org/10.1016/j.oregeorev.2022.104736
This work is co-authored by José Roseiro, a PhD candidate at the Earth and Space Sciences PhD program at the University of Évora and with whom a scientific cooperation was carried for this work. José has provided valuable assistance during field and laboratory work, as well as thorough discussions and revisions of early stages of the manuscript. The work is also co-authored by Mercedes Fuertes-Fuente and Antonia Cepedal, both Professors at the University of Oviedo (Spain) and have accompanied me during my scientific stay in Oviedo for the purpose of carrying EPMA analysis, assisting me in the scientific revision. The remaing co-authors are Pedro Nogueira, José Mirão, and Fernando Noronha which are the advisor and co-advisors of this PhD Thesis.

The third research paper is entitled “Geodiversity assessment through the Évora – Montemor-o-Novo region: On the scope of valorising the mining heritage of the Ossa-Morena Zone (SW Iberia, Portugal)” was published in **Geoheritage**, v. 14, 90. https://doi.org/10.1007/s12371-022-00728-2.

The co-authors of this research are Pedro Nogueira, José Mirão, and Fernando Noronha which are the advisors and co-advisors of this PhD Thesis and provided fruitful discussions, revisions, and scientific supervision.

The fourth research paper is entitled “Combining $\delta^{18}O$ isotope data and in-situ LA-ICP-MS trace element analysis of magnetite as a proxy for ore genesis: Constraints on the formation of Fe deposits from Ossa-Morena Zone (SW Iberian Peninsula)” and was published in **Journal of Geochemical Exploration**, v. 245, Article 107140. https://doi.org/10.1016/j.gexplo.2022.107140. The co-authors team is the same as the one from the first research paper.

The fifth research manuscript, entitled “A machine learning approach to the classification of ore deposits: Random Forest classification of in-situ LA-ICP-MS trace element analysis of

magnetite" is to be submitted. The co-authors team is the same as the one from the first and fourth research papers.

Conference Abstracts

Additionally, the following references correspond to conference abstracts with preliminary results that were presented in international meetings.

Maia, M., Nogueira, P., Barrulas, P., Mirão, J., and Noronha, F., Discrimination of Fe deposits from Ossa-Morena Zone (SW Iberia): Random Forest classification of in-situ LA-ICP-MS trace element analysis of magnetite. Congreso Ibérico de Geoquímica 2022, p. 84.

Maia, M., São Pedro, D., Nogueira, P., Mirão, J., and Noronha, F., 2019, Fluid constraints for Au deposition at the Monges iron deposit, Ossa-Morena Zone (Montemor-o-Novo, Portugal): 15th SGA Biennial Meeting 2019, Glasgow, v. 1, p. 252-255.

Other publications and outreach activities during the PhD

The following papers, conference abstracts and activities were developed throughout the PhD period although many of them not related to the topic under discussion on this PhD thesis.

Luz, F., Pereira, I., **Maia, M.**, Leal, S., Pereira, R., Roseiro, J., Casacão, J., São Pedro, D., and Moreira, N. (In press). Análise sobre empregabilidade e associativismo nas áreas das Geociências em Portugal. Geonovas.

Maia, M., Moreira, N., Vicente, S., Mirão, J., Noronha, F., and Nogueira P., 2020. Multi-Stage Fluid System Responsible for Ore Deposition in the Ossa-Morena Zone (Portugal): Constraints in Cu-Ore Deposits Formation. Geology of Ore Deposits, v. 62(6), p. 508-534. https://doi.org/10.1134/S1075701520060094

Moreira, N., Roseiro, J., **Maia, M.,** Pedro, D., Afonso, P., Mendes, P., and Nogueira, P., 2020. A Zona de Ossa-Morena e as suas matérias-primas críticas. Revista de Ciência Elementar, v. 8(01). https://doi.org/10.24927/rce2020.006

Araújo, A., Caldeira, B., Martins, A., Borges, J., Moreira, N., Araújo, J., **Maia, M.**, Vicente, S., Afonso, P., Espanhol, D., and Bezzeghoud, M., 2020. Macrossismicidade associada ao sismo

de Arraiolos do dia 15 de janeiro de 2018 com M = 4,9 e eventuais implicações na geometria da rutura. Comunicações Geológicas, v. 107(Especial I), p. 35-37. ISSN: 0873-948.

Nogueira, P., Afonso, P., Roseiro, J., **Maia, M.**, São Pedro, D., Moreira, N., Matos, J.X., and Batista, M.J., 2020. Portable X-ray fluorescence and clustering methods applied to mineral exploration: the significance and nature of Batigelas anomaly (Ossa-Morena Zone - Cabeço de Vide, Portugal). Comunicações Geológicas, v. 107(Especial II), p. 47-53. ISSN: 0873-948.

Nogueira, P., Moreira, N., **Maia, M.**, Roseiro, J., Silva, E., and Kullberg, J.C., 2020. Mais de 30 anos de encontros de Geoquímica Ibérica: contributos do XII Congresso Ibérico de Geoquímica e da XX Semana de Geoquímica. Comunicações Geológicas, v. 107(Especial II), p. 11-16. ISSN: 0873-948.

Nogueira, P., Vicente, S., **Maia, M.**, Roseiro, J., Moreira, N., and Matos, J.X., 2020. High-resolution geochemical mapping in the Mociços mine (Ossa-Morena Zone, Portugal). Contributions from machine learning methods. Comunicações Geológicas, v. 107(Especial II), p. 55-62. ISSN: 0873-948.

Roseiro, J., Moreira, N., Nogueira, P., **Maia, M.**, Araújo, A., and Pedro, J., 2020. Depositional environment and passive-to-active margin transition as recorded by trace elements chemistry of lower-middle Palaeozoic detrital units from the Ossa-Morena Zone (SW Iberia). Comunicações Geológicas, v. 107(Especial II), p. 39-46. ISSN: 0873-948.

Chapter 1

Introduction

1.1 Thesis outline

As aforementioned, this PhD thesis is the result of a compilation of five research papers currently published, accepted, under review or to be submitted in highly reputable journals, which are the scope of this thesis.

Chapter 1: Introduction

This chapter discloses the motivations and the structure behind the design of this PhD thesis project. The main issues addressed throughout the PhD thesis are presented in this chapter, including a brief complementary state of the art of the geological context of the mineral deposits of Ossa-Morena Zone and the research approach adopted throughout the elaboration of the thesis.

Chapter 2.

This chapter presents the identification and characterisation of the mechanisms behind gold deposition. This was carried out through the study of one gold deposit, which belongs to the gold bearing district of Escoural and is structurally controlled by the Montemor-o-Novo Shear Zone. This chapter corresponds to the published article "**New insights on the Escoural Orogenic gold district (Ossa-Morena Zone, SW Iberia): Geochemistry, fluid inclusions and stable isotope constraints from the Monfurado gold prospect**" which identifies the sulfur and gold sources, as well as the fluids, enrolled in gold transportation, for this combining the study of sulfide and gold chemistry with sulfur isotope analysis and fluid inclusions. This study relies on an extensive drilling campaign, where it was possible to sample six drill cores, performed during recent exploration works at the Monfurado Prospect. Our work identified two gold mineralisation types: Type i) where gold particles are found in close association with arsenopyrite and pyrite, disseminated in sulfide-rich layers, ubiquitously composed of pyrrhotite. Type ii) where gold is found hosted exclusively in pyrite which is found in thin veinlets of pyrite-chlorite-(quartz) crosscutting the metavolcanic rocks from the Monfurado Fm.. Evidence of gold being transported in metamorphic-derived fluids is found, with CH_4-rich fluid inclusions present in quartz veins. It is proposed that gold deposition was favoured from sulfidation reactions where a sulfur-rich fluid interacted with a magnetite rich host-rock.

This work draws attention to the fact that type i mineralisation style has not been previously acknowledged for the Escoural gold district, and that the magnetite-rich carbonate host-rocks at the Montemor-o-Novo Shear Zone could have been a preponderant control on gold deposition and should therefore be considered as a mineral exploration guide in the future.

Chapter 3.

In the fourth chapter the trace element composition of magnetite is investigated by electron probe microanalysis (EPMA) and laser ablation inductively coupled plasma mass spectrometry (LA-ICP-MS). Herein one of the main topics of this PhD project is introduced, focusing on the characterisation of iron ores by inspecting the chemical composition of magnetite aiming to constrain the conditions of formation of iron deposits from the Ossa-Morena Zone. This chapter is dedicated to the published article entitled "**In situ LA-ICP-MS trace element analysis of magnetite as a vector towards mineral exploration: A comparative case study of Fe-skarn deposits from SW Iberia (Ossa-Morena Zone)**", in which magnetite trace element composition is used to classify and characterise the conditions behind ore deposition at the Alvito and Azenhas Fe skarn deposits. A discussion regarding the previous classification of these deposits is presented, providing the geothermometric constraints to corroborate the proposed metallogenic models for both deposits. Additionally, magnetite chemistry shows interesting concentrations in metals such as Co, Ni, and Zn that might indicate initially enriched sources in such metals. This research provided valuable information to propose robust geological models for exploration and interesting geochemical proxies for targeting ore deposits in the Montemor-o-Novo – Ficalho metallogenic belt.

Chapter 4.

This chapter details the chemical and textural characterisation of magnetites from selected iron deposits of the Ossa-Morena Zone. Here the trace element analysis of magnetite from the iron deposits of the Montemor-o-Novo Iron Complex (MIC), debatably classified as SEDEX-VMS, are combined with the analyses of magnetite from the Arvito, Azenhas, and Orada skarn deposits. It corresponds to the manuscript entitled "**Combining $\delta^{18}O$ isotope data and in-situ LA-ICP-MS trace element analysis of magnetite as a proxy for ore genesis: Constraints on the formation of Fe deposits from Ossa-Morena Zone (SW Iberia)**" and displays a thorough textural and chemical characterisation of the orebodies from both deposit types, SEDEX-VMS and Skarn, in an effort of finding new criteria for the classification of the studied ore deposits and identifying geochemical proxies for the association to other metals present in these iron ores. This PhD thesis provides the first results of magnetite trace element analysis by LA-ICP-MS applied to Fe deposits from the Ossa-Morena Zone, combining them with the first results of oxygen isotope analysis ($\delta^{18}O$) of magnetite.

The combination of trace element and oxygen isotopes analysis is innovative in studying ore deposits in Iberia. It has proved to be a good discrimination for the processes behind ore deposition and ore sources. The constraint of such conditions by characterising the chemical

composition of magnetite was important in proposing a metallogenic evolution for the studied deposits, as well as in solidifying the geological models applied to these deposits. Such tasks will hopefully contribute to the future success of mineral exploration in the Montemor-o-Novo – Ficalho metallogenic belt.

Chapter 5.

Although the use of magnetite trace element composition has been applied in the classification of ore deposits for the past decade, it has been mostly used in the discrimination of magnetite composition using conventional scatterplots. These plots have a limitation of dimension visualisation, and the inspection of large datasets with multiple and multidimensional variables can become extremely difficult. For this, the application of data mining techniques, such as machine learning, has been increasingly applied to handle with large geochemical datasets.

In this chapter the manuscript entitled "**A machine learning approach to the classification of ore deposits: Random Forest classification of in-situ LA-ICP-MS trace element analysis of magnetite**" is presented. The trace element data collected by the LA-ICP-MS trace element analysis of magnetite analysis from the iron deposits selected for this PhD project is combined in a dataset of over 630 analyses. Random Forest classification is applied to the compiled dataset and a robust classification of the ore deposits depending on magnetite composition. For this work, four different Random Forest models were tested, in which literature data, combined with our own data, was used for the dataset used in the Random Forest classifier. The results show that, when using magnetite trace element data from VMS and Skarn deposits from the literature, the magnetites from the MIC deposits are classified as VMS and the magnetite from Alvito, Azenhas, and Orada are classified as Skarn, which corroborates the previous classification and indicates that a machine learning approach can successfully classify ore deposits by using mineral geochemistry results. Advances in the classification of ore deposits are extremely important since mineral exploration highly relies on the correct classification of a particular deposit. As soon as this classification is done time and money are saved, contributing to more robust decisions regarding exploration targets and which methods to apply.

Chapter 6.

This chapter is dedicated to the paper entitled "**Geodiversity assessment through the Évora – Montemor-o-Novo region: On the scope of valorising the mining heritage of the Ossa-Morena Zone (SW Iberia, Portugal)**" which is devoted to the geodiversity assessment of a geological transect between Évora and Montemor-o-Novo cities in which ancient mining activities took place during late 19th century and early 20th century. This paper provides a "Geodiversity Route" that integrates a uniqueness of geological settings, put in evidence by

the relation of the mining activities, with the surrounding historical and cultural heritage. This chapter serves as an introduction to the complex geology of Ossa-Morena Zone and focuses on geological aspects of the NW of the Montemor-o-Novo – Ficalho metallogenic belt (Mateus et al., 2013), evidencing the necessity of providing tools that contribute to efficient scientific communication strategies in what concerns mining and mineral exploration activities. Nevertheless, the use of geodiversity sites for formal and informal education activities should be fomented. These activities should not invalidate the potential of the areas for the exploration of mineral resources. In fact, Geoheritage and exploration activities must both contribute to the quest of a geologically informed society.

This chapter is framed in this PhD thesis as an output that can be directly applied for the benefit of local communities, such as future beneficiation of geotourism projects in the region between Évora and Montemor-o-Novo. It is my belief that every PhD project, besides its strict scientific compromise, most of the times inaccessible to non-specialised publics, should also focus on providing accessible outcomes, such as the educational routes proposed in this manuscript. Geology at the service of communities is not all about mineral resources, it is also the comprehensible dissemination of knowledge for better understanding the Earth.

Chapter 7.

In this chapter, the concluding remarks from this PhD thesis are presented. The main achievements are enumerated, and contingencies are identified. Clear recommendations for future research directions are provided in this chapter.

Appendices A to F.

The appendices were prepared so that all the acquired data and knowledge is provided. The appendices are organised as follows: In **Appendix A** the results from the quantitative geodiversity assessment presented in Chapter 2 is provided; the sample types, location, and analytical procedures applied to each sample are provided in **Appendix B**; in the **Appendix C** the complete results from the microthermometry study of fluid inclusions from the Monfurado gold prospect are provided; the complete results for whole rock geochemistry are given in **Appendix D**; the complete results from the EPMA analysis of silicates, sulfides, gold, and magnetite are provided respecting the sample location in **Appendix E**; and the complete results for the LA-ICP-MS trace element analysis of magnetite can be found in **Appendix F**.

1.2 The metallogenic subdivision of the Ossa-Morena Zone

The Ossa-Morena Zone is a complex geotectonic zone at the SW of the Iberian Massif (Julivert et al., 1972) that covers a large area from Portugal to Spain. The geological settings of OMZ are key to understand the puzzling transition and evolution of the Cadomian and Variscan orogeny´s. The Ossa-Morena Zone corresponds to terrains that were merged with the Central Iberian Zone during the Cadomian orogeny, and the Tomar-Badajóz-Córdoba Shear Zone is considered the remnant of the suture of this merging (Ribeiro et al., 2007), latter reactivated during the Variscan Orogeny.

The complex lithological and metallogenic units of OMZ mainly reflect the control of the Variscan cycle stages, from i) the early intracratonic rifting that promoted the detachment of the Avalonian terrains from Gondwana; ii) the complete development of the Rheic ocean; iii) the transition to a compressive regime with the beginning of oceanic crust subduction under the Gondwana terrains; iv) the collisional stage of the Variscan Orogeny marked by the oblique collision between Avalonia and Gondwana, setting the edification of the orogen and promoting the current framework of the Iberian Massif. The suture of this collision is attributed to the contact between OMZ and the South Portuguese Zone, represented by the Pulo do Lobo and the Beja Acebuches Ophiolitic Complex (Quesada et al., 1994; Fonseca and Ribeiro, 1993). As one can understand, the geodynamic evolution of the SW of Iberia was so diverse that, consequently, the metallogenic settings accompanied such diversity. The combination of such factors created the conditions for the formation of several ore deposit types during the evolution of OMZ, such as rift-related deposits (SEDEX and VMS) in the early stages of the Variscan cycle; deposits associated to carbonate platforms in passive margin environments (MVT-Mississippi Valley Type deposits); orogen related deposits associated to the emplacement of igneous bodies (skarns, W-Sn deposits); orogenic gold deposits associated to large crustal-scale shear zones formed during the collisional stages of the orogeny; and late epithermal lode deposits (e.g. Cu).

The diversity of ore deposits led to the proposal of a division for Ossa-Morena Zone that considered the metallogenic diversity, following the previous proposals for the lithostratigraphic division of OMZ (Apalagueti et al., 1990; Oliveira et al., 1991). The early metallogenic subdivision of OMZ was presented by Oliveira (1986) which defined the main metallogenic belts at the Portuguese domains of OMZ. Latter proposals were made by Tornos et al. (2004), for the Spanish domains of OMZ, and Mateus et al. (2013) that presented a modern metallogenic subdivision for the Portuguese OMZ domains (**Fig. 1.1**).

This subdivision successfully correlated ore deposits that shared similar tectonic conditions, ore assemblages, and host-rocks. This resulted in the definition of seven

metallogenic sectors that comprise ore deposits and occurrences that were prospected and mined intermittently over time.

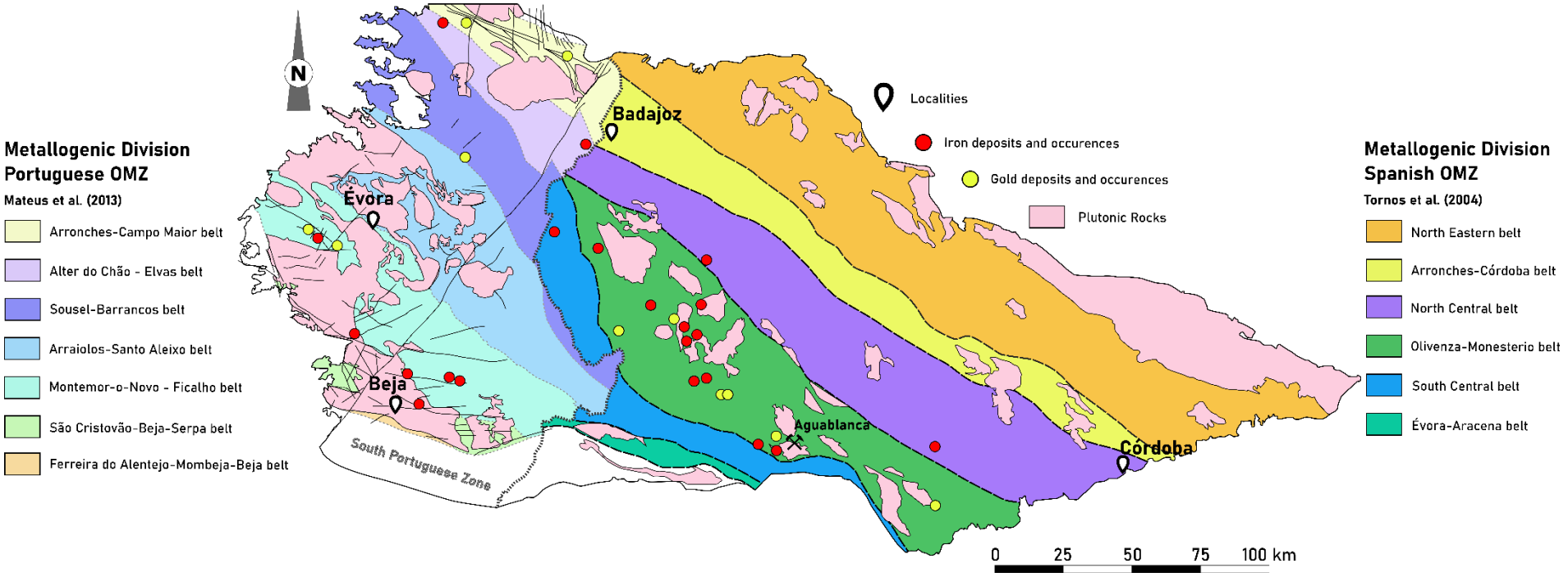

Figure 1.1 Metallogenic subdivision of Ossa-Morena Zone on the Portuguese and Spanish territories, with the location of the main iron and gold deposits and occurrences as well as the individualization of the main Variscan plutonic rocks (adapted from Tornos et al., 2004; Mateus et al., 2013).

1.2.1 The Montemor-o-Novo – Ficalho metallogenic belt

The Montemor-o-Novo - Ficalho metallogenic belt MFMB (**Fig. 1.1**), also known as the Magnetitic-Zinciferous belt (Goinhas, 1971; Oliveira, 1986), is perhaps one of the most complex metallogenic belts in the Portuguese OMZ. This belt comprises ore deposits formed in distinct geotectonic settings, and therefore the mechanisms behind ore source and deposition are controlled by "time" and "space" complex relations.

The metallogenic settings of the different ore deposits drive a fertile debate on the geological models that best fit their formation. Although this belt has been the target of much research by both academia and industry there is a general lack of recent work focusing on the definition of mineral exploration vectors based on the identification of geochemical proxies.

The MFMB is one of the most attractive for mineral exploration in the Portuguese side of OMZ, with several ore deposits and commodities identified, and in some cases exploited during the 20th century. The mine scale was small, in face of current supply and demand, and most of these deposits were intermittently mined until their economic viability ceased. Zn-Pb deposits are found in this belt, with examples of mining activity found at the Vila Ruiva and Preguiça deposits (Mateus et al., 2013) and a recognised potential for future mineral exploration at the Enfermarias prospect (Barroso et al., 2003; Martins et al., 2003).

However, the main mining activity in the Montemor-o-Novo – Ficalho belt was focused on the ubiquitous iron deposits, which display multiple metallogenic settings with a large time span for the ore genesis, ranging from the Cambrian in the case of the Montemor-o-Novo Iron Complex (MIC) to Devonian-Carboniferous ages in the case of the Alvito, Azenhas, and Orada deposits. The extent in which these deposits have formed indicates a large range of geological conditions that prevail during the ore deposition, and therefore different geological models are considered.

The Montemor-o-Novo Iron deposits (Andrade et al., 1949) have been recently studied (Salgueiro, 2011; Salgueiro et al., 2012). Recent ores shown that magnetite ores are hosted in Cambrian carbonates (Monfurado Formation; Chichorro, 2006) comprising evidence of rift-related volcanism (Sanchez-García et al., 2019) with metamorphosed rhyolite-rhyodacite rocks. Such geological settings have led the authors to suggest a VMS-SEDEX continuum model for their genesis. Such geological models imply that ore deposition occurred in a marine environment and that iron was introduced into the system by hydrothermal-venting systems associated with volcanism. These deposits are hosted in a deformation corridor with evidence for intense deformation and metamorphism (including high-pressure Moita et al., 2005; Pedro et al., 2013) promoted during the Variscan Orogeny. Such conditions presumably resulted in extensive epigenetic modifications (metamorphism and metasomatism) which might have imposed an overprinting of any primary textures of the iron ores at the MIC deposits. Due to

such complex settings, that suggest that other commodities could be associated to these deposits, the MIC deposits were selected as a case study for this PhD project. Further considerations on their genesis are given in the following chapters of this thesis.

The Alvito deposit corresponds to a Fe-skarn deposit located near the Alvito municipality which was mined during the 20th century. The genesis of this deposit is associated with the emplacement of a gabbro-dioritic complex (Cuba-Alvito Gabbro-Dioritic Complex) intruding a Cambrian carbonate sequence, that promoted the development of an exoskarn (Gomes and Fonseca, 2006; Gomes et al., 2004) and deposition of the iron ores. The plutonic rocks associated to the formation of this deposit belong to the Beja Igneous Complex (BIC), where the development of Ni-(Cu) ores associated to the layered gabbroic sequence was found (Jesus et al., 2020). The Alvito deposit lacked a thorough ore assemblage study that could favour future mineral exploration; hence this was one of the selected areas for this PhD project.

The Azenhas-Orada deposits correspond to three presumably independent orebodies, located near the Pedrogão village at the eastern and western margin of the Guadiana River. These deposits were exploited during the 20th century, with the Orada mine having prevailed until the 70´s. The iron ores are found hosted in intensely metasomatized amphibolite units, which are part of the Moura Phyllonitic Complex (e.g. Araújo et al., 2005; Araújo et al., 2013; Roseiro et al., 2019). These units correspond to an parauthochthonous volcano-sedimentary unit which is considered as an accretionary prism that was formed by the obduction of units with oceanic affinity during the Variscan Orogeny. The genesis of the orebodies is attributed to the imbrication of the amphibolite units over Cambrian carbonate rocks (Mateus et al., 2005; Salgueiro et al., 2010), promoted by Variscan overthrusts associated with the collisional stages of the orogeny. Such imbrication presumably set favourable conditions for the formation of a reaction skarn and deposition of the iron ores within the metasomatized amphibolite units. Due to this complex geologic and metallogenic setting attributed to the Azenhas-Orada deposits it was believed that it would favour from a more thorough study of the ore assemblages, allying the micro-scale geochemical techniques with the detailed cartography of the area.

Although the focus of this PhD project was mainly driven to the classification and geochemical characterisation of the iron deposits from the Montemor-o-Novo – Ficalho metallogenic belt in an attempt to improve the geological models applied to each deposit, and consequently contributing to future mineral exploration, the genesis of the gold deposits from the Escoural gold district was also one of the case studies selected.

The Escoural gold district corresponds to a set of gold deposits and occurrences hosted in the Montemor-o-Novo Shear Zone, curiously located in the vicinity of the iron deposits from the MIC (**Fig. 1.2**), with one of the gold deposits (Monfurado deposit) occupying the same area

as one of the ancient iron mines (Monges deposit). The Escoural gold district has been the target for several exploration campaigns during recent years, with several drillings done in the area. Through the partnership between COLT Resources Inc., the last exploration rights owner in the area, and the project "ZOM-3D Metallogenic Modelling of Ossa-Morena Zone: Valorisation of the Alentejo Mineral Resources" from the University of Évora it was possible to perform a thorough sampling of six drill cores performed in the Monfurado gold deposit. This gold prospect was selected due to the close association between the gold mineralisation and the iron ores. Although the lithostratigraphy of the Montemor-o-Novo Shear Zone is particularly well studied (Chichorro, 2006; Chichorro et al., 2008; Pereira et al., 2003; 2006; 2007; 2012; 2015), the identification of the processes behind gold transport and deposition, with characterisation of gold source and detailed ore assemblage description needed to be further investigated. The deposits from the Escoural gold district have been classified as Orogenic Gold Deposits (Inverno, 2001), based mainly on the lithological and structural controls on the mineralisation, which at the face of current knowledge (e.g. Goldfarb and Groves, 2015; Groves et al., 2019; Groves et al., 2020) lack important information. Nevertheless, previous works have characterised some of the deposits from the Escoural gold district, with the identification of geochemical anomalies and modelling of the deposits in order to improve the models applied to the exploration targets (e.g. Ribeiro et al., 1993; Reis et al., 2003; Matias et al., 2015). More recently the characterisation of gold particles collected in alluvial deposits (e.g. Chapman et al., 2021; 2022) associated with the main deposits of the Escoural gold district (Chaminé, Casas Novas, and Braços; **Fig. 1.2.**) has provided preliminary results (Elias et al., 2021) that suggest that this methodology can be used as a mineral exploration guideline, and should be further explored.

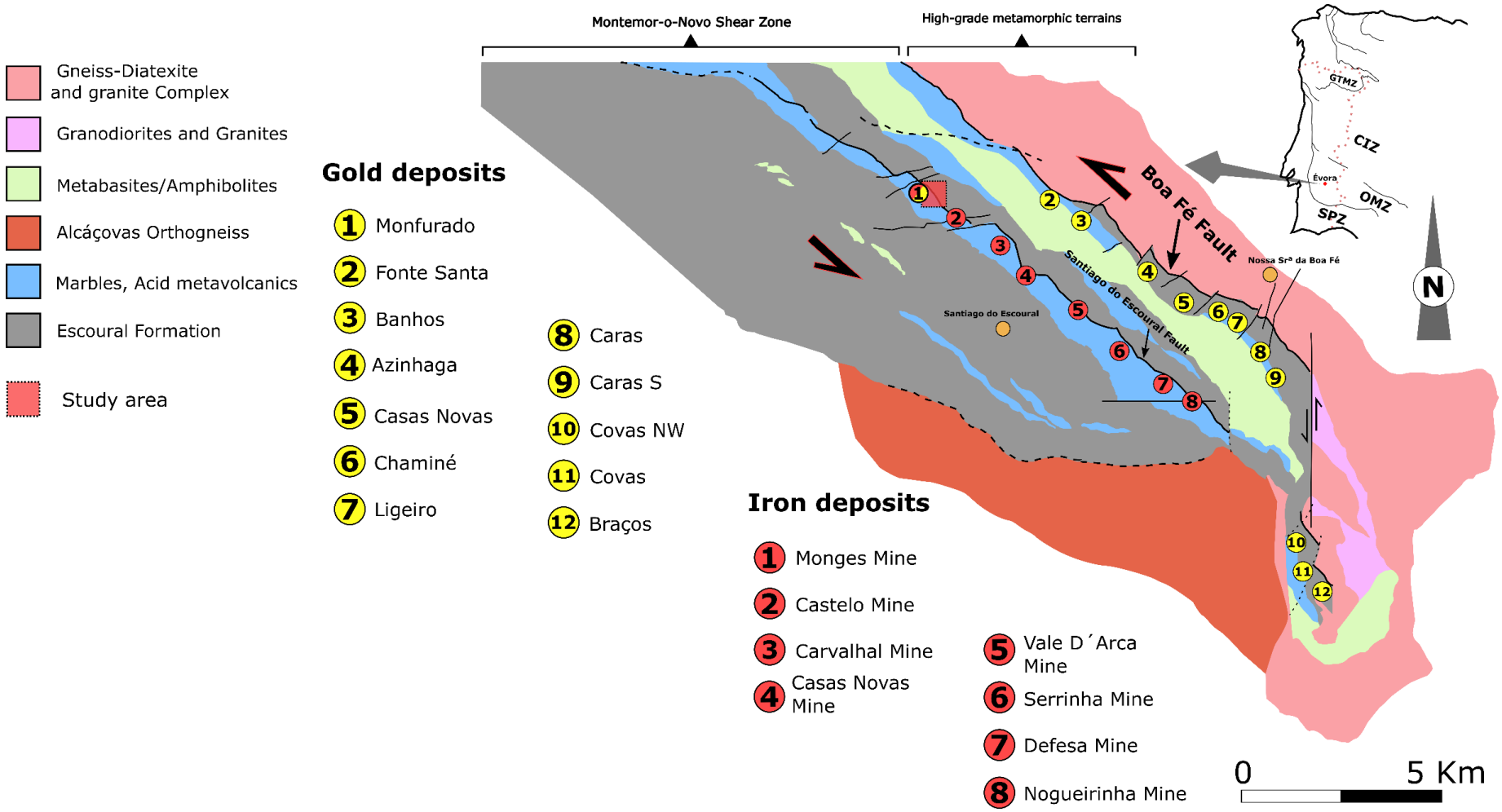

Figure 1.2 (a) Contextualization of the study area within the Ossa-Morena Zone and the Iberian Massif. **(b)** Simplified geological map of the Évora Massif terrains (adapted after Pereira et al 2003, 2015; Moita et al 2009). **(c)** Geological map of the Santiago do Escoural area and Montemor-o-Novo iron mining district (Andrade et al 1949), with delimitation of the mining areas (grey dashed rectangles). The map results from the reinterpretation and adaptation from seven Geological-Mining Maps at the scale 1: 5000 (nº0/-126; nº0/-124; nº-2/-122; nº-2/-124; nº-4/-122; nº-6/-120; nº-6/-122 - Serviço de Fomento Mineiro 1960) and from previous geological mapping works (Silva et al 1988; Chichorro 2006).

1.3 The importance of mineral chemistry as a mineral exploration tool

The current technological and industrial demand for raw material has made exploration and mining companies race for the discover of the next “needle in the haystack”. To accomplish the discovery of new ore deposits, or to increase the areas of currently known ones, the application of a wide range of analytical techniques is necessary. Such approach can contribute with results for the robust classification of ore deposits, contributing to obtain precise geological models that can be directly applied to mineral exploration.

Several factors are currently important limitations for the success of most mineral exploration projects, such as the ore grades and tonnage of a deposit and the social licence to operate (e.g. Mateus and Martins, 2021; Lesser et al., 2021). The social license to operate strongly depends on public opinion regarding the exploration and mining activities, which is highly influenced by the negative impacts of mining industry, particularly in the past. Public opinion is often contaminated by misinformation regarding a particular exploration or mining projects, but nonetheless part of the problem is within the industry and the geological community, which should also focus on information and the dissemination of geological themes that contribute to the scientific literacy. This topic is one of the mottos for Chapter 2, where the proposal of strategies for the valorisation of mining heritage are presented.

Ore grade is a limitation that is not in our hands, since it is a limitation that external fac tors cannot control by external factors, and every mining project stresses extending the activity, focusing in identifying new exploration targets. The fact that high-tonnage low-grade deposits are increasingly harder to find, since the discovery of new near-surface in-land deposits are decreasing over the last decades (e.g. Dan Wood and Hedenquist, 2019; Davies et al., 2021) forces the industry and exploration geologists to adapt and adopt new strategies. Many mineral exploration projects also face limited budgets, which oblige the exploration geologists to make the most with the available information (e.g., drill cores, geochemistry, structure etc.) and to have a professional profile with multidisciplinary skills that can face these challenges.

To contribute to successful mineral exploration, industry and academia have been long working together. Academia provides the opportunity to apply advanced analytical techniques that would otherwise be inaccessible to industry, and industry provide the access to e.g., drill cores, geochemistry results, and cartography which are key for the understanding of any ore system. In recent years, mineral chemistry has proved to be an important ally for mineral exploration, with the application of high-sensitive in-situ mineral analysis for the quantification of rare trace elements within. Mineral and host-rock geochemistry also contributes to the identification of the ore-forming processes; the most likely deposition horizons; identification

of geochemical proxies that can used to target orebodies; and for the early classification of ore deposits which contribute to the application of more robust mineral exploration models.

Mineral chemistry analysis by high-sensitive methods (e.g. LA-ICP-MS) is being widely applied as an approach to constrain the ore-forming processes and in defining geochemical criteria that can be applied to mineral exploration. This approach has been applied in different types of ore deposits, such as Iron-Oxide-Copper and Gold (IOCG) deposits (Tiddy et al., 2021), gold deposits (Pereira et al., 2019; Sciuba et al., 2021), Porphyry deposits (Cooke et al., 2020), and other magmatic-hydrothermal deposits (e.g. Codeço et al., 2021). Over the last decade trace element analysis of pyrite (e.g. Large et al., 2014; Nie et al., 2021; Zhai et al., 2021; Zhao et al., 2021) and magnetite (e.g. Nadoll et al., 2015; Huang et al., 2016; Wang et al., 2020; Peng et al., 2021), ubiquitous to most deposit types, have proved to provide excellent geochemical proxies to distinguish between ore deposit types and between barren and mineralised domains. Allying the trace element analysis of these minerals with isotope analysis ($\delta^{18}O$; $\delta^{34}S$; Pb) is a powerful method to identify ore sources and unveil the conduits of ore transport and the mechanisms behind its deposition (e.g. Madinabeitia et al., 2021)

Furthermore, the data mining of large geochemical datasets and the application of machine learning algorithms are being increasingly used and have proven successful in classifying ore deposits and in identifying lithological guide horizons for mineral exploration (e.g. Gregory et al., 2019; Luz et al., 2021; Nathwani et al., 2021).

It becomes clear that the research approach applied in the study of the ore deposits from the Ossa-Morena Zone should contemplate the myriad of geochemical approaches that proved useful to constrain the conditions of ore deposits formation and in identifying the extent of the ore endowments in other geologic and metallogenic settings.

1.3.1 Constraining the ore forming processes through magnetite geochemistry

The trace element analysis of magnetite for the characterisation of iron ores was one of the main objectives of this PhD thesis. Trace element analysis of magnetite has evolved alongside the evolution of the methods of in-situ analysis, from EPMA to LA-ICP-MS and the development of certified reference materials suitable for this kind of analysis (Nadol and Koenig, 2011).

Dupuis and Beoudoin (2011) have recently provided insights for trace element analysis of magnetite, with a work that has set the stage for many scientific articles on the scope of using trace element composition of magnetite for the classification of mineral deposits. These authors presented a thorough revision on magnetite composition from different metallogenic settings, identifying the chemical compositions indicative of a particular type of deposit. Latter

works by Dare et al. (2014), Nadoll et al. (2014; 2015), Knipping et al (2015), and others, have provided a solid basis for the identification of the chemical and physical conditions, such as temperature and oxygen fugacity, at the time of ore deposition. The characterisation of magnetite textures has proved to be a crucial factor for the interpretation of LA-ICP-MS and EPMA trace element data of magnetite (Hu et al., 2014; Huang et al., 2019; Huang and Beaudoin, 2021). The results from the chemical analysis of minerals usually result in large datasets, which are difficult to interpret by only using the most conventional statistical approach, whereas data mining methodologies have been proposed for the data treatment of magnetite trace element data (e.g. Makvandi et al., 2016a; 2016b; Hong et al., 2021). Many of these works have provided the literature support for the work presented in the following chapters of this PhD thesis, where the advantages and contingencies associated to each method are evaluated.

1.4 Research approach and main objectives

The research approach adopted during this PhD thesis was meticulously designed so that most of the objectives could be successfully achieved within the timeframe initially proposed. The identification of the most suitable methodologies was gathered from a thorough literature review, fruitful discussions, and research guidelines provided by the advisory team from this PhD thesis. Therefore, the following research steps were sequentially performed:

- Selection of the study areas for this PhD project and literature revision of previous works.
- Selection of methods and materials for the study of the selected ore deposits.
- Drill core and outcrop sampling campaigns.
- Detailed cartography of the outcrops and open-pit areas of the selected deposits.
- Sample preparation (thin sections; double polished thick sections for fluid inclusion studies; whole rock polished sections; milled samples for whole-rock geochemistry and x-ray diffraction; mineral separates for isotope analysis).
- Detailed host-rock and ore petrography
- Fluid inclusion petrography and microthermometry
- SEM-EDS analysis of the ore assemblages
- EPMA analysis at the University of Oviedo (two weeks laboratory visit).
- LA-ICP-MS analysis of the selected magnetite cross-sections, representative of the studied ore deposits.
- Data analysis (data mining/machine learning), interpretation and discussion.

- Article writing and thesis preparation.

With the presented research approach the main specific objectives of this PhD thesis were i) characterisation of the gold mineralisation styles in the Monfurado gold prospect and identification of the mechanisms responsible for gold transport and deposition; ii) provide useful vectors for future gold exploration in the Escoural gold district; iii) characterise the textures and chemistry of the iron ores from the deposits of the Montemor-o-Novo Iron Complex (Monges, Vale da Arca, and Serrinha mines), Alvito, Azenhas and Orada; iv) provide the first stable isotope analysis of sulfides and magnetite from the orogenic gold and iron deposits of OMZ; v) provide the first LA-ICP-MS analysis of magnetite for the classification of ore deposits in OMZ; vi) validate or refute the previous geological models attributed to the selected deposits, providing suitable alternative proposals when adequate; vii) provide suitable geological models for the iron deposits of Ossa-Morena Zone that can contribute for more robust mineral exploration models; viii) provide machine learning approaches for the classification of ore deposits; and ix) contribute to the geological literacy and valorisation of the mineral resources of Alentejo.

Chapter References

Andrade, A., Silva, J.M., Arruda, C.R, and Gameiro, J.C.S., 1949. Minas de Ferro de Montemor-o-Novo. Serviço de Fomento Mineiro, v. 15, p. 125.

Apalategui, O., Eguiluz, L., and Quesada, C., 1990. Ossa-Morena Zone: Structure. In: Martinez E and Dallmeyer RD (Eds.) Pre-Mesozoic Geology of Iberia, Springer Verlag, p. 280-291.

Araújo, A., Fonseca, P., Munhá, J., Moita, P., Pedro, J., Ribeiro, A., 2005. The Moura Phyllonitic Complex: An Accretionary Complex related with obduction in the Southern Iberia Variscan Suture. Geodinamica Acta, v.18(5), 375-388. https://doi.org/10.3166/ga.18.375-388

Araújo, A., Piçarra de Almeida, J., Borrego, J. Pedro, J. and Oliveira, T., 2013. As regiões central e sul da Zona de Ossa-Morena. In: Dias R, Araújo A, Terrinha P, Kullberg JC (Eds), Geologia de Portugal, Volume 1, Escolar Editora, pp 509-549.

Barroso, M., Mateus, A., Figueiras, J., Martins, R., Oliveira, V., 2003. Mineralogy and geochemical characteristics of different superimposed mineralisations at the Enfermarias prospect (Moura, Portugal). VI Congresso Nacional de Geologia, Lisboa (Portugal), Ciências da Terra (UNL), Lisboa, n.º esp. V, CD-ROM, F9-F12.

Chapman, R.J., Banks, D.A., Styles, M.T., Walshaw, M.T., Piazolo, S., Morgan, D.J., Grimshaw, M.R., Spence-Jones, C.P., Matthews, T.J., Borovinskaya, O., 2021. Chemical and physical heterogeneity within native gold: implications for the design of gold particle studies. Mineralium Deposita, v.56, pp. 1563-1588. https://doi.org/10.1007/s00126-020-01036-x

Chapman, R.J., Mortensen, J.K., Allan, M.M., Walshaw, R.D., Bond, J., and MacWilliam, K., 2022. A New Approach to Characterizing Deposit Type Using Mineral Inclusion Assemblages in Gold Particles. Economic Geology, v. 117(2), p. 361-381. https://doi.org/10.5382/econgeo.4863

Chichorro, M., 2006. A evolução tectónica da Zona de Cisalhamento de Montemor-o-Novo (Sudoeste da Zona de Ossa-Morena – Área de Santiago do Escoural – Cabrela). PhD Thesis, University of Évora, p.569, (in Portuguese with English abstract).

Chichorro, M., Pereira, M.F., Díaz-Azpiroz, M., Williams, I.S., Fernández, C., Pin, C., and Silva, J.B., 2008. Cambrian ensialic rift-related magmatism in the Ossa-Morena Zone (Évora–Aracena metamorphic belt, SW Iberian Massif): Sm–Nd isotopes and SHRIMP zircon U–Th–Pb geochronology. Tectonophysics, v. 461, p. 91-113. https://doi.org/10.1016/j.tecto.2008.01.008

Codeço, M.S., Weis, P., Trumbull, R.B., Hinsberg, V.H., Pinto, F., Lecumberri-Sanchez, P., and Schleicher, A.M., 2021. The imprint of hydrothermal fluids on trace-element contents in white mica and tourmaline from the Panasqueira W–Sn–Cu deposit, Portugal. Mineralium Deposita, v. 56, p. 481-508. https://doi.org/10.1007/s00126-020-00984-8

Cooke, D.R., Wilkinson, J.J., Baker, M., Agnew, P., Phillips, J., Chang, Z., Chen, H., Wilkinson, C.C., Inglis, S., Hollings, P., Zhang, L., Gemmell, J.B., White, N.C., Danyushevsky, L., and Martin, H., 2020. Using Mineral Chemistry to Aid Exploration: A Case Study from the Resolution Porphyry Cu-Mo Deposit, Arizona. Economic Geology, v. 115, p. 813-840. https://doi.org/10.5382/econgeo.4735

Dan Wood, A.O., and Hedenquist, J., 2019. Mineral Exploration: Discovering and Defining Ore Deposits. SEG Discovery, v. 116, p. 1-22. https://doi.org/10.5382/Geo-and-Mining-02

Dare, S.A.S., Barnes, S.-J., Beaudoin, G., Méric, J., Boutroy, E., and Potvin-Doucet, C., 2014. Trace elements in magnetite as petrogenetic indicators. Mineralium Deposita, v.49, pp. 785-796. https://doi.org/10.1007/s00126-014-0529-0

Davies, R.S., Davies, M.J., Groves, D., Davids, K., Brymer, E., Trench, A., Sykes, J.P., and Dentith, M., 2021. Learning and Expertise in Mineral Exploration Decision-Making: An Ecological Dynamics Perspective. International Journal of Environmental Research and Public Health, v. 18, 9752. https://doi.org/10.3390/ijerph18189752

Dupuis, C., and Beaudoin, G., 2011. Discriminant diagrams for iron oxide trace element fingerprinting of mineral deposit types. Mineralium Deposita, v. 46, pp. 319-335. https://doi.org/10.1007/s00126-011-0334-y

Elias, M., Tereso, V., Maia, M., Nogueira, P., 2021. Técnicas de prospeção aplicadas às mineralizações de ouro de Santiago do Escoural (Montemor-o-Novo): Caracterização de partículas de ouro enquanto indicadores de potenciais áreas de prospeção mineral. Unpublished Report, University of Évora, 25 pp. DOI: 10.13140/RG.2.2.16060.36482

Farias, P., Gallastegui, G., González Lodeiro, F., Marquínez, J., Martin Parra, L., Martínez Catalán, J., Paolo Macia, J., and Rodriguez Fernandez, L., 1987. Aportaciones al conocimiento de la litoestratigrafia y estrutura de Galiza Central. Memória, Fac. Ciênc. Univ. Porto 1, 411-431.

Fonseca, P., Ribeiro, A., 1993. The tectonics of Beja-Acebuches Ophiolite: A major suture in the Iberian Variscan Fold Belt. Geol. Rundsch., v. 3, p. 440 – 447.

García de Madinabeitia, S., Ibarguchi, J.I.G., and Zalduegui, J.F.S., 2021. IBERLID: A lead isotope database and tool for metal provenance and ore deposits research. Ore Geology Reviews, v. 137, 104279. https://doi.org/10.1016/j.oregeorev.2021.104279

Goinhas, J.A.C., 1971. Estudo geológico-económico preliminar dos jazigos de Zn/Pb da regiào de Portel (B. Alentejo Portugal) I Congreso Hispano-Luso-Americano de Geología Económica. Madrid-Lisboa, sec. 4, t. II. p. 621 -642.

Goldfarb, R.J., and Groves, D.I., 2015. Orogenic gold: common or evolving fluid and metal sources through time. Lithos 233, 2–26. https://doi.org/10.1016/j.lithos.2015.07.011

Gomes, E.M.C.G., Gama Pereira, L.C., and Pinto, A.F., 2004. Nódulos calcossilicatados zonados em mármores da região de Alvito, Alentejo (Sul de Portugal). Caderno Laboratório Xeolóxico de Laxe, v. 29, p. 171-185.

Gomes, E.M.C., and Fonseca, P.E., 2006. Eventos metamórfico/metassomáticos tardi-variscos na região de Alvito (Alentejo, sul de Portugal). Cadernos Xeológicos de Laxe, v.31, p. 67-85. ISSN: 0213 – 4497

Gregory, D.D., Cracknell, M.J., Large, R.R., McGoldrick, P., Kunh, S., Maslennikov, V.V., Baker, M.J., Fox, N., Belousov, I., Figueroa, M.C., Steadman, J.A., Fabris, A.J., and Lyons, T.W., 2019. Distinguishing Ore Deposit Type and Barren Sedimentary Pyrite Using Laser Ablation-Inductively Coupled Plasma-Mass Spectrometry Trace Element Data and Statistical Analysis of Large Data Sets. Economic Geology, v. 114(4), p. 771-786. https://doi.org/10.5382/econgeo.4654

Groves, D.I., Santosh, M., Deng, J., Wang, Q., Yang, L., and Zhang, L., 2019. A holistic model for the origin of orogenic gold deposits and its implications for exploration. Mineralium Deposita, v. 55, p. 275-292. https://doi.org/10.1007/s00126-019-00877-5

Groves, D.I., Santosh, M., and Zhang, L., 2020. A scale-integrated exploration model for orogenic gold deposits based on a mineral system approach. Geoscience Frontiers, v.11, p. 719-738. https://doi.org/10.1016/j.gsf.2019.12.007

Hu, H., Li, J.-W., Lentz, D., Ren, Z., Zhao, X.-F., Deng, X.-D., and Hall D., 2014. Dissolution–reprecipitation process of magnetite from the Chengchao iron deposit: Insights into ore genesis and implication for in-situ chemical analysis of magnetite. Ore Geology Reviews, v. 57, p. 393-405. http://dx.doi.org/10.1016/j.oregeorev.2013.07.008

Huang, X.-W., Gao, J.-F., Qi, L., Meng, Y.-M., Wang, Y.-C., and Dai, Z.-H., 2016. In-situ LA–ICP–MS trace elements analysis of magnetite: The Fenghuangshan Cu–Fe–Au deposit, Tongling, Eastern China. Ore Geology Reviews, v. 72, p. 746-759. http://dx.doi.org/10.1016/j.oregeorev.2015.09.012

Huang, X.-W., and Beaudoin, G., 2019. Textures and chemical and compositions of magnetite from Iron Oxide Copper-Gold (IOCG) and Kiruna-type Iron Oxide Apatite (IOA) deposits and their implications for ore genesis and magnetite classification schemes. Economic Geology, v.114, p. 953-979. https://doi.org/10.5382/econgeo.4651

Huang, X.-W., Sappin, A.-A., Boutroy, É., Beaudoin, G., and Makvandi, S., 2019. Trace element composition of igneous and hydrothermal magnetite from porphyry deposits: Relationship to deposit subtypes and magmatic affinity. Economic Geology, v.114(5), p. 917-952. https://doi.org/10.5382/econgeo.4648

Hong, S., Zuo, R., Juang, X., and Xiong, Y., 2021. Distinguishing IOCG and IOA deposits via random forest algorithm based on magnetite composition. Journal of Geochemical Exploration, v. 230, 106859. https://doi.org/10.1016/j.gexplo.2021.106859

Inverno, C.M.C., 2001. Comparison between orogenic (or mesothermal) gold deposits and intrusion-related gold deposits. Some extrapolation to Portugal. Cadernos Lab. Xeolóxico de Laxe, v.36, p.99-156 (in Portuguese with English abstract).

Jesus, A.P., Mateus, A., Benoit, M., Tassinari, C.C.G., and Bento dos Santos, T., 2020. The timing of sulfide segregation in a Variscan synorogenic gabbroic layered intrusion (Beja, Portugal): Implications for Ni-Cu-PGE exploration in orogenic settings. Ore Geology Reviews, v.126, 103767. https://doi.org/10.1016/j.oregeorev.2020.103767

Julivert, M., Fontboté, J.M., Ribeiro, A., and Nabais Conde, L.E., 1972. Mapa Tectónico de la Península Ibérica y Baleares. Scale 1:1.000.000. IGME.

Knipping, J.L., Bilenker, L.D., Simon, A.C., Reich, M., Barra, F., Deditius, A.P., Wälle, M., Heinrich, C.A., Holtz, F., and Munizaga, R., 2015. Trace elements in magnetite from massive iron oxide-apatite deposits indicate a combined formation by igneous and magmatic-hydrothermal processes. Geochimica et Cosmochimica Acta, v.171, pp. 15-38. http://dx.doi.org/10.1016/j.gca.2015.08.010

Large, R.R., Halpin, J.A., Danyushevsky, L.V., Maslennikov, V.V., Bull, S.W., Long, J.A., Gregory, D.D., Lounejeva, E., Lyons, T.W., Sack, P.J., McGoldrick, P.J., and Calver, C.R., 2014. Trace element content of sedimentary

pyrite as a new proxy for deep-time ocean–atmosphere evolution. Earth and Planetary Science Letters, v. 389, p. 209-220. http://dx.doi.org/10.1016/j.epsl.2013.12.020

Lesser, P., Gugerell, K., Poelzer, G., Hitch, M., and Tost, M., 2021. European mining and the social license to operate. The Extractive Industries and Society, v.8, 100787. https://doi.org/10.1016/j.exis.2020.07.021

Luz, F., Mateus, A., Ferreira, E., Tassinari, C.G., and Figueira, J., 2022. Pb-Nd-Sr Isotope Geochemistry of Metapelites from the Iberian Pyrite Belt and Its Relevance to Provenance Analysis and Mineral Exploration Surveys. Economic Geology, v. 117(2), p. 423-454. https://doi.org/10.5382/econgeo.4869

Makvandi, S., Ghasemzadeh-Barvarz, M., Beaudoin, G., Grunsky, E.C., McClenaghan, M.B., and Duchesne, C., 2016a. Principal component analysis of magnetite composition from volcanogenic massive sulfide deposits: Case studies from the Izok Lake (Nunavut, Canada) and Halfmile Lake (New Brunswick, Canada) deposits. Ore Geology Reviews, v. 72, p. 60-85. http://dx.doi.org/10.1016/j.oregeorev.2015.06.023

Makvandi, S., Ghasemzadeh-Barvarz, M., Beaudoin, G., Grunsky, E.C., McClenaghan, M.B., Duchesne, C., and Boutroy, E.C., 2016b. Partial least squares-discriminant analysis of trace element compositions of magnetite from various VMS deposit subtypes: Application to mineral exploration. Ore Geology Reviews, v.78, p. 388-408. http://dx.doi.org/10.1016/j.oregeorev.2016.04.014

Martins, R., Mateus, A., Figueiras, J., Barroso, M., Oliveira, V. 2003. Post-metamorphic evolution of the Lower Cambrian section at Enfermarias (Moura, Portugal): its record and metallogenic implications. VI Congresso Nacional de Geologia, Lisboa (Portugal), Ciências da Terra (UNL), Lisboa, n.º esp. V, CD-ROM, B60-B63.

Mateus, A., Araújo, A., Gonçalves, M.A., and Matos, J., 2005. Variscan overthrusting, fluid flow and genesis of magnetite ore-bodies at the Azenhas area (Pedrógão, Ossa-Morena Zona, SE Portugal). Boletín Geológico y Minero, v.116(1), p. 3-22. ISSN 0366-0176.

Mateus, A., Munhá, J., Inverno, C., Matos, J.X., Martins, L., Oliveira, D., Jesus, A., and Salgueiro, R., 2013. Mineralizações no sector português da Zona de Ossa-Morena. In R. Dias, A. Araújo, P. Terrinha, J.C. Kullberg (Eds.), Geologia de Portugal, v. 1, p. 577-619. Lisboa: Escolar Editora.

Mateus, A., and Martins, L., 2021. Building a mineral-based value chain in Europe: the balance between social acceptance and secure supply. Mineral Economics, v. 34, p. 239-261. https://doi.org/10.1007/s13563-020-00242-3

Matias, F.V., Almeida, J.A., and Chichorro, M., 2015. A Multistep Methodology for Building a Stochastic Model of Gold Grades in the Disseminated and Complex Deposit of Casas Novas in Alentejo, Southern Portugal. Resource Geology, v. 65(4), p. 361-374. https://doi.org/10.1111/rge.12077

Moita, P., Munhá, J., Fonseca, P., Pedro, J., Tassinari, C., Araújo, A., Palácios, T., 2005a. Phase equilibria and geochronology of Ossa Morena eclogites. Actas do XIV Semana de Gequímica//VIII Congresso de geoquímica dos Países de Língua Portuguesa, vol. 2, 463-466.

Nadoll, P., and Koenig, A.E., 2011. LA-ICP-MS of magnetite: methods and reference materials. Journal of Analytical Atomic Spectrometry, v. 26, pp. 1872-1877. https://doi.org/10.1039/c1ja10105f

Nadoll, P., Angerer, T., Mauk, J.L., French, D., and Walshe, J., 2014. The chemistry of hydrothermal magnetite: A review. Ore Geology Reviews, v. 61, pp. 1-32. http://dx.doi.org/10.1016/j.oregeorev.2013.12.013

Nadoll, P., Mauk, J.L., Leveille, R.A., and Koenig, A.E., 2015. Geochemistry of magnetite from porphyry Cu and skarn deposits in the southwestern United States. Mineralium Deposita, v. 50, p. 493-515. https://doi.org/10.1007/s00126-014-0539-y

Nathwani, C.L., Wilkinson, J.J., Fry, G., Armstrong, R.N., Smith, D.J., and Ihlenfeld, C., 2022. Machine learning for geochemical exploration: classifying metallogenic fertility in arc magmas and insights into porphyry copper deposit formation. Mineralium Deposita. https://doi.org/10.1007/s00126-021-01086-9

Nie, L., Zhou, T., White, N., Zhang, L., Olin, and Meffre, S., 2021. Textures, trace elements and Pb isotopes of pyrite from the Donggushan tungsten polymetallic deposit, eastern China: Deciphering the source of a skarn tungsten polymetallic deposit. Ore Geology Reviews, v. 133, 104077. https://doi.org/10.1016/j.oregeorev.2021.104077

Oliveira, J.T., Oliveira, V., and Piçarra, J.M., 1991. Traços gerais da evolução tectono-estratigráfica da Zona de Ossa Morena, em Portugal: síntese crítica do estado actual dos conhecimentos. Comum. Serv. Geol, Port., v.77, p.3-26.

Oliveira, V.M.J., 1986. Prospeção de minérios metálicos a Sul do Tejo. Geociências – Aveiro, v.1, p.15-22.

Pedro, J., Araújo, A., Fonseca, P., Munhá, J., Ribeiro, A., and Mateus, A., 2013. Cinturas Ofiolíticas e Metamorfismo de Alta Pressão no Bordo SW da Zona de Ossa-Morena. In: Dias R, Araújo A, Terrinha P, Kullberg JC (Eds), Geologia de Portugal, Volume 1, Escolar Editora, p. 641-665.

Peng, H.-J, Hou, L., Sun, C., Zou, H., Wang, T.-R, and Ma, Z.-Z., 2021. Geochemistry of magnetite from the Hongniu–Hongshan Cu skarn deposit in Yunnan Province, SW China. Ore Geology Reviews, v.134, 104237. https://doi.org/10.1016/j.oregeorev.2021.104237

Pereira, I., Storey, C., Darling, J., Lana, C., and Alkmim, A.R., 2019. Two billion years of evolution enclosed in hydrothermal rutile: Recycling of the São Francisco Craton Crust and constraints on gold remobilisation processes. Gondwana Research, v. 68, p. 69-92. https://doi.org/10.1016/j.gr.2018.11.008

Pereira, M.F., Silva, J.B., and Chichorro, M., 2003. Internal Structure of the Évora High-grade Terrains and the Montemor-o-Novo Shear Zone (Ossa-Morena Zone, Portugal), Geogaceta, v.33, p. 79-82.

Pereira, M. F., Chichorro, M., Linnemann, U., Eguiluz, L., and Silva, J. B., 2006. Inherited arc signature in Ediacaran and Early Cambrian basins of the Ossa-Morena zone (Iberian Massif, Portugal): paleogeographic link with European and North African Cadomian correlatives. Precambrian Research, v. 144(3-4), p. 297-315. https://doi.org/10.1016/j.precamres.2005.11.011

Pereira, M. F., Silva, J. B., Chichorro, M., Moita, P., Santos, J. F., Apraiz, A., and Ribeiro, C., 2007. Crustal growth and deformational processes in the northern Gondwana margin: Constraints from the Évora Massif (Ossa-Morena zone, southwest Iberia, Portugal). Special Paper 423: The Evolution of the Rheic Ocean: From Avalonian-Cadomian Active Margin to Alleghenian-Variscan Collision, p. 333–358. https://doi.org/10.1130/2007.2423(16).

Pereira, M.F., Solá, A.R., Chichorro, M., Lopes, L., Gerdes, A., and Silva, J.B., 2012. North-Gondwana assembly, break up and paleogeography: U–Pb isotope evidence from detrital and igneous zircons of Ediacaran and Cambrian rocks of SW Iberia. Gondwana Research, v.22(3-4), p. 866-881. https://doi.org/1016/j.gr.2012.02.010

Pereira, M.F., Chichorro, M., Moita, P., Santos, J.F., Solá, A.M.R., Williams, I.S., Silva, J.B., and Armstrong, R.A., 2015. The multistage crystallization of zircon in calc-alkaline granitoids: U–Pb age constraints on the timing of Variscan tectonic activity in SW Iberia. International Journal of Earth Sciences, v.104, p.1167-1183. https://doi.org/10.1007/s00531-015-1149-3

Quesada, C., Fonseca, P. E., Munhá, J., Oliveira, J. T., Ribeiro, A., 1994. The Beja-Acebuches Ophiolite (Southern Iberia Variscan fold belt): geological characterization and geodynamic significance. Boletín Geológico y Minero, v. 105(1), p. 3-49.

Reis, A.P., Sousa, A.J., and Cardoso Fonseca, E., 2003. Application of geostatistical methods in gold geochemical anomalies identification (Montemor-O-Novo, Portugal). Journal of Geochemical Exploration, v. 77, p. 45-63. https://doi.org/10.1016/S0375-6742(02)00269-8

Ribeiro, A., Munhá, J., Dias, R., Mateus, A., Pereira, E., Ribeiro, L., Fonseca, P., Araújo, A., Oliveira, O., Romão, J., Chaminé, H., Coke, C., and Pedro, J.C., 2007. Geodynamic evolution of the SW Europe Variscides. Tectonophysics, v.26, TC6009. https://doi.org/10.1029/2006TC002058

Ribeiro, C., Mateus, A., and Barriga, F., 1993. Gold mineralization of the Escoural area (Montemor, Évora, Portugal): a progress report. Comun. XII Reun. Geol. Oeste Penins., v.1, p.215-226.

Roseiro, J., Moreira, N., Fonseca, R., Araújo, A., Maia, M., Pedro, J., and Nogueira, P., 2019. Lithogeochemistry of metabasites from the Moura Phyllonitic Complex (Ossa Morena Zone, SW Portugal). EGU General Assembly 2019, Geophysical Research Abstracts.

Sánchez-García, T., Chichorro, M., Solá, A.R., Álvaro, J.J., Díez-Montes, A., Bellido, F., Ribeiro, M.L., Quesada, C., Lopes, J.C., Dias da Silva, Í., González-Clavijo, E., Gómez Barreiro, J., and López-Carmona, A., 2019. The Cambrian-Early Ordovician Rift Stage in the Gondwanan Units of the Iberian Massif. In: Quesada, C. & Oliveira J.T. (Eds) The Geology of Iberia: A Geodynamic Approach, Vol. 2: The Variscan Cycle. Springer Nature, Switzerland, p.27-74. https://doi.org/10.1007/978-3-030-10519-8

Salgueiro, R., 2011. Caracterização e génese das mineralizações de magnetite – sulfuretos em Monges (Santiago do Escoural, Montemor-o-Novo) e ensaio comparativo com as suas congéneres em Orada-Vale de Pães (Serpa-Vidigueira). PhD Thesis, Univ. Lisboa, 524 p., (in Portuguese with English abstract).

Salgueiro, R., Mateus, A., Inverno, C., 2010a. Caracterização e génese do skarn ferrífero de Orada (Zona de Ossa-Morena). E-Terra, v. 20(3).

Salgueiro, R., Mateus, A, and Inverno, C., 2012. Mineralizações de magnetite e sulfuretos de monges (Santiago do Escoural, Montemor-o-Novo), Vale de Pães (Cuba-Vidigueira) e Orada (Pedrógão, Serpa): Síntese de ensaio comparativo. Boletim de Minas, v. 47(1), p. 27-30.

Sciuba, M., and Beaudoin, G., 2021. Texture and Trace Element Composition of Rutile in Orogenic Gold Deposits. Economic Geology, v. 116, p. 1865-1892. https://doi.org/10.5382/econgeo.4857

Tiddy, C., Zivak, D., Hill, J., Giles, D., Hogkinson, J., Neumann, M., and Brotodewo, A., Monazite as an Exploration Tool for Iron Oxide-Copper-Gold Mineralisation in the Gawler Craton, South Australia. Minerals, v. 11, 809. https://doi.org/10.3390/min11080809

Tornos F., Inverno C.M.C., Casquet C., Mateus A., Ortiz G., and Oliveira V., 2004. The Metallogenic evolution of the Ossa-Morena Zone. J. Iber. Geol., v. 30, p. 143-181.

“To the scientific worker no subject is too vast for his research, no object so minute as to be unworthy of his most patient study”

Judd, 1888

Chapter 2

New insights on the Escoural Orogenic gold district (Ossa-Morena Zone, SW Iberia): Geochemistry, fluid inclusions and stable isotope constraints from the Monfurado gold prospect

Ore Geology Reviews, v. 142, Article Number 104736

https://doi.org/10.1016/j.oregeorev.2022.104736

Co-authors:

José Roseiro

Pedro Nogueira

Fernando Noronha

Mercedes Fuertes-Fuente

Antonia Cepedal

José Mirão

Abstract

The Escoural gold district belongs to the Montemor-Ficalho metallogenic belt which is part of the Portuguese section of Ossa-Morena Zone (OMZ), at the SW of Iberia. The Escoural gold district includes twelve gold prospects and/or deposits largely controlled by the NW-SE Montemor-o-Novo Shear Zone (MNSZ) and associated fault zones, extending for approximately 30 km. Ubiquitously, gold-arsenopyrite-loellingite assemblages hosted in quartz-sericite-chlorite veins are found in most deposits, although, in the Monfurado prospect, the gold-bearing assemblages are more complex. This prospect is located in the vicinity of a Cambrian SEDEX-VMS iron deposit, from which massive and disseminated iron-ores hosted in marbles and calcsilicate rocks, were exploited. The interplay of the gold mineralizing processes with the iron-rich host rocks has favored gold deposition at the Monfurado prospect. Selected samples from six drill cores allowed to define two mineralizing events: the pre-ore and ore stages. Two gold mineralization styles characterize the ore-stage: i) massive sulfide horizons in which gold (Au= 85.6 - 86.3 wt. %; Ag= 13.1 - 13.6 wt.%) is hosted in arsenopyrite and pyrite or, seldomly, gold particles (Au= 91.8 wt.%; Ag= 7.1 wt.%) found in an arsenopyrite-rich layer; and ii) quartz-chlorite-pyrite veins crosscutting acid metavolcanic rocks with rhyolite-rhyodacite affinities, in which gold (Au= 80.5 - 82.9 wt.%; Ag= 16.8 - 18.7 wt.%) is found as fracture filling in pyrite, sometimes accompanied by Bi-Te phases. Arsenopyrite geothermometer suggests that for type i the overall deposition temperature falls within the range of 188ºC to 372ºC. Type ii mineralization lacks arsenopyrite, and for this reason, thermodynamic constraints were gathered from fluid inclusions and chlorite geothermometer. CH_4-rich fluid inclusions are ubiquitous in transgranular fluid inclusion planes, suggesting that reduced fluids percolated the rocks that host type ii mineralization. The reduced fluids support the transport of gold in sulfide complexes, such as $AuHS^-$ and $Au(HS)^-_2$. Furthermore, secondary H_2O-NaCl fluid inclusions (Lw_2) were found, with mean salinities of 6.0 eq. w(NaCl) and mean homogenization temperature of 226ºC, with corresponding pressures of 3.0 MPa, thus suggesting late hydrostatic regimes. Chlorite geothermometer results are in the range of 229 ºC and 309 ºC, agreeing with the fluid inclusion homogenization temperatures for Lw_2 fluids.

Sulfur isotope ($\delta^{34}S$) analysis of representative sulfide phases collected from both mineralization types, revealed signatures ranging from 8.5 ‰ and 10.6 ‰, indicating a single sulfur source. The gathered results suggest that although fluid transport is structurally controlled by MNSZ activity, the sulfidation reactions promoted by fluid-rock interactions are the main control on gold deposition from type i mineralization. It is further

suggested that a coeval gold-event can lead to the deposition of two different types of mineralization, related to distinct gold deposition mechanisms.

The tectonic and geodynamic settings in which the Escoural gold district developed correlate it to worldwide Palaeozoic orogenic gold deposits, with the Monfurado prospect being an example of the complexity of such geological settings.

Keywords: Orogenic gold; vectoring gold exploration; Sulfide geochemistry; Fluid-rock interactions; SW Iberian Massif.

2.1 Introduction

The characterization of orogenic gold deposits and the identification of suitable vectoring tools to locate the most favorable locations for ore deposition, are challenging tasks for gold exploration projects. Their success depends on the significant understanding of the geodynamic and metallogenic settings that control the genesis of such deposits, as well as, clearly identifying the mineralization style. Such knowledge is highly reliable on the current accepted orogenic gold models but comparing such models to local field exploration data is extremely challenging and may sometimes lead to demotivating results.

The diverse ore-emplacement mechanisms described for this kind of deposit depends on factors such as time (geological age) and space (geological settings). Although, the collection of multidisciplinary data from orogenic gold deposits can ultimately allow the definition of successful exploration vectors.

We focus our research on developing an approach that can beneficiate gold exploration in SW Iberia, targeting the mechanisms behind gold transport and deposition, and the structural controls in the Escoural gold district.

The above-mentioned time and space dilemma generate prolific discussions and a fair amount of uncertainty regarding the conditions in which orogenic gold deposits form (Goldfarb and Groves, 2015; Wyman et al., 2016; and Gaboury, 2019). However, many physical and chemical conditions are shared by different orogenic gold deposits, such as the involvement of metamorphic fluids in gold transport, in relatively reduced conditions, and driven by regionally expressive crustal anisotropies. It is generally accepted that gold is transported in $AuHS^-$ and $Au(HS)^-_2$ complexes, and therefore sulfur activity in the system plays a major role in controlling the transport-deposition mechanisms (Lindgren, 1907, 1933; Goldfarb et al., 2005; Phillips and Powel, 2010; Goldfarb and Groves, 2015).

The separation of gold from the sulfur compounds can be promoted by the oxidation of the transporting fluid (Hodciewicz et al., 2008, LaFlamme et al., 2018a). Hence, comprehending the geochemical conditions that could trigger oxidation is of uttermost importance for understanding the mechanisms that lead to gold accumulation. Several authors have identified a fair amount of processes that contribute to the fluid oxidation, such as i) fluid mixing from different sources (Uemoto et al., 2002; Bateman and Hageman, 2004; Melfos et al., 2019); ii) cyclic fracturing causing pressure fluctuations in the fluid (Sibson et al., 1975; Hodciewicz et al., 2008; Peterson and Mavrogenes, 2014; Voisey et al. 2020); iii) fluid-rock interactions, such as, carbonation and sulfidation (Phillips, 1986; Phillips and Hughes, 1996; Palin and Xu 2000; Goldfarb et al., 2005;

Goldfarb and Groves, 2015; Petrella et al., 2020) or even iv) devolatilization by metamorphic fluids as discussed by Phillips and Powel, (2010).

Several gold deposits with genetic links to large shear zones are found throughout the Iberian Massif. Such deposits developed in the late stages of collisional event of the Variscan orogeny, in both orogenic and intrusion-related systems (e.g. Ribeiro et al., 1993; Noronha et al., 2000; Vallance et al., 2003; De Oliveira et al., 2007; Cepedal et al., 2013; 2018; Mortensen et al., 2014; Martinez-Abad et al., 2015; D´Angelico et al., 2016; Fuertes-Fuente et al., 2016; Rodríguez-Terente et al., 2018; MacKenzie et al., 2019; Neiva et al., 2019; Leal et al., 2022). In the north of Portugal, these deposits are found hosted in metasedimentary sequences (e.g. Tresminas or Valongo areas) and granitic units (e.g. the Penedono, Grovelas, or Castromil deposits), spatially associated with Variscan shear ductile-brittle structures. In such deposits the nature of the mineralizing hydrothermal solutions was identified as related with metamorphic fluids, displaying variable contribution of meteoric water to the system but without a recognizable input of magmatic fluids. Additionally, host rocks were identified as being the main source of metals and ligands to the mineralizing system, and the pronounced tectonism and associated structures, mostly shear zones and faults, served as pathways for fluid circulation (e.g. Noronha et al., 2000; Vallance et al., 2003; D´Angelico et al., 2016). Despite the extended time-space distribution, diverse metal sources, and the variety of ore-forming fluids, these deposits exhibit similarities, such as i) evidence of successive shearing with recurrent reactivation, ii) geodynamic settings that contributed to complex polyphasic fluid percolation; and iii) a typical gold-arsenopyrite ore-stage assemblage (e.g. Noronha, 2000; Fuertes-Fuente et al., 2016).

Gold deposits located on northern Iberia have been recently targeted for numerous multidisciplinary studies (Noronha et al., 2000; Vallance et al., 2003; Cepedal et al., 2013; Mortensen et al., 2014; Martinez-Abad et al., 2015; D´Angelico et al., 2016; Fuertes-Fuente et al., 2016; Rodríguez-Terente et al., 2018; MacKenzie et al., 2019; Cepedal et al., 2018; Neiva et al., 2019; Leal et al., 2022). On the contrary, at the SW of the Iberian Massif, particularly in Ossa-Morena Zone (OMZ), the characterization of gold deposits is not so well constrained. In this region, gold mineralization appears to be restricted to large Variscan shear zones with strike-slip kinematics. These geological settings are found at the São Martinho and Mosteiros deposits (De Oliveira et al., 2007) and at the numerous deposits and occurrences of the Escoural gold district, which are mainly hosted in Neoproterozoic to Lower Cambrian metasedimentary and metavolcanic units.

Because of this, identify and understand the mechanisms that promoted the gold precipitation is the main objective of this research, aiming to contribute to the comprehension of the Escoural gold district.

Herein a comprehensive study of the Monfurado gold prospect, part of the puzzling Escoural gold district, is provided. A wide range of techniques, including, mineralogical, geochemical, sulfur isotope, and fluid inclusion studies were employed, thus allowing to infer the sources of metals, fluid pathways, and fluid-rock interactions capable of triggering the mechanisms responsible for the anomalous gold concentrations in the area.

2.2 Geological Settings

2.2.1 Geodynamic Context of Iberia

The Iberian Massif represents the westernmost section of the European Variscides, and comprises a set of geological units formed during Palaeozoic that can be described in three different stages: i) the Cambrian-Early Ordovician rift stage, responsible for the separation of the Avalonia terrane at the northern Gondwana margin, forming the Rheic Ocean; ii) the Ordovician – Devonian passive margin stage, and iii) the middle-Devonian to Carboniferous subduction and posterior Gondwana-Laurussia oblique collision resulting in the closure of the Rheic Ocean and edification of Pangea (e.g. Franke, 2000; 2014 Matte, 2001; Nance et al., 2010; 2012; Pereira et al., 2012; 2017; Franke et al., 2017; Kroner et al., 2020).

The Cambrian-Early Ordovician rift stage at the northern Gondwana margin promoted the formation of several sedimentary basins in horst-graben structures, together with bimodal volcanic activity, which is well expressed throughout Iberia. The earlier expressions of rift-related volcanism are mainly restricted to the near-axis region in the southern domains, and late-stage assemblages are found widespread throughout the Iberian Massif (Chichorro et al., 2008; Sánchez Garcia et al., 2008; 2010; 2014; 2019, and references therein; Castro et al., 2020). The rift stage ended with the complete detachment of Avalonia, which drifted away from northern Gondwana, and gave birth to the Rheic Ocean during the Early Ordovician ages (ca 480 Ma; Pedro et al., 2010; Ribeiro et al., 2010). The Early Ordovician rift-drift transition set Iberia into a wide passive margin stage that persisted until Lower Devonian (e.g. Dias et al., 2016; Gutiérrez-Marco et al., 2019).

The subsequent compressional stage begins with an accretion and subduction period followed by the transcurrent collisional episode that presumably occurred before Visean times (Dallmeyer et al., 1993; Jesus et al., 2007; 2016; Pin et al., 2008; Pereira et al.,

2012). This period is characterized by i) extreme tectonism near the Avalonia-Gondwana suture zone; ii) orogenic metamorphism with considerable variations of the P-T regime; iii) the emplacement of parautocthonous and allochthonous terranes in the inner autochthon domains of the Iberian Massif, namely obduction of ophiolite fractions with the exhumation of high-pressure units, and iv) subduction and syn-collision magmatism (e.g. Quesada et al., 1994; 2019; Pedro, 1996; 2004; 2010; Fonseca et al., 1999; Leal, 2001; Dias et al., 2002; Araújo et al., 2005; Valle Aguado et al., 2005; Moita et al., 2005a; Ribeiro et al., 2007; 2010; Jesus et al., 2007; 2016; Rosas et al., 2008; Moita et al., 2009; Rubio Pascual et al., 2013; Dias et al., 2016; Azor et al., 2019).

Three main stages of deformation characterize the Variscan orogen, starting with D_1 which correspond to subduction-related crustal thickening as a result of thrust sheet stockpiling and recumbent or overturned folds that affect all units before Devonian ages; D_2 characterized by decompression and/or orogenic collapse and extension, and D_3 correspondent to a post-collisional thickening stage, implying vertical folds, ductile shears and strike-slip faults (Azor et al., 2019 and references therein).

2.2.2 Ossa-Morena Zone

The variety of tectonic-metamorphic and magmatic events that affected the Iberian Massif during the Variscan Cycle is expressed by a well-defined tectono-stratigraphic zonation (Lotze, 1945; Julivert et al., 1972; Ribeiro et al., 1995; 2007; Murphy et al., 2016; Simancas, 2019). In SW Iberia, the Rheic suture zone divides two important tectonic-stratigraphic units: the Ossa-Morena Zone, which represents the northernmost autochthonous terrane of Gondwana, and the South Portuguese Zone (SPZ), interpreted to embody a remnant of Avalonia separated in Cambrian - Early Ordovician times and posteriorly accreted during the collisional stages of the Variscan orogeny.

The OMZ comprises a thick sequence of variably metamorphosed rocks with ages ranging from Neoproterozoic to Carboniferous, packed with debris presumably resulting from the dismantlement of a pre-existing Cadomian arc (Apalategui et al., 1990; Oliveira et al., 1991; Araújo et al., 2013). The base sequence is characterized by the Lower Cambrian basal conglomerate and a calcite-dolomite carbonate formation, discordantly settled on top of the Neoproterozoic metasedimentary basement (locally named *Série Negra*), followed by a succession of siliciclastic strata culminated by syn-orogenic flysch, deposited from Middle-Upper Devonian to Lower Carboniferous (Oliveira et al., 1991; Piçarra, 2000; Robardet and Gutierrez-Marco, 2004; Borrego, 2009; Gutiérrez-Marco et al., 2019). The Cambrian-Early Ordovician rift events are accompanied by the emplacement of a series of acid-intermediate and basic volcanic rocks intercalated in the

carbonate and detrital units of Lower-Middle Cambrian age (Chichorro et al., 2008; Sánchez-Garcia et al., 2008; 2010; 2014; 2019).

The subduction and collisional episodes promoted the thrusting of ophiolitic and bordering units of the Iberian Terrane to the inner domains of the OMZ, as well as the exhumation of high-pressure rocks (e.g. the Moura Phyllonitic Complex; Araújo et al., 2005; Moita et al., 2005a; Rosas et al., 2008; Pedro et al, 2010; Ribeiro et al., 2010), and the emplacement of the Pulo do Lobo Terrane, an accretionary wedge overlaying the SPZ (e.g. Quesada et al., 1994). Additionally, several bimodal igneous suites were installed in the OMZ during different stages of the collisional event (Pereira et al., 2003; 2007; 2008; Jesus et al., 2007; 2016; Moita et al., 2005b; 2009; Dias da Silva et al. 2018; Ribeiro et al. 2019). The Variscan tectonic-metamorphic and magmatic events kept high-thermal regional regimes in Iberia and promoted the circulation of magmatic, metamorphic, and hydrothermal fluids responsible for the generation of some of the ore deposits widespread throughout OMZ.

2.2.3 The Montemor-o-Novo - Ficalho metallogenic belt

The Montemor-o-Novo – Ficalho metallogenic belt (Mateus et al., 2003; 2013; Tornos et al., 2004) is part of the Montemor-Ficalho lithostratigraphic Sector (Oliveira et al., 1991) delimited at North by the Estremoz-Barrancos Sector and at South by the Beja Igneous Complex. This belt displays an extremely complex evolution, evidenced by its structural, geological, and metallogenic features. The commodities are diverse, including Fe, Cu, Pb, Zn, and Au, and are represented by several ore assemblages hosted in diverse geological settings. Hence, several models are invoked to explain their occurrence, such as the SEDEX-VMS iron ores (Montemor-o-Novo iron deposits; Salgueiro, 2011); Zn-Pb deposits (Preguiça-Vila Ruiva and Enfermarias deposits; Barroso, 2003; Martins, 2003), or Skarn deposits (Orada, Azenhas, and Alvito Fe deposits; Carvalho, 1971, Oliveira, 1986; Matos et al., 1998, Caldeira et al., 2007; Salgueiro et al., 2010a, 2010b; Mateus et al., 2005; 2013; Maia et al., 2022).

Throughout the 18th and early 19th century this area was an important mining district with operations focusing on eight iron ore bodies (Andrade et al., 1949). The deposits are mainly composed of massive magnetite-pyrite (± chalcopyrite) and are hosted in Cambrian-Lower Ordovician units, for which recent studies suggest a Cambrian SEDEX-VMS continuum model (Salgueiro, 2011).

Aside from the iron ores found in the Montemor-o-Novo area, several gold deposits have been targeted during the last decades, forming what is here described as the Escoural gold district. This district was the focus of several gold-exploration projects and

scientific research, providing first descriptions of the gold endowment in the Escoural gold district deposits (Ribeiro et al., 1993). These earlier studies presented the first proposal that classified the deposits as Orogenic gold (Inverno, 2001). More recently, Lopes (2015) and Lopes et al. (2015) provided petrographic and isotopic (Sr-Nd) studies of host lithologies.

The calculated resources for the Escoural gold district reached 4.45 million tons of ore with a mean gold grade of 2.81 g/ton, translating into 440 000 ounces/12.5 tons of Au (Faria, 1997; Mateus et al., 2013; Lopes, 2015 and references therein), in which 45% are inferred mineral resources, 46% indicated and 9% measured. Previous authors tried to frame the ore deposition conditions, emphasizing on the sedimentary, structural, and geochemistry settings, whereas a multi-technique approach to the ores, as the one herein proposed, has never been endeavored.

2.2.4 Escoural gold district

The Escoural gold district is part of the Évora Massif, which is subdivided into three units: i) the high-grade metamorphic terrains, ii) the Montemor-o-Novo Shear Zone and iii) the Évora mid-grade metamorphic terrains (Pereira et al., 2003; 2006; Chichorro, 2006; Moita et al., 2009).

This gold district is structurally controlled by the wide (2 - 10 km) ductile NW-SE upper Carboniferous Montemor-o-Novo Shear Zone (MNSZ), which extends for over 30km and hosts 12 known deposits (**Fig. 3.1a**). Greenschist to amphibolitic facies metamorphism is ubiquitous in the area (**Fig. 3.1b**), and deformation is outlined by intense mylonitization that allowed to constrain the ages through which MNSZ was active (356 – 322 Ma; Pereira et al., 2015 and references therein). Most of the gold prospects (2-12 in **Fig. 3.1a**) occur near the contact between the MNSZ and the high-grade metamorphic terrains, structurally controlled by the Boa Fé fault zone (**Fig. 3.1a**), with exception of the Monfurado gold prospect which is located in the vicinity of the Santiago do Escoural fault. The units affected by the MNSZ can be defined as follow:

1. Escoural Fm. (Neoproterozoic): A metasedimentary formation, locally designated as *Série Negra*, mainly composed of biotitic schists and quartz-feldspar paragneiss, resulting from the dismantlement of a Cadomian-Avalonian magmatic arc with ages ranging from 560 to 550 Ma (Chichorro, 2006).

2. Monfurado Fm. (Lower Cambrian): This formation is individualized in two units (Chichorro, 2006), adopted subsequently by other authors (e.g. Salgueiro, 2011). The Lower unit is characterized by acid volcanism that is emplaced in the calcite-dolomite carbonate formations during the rift-related volcanic events (522.3 ± 5 Ma; Chichorro et

al., 2008), with metamorphism and deformation superimposed during the Variscan orogeny. The acid metavolcanics are locally referred to as Escoural Leptinites and display affinities to rhyodacites and rhyolites (Sánchez-Garcia et al., 2003; 2019, Chichorro, 2006). The Upper unit corresponds to the transition to an intermediate/basic volcanism, composed of amphibolites and amphibolic schists.

3. Carvalhal Fm. (Middle–Upper Cambrian): Mainly composed of basic metavolcanic rocks affected by greenschist to amphibole facies metamorphism and strongly deformed by the MNSZ activity. The Carvalhal Fm. is divided into two units, a Lower unit in which amphibolites (E-MORB) predominate, with intercalations of calcsilicate rocks (Carvalhosa, 1983; Carvalhosa and Zbyszweski, 1994) and an Upper unit composed of phyllites and metabasites with N-MORB signatures.

2.2.4.1 The Monfurado gold prospect

The Monfurado prospect is located at the NW of the Escoural gold district (**Fig. 2.1a**) and was one of the twelve targeted areas for mineral exploration. The Monfurado prospect is found near the ancient Monges iron mine (**Fig. 2.1c**; Andrade et al., 1949), north of the Santiago do Escoural village and mainly hosted by two geological units: the Escoural Fm. and Monfurado Fm (Lower and Upper units), described above (**Fig. 2.1**).

A drilling campaign (11 drill holes) was performed in 2012 by the COLT Resources exploration company to assess the Monfurado gold prospect potential. Outcrops are scarce, and the area is covered by a thin regolith. Therefore, the log interpretation provided by the company and later reinterpreted for this work, was essential to identify the main geological and structural controls over gold mineralization.

Drill core logs show a monocline structure generally dipping towards NE. The Escoural Fm. is found at the top of the logs (**Fig. 2.2; Fig. 2.3**), and it is differentiated by paragneisses and thin amphibolic schist intercalations. The contact between the Escoural Fm. and the Monfurado Fm. units is marked by tectonism that is interpreted as an overthrust (Araújo, 1995). The Upper unit of the Monfurado Fm. is composed by amphibolic schists (basic metavolcanic unit; **Fig. 2.1b, c; Fig. 2.2**) usually interbedded with pristine marbles. This unit transits to calcite-dolomite carbonated lithotypes at depth, ranging from pure marbles to calcsilicate metasomatized rocks. The transition to the acid metavolcanic rocks is marked by an abrupt contact and is evidenced by the presence of orthogneisses and sparse metacherts. The acid metavolcanic rocks are intensely fractured with several generations of veins, although two main types are consistent throughout the studied drill core samples and can be divided in i) thin quartz + tourmaline veins (<1 - 2 cm) perpendicular to bedding with sections of high density (4 veins/meter),

and ii) sparse thicker quartz-feldspar-chlorite veins (up to 5 cm) parallel to bedding cross-cutting the latter veins.

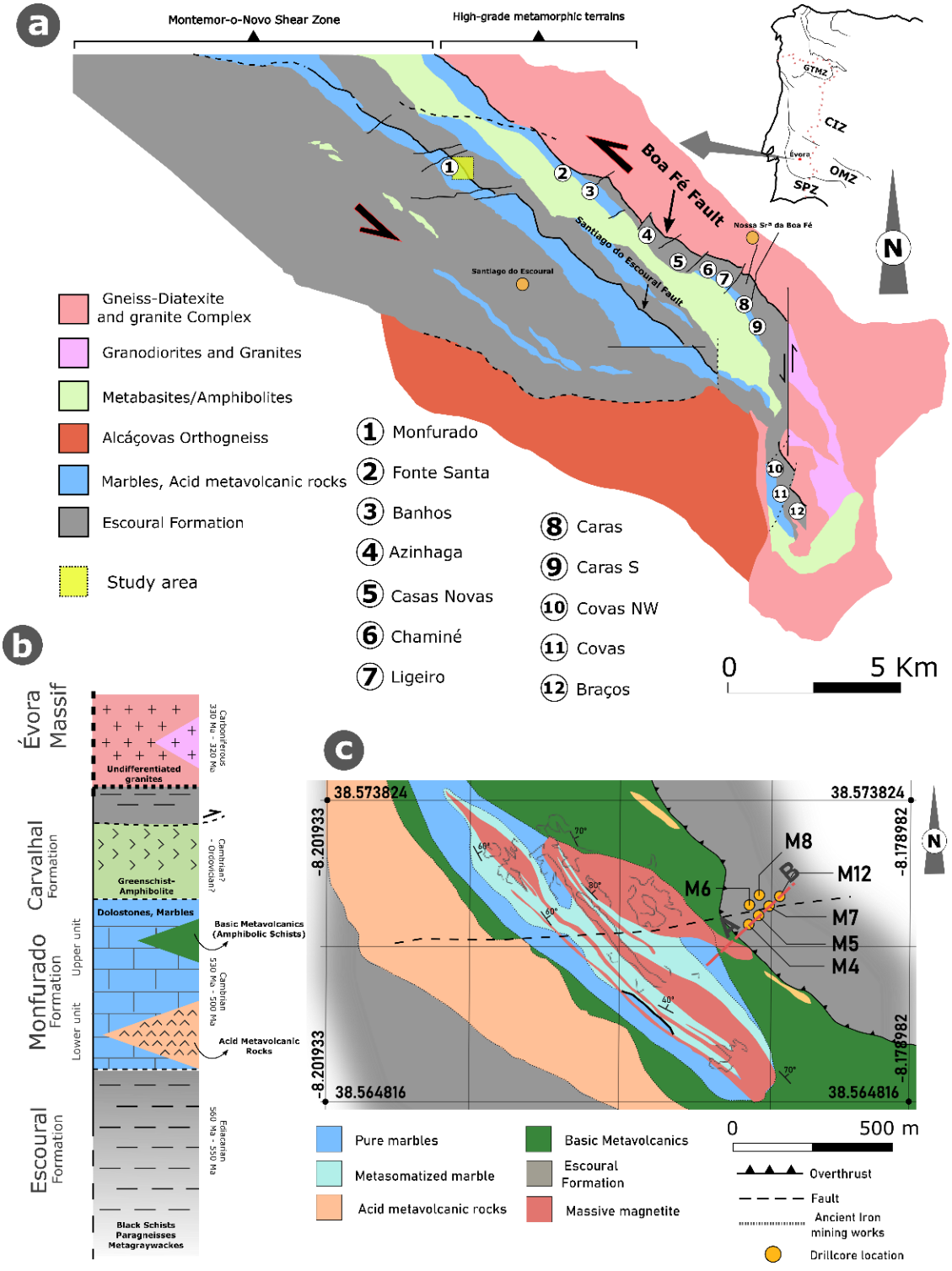

Figure 2.1. a. Location of the study area in the Iberian terrane and geological map of the Montemor-o-Novo area (adapted from Chichorro, 2006), with representation of the main geological formations. The numbered circles (1-12) represent the twelve gold prospects of the Escoural Gold district. The Monfurado prospect area is marked in the regional map by the yellow rectangle. The orange circles represent the closest villages

to the deposits, the Santiago do Escoural and Nossa Senhora da Boa Fé. **b.** Stratigraphic chart representative of the main formations observed in the Montemor-o-Novo and Santiago do Escoural areas (adapted from Carvalhosa and Zbyszweski, 1994; Chichorro, 2006). **c.** Geological map of the Monfurado prospect area (adapted from Andrade et al., 1949; Serviço de Fomento Mineiro, 1977), with location of the sampled drill cores performed in the vicinity of the ancient Monges iron mine. The A-B profile (red dashed line) corresponds to the geological section from drill cores M4 to M12 presented in Figure 3.3.

In some of the deeper sections of the cores, another transition to the Monfurado Fm. is observed hosting the richer ore sections (c.f. **Fig. 2.2**), mainly composed of massive sulfide layers with pyrrhotite and disseminated arsenopyrite. The Monfurado Fm. is identified as an important fluid pathway due to its intense mineralization, represented by massive layers of sulfides mainly composed of pyrrhotite, pyrite and arsenopyrite in which the higher gold grades are found. The massive sulfide layers are hosted in a carbonate iron-rich unit, in sections immediately below the acid metavolcanic rocks (**Fig. 2.2**).

Massive magnetite sections are observed throughout the drill cores, and pyrite is ubiquitous in all lithologies, mostly found in a disseminated form but locally occurring as massive layers.

The geochemical analysis of continuous log sections of 1m length, provided by COLT Resources company shows that the distribution of gold grades is controlled by i) the presence of massive sulfide layers with disseminated arsenopyrite hosted in calcsilicate units, ii) quartz-chlorite-pyrite veins that crosscut the acid metavolcanic rocks. Interesting gold grades along the drill cores are shown in **Figure 2.2**, and the mineralized envelope is defined in **Figure 2.3**.

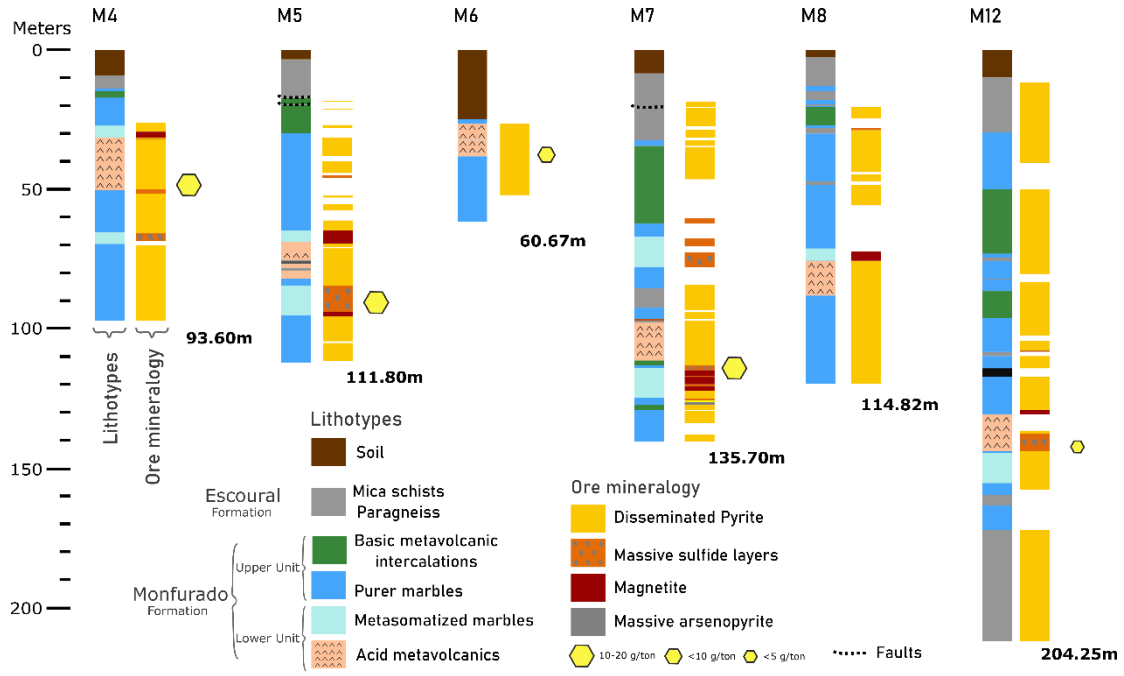

Figure 2.2. Log representation of the six studied drill cores, with individualization between lithology and ores. The yellow hexagons on the side of the drill cores refer to the range of the highest reported punctual gold grades (g/ton) on the respective drill core.

2.3 Sampling and analytical methods

2.3.1 Sampling

A total of 133 samples were collected at different depths from six of the eleven drill cores (M4; M5; M6; M7; M8; M12; **Fig. 2.1c**; **Fig. 2.2**) and are representative of the host rock lithologies and main mineralized sections. Sampling also focused on altered host rocks to identify the extent of alteration related with the mineralizing event, as well as with the regional metamorphism. The sampling resulted in the preparation of 143 polished thin sections and 62 polished cross-sections for petrographic and mineralogical studies, 8 milled samples for whole-rock geochemistry, 15 double polished thick sections for the fluid inclusion study, and 11 sulfide concentrates for sulfur isotope geochemistry.

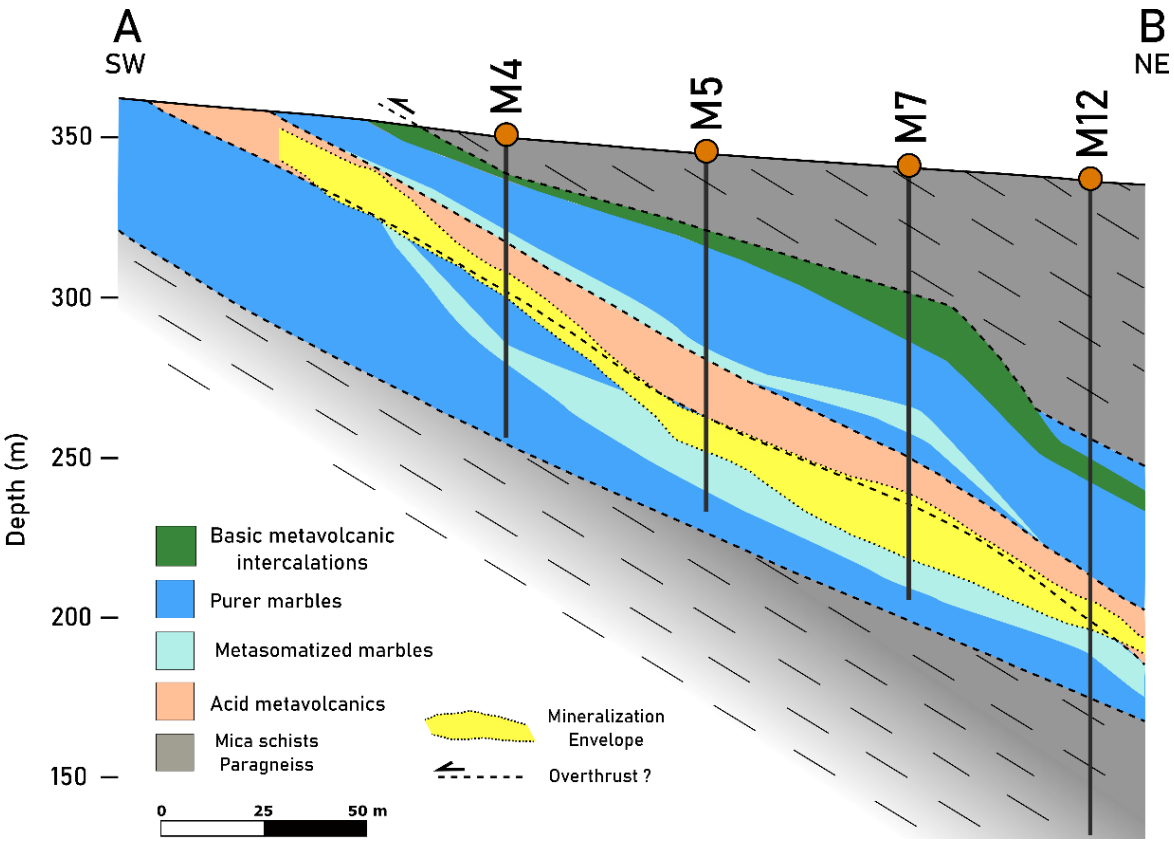

Figure 2.3. Interpretative section (adapted from COLT Resources unpublished reports) of four of the six studied drill cores in a SW-NE profile from M4 to M12 drill cores, as displayed by the A-B profile marked in Figure 3.1c. The mineralized envelope refers to gold grades above 0.2 g/ton.

2.3.2 Optical and Scanning Electron Microscopy

Polished cross-sections and polished thin sections were observed under an optical microscope to identify the main mineral phases and establish the ore paragenesis. Scanning electron microscopy with energy dispersive spectroscopy (SEM-EDS) analysis and image acquisition were performed using a VP-SEM-EDS Hitachi S3700N with a Bruker Xflash 5010SDD X-ray spectrometer at the HERCULES Laboratory of the University of Évora -Portugal-, and an MEB JEOL-6100 SEM-EDS at the Technical and Scientific Services of the University of Oviedo - Spain. All the mineralogical abbreviations adopted through this manuscript follow the proposals from Whitney and Evans (2010).

2.3.3 Electron probe microanalysis (EPMA)

In-situ arsenopyrite, pyrite, gold, chlorite, tourmaline, and feldspar analysis were performed using a CAMECA SX100 electron probe microanalyzer (EPMA) at the Technical and Scientific Services of the University of Oviedo (Spain). The analytical conditions were selected as follows: i) for arsenopyrite and pyrite a ~5 µm beam diameter was used, with an acceleration voltage of 20 kV and a 20 nA current for As, S, and Fe quantification, and a 20 kV acceleration voltage and 100nA current was used for Au quantification; ii) for gold particle analysis a ~5 µm beam was used to analyze the larger Au grains with an acceleration voltage of 20 kV and a current of 20 nA, and iii) for silicates and acceleration voltage of 15 kV and a 15 nA current was used.

The standards used for S, As, Fe were arsenopyrite, for Au, Cu, Se, Fe, Bi, Ag, and Hg the standards were pure gold, pure copper, pure selenium, pure iron, pure bismuth, silver telluride, and mercury sulfide respectively. All raw data including the limits of detection (LOD) for each element is disclosed in **Appendix E**.

2.3.4 Fluid inclusion studies

Fluid inclusion (FI) studies were performed at the Geoscience Department of the University of Évora using a LINKAM THMSG600 microthermometry stage coupled to a Nikon Eclipse 50Ipol microscope with a 100x long focus objective lens. Microthermomety cooling runs were performed using a 1 ºC to 10 ºC/min rates to ensure a cooling that allows the observation of the different phase changes, such as the first CH_4 melting temperatures (Tm_{CH4}), CO_2 melting temperature (Tm_{CO2}), eutectic temperature (Te), and ice melting temperature (Tm_{ice}). The heating runs were performed using a 5 ºC/min to 30 ºC/min step heating, assuring the accuracy of measurements of ±0.3 ºC and allowing to register CO_2 homogenization temperatures (Th_{CO2}) and final homogenization temperatures (Th).

Fluid inclusion salinities were calculated using the Tm_{ice} (Bodnar and Vityk, 1994) and Tm_{chl} when CO_2 was present, and when correct observation of this phase transition was possible. To constrain the P-T-V-x conditions of the fluids in the H_2O-NaCl system, the AqSo_NaCl Software (Bakker, 2018) was used, and for the H_2O-CH_4 system, the BULK package was used (Bakker, 2003).

2.3.5 Sulfur isotope geochemistry

Samples for sulfur isotope analysis were separated under the microscope to ensure the representativeness of the mineralization assemblages.

The selected samples were crushed for the selection of monomineralic grains of arsenopyrite, pyrite, and pyrrhotite. Arsenopyrite and pyrite were hand-picked under a binocular stereomicroscope, whereas pyrrhotite was separated using a hand-magnet and then hand-picked. Sulfur isotope analysis was performed by obtaining SO_2 for the determination of the $^{34}S/^{32}S$ isotopic ratio by isotope ratio mass spectrometry at the NUCLEUS Laboratory, University of Salamanca - Spain.

2.3.6 Whole-rock geochemistry

Major element bulk analysis was performed using X-ray fluorescence (XRF) whereas trace and rare earth element analysis were quantified by ICP-MS (Inductively Coupled Plasma – Mass Spectroscopy) through a fusing bead and acid digestion method. Both analyses were performed at ALS Seville Laboratories using the ME-XRF26 and ME-MS81 analytical packages.

2.4 Results

2.4.1 Host rock petrography and geochemistry

2.4.1.1 Escoural Formation

At the study area, the Escoural Fm. is composed of quartz-feldspar paragneiss with feldspar porphyroblasts visible in hand samples. The matrix displays strong deformation, and mineral strain is materialized by the presence of fine plates of biotite surrounding the porphyroblasts of feldspar (**Fig. 2.4a**). These crystals have pale polysynthetic twinning and are associated with recrystallized fine-grained quartz on strain shadows. The quartz from the paragneiss matrix displays the development of ribbon textures, which outline the stretching lineation. Some samples exhibit the growth of amphibole (mainly actinolite), agreeing with the greenschist-amphibolitic metamorphic conditions described for the region.

Geochemistry of a paragneiss from this unit (**Sample 1; Table 2.1; Appendix D**) revealed relatively high SiO_2 content, low Al_2O_3 values (70.5 wt.% and 12.8 wt.%, respectively), and Na_2O/K_2O of 3.41, as expected for coarse metasedimentary rocks. The REE diagram normalized to Chondrite (Palme and O´Neill, 2014; **Fig. 2.5**) show high fractionation of LREE over MREE (La/Sm_{CN} = 3.98), slightly flat HREE (Sm/Yb_{CN} = 1.13), and a marked positive Eu anomaly (McLennan 1989) of Eu/Eu* = 1.25. Such values are slightly different than other major element geochemical data of

metagraywackes and paragneisses from *Serie Negra* reported in literature (SiO_2 = 55 – 66 wt.%, Al_2O_3 = 15 – 19 wt.%; Pereira et al., 2006; Lopes, 2015; Díez-Fernández et al., 2017). Likewise, the steep LREE/MREE patterns are observed in bibliographic data, but contrast with the considerable negative Eu anomalies (Eu/Eu* = 0.43 – 0.87).

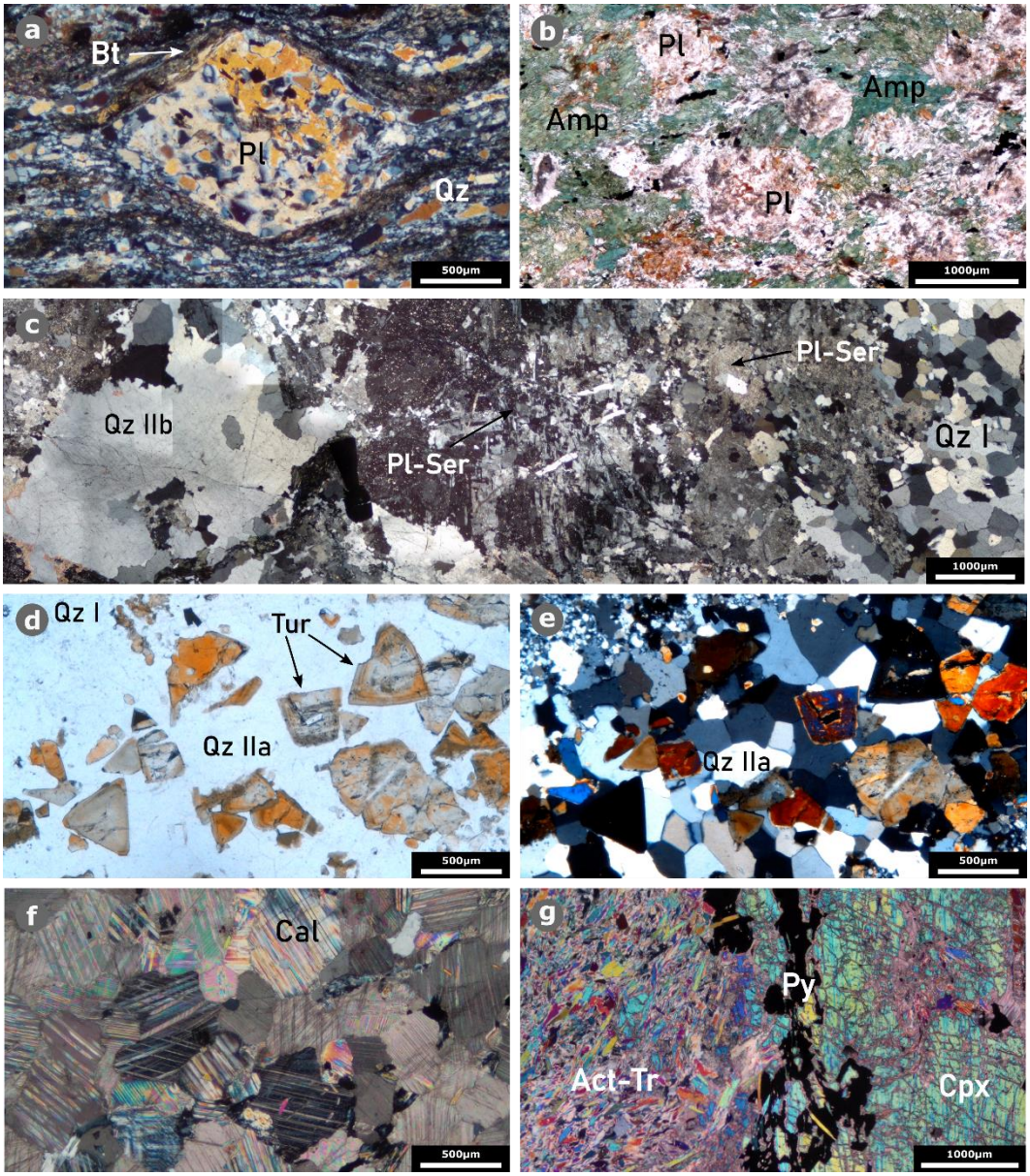

Figure 2.4. Representative petrography of host-rock thin sections is shown from (a.) to (g.). **a.** Example of macroscopic scale structures of the Paragneiss from the Escoural Fm., in which deformation is outlined by large plagioclase porphyroclasts surrounded by aligned plates of biotite and quartz ribbon structures. **b.** Composite image of microphotographs at x2 magnification, exemplifying the textures and mineral paragenesis of the basic metavolcanics (amphibolite?) of the Monfurado Fm. with relics of oval plagioclase surrounded by green hornblende. **c.** Composite microphotograph (x2 magnification) of the acid metavolcanic rocks from the Lower unit of the Monfurado Fm. This thin section outlines the quartz-feldspar matrix, with large porphyroclasts of plagioclase intensely sericitized (Pl-Ser). The volcanic matrix is crosscut by late quartz veins (Qz IIb), with large anhedral crystals. **d.** Plane nicols composite microphotograph of the quartz

(QzIIa)-tourmaline veins that crosscut the acid metavolcanics of the Monfurado Fm. **e.** Crossed nicols composite microphotograph of the section shown in (d.). **f.** Calcite-dolomite marbles of the Upper Monfurado Fm. unit. **g.** pervasive calcsilicate alteration of the marble units of the Monfurado Formation, with development of tremolite-actinolite and pyroxene paragenesis substituting the previous calcite-dolomite matrix.

2.4.1.2 Monfurado Formation (Lower unit)

The acid metavolcanic rocks are composed of a quartz-feldspar matrix, with a white to greyish color in hand sample, and are often crosscut by late-quartz veins. Local variations of this lithology display biotite development, observable in hand samples.

Thin section examination allows to describe this lithotype as medium-grained, mainly composed of euhedral quartz crystals (Qz I) with sparse large porphyroblasts of feldspar (**Fig. 2.4c**), mostly plagioclase which exhibit polysynthetic twinning. Hydrothermal alteration is pervasive and is materialized by intense sericite alteration of plagioclase (**Fig. 2.4c**). Quartz exhibits deformation features, such as undulatory extinction and ribbon textures in the most deformed sections, whereas biotite is found in fine plates, sub-parallel to the main foliation plane.

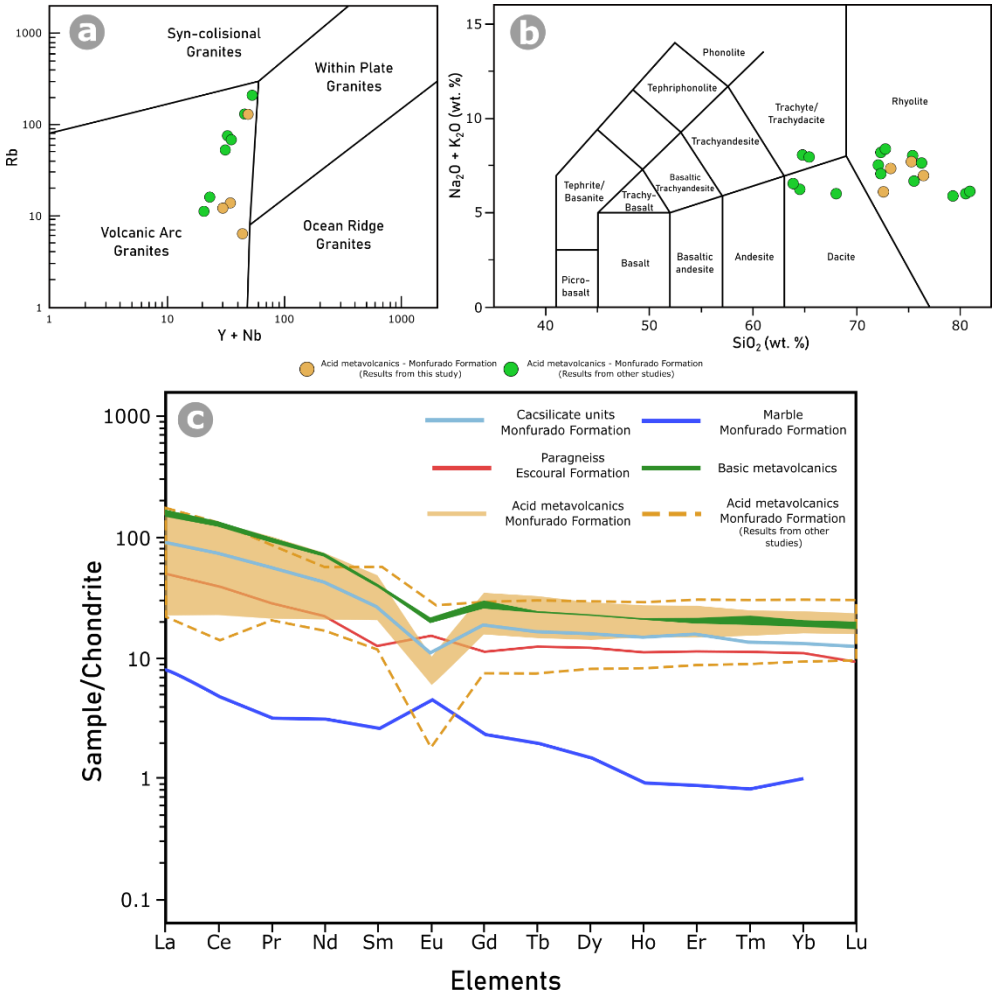

Figure 2.5. (previous page). a. Rb vs Y+Nb tectonomagmatic discriminant diagram (after Pearce et al., 1984) applied to the acid metavolcanic rocks of the Monfurado Fm.. **b.** Total alkali-silica diagram plot (after Le Maitre et al., 2012) of the acid metavolcanic rocks. **c.** Chondrite-normalized REE patterns representative of the host-rocks from the Monfurado deposit. In all diagrams a comparison is made to previous data for the acid metavolcanic rocks of the Montemor-o-Novo region (light-orange color dashed line; Chichorro, 2006; Pedro et al., 1996; Leal, 2001). Chondrite values after Palme and O´Neill (2014).

The acid metavolcanic rocks are strongly affected by brittle deformation that promoted the development of centimetric quartz veining (Qz IIa/IIb; **Fig. 2.4c, d**). The Qz IIa veins correspond to sub-vertical structures that generally crosscut bedding and are ubiquitously accompanied by tourmaline (**Fig. 2.4d**). These veins are perpendicularly crosscut by Qz IIb veins, which are mainly composed of quartz, feldspar and pyrite (**Fig. 2.4c**).

Tourmaline is cogenetic with quartz IIa, and displays characteristic triangular basal sections (**Fig. 2.4d, e**), with green to brownish optical zoning, and subhedral to euhedral shapes. Epidote aggregates are seldomly observed throughout the matrix, along with Qz I.

Samples of the acid metavolcanic rocks (**Sample 2, 3, 4, and 5; Table 2.1**) revealed chemical compositions consistent with a rhyolite to rhyodacite calc-alkaline affinity (**Fig. 2.5b**) and volcanic arc-like signature (Nb/Y = 0.21 - 0.44; **Fig. 2.5a**). CN REE generally displays flat patterns with subtle enrichments in LREE over MREE and HREE (La/SmCN = 1.1 – 3.4; Sm/YbCN = 1.1 – 1.9; **Fig. 2.5**), well pronounced negative Eu anomalies (Eu/Eu*= 0.25 – 0.49) and slightly demarked Ce anomaly (Ce/Ce*= 0.79 – 1.07), according to the McLennan (1989) equation. The herein presented geochemical data for the acid metavolcanic rocks is consistent with previously published data regarding other MNSZ rift-related volcanic events (Pedro, 1996; Leal, 2001; Sánchez-Garcia et al., 2003; 2019; Chichorro, 2006)

2.4.1.3 Monfurado Formation (Upper unit)

The transition from acid to basic metavolcanic rocks is identified by other authors (Chichorro, 2006; Salgueiro, 2011), and is distinguishably marked by the presence of amphibolic units, some with schistosity. These rocks are composed of amphibole, namely hornblende and medium-grained feldspar porphyroblasts with an oval shape and strongly sericitized cores (**Fig. 2.4b**). Geochemistry of intermediate/basic metavolcanic samples from these sections (**Samples 8 and 9; Table 2.1**) showed SiO_2 values between 60.8 wt.% and 49.1 wt.%., respectively. Both samples have relatively high alumina and alkali content (Al_2O_3 = 16.75 wt.% and 14.3 wt. %; $Na_2O + K_2O$ =7.3 wt.%

and 4.3 wt.%), although, in sample 8, trace element chemistry is characterized by low Nb/Y (0.41) and Zr/Ti (0.04), but high LILE components (Rb = 122 ppm; Ba = 823 ppm; Sr = 230 ppm), which is in accordance with volcanic-arc tectonic setting of emplacement. Sample 9 (**Table 2.1; Appendix D**), besides displaying lower SiO_2 values, has very high CaO content (17.4 wt.%); also, trace element ratios (Ti/V = 27.5, Zr/Y = 6.0) display affinities with basalts characteristic of E-MORB and within-plate environments, resembling the possible tectonic setting of the overlying Carvalhal Fm. (Pearce and Norry, 1979; Shervais, 1982; Chichorro, 2006; Sánchez-García, 2019).

Marbles (**Fig. 2.4f**) are ubiquitous to the upper unit of the Monfurado formation, usually displaying a calcite-dolomite matrix as revealed by the high CaO (29.3 wt.%) and MgO (18.3 wt.%) contents (Sample 6).

Hydrothermal alteration of marbles is revealed by the development of calcsilicate assemblages dominated by actinolite-tremolite, which is sometimes accompanied by pyrite (**Fig. 2.4g**). One selected calcsilicate sample (Sample 7) revealed higher SiO_2, Al_2O_3, and CaO values (6.88 wt.%, 1.51 wt.%, and 36.8 wt.%), with lower Fe_2O_3 and MgO contents (3.35 wt.% and 10.95 wt.%) when compared to the pristine marble sample.

2.4.2 Mineralized domains

Different mineralization styles can only be identified through detailed petrographic characterization of the ores. Such work is essential in understanding the succession of events related to ore deposition, providing the sequence of crystallization and its relationship with the complex geological history of the region.

2.4.2.1 Pre-Gold Ore Stage

Oxides

The Monfurado gold prospect is spatially associated with iron ore bodies that belong to the Monges mine and are mainly hosted in marbles and calcsilicate rocks (**Fig. 2.2**). The iron ores possibly formed through submarine hydrothermal activity during the Cambro-Ordovician intracratonic rifting settings (Salgueiro, 2011), which are prone to the formation of SEDEX-VMS deposits.

The iron-rich domains intersected by the drill cores are fundamentally composed of metric massive to disseminated magnetite sections hosted in a calcite-dolomite matrix, with minor pyrite and sparse chalcopyrite. Needle-like amphibole crystals, identified as actinolite-tremolite, accompany the iron oxides (**Fig. 2.6a**) that display intense

deformation as evidenced by the boudin-shaped magnetite crystals (**Fig. 2.6a**). Barite is found in close relation with magnetite and is, possibly, contemporary of its deposition.

Table 2.1. Representative major and trace elements data from drill core selected samples. Major elements in wt.%; trace elements in ppm.

Sample		1	2	3	4	5	6	7	8	9
	LOD*	M12@66m Paragneiss	M8@80m Acid Metavolcanics	M8@83m Acid Metavolcanics	M6@28m Acid Metavolcanics	Acid Metavolcanics (outcrop)	M10@76m Marble	M6@60m Calcsilicate rock	M12@95m Intermediate Metavolcanics	M12@98m Basic Metavolcanics
wt. %										
SiO_2	0.01	70.5	76.4	72.6	73.3	75.3	3.56	6.88	60.8	49.1
Al_2O_3	0.01	12.8	13.55	12.85	13.2	13.75	0.08	1.51	16.75	14.3
Fe_2O_3	0.01	4.58	1.35	4.35	1.66	0.64	6.07	3.35	5.01	5.09
CaO	0.01	0.58	1.1	1.19	0.56	0.96	29.3	36.8	5.94	17.4
MgO	0.01	2.83	0.41	1.77	1.87	1.07	18.3	10.95	1.47	2.49
Na_2O	0.01	2.83	6.42	5.49	1.58	7.59	0.02	0.14	3.22	1.52
K_2O	0.01	0.86	0.55	0.6	5.77	0.17	0.01	0.35	4.08	2.81
Cr_2O_3	0.002	0.006	<0.002	0.003	0.002	0.006	<0.002	<0.002	0.011	0.011
TiO_2	0.01	0.39	0.22	0.41	0.29	0.48	<0.01	0.09	0.68	0.57
MnO	0.01	0.01	<0.01	0.02	0.01	0.02	0.52	0.41	0.07	0.12
P_2O_5	0.01	0.11	0.13	0.13	0.1	0.07	0.02	0.05	0.15	0.13
SrO	0.01	<0.01	0.01	0.01	<0.01	<0.01	0.01	0.03	0.01	0.03
BaO	0.01	0.03	0.05	0.07	0.13	0.01	0.07	0.02	0.09	0.08
LOI	0.01	2.69	1.44	2.39	1.6	0.72	38.3	36	2.01	5.36
Total		98.22	101.63	101.88	100.07	100.79	96.26	96.58	100.29	99.01
	LOD									
ppm										
Ba	0.5	282	393	593	1130	46.2	584	659	823	686
Sr	0.1	91.1	240	210	50.9	87.8	181	212	230	352
Rb	0.2	31.5	13	12.3	126	6.2	0.6	65.9	122.5	91.7
Cs	0.01	0.48	0.44	0.53	1.72	0.09	0.12	1.1	1.77	1.37
V	5	102	11	33	21	78	7	23	110	124
Co	1	11	5	6	1	1	<1	2	8	5
Ni	1	19	2	5	3	7	<1	2	27	34
Cr	10	50	20	20	20	50	<10	30	90	90
Zr	2	117	249	265	215	193	5	120	177	179
Hf	0.1	3.5	7.4	7.8	7	5.4	0.2	3.7	5.2	5.3
Nb	0.1	5.8	5.8	9.3	9.6	9.5	<0.2	5.4	12.8	10.4
Ta	0.1	0.5	0.6	0.9	1.1	0.6	0.1	0.7	0.9	0.8
Ga	0.1	18.2	15.1	17	19.1	15.1	0.7	10.7	21.5	21.7
Tl	0.02	<10	10	<10	<10	<10	<10	<10	<10	<10
Li	10	10	<10	10	10	<10	<10	10	10	<10
Cd	0.5	<0.5	<0.5	<0.5	<0.5	<0.5	<0.5	<0.5	<0.5	<0.5
Mo	1	2	<1	1	1	1	2	<1	1	1
Sn	1	12	3	5	9	6	<1	5	3	6
W	1	6	2	3	5	4	1	5	3	3
Ag	0.5	<0.5	<0.5	<0.5	<0.5	<0.5	<0.5	1.8	<0.5	<0.5
As	0.1	<5	16	30	12	8	7	10	<5	<5
Pb	2	<2	6	2	10	3	3	8	6	8
Zn	2	6	16	11	10	18	16	20	15	20
Cu	1	1	27	79	4	6	17	11	25	8
Th	0.05	3.94	16.4	14.35	17	7.78	<0.05	8.56	10.95	9.58
U	0.05	1.65	5.88	6.13	9.52	4.72	0.13	5.04	3.88	3.46
Y	0.1	16.6	27.4	21.2	39.3	23.7	1.7	22.4	30.6	29.6
Sc	1	11	1	8	5	8	<1	4	15	14
La	0.1	11.8	5.3	11.7	37.7	10.1	1.9	21.2	39.7	34.6
Ce	0.1	24.2	14	27.8	78.9	19	2.9	44.8	81.8	74.5
Pr	0.02	2.65	1.98	3.4	9.14	3.35	0.29	5.14	8.97	8.34
Nd	0.1	10.2	9.2	14.8	33.8	14.2	1.4	19.2	32.5	31.9
Sm	0.03	1.85	3.1	3.3	7.01	4.11	0.38	3.92	5.76	5.91
Eu	0.02	0.84	0.49	0.52	0.57	0.33	0.25	0.61	1.08	1.19
Gd	0.05	2.26	3.63	3.13	6.86	3.52	0.46	3.67	5.05	5.84
Tb	0.01	0.45	0.7	0.53	1.15	0.67	0.07	0.59	0.85	0.87
Dy	0.05	3	5.21	3.48	7.09	4.28	0.36	3.87	5.5	5.43
Ho	0.01	0.61	1.09	0.81	1.49	0.82	0.05	0.79	1.16	1.14
Er	0.03	1.84	3.07	2.38	4.25	2.61	0.14	2.52	3.33	3.09
Tm	0.01	0.28	0.45	0.38	0.61	0.38	0.02	0.33	0.54	0.46
Yb	0.03	1.77	2.96	2.6	3.93	2.78	0.16	2.09	3.34	2.87
Lu	0.01	0.23	0.41	0.39	0.57	0.44	<0.01	0.3	0.49	0.41

Sulfides paragenesis

Two main pre-ore pyrite-rich sulfide domains were identified as (1) isolated pyrite crystals hosted in marbles from the Upper unit of the Monfurado Fm. (**Fig. 2.6b**), and usually accompanied by amphibole-chlorite assemblages; and (2) massive pyrite layers in a fine-grained and euhedral quartz matrix, in which pyrite is usually surrounded by chlorite-amphibole aggregates with minor epidote (**Fig. 2.6c**). The quartz matrix found in this section suggests a volcanogenic nature for these pyrite accumulations, possibly similar to the one associated with the iron ores (SEDEX-VMS; Salgueiro, 2011).

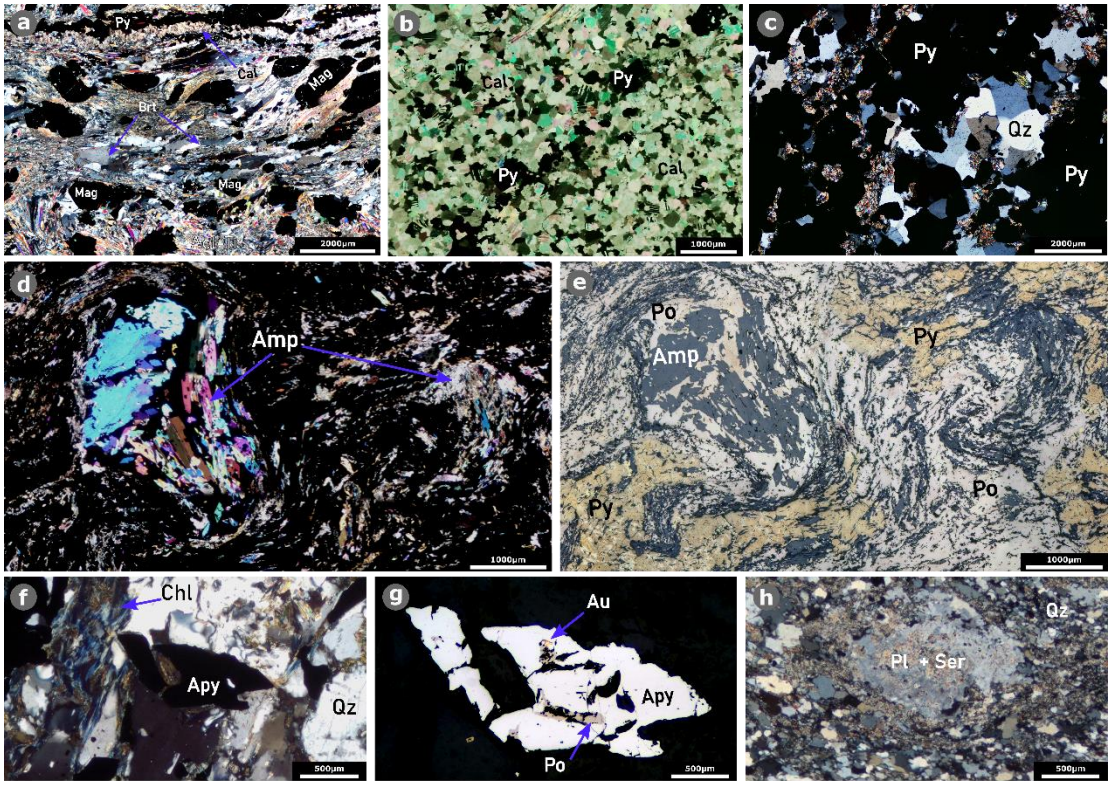

Figure 2.6. Mineralized domains petrography showing host-rock relations and translucid mineral identification. **a.** Crossed nicols composite microphotograph of the pre-gold oxide domain section in which dispersed opaques (Mag-magnetite) are accompanied by tremolite-actinolite in a calcsilicate matrix. Barite shows a ribbon texture which might indicate deformation. This section is crosscut by a late calcite-pyrite vein. **b.** Crossed nicols composite microphotograph of a pre-gold sulfide domain constituted mainly by pyrite in a calcite-dolomite matrix (Monfurado Fm. marbles), sometimes showing the development of tremolite in the pyrite-calcite contact. **c.** Crossed nicols composite microphotograph of a pre-gold sulfide domain mainly composed of massive pyrite in a quartz volcanogenic matrix. **d.** and **e.** Crossed nicols and reflected light composite microphotograph, respectively, of the gold-mineralization sulfide-rich layers in which amphibole develops along with pyrrhotite and pyrite. Pyrrhotite displays intense deformation (folding) with rotation of the larger amphibole crystals. **f.** Crossed nicols transmitted light composite microphotograph, of the gold-mineralization arsenopyrite-rich layers. Arsenopyrite is found in a quartz dominated matrix and develops along with Fe-rich chlorite (pennine). **g.** Reflected light of the section shown in (f.) at a x5 magnification,

showing gold inclusions in arsenopyrite. **h.** Crossed nicols transmitted light composite microphotograph of the acid metavolcanic matrix, composed by fine-grained subhedral quartz crystals and large sericitized plagioclase porphyroclasts.

2.4.2.2 Gold Ore Stage

Gold-sulfides assemblages in massive sulfide layers

A massive sulfide layer (MSL) is present in the majority of the studied drill cores, apparently marking a laterally continuous layer, with an approximate thickness of 3 to 15 meters. During the exploration campaigns the attention was drawn to M5, M7, and M12 drill cores (**Fig. 2.2**), which revealed gold grades up to 18 g/ton in the MSL intersected by these drill cores (**Fig. 2.2**).

The MSL is hosted in metasomatized marbles of the Monfurado Fm. (**Fig. 2.3**), having pyrrhotite as the dominant sulfide phase and usually accompanied by fine to medium-grained actinolite-tremolite crystals (**Fig. 2.6d, e; Fig. 2.7b**). Pyrite, arsenopyrite, and chalcopyrite are also present in variable proportions.

Magnetite is partially replaced by pyrrhotite, and sparse relicts of the iron oxide are found within pyrrhotite, outlining the presence of sulfidation processes, (**Fig. 2.7a and b**). Pyrrhotite preserves ductile deformation at all scales, displaying *durchbewegung* textures (e.g. Marshall and Gilligan, 1989) in hand samples (**Fig. 2.8a, b**) and, at a microscopic scale, corrugation lamellae/deformation twinning and strong anisotropy (**Fig. 2.7e**). Pyrrhotite mostly surrounds arsenopyrite and pyrite crystals (**Fig. 2.7c**) although, to a lesser extent, it is found in less deformed sections (**Fig. 2.7f**) in pyrrhotite-pyrite-chalcopyrite assemblages.

In these layers gold is mainly associated with arsenopyrite (Apy A in **Fig. 2.8**) and pyrite (Py A in **Fig. 2.9**), although not exclusively. Arsenopyrite A display syn-kinematic textures that are compatible with the high strain observed in the host rocks

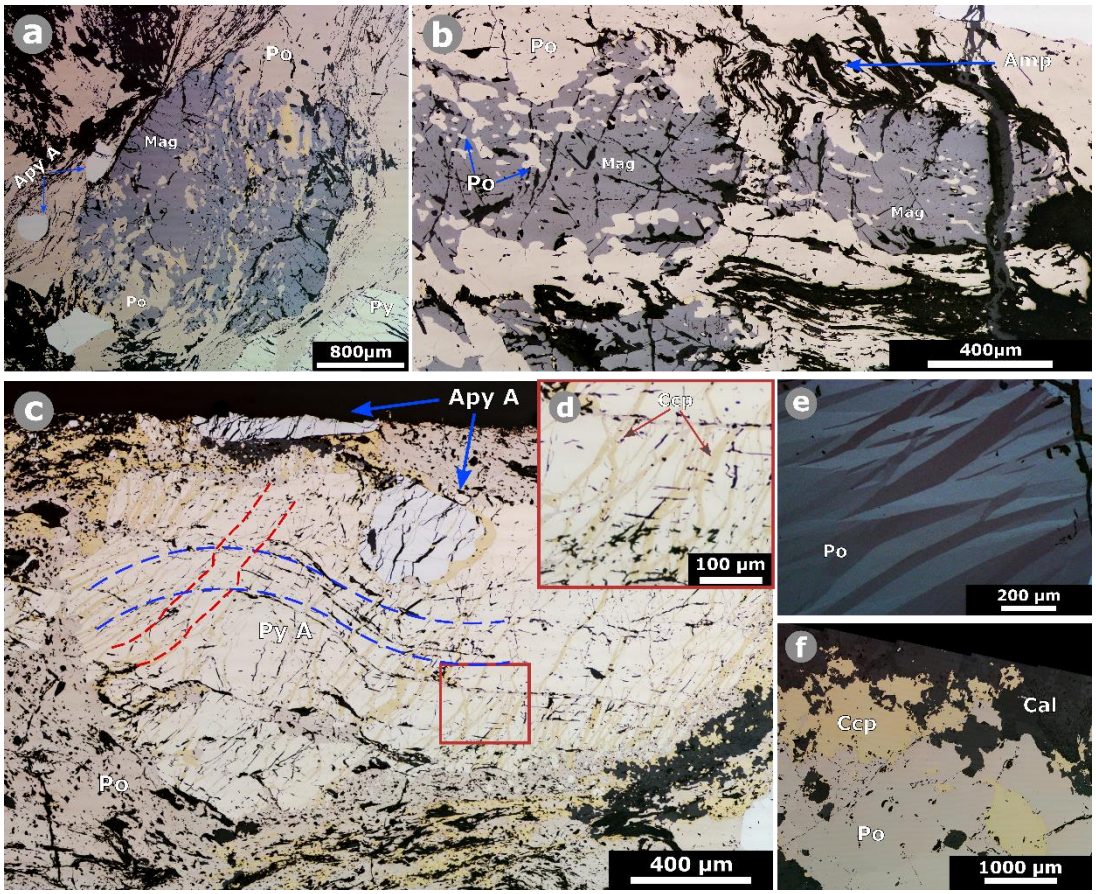

Figure 2.7. Composite microphotographs of ore petrography performed on cross sections from the massive sulfide horizons. **a.** and **b.** Sulfidation process in which alteration of magnetite to pyrrhotite occurs. Magnetite (grey) correspond to relics of the sulfidation process within pyrrhotite. **(c.)** composite image of 16 microphotographs (x5 magnification) showing pervasive brittle-ductile deformation, marked by the red and blue dashed lines. **d.** magnification of a section from figure (c.) showing a stock-work texture of late ore-stage chalcopyrite, filling fractures generated during brittle deformation. **e.** reflected light crossed nicols microphotograph of a pyrrhotite crystal section. The undulatory extinction is pronounced by the corrugation lamellae/deformation twinning. **f.** late-stage deposition of chalcopyrite around pyrrhotite in a low-deformed calcite-dolomite marble of the Monfurado Formation.

A small and localized arsenopyrite-rich layer (Apy B in **Fig. 2.8c**) was identified in a quartz-chlorite matrix in a 0.6m thick section of the M7 drill core (**Fig. 2.6f, g**). The relation between Apy B and the host rock is difficult to discern, nevertheless, it was possible to identify that the matrix is characterized by fine-grained anhedral quartz crystals and arsenopyrite is ubiquitously surrounded by chlorite with berlin-blue birefringence colors (**Fig. 2.6f**). Small and rare gold grains hosted in Apy B (**Fig. 2.6g**) and disperse in the quartz matrix (**Fig. 2.8n, o**) were identified, with no clear spatial relation to the MSL. The microscopic analysis of Apy A and Apy B suggests that they are homogeneous mineral phases, with no optical zonation, however, the backscatter electron images revealed a

faint compositional zonation, indicating a slight arsenic depletion towards the rims of Apy A (**Fig. 2.8g, h, i**).

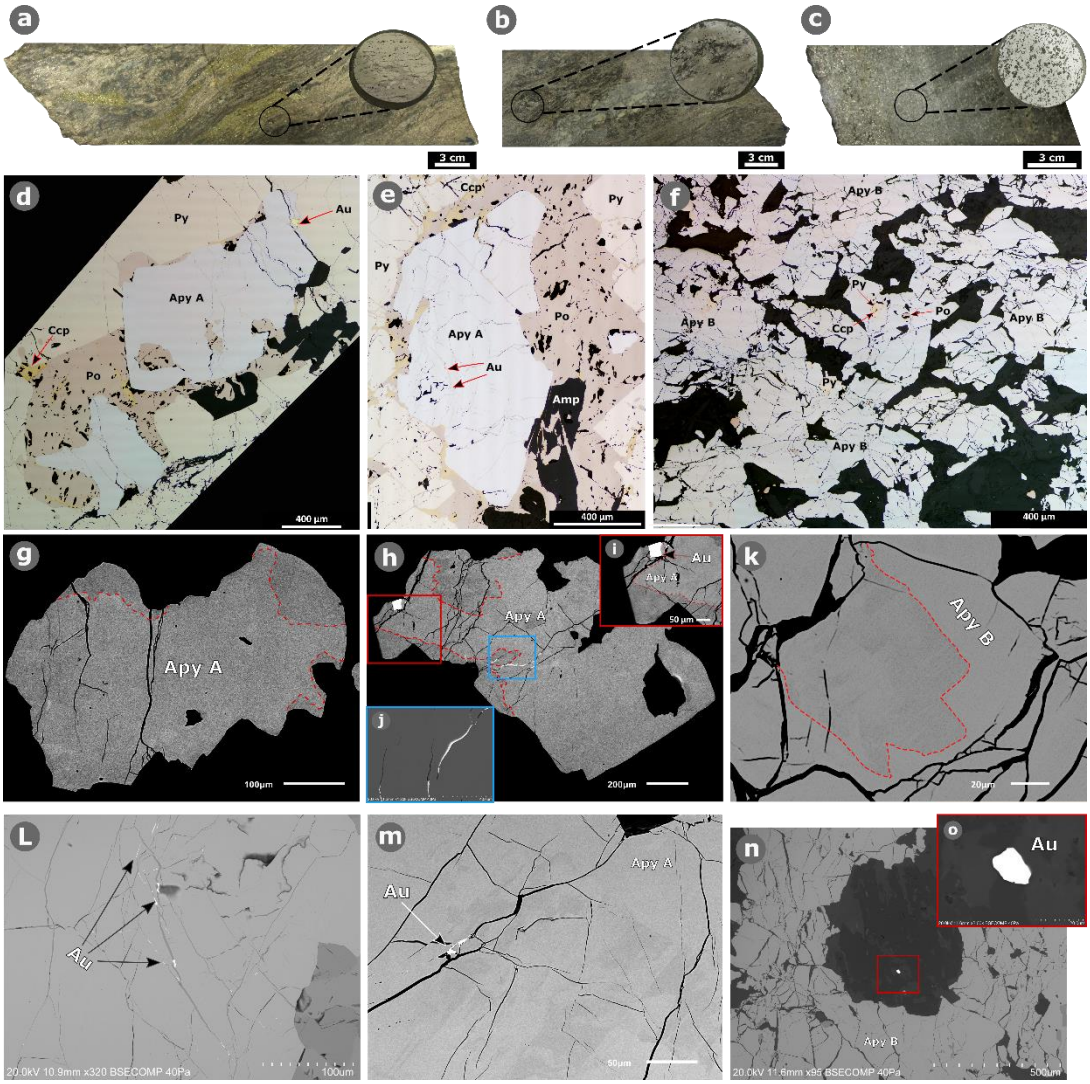

Figure 2.8. Representative samples, microphotographs and scanning electron microscopy (SEM) images of the main arsenopyrite paragenesis. **a.** massive sulfide horizon intersected by M5 drill core (@86 m) and one of the prepared polished drill core cross sections. **b.** massive sulfide horizon in a calcite-dolomite matrix intersected by M5 drill core (@87 m) and one of the prepared polished drill core cross sections. **c.** Massive arsenopyrite horizon intersected by M7 drill core (@123 m) and one of the prepared polished drill core cross sections. **d.** Composite image of 8 microphotographs (x5 magnification) from the cross section shown in (a.), in which gold occurs in arsenopyrite (ApyA) microfractures. **e.** Composite image of 6 microphotographs (x5 magnification) showing a massive sulfide layers (Po + Py + Apy) with gold particles being associated to fractures in arsenopyrite. **f.** Composite image of 6 microphotographs (x5 magnification) of an arsenopyrite-rich layers (Apy B) assemblage in a siliciclastic matrix. This image corresponds to the same cross section shown in (b.). **g.** SEM image of an arsenopyrite crystal (Apy A) from a massive sulfide layer in which it was possible to individualize a subtle zonation marked by the red dashed lines. Arsenopyrite rims are slightly impoverished in arsenic. **h.** SEM image of the same section shown in (d.) in which it is possible to identify gold (bright areas) distribution on arsenopyrite. Gold particles mainly occur in arsenopyrite rims (red square)

and as a fracture filling phase (blue square). Consistent zonation is individualized with a slight decrease in the arsenic content, marked by the red dashed lines. **i.** Zoom-in to the red square section from (h.), in which a 50 µm gold particle is identified as being associated to the Apy A arsenic depleted rim. **j.** Zoomed section of the blue square from (h.) in which fractures of arsenopyrite are filled by gold. **k.** SEM image of an arsenopyrite crystal (Apy B) from the arsenopyrite-rich layers in which it was possible to individualize a subtle zonation. The sample here presented corresponds to the same cross section shown in (c.) and (f.). **l.** SEM image showing distribution of gold inside arsenopyrite (Apy A) from a massivesulfide layers. **m.** SEM image showing distribution of gold inside arsenopyrite (Apy A) from a massive sulfide layer. **n.** SEM image of one free gold particle (red square) in a siliciclastic matrix from the arsenopyrite-rich layers shown in (c.) and (f.). **o.** Zoomed section to the free gold particle from (n.).

Gold grains are mostly found in arsenopyrite usually occurring as fracture filling in Apy A (**Fig. 2.8h to m**), and to a lesser extent in Py A (**Fig. 2.9c, d, g, h**). Ductile deformation in Py A crystals (**Fig. 2.7c**; blue dashed lines) is outlined by the presence of acicular amphibole, whereas brittle deformation is marked by perpendicular fracturing associated with micro-scale cataclasis (**Fig. 2.7c**; red dashed lines), affecting both Apy A and Py A. This type of deformation texture is particularly well preserved in the M4, M5 and M7 drill cores.

Chalcopyrite is abundant in the MSL, mostly found as fracture filling of Apy A, Py A and pyrrhotite (**Fig. 2.7c, Fig. 2.10b**). Other relatively late sulfide phases, such as inclusions of hedleyite and altaite, were identified mainly associated to pyrrhotite (**Fig. 2.10d, e**). Sphalerite is observed along some fractures of arsenopyrite (**Fig. 2.10c, g**), whereas galena is found in fractures along with pyrrhotite and/or chalcopyrite.

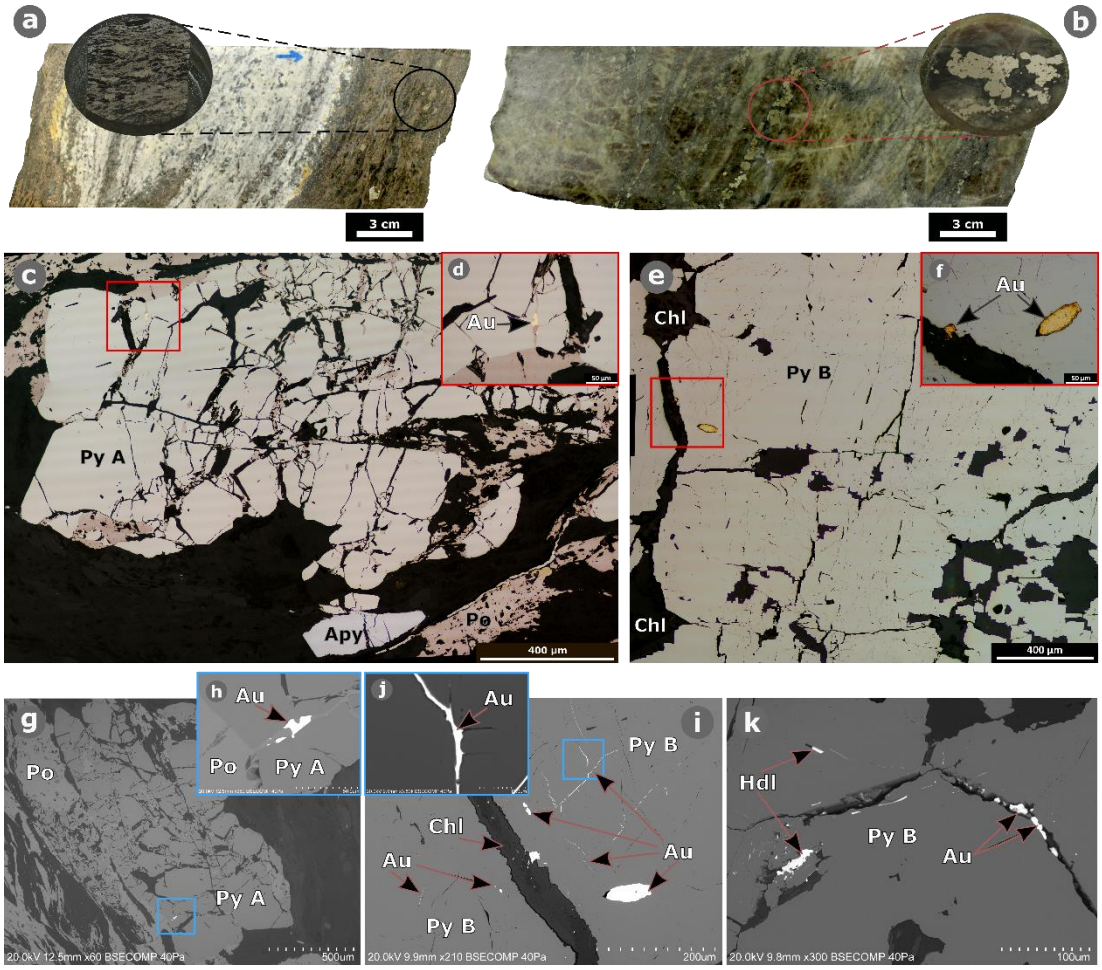

Figure 2.9. Representative samples, microphotographs and SEM images of the main pyrite paragenesis. **a.** massive sulfide layer in calcite-dolomite intercalations, intersected by M7 drill core (@110.5 m) and one of the prepared polished drill core cross sections. **b.** Pyrite-chlorite vein-type mineralization hosted in acid metavolcanic rocks. Drill core sample collected from M7 (@ 107.4 m) and one of the prepared polished drill core cross sections. **c.** Composite image of 10 microphotographs (x5 magnification) from the polished cross section shown in (a.). This section corresponds to a massive sulfide layer in which Pyrite A is identified. **d.** Zoomed section from the red square shown in (c.) in which a gold particle is identified in a pyrite fracture. **e.** Composite image of 8 microphotographs (x5 magnification) from the pyrite-chlorite vein structures shown in (b.). **f.** Zoomed in section from the red square shown in (e.) in which a large (80 µm) gold particle is individualized, along with a smaller particle. **g.** SEM imagery of the field of view shown in (c.), revealing that Py A do not show any relevant zonation. The blue square identifies the location of a gold. **h.** Zoomed in blue square section from (g.), the bright zone corresponds to a gold particle. **i.** SEM image showing the gold distribution and textures in Pyrite B. This image corresponds to the same field of view shown in (e.). Gold distribution in Py B fractures (blue square) were only possible to identify by SEM imagery, revealing a higher gold content. **j.** Zoomed blue square section from (i.) field of view, in which fracture filling by gold is observed. **k.** Gold and hedleyite distribution as fracture filling from Py B.

Gold-sulfides assemblages in acid metavolcanic rocks

Gold is also found in pyrite fractures (**Fig. 2.9i, j**) hosted in late veins crosscutting the acid metavolcanics, which exclusively occur at top of the MSL (Qz IIb; **Fig. 2.4c, d, e**). Pyrite hosting this gold mineralization type is addressed as Py B. The macroscopic analysis of hand samples suggests that pyrite is accompanied by chlorite and Qz IIb deposition and is controlled by late fracturing of the host rock (**Fig. 2.9b**).

Pyrite crystals (Py B) are usually euhedral, large (size > 400µm); **Fig. 2.9b, e**), and accompanied by intense chloritization of the host rock. At a microscopic scale, native gold is found in chlorite ± quartz assemblages (**Fig. 2.10a**), and filling thin fractures in Py B, as revealed by backscattered imagery (**Fig. 2.9i, j**). Hedleyite was also found in Py B microfractures (**Fig. 2.9k, Fig. 2.10f**).

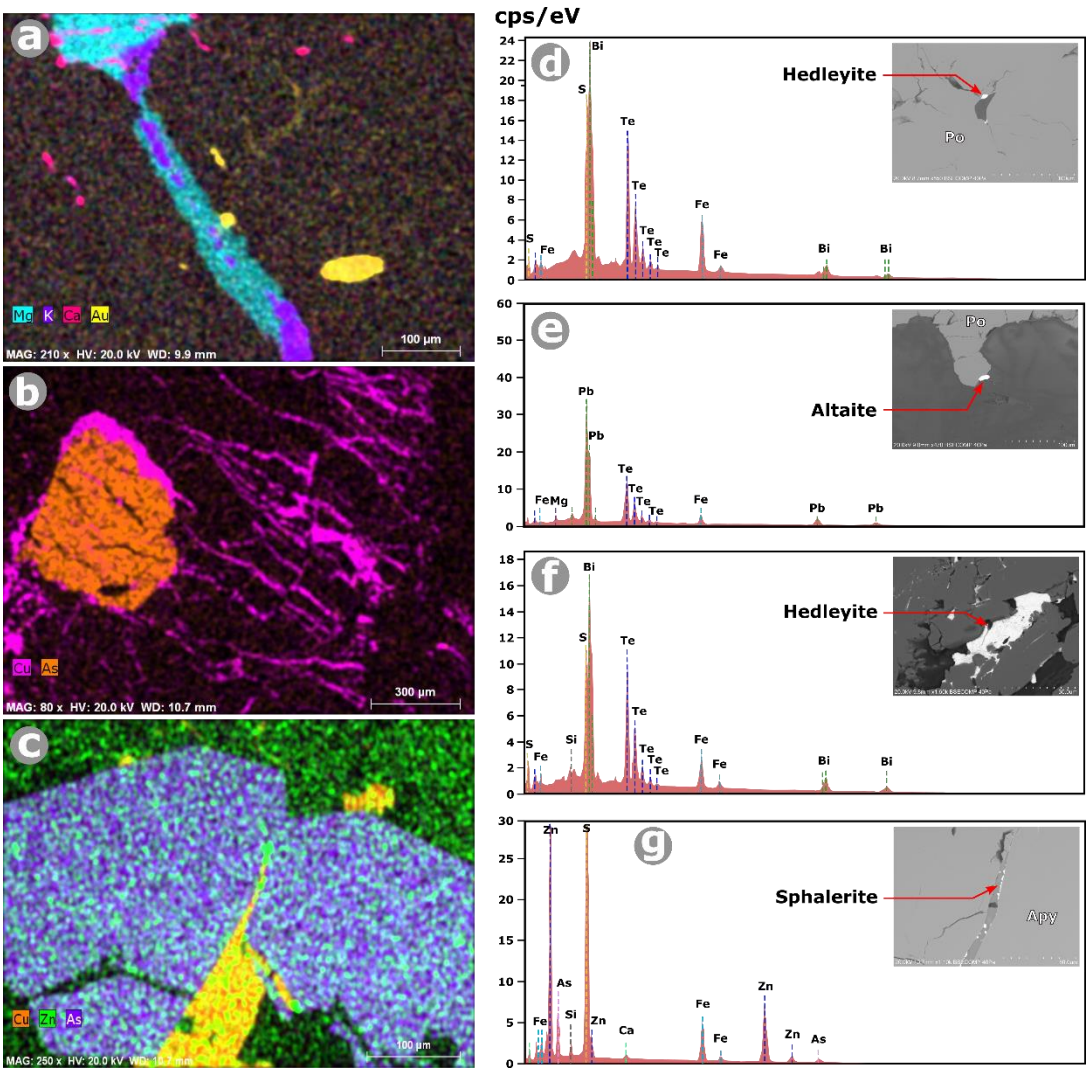

Figure 2.10. EDS mapping (a. to c.) and single spot analysis (d. to g.) of different sections and mineral phases representative of the Monfurado deposit paragenesis. **a.** EDS map of the field of view shown in Figure 3.9-(e.), in which the distribution of gold is observed (yellow) inside a pyrite crystal and a chlorite vein. **b.** EDS map acquired in the field of view shown in Figure 3.7-(c.) showing the stock-work distribution of

chalcopyrite, filling fractures in pyrite and arsenopyrite. **c.** EDS map of an arsenopyrite crystal from a sample collected from the massive sulfide layers, in which it is possible to identify late Cu and Zn mineral phases filling a fracture. **d.** Hedleyite identification in a pyrrhotite porosity. **e.** Altaite identification on the borders between pyrrhotite and a calcite-dolomite matrix. **f.** Hedleyite identification as fracture filling in Py B. **g.** Sphalerite identification filling a fracture of Apy A.

2.4.3 Sequence of crystallization

The sequence of crystallization for the Monfurado gold prospect (**Fig. 2.11**) was identified by petrography and descriptions of the textural features of the ores. Two main stages of metal input were identified: i) the pre-ore stage with an oxide and sulfide paragenesis and ii) the ore stage, in which gold mineralization is found in MSL, as well as in quartz-chlorite-pyrite veins hosted in the acid metavolcanic rocks.

Concerning the ore stage, two main types of gold mineralization were identified, as follows:

- Type i) correspond to gold in the MSL, which is ubiquitously composed of massive pyrrhotite and contains disseminated arsenopyrite (Apy A) and pyrite (Py A). These sulfide layers are sub-parallel to the surrounding iron-rich carbonate host rocks of the Monfurado Fm.. Gold deposition occurs in the rims and as fracture filling of arsenopyrite (**Fig. 2.8**) and, to a lesser extent, pyrite (**Fig. 2.9**). A single and constrained gold occurrence was found, in which Au is hosted in a layer composed almost exclusively of arsenopyrite (Apy B).
- Type ii) mineralization style is characterized by vein-hosted gold mineralization crosscutting the metavolcanic acid rocks. Gold is sometimes accompanied by Bi-Te phases (**Fig. 2.10**) and occurs as fracture filling of pyrite (Py B) associated with silicification and chloritization.

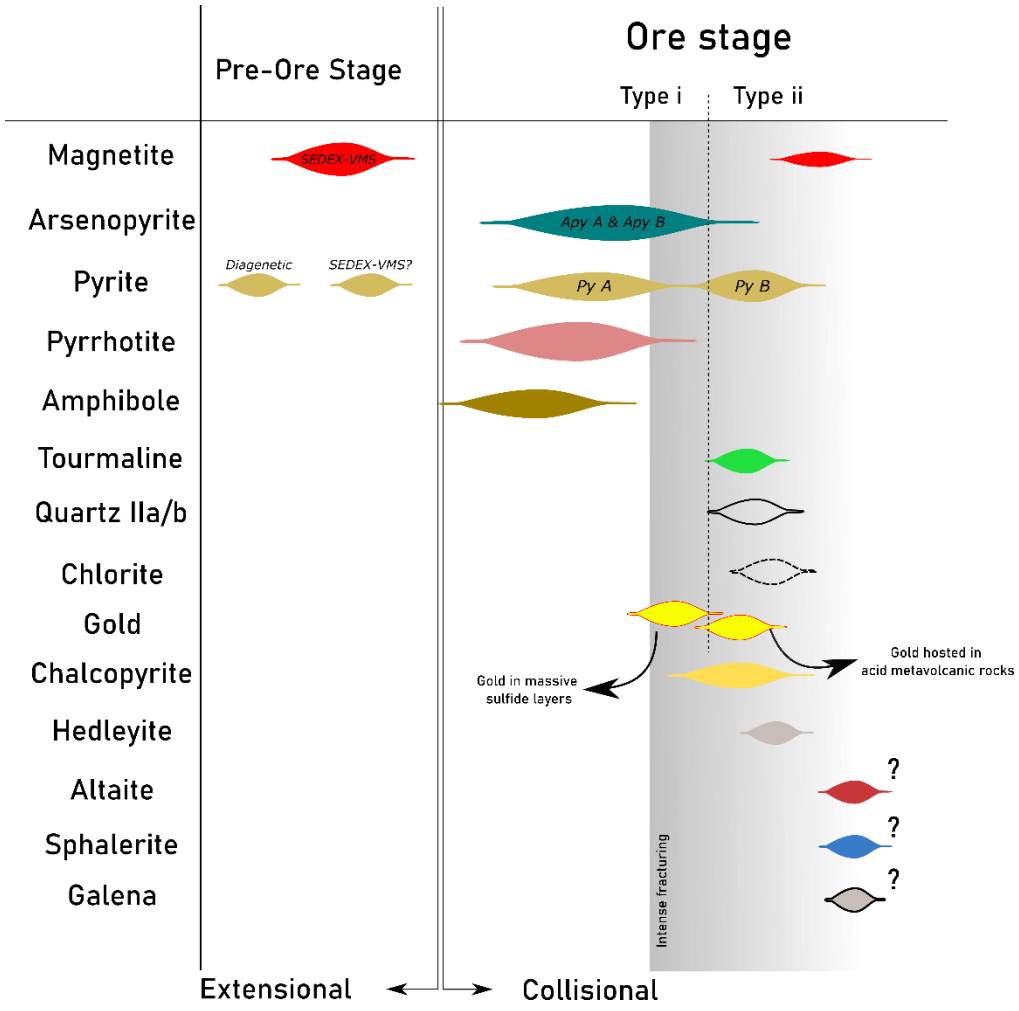

Figure 2.11. Mineral assemblages and sequence of crystallization representative of the Monfurado gold prospect.

2.4.4 Fluid inclusion studies

2.4.4.1 Fluid inclusion petrography

Quartz-hosted fluid inclusions are common throughout the studied samples, while inclusions hosted in tourmaline, barite and tremolite are rarer, smaller, and harder to study due to the color and cleavage of the host minerals. Quartz samples were prepared from veins crosscutting the acid metavolcanics and calcsilicate rocks of the Monfurado Fm., described as Qz IIb (**Fig. 2.4c; Fig. 2.12a-d**).

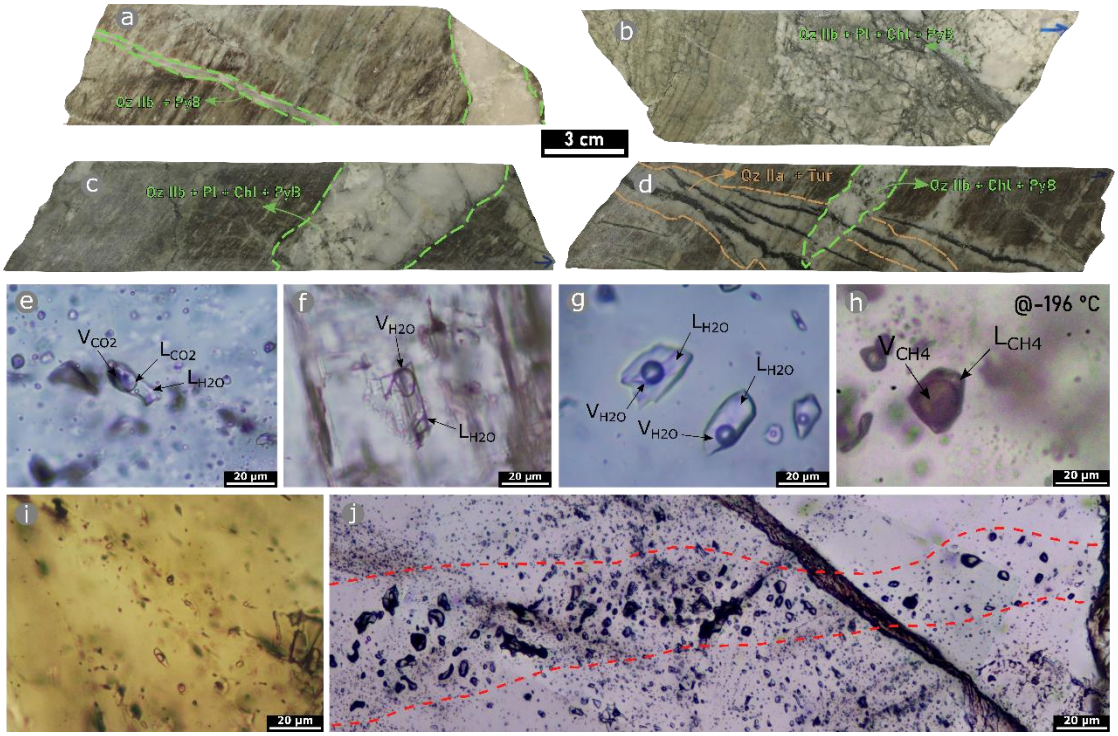

Figure 2.12. a. – d. Representative photos of the drill core samples that display the crosscutting relation among veins from which tourmaline and QzIIb were used in the fluid inclusion study. **e. – j.** Microphotographs representative of the fluid inclusion types individualized throughout this study. **e.** Lc-w three-phase aquo-carbonic fluid inclusions hosted in quartz. **f.** Lw_1 two-phase fluid inclusions hosted in a tremolite crystal. **g.** Lw_2 two-phase aqueous fluid inclusions hosted in Qz IIb. **h.** The figure shows a L_{CH4} fluid inclusions during the microthermometry studies under a temperature of -196 ºC. **i.** Lw1 fluid inclusions hosted in tourmaline prepared from the drill core sample shown in (d.). **j.** Composite microphotograph and image stacking showing a V_{CH4} fluid inclusion plane in Qz IIb prepared from the drill core sample shown in (a.).

Barite and tremolite samples were prepared from calcsilicate rocks of the Monfurado Fm., which is the result of regional metamorphism and metasomatic alteration of marbles. The crystals are disseminated in a tremolite dominated matrix. Tourmaline samples were prepared from quartz-tourmaline - Qz IIa veins (**Fig. 2.4d, e**) - which are cross-cut by Qz IIb veins in the acid-metavolcanic rocks (**Fig. 2.12d**).

Four types of fluid inclusions were identified, and the adopted fluid inclusion terminology is according to Boiron et al. (1992). Lc-w inclusions correspond to triphasic Fl´s ($L_{H2O-NaCl}$+L_{CO2}+V_{CO2}; **Fig. 2.12e**) with carbonic and aqueous volumetry varying significantly, occurring in transgranular fluid inclusion planes (FIP) in Qz IIb from veins that exclusively crosscut calcsilicate rocks. Lw_1 Fl´s occur as clusters of biphasic inclusions (L+V), hosted in baryte, tremolite (**Fig. 2.12f**) and tourmaline (**Fig. 2.12i**). Lw_2 inclusions are biphasic (L+V; **Fig. 2.12g**), mainly found in transgranular FIP in quartz-

plagioclase-chlorite-pyrite veins (Qz IIb; **Fig. 2.12a-d**). The volumetric proportion ratio between the liquid and vapor phase varies between 10-15 bubble vol. % for both Lw_1 and Lw_2 inclusions. The aqueous Lw_1 and Lw_2 fluid inclusions show a clear dominance over Lc-w and are found in samples from different depths.

Lastly, methane-rich fluid inclusions (**Fig. 2.12h**) hosted in quartz were identified in transgranular FIP (**Fig. 2.12j**) and were exclusively observed in samples from quartz veins (Qz IIb) crosscutting the acid metavolcanic-rocks from the Monfurado Fm. (**Fig. 2.12a-d**). These inclusions have an oval shape, with liquid CH_4 displaying a dark color and homogeneous aqueous H_2O-phase proportion (5%), at room temperature.

2.4.4.2 Microthermometry

Summarized microthermometry results are shown in **Table 2.2** and **Figure 2.13**, and the complete data is provided in the **Appendix C**. Lc-w fluid inclusions showed Tm_{CO2} ranging between -58.6ºC and -56.8ºC which indicates a near CO_2-pure phase, with minor concentrations of CH_4 (≈ 5% mol; Thiery et al., 1994; Maia et al., 2019). Th_{CO2} ranged from 0ºC to 24.6ºC and homogenization exclusively occurred into the liquid phase. Clathrate phases were identified in Lc-w inclusions, however, due to the small size and clustered occurrence of these FI´s, a correct measurement of Tm_{chl} was not possible, thus it was not possible to perform salinity and pressure estimations.

Ice melting temperatures measured in Lw_1 inclusions hosted in baryte range from -22.1 ºC to -3.7 ºC, and homogenization occurs into the liquid phase (L+V→L) with Th from 274ºC to 309ºC with a median of 290ºC. Salinities (eq. w(NaCl)) range from 6.0 to 23.1 eq. w(NaCl), with median pressure (*Md*) estimations of 5.0 MPa.

Lw_1 inclusions hosted in tremolite display Tm_{ice} between -16.6 ºC and -1.5 ºC, and Th ranging between 195ºC and 330ºC with a median of 305ºC. The calculated salinities range from 2.6 to 19.9 eq. w(NaCl) with a median of 12.1 eq. w(NaCl) and estimated pressures are in the range of 1.3 MPa to 11.8 MPa, with a median of 8.7 MPa. Fluid inclusions in tourmaline are small (5 µm), therefore only eight complete measurements were performed, with Tm_{ice} ranging between -6 ºC and -0.5 ºC and Th from 420ºC to 460ºC (*Md* = 425ºC). Correspondent salinities range from 0.9 to 9.2 eq. w(NaCl) with a median of 2.1 eq. w(NaCl), and the pressure estimations range from 27.6 MPa to 32.4 MPa, with a median of 29.8 MPa.

First ice melting temperatures (Te) measured in Lw_2 FI´s hosted by quartz, range from -33º C to -15 ºC, with a median of -26 ºC. Tm_{ice} ranges from -14.3 ºC to -0.1ºC and $Th_{(L+V→L)}$ are between 125 ºC and 327 ºC with a median of 226 ºC. Salinities range from

1.7 to 15.3 eq. w(NaCl), with a correspondent eq. w(NaCl) median of 6.5, with pressure estimations between 0.3 MPa to 19.7 MPa (*Md* = 3.1 MPa).

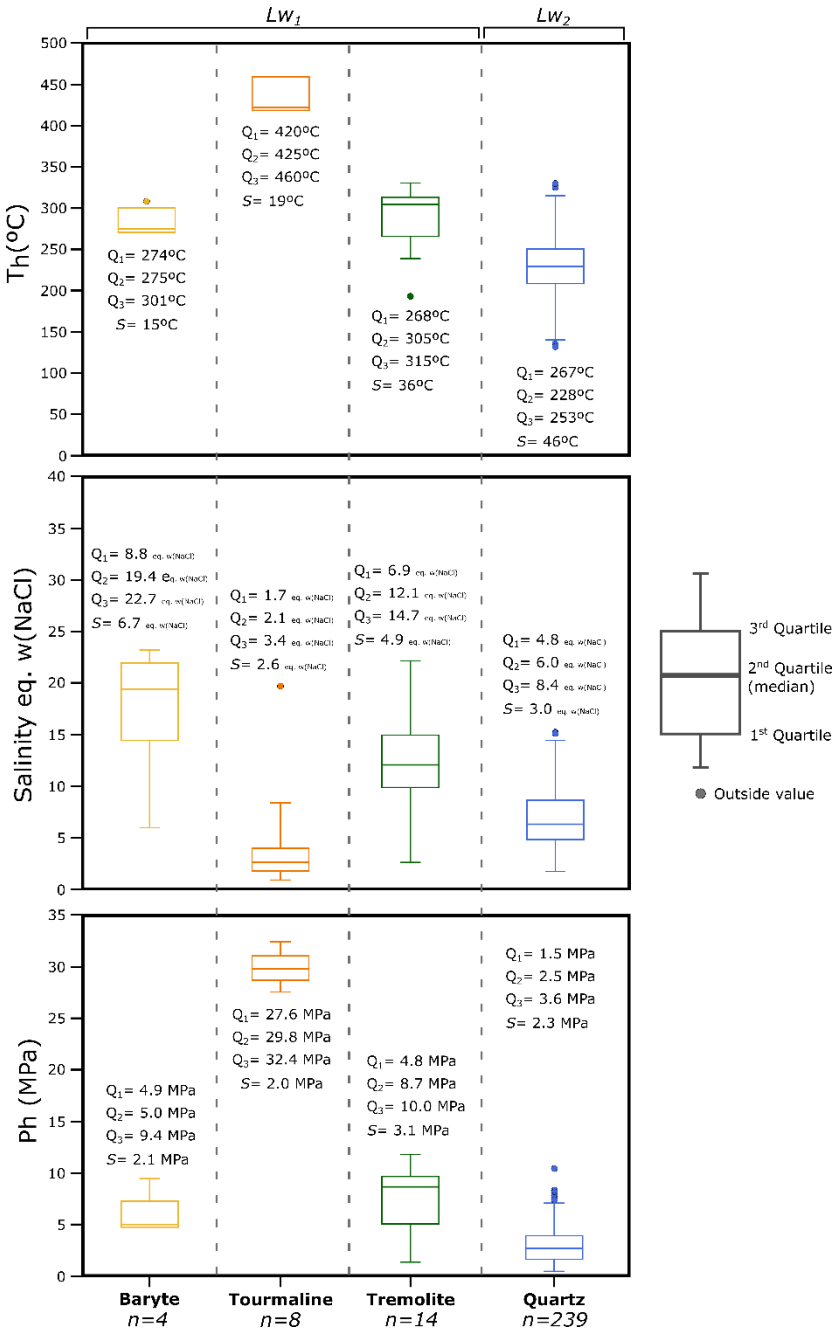

Figure 2.13. Boxplot diagrams in which representative P-T-x data from fluid inclusion microthermometry is plotted. 1st quartile, 2nd quartile, 3rd quartile and standard deviation (S) values are provided for each diagram. Data is here divided regarding the host-mineral, and the number of fluid inclusions studied in each one is provided by n.

Methane-rich fluid inclusions hosted in quartz (**Fig. 2.12h**) exhibited similar behaviors through the cooling runs (up to the -196.6 ºC), and although triple point temperature of

CH_4 was reached (-182.5 ºC) inclusions did not completely freeze. As shown by early studies from Roedder (1984), CH_4-rich fluid inclusions can sustain a metastable behavior through temperatures much lower than the triple point, thus not allowing salinity estimations. Microthermometry of these inclusions revealed phase transitions below the critical temperature of CH_4 (-82.6ºC), with Tm_{CH4} between -143.5 ºC and -136.3 ºC when homogenizing in the liquid-phase (L_{CH4}) and between -141.0 ºC and -136.0 ºC when homogenization into the vapor (V_{CH4}) phase occurs. Although the aqueous portion of the CH_4-rich inclusions is particularly small (approx. 5%), Tm_{ice} was limitedly observed in the range of -6.2 ºC and -0.9 ºC. Pressure at CH_4 homogenization was estimated between 0.35 MPa and 0.54 MPa for L_{CH4} and between 0.41 MPa and 0.55 MPa for V_{CH4} (**Table 2.2**).

Table 2.2. Summarized microthermometry results and descriptive statistics obtained from the fluid inclusions studies.

		Lc-w	**Lw_1**			**Lw_2**	**L_{CH4}**	**V_{CH4}**
		Quartz	Baryte	Tourmaline	Tremolite	Quartz	Quartz	
Te	Min.	N.D.	N.D.	N.D.	N.D.	-33	N.D.	N.D.
	Max.					-15		
	Mean					-24.9		
	Median					-25		
	Std. Dev.					3.9		
	1st Quartile					-27		
	3rd Quartile					-23		
Tm_{CO2}	Min.	-58.6	N.P.	N.P.	N.P.	N.P.	N.P.	N.P.
	Max.	-56.8						
	Mean	-57.4						
	Median	-57.3						
	Std. Dev.	0.5						
	1st Quartile	-57.8						
	3rd Quartile	-57.0						
Th_{CO2}	Min.	0	N.P.	N.P.	N.P.	N.P.	N.P.	N.P.
	Max.	24.6						
	Mean	10.1						
	Median	9.8						
	Std. Dev.	6.7						
	1st Quartile	4.5						
	3rd Quartile	16.7						
Tmice	Min.	-14.3	-21.2	-6	-16.6	-14.3	-6.2	N.D.
	Max.	-4.5	-3.7	-0.5	-1.5	-0.1	-0.9	
	Mean	-7.3	-12.6	-1.9	-7.6	-4.8	-3.05	
	Median	-6.0	-13.4	-1.2	-7.4	-4.0	-2.55	
	Std. Dev.	3.1	6.9	1.7	3.9	3.2	1.955	
	1st Quartile	-9.0	-20	-2	-10.1	-5.8	-5.375	
	3rd Quartile	-4.7	-4.9	-1	-5.8	-2.9	-1.225	
Th	Min.	N.D.	274	420	194.5	125.4	-143.5*[1]	-141
	Max.		309	460	330	327.0	-136.3	-136
	Mean		283	437.9	292.3	225.8	-140.9	-138.117
	Median		275	425	305	227.5	-141.8	-137.6

	Std. Dev.		15	19.3	35.5	46.0	2.2	1.4
	1st Quartile		274	420	267.5	203.2	-142.7	-139.45
	3rd Quartile		301	460	315.2	252.8	-138.3	-137.15
	Min.		6.0	0.9	2.6	1.7		
	Max.		23.1	9.2	19.9	15.3		
	Mean		17.0	3.2	11.1	6.8		
Salinity	Median	N.D.*	19.4	2.1	12.1	6.0	N.D.	N.D.
	Std. Dev.		6.7	2.6	4.9	3.0		
	1st Quartile		8.8	1.7	6.9	4.8		
	3rd Quartile		22.7	3.4	16.7	8.4		
	Min.		4.95	27.6	1.3	0.3	0.36*2	0.42
	Max.		9.4	32.4	11.8	11.9	0.54	0.55
	Mean		6.5	29.9	7.4	3.0	0.42	0.49
Ph(MPa)	Median	N.D.*	5.0	29.8	8.7	2.5	0.40	0.51
	Std. Dev.		2.1	1.9	3.1	2.3	0.06	0.04
	1st Quartile		4.95	27.6	4.7	1.5	0.38	0.46
	3rd Quartile		9.4	32.4	10.0	3.6	0.49	0.52

2.4.5 Sulfides, gold, and silicate geochemistry

A total of 278 EPMA spot analyses were performed in arsenopyrite (159), pyrite (48), gold (7), tourmaline (13), chlorite (18), and feldspars (23). Sample selection was done after a detailed mineralogical description and SEM-EDS analysis. The microprobe raw results can be consulted in **Appendix E**.

Arsenopyrite composition (**Table 2.3**) was acquired both for Apy A and Apy B, with As weight content below the typical stoichiometric composition for arsenopyrite (46 wt. %), with a median of 41.25 wt. % for the complete arsenopyrite data.

EPMA analysis considered the zoning observed in backscattered electron imagery, revealing Apy A arsenic content varying from 38.14 wt. % to 43.06 wt. % (*Md*= 41.55 wt. %) in crystal cores and from 40.05 wt. % to 41.26 wt. % (*Md*= 40.44 wt. %) at the rims.

Apy B revealed As contents ranging from 40.45 wt. % to 41.76 wt. % (*Md*= 41.06 wt. %) in the crystal cores and between 39.70 wt. % and 40.78 wt. % (*Md*= 40.03 wt. %) in the arsenic-depleted patchy areas (**Fig. 2.8k**). Although gold was analyzed as a trace element no concentrations above EPMA limits of detection (LOD; 308 ppm) were present. Both types of arsenopyrite displayed suitable values of Fe (< 34.3 at. %), for the application of the arsenopyrite geothermometer (Kretschmar and Scott, 1976).

Microprobe analysis of Py A and Py B (**Table 2.3**) revealed faint variation in As content, reinforcing their petrographic distinction (**Fig. 2.9**). Py A revealed arsenic values mostly below LOD (1734 ppm). Whereas, in Py B, the concentration of As ranges from 0.18 wt. % to 0.71 wt. % (*Md*= 0.32 wt. %). Although none of the above-mentioned pyrite types is considered As-rich, Py B shows a slight arsenic enrichment.

Gold hosted in Apy A from type i mineralization style revealed Au values ranging from 85.56 wt. % to 86.29 wt. % (**Table 2.4**), and Ag values between 13.15 wt. % and 13.56 wt. %. Low values of Fe were also detected, whereas the remaining analyzed elements are below EPMA LOD (disclosed in **Table 2.4**). Arsenopyrite-rich layers from type i mineralization display small gold grains with Au contents of 91.80 wt. % and Ag contents of 7.08 wt. %. Due to the small gold particle size, only one isolated gold particle was analyzed in these type i mineralized sections.

Gold filling microfractures in pyrite B from type ii mineralization shows a slightly different composition, with lower Au (between 80.54 wt. % and 82.90 wt. %) and higher Ag (between 16.83 wt. % and 18.68 wt. %) concentrations.

EPMA analysis were used to calculate gold fineness (Fisher, 1945), with results ranging from 863 to 868 for gold filling Apy A fractures from type i mineralization and from 812 to 831 for gold in Py B from type ii mineralization. The single free gold particle from type i showed the higher fineness value of 928.

Table 2.3. Representative EPMA analysis of arsenopyrite and pyrite crystals from the Type i and Type ii mineralization styles. The presented values correspond to the median values from several single-spot analysis (n) performed in each arsenopyrite crystal, in wt. % and atom per formula unit (a.p.f.u.). Structural formulae calculated on anionic basis of As + S = 1 for arsenopyrite, and S = 2 for pyrite.

Sample		**Apy Type**	**Mineral i-zation Style**	**S** (wt. %)	**As** (wt. %)	**Fe** (wt. %)	**S** (a.p.f.u)	**As** (a.p.f.u)	**Fe** (a.p.f.u)	***n****
005-31.3b	Arsenopyrite	Apy A	Type i	23.45	40.91	35.74	1.15	0.86	1.00	8
005-31.3b		Apy A	Type i	23.64	41.25	35.81	1.15	0.86	1.00	5
005-31.3b		Apy A	Type i	23.40	41.21	35.55	1.14	0.86	1.00	9
005-31.3b		Apy A	Type i	23.78	41.50	35.21	1.15	0.86	0.97	1
005-31.3b		Apy A	Type i	23.18	42.07	35.25	1.13	0.87	0.98	1
005-31.3b		Apy A	Type i	23.63	41.67	34.81	1.14	0.86	0.96	1
005-31.3b		Apy A	Type i	23.77	42.00	35.20	1.14	0.86	0.97	1
005-31.3b		Apy A	Type i	23.03	42.56	34.51	1.12	0.88	0.96	10
005-31.3b		Apy A	Type i	23.55	41.91	34.13	1.14	0.87	0.95	9
005-32.4b		Apy A	Type i	23.12	42.72	34.64	1.12	0.88	0.96	10
005-32.4b		Apy A	Type i	23.39	41.64	34.68	1.14	0.87	0.97	1
005-32.4b		Apy A	Type i	23.61	41.05	34.67	1.15	0.85	0.97	6
004-11.1b		Apy A	Type i	23.41	41.85	34.73	1.13	0.87	0.97	20
005-32.4c		Apy A	Type i	23.69	40.96	35.18	1.15	0.85	0.98	12
005-32.4c		Apy A	Type i	23.65	40.24	35.42	1.16	0.84	1.00	3
005-32.4c		Apy A	Type i	23.45	41.56	35.25	1.14	0.86	0.98	6
005-32.4c		Apy A	Type i	23.28	41.32	35.24	1.14	0.86	0.99	8
005-31.3b		Apy A rims	Type i	23.46	40.56	35.88	1.15	0.85	1.01	4
005-31.3b		Apy A rims	Type i	23.46	40.56	35.88	1.15	0.85	1.01	1
007-21.8a		Apy B	Type i	23.68	41.09	35.07	1.15	0.85	0.98	6
007-21.8a		Apy B	Type i	23.71	41.10	35.03	1.15	0.85	0.97	8
007-21.8a		Apy B	Type i	23.60	40.96	34.96	1.15	0.85	0.98	10
007-21.8a		Apy B	Type i	23.60	41.19	35.00	1.15	0.86	0.98	8
007-21.8a		Apy B rims	Type i	24.93	39.98	35.43	1.19	0.81	0.98	3
007-21.8a		Apy B rims	Type i	24.37	40.64	35.39	1.17	0.83	0.97	3
007-21.8a		Apy B rims	Type i	24.38	40.18	35.23	1.17	0.82	0.97	2
005-31.3b	Pyrite	Py A	Type i	53.720	0.24	45.35	2	0.002	0.97	6
007-10.3b		Py B	Type ii	53.76	0.57	45.22	2	0.008	0.97	18
007-10.3b		Py B	Type ii	53.89	0.24	45.48	2	0.004	0.97	15

Microprobe analysis was performed in mineral phases found on the host rocks of gold mineralization, as an auxiliary method to characterize the degree of hydrothermal alteration. This study was mostly applied to secondary minerals, namely feldspar from Qz IIb veins, and chlorite accompanying gold-bearing pyrite from to type ii mineralization (sample shown in **Fig. 2.9b**).

Feldspar characterization was performed using the microprobe analysis (**Table 2.5**; **Appendix E**) on samples of Escoural Fm. paragneisses, Carvalhal Fm. basic metavolcanic rocks, and veins crosscutting the Monfurado Fm acid metavolcanis rocks, based on An, Ab and Or percentages applying the classification diagram from **Figure 2.14a**. The results show that the paragneiss and basic metavolcanic rocks are mainly composed of orthoclase, whereas the analyzed feldspars from veins that crosscut acid metavolcanic rocks of rhyolite affinity are mainly albite (Ab84%; **Table 2.5**).

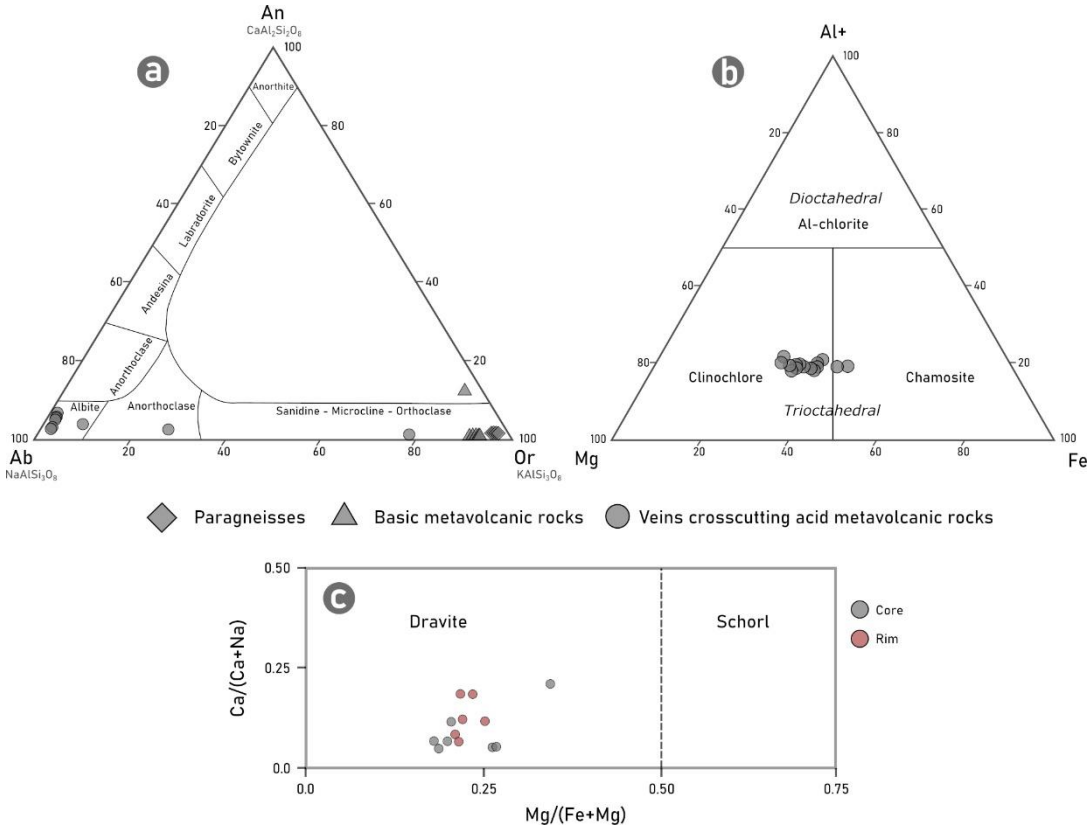

Figure 2.14. (**a.)** Feldspar ternary diagram classification with the plots of individual punctual EPMA analysis (provided in **Appendix E**) and following the nomenclature from Ribbe (1983). (**b.)** Chlorite compositional diagram (after Zane and Weiss, 1998) for the analysed chlorites from the Quartz-Chlorite-Pyrite-(Gold) veins hosted in acid metavolcanic rocks. (**c.)** Tourmaline classification using the ratios Ca / (Ca + Na) vs Mg / (Fe + Mg) (after Galbraith et al., 2009).

Chlorites were selected from samples of Qz IIb-plagioclase-pyrite veins that crosscut the acid metavolcanic rocks and are found to be related to type ii mineralization, therefore allowing the comparison between the chlorite geothermometer and the fluid inclusion data (**Table 2.2**) from Qz IIb (**Fig. 2.12 a – d**). The selected samples correspond to trioctahedral chlorites, classified as clinochlore by the Mg – Al^{+} - Fe classification diagram (**Fig. 2.14b**). The chlorite geothermometer was performed after Cathelineau (1988) using the EPMA data (**Table 2.5; Appendix E**).

Additionally, tourmaline crystals hosted in Qz IIa quartz crosscutting acid metavolcanic rocks (**Fig. 2.4d, e**) were selected for microprobe analysis (**Table 2.5**; **Appendix E**). The classification diagram using the Na / (Na + Ca) in the X site and Fe / (Fe + Mg) in the Y site (**Fig. 2.14c**) classify the samples as dravite.

Table 2.4. Representative EPMA analysis of gold particles from the Type i and Type ii mineralization styles.

Mineralization Type		**Type i)**				**Type ii)**		
Mode of occurence		**Filling Apy A fractures**			**Free particles**	**Filling Py B fractures**		
(wt. %)	**LOD (ppm)**	**1**	**2**	**3**	**4**	**5**	**6**	**7**
Au	5554	85.5623	86.2867	86.2194	91.8017	80.5427	82.8970	82.1758
Ag	861	13.5587	13.2686	13.1482	7.0838	18.6811	16.8268	17.4702
Fe	498	0.1247	0.1644	b.d.l.	0.1572	0.2442	0.1242	0.116
Cu	360	0.0368	b.d.l.	b.d.l.	b.d.l.	b.d.l.	b.d.l.	b.d.l.
Se	731	b.d.l.	b.d.l.	b.d.l.	b.d.l.	b.d.l.	b.d.l.	b.d.l.
Te	388	b.d.l.	b.d.l.	b.d.l.	b.d.l.	b.d.l.	b.d.l.	b.d.l.
Bi	1463	b.d.l.	b.d.l.	b.d.l.	b.d.l.	b.d.l.	b.d.l.	b.d.l.
Hg	3886	b.d.l.	b.d.l.	b.d.l.	b.d.l.	b.d.l.	b.d.l.	b.d.l.
Total		99.3163	99.8263	99.5365	99.1189	99.6290	99.9311	99.8498
Fineness	-	863	867	868	928	812	831	825

2.4.6 Sulfur Isotopes data ($\delta^{34}S_{CDT}$)

In the type i mineralization, the $\delta^{34}S_{CDT}$ was measured in arsenopyrite, pyrrhotite and pyrite. Apy A has values from 10.1 ‰ to 10.3 ‰ (**Table 2.6**), comparable to those found in Apy B, with a $\delta^{34}S_{CDT}$ of 10.6 ‰. Pyrite (Py A) shows signatures from 9.5 and 9.6 ‰ (**Table 2.6**), whereas pyrrhotite revealed lighter $\delta^{34}S_{CDT}$ values, from 8.5‰ and 9.7 ‰. In type ii mineralization, the $\delta^{34}S_{CDT}$ of the pyrite (Py B) shows a value of 10.2 ‰.

To compare $\delta^{34}S_{CDT}$ signatures, pyrites from the pre-ore stages were selected for sulfur source differentiation. Pyrites ubiquitously disseminated in the marbles, possibly diagenetic, yield $\delta^{34}S_{CDT}$ signature of 13.7 ‰ heavier than that of ore stage sulfides. The pyrites interpreted as being contemporary of the SEDEX-VMS iron mineralization events

display contrasting $\delta^{34}S_{CDT}$ signatures of 3 ‰ (**Table 2.6**) lighter than those of the ore-stage.

Table 2.5. **(next page).** Representative EPMA analysis (wt. %) of chlorite, tourmaline and feldspars. The presented values correspond to the average values from several single-spot analysis (n) performed in each phase. Additionally, standard deviation (σ) values of the analysis are provided in separate columns. For chlorite, the average temperatures are presented according to Chathelineau (1988) empirical geothermometric equation and structural formula was calculated using the WinCcac software from Yavuz et al. (2015), based on 14 oxygens. The structural formula for plagioclase and alkali feldspars was calculated based on 32 oxygens, and tourmaline in the basis of 29 oxygens.

Lithology	Quartz-Chlorite-Pyrite-(Gold) veins hosted in acid metavolcanic rocks					
Mineral	Chlorite					
	n=7	σ	n=9	σ	n=2	σ
Element (wt. %)						
SiO_2	28.9	0.3	28.3	0.6	27.9	0.6
TiO_2	0.1	0.0	0.0	0.0	0.0	0.0
Al_2O_3	17.6	0.3	17.8	0.7	20.4	0.5
FeO	20.1	0.3	23.0	2.1	17.6	0.4
MnO	0.2	0.0	0.2	0.0	0.2	0.0
MgO	18.3	0.4	16.1	1.3	19.7	0.1
CaO	0.1	0.0	0.1	0.0	0.1	0.0
Na_2O	0.0	0.0	0.0	0.0	0.0	0.0
K_2O	0.0	0.0	0.0	0.0	0.0	0.0
Total	85.3	0.9	85.6	0.7	86.1	0.5
Formula O=14						
Z						
Si	3.0	0.0	3.0	0.1	2.9	0.1
Al^{IV}	1.0	0.0	1.0	0.1	1.1	0.1
Total (IV)	4.0	0.0	4.0	0.0	4.0	0.0
R						
Al^{VI}	1.2	0.0	1.3	0.1	1.3	0.0
Ti	0.0	0.0	0.0	0.0	0.0	0.0
Cr	0.0	0.0	0.0	0.0	0.0	0.0
Fe^{3+}	0.0	0.0	0.0	0.0	0.0	0.0
Fe^{2+}	1.8	0.0	2.1	0.2	1.5	0.0
Mn	0.0	0.0	0.0	0.0	0.0	0.0
Mg	2.9	0.1	2.5	0.2	3.0	0.0
Total (VI)	5.9	0.0	5.9	0.0	5.9	0.0
Total	9.9	0.0	9.9	0.0	9.9	0.0
Fe/(Fe + Mg)	0.4	0.0	0.4	0.0	0.3	0.0
Mg + Fe	4.6	0.1	4.6	0.1	4.5	0.0
Mg/(Mg+Fe)	0.6	0.0	0.6	0.0	0.7	0.0
Al-chl (%)	18.6	0.4	19.0	0.8	20.7	0.4
Fe-chl (%)	32.5	0.8	37.5	3.4	28.4	0.0
Mg-chl (%)	48.9	1.1	43.5	3.4	50.9	0.4
Geothermometer (ºC)*	244.1	5.1	251.3	17.0	290.0	19.0

Lithology	Acid metavolcanic rocks			
Mineral	Tourmaline			
	Rim (n=6)	σ	Core (n=7)	σ
Element (wt. %)				
SiO_2	37.2	0.21	37.4	0.38
TiO_2	0.8	0.42	0.5	0.50
Al_2O_3	30.2	0.86	30.6	1.61
FeO	4.7	0.29	4.9	1.49
MgO	9.1	0.23	8.8	0.28
CaO	0.6	0.25	0.4	0.28
Na_2O	2.4	0.09	2.5	0.14
Total	85.0	0.38	85.2	0.49
Formula O=29				
B				
	3.0	0.00	3.0	0.00
Si	6.1	0.02	6.1	0.03
Ti	0.1	0.05	0.1	0.06
Al	5.8	0.13	5.9	0.25
Fe(ii)	0.6	0.04	0.7	0.21
Mn	0.0	0.00	0.0	0.00
Mg	2.2	0.05	2.1	0.06
Ca	0.1	0.04	0.1	0.05
Na	0.8	0.03	0.8	0.04
K	0.0	0.00	0.0	0.00
Total	18.8	0.04	18.8	0.06

Lithology	Paragneiss – Escoural Fm.		Basic metavolcanic rocks		Quartz – Feldspar – Chlorite veins in acid metavolcanic rocks	
Mineral	Feldspars					
	n=5	σ	n=8	σ	n=10	σ
Element (wt. %)						
SiO_2	63.4	1.20	64.18	0.46	66.77	1.18
TiO_2			0.03	0.00		
Al_2O_3	18.7	0.43	18.82	0.22	20.60	0.56
FeO	0.1	0.00	0.06	0.00	0.07	0.01
CaO	1.2	1.20	0.02	0.02	0.85	0.37
Na_2O	0.4	0.16	0.57	0.23	9.71	2.64
K_2O	16.2	0.49	16.17	0.40	1.87	3.88
BaO	0.4	0.11	0.45	0.13	1.73	0.00
Total	99.6	1.07	100.23	0.50	99.99	0.37
Formula O=32						
Si	11.8	0.07	11.89	0.03	11.77	0.06
Al	4.1	0.04	4.11	0.04	4.28	0.06
Fe(ii)	0.0	0.00	0.01	0.00	0.01	0.00
Ca	0.3	0.25	0.00	0.00	0.16	0.07
Na	0.2	0.06	0.21	0.08	3.30	0.88
K	3.9	0.08	3.82	0.10	0.44	0.92
Ba	0.0	0.01	0.03	0.01	0.13	0.00
Total	20.1	0.06	20.07	0.02	19.96	0.05
An (%)	2.3	4.50	0.11	0.10	4.11	1.75
Ab (%)	3.7	1.46	5.13	2.03	84.66	22.29
Or (%)	94.0	4.62	94.77	1.96	11.22	23.56

2.5 Discussion

2.5.1 Depositional stages

The Monfurado prospect is not only an interesting and complex case study from the Escoural gold district (**Fig. 2.1b, d**), as it is also an example of gold deposition that can be compared to worldwide Orogenic Gold deposits. In summary, two main gold mineralization types characterize the deposit: Type i mineralization is parallel to the host rock layering, with gold found in arsenopyrite (Apy A and Apy B) and pyrite (Py A) disseminated in massive sulfide layers (**Fig. 2.8a-c**) and mostly deposited in microfractures in those minerals (**Fig. 2.8l, m**). The presence of magnetite substitution by pyrrhotite suggest that fluid-rock interactions might have assisted gold deposition in type i mineralization.

Type ii mineralization occurs in veins parallel to bedding, in which gold is found to be hosted in pyrite (Py B) microfractures, usually accompanied by chlorite and quartz, and found in veins exclusively crosscutting the acid metavolcanic unit. The development of these veins is structurally controlled by late brittle deformation.

The identification of the paragenetic sequence is supported by the petrographic and mineralogical data, and is reinforced by the isotopic and geochemical data, constituting what is here described as the main gold stage (**Fig. 2.11**).

Table 2.6. Sulfur isotope data ($\delta^{34}S$) for the main sulfide phases of the Monfurado deposit.

Sample	Mineralization Style	Mineral	$\delta^{34}S_{CDT}$ (‰)
M7-15	Type i	Apy A	10.1
M4-11	Type i	Apy A	10.3
M5-32	Type i	Py A	9.6
M5-31	Type i	Py A	9.5
M5-30	Type i	Po	9.7
M4-11	Type i	Po	9.1
M7-15	Type i	Po	8.5
M7-21	Type i	Apy B	10.6
M7-10	Type ii	Py B	10.2
M7-19	Volcanogenic	Volcanogenic Pyrite	3
M4-14	Diagenetic	Diagenetic Pyrite	13.7

Type i mineralization has never been described for the Escoural gold district (**Fig. 2.1b, d**), whereas type ii shows a mode of occurrence similar to what is found in other deposits of the district (e.g. Casas Novas, Chaminé) where gold mainly occurs in quartz lodes, with

chloritization of the host rocks, in arsenopyrite-loellingite-pyrite-gold assemblages associated with native bismuth and bismuthinite (Ribeiro et al., 1993). Such features are consistent to type ii mineralization at the Monfurado prospect, where gold deposition is sometimes accompanied by hedleyite (**Fig. 2.9k**; **Fig. 2.10f**)

When inspecting gold fineness (**Table 2.4**) it becomes evident that gold from type i shows higher values (863-868) than those from type ii gold (812-831) which reinforces the distinct petrographic criteria.

2.5.2 Thermal and fluid evolution constraints

Fluid inclusion studies are extremely important in identifying the P-T-V-x conditions of the fluids responsible for gold transport in orogenic gold deposits, as well as in understanding host rock interactions promoted by those fluids, such as sulfidation and carbonation (Palin and Xu, 2000; Goldfarb et al., 2001; Goldfarb et al., 2005; Hodkiewicz, 2008; LaFlamme et al., 2018; Petrella et al., 2020). Nevertheless, the discussion regarding the fluid evolution of orogenic gold deposits is quite vast and presents weaknesses pointed out in detail by Goldfarb et al. (2005) and Goldfarb and Groves (2015). Ubiquitously, H_2O-CO_2-H_2S($\pm CH_4 \pm N_2$) reduced fluids, with low salinities have been identified in phanerozoic orogenic gold deposits, with temperatures ranging from 250ºC to 400ºC (Bierlein and Crowe, 2000; Goldfarb et al., 2005; Bodnar et al., 2014; Wyman et al., 2016).

The settings in which orogenic gold deposits occur are commonly associated with metasedimentary successions and metabasaltic rocks (Pitcairn et al., 2015) affected by greenschist to amphibolic regional metamorphism, displaying complex tectonic activity in which cyclic shear re-activations leads to successive fracturing and filling during several fluid circulation stages. This tectonism usually results in intricate fluid inclusion assemblages with unclear relation with ore deposition stages. The complexity of these hydrothermal systems often leads to uncertain fluid inclusion data interpretations, with unclear identification of the fluids responsible for ore transport (Groves et al., 2019).

Areas as the Monfurado gold prospect are examples of the above-mentioned fluid complexity, in which interpretation of fluids is highly conditioned by the geodynamic processes that occurred in pre- and post-ore deposition times. Nevertheless, the identification and characterization of the dominant fluids present in this hydrothermal system were possible. Combining the fluid inclusions results with arsenopyrite and chlorite geothermometer estimations allowed to describe the thermal evolution of the system.

Lw_1 inclusions (**Fig. 2.13**), especially those studied in tourmaline (dravite; **Fig. 2.14**), reflect the presence of fluids with higher temperature (> 400ºC) and under higher pressure (> 30MPa), contrasting to Lw_2 inclusions. Most quartz samples in which Lw_2, L_{CH4}/V_{CH4} were

identified correspond to late quartz-chlorite-feldspar veins that crosscut acid metavolcanic rocks (**Fig. 2.12a-d**) in which gold-bearing Py B (**Fig. 2.9b**) is found. Lw_2 fluid inclusions are ubiquitous in quartz (Qz IIb), and microthermometry revealed relatively low temperatures (*Md* = 230ºC) and low salinities (*Md* = 6.0 % eq. w(NaCl)), which are values compatible with the ones described for other orogenic gold deposits (**Fig. 2.15a**; Wilkinsson, 2001; Bodnar et al., 2014). Furthermore, Cathelineau (1988) geothermometer was applied to selected chlorite crystals, sampled from the same veins in which Lw_2 inclusions were identified (**Fig. 2.12a-d**). The chlorite geothermometer indicates temperatures ranging from 229ºC to 309ºC (**Table 2.5; Appendix E**), with average temperatures of 253ºC, which are compatible to those obtained from Lw_2 inclusions hosted in quartz (**Fig. 2.15a**).

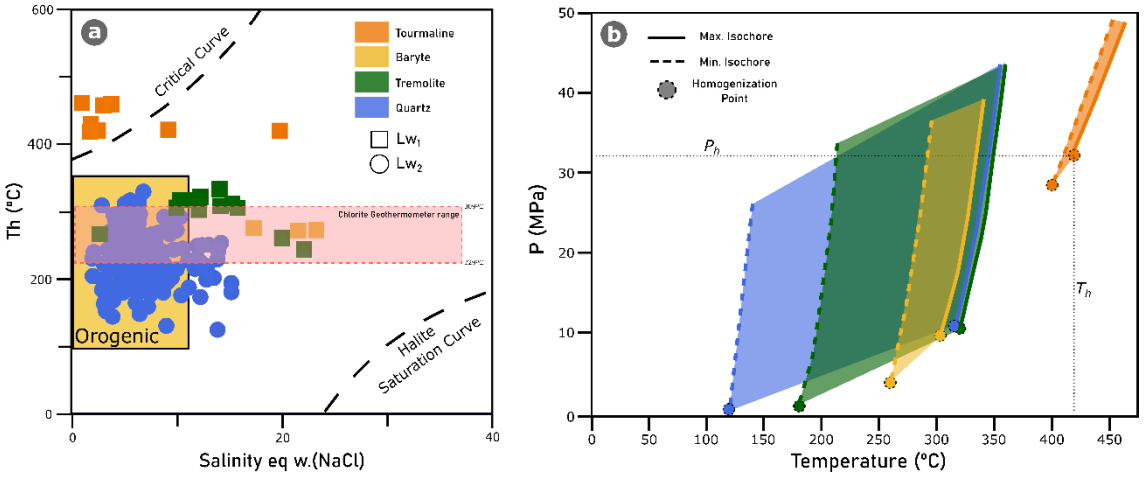

Figure 2.15. (a.) Th (°C) vs Salinity (eq. w(NaCl)) plot of the gathered data from fluid inclusion studies. The fields represent the temperature and salinity boundaries for the fluids identified as being associated to those metallogenic environments (after Wilkinson, 2001; Bodnar et al., 2014). The red rectangle marks the range of temperatures obtained for the chlorite geothermometer. **(b.)** P-T reconstruction based on the data collected from the studied fluid inclusions.

Arsenopyrite geothermometer was performed using the EPMA data following Kretshmar and Scott (1976) criteria. This methodology was applied assuming a pyrite-arsenopyrite equilibrium (**Table 2.7**). Crystal cores of Apy A show an As at. % content from 28.05 at. % to 30.43 at. % corresponding to a temperature range from 239ºC to 372ºC that are overlapped by the obtained temperatures for Apy B, indicating temperatures ranging from 252ºC to 308ºC (**Fig. 2.16**) and a mean log a(S_2) = -10.8 for crystal cores.

The slight As depletion found in Apy A crystal rims leads to a range of estimated temperatures from 213ºC to 279ºC (**Table 2.7**), suggesting a decrease in temperature from the center towards the rims. Sulfur fugacity also decreases from the cores (log a(S_2) = -10.5)

to the rims (log a(S_2) = -12.73; **Fig. 2.16; Table 2.7**) as a consequence of the lower arsenic contents.

Apy B also displayed As depleted areas with a patch zonation, to which temperature estimations from 188ºC to 246ºC and mean log a(S_2) = -12.7 (**Table 2.7**) were obtained.

Both arsenopyrites from massive sulfide layers (Apy A) and arsenopyrite-rich layers (Apy B) from mineralization type i (**Fig. 2.8c**) revealed similar arsenopyrite geothermometer (**Fig. 2.16**) and sulfur activity estimations which indicates that the processes that led to their formation are very similar. Additionally, the progressively lower P-T registered by fluid inclusions (**Fig. 2.15b**), is consistent with the chemical composition and correspondent geothermometer estimations attributed to arsenopyrite deposition.

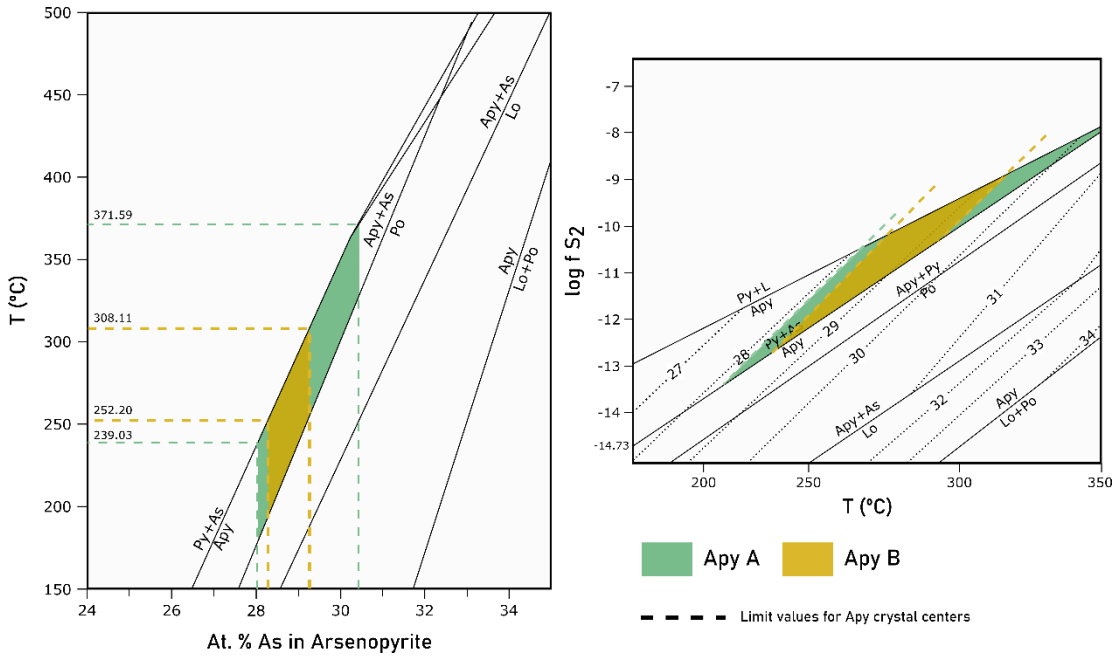

Figure 2.16. Arsenopyrite geothermometer (modified by Rajabpour et al., 2017 after Kretschmar and Scott, 1976) in which: the upper diagrams show the projection of T(°C) vs As at. % content of arsenopyrite in the arsenopyrite-pyrite stability field. Single plots are shown both for Apy A and Apy B crystal cores. Log fS_2 vs T(°C) projection for arsenopyrite chemical composition is shown in the right-side diagram.

2.5.3 Sulfide $\delta^{34}S_{CDT}$ signatures

Sulfur isotopic composition of sediment-hosted orogenic gold deposits, such as the Escoural gold district, share a similar trend to the seawater sulfate curve throughout geological time (Chang et al., 2008; Groves et al., 2020). Such evidence suggests that sulfur in these deposits is originated from reduced seawater sulfate, fractionated by biogenic or abiogenic processes, which justifies the lighter $\delta^{34}S_{CDT}$ signatures found in sulfides from orogenic gold deposits.

Considering this, the gathered $\delta^{34}S_{CDT}$ isotopic signatures of sulfides from the Monfurado ore assemblage suggest a sulfur fractionation of around 10 ‰ to 20 ‰ (coherent with abiogenic fractionation) from the initial seawater sulfate signature (Chang et al., 2008), considering the Neoproterozoic carbonaceous metasediments from Escoural Fm. to be the main sulfur provider to the system. The narrow $\delta^{34}S_{CDT}$ values of the ore assemblage sulfides (**Table 2.6**), from 8.5 ‰ to 10.6 ‰ (**Fig. 2.17**), indicate that although local paragenetic differences exist (**Fig. 2.11**), they share the same sulfur sources and are affected by the same, or at least similar, sulfur fractionation processes (LaFlamme et al., 2018). Furthermore, the narrow $\delta^{34}S_{CDT}$ variation, although revealing a slight shift in pyrrhotite towards lower $\delta^{34}S_{CDT}$ values, suggest that the variation of fO_2 in the fluid was not significant for major destabilization of $Au(HS)_2^-$, and therefore fluid oxidation is unlikely a major control on Au deposition as suggested by the sulfidation reaction modelling presented by Petrella et al. (2021).

The data obtained by different authors, for other NW Iberian gold districts, both in Portugal and Spain, are displayed in **Figure 2.17**. Similar $\delta^{34}S_{CDT}$ signatures were obtained in the NW Spain Vilalba gold district (Martinez-Abad et al., 2015) and Llamas de Cabrera (Gómez-Fernández et al., 2012), both hosted in Lower Palaeozoic metasediments, with positive values between 2.7 ‰ and 10.9 ‰ and from 8 ‰ to 23.1 ‰, respectively. Gold districts in NW Portugal, hosted in granite rocks, have distinct $\delta^{34}S_{CDT}$ values with contrastingly negative signatures. Examples of these differences are, the Limarinho deposit (-9.2 ‰ – -1.6 ‰; Fuertes-Fuente et al., 2016) and the Santo António (Penedono) gold deposit (-5.3 ‰ – -3.6 ‰; Neiva et al., 2019).

This study found meaningful $\delta^{34}S_{CDT}$ differences in massive pyrites, possibly related with the SEDEX-VMS ores, and diagenetic pyrites hosted in marbles from the Monfurado Fm., with $\delta^{34}S_{CDT}$ values of 3 ‰ and 13.7 ‰ respectively (**Fig. 2.17**). The difference of these values, when compared to sulfide phases representative of the ore stage, suggest a significant change in the sulfur fractionation throughout the geodynamic evolution of the area.

2.5.4 Possible gold source and deposition mechanisms

The geodynamic controls of OMZ favored the formation and preservation of several types of mineral deposits, from the ones related to the early rift stage (e.g. Cambrian SEDEX-VMS Montemor-o-Novo iron ore deposits) to the Carboniferous orogenic gold deposits under study. The compressional and oblique collision developed crustal-scale strike-slip shears, such as the MNSZ, and supra-crustal thermal anomalies that promoted the hydrothermal fluid circulation through dehydration of metal-rich sedimentary basins. Such crustal anisotropies acted as a pathway for metal-enriched metamorphic fluids, and at the same time conditioned the regional tectono-metamorphic regimes that favored the formation of orogenic gold systems

(Goldfarb and Groves, 2015; Groves et al., 2020). Combining these geodynamic conditions and considering the gathered data in this research, it is proposed that the Monfurado case study displays a distinct orogenic gold occurrence in SW Iberia, in which a supracrustal metamorphic model (Groves et al., 2019) is the most adequate to explain the genesis of these deposits (Goldfarb and Groves, 2015; Groves and Santosh, 2016). The Escoural gold district displays structural features that correlate it with an orogenic gold model, and the research here presented suggests that local redox destabilization promoted by fluid-rock interactions are the main control on gold deposition related to type i mineralization, which is the main type at the Monfurado gold prospect. In other Escoural gold district deposits, such as the Casas Novas, Chaminé and Braços, gold mineralization is mainly hosted in quartz-arsenopyrite veins associated with brittle deformation and crosscutting the Escoural Fm. (Ribeiro, 1993; Inverno, 2001; Lopes et al., 2015; Lopes, 2015), whereas in the Monfurado prospect two gold mineralization styles were identified.

Through this work we evidence for metamorphic derived fluids being responsible for Au transport at the Escoural gold district were found. The most likely origin for such fluids is the devolatilization of the Neoproterozoic metasedimentary basement, locally represented by the Escoural Fm., which could also be a key provider of Au and S. Nevertheless, Pitcairn et al. (2015) recently discussed the possibility of trace amounts of

Au, at the ppb levels, being remobilized from adjacent metabasaltic host rocks, such as the ones belonging to the Carvalhal Fm, which opens the possibility for other metal providers. For such devolatilization processes to occur several tectonic events can be invoked, such as i) slab break-off (Jesus et al., 2007; Pin et al., 2008; Ribeiro et al., 2010) and correspondent asthenosphere upwelling (Goldfarb and Groves, 2015); ii) radiogenic heat, provided by upper crust lithological pilling (Ribeiro et al., 2007) or even iii) igneous activity associated with the emplacement of magmatic bodies (e.g. Jesus et al., 2007; Moita et al., 2009).

Our research suggests that reduced metamorphic fluids capable of transporting gold in bisulfide complexes ($Au(HS)_2^-$) were enrolled in the process, as indicated by the presence of CH_4-fluids. One new type of gold mineralization (type i) has been identified in the Escoural gold district, in which gold deposition is believed to be triggered by the interaction of the reduced Au transporting fluids and the iron oxide-rich host rocks.

Additionally, the inspection of gold fineness reveals overall values from 812 and 868 which are consistent values for orogenic gold deposits (Morrison et al., 1991). Gold particle fineness is slightly higher for the type i mineralization (863-868) when compared to type ii (812-831) which, as pointed out by other authors (Pal´yanova, 2008; Petrella et al., 2021), could suggest different ore sources or different ore deposition mechanisms associated to the same mineralizing event. Considering that sulfides from type i and type ii mineralization show very narrow $\delta^{34}S_{CDT}$ signatures it is suggested that the source for sulfur is the same for both types

(**Fig. 2.17**) and therefore the differences in gold fineness are most likely associated to different ore deposition mechanisms being enrolled with type i and type ii mineralization.

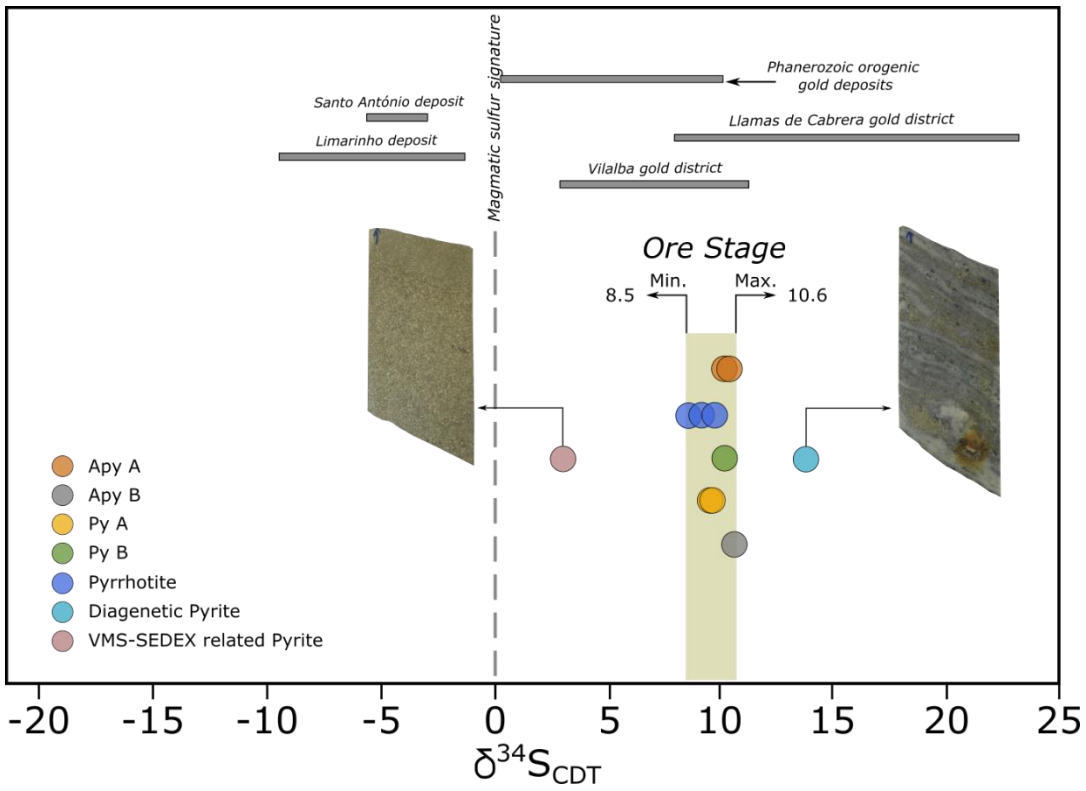

Figure 2.17. $\delta^{34}S$ values for the main sulfide phases described for the Monfurado deposit, with the constraining of $\delta^{34}S$ values for the analyzed ore stage sulfides. The grey horizontal bars show the range of $\delta^{34}S$ signatures for worldwide Paleozoic gold deposits (Nesbitt, 1991) and other NW Iberian gold districts. The Santo António deposit (Neiva et al., 2019), Limarinho deposit (Fuertes-Fuente et al., 2016), Llamas de Cabrera gold district (Gomez-Fernandéz et al., 2012) and Vilalba gold district (Martinez Abad et al., 2015) sulfur isotope ranges are displayed for comparison purposes.

2.5.4.1 Type i mineralization: sulfidation processes

For type i Au mineralization, destabilizing conditions for gold deposition were met when the initially reduced fluid interacted with the magnetite-rich host rocks (Monfurado Fm.). Sulfur concentrations in the fluid promoted magnetite sulfidation (Phillips, 1986; Phillips and Groves, 1984; Phillips and Hughes, 1996; Goldfarb et al., 2005), resulting in magnetite replacement by pyrrhotite (Palin and Xu, 2000, **Fig. 2.7a, b**). Sulfidation reactions are an important alteration associated to gold deposition in orogenic gold deposits (Goldfarb et al., 2005; Petrella et al., 2020; 2021), and are here interpreted as the main control for the deposition of gold in type i mineralization. The interaction between the reduced fluids transporting $Au(HS)^-_2$ and the iron-rich host rocks from the Monfurado Fm. led to the deposition of pyrrhotite by

substitution of magnetite and coeval deposition of sulfides such as arsenopyrite and pyrite. The deposition of these sulfide phases result in the consumption of H_2S from the fluid, thus leading to $Au(HS)^-_2$ destabilization and consequent gold deposition. These processes have been thoroughly discussed by Petrella et al. (2021), which disclose the chemical reactions that result from this fluid-rock interaction.

The fact that most of the gold particles from type i are found in arsenopyrite, suggests that arsenopyrite served as an electrochemical trap for Au (Möller and Kersten, 1994; Dubosq et al., 2018), which raises the question of Au possibly being incorporated in the atomic structure of arsenopyrite during its deposition as thoroughly discussed by Pokrovski et al. (2021). Post deposition metamorphism and deformation could have been an important mechanism in scavenging Au from arsenopyrite and pyrite structure (Fougerouse et al., 2016), leading to its deposition as fracture filling in type i mineralization.

Type i gold mineralization is exclusive to the Monfurado prospect and is part of the main gold mineralization stage, corresponding to gold grades up to 5.3 g/ton through an 8-meter section in one of the drill cores (**Fig. 2.2**). The contrasting rheological properties between the acid metavolcanic rocks and the carbonated units of the Monfurado Fm. are responsible for the focusing of type i gold mineralization endowment in these sections. This lithological contact served as an anisotropy for fluid circulation, thus focusing the fluid-rock interactions in the highly permeable iron-rich carbonate units of the Monfurado Fm. whereas, in the acid metavolcanic rocks, brittle-vein emplacement occurred. The result of sulfidation reactions (**Fig. 2.7a, b**) can be observed throughout the structural pathway in which a laterally consistent sulfide layer (MSL) was generated, which is observable in all core logs. The acid metavolcanics unit served as a low permeability barrier, concentrating fluid circulation at its base, and sulfidation reactions occurred in the lower calcsilicate /carbonate unit (**Fig. 2.2**; **Fig. 2.3**).

Table 2.7. Summarized statistical data calculated for Apy A and Apy B geothermometer according to Kretschmar and Scott (1976) method.

	Apy A						Apy B					
	Center			Rims			Center			Rims		
	As (at%)	T (°C)	Log $a(S_2)$	As (at%)	T (°C)	Log $a(S_2)$	As (at%)	T (°C)	Log $a(S_2)$	As (at%)	T (°C)	Log $a(S_2)$
Mean	29.05	305.31	-10.50	28.09	245.63	-12.14	28.68	280.16	-10.79	27.66	217.19	-12.66
Median	29.03	-	-	28.04	-	-	28.61	-	-	27.54	-	-
Std. Dev.	0.52	66.28	-2.64	0.32	32.81	-2.60	0.23	27.96	-1.93	0.37	29.13	-2.35
Min.	28.05	239.03	-13.1	27.58	212.82	-14.7	28.27	252.20	-12.7	27.15	188.06	-15
Max.	30.43	371.59	-7.9	28.73	278.43	-9.5	29.24	308.11	-8.9	28.17	246.32	-10.3
n*		111			9			32			7	

2.5.4.2 Type ii mineralization: evidence of reduced fluids

Type ii mineralization is found in quartz-veins (Qz IIb) hosted in acid metavolcanic rocks (**Fig. 2.12a-d**), contrasting to type i mineralization and thus suggesting that this mineralization type is structurally controlled. The veins bearing this mineralization type are usually sub-horizontal and parallel to the structural pathway, which is interpreted to be focused in the MSL.

Reduced CH_4-rich and H_2O-NaCl fluids were found in quartz from Qz IIb veins, and presumably assisted ore transport (**Fig. 2.9a; Fig. 2.12h, j**). The presence of CH_4-pure fluid inclusions is particularly interesting and indicates that such fluids are generated under reduced conditions, coherent to the fluids sustaining gold transport in bisulfide complexes (Goldfarb et al., 2005; Phillips and Powel, 2010; Pokrovski et al., 2014, Goldfarb and Groves, 2015). Several geological events are prone to contribute with CH_4 to the ore-forming fluids, from biogenic to abiotic sources (Etiope and Lollar, 2013). One commonly considered source of CH_4 is the thermal degradation of organic matter by the reactions between metamorphic-hydrothermal fluids and organic-rich and carbonate-rich rocks, during regional metamorphism (Fan et al., 2003; Etiope and Lollar, 2013; Gaboury, 2013; Zhang et al., 2019). Such reactions can be the main CH_4 supplier at the Monfurado gold prospect, owing to the metamorphism and metasomatism that affected the Escoural Fm. metasediments, and the Monfurado Fm. carbonate-rich units. A recent review by Gaboury (2021) addresses the role of organic matter on the formation of orogenic gold deposits since carbonaceous shales, such as the ones from Escoural Fm., are usually attributed as a common gold source. This evidence, together with the $\delta^{34}S_{CDT}$ values from Py B (**Table 2.6**; **Fig. 2.17**) is consistent with an input of sulfur, and possibly gold, from this Neoproterozoic basement.

In summary, the transport of gold was possibly assisted by CH_4-rich fluids and the partitioning of H_2S into the vapor and non-aqueous phases, such as CH_4, could impose destabilization of $Au(HS)^-_2$ complexes and subsequent gold deposition in type ii mineralization, as suggested by Naden and Shepherd (1989).

Aqueous-carbonic (Lc-w) fluid inclusions were exclusively found in clear-quartz veins cross-cutting the calcsilicate rocks of the Monfurado Fm., indicative that H_2O-CO_2-NaCl fluids have been locally incorporated in the system, and although such fluids are commonly found in orogenic gold deposits, in this case, such association could not be clearly disclosed.

The aqueous fluid inclusions found in Qz IIb veins revealed the presence of low-salinity (*Md*= 6.0 eq. w(NaCl)) and lower-temperature (*Md*= 230 ºC) H_2O-NaCl fluids, coherent with the chlorite and arsenopyrite geothermometer (**Table 2.5; Fig. 2.15a**). Such temperatures indicate probable input of meteoric water to the system (Lw_2; **Fig. 2.15**), although linking it to gold deposition was not possible.

2.6 Conclusions

2.6.1 Vectoring future exploration

The research approach presented throughout this work proved suitable for providing valuable insights on gold deposition mechanisms at the particularly interesting case study of the Escoural Orogenic gold district, the Monfurado gold prospect (**Fig. 2.1**).

The Monfurado gold prospect corresponds to a complex occurrence of gold displaying a unique mineralization style (type i) in which gold deposition was assisted by sulfidation processes that had not been recognized in the Escoural gold district (**Fig. 2.1a**). The spatial association of this gold prospect with the Santiago do Escoural fault and the precedent iron ores opens the possibility for other gold prospects to be found in the vicinity of this regional geological structures.

Considering the geochemistry, fluid inclusions, and isotopic data, the Neoproterozoic metasediments (i.e. Escoural Fm.) are suggested to be the most likely sulfur and gold supplier to the system. However, the role of the Cambrian volcanogenic iron-rich rocks from the Monfurado Fm. and metabasites from the Carvalhal Fm. (**Table 2.1**) as a source of metals is unknown and must not be ruled out considering the present evidence.

Additionally, the identification of gold-bearing sulfide layers - i.e. massive and arsenopyrite-rich - constitutes a valuable exploration vectoring tool for the sector. Understanding the role of the pre-existing iron-oxide domains in the evolution of the system provided insights for new gold deposition mechanisms and supports the possible existence of uncovered gold mineralization associated with the remaining massive iron bodies. Future exploration projects could benefit from this approach, focusing prospects on the contact between the acid metavolcanic and carbonate rocks from the Monfurado Fm., and addressing the relation between gold deposition and the iron-rich host rocks.

Chapter References

Andrade, A., Silva, J.M., Arruda, C.R, and Gameiro, J.C.S., 1949. Minas de Ferro de Montemor-o-Novo. Serviço de Fomento Mineiro, v. 15, p. 125.

Apalategui, O., Eguiluz, L., and Quesada, C., 1990. Ossa-Morena Zone: Structure. In: Martinez E and Dallmeyer RD (Eds.) Pre-Mesozoic Geology of Iberia, Springer Verlag, pp 280-291.

Araújo, A., 1995. Estrutura de uma geotransversal entre Brinches e Mourão (Zona Ossa Morena): Implicações na evolução geodinâmica da margem SW do terreno Autóctone Ibérico. PhD thesis Universidade de Évora, 200 p. (in Portuguese with English abstract)

Araújo, A., Fonseca, P., Munhá, J., Moita, P., Pedro, J., and Ribeiro, A. 2005. The Moura Phyllonitic Complex: an accretionary complex related with obduction in the Southern Iberia Variscan Suture. Geodinamica Acta, 18(5), 375-388. https://doi.org/10.3166/ga.18.375-388

Araújo, A., Piçarra de Almeida, J., Borrego, J. Pedro, J. and Oliveira, T., 2013. As regiões central e sul da Zona de Ossa-Morena. In: Dias R, Araújo A, Terrinha P, Kullberg JC (Eds), Geologia de Portugal, Volume 1, Escolar Editora, pp 509-549.

Azor, A., Dias da Silva, Í., Barreiro, J. G., González-Clavijo, E., Catalán, J. M., Simancas, J. F., Martínez Poyatos, D., Pérez-Cáceres, I. González Lodeiro, F., Expósito, I., Casas, J. M., Clariana, P., García-Sansegundo, J., Margalef, A., 2019. Deformation and Structure. In The geology of Iberia: A geodynamic approach (pp. 307-348). Springer, Cham. https://doi.org/10.1007/978-3-030-10519-8_10

Bakker, R.J., 2003. Package FLUIDS 1. Computer programs for analysis of fluid inclusion data and for modelling bulk fluid properties. Chemical Geology, v.194, p. 3-23. https://doi.org/10.1016/S0009-2541(02)00268-1

Bakker, R.J., 2018. AqSo_NaCl: Computer program to calculate p-T-V-x properties in the H_2O-NaCl fluid system applied to fluid inclusion research and pore fluid calculation. Comput. Geosci, v.115, p.122-133. https://doi.org/10.1016/j.cageo.2018.03.003

Barroso, M., Mateus, A., Figueiras, J., Martins, R., Oliveira, V., 2003. Mineralogy and geochemical characteristics of different superimposed mineralisations at the Enfermarias prospect (Moura, Portugal). VI Congresso Nacional de Geologia, Lisboa (Portugal), Ciências da Terra (UNL), Lisboa, n.º esp. V, CD-ROM, F9-F12.

Bateman, R., and Hagemann, S., 2004. Gold mineralization throughout about 45 Ma of Archean orogenesis: protracted flus of gold in the Golden Mile, Yilgarn craton, Western Australia. Mineralium Deposita, v.39, p.536-559. https://doi.org/10.1007/s00126-004-0431-2

Bierlein, F.P., and Crowe, D.E., 2000. Phanerozoic Orogenic Lode Gold Deposits. SEG Reviews, v. 13, p. 103-139.

Bodnar, R.J. and Vityk, M.O., 1994. Interpretation of microthermometric data for H2O–NaCl fluid inclusions, In Fluid Inclusions in Minerals: Methods and Applications, De Vivo, B. and Frezzotti, M.L., Eds., Sienna, pp. 117–130.

Bodnar, R.J., Lecumberri-Sanchez, P., Moncada, D., and Steele-MacInnis, M., 2014. Fluid inclusions in hydrothermal ore deposits. Treatise on Geochemistry, 2nd ed., v.13, p.119–142.

Boiron, M.C., Essarraj, S., Sellier, E., Cathelineau, M., Lespinasse, M., Poty, B., 1992. Identification of fluid inclusions in relation to their host microstructural domains in quartz

by cathodoluminescence. Geochim. Cosmochim. Acta 56, 175–185. https://doi.org/10.1016/0016-7037(92)90125-3

Borrego, J. 2009. Cartografia geológico-estrutural de um sector da Zona de Ossa-Morena (subsector de Estremoz-Barrancos-Ficalho) e sua interpretação tectónica. PhD thesis, 479 p. (in Portuguese with English abstract).

Caldeira, R., Ribeiro, M.L., and Moreira, M.E., 2007. Geoquímica das sequências máficas e félsicas entre Alvito, Torrão e Alcáçovas (SW da ZOM). Comunicações Geológicas, v.94, p. 5-28.

Carvalho, D., 1971. Observações sobre os jazigos de ferro da área Pedrógão-Orada. I Congresso Hispano – Luso – Americano de Geologia Económica, Madrid – Lisboa, v.1, p. 519-537.

Carvalhosa, A., 1983. Esquema geológico do Maciço de Évora. Comunicações dos Serviços Geológicos de Portugal, v.69(2), p. 201-208.

Carvalhosa, A., and Zbyszewski, G., 1994. Carta Geológica de Portugal, Notícia Explicativa da Folha 35-D (Montemor-o-Novo), Instituto Geológico e Mineiro, 1:50 000.

Castro, A., Pereira, M.F., Rodríguez, C., Fernández, C., and Jesús, D., 2020. Atypical peri-Gondwanan granodiorite–tonalite magmatism from Southern Iberia. Origin of magmas and implications. Lithos, 372, 105684. https://doi.org/10.1016/j.lithos.2020.105684

Cathelineau, M., 1988. Cation site occupancy in chlorites and illites as function of temperature. ClayMiner., v.23, p. 471–485. doi:10.1180/claymin.1988.023.4.13

Cepedal, A., Fuertes-Fuente, M., Martin-Izard, A., García-Nieto, J., and Boiron, M.C., 2013. Journal of Geochemical Exploration, v.124, p.101-126. http://dx.doi.org/10.1016/j.gexplo.2012.08.010

Cepedal, A., Fuertes-Fuente, M., Martin-Izard, A., Arias, D., and Aragón, D., 2018. The Portas deposit (Lugo, NW of Spain): An orogenic gold deposit related to Paleozoic ironstones. 15th Quadrennial IAGOD International Association on the Genesis of Ore Deposits Symposium, Salta, Argentina, 28-31 August 2018.

Chang, Z., Large, R.R. and Maslennikov, V., 2008. Sulfur isotopes in sediment-hosted orogenic gold deposits: Evidence for an early timing and a seawater sulfur source. Geology, v.36(12), p. 971-974. doi: 10.1130/G25001A.1

Chichorro, M., 2006. A evolução tectónica da Zona de Cisalhamento de Montemor-o-Novo (Sudoeste da Zona de Ossa-Morena – Área de Santiago do Escoural – Cabrela). PhD Thesis, University of Évora, p.569, (in Portuguese with English abstract).

Chichorro, M., Pereira, M.F., Díaz-Azpiroz, M., Williams, I.S., Fernández, C., Pin, C., and Silva, J.B., 2008. Cambrian ensialic rift-related magmatism in the Ossa-Morena Zone (Évora–Aracena metamorphic belt, SW Iberian Massif): Sm–Nd isotopes and SHRIMP zircon U–Th–Pb geochronology. Tectonophysics, v. 461, p. 91-113. https://doi.org/10.1016/j.tecto.2008.01.008

D'Angelico, A.J., Jenkin G.R.T., and James, D., 2016. Orogenic gold mineralisation in northwest Iberia, Portugal: role of meta-sediment source as a control on location, geochemistry and mineralogy. Applied Earth Science, v.125(2), p.73-74. https://doi.org/10.1080/03717453.2016.1166604

Dallmeyer, R.D., Fonseca, P.E., Quesada, C., and Ribeiro, A., 1993. 40Ar/39Ar mineral age constraints for the tectonothermal evolution of a Variscan suture in southwest Iberia. Tectonophysics, 222(2), 177-194. https://doi.org/10.1016/0040-1951(93)90048-O

de Oliveira, D.P.S, Robb, L.J., Inverno, C.M.C. and Charlesworth, E.G., 2007. Metallogenesis of the São Martinho and Mosteiros Gold Deposits, Tomar Cordoba Shear Zone, Portugal, International Geology Review, 49:10, 907-930. https://doi.org/10.2747/0020-6814.49.10.907

Dias, R., Ribeiro, A., Romão, J., Coke, C., and Moreira, N., 2016. A review of the Arcuate Structures in the Iberian Variscides; Constraints and Genetic Models. Tectonophysics, 681, 170-194. doi:10.1016/j.tecto.2016.04.011

Dias, G., Simões, P.P., Ferreira, N., and Leterrier, J., 2002. Mantle and crustal sources in the genesis of Late-Hercynian granitoids (NW Portugal): geochemical and Sr-Nd isotopic constraints. Gondwana Res 5:287–305. https://doi.org/10.1016/S1342-937X(05)70724-3

Dias da Silva, Í., Pereira, M.F., Silva, J.B., and Gama, C., 2018. Time-space distribution of silicic plutonism in a gneiss dome of the Iberian Variscan Belt: The Évora Massif (Ossa-Morena Zone, Portugal). Tectonophysics, 747, 298-317. https://doi.org/10.1016/j.tecto.2018.10.015

Díez-Fernández, R., Fuenlabrada, J.M., Chichorro, M., Pereira, M.F., Sánchez-Martínez, S., Silva, J. B., and Arenas, R., 2017. Geochemistry and tectonostratigraphy of the basal allochthonous units of SW Iberia (Évora Massif, Portugal): Keys to the reconstruction of pre-Pangean paleogeography in southern Europe, Lithos, v.268, p. 285-301. https://doi.org/10.1016/j.lithos.2016.10.031

Dubosq, R., Lawley, C.J.M., Rogowitz, A., Schneider, D.A., and Jackson, S., 2018. Pyrite deformation and connections to gold mobility: Insight from micro-structural analysis and trace element mapping. Lithos, v.310-311, p. 86-104. https://doi.org/10.1016/j.lithos.2018.03.024

Etiope, G., and Lollar, B.S., 2013. Abiotic methane on earth. Reviews of Geophysics, v.51, p. 276-299. https://doi.org/10.1002/rog.20011

Fan, H.,-R., Xie, Y.-H., Wang, K.-Y., and Wilde, S.A., 2004. Methane-rich fluid inclusions in skarn near the giant REE–Nb–Fe deposit at Bayan Obo, Northern China. Ore Geology Reviews, v.25, p. 301-309. doi:10.1016/j.oregeorev.2004.05.001

Faria, A.F., Chichorro, M., and Amaral, P.K., 1997. Montemor Gold Project, Southern Portugal – Geological Evaluation Report. Moriminas – Soc.Mineira de Montemor Lda., Montemor-o-Novo.

Fisher, N. H., 1945. The fineness of gold, with special reference to the Morobe gold field, New Guinea. Econonic Geology, v. 40, p. 449–495. https://doi.org/10.2113/gsecongeo.40.7.449

Fonseca, P.E., Munhá, J.M., Pedro, J., Rosas, F., Moita, P., Araújo, A., and Leal, N. 1999. Variscan ophiolites and high-pressure metamorphism in southern Iberia. Ofioliti, 24(2), 259-268.

Franke, W. 2000. The mid-European segment of the Variscides: tectonostratigraphic units, terrane boundaries and plate tectonic evolution. Geological Society, London, Special Publications, 179(1), 35-61. https://doi.org/10.1144/GSL.SP.2000.179.01.05

Franke, W. 2014. Topography of the Variscan orogen in Europe: failed–not collapsed. International Journal of Earth Sciences, 103(5), 1471-1499. https://doi.org/10.1007/s00531-014-1014-9

Franke, W., Cocks, L.R.M., and Torsvik, T.H., 2017. The Palaeozoic Variscan oceans revisited. Gondwana Research, 48, 257-284. http://dx.doi.org/10.1016/j.gr.2017.03.005

Fougerouse, D., Micklethwaite, S., Halfpenny, A., Reddy, S.M., Cliff, J.B., Martin, L.A.J., Kilburn, M., Guagliardo, P., and Ulrich, S., 2016. The golden ark: arsenopyrite crystal plasticity and the retention of gold through high strain and metamorphism. Terra Nova, v. 28, p. 181-187. https://doi.org/10.1111/ter.12206

Fuertes-Fuentes, M., Cepedal, A., Lima, A., Dória, A., Ribeiro, M.A., and Guedes, A., 2016. The Au-bearing vein system of the Limarinho deposit (northern Portugal): Genetic constraints from Bi-chalcogenides and Bi–Pb–Ag sulfosalts, fluid inclusions and stable isotopes. Ore Geology Reviews, v. 72, p. 213-231. http://dx.doi.org/10.1016/j.oregeorev.2015.07.009

Gaboury, D., 2013. Does gold in orogenic deposits come from pyrite in deeply buried

carbon-rich sediments?: Insight from volatiles in fluid inclusions. Geology, v. 41, p. 1207 – 1210. doi:10.1130/G34788.1

Gaboury, D., 2019. Parameters for the formation of orogenic gold deposits. Applied Earth Science. https://doi.org/10.1080/25726838.2019.1583310

Gaboury, D., 2021. The Neglected Involvement of Organic Matter in Forming Large and Rich Hydrothermal Orogenic Gold Deposits. geosciences, v. 11, 344. https://doi.org/10.3390/geosciences11080344

Galbraith, C.G., Clarke, D.B., Trumbull, R.B., and Wiedenbeck, M., 2009. Assessment of Tourmaline Compositions as an Indicator of Emerald Mineralization at the Tsa da Glisza Prospect, Yukon Territory, Canada. Economic Geology, v. 104, p. 713-731. https://doi.org/10.2113/gsecongeo.104.5.713

Goldfarb, R.J., Groves, D.I., and Gardoll, S., 2001. Orogenic gold and geologic time: a global synthesis. Ore Geol. Rev. 18, 1–71. https://doi.org/10.1016/S0169-1368(01)00016-6

Goldfarb, R.J., Baker, T., Dube′, B., Groves, D.I., Hart, C.J.R., and Gosselin, P., 2005. Distribution, character and genesis of gold deposits in metamorphic terranes. Econ. Geol. 407–450. https://doi.org/10.5382/AV100.14

Goldfarb, R.J., and Groves, D.I., 2015. Orogenic gold: common or evolving fluid and metal sources through time. Lithos 233, 2–26. https://doi.org/10.1016/j.lithos.2015.07.011

Gómez-Fernández, F., Vindel, E., Martín-Crespo, T., Sánchez, V., Clavijo, E.G., and Matías, R., 2012. The Llamas de Cabrera gold district, a new discovery in the Variscan basement of northwest Spain: A fluid inclusion and stable isotope study. Ore Geology Reviews, v.46, p.68-82. https://doi.org/10.1016/j.oregeorev.2012.02.001

Groves, D.I., and Santosh, M., 2016. The giant Jiaodong gold province: The key to a unified model for orogenic gold deposits? Geoscience Frontiers, v.7, p.409-417. http://dx.doi.org/10.1016/j.gsf.2015.08.002

Groves, D.I., Santosh, M., Deng, J., Wang, Q., Yang, L., and Zhang, L., 2019. A holistic model for the origin of orogenic gold deposits and its implications for exploration. Mineralium Deposita, v. 55, p. 275-292. https://doi.org/10.1007/s00126-019-00877-5

Groves, D.I., Santosh, M., and Zhang, L., 2020. A scale-integrated exploration model for orogenic gold deposits based on a mineral system approach. Geoscience Frontiers, v.11, p. 719-738. https://doi.org/10.1016/j.gsf.2019.12.007

Gutiérrez-Marco, J. C., Piçarra, J. M., Meireles, C. A., Cózar, P., García-Bellido, D. C., Pereira, Z., Vaz, N., Pereira, S., Lopes, G., Oliveira, J.T., Quesada, C., Zamora, S., Esteve, J., Colmenar, J., Bernardéz, E., Coronado, I., Lorenzo, S., Sá, A.A., Dias da Silva, Í., González-Clavijo, E., Díez-Montes, A., and Gómez-Barreiro, J., 2019. Early Ordovician–Devonian Passive Margin Stage in the Gondwanan Units of the Iberian Massif. In The geology of Iberia: A geodynamic approach (pp. 75-98). Springer, Cham. https://doi.org/10.1007/978-3-030-10519-8_3

Hodkiewicz, P. E., Groves, D. I., Davidson, G. J., Weinberg, R. F. and Hagemann, S. G., 2008. Influence of structural setting on sulphur isotopes in Archean orogenic gold deposits, Eastern Goldfields Province, Yilgarn Western Australia. Miner. Deposita 44, 129. https://doi.org/10.1007/s00126-008-0211-5

Inverno, C.M.C., 2001. Comparison between orogenic (or mesothermal) gold deposits and intrusion-related gold deposits. Some extrapolation to Portugal. Cadernos Lab. Xeolóxico de Laxe, v.36, p.99-156 (in Portuguese with English abstract).

Jesus, A.P., Munhá, J., Mateus, A., Tassinari, C., and Nutman, A.P., 2007. The Beja Layered Gabbroic Sequence (Ossa-Morena Zone, Southern Portugal): geochronology and geodynamic implications. Geodin Acta 20:139–15. doi:10.3166/ga.20.139-157

Jesus, A.P., Mateus, A., Munhá, J.M., Tassinari, C.C., dos Santos, T.M.B., and Benoit, M., 2016. Evidence for underplating in the genesis of the Variscan synorogenic Beja Layered Gabbroic Sequence (Portugal) and related mesocratic rocks. Tectonophysics, 683, 148-171. http://dx.doi.org/10.1016/j.tecto.2016.06.001

Julivert, M., Fontboté, J.M., Ribeiro, A., and Nabais Conde, L.E., 1972. Mapa Tectónico de la Península Ibérica y Baleares. Scale 1:1.000.000. IGME.

Kretschmar, U. and Scott, S., 1976. Phase relations involving arsenopyrite in the system Fe-As-S and their application. Can. Mineral., v.14(3), p.364-386.

Kroner, U., Stephan, T., Romer, R. L., Roscher, M., 2020. Paleozoic plate kinematics during the Pannotia–Pangea supercontinent cycle. Geological Society, London, Special Publications, 503. https://doi.org/10.1144/SP503-2020-15

LaFlamme, C., Jamieson J. W., Fiorentini, M. L., Thébaud, N., Caruso, S., and Selvaraja, V., 2018a. Investigating sulfur pathways through the lithosphere by tracing mass independent fractionation of sulfur to the Lady Bountiful orogenic gold deposit, Yilgarn Craton. Gondwana Res. 58, 27-38. https://doi.org/10.1016/j.gr.2018.02.005

Leal, N., 2001. Estudo petrológico e geoquímico de rochas metamórficas de alta pressão das regiões de Alvito-Viana do Alentejo e de Safira (Zona de Ossa-Morena, Maciço Ibérico). PhD Thesis, Universidade de Lisboa, 402 p. (in Portuguese with English abstract)

Leal, S., Lima, A., Noronha, F., Mortensen, J., Mackenzie, D., 2022. Geological setting of the Bigorne gold deposit, Iberian Variscan belt (Northern Portugal) and Au-Bi-Te mineral assemblages as indicators of the ore-forming conditions. Ore Geology Reviews, v.141, 104689. https://doi.org/10.1016/j.oregeorev.2021.104689

Le Maitre, R.W., Streckeisen, A., Zanetin, B., Le Bas, M.J., Bonin, B., Bateman, P., Bellieni, G., Dudek, A., Efremova, S., Keller, J., Lameyre, J., Sabine, P.A., Schmid, R., SØrensen, H., and Wooley, A.R., 2012. Igneous Rocks: A classification and Glossary of Terms, second editions, Cambridge University Press, 2012, 235 pp.

Lindgren, W., 1907, The relation of ore deposition to physical conditions: Economic Geology, V. 2, p. 105–127.

Lindgren, W., 1933, Mineral deposits, 4th edition: New York and London, McGraw Hill, 930 p.

Lopes, L.C.S., 2015. Litogeoquímica na área de concessão da Boa-Fé (COLT Resources). Master Thesis, Univ. Aveiro and Univ. Porto, p.152, (in Portuguese with English abstract).

Lopes, L.C.S., Santos, J.F., Sousa, J.C., and Ribeiro, S., 2015. New petrographic, geochemical and isotopic data on the Boa Fé gold prospect (Montemor-o-Novo, Ossa-Morena Zone). Comunicações Geológicas, v.102, Especial I, (in Portuguese with English abstract).

Lotze, F., 1945. Zur gliederung der Varisziden der Iberischen meseta. Geoteckt. Forsch., Berlin, v. 6, p. 78–92.

Maia, M., São Pedro, D., Mirão, J., Noronha, F., and Nogueira, P., 2019. Fluid constraints for Au deposition at the Monges iron deposit, Ossa-Morena Zone (Montemor-o-Novo, Portugal). Proceedings of the 15th SGA Biennal Meeting, 27-30 August 2019, Glasgow, Scotland, v.1, p. 252-255.

Maia, M., Barrulas, P., Nogueira, P., Mirão, J., and Noronha, F., 2022. In situ LA-ICP-MS trace element analysis of magnetite as a vector towards mineral exploration: A comparative case study of Fe-skarn deposits from SW Iberia (Ossa-Morena Zone). Journal of Geochemical Exploration, v. 234, 106941. https://doi.org/10.1016/j.gexplo.2021.106941

Marshall, B., and Gilligan, L.B., 1989. Durchbewegung structure, piercement cusps, and piercement veins in massive sulfide deposits: Formation and interpretation. Economic Geology, v. 84, p. 2311-2319. https://doi.org/10.2113/gsecongeo.84.8.2311

Martinez-Abad, I., Cepedal, A., Arias, D., and Martin-Izard, A., 2015. The Vilalba gold district, a new discovery in the Variscan terranes of the NW of Spain: A geologic, fluid inclusion and stable isotope study. Ore Geology Reviews, v. 66, p. 344-365. http://dx.doi.org/10.1016/j.oregeorev.2014.10.021

Martins, R., Mateus, A., Figueiras, J., Barroso, M., Oliveira, V. 2003. Post-metamorphic evolution of the Lower Cambrian section at Enfermarias (Moura, Portugal): its record and metallogenic implications. VI Congresso Nacional de Geologia, Lisboa (Portugal), Ciências da Terra (UNL), Lisboa, n.º esp. V, CD-ROM, B60-B63.

Mateus A., Matos J.X., Rosa C., and Oliveira V., 2003. Cu-ores in quartz-carbonate veins at Estremoz-Alandroal and Barrancos-Sto Aleixo regions (Ossa Morena Zone): a result of Late-Variscan hydrothermal activity. VI Congresso Nacional de Geologia, Lisboa (Portugal), Ciências da Terra (UNL), Lisboa, nº esp. V, CD-ROM, F90-F93.

Mateus, A., Araújo, A., Gonçalves, M.A., and Matos, J., 2005. Variscan overthrusting, fluid flow and genesis of magnetite ore-bodies at the Azenhas area (Pedrógão, Ossa-Morena Zona, SE Portugal). Boletín Geológico y Minero, v.116(1), p. 3-22. ISSN 0366-0176.

Mateus, A., Munhá, J., Inverno, C., Matos, J.X., Martins, L., Oliveira, D., Jesus, A., and Salgueiro, R., 2013. Mineralizações no sector português da Zona de Ossa-Morena. In R. Dias, A. Araújo, P. Terrinha, J.C. Kullberg (Eds.), Geologia de Portugal (p. 577-619, v.1). Lisboa: Escolar Editora.

Matos, J., Araújo, A., and Mateus, A., 1998. Cartografia de detalhe e controle estrutural das mineralizações na região de Pedrógão-Orada. Geologos, v.2, p. 101-104.

Matte, P. 2001. The Variscan collage and orogeny (480–290 Ma) and the tectonic definition of the Armorica microplate: a review. Terra nova, 13(2), p. 122-128. https://doi.org/10.1046/j.1365-3121.2001.00327.x

MacKenzie, D., Craw, D., and Mortensen, J.K., 2019. Orogenic gold deposits in the Variscan belt in northwestern Iberia. Proceedings of the 15th SGA Biennal Meeting, 27-30 August 2019, Glasgow, Scotland, v.2, p. 736-738.

McLennan, S.M., 1989. Rare Earth elements in sedimentary rocks: influence of provenance and sedimentary processes. In: Lipin, B.R., McKay, G.A. (Eds.), Geochemistry and mineralogy of Rare earth elements. Mineralogical Society of America, Rev. Mineral, v.21, p.169-200.

Melfos, V., Voudouris, P., Serafimovski, T., and Tasev, G., 2019. Fluid Inclusions at the Plavica Au-Ag-Cu Telescoped Porphyry–Epithermal System, Former Yugoslavian Republic of Macedonia (FYROM). Geosciences, 9, 88. doi:10.3390/geosciences9020088

Moita, P., Munhá, J., Fonseca, P.E., Pedro, J., Tassinari, C.C.G., Araujo, A., and Palácios, T., 2005a. Phase equilibria and geochronology of Ossa Morena eclogites. XIV Semana de Geoquímica/ VIII Congresso de Geoquímica dos Países de Língua Portuguesa, 463-466.

Moita, P., Munhá, J., Fonseca, P.E., Tassinari, C.C.G., Araujo, A., Palácios, T., 2005b. Dating orogenic events in Ossa-Morena Zone. XIV Semana de Geoquímica/ VIII Congresso de Geoquímica dos Países de Língua Portuguesa, 459-461.

Moita, P., Santos, J.F., and Pereira, M.F., 2009. Layered granitoids: interaction between continental crust recycling processes and mantle-derived magmatism: examples from the Évora Massif (Ossa–Morena Zone, southwest Iberia, Portugal). Lithos 111,125–141. https://doi.org/10.1016/j.lithos.2009.02.009

Möller, P., and Kersten, G., 1994. Electrochemical accumulation of visible gold on pyrite andcarsenopyrite surfaces. Mineralium Deposita, v. 29, p. 404-413.

Morrison, G.W., Rose, W.J. and Jaireth, S., 1991. Geological and geochemical controls on the silver content (fineness) of gold in gold–silver deposits. Ore Geology Reviews, v. 6, p. 333–364. https://doi.org/10.1016/0169-1368(91)90009-v

Mortensen, J.K., Martin Izard, A., Cepedal, M.A.H., Fuertes-Fuente, M., Lima, A., Creaser, R., 2014. Gold metallogeny of northwestern Iberia: superimposed orogenic and intrusion related mineralization in an evolving Variscan Orogen. SEG Denver 2014 Conference, Denver, Colorado.

Murphy, J.B., Quesada, C., Gutiérrez-Alonso, G., Johnston, S.T., and Weil, A., 2016. Reconciling competing models for the tectono-stratigraphic zonation of the Variscan orogen in Western Europe. Tectonophysics, 681, 209-219. https://doi.org/10.1016/j.tecto.2016.01.006

Naden, J., and Shepherd, T. 1989. Role of methane and carbon dioxide in gold deposition. Nature v.342, p.793–795 (1989). https://doi.org/10.1038/342793a0

Nance, R. D., Gutiérrez-Alonso, G., Keppie, J. D., Linnemann, U., Murphy, J. B., Quesada, C., Strachan, R. A., Woodcock, N. H. 2010. Evolution of the Rheic ocean. Gondwana Research, v.17(2-3), p.194-222. https://doi.org/10.1016/j.gr.2009.08.001

Nance, R. D., Gutiérrez-Alonso, G., Keppie, J. D., Linnemann, U., Murphy, J. B., Quesada, C., Strachan, R. A, Woodcock, N. H. 2012. A brief history of the Rheic Ocean. Geoscience Frontiers, v.3(2), p.125-135. https://doi.org/10.1016/j.gsf.2011.11.008

Neiva, A.M., Moura, A., Gomes, C.A.L., Pereira, M.F., and Corfu, F. 2019. The granite-hosted Variscan gold deposit from Santo António mine in the Iberian Massif (Penedono, NW Portugal): constraints from mineral chemistry, fluid inclusions, sulfur and noble gases isotopes. J. Iber. Geol., v. 45(3), p. 443-469. https://doi.org/10.1007/s41513-019-00103-1

Nesbitt, B.E., 1991. Phanerozoic gold deposits in tectonically active continental margins. In: Foster, R.P., Ed., Gold metallogeny and exploration: London, Blackie, p. 63–103.

Noronha, F., Cathelineau, M., Boiron, M.C., Banks, D.A., Dória, A., Ribeiro, M.A., Nogueira, P., and Guedes, A. 2000. A three stage fluid flow model for Variscan gold metallogenesis in northern Portugal. J. Geol. Explor., v. 71(2), p. 209-224. https://doi.org/10.1016/S0375-6742(00)00153-9

Oliveira, J.T., Oliveira, V., and Piçarra, J.M., 1991. Traços gerais da evolução tectono-estratigráfica da Zona de Ossa Morena, em Portugal: síntese crítica do estado actual dos conhecimentos. Comum. Serv. Geol, Port., v.77, p.3-26.

Oliveira, V.M.J., 1986. Prospeção de minérios metálicos a Sul do Tejo. Geociências – Aveiro, v.1, p.15-22.

Palin, J.M., and Xu, Y., 2000. Gilt by association? Origins of pyritic gold ores in the Victory mesothermal gold deposit, Western Australia. Economic Geology, v.95, p. 1627–1634. https://doi.org/10.2113/gsecongeo.95.8.1627

Pal´yanova G. 2008. Physicochemical modeling of the coupled behavior of gold and silver in hydrothermal processes: Gold fineness, Au/Ag ratios and their possible implications. Chem. Geol., v. 255, p. 399–413. https://doi.org/10.1016/j.chemgeo.2008.07.010

Palme, H., and O´Neill, HStC., 2014. Cosmochemical Estimates of Mantle Composition. In: Holland, H.D. & Turekian K.K. (Eds) Treatise on geochemistry. Vol. 15: Analytical geochemistry/inorganic instrument analysis. Elsevier, Oxford, p. 1-39. http://dx.doi.org/10.1016/B978-0-08-095975-7.00201-1

Pearce, J. A., and Norry, M. J. (1979). Petrogenetic implications of Ti, Zr, Y, and Nb variations in volcanic rocks. Contributions to mineralogy and petrology, v. 69(1), p. 33-47. https://doi.org/10.1007/BF00375192

Pearce, J.A., Harris, N.B.W, and Tindle, A.G., 1984. Trace element discrimination diagrams for the tectonic interpretation of granitic rocks. Journal of Petrology, v.25, p.956-983. https://doi.org/10.1093/petrology/25.4.956

Pedro, J., 1996 Estudo do metamorfismo de alta pressão na área de Safira (Montemor-o-Novo) Zona de Ossa-Morena. MSc. Thesis, Universidade de Lisboa, 69p. (in Portuguese with English abstract)

Pedro, J., 2004. Estudo geológico e geoquímico das sequências ofiolìticas da zona de Ossa-Morena (Portugal). PhD Thesis, Universidade de Lisboa, 225p. (in Portuguese with English abstract)

Pedro, J., Araújo, A., Fonseca, P.E., Tassinari, C., Ribeiro, A. 2010. Geochemistry and U-Pb zircon age of the internal Ossa-Morena Zone ophiolite sequences: a remnant of Rheic ocean in SW Iberia. Ofioliti, 35(2), 117-130

Pereira, M.F., Silva, J.B., and Chichorro, M., 2003. Internal Structure of the Évora High-grade Terrains and the Montemor-o-Novo Shear Zone (Ossa-Morena Zone, Portugal), Geogaceta, v.33, p.79-82.

Pereira, M. F., Chichorro, M., Linnemann, U., Eguiluz, L., and Silva, J. B., 2006. Inherited arc signature in Ediacaran and Early Cambrian basins of the Ossa-Morena zone (Iberian Massif, Portugal): paleogeographic link with European and North African Cadomian correlatives. Precambrian Research, v. 144(3-4), p. 297-315. https://doi.org/10.1016/j.precamres.2005.11.011

Pereira, M. F., Silva, J. B., Chichorro, M., Moita, P., Santos, J. F., Apraiz, A., and Ribeiro, C., 2007. Crustal growth and deformational processes in the northern Gondwana margin: Constraints from the Évora Massif (Ossa-Morena zone, southwest Iberia, Portugal). Special Paper 423: The Evolution of the Rheic Ocean: From Avalonian-Cadomian Active Margin to Alleghenian-Variscan Collision, 333–358. https://doi.org/10.1130/2007.2423(16).

Pereira, M. F., Chichorro, M., Williams, I. S., and Silva, J. B. 2008. Zircon U–Pb geochronology of paragneisses and biotite granites from the SW Iberian Massif (Portugal): evidence for a palaeogeographical link between the Ossa–Morena Ediacaran basins and the West African craton. Geological Society, London, Special Publications, 297(1), 385–408. doi:10.1144/sp297.18

Pereira, M.F., Solá, A.R., Chichorro, M., Lopes, L., Gerdes, A., and Silva, J.B., 2012. North-Gondwana assembly, break up and paleogeography: U–Pb isotope evidence from detrital and igneous zircons of Ediacaran and Cambrian rocks of SW Iberia. Gondwana Res., 22(3-4), 866-881.

Pereira, M.F., Chichorro, M., Moita, P., Santos, J.F., Solá, A.M.R., Williams, I.S., and Silva, J.B., 2015. The multistage crystallization of zircon in calc-alkaline granitoids: U–Pb age constraints on the timing of Variscan tectonic activity in SW Iberia. International Journal of Earth Sciences, v. 104, p. 1167 – 1183. https://doi.org/10.1007/s00531-015-1149-3

Pereira, M.F., Gutíerrez-Alonso, G., Murphy, J.B., Drost, K., Gama, C., Silva, J.B., 2017. Birth and demise of the Rheic Ocean magmatic arc(s): combined U–Pb and Hf isotope analyses in detrital zircon from SW Iberia siliciclastic strata. Lithos v.278, 383–399. https://doi.org/10.1016/j.lithos.2017.02.009

Peterson, E.C. and Mavrogenes, J.A., 2014. Linking high-grade gold mineralization to earthquake-induced fault-valve processes in the Porgera gold deposit, Papua New Guinea. Geol. 42, 383– 386. https://doi.org/10.1130/G35286.1

Petrella, L., Thébaud, N., Laflamme, C., Martin, L., Occhipinti, S., and Bigelow, J., 2020. In-situ sulfur isotopes analysis as an exploration tool for orogenic gold mineralization in the Granites-Tanami Gold Province, Australia: Learnings from the Callie deposit. J. Geochem. Explor., v. 214. https://doi.org/10.1016/j.gexplo.2020.106542

Petrella, L., Thébaud, N., Evans, K., LaFlamme, C., and Occhipinti, S., 2021. The role of competitive fluid-rock interaction processes in the formation of high-grade gold deposits. Geochimica et Cosmochimica Acta, v. 310, p. 38-54. https://doi.org/10.1016/j.gca.2021.08.024

Phillips, G.N., 1986, Geology and alteration in the Golden Mile, Kalgoorlie: Economic Geology, v.81, p.779–808. https://doi.org/10.2113/gsecongeo.81.4.779

Phillips, G. N., and Groves, D. I., 1984. Fluid access and fluid-wall rock interaction in the genesis of the Archaean gold-quartz vein deposit at Hunt mine, Kambalda, Western Australia, in Foster, R. P., ed., Gold ’82—the geology, geochemistry and genesis of gold deposits: Rotterdam, Balkema, p. 389–416.

Phillips, G.N., and Hughes, M.J., 1996, The geology and gold deposits of the Victorian gold province. Ore Geology Reviews, v. 11, p. 255–302. https://doi.org/10.1016/S0169-1368(96)00006-6

Phillips, G.N., and Powell, R., 2010. Formation of gold deposits: a metamorphic devolatilization model. J. Metamorph. Geol. 28, p.689–718. https://doi.org/10.1111/j.1525-1314.2010.00887.x

Piçarra, J.M., 2000. Estudo estratigráfico do sector de Estremoz-Barrancos, Zona de Ossa Morena, Portugal. Volume 1: Litoestratigrafia do intervalo Câmbrico médio? - Devónico inferior. PhD Thesis, Universidade de Évora, p. 95. (in Portuguese with English abstract)

Pin, C., Fonseca, P.E., Paquette, J.-L., Castro, P., and Matte, P., 2008. The ca. 350 Ma Beja Igneous Complex: a record of transcurrent slab break-off in the Southern Iberia Variscan Belt? Tectonophysics, v.461, p. 356–377. https://doi.org/10.1016/j.tecto.2008.06.001

Pitcairn, I.K., Craw, D., and Teagle, D.A.H., 2015. Metabasalts as sources of metals in orogenic gold deposits. Mineralium Deposita, v. 50, p. 373-390. https://doi.org/10.1007/s00126-014-0547-y

Pokrovski, G.S., Akinfiev, N.N., Borisova, A.Y., Zotoz, A.V., and Kouzmanov, K., 2014. Gold speciation and transport in geological fluids: insights from experiments and physical-chemical modelling. In: Garofalo, P. S. & Ridley, J. R. (Eds) 2014. Gold-Transporting Hydrothermal Fluids in the Earth's Crust. Geological Society, London, Special Publications, v. 402, p. 9–70. http://dx.doi.org/10.1144/SP402.4

Pokrovski, G.S., Escoda, C., Blanchard, M., Testemale, D., Hazemann, J.-L., Gouy, S., Kokh, M.A., Boirn, M.-C., de Parseval, F., Aigouy, T., Menjot, LL., de Parseval, P., Proux, O., Rovezzi, M., Béziat, D., Salvi, S., Kouzmanov, K., Barstch, T., Pöttgen, R., and Doert, T., 2021. An arsenic-driven pump for invisible gold in hydrothermal systems. Geochemical Perspectives Letters, v. 17, p. 39-44. doi: 10.7185/geochemlet.2112

Quesada, C., Fonseca, P. E., Munhá, J., Oliveira, J. T., Ribeiro, A., 1994. The Beja-Acebuches Ophiolite (Southern Iberia Variscan fold belt): geological characterization and geodynamic significance. Boletín Geológico y Minero, v. 105(1), p. 3-49.

Quesada, C., Braid, J.A., Fernandes, P., Ferreira, P., Jorge, R. S., Matos, J. X., Murphy, J.B., Oliveira, J.T., Pedro, J., and Pereira, Z., 2019. SW Iberia Variscan Suture Zone: Oceanic Affinity Units. In The Geology of Iberia: A Geodynamic Approach (pp. 131-171). Springer, Cham. https://doi.org/10.1007/978-3-030-10519-8_5

Rajabpour, S., Behzadi, M., Jiang, S.-Y., Rasa, I., Lehmann, B., and Ma, Y., 2017. Sulfide chemistry and sulfur isotope characteristics of the Cenozoic volcanic-hosted Kuh-Pang copper deposit, Saveh county,

northwestern central Iran. Ore Geology Reviews, v.86, p. 563-583. http://dx.doi.org/10.1016/j.oregeorev.2017.03.001

Ribbe, P. H., 1983. Feldspar mineralogy. Mineralogical Society of America. 2nd. Ed., pp 362.

Ribeiro, A., Dias, R., and Brandão Silva, J., 1995. Genesis of the Ibero-Armorican arc. Geodinamica Acta, v. 8(4), p. 173-184

Ribeiro, A., Munhá, J., Dias, R., Mateus, A., Pereira, E., Ribeiro, L., Fonseca, P., Araújo, A., Oliveira, O., Romão, J., Chaminé, H., Coke, C., and Pedro, J.C., 2007. Geodynamic evolution of the SW Europe Variscides. Tectonophysics, v.26, TC6009. https://doi.org/10.1029/2006TC002058

Ribeiro, A., Munhá, J., Fonseca, P.E., Araújo, A., Pedro, J.C., Mateus, A., Tassinari, C., Machado, G., and Jesus, A., 2010. Variscan ophiolite belts in the Ossa-Morena Zone (Southwest Iberia): Geological characterization and geodynamic significance. Gondwana Research, v.17, p. 408-421. https://doi.org/10.1016/j.gr.2009.09.005

Ribeiro, C., Mateus, A., and Barriga, F., 1993. Gold mineralization of the Escoural area (Montemor, Évora, Portugal): a progress report. Comun. XII Reun. Geol. Oeste Penins., v.1, p.215-226.

Ribeiro, M.L., Castro, A., Almeida, A., Menéndez, L. G., Jesus, A., Lains, J.A., Carrilho Lopes, J., Martins, H.C.B.; Mata, J., Mateus, A., Moita, P., Neiva, A., Ribeira, M.A., Santos, J.F., and Solá, A.R., 2019. Variscan Magmatism. In The Geology of Iberia: A Geodynamic Approach (pp. 497-526). Springer, Cham. https://doi.org/10.1007/978-3-030-10519-8_13

Robardet, M., and Gutiérrez-Marco, J.C., 2004. The Ordovician, Silurian and Devonian sedimentar rocks of the Ossa-Morena Zone (SW Iberian Peninsula, Spain). J. Iber. Geol. v. 30, p. 73-92. https://doi.org/10.1016/j.gexplo.2018.02.011

Roedder, E., 1984. Fluid inclusions, Rev. Mineral., Ribbe, P.H.,Ed., Mineralogical Society of America, 1984, vol. 12.

Rodríguez-Terente, L.M., Martin-Izard, A., Aria, D., Fuertes-Fuente, M., Cepedal, A., 2018. The Salave Mine, a Variscan intrusion-related gold deposit (IRGD) in the NW of Spain: Geological context, hydrothermal alterations and ore features. J. Geoch. Explor., V.188, p.364-389.

Rosas, F. M., Marques, F. O., Ballevre, M., and Tassinari, C., 2008. Geodynamic evolution of the SW Variscides: Orogenic collapse shown by new tectonometamorphic and isotopic data from western Ossa-Morena Zone, SW Iberia. Tectonics, 27(6), TC6008. https://doi.org/10.1029/2008TC002333

Rubio Pascual, F.J.R., Matas, J., and Parra, L.M.M., 2013. High-pressure metamorphism in the Early Variscan subduction complex of the SW Iberian Massif. Tectonophysics, 592, 187-199. https://doi.org/10.1016/j.tecto.2013.02.022

Salgueiro, R., 2011. Caracterização e génese das mineralizações de magnetite – sulfuretos em Monges (Santiago do Escoural, Montemor-o-Novo) e ensaio comparativo com as suas congéneres em Orada-Vale de Pães (Serpa-Vidigueira). PhD Thesis, Univ. Lisboa, 524 p., (in Portuguese with English abstract).

Salgueiro, R., Mateus, A., Inverno, C., 2010a. Caracterização e génese do skarn ferrífero de Orada (Zona de Ossa-Morena). E-Terra, v. 20(3).

Salgueiro, R., Inverno, C., and Mateus, A., 2010b. Main characteristics and genesis of the Vale de Pães skarn (Cuba-Vidigueira, Ossa Morena Zone, Portugal). Estudios Geológicos, v.66(1), p. 65-74. doi:10.3989/egeol.40150.101

Sánchez-Garcia, T., Bellindo, F., and Quesada, C., 2003. Geodynamic setting and geochemical signatures of Cambrian-Ordovician rift-related igneous rocks (Ossa-Morena Zone, SW Iberia). Tectonophysics 365, p.233-255. https://doi.org/10.1016/S0040-1951(03)00024-6

Sánchez-García, T., Quesada, C., Bellido, F., Dunning, G.R., Tánago, J.G. 2008. Two-step magma flooding of the upper crust during rifting: the Early Paleozoic of the Ossa Morena Zone (SW Iberia). Tectonophysics 461(1-4):72-90. https://doi.org/10.1016/j.tecto.2008.03.006.

Sánchez-Garcia, T., Bellido, F., Pereira, M.F., Chichorro, M., Quesada, C., Pin, C., Silva, J.B. 2010. Rift-related volcanism predating the birth of the Rheic Ocean (Ossa-Morena zone, SW Iberia). Gondwana Res 17(2):392-407. https://doi.org/10.1016/j.gr.2009.10.005.

Sánchez-García, T., Pereira, M. F., Bellido, F., Chichorro, M., Silva, J. B., Valverde-Vaquero, P., Pin, C., Solá, A.R. 2014. Early Cambrian granitoids of North Gondwana margin in the transition from a convergent setting to intra-continental rifting (Ossa-Morena Zone, SW Iberia). International Journal of Earth Sciences, 103(5), 1203-1218. https://doi.org/10.1007/s00531-013-0939-8

Sánchez-García, T., Chichorro, M., Solá, A.R., Álvaro, J.J., Díez-Montes, A., Bellido, F., Ribeiro, M.L., Quesada, C., Lopes, J.C., Dias da Silva, Í., González-Clavijo, E., Gómez Barreiro, J., and López-Carmona, A., 2019.

The Cambrian-Early Ordovician Rift Stage in the Gondwanan Units of the Iberian Massif. In: Quesada, C. & Oliveira J.T. (Eds) The Geology of Iberia: A Geodynamic Approach, Vol. 2: The Variscan Cycle. Springer Nature, Switzerland, p.27-74. https://doi.org/10.1007/978-3-030-10519-8

Serviço de Fomento Mineiro, 1977, 1:5 000 Geologic map of the Escoural-Monges region.

Shervais, J. W., 1982. Ti-V plots and the petrogenesis of modern and ophiolitic lavas. Earth and planetary science letters, v. 59(1), p. 101-118. https://doi.org/10.1016/0012-821X(82)90120-0

Sibson, R., Moore, J.M.M., and Rankin, A., 1975, Seismic pumping—a hydrothermal fluid transport mechanism: Journal of the Geological Society, v. 131, p. 653–659.

Simancas, J.F., 2019. Variscan Cycle. In: Quesada. C., Oliveira, J.T. (Eds.), The Geology of Iberia: a geodynamic approach. Vol.2: The Variscan Cycle. Springer (Berlin), Regional Geology Series, pp 1-25. https://doi.org/10.1007/978-3-030-10519-8_1.

Thiery, R., Vidal, J., and Dubessy, J., 1994. Phase equilibria modelling applied to fluid inclusions: Liquid-vapour equilibria and calculation of the molar volume in the CO2-CH4-N2 system. Geoch. Cosm. Acta, v.58, p.1073-1082. https://doi.org/10.1016/0016-7037(94)90573-8

Tornos F., Inverno C.M.C., Casquet C., Mateus A., Ortiz G., and Oliveira V., 2004. The Metallogenic evolution of the Ossa-Morena Zone. J. Iber. Geol., v. 30, p. 143-181.

Uemoto, T., Ridley, J., Mikucki, E., Groves, D.I., and Kusakabe, M., 2002. Fluid chemical evolution as a factor in controlling the distribution of gold at the Archean Golden Crown lode gold deposit, Murchison province, Western Australia. Economic Geology, v.97, p.1227–1248. https://doi.org/10.2113/gsecongeo.97.6.1227

Valle Aguado, B., Azevedo, M.R., Schaltegger, U., Martínez Catalán, J.R., and Nolan, J., 2005. U-Pb zircon and monazite geochronology of Variscan magmatism related to syn-convergence extension in Central Northern Portugal. Lithos, 82, 169–184. https://doi.org/10.1016/j.lithos.2004.12.012

Vallance, J., Cathelineau, M., Boiron, M. C., Fourcade, S., Shepherd, T. J. and Naden, J. 2003. Fluid–rock interactions and the role of late Hercynian aplite intrusion in the genesis of the Castromil gold deposit, northern Portugal. Chem. Geol., v. 194(1-3), p. 201-224. https://doi.org/10.1016/S0009-2541(02)00278-4

Voisey, C. R., Willis, D., Tomkins A. G., Wilson C. J. L., Micklethwaite, S., Salvemini, F., Bougoure, J., and Rickard, W. D. A., 2020. Aseismic Refinement of Orogenic Gold Systems. Econ. Geol., v. 115, p. 33-50. https://doi.org/10.5382/econgeo.4692

Whitney D.L., and Evans B.W. 2010. Abbreviations for names of rock-forming minerals. Amer. Miner., v.95, p.185-187. https://doi.org/10.2138/am.2010.3371

Wilkinson, J. J., 2001. Fluid inclusions in hydrothermal ore deposits. Lithos, v.55, p. 229, https://doi.org/10.1016/S0024-4937(00)00047-5

Wyman, D.A., Cassidy, K.F., Hollings, P., 2016. Orogenic gold and the mineral systems approach: Resolving fact, fiction and fantasy. Ore Geology Reviews, v. 78, p. 322-335. https://doi.org/10.1016/j.oregeorev.2016.04.006

Yavuz, F., Kumral, M., Karakaya, N., Karakaya, M.Ç., and Yildirim, D.K., 2015. A Windows program for chlorite calculation and classification. Computer & Geoscience, v. 81, p. 101-113. http://dx.doi.org/10.1016/j.cageo.2015.04.01

Zane, A., and Weiss, Z., 1998. Aprocedure for classifying rock-forming chlorites based on microprobe data. Rend. Lincei Sci. Fis. Nat. Ser., v.9, p. 51–56.

Zhang, W., Williams-Jones, A.E., Leng, C.-L., Zhang, X.-C., Chen, W., Qin, C.-J., Su, W.-C., and Yan, J.-H., 2019. The origin of CH4-rich fluids in reduced porphyry–skarn Cu–Mo–Au systems. Ore Geology Reviews, v. 114, 103135. https://doi.org/10.1016/j.oregeorev.2019.103135

Chapter 3

In situ LA-ICP-MS trace element analysis of magnetite as a vector towards mineral exploration: A comparative case study of Fe-skarn deposits from SW Iberia (Ossa-Morena Zone)

Journal of Geochemical Exploration, v. 234, Article Number 106941

https://doi.org/10.1016/j.gexplo.2021.106941

Co-authors:

Pedro Barrulas

Pedro Nogueira

José Mirão

Fernando Noronha

Abstract

The Azenhas and Alvito Fe-deposits are located at SW of the Iberian Variscan belt, in a wide Fe-Zn ore district (Montemor-Ficalho Belt), part of the Ossa-Morena Zone. Both deposits are dominantly composed of magnetite ores that display distinct ore formation processes and, at the Azenhas deposit, massive magnetite ores are mainly hosted in amphibolites (Middle Cambrian – Ordovician), with a genesis arguably associated with metamorphic-metasomatic reactions promoted by fluid circulation through several thrust faults that led to and expressive tectonic pilling. Contrastingly, the Alvito massive magnetite ores are formed by the emplacement of a gabbro-dioritic suite in contact with calcite-dolomite marbles, constituting a typical calcic exoskarn Fe-skarn deposit. Primary and secondary magnetite were identified and characterized, and further selected for *in situ* laser ablation coupled inductively mass spectroscopy (LA-ICP-MS) trace element analysis. Results show that primary magnetite (Mag I) from the Azenhas deposit is discriminated by higher concentrations of Mg, Cr, Mn, Zn, Co, and Sn, whereas secondary magnetite (Mag II) is depleted in most trace elements, although displaying relatively higher concentrations of V, Ga, Mo, and Pb. The application of $T_{Mg\text{-}Mag}$ geothermometer reinforced the discriminatory indexes, with Mag I displaying higher-temperature estimations (ca. 770 ºC) when compared to Mag II (ca. 420 ºC), thus suggesting that primary ores are associated to higher temperature processes than previously assumed.

Characterization of the ores from Alvito deposit revealed primary magnetite characterized by abundant ilmenite and Al-spinel oxy-exsolutions which led to high measured Al concentrations in magnetite. The trace element content indicates high-temperature hydrothermal magnetite, underlining the contribution of hot hydrothermal fluids from the igneous body emplacement, also supported by the $T_{Mg\text{-}Mag}$ geothermometer (ca. 685 ºC). The anomalous presence of Co (max. 156 ppm) and Ni (max. 100 ppm) concentrations in Mag I from Alvito, along with pentlandite-magnetite assemblages, suggest that prone conditions were sustained for the development of Ni-bearing ores and that magnetite composition could be an interesting geochemical proxy for the exploration of such mineralization.

The Mn + Al versus Ti + V discriminant diagram shows that primary ores from both deposits plot in the skarn field. The combination of magnetite analyses with whole-rock geochemistry and field geology, allowed us to define criteria that can be applied in the discrimination of Fe-deposits and contribute to improve the geological models of the studied ore deposits, thus beneficiating future exploration in SW Iberia.

Keywords: Fe-deposits; LA-ICP-MS; Magnetite; Trace element analysis; Geothermometry; Exploration vectoring.

3.1 Introduction

Mineral chemistry is used as a pathfinder in geological exploration of greenfield and brownfield areas, particularly focusing on hydrothermal alteration of the host rocks and aiming for deep-seated or partially obscure exploration targets (e.g. Baker et al., 2020; Cooke et al., 2020). In appropriate cases, when magnetite is present its composition can be used to refine the geological models of the ore deposits, which can contribute to vector future mineral exploration (e.g. Pisiak et al., 2017; Ward et al., 2018).

Magnetite is a widespread mineral throughout many metallogenic and geodynamic settings and is found in numerous deposit types including skarn, volcanogenic massive sulphides (VMS), and Iron-Oxide Copper and Gold Deposits (IOCG). Nadoll et al. (2014) discussed in detail the incorporation and substitution of several elements in magnetite structure and its control by the physical and chemical parameters, mainly influenced by the depositional conditions, namely temperature and oxygen fugacity (fO_2). Incorporation of such elements in magnetite structure usually happens at trace concentrations, therefore, micro-analysis of these elements can be used as a tool in identifying the mechanisms that control their presence, providing valuable clues for characterizing the depositional conditions of the ores. Understanding these mechanisms and constraining ore-forming fluid conditions could provide innovative insights regarding the metallogenic potential of the Montemor-Ficalho Belt (MFB). MFB is a metallogenic province (Mateus et al., 2013) located at the SW of Ossa-Morena Zone (OMZ) that comprises several metasedimentary units and intrusive bodies with ages spanning from the Neoproterozoic up to the Carboniferous.

Montemor-Ficalho belt is described as a magnetitic-zinciferous province displaying several Fe (Montemor-o-Novo, Azenhas, Alvito, Orada, etc.) and Zn-(Pb) deposits (Preguiça and Vila Ruiva deposits; **Fig. 3.1a**) whose genesis is intrinsically controlled by the OMZ geodynamic context and associated tectonic structures. Almost 20 iron deposits and occurrences were identified in MFB including SEDEX-VMS iron deposits (Salgueiro, 2011; Salgueiro et al. 2012) such as the Montemor-o-Novo iron deposits (Andrade et al. 1949), and Fe-Skarn deposits, such as, the Azenhas, Alvito, Orada and Vale de Pães deposits (Carvalho 1971, Oliveira et al. 1986; Matos et al. 1998, Caldeira et al. 2007; Salgueiro et al. 2010a, 2010b; Mateus et al. 2005; 2013). Other examples of Fe-skarn deposits can be found at the Spanish counterpart, such as the Cala, Colmenar, and Monchi deposits (Velasco and Amigó, 1981; Carriedo et al., 2006; 2021; Tornos et al., 2002; 2021). Additionally, MFB displays several other base-metal deposits, that have attracted exploration projects throughout recent years, and special interest has been addressed to the Escoural gold district (Maia et al. 2022) and the Ni-Cu Odivelas prospect (Jesus 2011; Jesus et al. 2020).

Fe-deposits of MFB, particularly the case studies herein presented, display contrasting ore-forming conditions, hence, its comprehension can benefit from *in situ* LA-ICP-MS trace element analysis of magnetite samples collected from the ore horizons, by following the methodologies proposed by several authors (Dupuis & Beaudoin 2011: Dare et al. 2012; 2014; Nadoll et al. 2012; 2014; Knipping et al. 2015; Makvandi et al. 2016; 2021; Huang and Beaudoin, 2019; Wu et al., 2019).

Through this work, we intend to provide the first comprehensive description of Fe-deposits in SW Portugal based on magnetite chemical composition. A detailed mineralogical ore deposit description along with a thorough mineral geochemistry is provided, aiming to, i) constrain the physical and chemical conditions of the ore-forming events; ii) evaluate the geochemical composition of magnetite allying it with lithogeochemistry and mineralogy, aiming to contribute for the comprehension of Fe-deposits formation in SW Iberia; iii) use trace element content in magnetite as a fingerprinting method to identify potential mineral exploration targets in MFB, and iv) identify the implications of the geodynamic evolution of OMZ in controlling the iron deposits metallogenic evolution and consequently trace element incorporation into magnetite.

3.2 Regional geologic context

The Montemor-Ficalho sector (Oliveira et al., 1991) is the Portuguese portion of the Évora-Aracena/Beja-Aracena domains (Chacón et al., 1983; Apalagueti et al., 1990). These domains have a distinct and complex geologic evolution, that reflect different stages of the Variscan cycle.

OMZ (Julivert, 1972) is limited at north by the Tomar-Badajoz-Córdoba shear zone which was active throughout the Cadomian and Variscan cycles, and at SW by the Beja-Acebuches Ophiolitic Complex, which also marks the contact with the South Portuguese Zone (SPZ). The contact between OMZ and SPZ is the result of the Gondwana-Avalonia oblique collision (Devonian-Carboniferous; Dallmeyer et al. 1993; Jesus et al., 2007; 2016; Pin et al., 2008; Pereira et al., 2012), which led to the Rheic ocean closure during the Variscan cycle.

Several deformation stages have been identified and interpreted as a result of the geodynamic evolution of the area and are described as D_1, expressed by metasedimentary pilling and folding, affecting all units until Devonian ages; D_2 characterized by isoclinal folding generally with low angle axial planes and magmatic-anatectic events, and D_3 stage, materialized by mostly vertical axial planes and by deep-seated strike-slip faults (Azor et al., 2019).

In the inner domains of OMZ, notably at the Montemor-Ficalho belt, several ophiolite sequences (Pedro et al., 2010), high-pressure rocks (Araújo et al. 1995, Ribeiro et al., 2010;

Pedro et al., 2013) and an accretionary wedge - Pulo do Lobo terrane – are individualized (Quesada et al., 1994; Quesada et al., 2019). As compression begins and closing of the Rheic ocean leads to the collision between Avalonia and Gondwana, subduction-obduction episodes give rise to the emplacement of allochthonous ophiolite remnants and parauthochthonous sedimentary-volcanic units thrusted to the inner domains of OMZ, constituting the Moura Phyllonitic Complex (Upper Ordovician – Lower Devonian). This unit is composed of mica schists with intercalations of basic and felsic metavolcanic rocks, as well as segments of lower Cambrian – Silurian sedimentary succession of the OMZ authochthonous sequence chaotically dispersed within the schistose matrix (Araújo, 1995; Araújo et al., 2005; 2013; Roseiro et al., 2019) and furthermore exhibiting evidence for HT-HP metamorphism evidenced by the presence of eclogites and blue schists (Ribeiro et al., 2010).

At the MFB several expressions of calc-alkaline magmatism are observed, such as 1) at the Évora massif where high-grade metamorphic terrains are materialized by the anatectic Gneiss-Migmatite Complex (341 Ma; Pereira et al., 2015), and are accompanied by calc-alkaline magmatism (Hospitais tonalite massif - 336 Ma; Moita et al., 2015); 2) the late to post tectonic Pedrógão granite in the inner domain of MFB (**Fig. 3.1a-b**) which possibly register the late stages of calc-alkaline magmatism in OMZ (ca. 300 Ma; Moita et al., 2005); and 3) the Beja Igneous Complex at SW (**Fig. 3.1a**) which marks a complex and partitioned calc-alkaline body associated with different magmatic pulses triggered by the collisional settings near the suture of OMZ and SPZ, and aided by slab-break off of the subducted oceanic plate (Pinto and Soares de Andrade, 1987; Pereira et al., 2003, 2007; 2008; Jesus et al., 2007; 2016; Moita et al., 2005; 2009; Dias da Silva et al., 2018; Ribeiro et al., 2019).

The evolution of the Variscan Orogen provided suitable conditions for the formation of several ore deposits both in the OMZ and in SPZ (**Fig. 3.1a**). Examples of world-class deposits are found at the Iberian Pyrite Belt (IPB) in the SPZ, such as the giant massive sulfide Neves Corvo deposit. Contrastingly, the OMZ, and particularly MFB, comprise diverse ore deposits which were mined intermittently over the last century. The selected study areas lie within the MFB and conceal Fe-deposits with distinctive emplacement conditions, and therefore their study and comparison provide valuable information on the metallogenic settings of the Fe-Zn Montemor-Ficalho belt.

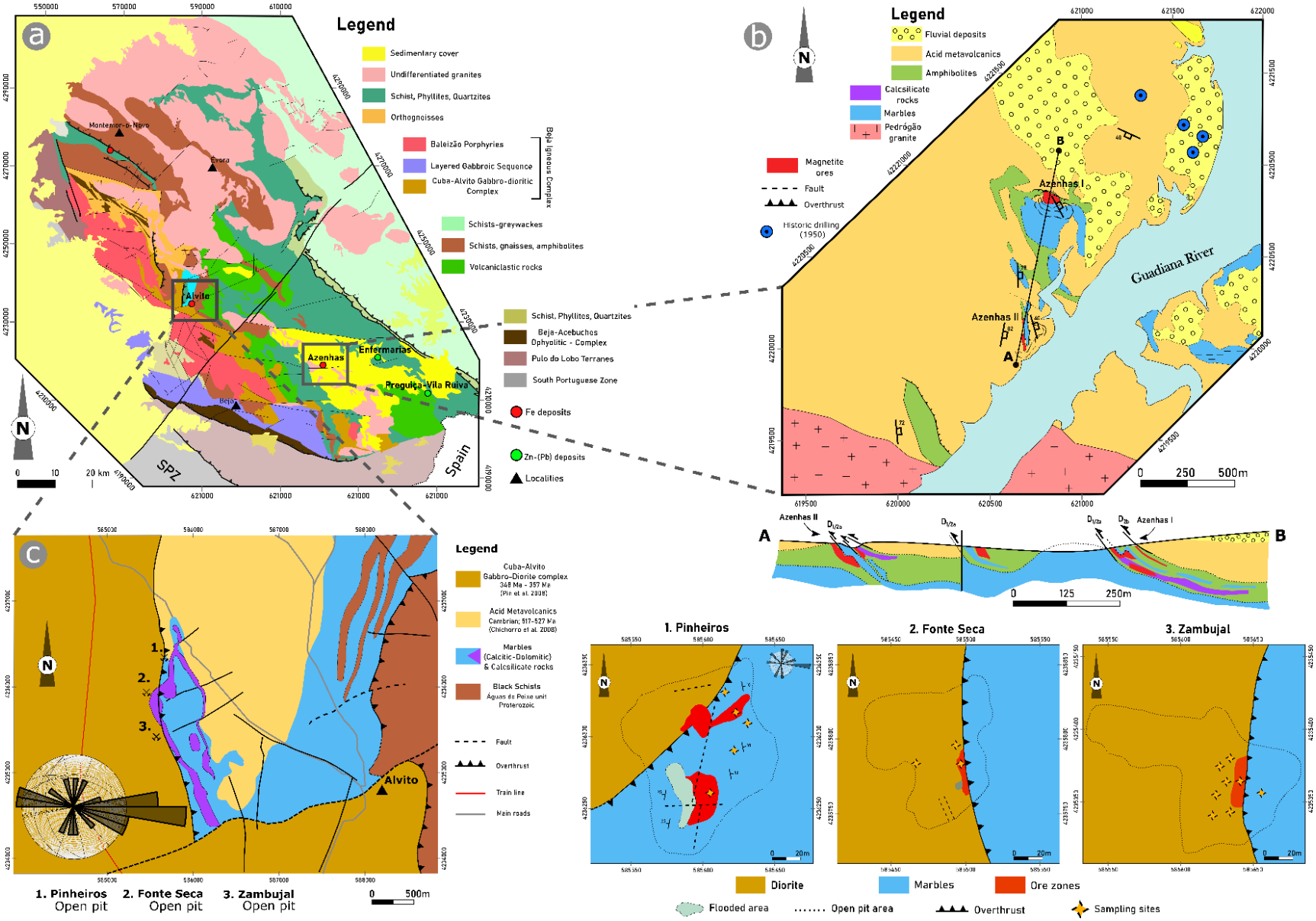
a
Legend
Sedimentary cover
Undifferentiated granites
Schist, Phyllites, Quartzites
Orthogneisses
Baleizão Porphyries
Layered Gabbroic Sequence
Cuba-Alvito Gabbro-dioritic Complex
Beja Igneous Complex
Schists-greywackes
Schists, gnaisses, amphibolites
Volcaniclastic rocks
Schist, Phyllites, Quartzites
Beja-Acebuchos Ophyolitic - Complex
Pulo do Lobo Terranes
South Portuguese Zone
Fe deposits
Zn-(Pb) deposits
Localities
Montemor-o-Novo
Évora
Alvito
Azenhas
Entremarias
Preguiça-Vila Ruiva
Beja
SPZ
Spain
N
0 10 20 km
b
Legend
Fluvial deposits
Acid metavolcanics
Amphibolites
Calcsilicate rocks
Marbles
Pedrógão granite
Magnetite ores
Fault
Overthrust
Historic drilling (1950)
Azenhas I
Azenhas II
Guadiana River
0 250 500m
A
B
0 125 250m
c
Legend
Cuba-Alvito Gabbro-Diorite complex 348 Ma - 357 Ma (Pin et al. 2008)
Acid Metavolcanics Cambrian; 517-527 Ma (Chichorro et al. 2008)
Marbles (Calcitic-Dolomitic) & Calcsilicate rocks
Black Schists Águas de Peixe unit Proterozoic
Fault
Overthrust
Train line
Main roads
Alvito
1. Pinheiros Open pit
2. Fonte Seca Open pit
3. Zambujal Open pit
0 500m
1. Pinheiros
2. Fonte Seca
3. Zambujal
Diorite
Marbles
Ore zones
Flooded area
Open pit area
Overthrust
Sampling sites

Figure 3.1. (previous page). (**a.)** Geological map of the SW of Ossa-Morena Zone, adapted from the 1: 500 000 cartography (Serviços Geológicos de Portugal, 1992). In the figure the main geological units are shown, along with the location of the study areas and other deposits referred throughout the text. **(b.)** Geological map of the Azenhas area at the scale 1: 5 000 (adapted from Serviço de Fomento Mineiro, 1965) with location of the Azenhas open pit at the left margin of the Guadiana River. The bottom image corresponds to a cross-section (A-B) shown in figure 1b. **(c.)** Geological map of the Alvito area at the scale 1: 50 000 (adapted from Carvalhosa, 1971; Gomes, 2000; Gomes and Fonseca, 2006) and the geological mapping of the sampled open-pit areas from the Alvito deposit (1. Pinheiros open pit; 2. Fonte Seca open pit; 3. Zambujal open pit). All coordinates are presented in the WGS 84-UTM 29N referencing system.

3.3 Ore deposit geology

3.3.1 The Azenhas deposit

Azenhas is an ancient iron mining area composed of two main open-pits (Azenhas I and Azenhas II; **Fig. 3.1b**) that focused exploitation in massive and disseminated magnetite ores hosted in basic metavolcanic units – amphibolites – part of the Moura Phyllonitic Complex. The mining areas are located at the west margin of the Guadiana River 3km northeast of the *Pedrogão* village (**Fig. 3.1b**). The Pedrogão region was exploited from the late 19th century until the '70s decade of the 20th century, particularly in the Orada iron mine (3 km to SE of Azenhas). Several drill cores were performed in the area by the former Portuguese governmental mining services during the 40s of the 20th century (**Fig. 3.1b**) to evaluate the mining potential of the deposits. Currently, mining works are inactive due to the lack of economically viable tonnage of the currently recognized ore bodies, although up to date feasibility assessment of the area is absent with perspectives for other mineral exploration targets to be found.

At the Azenhas area three main geological units prevail, as defined by Araújo (1995), i) the allochthonous (Araújo 1995; Mateus et al., 2005) *Mina do Pequito* Unit (MPU) composed of intricate successions of basic metavolcanic rocks, marbles (Cambrian), and skarns (Meinert et al., 1992; Meinert et al., 2005) composed of calcsilicate mineral assemblages. This unit is interpreted as being part of the Moura Phyllonitic Complex; ii) The allochthonous *Azenha da Rabadoa* Unit (ARU) composed of felsic metavolcanic rocks, and iii) the *Pedrógão* two-mica post-tectonic granite (308 ± 4 Ma.; Carvalho, 1971; **Fig. 3.1b**) which intrudes the former units.

At the Azenhas I open-pit (**Fig. 3.1b**), MPU is individualized in several lithotypes, such as, marbles amphibolites, and calcsilicate rocks that host most of the iron ore bodies. This unit results from the tectonic pilling of the amphibolites over marbles (Middle Cambrian – Upper Cambrian) during two main thrusting episodes (Araújo, 1995), which presumably promoted a thermal gradient inversion generating local metasomatic reactions and favouring ore deposition during the retrograde stage, thus having been classified as a skarn deposit (Mateus

et al., 2005; Salgueiro et al., 2010b; Salgueiro, 2011; Mateus et al., 2013). The genesis of Azenhas Fe-skarn deposit has been previously attributed to the intrusive post-tectonic granitic suite of *Pedrógão*, but latter works (e.g. Mateus et al., 2005) have excluded this hypothesis due to the cross-cutting criteria observed at the outcrops, which suggest that the *Pedrógão* intrusion intersects the D_1/D_{2a} thrusting, and therefore its emplacement is posterior to the tectonic pilling and ore genesis (Mateus et al., 2005; 2013; Salgueiro, 2011).

A suite of felsic metavolcanic rocks of the ARU is observed at top of the MRU succession. The contact is marked by a thrust structure striking WNW-ESE and dipping NE, corresponding to D_{2b} structures, as defined by Araújo (1995). This thrust truncates, at the top, the MPU pilling and ore bodies, suggesting that mineralization is previous to this major structural event. Alteration of the felsic metavolcanic rocks is observed towards the contact, by strong silicification associated with the local fluid circulation and heat transfer promoted by the thrusting and its latter reactivations (Mateus et al., 2005).

3.3.2 The Alvito deposit

The Alvito iron deposit is located approximately 3km northwest from the Alvito municipality and consists of four open-pit mining sites that explored magnetite bodies hosted in metasomatic aureoles at the contact between the Cuba-Alvito gabbro-diorite suite (CAGD) and the Viana do Alentejo-Alvito marbles. Our work focused on ore bodies from three of those mining sites (**Fig. 3.1c**), in which sampling and geological mapping were carried out.

At the Alvito area, four main units can be individualized, as follows (Rosas et al., 2008; Akker et al., 2020), i) an acid metavolcanic orthogneiss unit with an oriented texture (S_N: N80ºE; 25ºS) and E-W fracturing dipping towards N (**Fig. 3.1c**). This unit can be correlated to the Cambro-Ordovician (522.3 ± 5 Ma.) rift-related acid volcanism (Chichorro et al., 2008; Sánchez-Garcia et al., 2003; 2019), observed throughout the MFB and more particularly in the Monfurado Formation units, to whom they share several petrographic and geochemical features - see section 5.1 - (Carvalhosa, 1985; Caldeira et al., 2007; Maia et al., 2022); ii) the (Ca-Mg)-marbles of the Viana do Alentejo antiform. iii) the Proterozoic metasedimentary units, designated as *Série Negra* in Iberia, mainly composed of graphitic and biotitic schists - *Águas de Peixe* unit (**Fig. 3.1c**) - which are relatable to the *Escoural* Formation at the Montemor-o-Novo sector (Chichorro, 2006; Maia et al., *submm*.). iv) the Cuba-Alvito gabbro-diorite suite, which outcrops at W and S of the study area (**Fig. 3.1c**). This suite belongs to the Beja Igneous Complex (BIC), which also includes a Layered Gabbroic Sequence (Jesus et al., 2007; 2016; Jesus, 2011). CAGD U-Pb ages were estimated around 350 Ma. (Pin et al., 2008), although K-Ar ages in biotite revealed younger ages, in the range of 338 – 325 Ma. (Gomes, 2000), which could register the cooling of the massif.

The iron ores are controlled by the emplacement of the CAGD at the margin of the Viana do Alentejo – Alvito marbles, which induced contact metamorphism and metasomatic reactions that led to the formation of an Fe-exoskarn deposit (Einaudi and Burt, 1982).

3.4 Analytical Methods

Thirty-four samples representative of the ore horizons and host rocks were collected at the Azenhas and Alvito deposits, subsequently prepared in 35 thin sections and 20 cross-sections for further observation under transmitted and reflected light microscopy. Sample preparation and mineralogical description were conducted at the Geosciences Department of the University of Évora (Portugal). Subsequently, detailed description of magnetite and associated mineral assemblages were performed, and cross-sections underwent scanning electron microscopy (SEM) and energy dispersive spectroscopy using a VP-SEM-EDS Hitachi 3700N scanning electron microscope with a Bruker Xflash 5010 SDD x-ray spectrometer at the HERCULES Laboratory of the University of Évora (Portugal), using an acceleration voltage of 20 kV at 40 Pa. SEM-EDS was an important step in identifying and characterizing possible inclusions, exsolutions, and zoning that could affect analytical interpretation. Mineralogical abbreviations used throughout the manuscript are accordingly to Whitney and Evans (2010).

Magnetite major and minor element composition were determined using a CAMECA SX 100 equipment at the University of Oviedo (Spain). The selected cross-sections were analysed using a 5 *µm beam diameter, with a 15 kV and 40 nA for Mg, Al, Si, Ca, Ti, Fe, Cr, Mn, and Ni, whereas for V, Co, and Zn an acceleration voltage of 25 kV and a current of 60 nA was used.*

LA-ICP-MS is commonly part of the analytical procedures used in the geochemical characterization of magnetite. The selected magnetite grains were photographed throughout this study and a total of 230 spot analyses were performed in 45 grains, matching the areas previously analysed by EPMA. A total of 28 isotopes (^{24}Mg, ^{27}Al, ^{28}Si, ^{42}Ca, ^{45}Sc, ^{49}Ti, ^{51}V, ^{52}Cr, ^{55}Mn, ^{57}Fe, ^{59}Co, ^{62}Ni, ^{65}Cu, ^{66}Zn, ^{71}Ga, ^{73}Ge, ^{75}As, ^{89}Y, ^{90}Zr, ^{93}Nb, ^{97}Mo, ^{118}Sn, ^{178}Hf, ^{181} Ta, ^{182}W, ^{208}Pb, ^{232}Th, ^{238}U) were determined in representative magnetite types of the deposits, following the methodology proposed by Nadoll and Koenig (2011). REEs (rare earth elements) were also included in the analytical package to identify contamination during signal acquisition, which could indicate the presence of inclusions such as calcite and calcsilicate minerals (common in skarn deposits).

Analysis was conducted at the HERCULES Laboratory (University of Évora, Portugal) by means of a CETAC LSX-213 G2+ laser ablation system coupled to a Triple Quad ICP-MS (Agilent 8800).

Prior to the analysis, ICP-MS was calibrated using NIST 610 glass standard for sensitivity optimization as well as for minimizing both elemental fractionation ($^{238}U/^{232}Th$ ratio) and oxide formation ($^{248}ThO/^{232}Th$ ratio). The samples were studied through spot analysis using a 400 burst with a 50 µm laser beam, a repetition rate of 10 Hz, and 100% energy, using helium as carrier gas at 1 L/min. Each spot analysis had a total acquisition time of 70 seconds, including 15 s for a gas blank, 40 s of ablation, and 15 s for cell washout. Method validation, namely quantification of accuracy and precision, was performed using the GSE-1G reference material (Jochum et al. 2005; Guillong et al., 2005) as an external standard, which was also analysed three times every 20-25 sample spot analysis to check for potential instrumental drift. Reference materials GSC-1G and BCR-2G were also analysed every 20-25 spots as unknowns (quality controls) to check for elemental recovery (%) assays.

With the presented methodology a total quantification accuracy (mean) -0.242% was obtained for all elements, as well as a 3.12% total method precision (mean), and a LOD for trace elements (mean) of 0.10 ppm. In this study, mean and representative FeO (wt. %) was used as an internal standard element (data collected by EPMA analysis) and for data reduction and elemental quantification purposes data was processed using Glitter® software.

In **the Appendix E and Appendix F** all the previously mentioned data can be found in **tables 4.3** and **4.4**. REE data is not disclosed due to their relatively low concentration in magnetite (Nadoll and Koenig 2011), although they were important guidelines during time-resolved data reduction to exclude spots in which inclusions were ablated along with magnetite. The correlation between Ti (EPMA) and Ti (LA-ICP-MS) for similar analysed areas revealed r^2 of 0.84; and between V (EPMA) and V (LA-ICP-MS) an r^2 of 0.57, which indicated a good correlation of analysis from both equipment.

Additionally, major and trace element bulk analyses were performed in 11 samples from the Azenhas deposit and 22 milled samples from Alvito deposit. Major element analysis was performed using X-ray fluorescence (XRF), whereas trace and REE content were quantified by ICP-MS through a fusing bead and acid digestion method. Both analyses were performed at the ALS Seville Laboratories using the selected ME-XRF26 and ME581 analytical packages.

3.5 Results

3.5.1 Host-rock features

Distinctive host-rock features are found in the Azenhas and Alvito deposits, which contributes significantly to the differences found in both Fe-deposit genesis.

3.5.1.1 Azenhas deposit

The MPU displays variable degrees of hydrothermal alteration as a result of D_1 and D_{2a} thrusting episodes. The high contents of MgO (7.2 wt.% - 16.9 wt.%; **Table 3.1**) reflect the mineralogical composition of the marbles, with variable amounts of dolomite and olivine (**Fig. 3.2a**). A general LREE enrichment over MREE and HREE (**Fig. 3.2a**) is observed (La/Sm_{CN}= 2.8 – 4.2; Sm/Yb_{CN}= 1.9 – 2.9), and two of the samples display a positive Eu anomaly (Eu/Eu*= 1.2 – 2.2).

The MPU amphibolites host most of the massive magnetite ores, and the ore horizons mainly comprise amphibole and olivine (**Fig. 3.2c – e**). The Zr/TiO_2 versus Nb/Y plot indicates that the amphibolites display geochemical affinities with andesitic and basaltic rocks (**Fig. 3.3c**), coherent with other author´s data for the Azenhas area (Salgueiro, 2011). The relatively flat REE patterns revealed distinct positive anomalies of redox-sensible elements, such as Ce/Ce*= 1.1 – 1.2 and Eu/Eu*= 2.1 – 2.6 (**Fig. 3.3a**). Sections of the MPU unit are rich in calcsilicate mineral assemblages, in which amphibole and epidote (**Fig. 3.2f**) are the dominant minerals. These sections are considered to be skarns (Meinert 1992; Meinert et al., 2005) and are crosscut by thin calcite veins (**Fig. 3.2f**), and by late quartz-feldspar veins which are composed of quartz with sub granulation and anhedral shapes, along with plagioclase crystals and, frequently, calcite (**Fig. 3.2b**). These veins display distinct geochemical compositions with high SiO_2 contents, up to 55.5 wt.%, and CaO and Na_2O concentrations of 9.5 wt.% and 8.9 wt.%, respectively (c.f. **Table 3.1 - Sample AZ5**).

The ARU felsic metavolcanic rocks display a matrix dominantly composed of a quartz-feldspar assemblage (**Fig. 3.2g-h**). Quartz displays a sub granulation texture, that is related to the deformation imposed by the thrusting of this unit. Feldspar is mainly albite with anhedral shapes sometimes displaying irregular rims, and green hornblende crystals are seldomly found (**Fig. 3.2g-h**).

The geochemical analysis of the ARU displays a flat REE pattern with slightly negative Eu anomalies (Eu/Eu*= 0.70), and a subtle enrichment of LREE over HREE and MREE, with La/Sm_{CN}= 1.27 and Sm/Yb_{CN}= 1.24 (**Fig. 3.3a**). Contrastingly, rocks that are found closer to the D_{2b} thrust plane are extremely silicified, displaying an REE pattern outlining depleted LREE over MREE and HREE, with La/Sm_{CN}= 0.75 and Sm/Yb_{CN}= 0.13 (**Fig. 3.3a**). The new ARU

geochemical data is consistent with previously published data for the area (Mateus et al., 2005; Salgueiro, 2011) and reveal affinities to rhyolite and rhyodacite compositions displaying SiO_2 in the range 71.9 – 77.7 wt. %, , similar to what was found in other felsic metavolcanic units of OMZ (Pedro, 1996; Leal, 2001; Sánchez-Garcia et al., 2003; 2019; Chichorro, 2006; Telhado, 2018; Maia et al., 2022), some of which also plotted in **Figure 4.3d**.

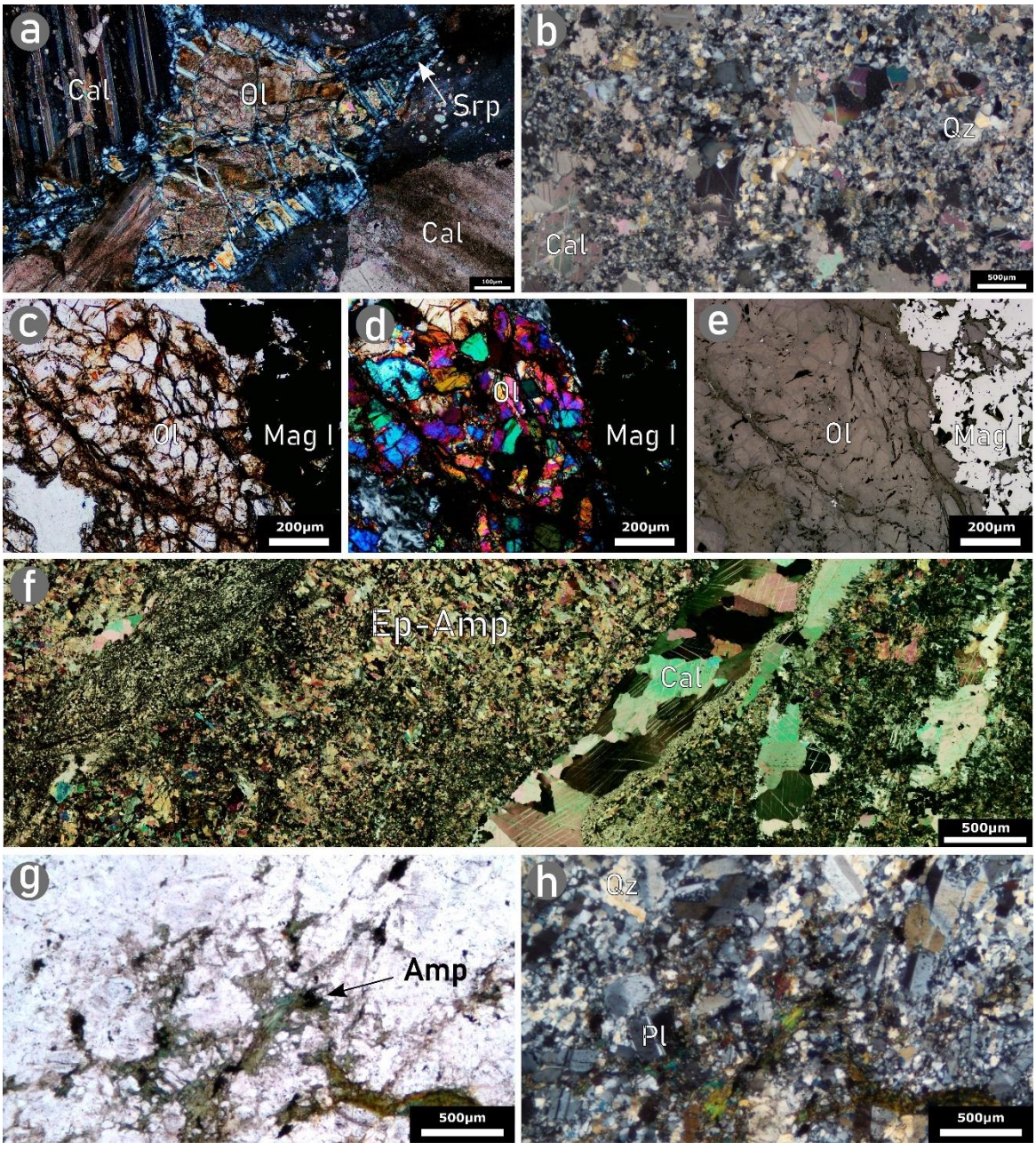

Figure 3.2. (a.) Crossed polarized light (CPL) microscopy image of the MPU olivinic marbles, with remnant olivine (Ol) crystals displaying intense serpentinization (Srp), particularly at the rims. **(b.)** CPL image showing a silicified section of the marbles from the MPU, where anhedral calcite (Cal) and quartz (Qz) crystals are observed. **(c.)** Plane polarized light (PPL) microscopy image showing the matrix of the magnetite ores hosted in the MPU

amphibolite, displaying olivine crystals (Ol) at the contact with primary magnetite (Mag I). **(d.)** CCP image of the same section shown in (c.). **(e.)** Reflected light image of the same section shown in (c.) and (d.), with identification of primary magnetite (Mag I). **(f.)** CPL image displaying the mineral assemblage observed in extremely metasomatized amphibolites (MPU) sections, the groundmass is dominantly composed of Epidote (Ep) and amphibole (Amp). **(g.)** PPL image of representative textural and mineralogical features of the acid metavolcanics (ARU, see text), where amphibole (Amp) is observed in interstitial spaces of quartz and feldspar crystals. **(h.)** CPL image from the same section shown in (g.), with identification of the main minerals composing the matrix of the ARU metavolcanic rocks.

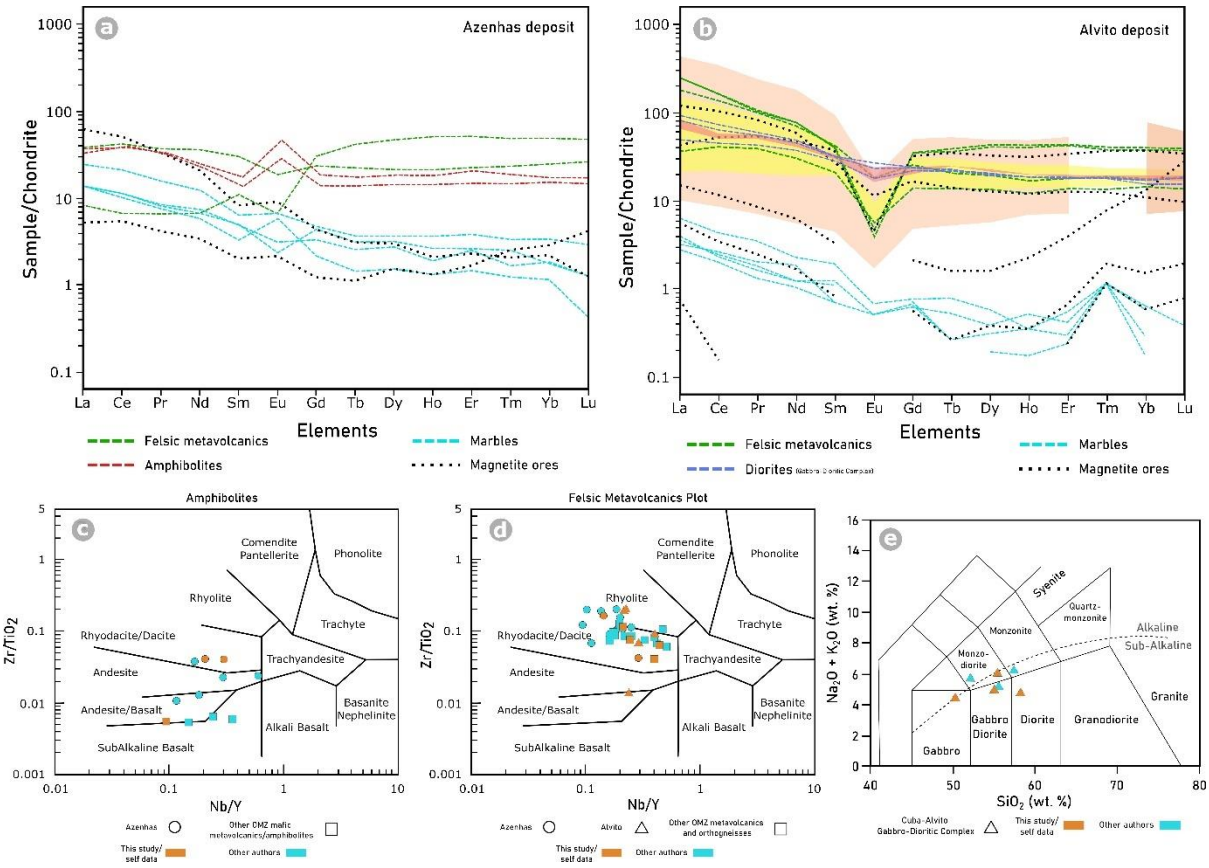

Figure 3.3. (a.) REE pattern of the analyzed representative samples from the Azenhas deposit, chondrite values after Palme and O´Neill (2014). **(b.)** REE pattern of the analyzed representative samples from the Alvito deposit. The shadowed patterns represent data from literature as follows: orange field corresponds to data from the Alcáçovas Orthogneiss (Telhado, 2018); yellow field refers to data of acid metavolcanic rocks from the Monfurado Formation (Montemor-o-Novo area) after Maia et al., 2022.; red field refers to Gabbro-Dioritic data from Caldeira et al. (2007). **(c.)** Volcanic rocks discriminant diagram (after Windchester and Floyd, 1977) applied to basic metavolcanic data (amphibolites – ARU) and compared to literature data, as follows: data from the Azenhas area from Salgueiro (2011); data from another mafic metavolcanics of the Ossa-Morena Zone from Chichorro (2005). **(d.)** Volcanic rocks discriminant diagram (after Winchester and Floyd, 1977) applied to acid metavolcanic rocks of the Azenhas and Alvito area and compared to literature data from other acid metavolcanic units from the MFB of the Ossa-Morena Zone, outlining the affinity of these lithotypes to rhyodacite-rhyolite rocks. Literature data as follows: Azenhas felsic metavolcanics from Salgueiro (2011) and other OMZ metavolcanic and orthogneisses from

Telhado (2018), referring to the Alcáçovas Orthogneisses. **(e.)** Total alkali-silica discriminant diagram for plutonic rocks (after Middlemost, 1994) applied to the Gabbro-Diorite data and compared to data from Caldeira et al. (2007).

3.5.1.2 Alvito deposit

The Alvito area is largely controlled by the calc-alkaline Cuba-Alvito gabbro-diorite suite (ca. 350 Ma, Pin et al., 2008) which, at the deposit area, is constituted by a medium to fine-grained diorite with quartz, feldspar and hornblende as the main constituents. At the microscopic scale, quartz exhibits strong sub-granulation (**Fig. 3.4a**) and recrystallization, with lobated rims. Plagioclase phenocrysts are consistently observed throughout the ground mass, displaying concentric zonation (**Fig. 3.4a**) and frequently sericitized cores (**Fig. 3.4a**).

The geochemical analysis (**Table 3.2**) from the CAGD display compositions compatible with gabbro-diorite rocks, with SiO_2= 50.3 – 58.3 wt.% and $Na_2O + K_2O$= 4.5 – 6 wt.% (**Fig. 3.3b**), consistent with published data for this suite (Caldeira et al., 2007). REE patterns are flat, with a slight enrichment of LREE over HREE and absent, to slightly negative, Eu anomalies, with Eu/Eu*= 0.72 – 0.96 (**Fig. 3.3b**). The $Na_2O + K_2O$ versus SiO_2 plot reveals its affinity to the gabbro-diorite compositions (**Fig. 3.3d**), also coherent with previous data (Caldeira et al., 2007).

The described samples from the Viana do Alentejo – Alvito marbles allowed to distinguish two main facies, one exclusively constituted by calcite (**Table 3.2 – Samples AL 5 and AL 16**) and another correspondent to olivine marbles (**Table 3.2 – Sample AL 7; AL 21 and AL 22**), with pervasive serpentinization (**Fig. 3.4g-h**). Such differences are distinguishably identified by the geochemical compositions of both lithotypes, with calcite-dominated facies displaying CaO content between 53.1 wt.% to 54 wt.% and MgO from 0.77 wt.% and 2.1 wt.%, whereas the olivine-rich marbles exhibit lower CaO values (31.1 wt.% - 33.4 wt.%) and higher MgO (19.1 wt.% - 19.5 wt.%). A descending REE pattern with a slight enrichment of LREE over HREE is consistent throughout the analysed samples.

The intrusion of the CAGD at the contact with Viana do Alentejo – Alvito marbles promoted metasomatic alteration which led to the formation of skarns, in which textures and mineral assemblages contrast with the surrounding rocks. These lithotypes are mainly composed by diopside – hedenbergite assemblages, in which distinctive vesuvianite-rich calcsilicate-rock nodules were identified, consistent with other author´s observations (Gomes, 2000; Gomes et al. 2004). These lithotypes have SiO_2 contents between 40.0 wt.% and 44.3 wt.%, and high CaO values 7.69 wt.% and 21.8 wt.% (**Table 3.2**). Variable Al_2O_3 content is consistent with the identified mineral assemblage (Al_2O_3= 1.17 – 21.2 wt.%).

The Alvito area is also characterized by acid metavolcanic rocks, that display rhyolite – rhyodacite affinity (SiO_2= 68.5 – 78.1 wt.%), with geochemical compositions similar to the felsic

metavolcanic rocks of the Azenhas deposit (Pedro, 1996; Leal, 2001; Sánchez-Garcia et al., 2003;2019; Chichorro, 2006, Mateus et al., 2005; Salgueiro, 2011; Telhado, 2015; Carvalhosa, 1985; Maia et al., 2022)

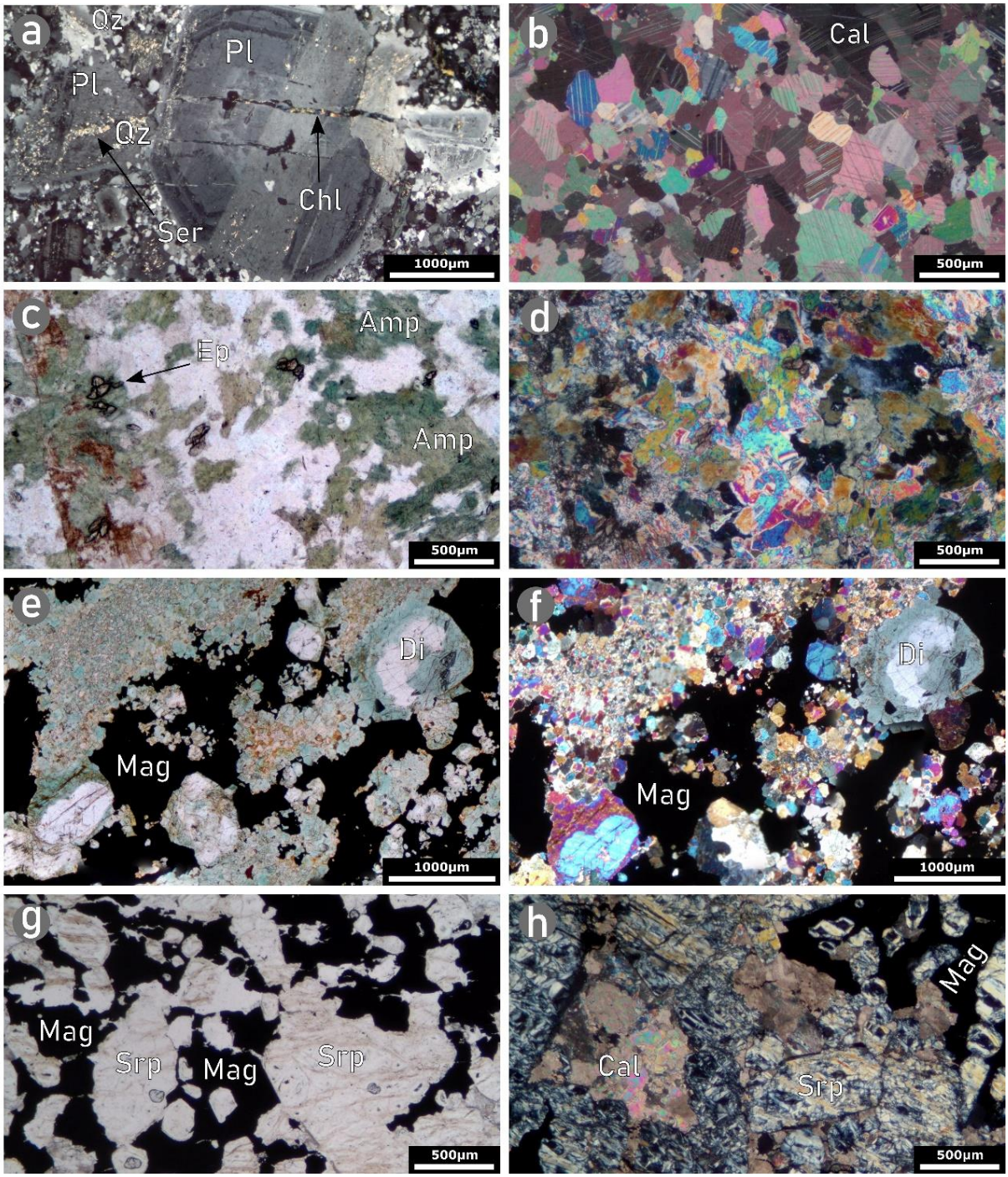

Figure 3.4. (a.) CPL image of the characteristic feldspar porphyroblasts displaying concentric zoning and sericitization identified in diorite from the Cuba-Alvito Gabbro-Dioritic Complex. **(b.)** Calcitic marble matrix CPL image observed in the Viana do Alentejo – Alvito marbles. **(c.)** PPL image from the metasomatic assemblages, displaying amphibole-pyroxene assemblages. **(d.)** CPL image from the section shown in (c.). **(e.)** Magnetite ores matrix displaying pervasive pyroxene assemblages, with large crystals that display green-rims (hedenbergite, Hdn) and colorless cores (diopside; Di); PPL image. **(f.)** CPL image of the same section shown in (e.). **(g.)** Olivine-serpentine matrix hosting massive magnetite ores. Serpentine is the main constituent of the matrix due to intense serpentinization. Relics of olivine are preserved, and sparse calcite crystals are observed, PPL image. **(h.)** CPL image of the same section shown in (g.).

3.5.2 Magnetite ores

3.5.2.1 Azenhas deposit

Two main types of magnetite were identified at the macroscopic and mesoscopic scale at the Azenhas deposit, individualized in primary and secondary ores. Primary magnetite ores (Mag I) are mainly composed by massive magnetite horizons, ubiquitous at the mining area and hosted by the amphibolitic rocks (**Fig. 3.2e-g; Fig. 3.5a**), although in restricted sections banded disseminated magnetite ores were identified hosted in the marbles. Massive magnetite exhibits a sub euhedral to euhedral habit (**Fig. 3.6a**), extremely porous with sparse micro-inclusions of silicates and carbonates. Backscattered electron imagery (BSE) by SEM-EDS indicates that this magnetite does not display significant geochemical zonation (**Fig. 3.6c, f, h**).

Secondary magnetite (Mag II) is found in small centimetric to millimetric veins which crosscut the skarns (**Fig. 3.2f**), sidewise, small calcite veins are also found in this lithotype (**Fig. 3.2f**). Magnetite II is usually fine-grained, found as aggregates accompanied by calcsilicate mineral assemblages (**Fig. 3.6g**). The larger crystals of this type have homogeneous textures with no representative geochemical zonation and were therefore selected for the EPMA and LA-ICP-MS trace element analysis (**Fig. 3.6f, g, h**). Whole-rock geochemistry of the magnetite ores revealed Fe_2O_3 contents between 21 wt.% and 59.3 wt.%, when hosted by carbonate dominated rocks (**Table 3.2 – Sample 11**) and amphibolite (**Table 3.2 – Sample 8**), respectively.

The magnetite ores hosted by amphibolite display higher SiO_2, Al_2O_3, and TiO_2 content when compared to iron ores hosted by the marbles, which on the contrary display higher CaO and MgO contents, consistent with the more dolomitized facies. REE patterns display a notorious enrichment of LREE over MREE and HREE (La/Sm_{CN}= 2.58 - 7.61; Sm/Yb_{CN}= 0.70 - 3.7).

Table 3.1. Whole-rock analysis of the host-rocks and magnetite ores from the Azenhas deposit. Major elements in wt.%; trace elements and REE in ppm.

Sample Reference	AZ 1	AZ 2	AZ 5	AZ 6	AZ 7	AZ 9	AZ 10	AZ 4	AZ 12	AZ 8	AZ 11
ithology	Felsic Metavolcanic rocks		Marbles and caclsilicate rocks					Metassomatized amphibolites		Magnetite ores	
wt. %											
SiO_2	71.9	77.7	55.5	11.6	11.8	8.75	9.46	49.7	48.2	18.65	11.8
Al_2O_3	13.9	12.3	16.3	0.98	1.78	1.21	1.27	9.83	10.8	1.88	0.57
Fe_2O_3	2.07	1.45	1.02	4.3	6.25	5.41	2.81	10.3	10.55	59.3	21
CaO	1.19	0.32	9.51	39.9	28.9	41.1	41.3	17.3	17.9	3.03	17.65
MgO	0.46	0.7	0.45	7.19	16.85	9.39	9.55	7.52	6.36	15.15	21.1
Na_2O	7.64	6.74	8.89	0.03	0.03	0.02	0.02	3.04	2.81	0.03	0.02
K_2O	0.09	0.04	0.06	<0.01	<0.01	<0.01	<0.01	0.02	0.02	0.01	<0.01
TiO_2	0.65	0.22	0.17	0.04	0.09	0.06	0.06	0.37	0.37	0.18	0.01
MnO	0.04	0.02	0.05	0.39	0.83	0.43	0.36	0.21	0.2	0.6	0.64
P_2O_5	0.12	0.02	0.03	0.02	0.02	0.01	0.02	0.17	0.11	0.01	<0.01
LOI	0.91	0.73	6.73	34.4	33.4	32.9	34.3	1.69	2.23	2.34	27.2
Total	98.97	100.24	98.74	98.86	99.96	99.3	99.16	100.18	99.59	101.18	99.99
ppm											
Ba	225	417	53.8	8.8	4.1	10.5	13.9	31.9	22.6	9.1	7.2
Sr	378	313	282	220	147	245	215	322	392	6.9	52.4
Rb	48.1	34.9	1.2	0.2	0.2	<0.2	0.2	0.8	0.5	0.2	0.2
Cs	2.69	0.7	0.13	0.09	0.11	0.02	0.06	0.09	<10	0.13	0.07
V	167	139	7	27	23	21	17	28	14	98	28
Co	16	20	<1	1	3	3	<1	3	5	56	56
Ni	<1	17	<1	5	6	11	11	6	6	8	4
Cr	10	50	10	20	20	20	20	10	<10	20	10
Zr	148	195	164	11	17	16	20	155	156	7	4
Hf	4	5	5.6	0.4	0.6	0.6	0.6	4.8	4.5	0.3	0.2
Nb	6.3	7.6	5.2	0.8	1.2	1.1	1.2	6.5	5.6	0.7	0.6
Ta	0.6	0.7	0.5	0.1	0.2	0.1	0.2	0.4	0.1	0.1	<0.1
Ga	20.2	19.9	9	1.8	3.1	2.2	2.4	14.9	16.7	12.8	1.8
Tl	<10	<10	<10	<10	<10	<10	<10	<10	<10	<10	<10
Li	10	10	<10	10	10	<10	<10	20	20	<10	<10
Cd	<0.5	<0.5	0.7	<0.5	0.7	0.5	<0.5	<0.5	1.2	<0.5	<0.5
Mo	<1	<1	2	<1	1	1	1	1	<1	<1	1
Sn	2	2	3	1	2	1	1	7	7	6	12
W	1	1	2	1	2	2	1	1	1	5	2
Ag	<0.5	<0.5	<0.5	<0.5	<0.5	<0.5	<0.5	<0.5	<0.5	<0.5	<0.5
As	5	<5	<5	10	6	8	<5	8	8	<5	255
Pb	<2	6	16	8	5	11	8	12	20	<2	2
Zn	51	65	32	217	601	99	53	139	119	590	421
Cu	<1	18	932	3	8	4	3	1	1	1	1
Th	2.7	4.97	9.9	0.63	0.98	0.8	0.88	2.91	2.54	0.1	0.08
U	1.05	1.81	1.48	3.17	3.43	2.58	3.34	2.4	2.97	0.24	0.65
Y	25.9	26.7	11.6	2.5	6.1	3.9	4.7	21.6	27.3	2.5	4.2
Sc	16	19	3	1	2	1	1	9	9	1	<1
La	11.9	22.1	0.7	3.2	5.7	3.3	3.3	7.8	8.7	1.2	14.5
Ce	27.9	45	2.2	6.1	12.6	6.8	6.6	24.1	23.9	3.3	30.5
Pr	4.03	5.61	0.42	0.69	1.43	0.77	0.75	3	3.08	0.38	3.03
Nd	17.1	22.5	2.1	2.6	5.5	3.3	3	10.2	11	1.5	9.3
Sm	4.2	4.8	0.82	0.48	0.93	0.71	0.73	2.03	2.6	0.29	1.19
Eu	1.02	1.53	0.2	0.32	0.37	0.17	0.13	1.62	2.63	0.12	0.5
Gd	4.38	4.83	1.03	0.42	0.92	0.64	0.86	2.82	3.74	0.24	0.86
Tb	0.79	0.81	0.26	0.05	0.13	0.09	0.11	0.5	0.62	0.04	0.11
Dy	4.96	5.11	1.87	0.37	0.88	0.66	0.77	3.6	4.56	0.37	0.71
Ho	1.02	1.02	0.39	0.07	0.19	0.1	0.14	0.78	0.99	0.07	0.11
Er	2.97	2.83	1.38	0.23	0.61	0.39	0.41	2.41	3.33	0.26	0.36
Tm	0.45	0.46	0.27	0.03	0.08	0.04	0.06	0.36	0.46	0.06	0.05
Yb	2.74	2.75	1.8	0.18	0.54	0.29	0.28	2.48	2.77	0.45	0.35
Lu	0.45	0.45	0.3	0.01	0.07	0.03	0.03	0.36	0.42	0.1	0.03

Table 3.2. Whole-rock analysis of the host-rocks and magnetite ores from the Alvito deposit. Major elements in wt.%; trace elements and REE in ppm.

Sample Reference	AL 2	AL 14	AL 17	AL 34	AL 9	AL 15	AL 29	AL 30	AL 5	AL 7	AL 16	AL 21	AL 22	AL 1	AL 4	AL 31	AL 3	AL 6	AL 8	AL 10	AL 19	AL 20
Lithology	Diorites				Felsic Metavolcanic rocks				Marbles					Calcsilicate			Magnetite ores					
wt. %																						
SiO_2	58.3	50.3	55.1	55.4	75.8	68.5	77.7	78.1	5.78	2.1	1.26	0.52	1.24	44.3	41.3	40	17.85	31.2	44.7	42.5	31.6	18.3
Al_2O_3	17.85	15.25	16.85	16.75	13.55	15.4	11.5	11.6	0.17	0.45	0.17	0.11	0.43	20.8	21.2	1.17	0.52	0.16	2.62	4.95	4.24	0.91
Fe_2O_3	6.81	6.44	8.06	5.22	0.28	3.45	1.19	1.21	0.14	3.06	0.17	1.87	1.66	7.18	9.33	19.9	54.8	36.9	22.6	29.3	46.5	48.8
CaO	6.06	5.62	8.2	6.38	1.27	2.01	0.03	0.04	54	31.1	53.1	33.4	31.3	16.95	7.69	21.8	0.09	1.39	21.2	15.45	13.4	2.68
MgO	3.22	3.07	4.18	6.5	0.15	0.99	0.23	0.24	0.77	19.2	2.08	19.45	19.05	2.68	8.87	5.76	22.2	28.2	9.67	3.8	4.6	21.3
Na_2O	3.64	3.53	4.14	3.81	3.61	4.29	0.15	0.15	0.02	0.01	0.02	0.01	0.01	0.44	0.56	0.17	0.02	0.02	0.12	0.44	0.2	0.01
K_2O	1.06	0.95	0.77	2.18	4.54	2.1	6.39	6.49	0.08	<0.01	0.07	<0.01	0.01	2.86	3.23	0.05	<0.01	<0.01	0.07	0.71	0.29	0.01
TiO_2	0.88	0.86	1.6	0.58	0.11	0.38	0.13	0.13	0.01	0.03	0.01	<0.01	0.03	0.77	0.83	0.04	0.02	0.01	0.03	0.15	0.04	0.07
MnO	0.1	0.11	0.14	0.11	0.01	0.06	<0.01	<0.01	0.09	0.52	0.08	0.43	0.42	0.26	1.24	0.83	0.3	0.72	0.3	0.58	0.24	0.22
P_2O_5	0.14	0.15	0.21	0.08	0.07	0.1	0.01	0.01	<0.01	<0.01	<0.01	<0.01	<0.01	0.18	0.17	0.02	0.01	0.11	<0.01	0.52	<0.01	0.01
LOI	1.91	1.72	1.2	2.95	0.64	1.69	1.61	1.68	38.5	43	42.7	42.8	44.6	3.73	6.07	9.06	4.65	1.9	0.13	0.33	-0.41	8.66
Total	100.01	88.07	100.54	100.12	100.2	99.07	99.02	99.73	99.6	99.47	99.67	98.6	98.75	100.26	100.62	98.81	100.46	100.61	101.44	98.74	100.71	100.97
ppm																						
Ba	225	417	475	989	1455	770	676	693	159.5	7.2	16.7	17	14.4	681	954	46.9	3.3	8.2	11.3	114	127.5	2.6
Sr	378	313	418	343	208	257	83.5	82.8	276	64	146.5	109.5	94.1	249	248	90.4	1.1	2.5	18	47.9	40.2	11.6
Rb	48.1	34.9	21.1	60.6	87.6	52.4	179.5	184	3	0.4	3	0.3	0.4	145	180.5	0.6	0.3	0.8	1	3.9	11.3	0.3
Cs	2.69	0.7	0.81	190	0.57	0.4	10	10	0.12	0.03	0.2	0.03	0.08	8.17	8.08	10	0.02	0.12	0.18	0.48	0.34	0.03
V	167	139	233	106	12	39	<5	<5	13	16	8	7	10	44	88	12	11	9	11	25	17	23
Co	16	20	23	24	1	4	<1	1	<1	<1	<1	<1	<1	15	7	28	63	146	39	41	83	63
Ni	<1	17	5	83	<1	1	4	5	9	3	7	3	3	9	11	11	5	179	3	15	4	43
Cr	10	50	30	190	10	20	10	10	10	10	10	60	10	70	30	10	10	10	10	130	20	20
Zr	148	195	75	75	94	252	254	251	15	14	6	8	8	299	136	12	11	7	40	68	40	21
Hf	4	5	2.3	2.4	3.4	6.4	8.8	8.6	0.2	0.4	<0.2	0.2	0.2	8.1	3.8	0.3	0.2	<0.2	1.7	2.6	2	0.6
Nb	6.3	7.6	6.4	4.1	8.4	8.1	15.3	15.7	<0.2	0.4	<0.2	0.3	0.4	13.8	7.5	0.6	4	1	3	6.9	6.9	5.2
Ta	0.6	0.7	0.5	0.4	1.3	0.7	1.1	1	0.1	0.1	0.1	<0.1	0.1	0.8	0.5	<0.1	0.1	0.1	0.1	0.5	1.1	0.2
Ga	20.2	19.9	19.3	18.1	16.6	18.1	23.3	22.6	0.7	1.3	0.4	0.7	1.2	23	18.2	3.7	3.1	6.1	8	13.9	19.7	17.9
Tl	<10	<10	10	<10	<10	10	<10	<10	<10	<10	<10	<10	<10	<10	<10	<10	<10	<10	<10	<10	<10	<10
Li	10	10	<10	20	<10	10	20	20	<10	<10	<10	<10	<10	110	80	<10	<10	<10	10	<10	10	<10
Cd	<0.5	<0.5	<0.5	<0.5	<0.5	<0.5	<0.5	<0.5	<0.5	<0.5	<0.5	<0.5	<0.5	<0.5	<0.5	2.1	<0.5	<0.5	0.8	0.5	<0.5	<0.5
Mo	<1	<1	1	<1	<1	1	1	1	1	1	1	1	<1	1	<1	<1	3	1	<1	1	2	<1
Sn	2	2	1	1	2	1	3	3	<1	1	<1	<1	<1	13	23	6	32	4	12	27	11	26
W	1	1	2	2	<1	6	5	5	<1	1	<1	2	1	16	2	1	1	6	<1	4	2	6
Ag	<0.5	<0.5	<0.5	<0.5	<0.5	<0.5	<0.5	<0.5	<0.5	<0.5	<0.5	<0.5	<0.5	<0.5	<0.5	<0.5	<0.5	<0.5	<0.5	<0.5	<0.5	<0.5
As	5	<5	7	<5	<5	<5	<5	<5	<5	<5	<5	6	5	<5	<5	<5	<5	5	<5	7	<5	5
Pb	<2	6	7	2	5	3	3	2	<2	9	3	3	<2	7	10	<2	<2	<2	3	<2	3	6
Zn	51	65	63	40	3	40	6	6	5	21	6	16	12	109	53	78	222	257	110	130	86	236
Cu	<1	18	18	2	1	<1	4	5	<1	22	<1	2	<1	1	<1	<1	4	353	3	86	1	23
Th	2.7	4.97	3.49	4.83	11	11.7	14.3	15.05	0.1	<0.05	0.14	0.08	0.29	17.15	3.57	0.33	0.07	0.77	0.25	20.2	2.1	0.09
U	1.05	1.81	1.23	1.05	3.48	3.5	2.74	2.73	1.84	0.06	0.81	0.06	0.47	4.76	2.61	0.31	0.29	0.24	0.33	2.5	1.34	0.1
Y	25.9	26.7	25.9	17.1	20.6	27.7	67.5	69.8	0.6	0.9	1.2	0.6	0.7	39.4	21.2	1	0.2	3.3	5.6	19.1	47.2	1
Sc	16	19	26	24	2	8	4	4	<1	<1	<1	<1	<1	10	12	1	<1	1	2	4	1	1
La	11.9	22.1	19.1	7.6	9.1	44.7	62.3	62.1	0.7	0.9	1.6	1	0.8	101	10.1	0.5	0.2	3.7	6	29.6	10.6	1.4
Ce	27.9	45	39.4	16.2	26.6	88.5	105.5	105	1.3	1.6	2.8	1.5	1.7	162	25.7	0.8	0.1	7.5	20	66.8	33.8	2.2
Pr	4.03	5.61	5.13	2.02	3.81	9.88	10.45	10.15	0.13	0.18	0.34	0.16	0.2	16.1	3.53	0.12	<0.03	0.85	3	8.08	5.23	0.24
Nd	17.1	22.5	21.1	9.6	14.4	34.4	37	36.8	0.5	0.6	1.1	0.6	0.9	51.5	14.7	0.4	0.1	3	10.7	28.4	22.7	0.8
Sm	4.2	4.8	4.7	2.41	3.28	6.54	6.2	6.2	0.11	0.19	0.3	0.17	0.11	8.89	3.41	0.08	<0.03	0.51	1.69	4.29	5.73	0.13
Eu	1.02	1.53	1.32	0.53	0.34	1.09	0.28	0.23	<0.03	0.03	0.04	<0.03	0.03	1.05	0.92	0.02	<0.03	<0.03	0.2	0.68	0.26	<0.03
Gd	4.38	4.83	4.74	2.79	2.94	5.39	7.23	7.32	0.1	0.13	0.16	0.15	0.14	7.82	3.7	0.15	<0.05	0.44	1.18	3.46	6.62	0.12
Tb	0.79	0.81	0.83	0.44	0.52	0.79	1.39	1.46	<0.01	0.02	0.03	0.01	0.01	1.23	0.59	0.02	<0.01	0.06	0.19	0.53	1.31	0.01
Dy	4.96	5.11	4.84	3.29	3.53	5.02	10.7	11.15	0.05	0.1	0.15	<0.05	0.08	7.64	4.04	0.12	<0.05	0.42	1.17	3.32	8.43	0.1
Ho	1.02	1.02	1.02	0.66	0.7	0.96	2.35	2.46	0.01	0.03	0.02	0.01	0.02	1.53	0.8	0.04	<0.01	0.13	0.22	0.68	1.78	0.02
Er	2.97	2.83	2.92	1.85	2.33	3.02	7.3	7.4	<0.03	0.07	0.09	0.04	0.05	4.55	2.54	0.13	0.04	0.66	0.69	2.16	5.69	0.11
Tm	0.45	0.46	0.44	0.28	0.35	0.49	0.97	1.05	0.03	0.03	0.03	0.03	0.03	0.65	0.42	0.03	0.03	0.2	0.13	0.32	0.95	0.05
Yb	2.74	2.75	2.51	1.76	2.44	2.98	6.39	6.73	0.03	0.11	0.05	0.03	0.1	3.85	2.57	0.17	0.1	2.2	0.57	1.84	6.28	0.26
Lu	0.45	0.45	0.38	0.28	0.35	0.48	0.96	1	<0.01	0.01	<0.01			0.6	0.37	0.02	0.02	0.71	0.1	0.25	0.89	0.05

3.5.2.2 Alvito deposit

Magnetite massive ores are hosted in metasomatized marbles in which olivine is extremely serpentinized (**Fig. 3.4g, h; Fig. 3.5b**) and skarn mineral assemblages were identified. Magnetite bearing rocks display a medium-grained matrix in which olivine and abundant clinopyroxene crystals are found. Clinopyroxene crystals display a concentric zonation in which the crystal rims are composed of green pyroxene hedenbergite and the cores by diopside (**Fig. 3.4e, f; Fig. 3.5b**), this feature was also identified by other authors (Gomes et al., 2004). Optical observations of polished rock sections suggests that primary magnetite does not display major post-depositional alteration. BSE imagery reveals that magnetite crystals are usually round-shaped and display pervasive exsolutions (**Fig. 3.7b, d, e, f**) identified as ilmenite and Al-spinel exsolutions (**Fig. 3.7c, g**). To a lesser extent magnetite is accompanied by sulfide phases (**Fig. 3.7h**) with dissolution and precipitation textures (**Fig. 3.7i**) in which pyrrhotite, Co-rich pentlandite, and sphalerite were found (**Fig. 3.7h, i, j**).

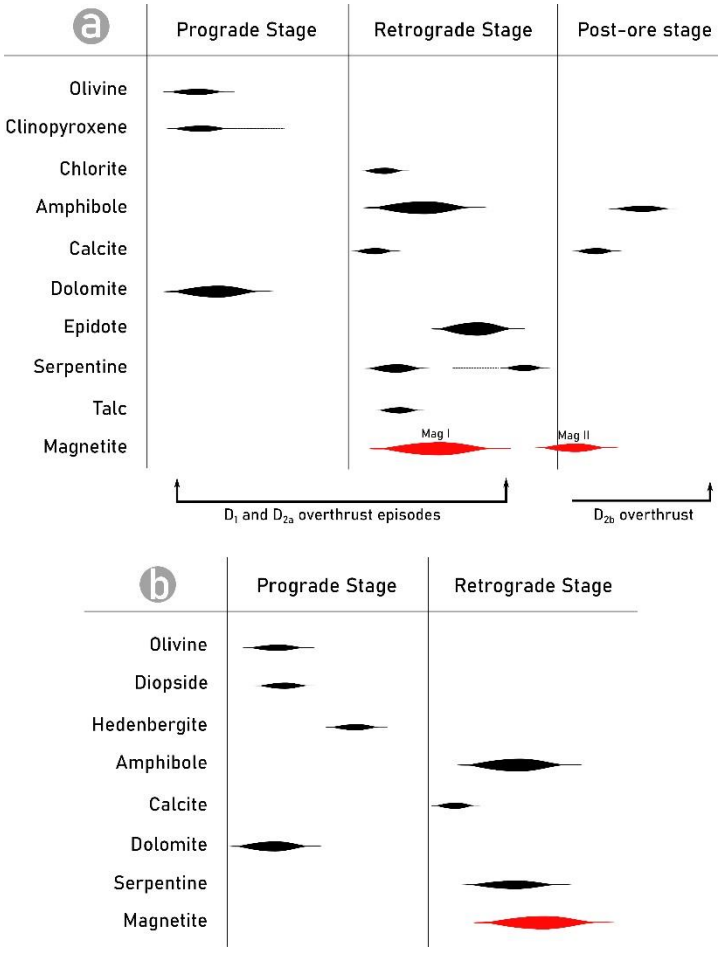

Figure 3.5. Sequence of crystallization for the Azenhas **(a.)** and Alvito **(b.)** deposit mineral assemblages.

Whole-rock analysis of massive magnetite ores revealed Fe_2O_3 contents between 22.6 wt.% and 54.8 wt.% with variable SiO_2 and MgO contents, from 17.9 – 44.7 wt.% and 3.8 – 28.2 wt.%, respectively. REE pattern of the magnetite ores exhibit two main profiles: one flatter with slight enrichment of LREE over HREE (**Fig. 3.3b**) and pronounced Eu anomalies (Eu/Eu*= 0.13 – 0.54), closer to the CAGD REE patterns; the other displays similarities to those obtained from olivine-rich marbles samples.

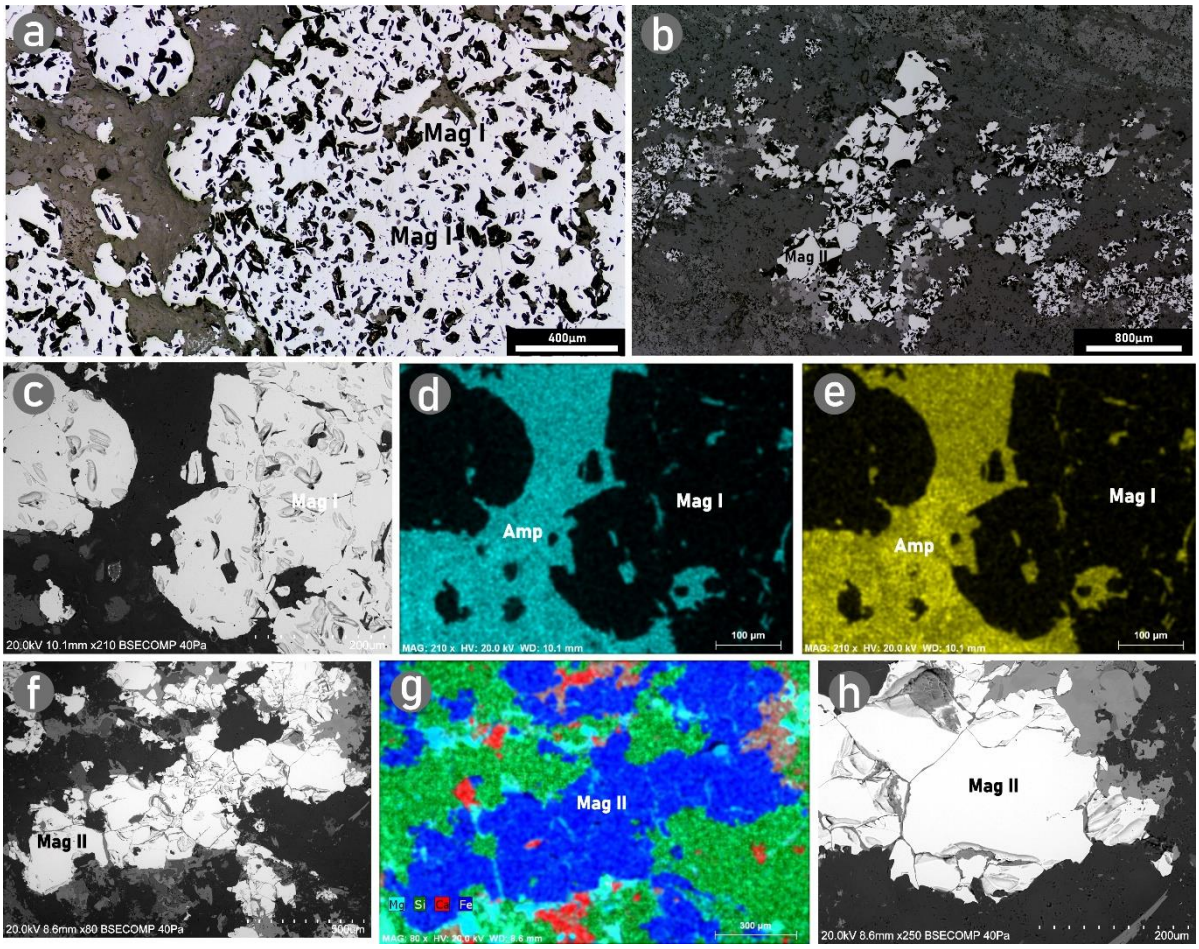

Figure 3.6. (a.) Reflected light microscopy (RLM) image of Mag I from the Azenhas deposit, which display a porous textural and several carbonate inclusions. **(b.)** RLM image of secondary magnetite from the Azenhas deposit. The image shows that magnetite is fine grained, found in small veinlets, with larger grains displaying homogenous textures. **(c.)** Backscattered electron imagery of the Azenhas Mag I, indicating porous textures with several inclusions. **(d.)** EDS map displaying the distribution of Mg, in the same section shown in (c.). **(e.)** EDS map displaying the distribution of Si, in the same section shown in (c.). **(f.)** Backscattered electron imagery of the Azenhas secondary magnetite. **(g.)** EDS map displaying the distribution of Mg, Si, Ca, Fe in the same section shown in (f.). **(h.)** Backscattered electron imagery of an approximation of the section shown in (f.), revealing a homogeneous texture for secondary magnetite.

3.5.3 Magnetite Composition

Representative Mag I and Mag II from the Azenhas deposit and primary magnetite from the Alvito deposit samples were analysed by EPMA and LA-ICP-MS.

3.5.3.1 EPMA

Mg, Al, Si, Ca, Ti, Fe, Mn, Zn, and O were analysed by EPMA; Cr, Ni, V, and Co were frequently close or below the limits of detection and therefore are ignored for this study. The summarized statistics of the data are supplied in **Table 3.3**. Mag I and Mag II from Azenhas display an average Fe of 69.36 wt.% and 71.69 wt.% respectively, whereas the Alvito magnetite displays an average Fe of 69.32 wt.%.

Although EPMA analysis was used as a procedure to obtain the FeO contents for LA-ICP-MS analysis, higher concentrations of Zn, Mn, Ti, Al, and Mg were found in primary magnetite from both deposits, when compared to Mag II from the Azenhas deposit.

3.5.3.2 LA-ICP-MS

Due to the larger sample volume created by the ablation spot, the LA-ICP-MS data display higher trace element variability when compared to EPMA, although similar trends were identified. Marked differences in trace element content were found between Azenhas and Alvito magnetite ores (**Table 3.4; Appendix E and F**), although the most significant variations are identified when comparing primary massive ores and secondary vein-like magnetite, exclusive to the Azenhas deposit.

Primary magnetite samples from the Azenhas and Alvito deposits display higher contents of most trace elements when compared to secondary magnetite samples, as shown by the boxplot and whisker plots (**Fig. 3.8**). Alvito primary magnetite revealed higher average contents of Al (9914 ppm), Cr (48 ppm), Co (86 ppm), Ni (41 ppm), Ga (40 ppm), and Sn (25 ppm), although Azenhas Mag I comprises higher average values of Mg (8534 ppm), Mn (4859 ppm) and Zn (659 ppm). Contrastingly, Mag II from the Azenhas deposit is depleted in most of the trace elements analysed, with exception of Pb (Ave. 81 ppm).

Higher values of Al were expected in the Alvito magnetite due to the abundant Al-spinel exsolutions outlined by BSE imagery (**Fig. 3.7b – g**), and consequently, the number of spot analyses per grains and sample was substantially increased to obtain results that reflect the composition of Alvito magnetites (Dupuis and Beaudoin, 2011; Dare et al., 2012; Nadoll et al., 2014; Hu et al., 2015; Chen et al., 2019; Huang et al., 2019).

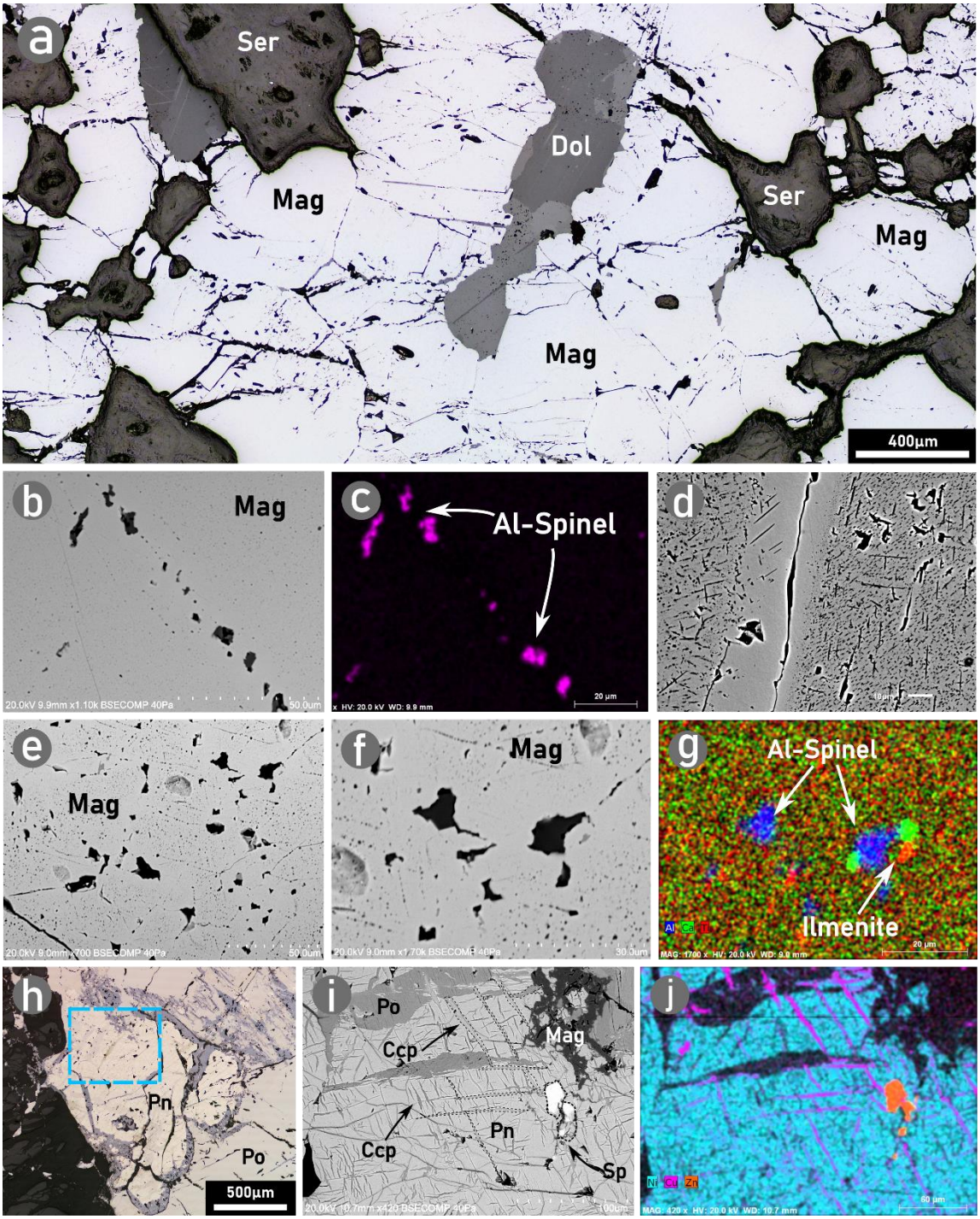

Figure 3.7. (a.) RLM image of the primary magnetites from the Alvito deposit, displaying dolomite and calcite inclusions. **(b.)** Backscattered electron imagery of the textural characteristics found in the primary Alvito magnetite, with pervasive exsolutions. **(c.)** EDS map of the section shown in (b.) displaying the distribution of Al in the Al-rich spinel exsolutions found in magnetite. **(d.)** Backscattered electron imagery of other textural examples from Alvito primary magnetite where pervasive oxy-exsolutions are observed. **(e.)** Backscattered electron imagery of the primary magnetite exsolutions. **(f.)** BSE imagery from a magnified section of the image shown in (e.). **(g.)** EDS map of the section shown in (f.) displaying the distribution of Al (blue), Ca (green) and Ti (red) with identification of Al-spinel and ilmenite exsolutions. **(h.)** RLM image of the sulfide assemblages sparsely found associated with primary magnetite at the Alvito deposit. These sulfide assemblages are mainly constituted by pyrrhotite (Po) and pentlantite

(Pn). **(i.)** BSE image of the textural characteristics found in pentlandite from the sulfide assemblages, with identification of fracture-filling textures in pentlandite. **(j.)** EDS map of the section shown in (i.) displaying the distribution of Ni (blue), Cu (purple) and Zn (orange) in pentlandite, chalcopyrite and sphalerite, respectively. EDS spot analysis revealed Co contents in pentlandite up to 8 wt.%.

3.6 Discussion

In recent years several studies have focused on constraining the factors that control trace element incorporation and subsequent textural and chemical variances in hydrothermal magnetite (Dupuis and Beaudoin et al., 2011; Dare et al., 2012; 2014; Huang and Beaudoin 2019; Nadoll et al., 2014; 2015), and also concerning the genesis of Fe skarn deposits (Hu et al., 2014; 2015; Hu et al., 2017; Chen et al., 2019; Xiao et al., 2019; Alaminia et al., 2020; Sarjoughian et al., 2020; Liu et al., 2019; Sun et al., 2019; Marbouti et al., 2020). Such conditions can be used to constrain the ore deposit formation, and to define new vectors for mineral exploration, using magnetite as a pathfinder when targeting anomalous concentrations of rare metals.

Despite significant advances in data acquisition and statistical treatment (Makvandi et al., 2016a; 2016b; 2021) the factors that control trace element variations in hydrothermal magnetite from different Fe deposit types are still quite obscure when compared to magmatic-related deposits (Nadoll et al., 2014; 2015; Huang et al., 2019; Duan et al., 2019; Mehrabi et al., 2019; Wu et al., 2019; Rodriguez-Mustafa et al., 2020), these considerations also apply when the subject is the iron deposits from SW Iberia.

3.6.1 Factors controlling magnetite composition

The factors that control trace element incorporation in magnetite are described by Nadoll et al. (2014), and, as discussed by these authors, in hydrothermal settings the main controlling factors are the temperature of the system at the time of deposition; the fluid-rock interactions; ionic radii proportions of the compatible elements, such as the lithophile and siderophile elements (Dare et al., 2014), and the spinel-structure of the magnetite and the oxygen fugacity conditions (Dare et al., 2012; 2014; Nadoll et al., 2014; 2015; Huang et al., 2019; Chen et al., 2019; Qi et al., 2019). The last is very well described for magmatic processes, whereas for hydrothermal systems of lower temperature (< 600ºC), the constraints are not yet well defined, nevertheless, the behaviour of redox-sensible elements, such as V and Cr can provide valuable insights.

Aluminium displays faint correlation with Ti (**Fig. 3.9c**), with values of Al progressively lower from Alvito primary magnetite → Azenhas Mag I → Azenhas Mag II, and with Ti varying

significantly in the studied cases. Due to its immobile nature, Al incorporation is greatly controlled by the temperature of the system at the time of magnetite deposition (Nielsen et al., 1994; Nadoll et al., 2014; 2015; Huang et al., 2019), therefore its relative abundance may suggest higher temperatures of formation.

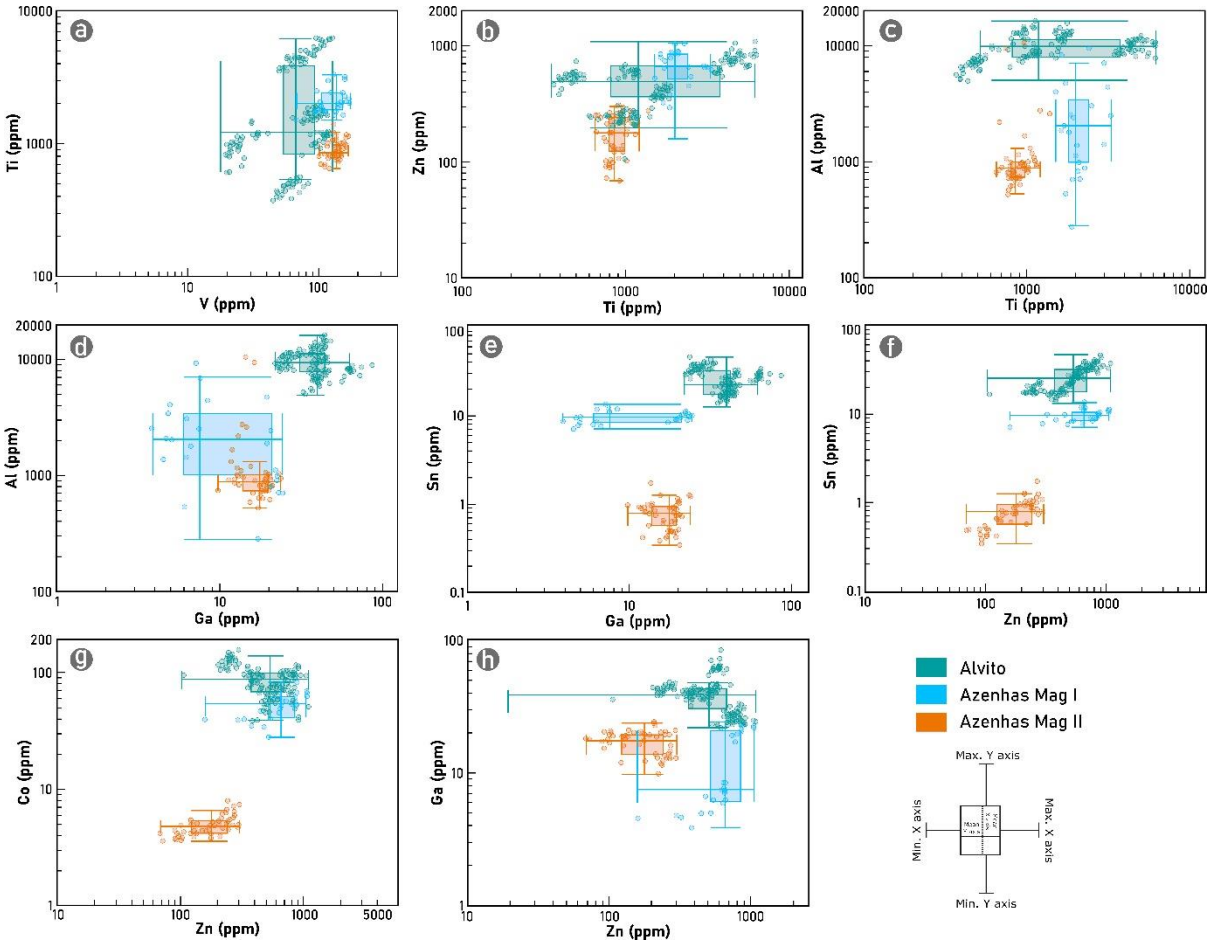

Figure 3.8. Boxplots of trace element data from the LA-ICP-MS analysis of the primary and secondary magnetite from both Azenhas as Alvito deposit. Data is organized according to the sample names and deposits as shown in the legend.

Sn and Ga behaviour are suggested as a good magnetite provenance discriminator (Kamvong et al., 2007) and also referred to reflect the temperature of formation (Nadoll et al., 2014). The Sn versus Ga plot (**Fig. 3.9e**) shows that the higher concentration of these elements are found in primary magnetite from Alvito, followed by the Azenhas Mag I, and lastly the Azenhas Mag II analysis, thus suggesting that the magnetite from Alvito deposit is related to relatively higher temperatures. Furthermore, the Sn versus Ga plot suggest that Mag II deposition is controlled by lower temperature conditions.

Positive correlations are found between Sn – Zn and Co – Zn, with Azenhas Mag I displaying values of Zn up to 1085 ppm (**Table 3.4; Appendix F** and Alvito magnetite displaying Co and Sn values up to 157 ppm and 46 ppm respectively. The Mg and Mn values found in the primary magnetite of both deposits (**Table 3.4; Appendix E and F; Fig. 3.8**) are consistent with extensive fluid-rock interactions usually described for metasomatized deposits (Einaudi et al., 1981; Meinert, 1987).

The incorporation of elements such as vanadium and nickel are highly dependent on oxygen activity and fugacity. V^{3+} is the dominant vanadium cation incorporated into magnetite due to similar ionic radii with Fe^{3+}, and at lower oxygen fugacity its behaviour is similar to Cr^{3+}, whereas at higher oxygen fugacity the incorporation of V^{4+} is favoured (Papike et al., 2005; Toplis and Corgne, 2002), exhibiting similar behaviour to Ti^{4+}. Consistently, the correlation of V, Cr, and Ti reflects the oxygen fugacity evolution throughout depositions. At the Azenhas deposit, Mag I display a stronger correlation between V and Ti (r^2= 0.28) which contrast with the weak correlation in Mag II (r^2= 0.02), that otherwise display a stronger correlation between V and Cr (r^2= 0.26). Such results suggest that in Mag I vanadium was possibly incorporated as V^{4+} suggesting that primary ores were associated with more oxidized conditions. In Mag II vanadium is presumably incorporated as V^{3+}, suggesting a decrease in oxygen fugacity, thus indicating progressively reduced conditions.

The magnetite from the Alvito deposit has a V and Cr correlation of r^2= 0.11, and a correlation between V and Ti of r^2= 0.27, suggesting that incorporation of V^{4+} was favoured. Such evidence seems to contrast to the incorporation of Ni into the spinel structure, which is described to only occur at very low oxygen fugacity (Nadoll et al., 2014). Nevertheless, the presence of Co-Ni-bearing sulphide phases implies that Ni was available in the original fluid at the time of deposition, which can affect the partitioning coefficient of Ni into the magnetite structure (Righter et al., 2006).

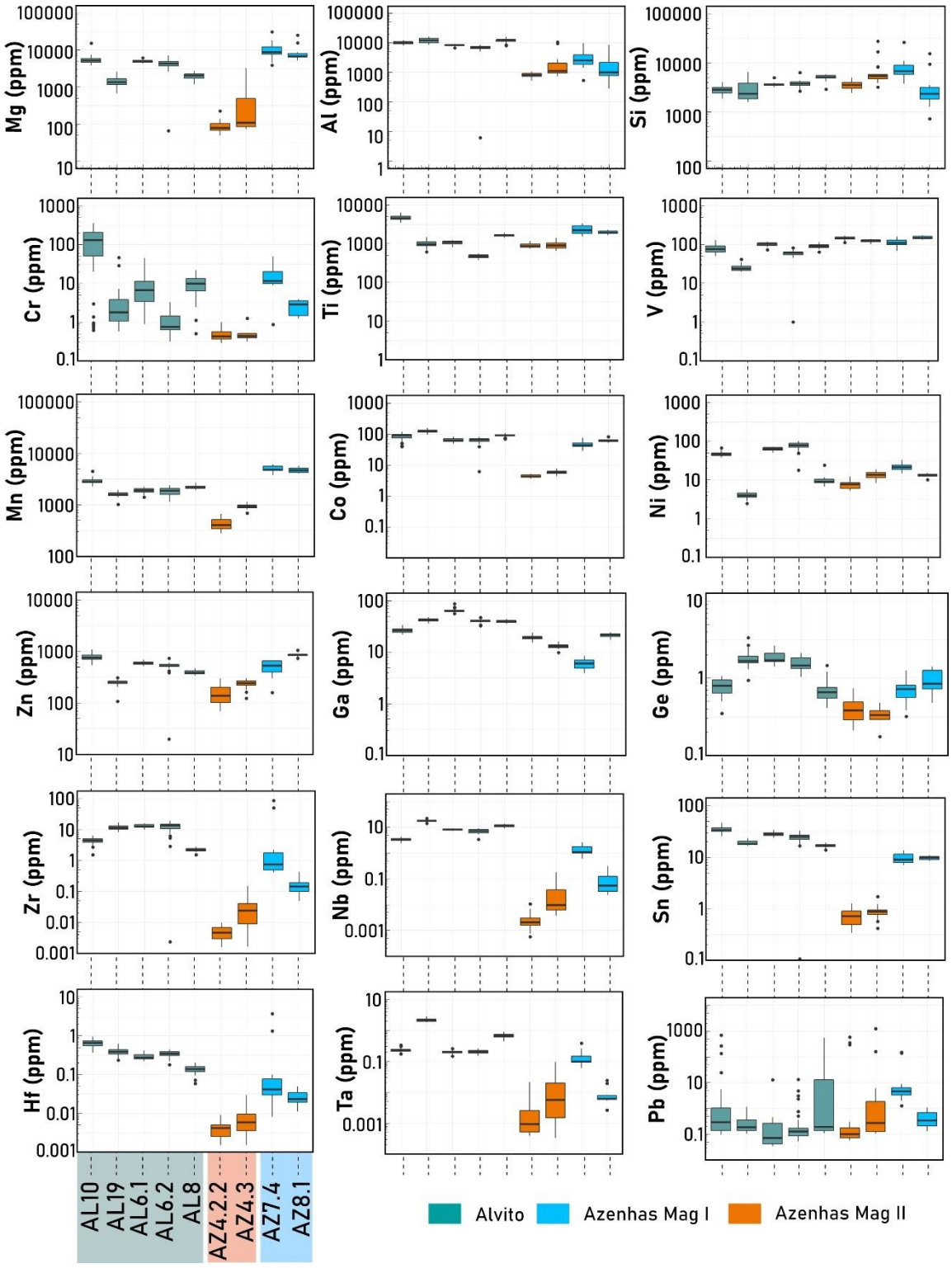

Figure 3.9. Combined double boxplot and scatterplot diagrams of several trace element data from the LA-ICP-MS analysis of primary and secondary magnetite from Azenhas and Alvito deposits. **(a.)** Titanium versus Vanadium. **(b.)** Zinc versus Titanium. **(c.)** Aluminium versus Titanium. **(d.)** Aluminium versus Gallium. **(e.)** Tin versus Gallium. **(f.)** Tin versus Zinc. **(g.)** Cobalt versus Zinc. **(h.)** Gallium versus Zinc.

3.6.2 Discriminating Skarn deposits in SW Iberia

The application of discriminant criteria based on geochemical composition of magnetite can provide valuable insights regarding the mechanisms behind ore deposition.

3.6.2.1 Discriminant diagrams

As proposed by Dupuis and Beaudoin (2011) and Nadoll et al. (2014) several elements (Ni, Cr, Si, Mg, Al, Zn, Ca, Cu, Mn, Ti, V) can be used in discriminatory diagrams in a tentative approach to classify ore deposits, although several other indexes should be used to strengthen the discrimination. The Ca + Al + Mn versus Ti + V diagram (Dupuis and Beaudoin, 2011) was altered by Nadoll et al. (2014) and Nadoll et al. (2015), that proposed the removal of Ca due to its negligible contribution in the Ca + Al + Mn cation sum, which agrees with our data with Ca having 75 % of non-detects. The Al + Mn versus Ti + V is currently one of the most widely applied discriminatory indexes in skarn deposits (Xiao et al., 2019; Alaminia et al., 2020; Sarjoughian et al., 2020; Liu et al., 2019; Sun et al., 2019; Marbouti et al., 2020; Hu et al., 2014; 2015; Hu et al., 2017; Ayupova et al., 2020), which allow to decipher the behaviour of usually immobile elements such as titanium (Wen et al., 2017). The Ti + V axis is interpreted by several authors as a good indication of the temperature of the system at the time of magnetite deposition. Such statement is supported by the direct relation found between higher Ti concentrations and magmatic magnetite (e.g. Dupuis and Beaudoin, 2011; Nadoll et al. 2014; 2015; Huang et al., 2019; Duan et al., 2019; Mehrabi et al., 2019; Wu et al., 2019; Rodriguez-Mustafa et al., 2020), whereas the Mn + Al axis is interpreted to reflect the extent of fluid-rock interactions.

The plots displayed in **Figure 4.10a and 4.10b** reveal that the primary magnetite from both deposits (Azenhas and Alvito) show affinities to the skarn fields of the diagrams. The Alvito primary magnetite displays a wide dispersion in the Ti + V axis, due to the wide Ti contents throughout the studied samples (371 ppm – 6188 ppm). Such dispersion can be attributed to the titanium-rich oxy-exsolutions (**Fig. 3.7b, d, e, f**) found in many of these magnetite crystals. These kinds of textures are interpreted to deplete the surrounding magnetite grain in the elements that compose said exsolution (e.g. Ti, Al), therefore masking the primary composition of the magnetite (Dupuis and Beaudoin, 2011; Dare et al., 2012; Nadoll and Koenig, 2014; Hu et al., 2015; Chen et al., 2019; Huang and Beaudoin, 2019), which outlines the importance of having a statistically significant number of spot analysis per grain. Alvito primary magnetite also displays the higher Al content (**Table 3.4; Appendix F**), partially influenced by the presence of Al-exsolutions (**Fig. 3.7b, d, e, f**). Nevertheless, in such cases high number of ablation spots were performed and therefore the trace element data is

considered as representative of magnetite composition (Dupuis and Beaudoin, 2011; Dare et al., 2012; Nadoll and Koenig, 2014; Hu et al., 2015; Chen et al., 2019; Huang et al., 2019).

Table 3.3. Representative EPMA data collected from the analysis of primary and secondary magnetite from the Azenhas and Alvito deposits.

Magnetite Type	**Magnetite I - Azenhas deposit**				**Magnetite II - Azenhas deposit**				**Primary Magnetite - Alvito deposit**			
Analysis	Min.	Max.	Ave.	Med.	Min.	Max.	Ave.	Med.	Min.	Max.	Ave.	Med.
Element (wt. %)												
Mg	0.1345	1.4269	0.404571	0.3665	0.0747	0.0747	0.0747	0.0747	0.0491	1.807	0.764732	0.328
Al	0.0263	1.156	0.179121	0.1059	0.0578	0.4589	0.101711	0.09965	0.5994	1.7681	1.103321	1.05845
Si	0.0188	0.6818	0.1613	0.0785	0.0177	0.9124	0.082148	0.0298	0.0201	0.6009	0.051181	0.0356
Ca	0.0182	0.8385	0.103449	0.0427	0.0172	0.1411	0.042793	0.03015	0.0187	0.3475	0.05564	0.0382
Ti	0.1007	0.4556	0.209141	0.19995	0.0572	0.122	0.081303	0.0793	0.0361	0.2009	0.083328	0.0864
Fe	61.3562	71.4383	69.35915	69.91935	69.58	72.4242	71.68543	71.69425	66.8593	71.9301	69.32145	69.85775
Mn	0.334	1.0243	0.455142	0.4433	0.0528	0.1	0.077308	0.0781	0.0494	0.2283	0.174971	0.17745
Zn	0.0279	0.2067	0.072958	0.05015	0.0277	0.0411	0.03078	0.0284	0.0283	0.091	0.043797	0.0387
O	19.2011	22.3029	19.64694	19.50895	19.1593	20.3627	19.41194	19.3493	19.2314	20.9369	20.09165	20.10455

Table 3.4. Summarized representative statistics of the trace element LA-ICP-MS analysis of primary and secondary magnetite from the Azenhas and Alvito deposits.

Magnetite Type	**Magnetite I - Azenhas deposit**				**Magnetite II - Azenhas deposit**				**Primary Magnetite – Alvito deposit**			
	n^1=2; n^2=8; n^3=20				**n^1=2; n^2=20; n^3=49**				**n^1=5; n^2=17; n^3=156**			
Analysis	Min.	Max.	Ave.	Med.	Min.	Max.	Ave.	Med.	Min.	Max.	Ave.	Med.
Element (ppm)												
Mg	3880.3	18241.56	8534.005	7545.76	48.55	3195.36	202.6429	90.45	676.1	15244.57	3754.179	4291.65
Al	280.33	7059.03	2222.047	1887.78	525.98	10704.13	1357.324	878.85	5030.38	16280.62	9913.487	9656.83
Si	724.45	10848.82	5040.921	4360.39	2411.07	27240.1	4819.311	3929.66	1570.11	6422.62	3580.744	3561.92
Ca	41.69	4321.64	1063.537	372.17	32.69	436.71	119.5107	74.34	36.88	1938.43	665.1327	414.33
Sc	0.43	1.04	0.580929	0.5275	0.127	0.171	0.15325	0.1575	0.149	3.95	1.426372	0.842
Ti	1506.18	3290.05	2149.445	2000.46	651.55	1386.21	899.1486	853.8	370.52	6187.86	2070.801	1199.41
V	67.49	174.06	131.17	137.13	101.23	168.81	136.6994	137.48	19.81	128.16	70.87222	72.375
Cr	0.87	49.87	11.70095	9.16	0.28	1.24	0.487556	0.43	0.31	359.17	48.28069	6.23
Mn	3787.49	6109.59	4858.774	4759.07	274.85	1135.55	612.9169	536.85	1012.44	4501	2155.266	2095.67
Co	28.2	82.68	52.07957	51.84	3.58	7.77	4.957143	4.78	38.82	156.72	86.43089	87.49
Ni	10.16	33.07	17.70739	15.27	5.23	18.51	9.73449	8.52	2.46	100.87	40.5869	44.86
Cu	0.198	3.5	0.942364	0.65	0.059	0.829	0.2555	0.067	0.074	25.87	1.247886	0.1735
Zn	158.51	1052.2	658.4991	659.44	68.98	301.78	183.1133	178.66	106.63	1085.13	526.914	532.805
Ga	3.88	24.22	12.55087	7.53	9.76	23.73	16.94122	17.63	21.91	86.68	39.87525	39.885
Ge	0.32	1.41	0.821818	0.745	0.175	0.74	0.380889	0.3715	0.35	3.36	1.242848	1.13
As	0.58	11.42	3.131905	2.64	0.182	4.83	0.561239	0.46	0.166	7.12	0.580275	0.43
Y	0.0095	2.61	0.417895	0.224	0.00042	0.183	0.01454	0.00505	0.00064	3.63	0.134658	0.0096
Zr	0.047	86	6.674273	0.4345	0.0015	0.149	0.024211	0.0084	1.522	19.11	8.215456	6.8
Nb	0.023	2.64	0.832683	0.831	0.00056	0.178	0.015464	0.0052	2.44	22.45	9.088165	8.25
Mo	0.076	0.292	0.188238	0.185	0.153	104.62	13.82753	3.1	0.572	7.93	2.587525	2.64
Sn	7.04	11.9	9.532609	9.65	0.341	1.71	0.785041	0.788	13.85	46.06	25.315	25.205
Hf	0.008	3.65	0.28077	0.0324	0.0015	0.0296	0.005988	0.0043	0.059	0.948	0.389405	0.367
Ta	0.0026	0.375	0.079295	0.07	0.00033	0.093	0.011863	0.0024	0.145	2.75	0.652044	0.238
W	0.0074	1.8	0.568018	0.4505	0.0017	28.54	4.52454	1.94	0.002	1.76	0.095909	0.03915
Pb	0.127	148.15	15.41677	2.415	0.057	1248.47	81.19022	0.134	0.034	710.15	19.08651	0.171
Th	0.0024	1.6	0.314615	0.2115	0.00056	0.303	0.027109	0.0114	0.00047	0.245	0.018862	0.0047
U	0.0049	5.37	0.941432	0.5695	0.00071	0.321	0.033907	0.00715	0.00064	1.172	0.040053	0.0135

The Azenhas Mag I data also plot in the skarn field (**Fig. 3.10a - b**), revealing a constrained Ti, V, Al, and Mn contents, whereas Mag II plots towards the IOCG field in the **Figure 4.10a** plot, which does not reflect the metallogenic conditions at the time of deposition and hence suggesting that the fields defined by Dupuis and Beaudoin (2011) to discriminate skarn deposits do not fit the discrimination of Azenhas Mag II. As stated previously, Mag II is associated with late-hydrothermal remobilization, and is found in thin veins hosted in strongly metasomatized amphibolites. This magnetite type exhibits the lowest contents of trace elements which incorporation into the magnetite structure is temperature controlled, which may indicate that the genesis of this magnetite type is associated with lower-temperature hydrothermal processes. For this, the use of the **Figure 4.10b** plot from Nadoll et al. (2015) is here suggested to better reflect the metallogenic conditions of both deposits, in which the grey arrow represents the direction of trace element depletion from Azenhas Mag I to Mag II.

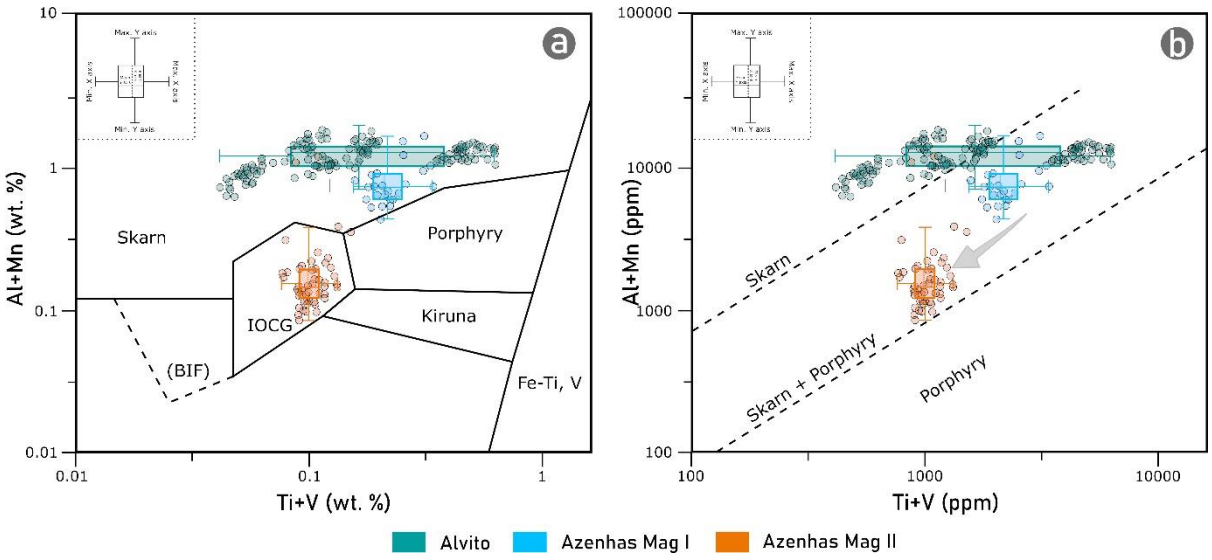

Figure 3.10. Al + Mn versus Ti + V discriminant diagrams where a. was adapted from the reinterpretation of Nadoll et al. (2014) to the Dupuis and Beaudoin (2011) discriminant diagram; and b. was adapted from Nadoll et al. (2015). These diagrams were applied to the magnetite LA-ICP-MS from Azenhas and Alvito in a tentative approach to classify both Fe deposits.

3.6.2.2 Trace element patterns

Multielement variation diagrams (Dare et al., 2012; 2014; Knipping et al., 2015), using trace element analysis of magnetite normalized to the bulk continental crust (Rudnick and Gao, 2003) have been used as a good petrogenetic discrimination. Magmatic, high-temperature hydrothermal, and low-temperature hydrothermal magnetite is used as a comparison to discriminate the data from Alvito and Azenhas magnetite (**Fig. 3.11**). The trace element

pattern from the primary magnetite of the Alvito and Azenhas deposits reveals enrichment in several transition metals, such as Sn, Mn, Zn, Co, and Ni. However, this petrogenetic criteria outlines that the primary magnetite from Alvito deposit bear the higher concentrations of the analysed trace elements (**Figure 4.11**), displaying an enriched pattern when compared to Azenhas Mag I, and best-fitting with the high-temperature hydrothermal magnetite field (Dare et al., 2014).

Primary magnetite from both deposits displays a closer affinity to the high-temperature hydrothermal magnetite field (**Fig. 3.11**), although Alvito magnetite displays Ta and Nb contents (high field strength elements) higher than is expected for such provenances (Dare et al., 2014). On the opposite, Azenhas Mag II revealed the lower content in most trace elements, which is reflected on the variation diagram (**Fig. 3.11**), with the trace element patterns falling close to what is referred to as low-temperature hydrothermal magnetite (Dare et al., 2014).

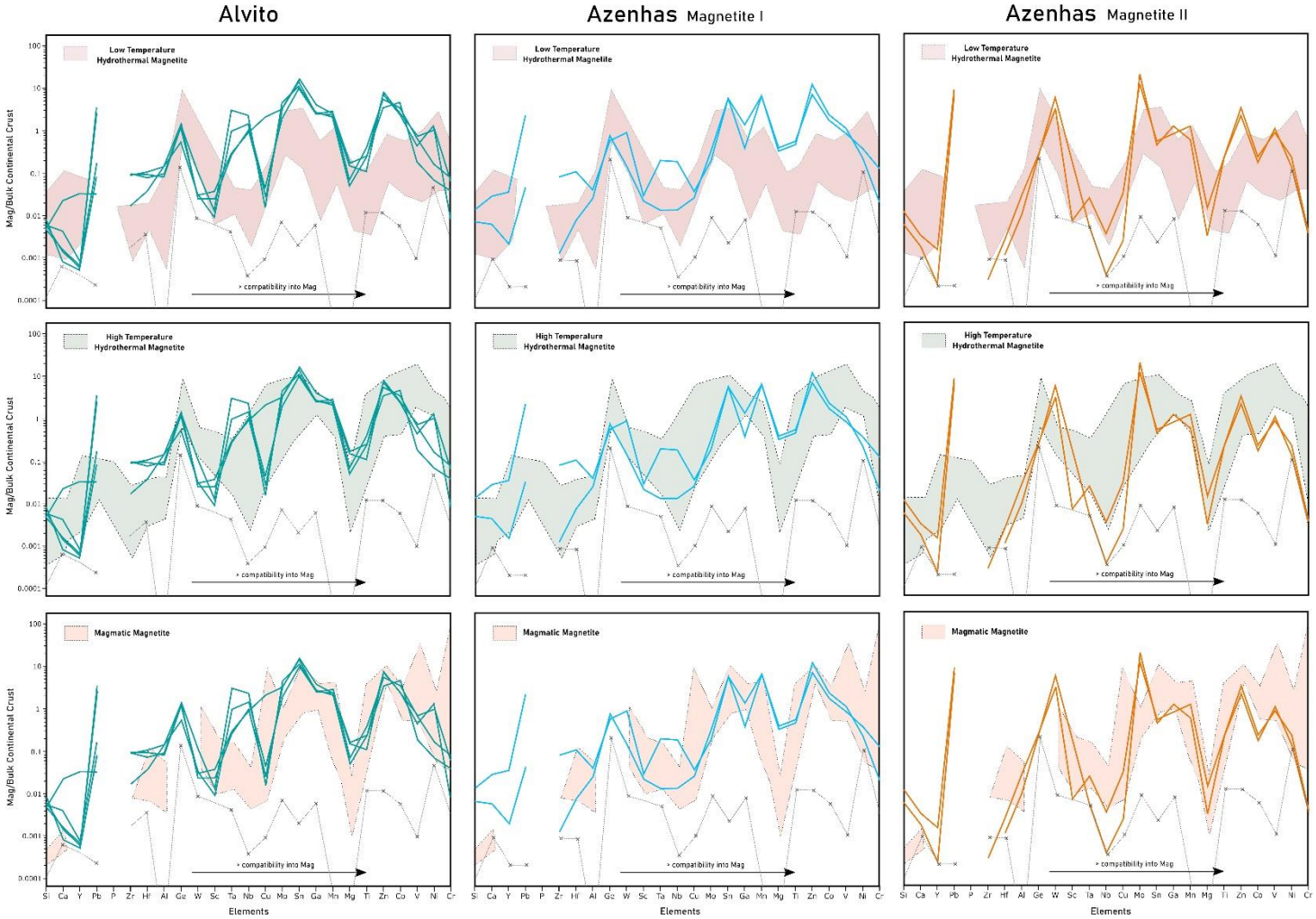

Figure 3.11. Multi-trace element variation diagrams of the LA-ICP-MS data from the Azenhas and Alvito deposits, normalized to the Bulk Continental Crust values (Rudnick and Gao, 2003). Obtained analyses were compared to literature data for low-temperature hydrothermal magnetite, high-temperature hydrothermal magnetite and magmatic magnetite (after Dare et al., 2014; Knipping et al., 2015). The limits of the detection are represented in the plot by the dashed grey lines.

3.6.2.3 Principal components analysis

Principal Components Analysis (PCA) is a multivariate statistical approach that has been widely applied to large geochemical datasets, like the ones obtained from oxides and hydroxides analysis by LA-ICP-MS (Nadoll et al., 2012; 2015; Canil et al., 2016; Makvandi et al., 2016a; 2016b; 2021). One of the main issues to address in such large datasets is the presence of censored data, in other words, the observations displaying values below the detection limit of the LA-ICP-MS equipment. Censored data substitution was applied using the zCompositions package in R software environment (Palarea-Albaladejo and Martín-Fernandez, 2015), based on the average limits of detection of all analysis and using the single and multiple imputations based on the log-ratio MCMC Data Augmentation (DA) algorithm (lrDA). The zPatterns function was applied and the data with over 40% censored values were excluded from the analysis (Hron et al., 2010) which led to the exclusion of Ca and Cu. Substitution of data was followed by centered log-ratio application so that closure of geochemical data was achieved (Egozcue et al. 2003).

PCA of all the magnetite data revealed that the first three principal components (PC1, PC2, PC3) explain 43.0 %, 12.9 %, and 11.9 % of the data (**Fig. 3.12**). The plot of PC1-PC2 and PC1-PC3 allows the separation of the three types of magnetite (Alvito primary magnetite, Azenhas Mag I, and Mag II), giving clues to define the criteria towards discriminating and characterizing these ore deposits (**Fig. 3.12**).

The PC1 is mainly influenced by Si, V, Zn, at the positive part of this axis and Zr, Nb, Hf, and Ta in the negative part. This axis allows the overall separation of the different ores, where Alvito corresponds to samples influenced by Zr, Nb, Hf, and Ta and Azenhas Mag II is influenced by the Si, V, and Zn. The PC2 axis is mainly influenced by Mg and Sc at the positive quadrants and Al and Mo in the negative quadrants of the axis. This analysis outlines the enrichment of Alvito magnetite in the immobile high field strength elements (Zr, Nb, Hf, and Ta), unusual in Fe-skarn deposits and which may suggest a stronger magmatic-hydrothermal fluid contribution to ore genesis.

Principal component analysis shows that Azenhas Mag I (**Fig. 3.12**) are mainly influenced by the Mg and Sc elemental composition, and inspection of Mag II reaffirm their differentiated composition when compared to primary magnetite from both deposits (**Fig. 3.12**). The separation in the opposite axis between the Alvito and the Mag I and Mag II from Azenhas (c.f. **Fig. 3.12**), implies different elemental behaviour and therefore suggests a distinct genesis when comparing the three magnetite types. This difference was expected because they are after all from distinct Fe-deposits with different geodynamic contexts, and in the case of Mag II, with different timing of formation.

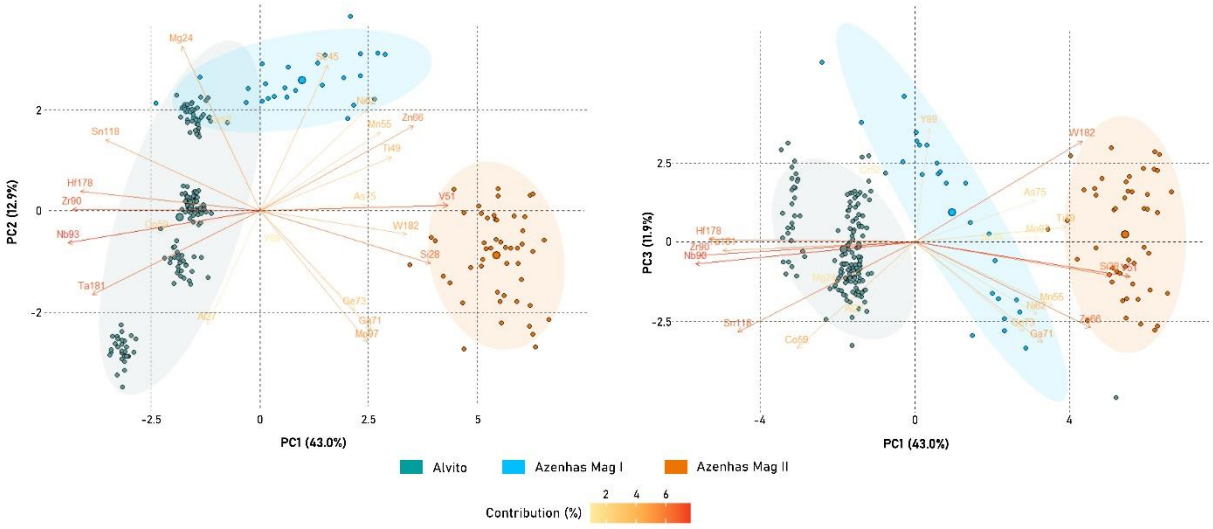

Figure 3.12. Biplot of PC1-PC2 (left site) and PC1-PC3 (right side) clusters, correspondent to the LA-ICP-MS data from the primary and secondary magnetites from the Azenhas and Alvito deposits.

3.6.3 Fluid and geothermometric constraints

The geodynamic and metallogenic conditions in which Azenhas and Alvito Fe-deposits have formed are contrastingly different. The genesis of Alvito ores is distinctively associated with the emplacement of the CAGD suite which contributed with magmatic-hydrothermal fluids to the system, promoting the metasomatic alteration of the surrounding carbonated host-rocks giving origin to a skarn deposit (*sensu stricto*; Meinert, 1992; Meinert et al., 2005). The chemistry and textures indicate that the Alvito magnetite is formed in higher temperature, which is also corroborated by higher concentrations of temperature-sensible elements (Ti, Sn, Ga) and by the discriminant methods presented in previous sections (**Fig. 4.9; Fig. 4.10; Fig. 4.11**).

Magnetite chemistry corroborates the direct relation of Alvito magnetite ores to the emplacement of the Cuba-Alvito gabbro-dioritic suite, with estimated temperatures around 820 ºC (Gomes, 2000). To constraint temperature of the system at the time of ore deposition, the $T_{Mg\text{-}Mag}$ magnetite geothermometer proposed by Canil and Lacourse (2020) with a confidence of ± 60ºC was applied to the gathered LA-ICP-MS data from both deposits. The $T_{Mg\text{-}Mag}$ geothermometer revealed the minimum and maximum average temperatures of 676 ºC and 689 ºC (**Table 3.5; Fig. 3.13a**) for Alvito magnetite, which is consistent with the fluid circulation and metasomatic reactions responsible for the genesis of the skarn mineral assemblages (Gomes, 2000; Gomes and Fonseca, 2006). Furthermore, the CAGD geochemistry (**Table**

3.2) falls in the range of the compositional variations identified for intrusions related with Fe-skarn deposits, as proposed by Meinert (1993).

In the Azenhas deposit, Mag I and Mag II revealed geochemical features that clearly distinguish them, where Mag II is depleted in most of the analysed trace elements (**Fig. 3.8; Fig. 3.9**) with a clear indication that primary ores are associated with higher formation temperatures. The $T_{Mg\text{-}Mag}$ geothermometer corroborates these observations, with Azenhas Mag II displaying minimum and the maximum average temperatures of 408 ºC and 429 ºC, and Mag I between 765 ºC and 773 ºC (**Fig. 3.13a**). $T_{Mg\text{-}Mag}$ geothermometer outlines the latter and lower temperature origin of Mag II, whereas the primary ores from the Azenhas Fe-deposits display $T_{Mg\text{-}Mag}$ estimations higher than those previously modelled for the system at the time of ore deposition (Mateus et al., 2005).

Table 3.5. Summarized and representative statistics of $T_{Mg\text{-}Mag}$ geothermometry (Canil and Lacourse 2020) for the primary and secondary magnetite of the Azenhas and Alvito deposits.

Magnetite type	$T_{Mg\text{-}mag}$				
	Min.	Max.	Ave.	Med.	Std.
Azenhas Mag I	765.1	772.6	768.8	776.1	31.1
Azenhas Mag II	40.7.6	428.7	418.1	402.4	54.3
Alvito primary magnetite	676.4	688.6	682.5	710.2	62.9

The data from this research raises questions regarding the genesis of the Azenhas skarn deposit, which is attributed to the tectonic pilling of amphibolite units over Middle Cambrian – Ordovician marbles (Oliveira et al., 1991) promoted by two main thrusting episodes (D_1 / D_{2a}; Araújo et al., 1995). Mateus A. (2005; 2013) proposed that the thermic conditions estimated for these events suggest that, presumably, an inverted thermal gradient was sustained for over 4.5 Ma. at a temperature of 400 ºC – 500 ºC, responsible for the favourable chemical conditions associated with magnetite deposition. Such temperatures fall in the range of the late Mag II, but short to the ones obtained for primary magnetite – Mag I - (Canil and Lacourse 2020). Furthermore, the $T_{Mg\text{-}Mag}$ geothermometer was applied to the EPMA data published for the Azenhas magnetite (Salgueiro, 2011) and similar temperature ranges are acquired for primary and secondary magnetite, with average temperatures of 801 ºC for primary ores and 623 ºC for secondary ores (**Fig. 3.13**), coherent with the data presented in this manuscript.

It should be stated that, although believing that the $T_{Mg\text{-}Mag}$ geothermometer results are a good indication for the temperature in which magnetite was formed, these results should be

handled with care. $T_{Mg\text{-}Mag}$ geothermometer in based upon the partitioning of Mg into the magnetite structure for high-temperature systems (Canil and Lacourse, 2020), and is necessarily influenced by the concentration of magnesium in magnetite. With this said, the higher the Mg concentration in magnetite the higher the temperature, and therefore it is important to recognise that several factors, other than temperature, can contribute to such high Mg contents. Extensive interaction between ore fluids and Mg-rich host rocks can contribute to the incorporation of Mg into the magnetite structure, which could be the case at the Azenhas deposit, where fluids interacted with dolomite and forsterite rich host rocks (marbles and amphibolites).

Nevertheless, good correlation was found in bivariate plots between magnetite temperature and elements whose incorporation in magnetite is typically controlled by temperature (e.g., Sn; **Fig. 3.13a**). Cobalt was tentatively used in such bivariate plots (**Fig. 3.13b**) and similar behaviours to the ones observed for tin were obtained (**Fig. 3.13a**), suggesting that the incorporation of Co into the magnetite structure can be temperature dependent. Thereafter it is here suggested that Co can be used as a discriminatory element between low temperature and high temperature magnetite.

Zinc partitioning into the hydrothermal fluid has been studied by Ilton and Eugster (1989) and further inspected by Wu et al. (2019), whose findings suggest that Zn is fractionated into hydrothermal fluids with more effectiveness at lower temperatures. Considering these observations, it is not yet possible to explain the high Zn contents found in high-temperature hydrothermal primary magnetite from the Azenhas and Alvito deposits. At the Alvito deposit, the CAGD emplacement was prone to provide anomalous concentrations of Co and Ni, as supported by the presence of Ni-(Co)-bearing sulfide phases (**Fig. 3.7h-j**).

3.6.4 Constraining the metallogenic conditions

Trace element composition of primary magnetite from the Azenhas and Alvito deposits have been used to characterize the conditions in which ore deposition occurred. The application of discriminant diagrams such as the Al + Mn versus Ti + V shows that both deposits plot in the skarn deposits field (**Fig. 3.10a -b**; Dupuis and Beaudoin, 2011; Nadoll et al., 2014) exhibiting trace element patterns with affinities to the high-temperature hydrothermal magnetite field (**Fig. 3.11**; Dare et al., 2014; Knipping et al., 2015).

In the case of the Alvito deposit, it becomes evident that ore genesis and mineral assemblage is typical of an exoskarn deposit developed at the contact between the CAGD suite and the surrounding marbles, with magnetite ores revealing higher concentration in elements that are interpreted to be incorporated as a function of temperature (Sn, Ga, and Co) at the time of deposition.

At the Azenhas deposit, Mag I is found in massive magnetite bodies hosted in amphibolites and marbles affected by thrusting episodes which facilitated fluid circulation. Although the mineral assemblages found at the Azenhas deposit are similar to those of typical pluton-related skarn-deposits (Meinert, 1992; 1993; 1995) the genesis of the mineralization is, at the light of the current knowledge, discarded to be related with the emplacement of any pluton. The Azenhas area remains enigmatic concerning the comprehensive identification of ore provenance, and besides the spatial relation to the *Pedrogão* granitic suite ene must mphasize that the ore bodies are intersected by the granitic body, and therefore necessarily pre-date it.

The evidence gathered throughout this work regarding the trace element composition of Azenhas magnetite fuels the discussion concerning the physical and chemical conditions at the time of iron ore deposition. The trace element contents, and all the discriminant methods applied to the Azenhas magnetite indicate that the primary ores were generated under geochemical conditions compatible to the formation of skarn deposits (**Fig. 3.10a – b**), with affinities to high-temperature hydrothermal magnetite (**Fig. 3.11**) favouring the incorporation of elements such as Sn, Ga and Co into Mag I structure (**Fig. 3.9e – h**). The evidence for high temperature conditions at the time of primary ore deposition (Mag I) is also corroborated by the V and Ti correlation, suggesting ore deposition under oxidized conditions which are found to be associated with higher temperature settings (Wood, 1990; Bau and Dulski, 1996; Tostevin et al., 2016). The $T_{Mg\text{-}Mag}$ geothermometer (765 ºC – 773 ºC; **Fig. 3.13**; **Table 3.5**), revealed higher temperatures than the ones previously modelled for the genesis of the deposit (Mateus et al., 2005; 2013). As previously stated (see section 6.3), these temperatures could be reflecting the high contents of Mg found on Azenhas primary magnetite (**Table 3.5**; **Appendix F**). Such concentrations could be the result of extensive fluid-rock (amphibolite and Mg-marbles) interactions, which would end in an over-estimation of the $T_{Mg\text{-}Mag}$. Our data puts in evidence the importance of allying several discriminatory indexes for the classification of ore deposits since, individually, they may lead to erroneous assumptions. Nonetheless, several data, other than the $T_{Mg\text{-}Mag}$, indicates that Azenhas primary magnetite has formed under high-temperature conditions (**Fig. 3.11**), which contradicts the previously modelled conditions for the deposit (Mateus et al., 2005).

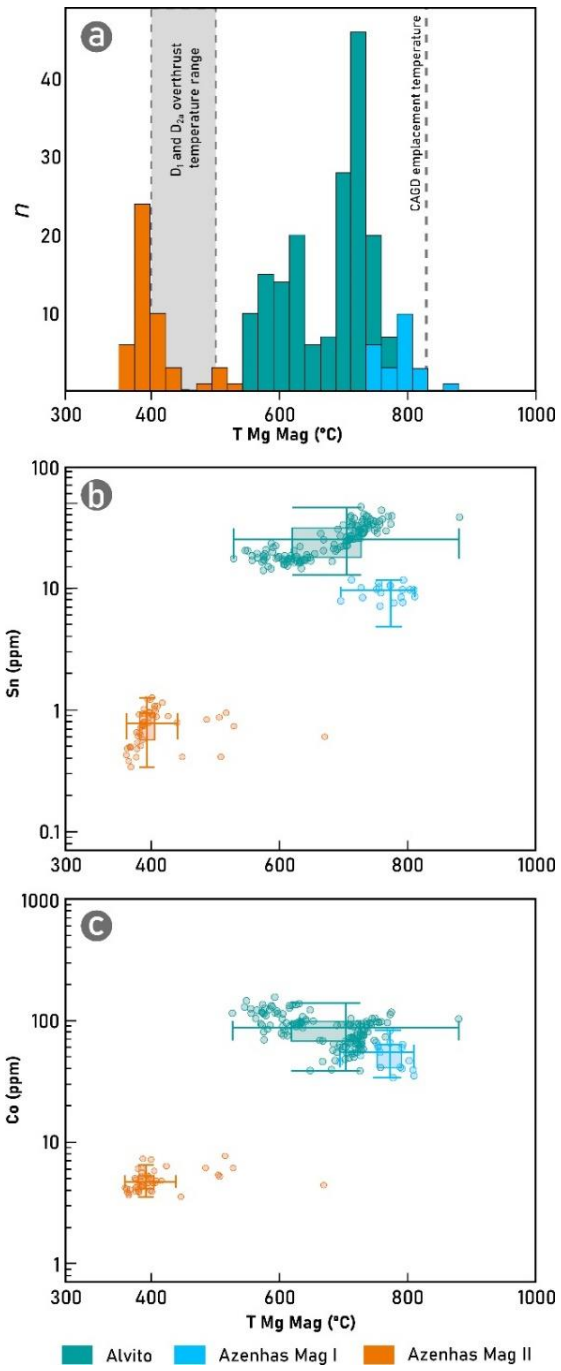

Figure 3.13. (a.) $T_{Mg\text{-}Mag}$ geothermometer (Canil and Lacourse, 2020) applied to the LA-ICP-MS data of primary and secondary magnetite of the Azenhas and Alvito deposits. The CAGD emplacement temperatures are displayed by the grey dashed lines after Gomes and Fonseca (2006) and Gomes (2000). Combined double boxplot and scatterplot diagrams showing the tin versus the $T_{Mg\text{-}Mag}$ data **(b.)** and Co versus $T_{Mg\text{-}Mag}$ **(c.)**, suggesting that tin and cobalt are incorporated in magnetite as a factor of temperature.

The $T_{Mg\text{-}Mag}$ estimation suggests temperatures that could only be sustained if considering an igneous source for the genesis of the Azenhas deposit. The source of the ores remains unidentified, reinforcing the need of broadening the study to adjacent ore deposits (e.g. Orada

mine), and performing detailed petrologic and geochemical studies in order to identify the geodynamic conditions at the time of deposition and providing new insights for the improvement of the metallogenic model for the Azenhas deposit. Nevertheless, the geological evidence from the Azenhas area could suggests that ore formation could be associated to the basic magmatism, represented in the area by the MPU amphiboles. Such interpretation suggest that the Azenhas ore bodies were formed under high-temperature settings at a relatively older age than currently acknowledged (Mateus et al., 2005), associated to a different geodynamic setting during the Variscan cycle, possibly prior to the collisional stages.

The gathered data has shown that applying conventional discriminatory diagrams to Mag II from the Azenhas deposit may lead to erroneous conclusions regarding the deposit classification (**Fig. 3.10a**). Nevertheless, Mag II trace element contents show an affinity to lower temperature hydrothermal magnetites (**Fig. 3.11; Fig. 3.13**), and their generalized trace element depletion (**Fig. 3.14**) may be a result of Mag I remobilization. The V and Cr correlation (r^2= 0.26) in Mag II additionally suggest low oxygen fugacity activities (Papike et al., 2005; Toplis and Corgne, 2002). It is noteworthy that the temperatures obtained for Mag II are comparable to the ones modelled for the thrust-fault episodes at the Azenhas deposit (Mateus et al., 2005; 2013), which could indicate that the D_1 and D_{2a} thrusting episodes could have promoted a late fluid input responsible for secondary ore deposition.

Additionally, although $T_{Mg\text{-}Mag}$ geothermometer indicates that Azenhas primary ores were formed at higher temperatures than Alvito primary ores other trace element data suggest differently, such as 1) the Sn versus Ga diagrams (**Fig. 3.9**); 2) the higher Ti contents as evidenced by the Mn + Al versus Ti + V diagram (**Fig. 3.10**), and 3) the higher Co concentrations, an element which incorporation into magnetite structure is proposed to be temperature sensitive on the studied skarn deposits. These conclusions put in evidence the importance of utilizing several discriminatory approaches in the classification of ore deposits since, individually, they may lead to erroneous assumptions.

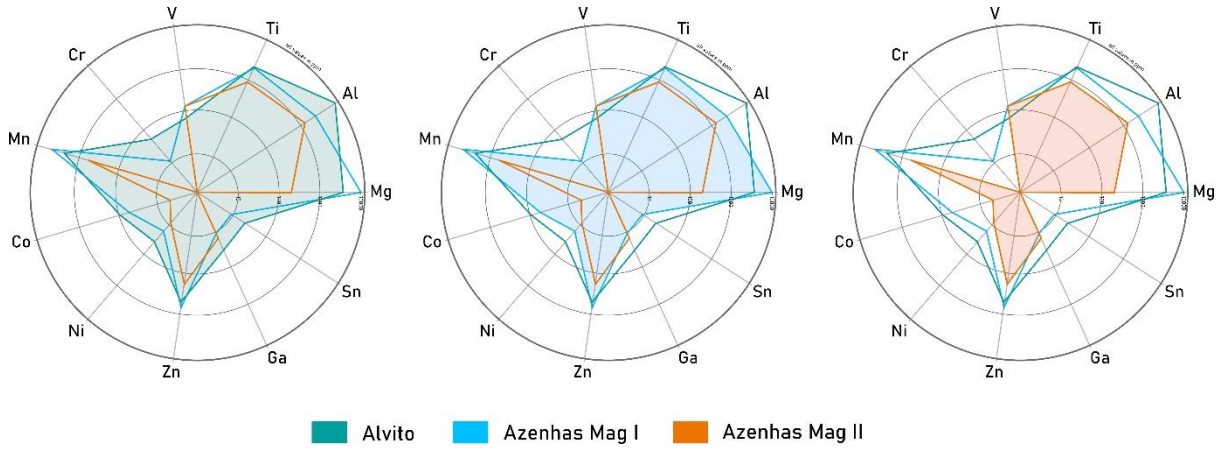

Figure 3.14. (previous oage) Radar diagram displaying the variation of LA-ICP-MS trace elements data (Mg, Sn, Ga, Zn, Ni, Co, Mn, Cr, V, Ti, Al), comparing the primary and secondary magnetites from the Azenhas and Alvito deposits, as described in the legend. These kinds of plots allow to compare the trace element differences between each type, clearly demonstrating that secondary magnetite from Azenhas is depleted in most elements.

3.7 Conclusions

The results obtained from trace element analysis in magnetite from the Azenhas and Alvito Fe-deposits suggest that broadening this kind of study for other magnetite-bearing ore deposits in OMZ could be an important contribution in identifying areas prone to ore deposition, and further characterize the metallogenic models associated with them. The studied deposits are dominantly composed of magnetite ores which are hosted in distinctive units and have formed from contrastingly different metal sources and transporting fluids, as reflected by the trace element compositions.

Studies carried out at the Azenhas deposit indicate two stages of ore deposition, one associated to the primary massive magnetite ores (Mag I), and second event outlined by secondary ores deposited in thin veinlets (Mag II). Primary ores were formed under oxidizing conditions, probably at higher temperatures than the ones previously modelled for the deposit (Mateus et al., 2005), as suggested by $T_{Mg\text{-}Mag}$. Azenhas Mag I displays an enrichment in Zn (up to 1060 ppm), which is consistent with the prevailing conditions present in the surrounding marbles from the MPU (**Table 3.1**). Such evidence indicates that surrounding rocks at the Azenhas deposit were prone to provide elements, such as Zn, during ore genesis through fluid-rock interactions. Azenhas deposit Mag II displays Pb values up to 1249 ppm and was formed under more reducing conditions. Such geochemical evidence allied with the fact that MFB comprises several Zn – (Pb) – (Fe) deposits and occurrences (e.g. Enfermarias, Santo André, Preguiça-Vila Ruiva; **Fig. 3.1a**), particularly at the SE of the belt (Barroso et al., 2003; Martins et al., 2003), can be good indications for the possibility of Zn – (Pb) ores to occur at the Azenhas-Orada area.

The results obtained from the study of the Alvito deposit indicate that magnetite ores are associated with the emplacement of the Beja Igneous Complex at the SW border of the MFB, and particularly to the Cuba-Alvito gabbro dioritic suite, making Alvito an classic example of an exoskarn Fe-deposit. Such tectonic settings are reflected by the lithotypes, and mineral assemblages present at the deposit scale, and by the textural and chemical composition of magnetite. Primary ores from Alvito Fe-skarn deposit display distinctive ilmenite and Al-spinel exsolutions, usually found associated with high temperatures (Huang and Beaudoin, 2019). Trace element contents are concordant to high-temperature hydrothermal magnetite (**Fig. 3.11; Fig. 3.12**) and corroborated by the $T_{Mg\text{-}Mag}$ geothermometer (**Fig. 3.13**), compatible with

the CAGD emplacement temperatures (Gomes, 2000). The magmatic activity allied with the fact that Ni-(Co) sulfide phases (pentlandite; **Fig. 3.7h – j**) were identified in magnetite ore assemblages, indicate that the magmatic suite was prone to contribute with other base metals (e.g. Ni), which have already been identified and characterized in Layered Gabbroic Sequences of the Beja Igneous Complex (Jesus et al., 2011; Jesus et al., 2020).

The data gathered throughout this study outlines the importance of magnetite in identifying and characterising the physical and chemical processes enrolled in ore transport and deposition. Geochemical analysis of trace elements in magnetite by LA-ICP-MS has proved to be an important ally to redefine and review the geological models associated to the genesis of ore deposits, thus contributing to vector future mineral exploration in SW Iberia. Furthermore, the anomalous concentrations of elements such as Co, Ni, and Zn could be important guidelines to unveil other commodities associated with the Alvito and Azenhas deposits.

Chapter References

Akker, I.V., Tajčmanová, L., Marques, F.O., and Burg, J.-P., 2020. U–Pb zircon geochronology and phase equilibria modelling of HP-LT rocks in the Ossa-Morena Zone, Portugal. International Journal of Earth Sciences, v.109, p. 2719-2738. https://doi.org/10.1007/s00531-020-01921-w

Alaminia, Z., Tadayon, M., Finger, F., Lentz, D.R., and Waitzinger, M., 2020. Analysis of the infiltrative metasomatic relationships controlling skarn mineralization at the Abbas-Abad Fe-Cu Deposit, Isfahan, north Zefreh Fault, Central Iran. Ore Geology Reviews, v. 117, 103321. https://doi.org/10.1016/j.oregeorev.2020.103321

Andrade, A., Silva, J.M., Arruda, C.R, and Gameiro, J.C.S., 1949. Minas de Ferro de Montemor-o-Novo. Serviço de Fomento Mineiro, v. 15, p. 125.

Apalategui, O., Eguiluz, L., and Quesada, C., 1990. Ossa-Morena Zone: Structure. In: Martinez E and Dallmeyer RD (Eds.) Pre-Mesozoic Geology of Iberia, Springer Verlag, p. 280-291.

Araújo, A., 1995. Estrutura de uma Geotransversal entre Brinches e Mourão (Zona de Ossa-Morena): Implicações na evolução geodinâmica da margem Sudoeste do Terreno Autóctone Ibérico. PhD Thesis, Universidade de Évora, Portugal, 200p.

Araújo, A., Fonseca, P., Munhá, J., Moita, P., Pedro, J., Ribeiro, A., 2005. The Moura Phyllonitic Complex: An Accretionary Complex related with obduction in the Southern Iberia Variscan Suture. Geodinamica Acta, v.18(5), 375-388. https://doi.org/10.3166/ga.18.375-388

Araújo, A., Piçarra de Almeida, J., Borrego, J. Pedro, J. and Oliveira, T., 2013. As regiões central e sul da Zona de Ossa-Morena. In: Dias R, Araújo A, Terrinha P, Kullberg JC (Eds), Geologia de Portugal, Volume 1, Escolar Editora, pp 509-549.

Ayupova, N.R., Novoselov, K.A., Maslennikov, V., Melekestseva, I.Y., Hollis, S.P., Artemyev, D.A., and Tessalina, S.G., 2020. The formation of magnetite ores of the Glubochenskoe deposit, Turgai iron belt, Russia: new structural, mineralogical, geochemical, and isotopic constraints. Mineralium Deposita, v.56, 103-123. https://doi.org/10.1007/s00126-020-00994-6

Azor, A., Dias da Silva, Í., Barreiro, J. G., González-Clavijo, E., Catalán, J. M., Simancas, J. F., Martínez Poyatos, D., Pérez-Cáceres, I. González Lodeiro, F., Expósito, I., Casas, J. M., Clariana, P., García-Sansegundo, J., Margalef, A. 2019. Deformation and Structure. In The geology of Iberia: A geodynamic approach (pp. 307-348). Springer, Cham. https://doi.org/10.1007/978-3-030-10519-8_10

Baker, M.J., Wilkinson, J.J., Wilkinson, C.C., Cooke, D.R., and Ireland, T., 2020. Epidote Trace Element Chemistry as an Exploration Tool in the Collahuasi District, Northern Chile. Economic Geology, v. 115, p. 749-770. https://doi.org/10.5382/econgeo.4739

Barroso, M., Mateus, A., Figueiras, J., Martins, R., and Oliveira, V., 2003. Mineralogy and geochemical characteristics of different superimposed mineralisations at the Enfermarias prospect (Moura, Portugal). VI Congresso Nacional de Geologia, Lisboa (Portugal), Ciências da Terra (UNL), Lisboa, n.º esp. V, CD-ROM, F9-F12.

Bau, M., and Dulski, P., 1996. Distribution of yttrium and rare-earth elements in the Penge and

Kuruman iron-formations, Transvaal Supergroup, South Africa. Precambrian Res. v.79, p. 37–55. https://doi.org/10.1016/0301-9268(95)00087-9

Caldeira, R., Ribeiro, M.L., and Moreira, M.E., 2007. Geoquímica das sequências máficas e félsicas entre Alvito, Torrão e Alcáçovas (SW da ZOM). Comunicações Geológicas, v. 94, p. 5-28.

Canil, D., Grondahl, C., Lacourse, T., and Pisiak, L.K., 2016. Trace elements in magnetite from porphyry Cu–Mo–Au deposits in British Columbia, Canada. Ore Geology Reviews, v.72, p. 1116-1128. http://dx.doi.org/10.1016/j.oregeorev.2015.10.007

Canil, D., and Lacourse, T., 2020. Geothermometry using minor and trace elements in igneous and hydrothermal magnetite. Chemical Geology, v.541, 119576. https://doi.org/10.1016/j.chemgeo.2020.119576

Carriedo, J., Tornos, F., Velasco, F., and Terrón, A., 2006. Mineralizaciones de magnetita asociadas a skarns y bandas de cizalla: La mina de Cala (Huelva). Geogaceta, v.40, p. 235-238. ISSN: 0213683X

Carriedo, J., Tornos, F., Chiaradia, M., and Galindo, C., 2021. A genetic link between albitic magmas and IOCG mineralization in the Ossa Morena Zone (SW Iberia). Journal of Iberian Geology. https://doi.org/10.1007/s41513-021-00162-3

Carvalho, D., 1971. Observações sobre os jazigos de ferro da área Pedrógão-Orada. I Congresso Hispano – Luso – Americano de Geologia Económica, Madrid – Lisboa, v.1, p. 519-537

Carvalhosa, 1971. Carta Geológica de Portugal 1:50.000 Folha 40-C, 1:50 000. Serviços Geológicos de Portugal.

Carvalhosa, A.B., 1985. Sobre os gnaisses leptiníticos da faixa de Escoural-Alvito (Alentejo) – Nota Preliminar. Boletim da Sociedade Geológica de Portugal, v.25, p. 213-220.

Chacón, J., Oliveira, V., Ribeiro, A., and Oliveira, J.T., 1983. La estructura de la Zona de Ossa Morena. Eds: Comba, J.A. (Coord) - Libro Jubilar J. M. Rios – Geologia de España, Tomo I. Instituto Geológico y Minero de España, Madrid, p. 490-504.

Chen, W., Ying, Y.-C., Bai, T., Zhang, J.-J., Jiang, S.-Y., Zhao, K.-D., Shin, D., and Kynicky, J., 2019. In situ major and trace element analysis of magnetite from carbonatite related complexes: Implications for petrogenesis and ore genesis. Ore Geology Reviews, v.107, p. 30-40. https://doi.org/10.1016/j.oregeorev.2019.01.029

Chichorro, M., 2006. A evolução tectónica da Zona de Cisalhamento de Montemor-o-Novo (Sudoeste da Zona de Ossa-Morena – Área de Santiago do Escoural – Cabrela). PhD Thesis, Universidade de Évora, p.569.

Chichorro, M., Pereira, M.F., Díaz-Azpiroz, M., Williams, I.S., Fernández, C., Pin, C., and Silva, J.B., 2008. Cambrian ensialic rift-related magmatism in the Ossa-Morena Zone (Évora–Aracena metamorphic belt, SW Iberian Massif): Sm–Nd isotopes and SHRIMP zircon U–Th–Pb geochronology. Tectonophysics, v. 461, p. 91-113. https://doi.org/10.1016/j.tecto.2008.01.008

Cooke, D.R., Wilkinson, J.J., Baker, M., Agnew, P., Phillips, J., Chang, Z., Chen, H., Wilkinson, C.C., Inglis, S., Hollings, P., Zhang, L., Bruce Gemmel, J., White, N.C., Danyushevsky, L., and Martin, H., 2020. Using Mineral Chemistry to Aid Exploration: A Case Study from the Resolution Porphyry Cu-Mo Deposit, Arizona. Economic Geology, v. 115(4), p. 813-840. https://doi.org/10.5382/econgeo.4735

Dallmeyer, R.D., Fonseca, P.E., Quesada, C., and Ribeiro, A., 1993. 40Ar/39Ar mineral age constraints for the tectonothermal evolution of a Variscan suture in southwest Iberia. Tectonophysics, v. 222(2), p. 177-194. https://doi.org/10.1016/0040-1951(93)90048-O

Dare, S.A.S., Barnes, S.-J., and Beaudoin, G., 2012. Variation in trace element content of magnetite crystallized from a fractionating sulfide liquid, Sudbury, Canada: Implications for provenance discrimination. Geochimica et Cosmochimica Acta, v.88, p. 27-50. http://dx.doi.org/10.1016/j.gca.2012.04.032

Dare, S.A.S., Barnes, S.-J., Beaudoin, G., Méric, J., Boutroy, E., and Potvin-Doucet, C., 2014. Trace elements in magnetite as petrogenetic indicators. Mineralium Deposita, v.49, p. 785-796. https://doi.org/10.1007/s00126-014-0529-0

Dias da Silva, Í., Pereira, M.F., Silva, J.B., and Gama, C., 2018. Time-space distribution of silicic plutonism in a gneiss dome of the Iberian Variscan Belt: The Évora Massif (Ossa-Morena Zone, Portugal). Tectonophysics, v.747, p. 298-317. https://doi.org/10.1016/j.tecto.2018.10.015

Duan, C., Li, Y., Mao, J., Hou, K., Wang, C., Yang, B., Wang, Q., and Li, W., 2019. Ore formation at the Washan iron oxide–apatite deposit in the Ningwu Ore District, eastern China: Insights from in situ LA-ICP-MS magnetite trace element geochemistry. Ore Geology Reviews, v.112, 103064. https://doi.org/10.1016/j.oregeorev.2019.103064

Dupuis, C., and Beaudoin, G., 2011. Discriminant diagrams for iron oxide trace element fingerprinting of mineral deposit types. Mineralium Deposita, v.46, p. 319-335. https://doi.org/10.1007/s00126-011-0334-y

Egozcue, J.J., Pawlowsky-Glahn, V., Mateu-Figueraz, G., and Barceló-Vidal, C., 2003. Isometric logratio transformations for compositional data analysis. Mathematical Geoscience, v. 35, p. 279–300. https://doi.org/10.1023/A:1023818214614

Einaudi, M. T., and Burt, D.M., 1982. Introduction - terminology, classification, and composition of skarn deposits. Economic Geology, v.77(4), p. 745-754. https://doi.org/10.2113/gsecongeo.77.4.745

Einaudi, M.T., Meinert, L.D., and Newberry, R.J., 1981. Skarn deposits. Economic Geology 75th Anniversary Volume, p. 317–391.

Gomes, E.M.C., 2000. Metamorfismo de rochas carbonatadas siliciosas da região de Alvito (Alentejo, Sul de Portugal). PhD Thesis, Universidade de Coimbra, pp. 240.

Gomes, E.M.C.G., Gama Pereira, L.C., and Pinto, A.F., 2004. Nódulos calcossilicatados zonados em mármores da região de Alvito, Alentejo (Sul de Portugal). Caderno Laboratório Xeolóxico de Laxe, v.29, p. 171-185.

Gomes, E.M.C., and Fonseca, P.E., 2006. Eventos metamórfico/metassomáticos tardi-variscos na região de Alvito (Alentejo, sul de Portugal). Cadernos Xeológicos de Laxe, v.31, p. 67-85. ISSN: 0213 – 4497

Guillong, M., Hametner, K., Reusser, E., Wilson, S.A., and Günther, D., 2005. Preliminary Characterisation of New Glass Reference Materials (GSA-1G, GSC-1G, GSD-1G and GSE-1G) by Laser Ablation-Inductively Coupled Plasma-Mass Spectrometry Using 193 nm, 213 nm and 266 nm Wavelengths. Geostandards and Geoanalytical Research, v. 29(3), p. 315-331. https://doi.org/10.1111/j.1751-908X.2005.tb00903.x

Hron, K., Templ, M., and Filzmoser, P., 2010. Imputation of missing values for compositional data using classical and robust methods. Computational Statistics and Data Analysis, v.54, p.3095-3107. https://doi.org/10.1016/j.csda.2009.11.023

Hu, H., Li, J.-W., Lentz, D., Ren, Z., Zhao, X.-F., Deng, X.-D., and Hall D., 2014. Dissolution–reprecipitation process of magnetite from the Chengchao iron deposit: Insights into ore genesis and implication for in-situ chemical

analysis of magnetite. Ore Geology Reviews, v. 57, p. 393-405. http://dx.doi.org/10.1016/j.oregeorev.2013.07.008

Hu, H., Lentz, D., Li, J.-W., McCarron, T., Zhao, X.-F., and Hall, D., 2015. Reequilibration processes in magnetite from iron skarn deposits. Economic Geology, v.110, pp. 1-8. https://doi.org/10.2113/econgeo.110.1.1

Hu, X., Chen, H., Zhao, L., Han, J., and Xia, X., 2017. Magnetite geochemistry of the Longqiao and Tieshan Fe–(Cu) deposits in the Middle-Lower Yangtze River Belt: Implications for deposit type and ore genesis. Ore Geology Reviews, v. 89, p. 822-835. http://dx.doi.org/10.1016/j.oregeorev.2017.07.019

Huang, X.-W., and Beaudoin, G., 2019. Textures and chemical and compositions of magnetite from Iron Oxide Copper-Gold (IOCG) and Kiruna-type Iron Oxide Apatite (IOA) deposits and their implications for ore genesis and magnetite classification schemes. Economic Geology, v.114, p. 953-979. https://doi.org/10.5382/econgeo.4651

Huang, X.-W., Sappin, A.-A., Boutroy, É., Beaudoin, G., and Makvandi, S., 2019. Trace element composition of igneous and hydrothermal magnetite from porphyry deposits: Relationship to deposit subtypes and magmatic affinity. Economic Geology, v.114(5), p. 917-952. https://doi.org/10.5382/econgeo.4648

Ilton, E.S., and Eugster, H.P., 1989. Base metal exchange between magnetite and a chloride-rich hydrothermal fluid. Geochimica et Cosmochimica Acta, v. 53, p. 291-301. https://doi.org/10.1016/0016-7037(89)90381-5

Jesus, A.P., Munhá, J., Mateus, A., Tassinari, C., and Nutman, A.P., 2007. The Beja Layered Gabbroic Sequence (Ossa-Morena Zone, Southern Portugal): geochronology and geodynamic implications. Geodin Acta 20:139–15. https://doi.org/10.3166/ga.20.139-157

Jesus, A.P., 2011. Ore forming systems in the western compartment of the Beja Layered Gabbroic Sequence (Ossa Morena Zone Portugal). PhD Thesis, Univ. Lisboa.

Jesus, A.P., Mateus, A., Munhá, J.M., Tassinari, C.C.G., Bento dos Santos, T., and Benoit, M., 2016. Evidence for underplating in the genesis of the Variscan synorogenic Beja Layered Gabbroic Sequence (Portugal) and related mesocratic rocks. Tectonophysics, v. 683, p. 148-171. http://dx.doi.org/10.1016/j.tecto.2016.06.001

Jesus, A.P., Mateus, A., Benoit, M., Tassinari, C.C.G., and Bento dos Santos, T., 2020. The timing of sulfide segregation in a Variscan synorogenic gabbroic layered intrusion (Beja, Portugal): Implications for Ni-Cu-PGE exploration in orogenic settings. Ore Geology Reviews, v.126, 103767. https://doi.org/10.1016/j.oregeorev.2020.103767

Jochum, K.P., Willbold, M., Raczek, I., Stoll, B., and Herwig, K., 2005. Chemical Characterisation of the USGS Reference Glasses GSA-1G, GSC-1G, GSD-1G, GSE-1G, BCR-2G, BHVO-2G and BIR-1G Using EPMA, ID-TIMS, ID-ICP-MS and LA-ICP-MS. Geostandards and Geoanalytical Research, v. 29(3), p. 285.302. https://doi.org/10.1111/j.1751-908X.2005.tb00901.x

Julivert, M., Fontboté, J.M., Ribeiro, A., and Nabais Conde, L.E., 1972. Mapa Tectónico de la Península Ibérica y Baleares. Scale 1:1.000.000. IGME.

Kamvong T, Zaw K, and Siegele, R., 2007. PIXE/PIGE microanalysis of trace elements in hydrothermal magnetite and exploration significance: a pilot study 15th Australian Conference on Nuclear and Complementary Techniques of Analysis and 9th Vacuum Society of Australia Congress. University of Melbourne, Melbourne.

Knipping, J.L., Bilenker, L.D., Simon, A.C., Reich, M., Barra, F., Deditius, A.P., Wälle, M., Heinrich, C.A., Holtz, F., and Munizaga, R., 2015. Trace elements in magnetite from massive iron oxide-apatite deposits indicate a combined formation by igneous and magmatic-hydrothermal processes. Geochimica et Cosmochimica Acta, v.171, p. 15-38. http://dx.doi.org/10.1016/j.gca.2015.08.010

Leal, N., 2001. Estudo petrológico e geoquímico de rochas metamórficas de alta pressão das regiões de Alvito-Viana do Alentejo e de Safira (Zona de Ossa-Morena, Maciço Ibérico). PhD Thesis, Universidade de Lisboa, pp. 402.

Liu, Y., Fan, Y., Zhou, T., Xiao, X., White, N.C., Thompson, J., Hong, H., and Zhang, L., 2019. Geochemical characteristics of magnetite in Longqiao skarn iron deposit in the Middle-Lower Yangtze Metallogenic Belt, Eastern China. Mineralium Deposita, v. 54, p. 1229-1242. https://doi.org/10.1007/s00126-019-00871-x

Maia, M., Roseiro, J., Nogueira, P., Noronha, F., Fuertes.Fuente, M., Cepedal, A., and Mirão, J., 2022. New insights on the Escoural Orogenic gold district (Ossa-Morena Zone, SW Iberia): Geochemistry, fluid inclusions and stable isotope constraints from the Monfurado gold prospect: Ore Geology Reviews, v. 142, 104736. https://doi.org/10.1016/j.oregeorev.2022.104736

Makvandi, S., Ghasemzadeh-Barvarz, M., Beaudoin, G., Grunsky, E.C., McClenaghan, M.B., and Duchesne, C., 2016a. Principal component analysis of magnetite composition from volcanogenic massive sulfide deposits: Case studies from the Izok Lake (Nunavut, Canada) and Halfmile Lake (New Brunswick, Canada) deposits. Ore Geology Reviews, v. 72, p. 60-85. http://dx.doi.org/10.1016/j.oregeorev.2015.06.023

Makvandi, S., Ghasemzadeh-Barvarz, M., Beaudoin, G., Grunsky, E.C., McClenaghan, M.B., Duchesne, C., and Boutroy, E.C., 2016b. Partial least squares-discriminant analysis of trace element compositions of magnetite

from various VMS deposit subtypes: Application to mineral exploration. Ore Geology Reviews, v.78, p. 388-408. http://dx.doi.org/10.1016/j.oregeorev.2016.04.014

Makvandi, S., Huang, X., Beaudoin, G., Quirt, D., Ledru, P., and Fayek, M., 2021. Trace element signatures in hematite and goethite associated with the Kiggavik–Andrew Lake structural trend U deposits (Nunavut, Canada). Mineralium Deposita, v. 56, p. 509-535. https://doi.org/10.1007/s00126-020-00980-y

Marbouti, Z., Ehya, F., Paydar, G.R., and Maleki, S., 2020. Geochemical, microthermometric, and sulfur isotopic constraints on the origin of the Sarviyan iron deposit, Markazi Province, Iran. Journal of Geochemical Exploration, v. 210, 106451. https://doi.org/10.1016/j.gexplo.2019.106451

Martins, R., Mateus, A., Figueiras, J., Barroso, M., and Oliveira, V. 2003. Post-metamorphic evolution of the Lower Cambrian section at Enfermarias (Moura, Portugal): its record and metallogenic implications. VI Congresso Nacional de Geologia, Lisboa (Portugal), Ciências da Terra (UNL), Lisboa, n.º esp. V, CD-ROM, B60-B63.

Mateus, A., Araújo, A., Gonçalves, M.A., and Matos, J., 2005. Variscan overthrusting, fluid flow and genesis of magnetite ore-bodies at the Azenhas area (Pedrógão, Ossa-Morena Zona, SE Portugal). Boletín Geológico y Minero, v.116(1), p. 3-22. ISSN 0366-0176.

Mateus, A., Munhá, J., Inverno, C., Matos, J.X., Martins, L., Oliveira, D., Jesus, A., and Salgueiro, R., 2013. Mineralizações no sector português da Zona de Ossa-Morena. In R. Dias, A. Araújo, P. Terrinha, J.C. Kullberg (Eds.), Geologia de Portugal, v. 1, p. 577-619. Lisboa: Escolar Editora.

Matos, J., Araújo, A., and Mateus, A., 1998. Cartografia de detalhe e controle estrutural das mineralizações na região de Pedrógão-Orada. Geologos, v.2, p. 101-104.

Mehrabi, B., Karimishahraki, B., Banks, D., Boyce, A., and Yardley, B.W.D., 2019. Hydrothermal iron oxide-Cu-Au (IOCG) mineralization at the Jalal-Abad deposit, northwestern Zarand, Iran. Ore Geology Reviews, v. 106, p. 300-317. https://doi.org/10.1016/j.oregeorev.2019.01.019

Meinert, L.D., 1987. Skarn zonation and fluid evolution in the Groundhog Mine, Central mining district, New Mexico. Economic Geology, v.82, p.523–545. https://doi.org/10.2113/gsecongeo.82.3.523

Meinert, L.D., 1992. Skarns and skarn deposits. Geoscience Canada, v. 19, p. 145-162.

Meinert, L.D., 1993. Igneous petrogenesis and skarn deposit. In: R.V. Kirkham, W.D. Sinclair, R.I. Thorpe, & J.M.Duke, eds. Geol. Assoc. Can. Special Paper, v. 40, p. 569-583.

Meinert, L.D., Dipple, G.M., and Nicolescu, S., 2005. World skarn deposits. Economic Geology 100th Anniversary Volume, pp. 299–336. https://doi.org/10.5382/AV100.11

Middlemost, E.A.K., 1994. Naming materials in the magma/igneous rock system. Earth-Science Reviews, v.37, p.215-224. https://doi.org/10.1016/0012-8252(94)90029-9

Moita, P., Munhá, J., Fonseca, P.E., Tassinari, C.C.G., Araujo, A., and Palácios, T., 2005. Dating orogenic events in Ossa-Morena Zone. XIV Semana de Geoquímica/ VIII Congresso de Geoquímica dos Países de Língua Portuguesa, p. 459-461.

Moita, P., Santos, J.F., and Pereira, M.F., 2009. Layered granitoids: interaction between continental crust recycling processes and mantle-derived magmatism: examples from the Évora Massif (Ossa–Morena Zone, southwest Iberia, Portugal). Lithos v. 111, p. 125–141. https://doi.org/10.1016/j.lithos.2009.02.009

Moita, P., Santos, J.F., Pereira, M.F., Costa, M.M., and Corfu, F., 2015. The quartz-dioritic Hospitais intrusion (SW Iberian Massif) and its mafic microgranular enclaves — Evidence for mineral clustering. Lithos, v.224-225, p. 78-100. https://doi.org/10.1016/j.lithos.2015.02.012

Nadoll, P., and Koenig, A.E., 2011. LA-ICP-MS of magnetite: methods and reference materials. Journal of Analytical Atomic Spectrometry, v. 26, p. 1872-1877. DOI: 10.1039/c1ja10105f

Nadoll, P., Mauk, J.L., Hayes, T.S., Koenig, A.E., and Box, S.E., 2012. Geochemistry of Magnetite from Hydrothermal Ore Deposits and Host Rocks of the Mesoproterozoic Belt Supergroup, United States. Economic Geology, v.107, p. 1275-1292. https://doi.org/10.2113/econgeo.107.6.1275

Nadoll, P., Angerer, T., Mauk, J.L., French, D., and Walshe, J., 2014. The chemistry of hydrothermal magnetite: A review. Ore Geology Reviews, v. 61, p. 1-32. http://dx.doi.org/10.1016/j.oregeorev.2013.12.013

Nadoll, P., Mauk, J.L., Leveille, R.A., and Koenig, A.E., 2015. Geochemistry of magnetite from porphyry Cu and skarn deposits in the southwestern United States. Mineralium Deposita, v. 50, p. 493-515. https://doi.org/10.1007/s00126-014-0539-y

Nielsen, R.L., Forsythe, L.M., Gallahan, W.E., and Fisk, M.R., 1994. Major-and trace-element magnetite-melt equilibria. Chemical Geology, v.117 (1–4), p.167–191. https://doi.org/10.1016/0009-2541(94)90127-9

Oliveira, V.M.J., 1986. Prospeção de minérios metálicos a Sul do Tejo. Geociências – Aveiro, v.1, p.15-22.

Oliveira, J.T., Oliveira, V., and Piçarra, J.M., 1991. Traços gerais da evolução tectono-estratigráfica da Zona de Ossa Morena, em Portugal: síntese crítica do estado actual dos conhecimentos. Comum. Serviços Geológicos de Portugal, v.77, p.3-26.

Palarea-Albaladejo, J., and Martín-Fernández, J.A., 2015. zCompositions — R package for multivariate imputation of left-censored data under a compositional approach. Chemometrics and Intelligent Laboratory Systems, v. 143, p. 85-96. http://dx.doi.org/10.1016/j.chemolab.2015.02.019

Palme, H., and O´Neill, HStC., 2014. Cosmochemical Estimates of Mantle Composition. In: Holland, H.D. & Turekian K.K. (Eds) Treatise on geochemistry. Vol. 15: Analytical geochemistry/inorganic instrument analysis. Elsevier, Oxford, p. 1-39. http://dx.doi.org/10.1016/B978-0-08-095975-7.00201-1

Papike, J.J., Karner, J.M., and Shearer, C.K., 2005. Comparative planetary mineralogy: valence state partitioning of Cr, Fe, Ti, and Vamong crystallographic sites in olivine, pyroxene, and spinel from planetary basalts. American Mineralogy, v. 90, p. 277–290. https://doi.org/10.2138/am.2005.1779

Pedro, J., 1996 Estudo do metamorfismo de alta pressão na área de Safira (Montemor-o-Novo) Zona de Ossa-Morena. MSc. Thesis, Universidade de Lisboa, pp. 69.

Pedro, J., Araújo, A., Fonseca, P.E., Tassinari, C., Ribeiro, A. 2010. Geochemistry and U-Pb zircon age of the internal Ossa-Morena Zone ophiolite sequences: a remnant of Rheic ocean in SW Iberia. Ofioliti, v. 35(2), p. 117-130.

Pedro, J., Araújo, A., Fonseca, P., Munhá, J., Ribeiro, A., and Mateus, A., 2013. Cinturas Ofiolíticas e Metamorfismo de Alta Pressão no Bordo SW da Zona de Ossa-Morena. In R. Dias, A. Araújo, P. Terrinha, J.C. Kullberg (Eds.), Geologia de Portugal (p. 641-665, v.1). Lisboa: Escolar Editora.

Pereira, M.F., Silva, J.B., and Chichorro, M., 2003. Internal Structure of the Évora High-grade Terrains and the Montemor-o-Novo Shear Zone (Ossa-Morena Zone, Portugal), Geogaceta, v.33, p. 79-82.

Pereira, M. F., Silva, J. B., Chichorro, M., Moita, P., Santos, J. F., Apraiz, A., and Ribeiro, C., 2007. Crustal growth and deformational processes in the northern Gondwana margin: Constraints from the Évora Massif (Ossa-Morena zone, southwest Iberia, Portugal). Special Paper 423: The Evolution of the Rheic Ocean: From Avalonian-Cadomian Active Margin to Alleghenian-Variscan Collision, p. 333–358. https://doi.org/10.1130/2007.2423(16).

Pereira, M. F., Chichorro, M., Williams, I. S., and Silva, J. B. 2008. Zircon U–Pb geochronology of paragneisses and biotite granites from the SW Iberian Massif (Portugal): evidence for a palaeogeographical link between

the Ossa–Morena Ediacaran basins and the West African craton. Geological Society, London, Special Publications, v.297(1), p. 385–408. https://doi.org/10.1144/SP297.18

Pereira, M.F., Solá, A.R., Chichorro, M., Lopes, L., Gerdes, A., and Silva, J.B., 2012. North-Gondwana assembly, break up and paleogeography: U–Pb isotope evidence from detrital and igneous zircons of Ediacaran and Cambrian rocks of SW Iberia. Gondwana Research, v.22(3-4), p. 866-881. https://doi.org/1016/j.gr.2012.02.010

Pereira, M.F., Chichorro, M., Moita, P., Santos, J.F., Solá, A.M.R., Williams, I.S., Silva, J.B., and Armstrong, R.A., 2015. The multistage crystallization of zircon in calc-alkaline granitoids: U–Pb age constraints on the timing of Variscan tectonic activity in SW Iberia. International Journal of Earth Sciences, v.104, p.1167-1183. https://doi.org/10.1007/s00531-015-1149-3

Pin, C., Fonseca, P.E., Paquette, J.-L., Castro, P., and Matte, P., 2008. The ca. 350 Ma Beja Igneous Complex: a record of transcurrent slab break-off in the Southern Iberia Variscan Belt? Tectonophysics, v.461, p. 356–377. https://doi.org/10.1016/j.tecto.2008.06.001

Pinto, S.M.C., Soares de Andrade, A.A., 1987. Geocronologia dos granitóides da Zona de Ossa-Morena (Maciço Hespérico) no contexto do arco Ibero-Armoricano. Geociências – Aveiro, v.2, p. 95-103.

Pisiak, L.K., Canil, D., Lacourse, T., Plouffe, A., and Ferbey, T., 2017. Magnetite as an Indicator Mineral in the Exploration of Porphyry Deposits: A Case Study in Till near the Mount Polley Cu-Au Deposit, British Columbia, Canada. Economic Geology, v. 112, p. 919-940. https://doi.org/10.2113/econgeo.112.4.919

Qi, Y., Hu, R., Gao, J., Gao, W., and Gong, H., 2021. Trace element characteristics of magnetite: Constraints on the genesis of the Lengshuikeng Ag–Pb–Zn deposit, China. Ore Geology Reviews, v. 129, 103943. https://doi.org/10.1016/j.oregeorev.2020.103943.

Quesada, C., Fonseca, P., Munhá, J., Oliveira, J., and Ribeiro, A., 1994. The Beja-Acebuches Ophiolite (Southern Iberia Variscan fold belt): geological characterization and geodynamic significance. Bolletin Geologico y Minero, v.105(1), p. 3-49.

Quesada, C., Braid, J.A., Fernandes, P., Ferreira, P., Jorge, R. S., Matos, J. X., Murphy, J.B., Oliveira, J.T., Pedro, J., and Pereira, Z., 2019. SW Iberia Variscan Suture Zone: Oceanic Affinity Units. In The Geology of Iberia: A Geodynamic Approach (pp. 131-171). Springer, Cham. https://doi.org/10.1007/978-3-030-10519-8_5

Ribeiro, A., Munhá, J., Fonseca, P.E., Araújo, A., Pedro, J.C., Mateus, A., Tassinari, C., Machado, G., and Jesus, A., 2010. Variscan ophiolite belts in the Ossa-Morena Zone (Southwest Iberia): Geological characterization

and geodynamic significance. Gondwana Research, v.17, p. 408-421. https://doi.org/10.1016/j.gr.2009.09.005

Ribeiro, M.L., Castro, A., Almeida, A., Menéndez, L. G., Jesus, A., Lains, J.A., Carrilho Lopes, J., Martins, H.C.B.; Mata, J., Mateus, A., Moita, P., Neiva, A., Ribeira, M.A., Santos, J.F., and Solá, A.R., 2019. Variscan Magmatism. In The Geology of Iberia: A Geodynamic Approach (pp. 497-526). Springer, Cham. https://doi.org/10.1007/978-3-030-10519-8_13

Righter, K., Leeman, W.P., and Hervig, R.L., 2006. Partitioning of Ni, Co and V between spinel-structured oxides and silicate melts: importance of spinel composition. Chemical Geology, v. 227, p. 1–25. https://doi.org/10.1016/j.chemgeo.2005.05.011

Rodriguez-Mustafa, M.A., Simon, A.C., del Real, I., Thompson, J.F.H., Bilenker, L.D., Barra, F., Bindeman, I., and Cadwell, D., 2020. Economic Geology, v. 115(7), p. 1443-1459. https://doi.org/10.5382/econgeo.4752

Rosas, F., Marques, F.O., Ballevre, M., and Tassinari, C., 2008. Geodynamic evolution of the SW Variscides: Orogenic collapse shown by new tectonometamorphic and isotopic data from western Ossa-Morena Zone, SW Iberia. Tectonics, v.27(6). https ://doi.org/10.1029/2008T C002333

Roseiro, J., Moreira, N., Fonseca, R., Araújo, A., Maia, M., Pedro, J., and Nogueira, P., 2019. Lithogeochemistry of metabasites from the Moura Phyllonitic Complex (Ossa Morena Zone, SW Portugal). EGU General Assembly 2019, Geophysical Research Abstracts.

Rudnick, R.L., and Gao, S., 2003. The composition of continental crust. Treatise Geochemistry, v.3, p. 1–64. https://doi.org/10.1016/0016-7037(95)00038-2

Salgueiro, R., Mateus, A., Inverno, C., 2010a. Caracterização e génese do skarn ferrífero de Orada (Zona de Ossa-Morena). E-Terra, v. 20(3).

Salgueiro, R., Inverno, C., and Mateus, A., 2010b. Main characteristics and genesis of the Vale de Pães skarn (Cuba-Vidigueira, Ossa Morena Zone, Portugal). Estudios Geológicos, v.66(1), p. 65-74. doi:10.3989/egeol.40150.101

Salgueiro, R., 2011. Caracterização e génese das mineralizações de magnetite – sulfuretos em Monges (Santiago do Escoural, Montemor-o-Novo) e ensaio comparativo com as suas congéneres em Orada-Vale de Pães (Serpa-Vidigueira). PhD Thesis, Universidade de Lisboa, 524 p.

Salgueiro, R., Mateus, A, and Inverno, C., 2012. Mineralizações de magnetite e sulfuretos de monges (Santiago do Escoural, Montemor-o-Novo), Vale de Pães (Cuba-Vidigueira) e Orada (Pedrógão, Serpa): Síntese de ensaio comparativo. Boletim de Minas, v. 47(1), p. 27-30.

Sánchez-Garcia, T., Bellindo, F., and Quesada, C., 2003. Geodynamic setting and geochemical signatures of Cambrian-Ordovician rift-related igneous rocks (Ossa-Morena Zone, SW Iberia). Tectonophysics, v. 365, p.233-255. https://doi.org/10.1016/S0040-1951(03)00024-6

Sánchez-García, T., Chichorro, M., Solá, A.R., Álvaro, J.J., Díez-Montes, A., Bellido, F., Ribeiro, M.L., Quesada, C., Lopes, J.C., Dias da Silva, Í., González-Clavijo, E., Gómez Barreiro, J., and López-Carmona, A., 2019. The Cambrian-Early Ordovician Rift Stage in the Gondwanan Units of the Iberian Massif. In: Quesada, C. & Oliveira J.T. (Eds) The Geology of Iberia: A Geodynamic Approach, Vol. 2: The Variscan Cycle. Springer Nature, Switzerland, p.27-74. https://doi.org/10.1007/978-3-030-10519-8

Sarjoughian, F., Habibi, I., Lentz, D.R., Azizi, H., and Esna-Ashari, A., 2020. Magnetite compositions from the Baba Ali iron deposit in the Sanandaj-Sirjan zone, western Iran: Implications for ore genesis. Ore Geology Reviews, v. 126, 103728. https://doi.org/10.1016/j.oregeorev.2020.103728

Serviço de Fomento Mineiro, 1965. 1: 5000 cartographic map of the Azenhas-Orada area. Unpublished map.

Serviços Geológicos de Portugal, 1992. Carta Geológica de Portugal à escala 1:500 000. Serviços Geológicos de Portugal, Lisboa.

Sun, W., Yuan, F., Jowitt, S.M., Zhou, T., Liu, G., Li, X., Wang, F., and Troll, V.R., 2019. In situ LA–ICP–MS trace element analyses of magnetite: genetic implications for the Zhonggu orefield, Ningwu volcanic basin, Anhui Province, China. Mineralium Deposita, v. 54, p. 1243-1264. https://doi.org/10.1007/s00126-019-00872-w

Telhado, F. M., 2018. Petrologia e geoquímica do Ortognaisse das Alcáçovas e rochas associadas: contributo para a compreensão da evolução geodinâmica da Zona de Ossa Morena. MsC Thesis, Universidade de Lisboa, pp. 107.

Toplis, M.J., and Corgne, A., 2002. An experimental study of element partitioning between magnetite, clinopyroxene and iron-bearing silicate liquids with particular emphasis on vanadium. Contributions to Mineralogy and Petrology, v. 144, p. 22–37. https://doi.org/10.1007/s00410-002-0382-5

Tornos, F., Casquet, C., Relvas, J.M.R.S., Barriga, F.J.A.S., and Sáez, R., 2002. The relationship between ore deposits and oblique tectonics: the SW Iberian Variscan Belt. In: BLUNDELL, D.J., NEUBAUER, E & VON

QUADT, A. (eds) 2002. The Timing and Location of Major Ore Deposits in an Evolving Orogen. Geological Society, London, Special Publications, v.204, p. 179-198. https://doi.org/10.1144/GSL.SP.2002.204.01.11

Tornos, F., Galindo, C., Darbyshire, F., Casquet, C., and Noble, S.R., 2021. Isotope geochemistry, age, and origin of the magnetite-vonsenite mineralization of the Monchi Mine, SW Iberia. Journal of Iberian Geology. https://doi.org/10.1007/s41513-020-00159-4

Tostevin, R., Shields, G.A., Tarbuck, G.M., He, T., Clarkson, M.O., and Wood, R.A., 2016. Effective use of cerium anomalies as a redox proxy in carbonate-dominated marine settings. Chemical Geology, v. 438, p. 146-162. http://dx.doi.org/10.1016/j.chemgeo.2016.06.027

Velasco, F., and Amigó, J.M., 1981. Mineralogy and origin of the skarn from Cala (Huelva). Economic Geology, v.76(3), p.719-727. https://doi.org/10.2113/gsecongeo.76.3.719

Ward, L.A., Holwell, D.A.M Barry, T.L., Blanks, D.E., and Graham, S.D., 2018. The use of magnetite as a geochemical indicator in the exploration for magmatic Ni-Cu-PGE sulfide deposits: A case study from Munali, Zambia. Journal of Geochemical Exploration, v.188, p.172-184. https://doi.org/10.1016/j.gexplo.2018.01.018

Wen, G., Li, J.-W., Hofstra, A.H., Koenig, A.E., Lowers, H.A., and Adams, D., 2017. Hydrothermal reequilibration of igneous magnetite in altered granitic plutons and its implications for magnetite classification schemes: Insights from the Handan-Xingtai iron district, North China Craton. Geochimica Cosmochimica Acta, v.213, p. 255–270. https://doi.org/10.1016/j.gca.2017.06.043

Whitney D.L., and Evans B.W. 2010. Abbreviations for names of rock-forming minerals. Amer. Miner., v.95, p.185-187. https://doi.org/10.2138/am.2010.3371

Winchester, J.A, and Floyd, P.A., 1977. Geochemical discrimination of different magma series and their differentiation products using immobile elements. Chemical Geology, v.20, p.325-343. https://doi.org/10.1016/0009-2541(77)90057-2

Wu, C., Chen, H., Hong, W., Li, D., Liang, P., Fang, J., Zhang, L., and Lai, C., 2019. Magnetite chemistry and implications for the magmatic-hydrothermal ore-forming process: An example from the Devonian Yuleken porphyry Cu system, NW China. Chemical Geology, v. 522, p. 1-15. https://doi.org/10.1016/j.chemgeo.2019.04.022

Wood, S.A., 1990. The aqueous geochemistry of the rare-earth elements and Yttrium. Theoretical predictions of speciation in hydrothermal solutions to 350°C at saturation water vapor pressure. Chemical Geology, v. 88, p. 99–125. https://doi.org/10.1016/0009-2541(90)90106-H

Xiao, Q.-L., Zhou, T.-F., Wang, S.-W., Yuan, F., White, N.C., Wang, F.-Y., Xie, Z.-J., and Jing, L., 2019. Genesis of Chating Cu-Au deposit in the Middle-Lower Yangtze River Metallogenic Belt, Eastern China: Implications from magnetite and biotite geochemistry. Ore Geology Reviews, v. 109, p. 113-133. https://doi.org/10.1016/j.oregeorev.2019.01.017

Chapter 4

Combining $\delta^{18}O$ isotope data and in-situ LA-ICP-MS trace element analysis of magnetite as a proxy for ore genesis: Constraints on the formation of Fe deposits from Ossa-Morena Zone (SW Iberia)

Journal of Geochemical Exploration, v. 245, Article Number 107140

https://doi.org/10.1016/j.gexplo.2022.107140

Co-authors:

Pedro Barrulas

Pedro Nogueira

José Mirão

Fernando Noronha

Abstract

The Ossa-Morena Zone (OMZ, SW of the Iberian Peninsula) is a geotectonic domain that comprises a set of diversified ore deposits formed from Cambrian to Carboniferous-Permian ages. The Montemor-o-Novo – Ficalho Fe-Zn-(Pb) belt was a productive mining sector until the first half of the 20th century with potential for future mineral exploration, although the mechanisms responsible for ore deposition are, in some cases, poorly constrained. In this study the trace element composition of a large set of orebodies belonging to three iron deposits is examined, and the first $\delta^{18}O$ analysis of magnetite from the Portuguese sector of OMZ is reported.

Outcrop and drill core magnetite samples were collected from the Montemor-o-Novo Iron Complex (MIC), and from the Alvito and Azenhas-Orada deposits. New magnetite LA-ICP-MS data from the carbonate-hosted MIC deposits, classified as SEDEX-VMS, and from the Alvito and Azenhas-Orada skarn deposits are complemented by previously published data. This approach contributes to the classification of these deposits and provides new discriminatory proxies for skarn deposits worldwide. Close to 1000 LA-ICP-MS and EPMA magnetite spot analyses is explored, complemented by EPMA analysis of representative mineral phases from the host rocks. Three deposits from the MIC (Monges, Vale da Arca, and Serrinha) were studied, in which magnetite reveals a wide range of textures and trace element compositions. Using the Al + Mn vs Ti + V diagram the magnetite from the MIC is hardly discriminated from the magnetite data from the skarn deposits. Hence other discriminant factors have been used. Magnetite from the MIC is characterized by low contents of Co, Zn, and HFSE (e.g. Ta, Nb), and shows a close relation with low-temperature hydrothermal magnetite as revealed by the multivariate diagrams of trace elements. Skarn magnetite display high concentrations of temperature-dependent elements such as Ti, V, Al, Ga, Sn, Cr, and HSFE. Additionally, high contents of Co and Zn are ubiquitous for first generation magnetite from the skarn deposits, which might indicate that the ore source was enriched in such elements.

Primary magnetite from the MIC deposits revealed $\delta^{18}O$ signatures in the range 4.3 ‰ to 9.0 ‰ which, combined with magnetite trace element composition, suggests extensive overprinting of the primary signatures by late metamorphic events. Primary magnetite from the Azenhas-Orada deposits revealed $\delta^{18}O$ signatures (4.0 ‰ – 5.6 ‰) suggesting a magmatic derived source for the mineralization, corroborating the hypothesis proposed in recent works. The $\delta^{18}O$ signatures of magnetite from the Alvito skarn deposit indicate that extensive interactions between a magmatic fluid, with lighter 18O signatures, and the dolomite-calcite host rock, with heavier ^{18}O signatures, have occurred. The results outline the potential of allying powerful multielement analysis of magnetite with stable isotope analysis

and contribute to the refinement of geological models in the Ossa-Morena Zone that can be used in future mineral exploration.

Keywords: Magnetite; Trace elements; Oxygen isotopes; LA-ICP-MS; Geochemical fingerprinting.

4.1 Introduction

Advances in analytical techniques allowed the application of high-sensitive methods to the analysis of trace elements and stable isotopes in a wide range of minerals, which have been used to fingerprint the processes behind the formation of ore deposits and to identify the exchanges between ore transporting fluids and host rocks (e.g., Cook et al., 2016; Codeço et al., 2021, Sciuba et al., 2021; Steadman et al., 2021). Such developments have shed light on possible sources and processes thus defining new exploration vectors for selecting locations prone to the concentration of metals, hence helping in mineral deposit exploration campaigns. This goal has been successfully achieved using magnetite trace element composition to construct discriminatory indexes that can be applied to the classification of ore deposits (Dupuis and Beaudoin, 2011; Dare et al., 2014; Nadoll et al., 2014; 2015). The identification of the mechanisms that control trace element incorporation into the magnetite structure provides valuable information regarding the ore sources, which can ultimately help in targeting new prospects.

Conventional and unconventional isotope analysis of magnetite has been recently used to evaluate the source of the ores in Iron-Oxide-Apatite (IOA) deposits and Iron-Oxide-Copper and Gold (IOCG) deposits (Nyström et al., 2008; Johnson et al., 2016; Ghazi et al., 2019; Duan et al., 2019; Peters et al., 2019; Troll et al., 2019; Childress et al., 2020; Rodriguez-Mustafa et al., 2020; Palma et al., 2021), whereas magnetite from other deposit types, such as, Fe skarns has not been inspected in most of these studies (Rose et al., 1985, Xie et al., 2017; Dong et al., 2021, Tornos et al., 2021). For the latter, other ore-assemblage minerals and whole-rock samples have been preferred for the analysis of oxygen isotopes to constrain the geological conditions that assisted the mineralizing events (Ayupova et al., 2020; Morris & Canil, 2021).

Several types of iron deposits are found at the SW of the Iberian Massif, in the Ossa-Morena Zone (OMZ) (Velasco and Amigó, 1981; Carriedo et al., 2021; Tornos et al., 2021). At the Portuguese sector of OMZ, the iron deposits mainly concentrate in the Montemor-o-Novo – Ficalho belt (MFB; Mateus et al., 2013). The ore deposition is controlled by multiple geological features that actuated during the geodynamic history of this sector.

This study provides the first results that combine in-situ LA-ICP-MS trace element analysis and oxygen isotope signatures of magnetite to characterize iron deposits from the Ossa-Morena Zone (**Fig. 4.1a**). We focus our study on some of the abandoned mines that are part of the Montemor-o-Novo Iron Complex (MIC; **Fig. 4.1b**), from which three ore bodies were selected, the Monges, Vale da Arca, and Serrinha ancient mines (**Fig. 4.1b**). Additionally, two distinctive abandoned mining areas were investigated: the Alvito and the Azenhas-Orada skarn deposits (**Fig. 4.1c, d**). Previous studies investigated the ore-assemblages and

gathered data to propose a SEDEX-VMS metallogenic model for the MIC deposits (Salgueiro, 2011) and a skarn deposit model for the genesis of the Alvito and Azenhas-Orada orebodies (Mateus et al., 2005; Salgueiro 2011; Salgueiro et al., 2012). The Azenhas and Alvito skarn deposits have recently been the subject of a research focusing on magnetite trace element analysis (Maia et al., 2022a). The presented research aims to provide new results for these iron ores, which are complemented by the analysis of magnetite from the Orada skarn deposit and three ore bodies from the MIC deposits, as well as inspecting the oxygen isotopes signatures of magnetite for all the deposit types of the sector.

The goals of this research are: i) fingerprint the source of the ores for the selected case studies, ii) constrain the conditions of magnetite deposition, and contribute to the understanding of the ore-systems based on the mechanisms of element mobility and incorporation in the magnetite structure, iii) identify the extent of post-deposition processes, iv) contribute for the understanding of the metallogenic evolution of the sector and v) provide exploration vectors for the mineral exploration in OMZ that can be replicated for other case studies associated to diverse geotectonic settings.

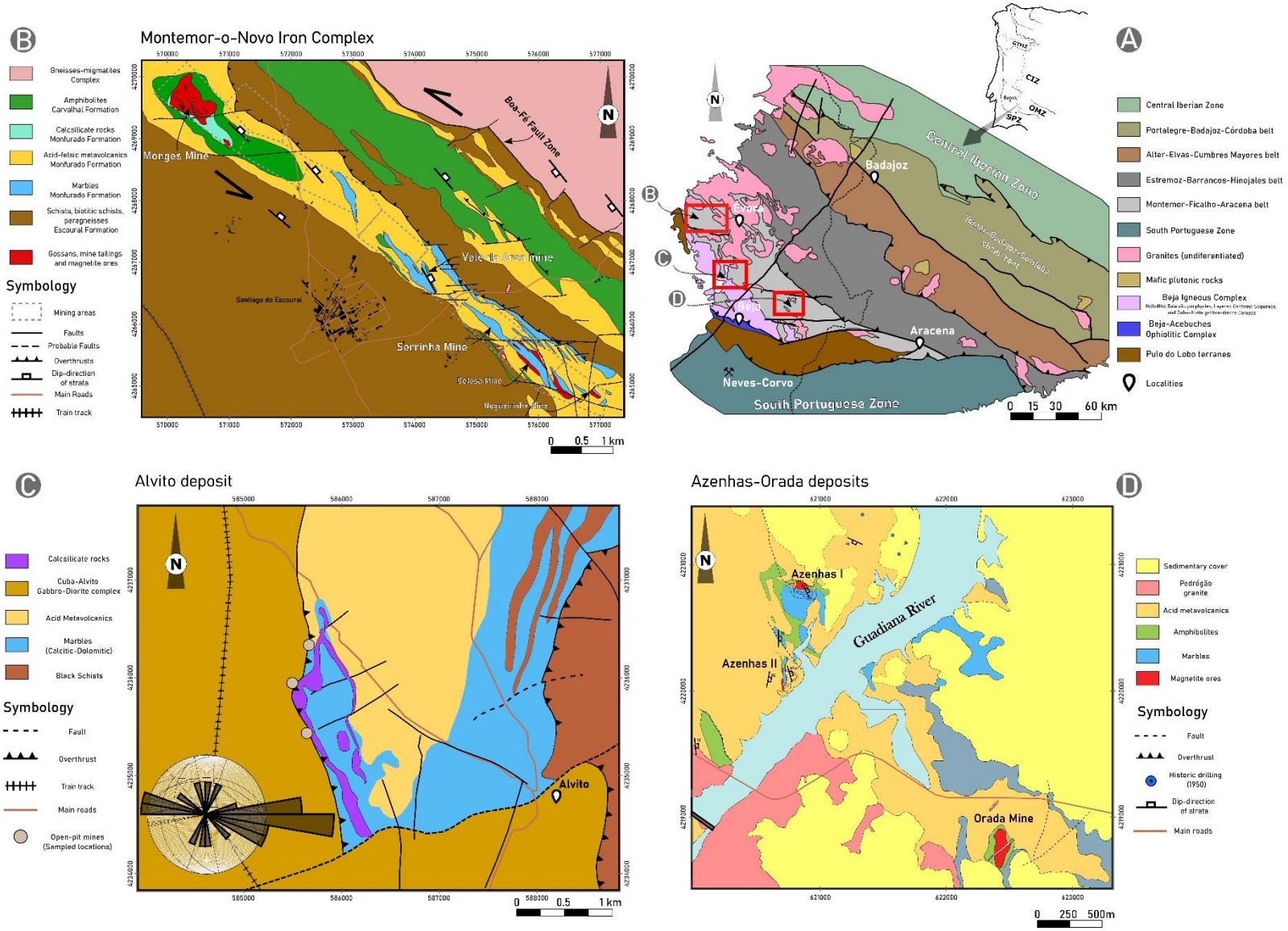
B
Montemor-o-Novo Iron Complex
Gneisses-migmatites Complex
Amphibolites Carvalhal Formation
Calcsilicate rocks Monfurado Formation
Acid-felsic metavolcanics Monfurado Formation
Marbles Monfurado Formation
Schists, biotitic schists, paragneisses Escoural Formation
Gossans, mine tailings and magnetite ores
Symbology
Mining areas
Faults
Probable Faults
Overthrusts
Dip-direction of strata
Main Roads
Train track
Monges Mine
Boa-Fé Fault Zone
Vale de Areia mine
Santiago do Escoural
Serrinha Mine
Defesa Mine
Negrinha Mine
0 0.5 1 km
A
Central Iberian Zone
Portalegre-Badajoz-Córdoba belt
Alter-Elvas-Cumbres Mayores belt
Estremoz-Barrancos-Hinojales belt
Montemor-Ficalho-Aracena belt
South Portuguese Zone
Granites (undiferentiated)
Mafic plutonic rocks
Beja Igneous Complex
Beja-Acebuches Ophiolitic Complex
Pulo do Lobo terranes
Localities
CTZ
OMZ
SPZ
Badajoz
Beja
Aracena
Neves-Corvo
South Portuguese Zone
0 15 30 60 km
C
Alvito deposit
Calcsilicate rocks
Cuba-Alvito Gabbro-Diorite complex
Acid Metavolcanics
Marbles (Calcitic-Dolomitic)
Black Schists
Symbology
Fault
Overthrust
Train track
Main roads
Open-pit mines (Sampled locations)
Alvito
0 0.5 1 km
D
Azenhas-Orada deposits
Azenhas I
Azenhas II
Guadiana River
Orada Mine
Sedimentary cover
Pedrógão granite
Acid metavolcanics
Amphibolites
Marbles
Magnetite ores
Symbology
Fault
Overthrust
Historic drilling (1950)
Dip-direction of strata
Main roads
0 250 500m

Figure 4.1 (previous page) Representative geological maps of the areas selected for this study. (A) Geotectonic sectioning of SW Iberia (Julivert et al., 1972) with individualization of the lithostratigraphic terranes of Ossa-Morena Zone and main magmatic bodies (adapted from Jesus et al., 2020). In this figure the red rectangles correspond to the location of the selected areas and the letters have their due correspondence to the Figure 1B, Figure 1C, and Figure 1D. (B) Close-up of the area marked in Figure 1A as B. The image shows the geological map of the Montemor-o-Novo Iron Complex (MIC) area (adapted from Serviço de Fomento Mineiro 1960; Silva et al., 1988). In the map the delimitation of the Montemor-o-Novo Iron Complex mining areas deposits are shown (Andrade et al., 1949; Goínhas and Martins, 1986). (C) Geological map of the surrounding area of the Alvito Fe Skarn deposit (adapted from Carvalhosa and Zbyszewski, 1971; Gomes, 2000; Gomes and Fonseca, 2006; Maia et al., 2022a), with the indication of the sampled locations. (D) Geological map of the Azenhas-Orada Fe skarn deposits area, with individualization of the Azenhas and Orada mines (adapted from Serviço de Fomento Mineiro, 1965).

4.2 Geologic Background

The geotectonic arrangement of the Iberian Massif divides it in several zones as follows, Cantabrian Zone, Galiza Trás-os-Montes Zone, Central Iberian Zone, Ossa-Morena Zone, South Portuguese Zone (Julivert et al., 1972; Farias et al., 1987), and additionally the Pulo do Lobo (e.g. Pereira et al., 2017) and Finisterra terranes (e.g. Moreira et al., 2019). This geotectonic arrangement is highly controlled by the edification of the Variscan Orogen, as well as by the oceanization events that preceded it (e.g. Matte, 2001; Araújo et al., 2005; Ribeiro et al., 2007; 2010; Diéz Fernández et al., 2016; Dias et al., 2017). The Ossa-Morena Zone is a geotectonic unit that is key to understand the geodynamic evolution of the European Variscides, with an internal tectonostratigraphic arrangement that reflects not only the evolution of the Variscan cycle, but also the prior Cadomian Orogeny (e.g. Eguiluz et al., 2000; Ribeiro et al., 2007; Rojo-Pérez et al., 2021). The Variscan cycle began in early to middle Cambrian ages (Ribeiro et al., 2007; Simancas, 2019) defined by an intracontinental rifting stage at Cambrian-Ordovician times that marks the initial stages of the Rheic ocean opening. The early stages of oceanization are accompanied by intense magmatic activity, registered by felsic metavolcanic rocks observed throughout OMZ (ca. 535 – 515 Ma.; Chichorro et al., 2008; Sanchéz-Garcia et al. 2019). The rifting stage led to the detachment of Avalonia from Gondwana; during the early stages a horst-graben basin developed, leading to the formation of an extensive shallow-water carbonate platform. With the Rheic ocean fully developed (early Ordovician) a transition to a passive margin regime occurred (Ordovician-Devonian), which was then followed by a compressional regime that settled the beginning of the Rheic ocean closure (Silurian-Devonian boundary; Ribeiro et al., 2007). Subduction of the oceanic crust initiates in this stage, leading to the progressive approximation of the Avalonian terranes. During this stage, the emplacement of an ophiolitic suite occurs (Beja-Acebuches Ophyolitic Complex; Quesada et al., 1994; Ribeiro et al., 2010), and as compression continues, several

slabs of oceanic crust were obducted over the OMZ terranes. Evidence of these processes are observed at the inner domains of OMZ, particularly at the Montemor-Ficalho lithostratigraphic sector (Oliveira et al., 1991; Pedro et al., 2010; Ribeiro et al., 2010) extending through Aracena (Fig. 1A; Apalategui, 1990). Edification of the orogen started circa 390-370 Ma with the oblique collision between Laurussia and Gondwana (Ribeiro et al., 2007). Intense calc-alkaline magmatism is triggered during these collisional stages, which can be observed at the Évora Massif (Pereira et al., 2007; 2015; Moita et al., 2009; 2015; Dias da Silva et al., 2018) and the Beja Igneous Complex (Jesus et al., 2016; 2020). The stress field settled during these stages is responsible for the development of large NW-SE shear zones and shear faults near the suture.

The metallogenic diversity of OMZ is evidenced by the diverse ore deposit types, such as epithermal lode Cu deposits (Bugalho, Miguel Vacas, Mociços; e.g. Maia et al., 2020), Zn-Pb MVT deposits (Vila Ruiva and Preguiça; e.g., Barroso, 2003; Martins, 2003), orogenic gold deposits (Santiago do Escoural; e.g. Maia et al., 2022b), as well as the numerous iron deposits, some of which are part of this research. The relation of these deposits with the regional geologic settings led to the division of OMZ into several metallogenic belts (Tornos et al., 2004; Mateus et al., 2013). Herein, we focus on the iron deposits from the Montemor-o-Novo-Ficalho metallogenic belt (MFB; Mateus et al., 2013), which correspond to the Évora-Aracena belt described by Tornos et al. (2004).

4.2.1 Montemor-o-Novo Iron Complex

The Montemor-o-Novo Iron Complex (MIC) (**Fig. 4.1b**) corresponds to a set of iron deposits whose genesis is attributed to the intracratonic rifting stages of the Variscan cycle (Salgueiro, 2011). The ores are hosted in a volcano-sedimentary sequence, mainly composed of marbles, calc-silicate rocks (amphibole-rich), and acid metavolcanic rocks of rhyolite-rhyodacite affinity. This sequence is of Cambrian age and the acid metavolcanic rocks are evidence of the intracontinental rift-related magmatism, ubiquitous throughout OMZ (Chichorro et al., 2008; Sánchez-Garcia et al., 2019). Carbonates have formed in a restricted marine basin, and recent works (Salgueiro, 2011) attributed the genesis of the iron ores, mainly composed of magnetite and sulfides, to hydrothermal-exhalative processes during the rifting stages of the Variscan cycle (Rheic oceanization), therefore framing it as a SEDEX-VMS deposits (Salgueiro, 2011). Nevertheless, one must emphasize that most of the primary mineral assemblages and textures have been overprinted by later episodes of tectonism and metamorphism during the collisional stages of the Variscan orogeny.

A complex geological setting frames the MIC iron deposits, highly influenced by the development of the large left-lateral shear zone that affects a metasedimentary sequence with

ages from the Neoproterozoic up to the Ordovician. The metamorphic conditions attained the greenschist to amphibolite facies, which imposed the development of amphibole assemblages (tremolite-actinolite) in the marbles hosting the mineralization (Pereira et al., 2003; 2007). Fluid circulation is acknowledged as important in the metamorphic-hydrothermal overprinting of the ores (Salgueiro, 2011; Maia et al. 2022b). Due to this long-lived tectonic-metamorphic history and the difficulty in identifying primary unmetamorphosed ores, the classification of the deposits as SEDEX-VMS is debatable, hence the relevance of applying new discriminatory geochemistry criteria such as the one presented in this research.

4.2.2 Alvito Fe skarn deposit

The Alvito deposit (**Fig. 4.1c**) is located at the SW of the MFB and corresponds to a Fe skarn deposit generated by late metasomatic events associated with the emplacement of a gabbro-diorite suite (Gomes and Fonseca, 2006), part of the large Beja Igneous Complex (BIC), within carbonate units of Cambrian age. The genesis of the Beja Igneous Complex is related with a compressional regime during the collisional stages of the Variscan orogeny. The emplacement of BIC started at 350 ± 5 Ma (Pin et al., 2008) and encompassed a Layered Gabbroic Sequence (Jesus et al., 2016; 2020), the Cuba-Alvito gabbro-diorite suite (CAGD; **Fig. 4.1c**), and the Baleizão porphyry complex.

Through this work, we focus on the ore-forming processes promoted by the installment of the CAGD and in constraining the conditions for the formation of the Alvito Fe skarn, aiming to compare the SW Iberian geochemical signature of the iron ores and provide supplementary data and new insights for this deposit (c.f. Maia et al., 2022a). Furthermore, Ni-Cu-PGE ore formation processes have been described as related to the BIC emplacement (Jesus et al., 2020), with other analogues found in Spain (e.g. in Aguablanca; Tornos et al., 2006).

4.2.3 Azenhas-Orada Fe skarn deposits

The Azenhas-Orada area comprises two main inactive mining complexes corresponding to the Azenhas and Orada Fe skarn deposits (**Fig. 4.1d**).

The iron ores are found mainly hosted in allochthonous basic metavolcanic rocks (amphibolites; Araújo, 1995) imbricated along with Cambrian carbonate units. This tectonic imbrication was generated by an early-Variscan thrusting (D1/D2). The tectonic pilling and iron ores are truncated at the top by an acid metavolcanic unit with rhyolite-rhyodacite affinity (Maia et al., 2022a). This thrusting episode is responsible for metasomatic reactions with the development of epidote-rich skarn-like rocks, and remobilization of first-generation magnetite (Maia et al., 2022a). The Azenhas-Orada area is intruded by the Pedrogão granite, which

corresponds to a two-mica granite (308 ± 4 Ma; Carvalho et al., 1971) that crosscuts the tectonic pilling and the ore bodies.

The genesis of these deposits was addressed in previous works (Mateus et al., 2005; Salgueiro, 2011; Salgueiro, et al., 2010; 2012) with discussions that attribute the genesis of the ore bodies to a thermal gradient inversion promoted by the D1/D2 thrusting events, with a model closer to a reaction skarn (Meinert et al., 2005). Recent works (Maia et al, 2022a) showed results from the geochemical composition of magnetite from the Azenhas orebodies that indicate that the temperatures at the time of deposition should have been much higher than previously estimated, closer to those derived from a magmatic-hydrothermal origin.

4.3 Sampling and analytical methods

Sampling was performed in the ascribed iron deposits, and, for representativeness purposes, three deposits from the MIC were sellected, as follows:

(1) The Monges deposit, outcrop samples of massive magnetite ± sulfide masses were collected at the mining area. Near the Monges orebodies a drilling campaign, focused on targeting gold mineralization, was performed in 2014 by COLT Resources, Ltd. Access to the cores was provided by the company and samples from 4 drill cores were collected for the mineralogical and textural characterization of the ores and respective host rocks.
(2) Samples were collected in outcrops from the Vale da Arca ancient mining area. These outcrops are mostly composed of pristine and hydrothermally altered marbles in which disseminated iron oxides and sulfides, mainly magnetite and pyrite, were found.
(3) The Serrinha deposit was one of the targets of iron exploration in the MIC; for this deposit massive magnetite from mining outcrops was sampled.

Regarding the Fe skarn deposits, the sampling was carried out at the Alvito Fe skarn deposit in outcrops accessible through ancient mining works, as shown in **Fig. 4.1c**. Massive magnetite orebodies were sampled for textural characterization of the ores, as well as for the geochemical approach adopted in this research. Additionally, host rock samples were collected for characterization of the metasomatic alteration adjacent to the mineralization. At the Azenhas and Orada Fe skarn deposit, samples were collected from the open pits (**Fig. 4.1d**), although detailed outcrop sampling was only possible in the Azenhas deposit.

4.3.1 SEM-EDS

Mineralogical and textural characterization was performed in 40 polished sections representative of the sampled magnetite ores and in 64 polished thin sections representatives of the host rocks. Magnetite texture was further examined using a VP-SEM-EDS Hitachi S-3700N scanning electron microscope with a Bruker Xflash 5010 SDD x-ray spectrometer at the HERCULES Laboratory of the University of Évora (Évora, Portugal). This step was critical in the identification of exsolutions and inclusions, which could influence the analysis (Huang and Beaudoin, 2019; 2021) and, if possible, should be avoided throughout laser ablation inductively coupled mass spectroscopy (LA-ICP-MS). Semiquantitative analyses of magnetite were performed using an acceleration voltage of 20 kV at 40 Pa.

4.3.2 EPMA

Electron probe microanalysis (EPMA) is a standard method for determining the major and minor element composition of magnetite. Magnetites representative of the selected deposits were analyzed using a CAMECA SX100 EPMA at the University of Oviedo (Oviedo, Spain). Over 540 spot analyses were performed using a 5 μm beam diameter, with a 15 kV and 40 nA for the analyses of Mg, Al, Si, Ca, Ti, Fe, Cr, Mn, and V. For Co, and Zn an acceleration of 25 kV and a 60 nA current was adopted. Due to the lower limits of detection (LOD) for most of the trace elements present in magnetite the analysis by LA-ICP-MS was preferred over EPMA.

EPMA analyses were also conducted in amphiboles, feldspar, epidote, and pyroxene crystals for the characterization of host rocks. Analysis of K, Ca, Ti, Fe, Mn, Na, Si, Al, Mg, P, Cl, F, Cr, Ba, and O used a 5 μm beam diameter, 15 kV acceleration voltage, and 15 nA current.

4.3.3 LA-ICP-MS

For this study, the results from 631 ablation spots in 150 magnetite grains from 23 polished cross-sections prepared from representative samples of the selected orebodies are inspected. A total of 27 isotopes (^{24}Mg, ^{27}Al, ^{28}Si, ^{42}Ca, ^{45}Sc, ^{49}Ti, ^{51}V, ^{52}Cr, ^{55}Mn, ^{59}Co, ^{62}Ni, ^{65}Cu, ^{66}Zn, ^{71}Ga, ^{73}Ge, ^{75}As, ^{89}Y, ^{90}Zr, ^{93}Nb, ^{97}Mo, ^{118}Sn, ^{178}Hf, ^{181}Ta, ^{182}W, ^{208}Pb, ^{232}Th, ^{238}U) were determined following the methodology proposed by Nadoll & Koenig (2011). LA-ICP-MS was performed at the HERCULES Laboratory (University of Évora), using a CETAC LSX-213 G2+ system coupled to an Agilent 8800 Triple Quad ICP-MS. The NIST 610 glass standard (Jochum et al., 2011) was selected for ICP-MS calibration to optimize sensitivity and minimize both elemental fractionation (238U/232Th) and oxide formation (^{248}ThO/^{232}Th). Spot analyses

using a 400 burst with a 50 µm laser beam were selected for sample analysis, using a repetition rate of 10 Hz, with 100% energy, and using helium as carrier gas at 1 L/min. Each spot analysis had a total acquisition time of 70 seconds, comprising 15 s of gas blank, 40 s of ablation, and 15 s for cell washout. The GSE-1G reference glass (Jochum et al. 2005; Guillong et al., 2005) was used as the external standard, and was analyzed three times every 20-25 sample spot analysis. This approach guarantied method validation, namely quantification of accuracy and precision (App. Table A1), avoiding potential instrumental drift. Additionally, the GSC-1G and BCR-2G standards were also analyzed every 20-25 spots as unknowns (quality controls) to check for elemental recovery (%) assays. With the presented methodology a total average quantification accuracy of -0.262% was obtained for all elements, as well as a 3.09% total average method precision, and an average LOD for trace elements of 0.111 ppm (App. Table A1). Three different methods for internal standardization were applied as follows: 1) Fe concentrations, previously determined by EPMA analysis, as aforementioned, which was the preferred methodology, 2) Fe concentrations acquired from SEM-EDS analysis, and 3) internal standardization using the stoichiometric Fe proportion of 72.36 wt.%, as described by several authors (Pisiak et al., 2017, Chen et al., 2019; Huang et al., 2019).

4.3.4 Oxygen Isotopes

Representative samples of the primary ores were selected for oxygen isotope analyses. Samples were cut and milled to a 2 mm granulometry and then separated using a hand-magnet. The selected grains were observed under a binocular loupe and only the ones that did not display evidence for the presence of other minerals (e.g., silicates) were selected for the analysis. Oxygen isotope analyses were conducted at the NUCLEUS Laboratory from the University of Salamanca (Salamanca, Spain). The adopted methodology followed the acquisition of CO_2 by laser fluorination and determination of $^{18}O/^{16}O$ isotope ratios using a SIRA-II mass spectrometer in Dual-Inlet mode.

4.4 Results

4.4.1 Magnetite Characterization

Reflected light microscopy complemented by backscattered electron imaging (BSE) revealed magnetite crystals with different textural features throughout the studied deposits. Characterization of magnetite led to the subdivision of magnetite in several types according to the sampling site and iron deposit.

4.4.1.1 Montemor-o-Novo Iron Complex

Magnetite samples from drill cores were subdivided into first generation (Mag I) and second generation (Mag II). Mag I constitutes the primary ore assemblage and is found in semi-massive ore bodies with euhedral crystals and homogeneous textures, although sometimes fractured (**Fig. 4.2a, b**). The Mag I is usually accompanied by barite (**Fig. 4.2a**) and amphibole, found in calc-silicate rocks that result from metamorphism of carbonate rich rocks (**Fig. 4.3a, b**). As revealed by SEM imaging, Mag I show no evident of chemical zoning, but sparse monazite inclusions are present (**Fig. 4.2b**). Mag II is a magnetite disseminated in the carbonate rocks (**Fig. 4.2c, d, e**), usually associated with pyrite. Mag II texture is extremely porous with sparse inclusions of chalcopyrite (**Fig. 4.2c, e**).

At the MIC Vale da Arca deposit, magnetite occurs as a disseminated ore in calc-silicate rocks. Only one type of magnetite was distinguished and is referred as Vale da Arca Mag I, even though there is no significant evidence that proves these magnetites to be associated with primary processes. Vale da Arca Mag I usually display a homogeneous texture in the crystal cores, but highly porous towards the crystal rims (**Fig. 4.2f**). EDS mapping shows that the porous edges contain sulfides, namely sphalerite and pyrite (**Fig. 4.2g**). The homogeneous crystal cores were chosen for LA-ICP-MS analysis.

The magnetite (Mag I) from the Serrinha deposit occurs in massive bodies. At a microscopic scale, the crystals are usually found as euhedral fine-grained aggregates, exhibiting abundant intergrowths with elongated silicates (**Fig. 4.2h**), which were avoided during LA-ICP-MS analysis.

4.4.1.2 Skarn deposits

Magnetite from the Alvito Fe skarn deposit is coarse-grained (Mag I) and was found hosted in a skarn rich in pyroxene and garnet (**Fig. 4.3c, d**). Scanning electron microscopy revealed that Mag I has abundant inclusions, mostly composed of Al-rich spinel (Maia et al., 2022a) and Ti-rich oxyexsolutions (**Fig. 3.2i, j, k**). This magnetite occurs in association with pyrrhotite and (Co)-pentlandite (Maia et al., 2022a).

At the Azenhas-Orada Fe skarn, two magnetite types were identified (Maia et al., 2022a), in which Mag I correspond to first generation massive magnetite (**Fig. 3.2l**) hosted in metabasic volcanic rocks (**Fig. 4.3e**), and Mag II is hosted in an epidote-rich skarn (**Fig. 4.3f**).

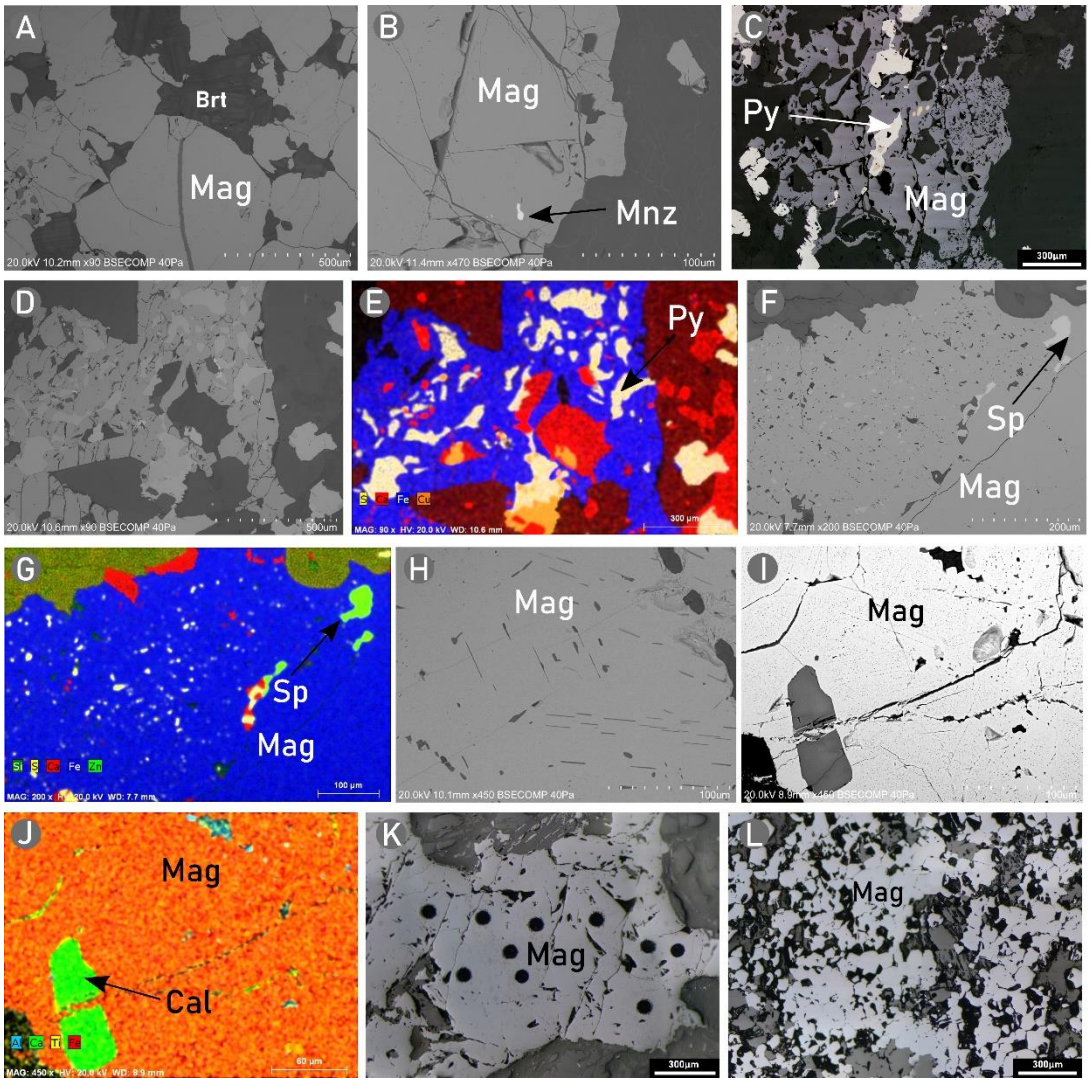

Figure 4.2. Images representative of the identified magnetite types and textures. (A) Backscattered electron (BSE) image of the primary ore assemblages from the Monges deposit of the MIC, where euhedral magnetite along with barite is observed. (B) Backscattered electron (BSE) image of a fractured primary magnetite crystal (Mag I) from the Monges deposit. The image shows the identification of small inclusions of monazite crystals. (C) RLM image of assemblages in which secondary magnetite (Mag II) from the Monges deposit. In the image, a magnetite-pyrite-chalcopyrite assemblage is identified. (D) BSE imagery of the Monges deposit Mag II assemblages. (E) Energy dispersive x-ray spectroscopy (EDS) map analysis of the area shown in (D) in which distribution of S, Ca, Fe, and Cu is displayed. (F) BSE imagery of Mag I from the Vale da Arca deposit. This magnetite section corresponds to the porous rims of Mag I in which inclusions of pyrite and sphalerite have been identified. (G) EDS map analysis of the area shown in figure 2F in which the distribution of Si, S, Ca, Fe, and Zn are displayed. (H) BSE imaging of inclusions of thin plates of silicate minerals in Mag I from the Serrinha deposit. (I) BSE imagery of a magnetite crystal from the Alvito deposit in which abundant inclusions and exsolutions are evident. (J) EDS map analysis of the area sown in figure 2I with the distribution of Al, Ca, Ti, and Fe is displayed. This image shows a clear relation between Al and Ti in the exsolution, and inclusions identified in this magnetite type. (K) Fractured magnetite crystal from a sample from the Alvito Fe skarn deposit in which several ablation spots (50 µm) are shown. (L) RLM microphotograph composition of magnetite aggregates from the Orada deposit.

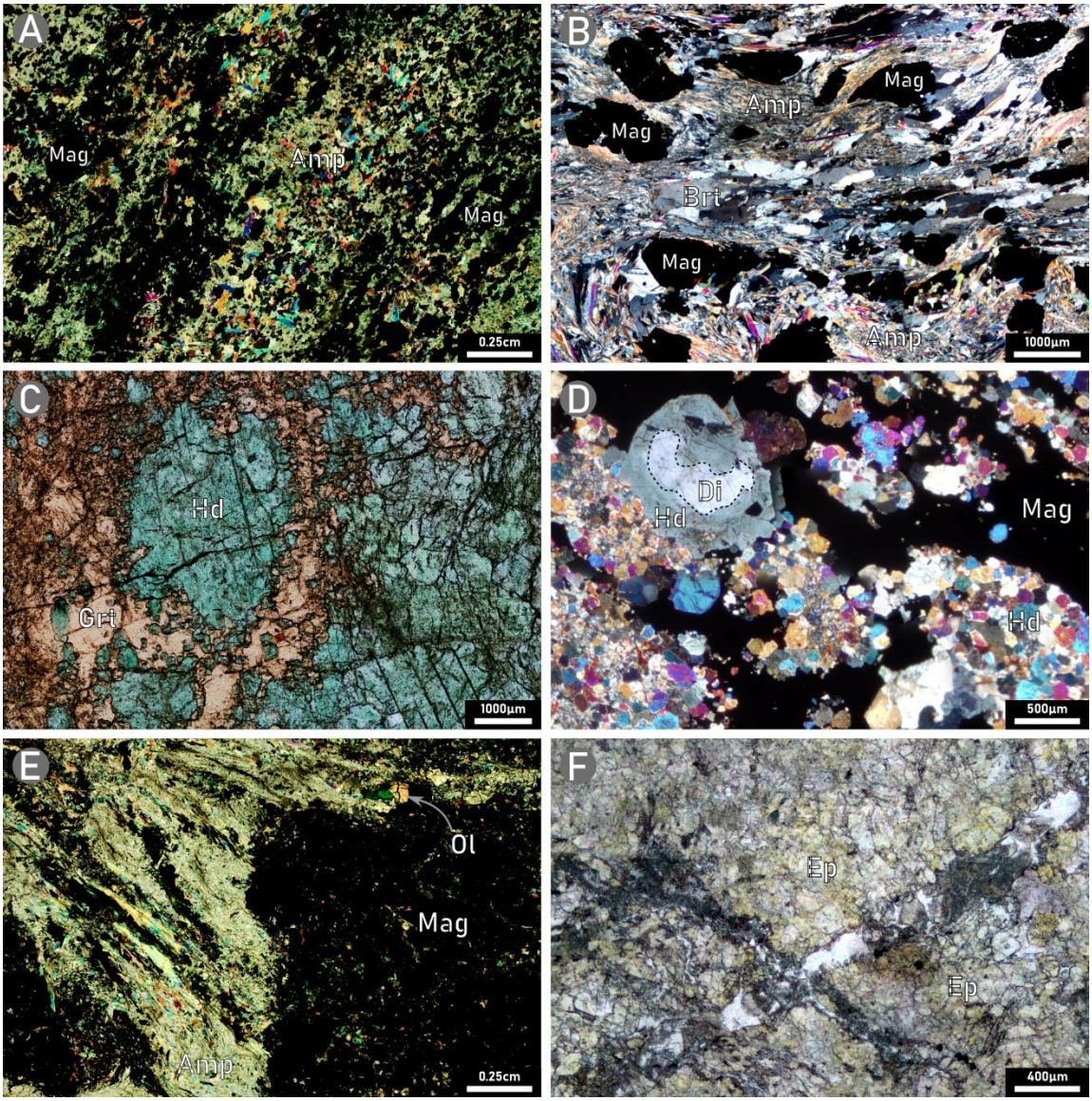

Figure 4.3 Representative images of host rock petrography. (A) Crossed polarized light (CPL) microphotograph composite of magnetite-rich section from drill core samples of Monges deposit. Magnetite (opaque) is exclusively accompanied by amphibole (high interference colors) generated during amphibolite facies metamorphism. (B) CPL microphotograph composite of disseminated magnetite in an amphibole-barite-calcite matrix from the Monges deposit. The amphibole alignment suggests ductile deformation of these sections. (C) CPL microphotograph composite image of typical garnet-clinopyroxene (hedenbergite) mineral assemblage found in the exoskarn from the Alvito deposit. (D) CPL microphotograph of magnetite-clinopyroxene (hedenbergite) assemblage found at the Alvito skarn deposit. (E) CPL microphotograph composite image of the ore sections from the Azenhas Fe skarn deposit in which massive magnetite is surrounded by fine amphibole crystals and relics of olivine. (F) CPL microphotograph composite image of the epidote-rich magnetite-poor skarn found at the Azenhas deposit.

4.4.2 Magnetite chemistry

Trace element composition of magnetite from the selected outcrops and drill core samples are given as minimum, maximum, average, and median values in Table 1. The complete dataset of EPMA and LA-ICP-MS analysis can be consulted in **Appendix E** and **F**, in which data from previous studies (Maia et al., 2022a) is also disclosed. Mag I from the Serrinha deposit and Mag I from the Orada deposit were only analyzed by LA-ICP-MS.

4.4.2.1 Montemor-o-Novo Iron Complex

Magnetite from drill core samples collected at the MIC Monges deposit revealed Fe concentrations from 65.88 wt.% to 71.62 wt.% for Mag I, and from 63.82 wt.% to 72.25 wt.% for Mag II. Comparing both magnetite types reveals that Mag I has higher average contents of Al (907 ppm), Ti (568 ppm), and Mn (7004 ppm), whereas Mag II has relatively higher Mg (3265 ppm), Ca (2168 ppm), and Zn (99.6 ppm).

The higher contents of Ni (16 ppm) and Zn (109 ppm) in magnetite of the studied deposits from the MIC are found in the Vale da Arca orebodies (**Fig. 4.4**). The magnetite from the Serrinha deposit shows the higher concentration of Mg (4428 ppm), Si (4267 ppm), and Mn (11268 ppm) of all the studied MIC deposits. Contrastingly, in Mag I from Serrinha the lower values of Ti, V, Cr, and Ga are found (**Table 4.1**).

4.4.2.2 Alvito Fe deposit

The magnetite (Mag I) from this deposit revealed the higher trace element concentrations of all the dataset. This magnetite type has the higher average contents of Al (9914 ppm), Ti (2071 ppm), Cr (48 ppm), Co (86 ppm), Ni (41 ppm), Zn (527 ppm), Ga (40 ppm), Zr (8 ppm), Nb (9 ppm), and Sn (25 ppm).

Table 4.1 Summarized representative statistics of the trace element LA-ICP-MS analysis of primary and secondary magnetite from drill core and outcrop samples of the MIC deposits.

	Drill core samples								Outcrop Samples											
Magnetite Type	Magnetite I – Monges deposit				Magnetite II - Monges deposit				Weathered Magnetite I – Monges deposit				Primary Magnetite – Serrinha deposit				Primary Magnetite – Vale da Arca deposit			
	$n^1=3$; $n^2=33$; $n^3=99$				$n^1=3$; $n^2=5$; $n^3=53$				$n^1=4$; $n^2=52$; $n^3=158$				$n^1=2$; $n^2=4$; $n^3=45$				$n^1=1$; $n^2=1$; $n^3=10$			
	Min.	Max.	Ave.	Med.	Min.	Max.	Ave.	Med.	Min.	Max.	Ave.	Med.	Min.	Max.	Ave.	Med.	Min.	Max.	Ave.	Med.
LA-ICP-MS (ppm)																				
Mg	172.17	26572.30	3110.19	2416.92	884.33	12062.75	3265.02	3146.91	251.16	4001.36	983.81	813.00	2719.72	10230.74	4427.55	1124.37	1273.27	3060.44	2254.57	2239.77
Al	50.35	9357.10	907.98	701.32	11.04	504.28	219.57	212.05	85.08	666.10	372.63	370.34	477.31	1109.67	715.37	418.71	17.93	155.27	67.14	61.40
Si	483.59	31374.15	5040.92	4320.99	1226.99	24264.88	4049.83	3140.32	1556.54	7124.02	3579.18	3457.79	2347.67	11437.63	4267.08	3634.20	1064.38	3124.99	2017.62	1779.54
Ca	46.39	6010.46	981.16	310.44	36.57	7893.95	2168.44	942.03	33.32	81.14	55.77	51.68	52.40	379.52	142.65	81.14	101.39	347.67	209.58	186.40
Sc	0.22	1.39	0.74	0.80	0.09	0.61	0.26	0.26	0.11	0.49	0.21	0.20	0.09	0.25	0.15	0.17	0.00	0.00	#DIV/0!	#NÚM!
Ti	157.86	1179.45	568.52	486.04	5.69	768.03	274.09	261.97	50.86	135.31	90.09	83.76	22.94	160.30	69.27	80.18	34.73	196.32	142.46	146.01
V	13.31	81.74	37.50	34.62	0.44	811.95	93.56	20.07	9.60	36.18	15.82	15.17	0.99	32.22	8.95	13.34	21.87	165.18	132.05	140.82
Cr	0.67	123.57	20.78	12.72	0.35	53.87	4.52	0.83	0.28	91.95	4.40	0.83	0.31	14.96	2.98	0.83	0.58	1.18	0.90	0.94
Mn	965.55	15064.85	7004.83	6152.78	488.41	7858.20	3117.77	966.00	320.74	2475.55	1292.90	1124.96	8396.39	14430.19	11267.92	1743.08	5953.76	8402.91	7250.09	7122.83
Co	0.07	1.16	0.46	0.25	0.02	0.56	0.21	0.03	0.33	1.08	0.59	0.58	0.43	0.77	0.53	0.53	0.05	0.05	0.05	0.05
Ni	0.64	11.56	2.19	1.54	0.70	1.89	1.04	0.83	0.47	2.70	0.92	0.79	0.30	3.37	1.24	1.03	2.34	47.20	15.84	9.06
Cu	0.07	1.63	0.50	0.27	0.06	108.85	9.83	0.20	0.06	0.50	0.17	0.09	0.07	76.37	12.86	0.15	0.13	0.18	0.16	0.16
Zn	13.06	79.85	50.04	49.51	37.69	257.11	99.61	93.60	34.88	99.61	64.47	64.90	32.09	66.10	46.59	55.34	79.99	131.98	109.27	108.03
Ga	2.40	12.17	6.19	5.99	0.69	31.67	8.89	4.60	2.99	5.52	4.10	4.09	0.39	1.01	0.62	3.70	2.64	4.39	3.47	3.54
Ge	0.59	6.60	1.42	1.19	0.25	1.92	0.76	0.71	0.32	2.91	1.04	1.00	0.25	0.93	0.53	0.78	0.48	2.01	1.30	1.20
As	0.14	5.20	1.33	0.92	0.22	43.85	2.62	0.85	0.13	3.57	0.95	0.73	0.18	78.52	6.26	0.57	0.50	8.43	2.90	2.29
Y	0.01	4.04	0.62	0.36	0.00	0.88	0.06	0.01	0.00	0.26	0.05	0.02	0.00	0.08	0.02	0.01	0.01	0.45	0.19	0.18
Zr	0.00	26.96	0.53	0.04	0.00	0.06	0.01	0.01	0.00	7.62	0.17	0.01	0.77	2.24	1.33	0.04	0.00	0.41	0.15	0.14
Nb	0.00	2.24	0.22	0.09	0.00	0.14	0.03	0.02	0.00	0.52	0.07	0.03	0.01	0.08	0.03	0.03	0.01	0.23	0.09	0.11
Mo	0.05	5.63	0.34	0.11	0.05	0.16	0.09	0.09	0.04	0.26	0.13	0.13	0.22	1.35	0.86	0.15	0.06	0.15	0.09	0.08
Sn	1.25	21.40	9.94	10.56	5.27	11.93	8.77	9.24	7.54	15.35	11.57	11.61	13.18	23.27	17.57	12.29	1.95	10.46	5.58	5.10
Hf	0.00	0.87	0.06	0.01	0.00	0.01	0.00	0.00	0.00	0.13	0.01	0.00	0.02	0.08	0.04	0.02	0.01	0.01	0.01	0.01
Ta	0.00	0.82	0.03	0.02	0.00	0.07	0.01	0.00	0.00	0.08	0.01	0.01	0.00	0.01	0.01	0.01	0.00	0.02	0.01	0.01
W	0.01	1.29	0.13	0.08	0.00	0.17	0.04	0.03	0.00	0.88	0.05	0.01	0.05	1.33	0.44	0.05	0.00	0.30	0.13	0.08
Pb	0.09	676.69	22.60	0.18	0.07	813.92	25.15	0.15	0.03	10.30	0.64	0.08	0.04	94.53	3.75	0.13	0.08	0.24	0.13	0.10
Th	0.00	0.67	0.02	0.01	0.00	0.03	0.01	0.00	0.00	0.02	0.00	0.00	0.00	0.16	0.03	0.01	0.00	0.09	0.02	0.02
U	0.00	1.73	0.12	0.05	0.00	0.25	0.03	0.01	0.00	0.66	0.03	0.02	0.00	0.24	0.05	0.01	0.00	0.26	0.06	0.05

4.4.2.3 Azenhas-Orada deposits

The Azenhas deposit dataset was compiled from Maia et al., (2022a), to which the analyses of magnetite from the Orada deposit were added. Samples from Orada were only analyzed by LA-ICP-MS, therefore stoichiometric Fe (72.4 wt.%) value was used as the internal standard, which can, somewhat, bias the results (Pisiak et al., 2017).

Mag I from the Azenhas deposit has higher average contents of Mg (8534 ppm), Mn (4859 ppm), Co (86 ppm), Ni (41 ppm), Zn (527 ppm), and Ga (40 ppm) when compared to Mag II (Fig. 4; Table 2). Mag I from the Orada tailings showed average concentrations of Mg (2597 ppm), Si (4633 ppm), Ti (144 ppm), Co (29 ppm), and Ni (24 ppm) closer to those found in Mag I from the Azenhas deposit.

4.4.3 Mineral chemistry of host rocks

4.4.3.1 Montemor-o-Novo Iron Complex

Representative analyses of amphibole accompanying the ore assemblage at the Monges deposit (**Fig. 4.3a, b**) are presented in **Table 4.3** and plotted in **Figure 4.5a**, the complete results can be found in **Appendix Table D**. These amphiboles were formed during regional metamorphism and correspond to actinolite-tremolite (**Table 4.3**).

At the Vale da Arca deposit pyroxene accompanying the magnetite crystals were analyzed (**Table 4.4),** revealing compositions consistent with Mg-rich (Avg. 17.6 wt.%), Fe-poor (0.71 wt.%) diopside (**Fig. 4.5c**). Amphibole, feldspar, and epidote were analyzed in a basic metavolcanic rock. Amphibole is mostly actinolite, with minor magnesian-hornblende, as shown in **Figure 4.5a**. In this basic metavolcanic rock, feldspars are exclusively orthoclase (**Fig. 4.5d**) and occur as large porphyroblasts, whereas epidote composition plots in the Mn-Al-Fe diagram and is classified as clinozoisite (**Fig. 4.5b**).

Table 4.2 Summarized representative statistics of the trace element LA-ICP-MS data of primary and secondary magnetite from skarn deposits used in this study.

Magnetite Type	**Primary Magnetite – Alvito deposit**				**Magnetite I - Azenhas deposit**				**Magnetite II - Azenhas deposit**				**Primary Magnetite – Orada deposit**			
	n^1=5; n^2=17; n^3=156				**n^1=2; n^2=8; n^3=20**				**n^1=2; n^2=20; n^3=49**				**n^1=1; n^2=10; n^3=35**			
	Min.	Max.	Ave.	Med.	Min.	Max.	Ave.	Med.	Min.	Max.	Ave.	Med.	Min.	Max.	Ave.	Med.
LA-ICP-MS (ppm)																
Mg	676.1	15244.57	3754.179	4291.65	3880.3	18241.56	8534.005	7545.76	48.55	3195.36	202.6429	90.45	1895.07	4915.11	2597.43	2526.91
Al	5030.4	16280.62	9913.487	9656.83	280.33	7059.03	2222.047	1887.78	525.98	10704.13	1357.324	878.85	1451.80	3956.65	2772.54	2783.53
Si	1570.1	6422.62	3580.744	3561.92	724.45	10848.82	5040.921	4360.39	2411.07	27240.1	4819.311	3929.66	2851.16	7441.73	4633.32	4610.94
Ca	36.88	1938.43	665.1327	414.33	41.69	4321.64	1063.537	372.17	32.69	436.71	119.5107	74.34	53.98	2143.14	298.36	129.14
Sc	0.149	3.95	1.426372	0.842	0.43	1.04	0.580929	0.5275	0.127	0.171	0.15325	0.1575	0.10	0.29	0.18	0.19
Ti	370.52	6187.86	2070.801	1199.41	1506.18	3290.05	2149.445	2000.46	651.55	1386.21	899.1486	853.8	119.28	169.54	144.14	143.04
V	19.81	128.16	70.87222	72.375	67.49	174.06	131.17	137.13	101.23	168.81	136.6994	137.48	30.74	52.66	44.18	44.20
Cr	0.31	359.17	48.28069	6.23	0.87	49.87	11.70095	9.16	0.28	1.24	0.487556	0.43	0.32	7.95	1.86	1.41
Mn	1012.4	4501	2155.266	2095.67	3787.49	6109.59	4858.774	4759.07	274.85	1135.55	612.9169	536.85	360.93	648.95	497.61	493.67
Co	38.82	156.72	86.43089	87.49	28.2	82.68	52.07957	51.84	3.58	7.77	4.957143	4.78	20.04	33.90	28.97	28.84
Ni	2.46	100.87	40.5869	44.86	10.16	33.07	17.70739	15.27	5.23	18.51	9.73449	8.52	16.75	29.34	24.40	24.19
Cu	0.074	25.87	1.247886	0.1735	0.198	3.5	0.942364	0.65	0.059	0.829	0.2555	0.067	0.25	0.77	0.42	0.37
Zn	106.63	1085.13	526.914	532.805	158.51	1052.2	658.4991	659.44	68.98	301.78	183.1133	178.66	46.69	100.21	68.82	69.10
Ga	21.91	86.68	39.87525	39.885	3.88	24.22	12.55087	7.53	9.76	23.73	16.94122	17.63	5.57	10.01	8.38	8.39
Ge	0.35	3.36	1.242848	1.13	0.32	1.41	0.821818	0.745	0.175	0.74	0.380889	0.3715	0.38	1.61	0.95	0.97
As	0.166	7.12	0.580275	0.43	0.58	11.42	3.131905	2.64	0.182	4.83	0.561239	0.46	0.12	1.04	0.38	0.33
Y	0.0006	3.63	0.135	0.0096	0.0095	2.61	0.417895	0.224	0.00042	0.183	0.01454	0.00505	0.00	0.16	0.03	0.01
Zr	1.522	19.11	8.215456	6.8	0.047	86	6.674273	0.4345	0.0015	0.149	0.024211	0.0084	1.23	4.11	2.44	2.37
Nb	2.44	22.45	9.088165	8.25	0.023	2.64	0.832683	0.831	0.00056	0.178	0.015464	0.0052	0.12	1.01	0.41	0.36
Mo	0.572	7.93	2.587525	2.64	0.076	0.292	0.188238	0.185	0.153	104.62	13.82753	3.1	1.97	3.83	3.05	3.14
Sn	13.85	46.06	25.315	25.205	7.04	11.9	9.532609	9.65	0.341	1.71	0.785041	0.788	8.41	14.48	12.05	12.08
Hf	0.059	0.948	0.389405	0.367	0.008	3.65	0.28077	0.0324	0.0015	0.0296	0.005988	0.0043	0.03	0.12	0.07	0.08
Ta	0.145	2.75	0.652044	0.238	0.0026	0.375	0.079295	0.07	0.00033	0.093	0.011863	0.0024	0.00	0.01	0.01	0.01
W	0.002	1.76	0.095909	0.03915	0.0074	1.8	0.568018	0.4505	0.0017	28.54	4.52454	1.94	0.00	0.27	0.06	0.04
Pb	0.034	710.15	19.08651	0.171	0.127	148.15	15.41677	2.415	0.057	1248.47	81.19022	0.134	0.05	10.57	0.61	0.18
Th	0.00047	0.245	0.018862	0.0047	0.0024	1.6	0.314615	0.2115	0.00056	0.303	0.027109	0.0114	0.00	0.24	0.04	0.01
U	0.00064	1.172	0.040053	0.0135	0.0049	5.37	0.941432	0.5695	0.00071	0.321	0.033907	0.00715	0.00	0.14	0.03	0.02

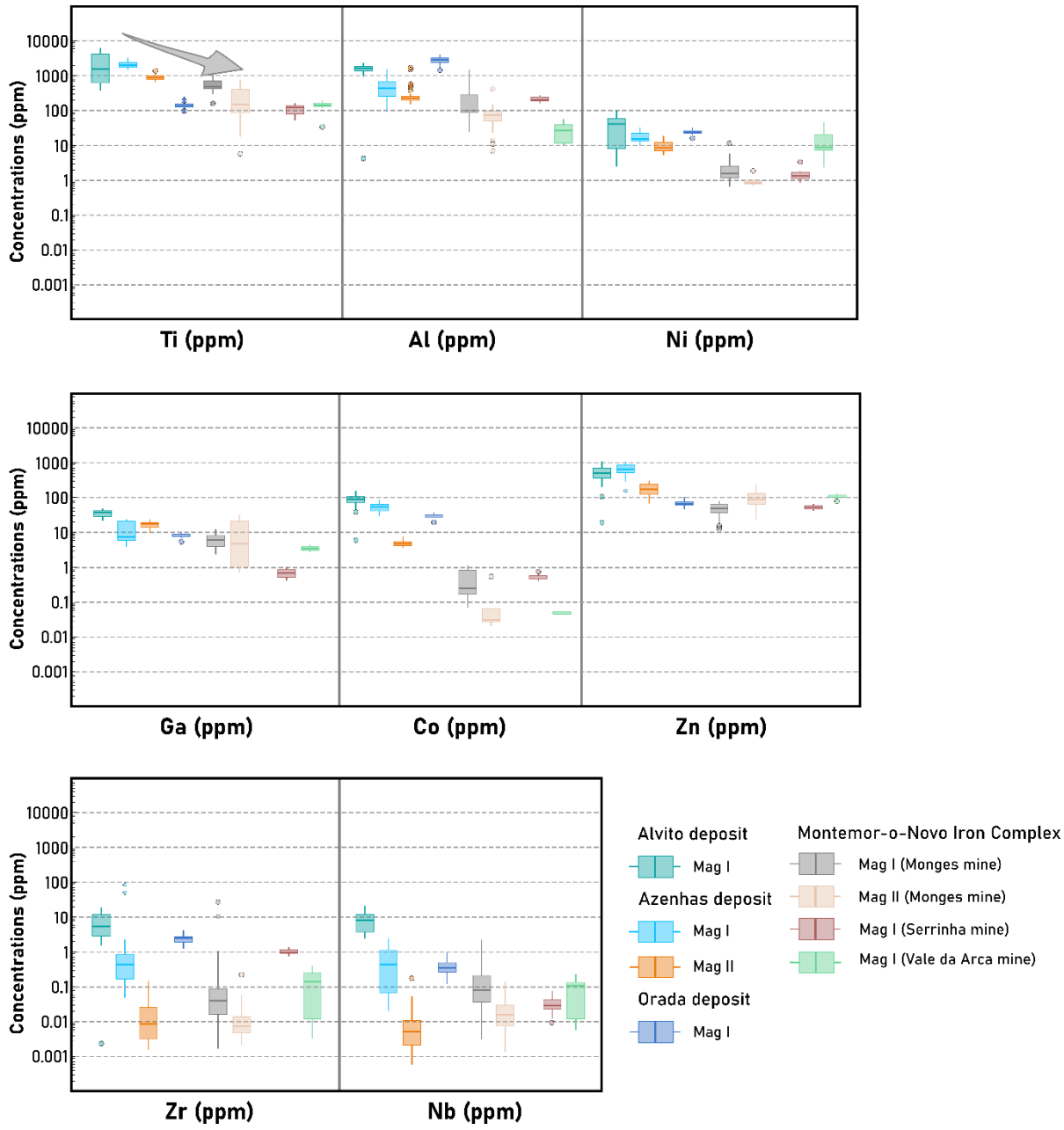

Figure 4.4 Boxplot display of selected trace elements (Ti, Al, Ni, Ga, Co, Zn, and Zr) analyzed in magnetite by LA-ICP-MS. The color code is divided according to the magnetite type and deposit. A depletion in Ti, Al, Ni, Ga, Co, Zn, and Zr content is observed from the skarn deposits towards the deposits that belong to the MIC (grey arrow).

4.4.3.2 Alvito deposit

The Alvito diorite suite, part of the CAGD, is mainly constituted by quartz, feldspar, and amphibole. Amphiboles from the diorite are mainly magnesian-hornblende with SiO2 contents of 48.1 wt. %, relatively high FeO contents (15.4 ± 1.7 wt.%; **Table 4.3**). The analyzed feldspars from diorite samples (Table 4) are mainly andesine, with $Ab_{58.06\text{-}60.67}An_{34.01\text{-}39.91}Or_{2.03\text{-}5.32}$ (**Fig. 4.5d**), with frequent concentric zonation and strongly sericitized cores.

The mineralized horizons display a typical prograde diopside-garnet skarn paragenesis (Meinert et al., 2005). Pyroxenes show a clear zoning with cores composed of Mg-rich (Avg. 16.8 wt.%) Fe-poor (Avg. 1.3 wt.%) diopside. In contrast, the green rims (**Fig. 4.3c, d**) correspond to the Fe-rich endmember, hedenbergite (**Fig. 4.5c**).

4.4.3.3 Azenhas-Orada deposits

Olivine is found in the amphibolites hosting the massive magnetite ore bodies and corresponds to the forsterite-rich term (Avg. $Fo_{83.3}Fa_{15}Tp_{1.7}$; Table 4). The amphiboles accompanying the ores are mainly tremolite-actinolite (**Fig. 4.5a**). Additionally, epidote from the epidote-rich skarns (**Fig. 4.3f**) were analyzed by EPMA, plotting in the clinozoisite field (**Fig. 4.5b**) and are possibly associated to the retrograde alteration stage responsible for the genesis of the skarn (Meinert et al., 2005).

4.4.4 Oxygen isotope composition

Oxygen isotope signatures of magnetite are reported as $\delta^{18}O_{SMOW}$ and are provided in **Table 4.4**, respecting the previously described nomenclature and classification of magnetite.

4.4.5 Montemor-o-Novo Iron Complex

Seven analyses were performed on magnetite from deposits that belong to the MIC. The Mag I from the Monges deposit revealed $\delta^{18}O$ values ranging from 7.7 ‰ – 9.0 ‰. Mag I from the Serrinha deposit shows values of 8.1 ‰, closer to those of Monges deposit Mag I. Contrastingly, lighter $\delta^{18}O$ values were gathered from Vale da Arca deposit Mag I analyses (4.3 ‰).

4.4.6 Fe skarn deposits

Magnetite I from the Alvito Fe skarn has $\delta^{18}O$ values ranging from 10.1 ‰ to 10.6 ‰. The magnetite from the Azenhas Fe skarn deposit revealed signatures between 4.0 ‰ and 4.2 ‰, whereas the magnetite sample from the Orada deposit revealed a $\delta^{18}O$ value of 5.6 ‰.

Table 4.3 Representative EPMA data of silicate phases from the host rocks.

Deposit	Monges										Vale da Arca		Alvito		Azenhas orebodies			
Mineral	Amphibole																	
Sample	007-15.6a		007-14.2a		005.30.8a		005-32.1a		004-13.3b		MV6		AL17		AZ4.3		AZ8.1	
	n=6*	σ	n=12	σ	n=10	σ	n=8	σ	n=13	σ	n=4	σ	n=14	σ	n=4	σ	n=6	σ
Element (wt. %)																		
SiO_2	57.6	0.7	57.0	0.5	55.9	0.6	60.3	2.3	57.5	0.3	50.6	3.6	48.1	0.6	51.6	1.6	58.6	0.4
Al_2O_3	0.3	0.3	0.5	0.1	1.4	0.6	0.2	0.1	0.2	0.1	4.5	2.9	6.0	0.4	4.5	1.2	0.1	0.1
MnO	0.4	0.2	0.1	0.0	0.1	0.0	0.2	0.2	0.3	0.1	0.2	0.03	0.3	0.04	0.3	0.01	0.5	0.1
FeO	4.9	1.4	6.5	1.7	5.8	0.7	2.9	2.1	4.7	1.2	15.4	1.7	16.4	0.4	8.0	0.9	1.7	0.2
MgO	21.3	1.3	20.0	1.2	19.8	0.6	26.5	3.4	21.0	0.7	12.5	1.8	11.3	0.3	18.0	0.8	23.2	0.3
CaO	12.2	0.4	12.5	0.3	12.6	0.3	5.6	5.9	12.7	0.2	11.9	0.5	11.3	0.2	12.0	0.2	12.9	0.2
Na_2O	0.1	0.1	0.2	0.0	0.2	0.1	0.1	0.04	0.1	0.04	0.6	0.3	0.8	0.1	1.7	0.3	0.1	0.00
K_2O	0.0	0.0	0.03	0.0	0.1	0.03	0.2	0.00	0.05	0.01	0.4	0.3	0.5	0.1	0.2	0.1	0.1	0.01
Initial Total	96.9	0.7	96.9	0.5	95.9	0.5	95.3	1.3	96.5	0.3	96.2	0.5	94.7	0.4	96.3	0.5	96.9	0.3
T (ideally 8 apfu)																		
Si	8.0	0.0	8.0	0.0	7.9	0.1	8.2	0.2	8.0	0.02	7.5	0.4	7.3	0.1	7.4	0.2	8.0	0.03
Al	0.0	0.0	0.0	0.0	0.1	0.1	0.00	0.00			0.5	0.4	0.7	0.1	0.6	0.2	0.02	0.00
T subtotal	8.0	0.0	8.0	0.0	8.0	0.0	8.2	0.2	8.0	0.02	8.0	0.00	8.0	0.00	8.0	0.00	8.0	0.02
C																		
Al	0.0	0.0	0.1	0.0	0.1	0.1	0.04	0.02	0.03	0.02	0.3	0.2	0.4	0.05	0.2	0.1	0.01	0.01
Fe3+			0.01	0.0	0.1	0.01			0.00	0.00	0.1	0.1	0.2	0.04	0.1	0.05	0.01	0.00
Mn2+	0.0	0.0	0.01	0.0	0.01	0.01	0.02	0.00	0.04	0.01	0.02	0.01	0.02	0.00	0.02	0.01	0.1	0.01
Fe2+	0.5	0.2	0.7	0.2	0.7	0.1	0.3	0.1	0.5	0.1	1.8	0.2	1.9	0.1	0.8	0.1	0.2	0.04
Mg	4.4	0.2	4.2	0.2	4.2	0.1	4.8	0.2	4.4	0.1	2.8	0.4	2.6	0.1	3.8	0.1	4.7	0.1
C subtotal	5.0	0.0	5.0	0.0	5.0	0.0	5.0	0.0	5.0	0.04	5.0	0.0	5.0	0.00	5.0	0.00	5.0	0.02
B																		
Mn2+	0.0	0.0	0.02	0.0	0.02	0.00	0.02	0.03	0.02	0.01	0.02	0.0	0.04	0.01	0.03	0.01	0.03	0.02
Fe2+	0.1	0.1	0.1	0.0	0.02	0.02	0.3	0.3	0.02	0.01	0.01	0.01	0.02	0.01	0.02	0.01	0.1	0.00
Ca	1.8	0.1	1.9	0.0	1.9	0.04	0.7	0.9	1.9	0.03	1.9	0.1	1.8	0.03	1.8	0.02	1.9	0.02
Na	0.0	0.0	0.0	0.0	0.05	0.02	0.0	0.01	0.0	0.01	0.1	0.1	0.1	0.02	0.1	0.01	0.0	0.01
B subtotal	1.9	0.0	2.0	0.0	2.0	0.03	1.5	0.4	1.9	0.02	2.0	0.0	2.0	0.00	2.0	0.00	1.9	0.04
A																		
Na																		
K	0.0	0.0	0.01	0.0	0.01	0.01	0.03	0.00	0.01	0.0	0.1	0.1	0.1	0.01	0.04	0.01	0.01	0.00
A subtotal	0.0	0.0	0.01	0.0	0.02	0.02	0.00	0.01	0.0	0.0	0.2	0.2	0.2	0.04	0.4	0.1	0.00	0.01

Lithology																						
Deposit	**Vale da Arca**		**Alvito**				**Azenhas**		**Vale da Arca**			**Azenhas**		**Alvito**				**Vale da Arca**		**Azenhas**		
Mineral	Feldspar								Epidote					Pyroxene - Cores		Pyroxene -Rims		Pyroxene		Olivine		
Sample	MV6		AL14		AL17		AZ1.1		MV6			AZ4.3		AL19				MV3		AZ8.1		
	n=9*	σ	n=7	σ	n=5	σ	n=8	σ		n=14	σ	n=8	σ		n=6	σ	n=7	σ	n=8	σ		n=4	σ
Element (wt. %)									**Element (wt. %)**					**Element (wt. %)**							**Element (wt. %)**		
SiO_2	64.32	1.38	57.36	0.56	59.57	0.99	67.87	0.74	**SiO_2**	37.54	0.29	37.36	0.32	**SiO_2**	54.89	0.45	47.21	0.57	55.32	0.49	**SiO_2**	39.8	0.43
TiO_2			0.03	0.01	0.07	0.00			**TiO_2**	0.13	0.05	0.10	0.08	**TiO_2**	0.14	0.07			0.04	0.00	**Al_2O_3**	0.1	0.13
Al_2O_3	18.89	0.55	27.04	0.30	25.79	0.92	20.07	0.35	**Al_2O_3**	23.34	0.91	22.01	0.71	**Al_2O_3**	0.44	0.24	3.50	0.51	0.08	0.05	**FeO**	13.8	0.38
FeO			0.17	0.05	0.09	0.03	0.57	0.92	**Fe_2O_3**	13.10	0.93	15.06	0.79	**FeO**	1.32	0.52	18.49	1.09	0.71	0.15	**MnO**	1.5	0.16
CaO	0.09	0.03	8.14	0.22	6.95	0.98	0.39	0.25	**MnO**	0.27	0.11	0.13	0.00	**MnO**	0.51	0.07	0.33	0.03	0.41	0.05	**MgO**	43.1	0.71
Na_2O	1.77	3.31	6.54	0.10	6.85	0.28	11.04	0.55	**MgO**			0.11	0.00	**MgO**	16.78	0.56	5.36	0.71	17.64	0.24	**Total**	98.3	0.33
K_2O	14.47	5.07	0.35	0.06	0.92	1.15	0.22	0.39	**CaO**	23.01	0.24	22.92	0.13	**CaO**	25.32	0.13	22.57	0.17	25.26	0.15			
BaO	0.26	0.05							**P_2O_5**	0.28	0.04	0.28	0.05	**Na_2O**	0.05	0.00	0.12	0.04	0.06	0.01	***O=4***		
Total	99.70	0.34	99.63	0.26	100.17	0.23	99.91	0.51	**Total**	97.54	0.70	97.75	0.39	**Total**	99.41	0.42	97.58	0.39	99.44	0.42	**Si**	1.0	0.01
																					Ti	0.0	0.00
Formula *O=32*									***O=12.5***					***O=6***							**Al**	0.0	0.00
									Si	3.21	0.02	3.24	0.02	**Si**	2.00	0.01	1.91	0.02	2.01	0.01	**Cr**	0.0	0.00
Si	11.89	0.02	10.31	0.07	10.62	0.18	11.88	0.07	**Ti**	0.01	0.00	0.01	0.00	**Al**	0.00	0.01	0.09	0.02	-0.01	0.01	**Fe(ii)**	0.3	0.01
Al	4.11	0.04	5.73	0.08	5.42	0.19	4.14	0.08	**Al**	2.35	0.06	2.25	0.05	**Al**	0.02	0.01	0.07	0.01	0.01	0.01	**Mn**	0.0	0.00
Fe(ii)	0.01	0.00	0.03	0.01	0.01	0.01	0.08	0.14	**Fe(iii)**	0.42	0.04	0.49	0.03	**Fe(iii)**			0.05	0.02	0.00	0.00	**Mg**	1.6	0.02
Ca	0.02	0.01	1.57	0.04	1.33	0.19	0.07	0.05	**Mn**	0.01	0.01	0.00	0.00	**Ti**	0.00	0.00	0.00	0.00	0.00	0.00	**Ni**	0.0	0.00
Na	0.61	1.12	2.28	0.04	2.37	0.09	3.75	0.17	**Mg**	0.00	0.00	0.00	0.00	**Fe(ii)**	0.04	0.02	0.57	0.03	0.02	0.00	**Ca**	0.0	0.00
K	3.44	1.21	0.08	0.01	0.21	0.26	0.05	0.09	**Ca**	2.11	0.03	2.13	0.02	**Mn**	0.02	0.00	0.01	0.00	0.01	0.00	**Total**	3.0	0.01
Ba	2.23	6.25							**P**	0.01	0.00	0.01	0.00	**Mg**	0.91	0.03	0.32	0.04	0.96	0.01	**Fo (%)**	83.3	0.66
Total	20.10	0.02	20.00	0.04	19.96	0.02	19.94	0.03	**Total**	8.11	0.01	8.13	0.01	**Ca**	0.99	0.01	0.98	0.01	0.98	0.01	**Fa (%)**	15.0	0.48
An (%)	0.17	0.22	39.91	1.08	34.01	4.90	1.93	1.26						**Na**	0.00	0.00	0.01	0.00	0.01	0.00	**Tp (%)**	1.7	0.19
Ab (%)	15.70	29.43	58.06	0.84	60.67	2.47	96.78	3.18						**Total**	3.99	0.01	4.01	0.00	4.00	0.02			
Or(%)	84.18	29.60	2.03	0.37	5.32	6.65	1.29	2.31															

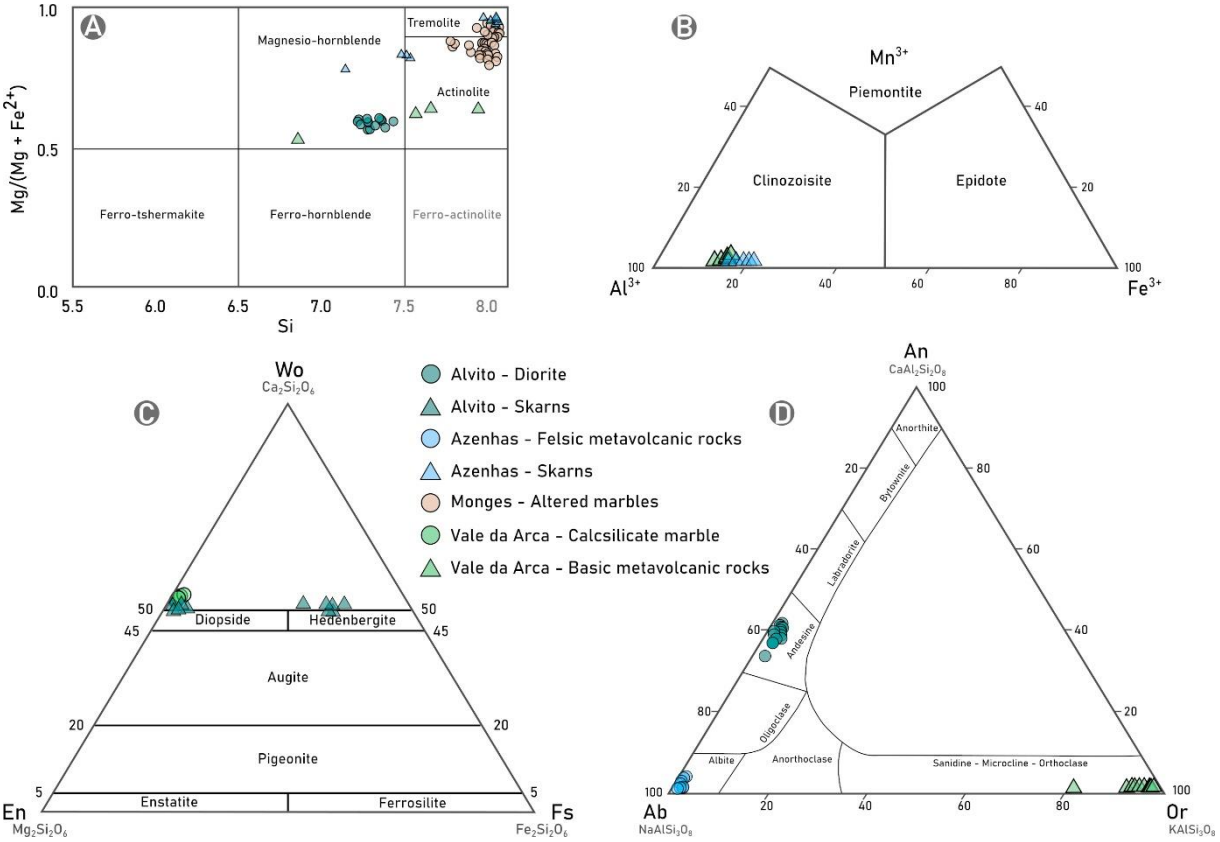

Figure 4.5 Plots of EPMA data in classification diagrams of amphibole, epidote, pyroxene, and feldspars. (A) Mg/(Mg+Fe2+) vs Si classification diagram for amphibole (Leake et al., 1997). (B) Ternary classification diagram for epidote with all EPMA data plotting in the clinozoisite field (Armbruster et al., 2006). (C) Ternary diagram applied to the classification of pyroxene (Marimoto et al., 1988) from the Vale da Arca and Alvito deposit. (D) Ternary diagram for the classification of feldspars applied to EPMA data from feldspars of the Vale da Arca, Alvito and Azenhas deposit host rocks.

4.5 Discussion

4.5.1 Identification of factors that control magnetite composition

Respecting the inverse spinel structure and stoichiometry of magnetite, a range of divalent and trivalent elements are more or less prone to substitute Fe2+ and Fe3+ depending on several factors (Dupuis and Beaudoin, 2011; Dare et al., 2014; Nadoll et al., 2014), such as the temperature of the system at the time of deposition, country rock composition and subsequent fluid-rock interactions, precipitation of other mineral phases concomitantly with magnetite, as well as, the oxygen fugacity conditions that influence the valance state of several elements (e.g. V, Cr).

The incorporation of elements compatible with the magnetite structure are controlled by several factors. For example, higher concentrations of V and Ti are usually found in magmatic and high temperature / magmatic derived hydrothermal magnetite (Nadoll et al., 2014; 2015), whereas the incorporation of elements such as Ge seems to be temperature independent (Meng et al., 2017).

The data examination revealed that the higher concentrations of V and Ti are found in primary magnetite from the Alvito and Azenhas-Orada skarn deposits (**Table 4.1** and **Table 4.2**), whereas those from the Montemor-o-Novo Iron Complex show the lowest contents. The Ti vs V scatterplot (**Fig. 4.6a**) displays a consistent correlation, with a decrease in concentrations towards the deposits from the MIC, which indicates lower temperatures at the time of ore deposition. Additionally, the Al behavior in magnetite composition follows the same trend (**Fig. 4.6b**). Aluminum is a relatively immobile element (Nadoll et al., 2015) and its coupled behavior with V and Ti (**Fig. 4.6b**) suggests that its incorporation in magnetite is mostly controlled by temperature.

Table 4.4 Complete magnetite oxygen isotope results ($\delta^{18}O_{SMOW}$) with disclosure of deposit orebody, sample, and magnetite type.

Sample	Deposit	Orebody	Sample Type	Magnetite type	$\delta^{18}O_{SMOW}$ (‰)
005-17	MIC	Monges	Drill core	Mag I	8.6
005-17	MIC	Monges	Drill core	Mag I	9.0
005-20	MIC	Monges	Drill core	Mag I	7.7
005-21	MIC	Monges	Drill core	Mag I	8.5
005-21	MIC	Monges	Drill core	Mag I	8.7
MNG 1	MIC	Monges	Outcrop	Weathered Mag I	6.5
MNG 1	MIC	Monges	Outcrop	Weathered Mag I	6.8
SER 1	MIC	Serrinha	Outcrop	Mag I	8.1
MV 4	MIC	Vale da Arca	Outcrop	Mag I	4.3
AL19	Alvito	Alvito	Outcrop	Mag I	10.1
AL19	Alvito	Alvito	Outcrop	Mag I	10.6
AL20	Alvito	Alvito	Outcrop	Mag I	10.2
AL20	Alvito	Alvito	Outcrop	Mag I	10.3
AZ 8	Azenhas-Orada	Azenhas	Outcrop	Mag I	4.0
AZ 8	Azenhas-Orada	Azenhas	Outcrop	Mag I	4.2
ORA 2	Azenhas-Orada	Orada	Outcrop	Mag I	5.6

Gallium has also been identified as a temperature dependent element, usually found at higher concentrations in magnetite formed under the influence of high-temperature hydrothermal and/or magmatic derived fluids (Nadoll et al., 2014; Peng et al., 2021). The

scatterplot of Al vs. Ga (**Fig. 4.6c**) reveals a good correlation between both elements, showing a similar trend to that observed in the previous figures. Such results are consistent with the higher concentrations being found in magnetite from skarn deposits, presumably formed under higher temperatures than those from the MIC.

Other elements, such as Mn and Mg, are important clues in identifying the extent of the fluid-rock interaction processes (Nadoll et al., 2015 and references therein). The incorporation of such elements usually marks the remobilization of elements from the host rocks by the mineralizing fluids or by post-deposition alteration processes. The plot of Mn vs. Mg (**Fig. 4.6d**) aids in the visualization of the intensity of such processes, and for the selected case studies it becomes evident that magnetite from the MIC deposits has the higher contents of Mg and Mn, reaching 1 wt. % in the Serrinha massive magnetite. Contrastingly, the second-generation magnetite (Mag II) from Azenhas hosted in an epidote-rich skarn possesses the lowest contents of Mn and Mg. However, Mag II from the Monges deposit, despite having low Mn contents, keeps the Mg contents high.

4.5.2 Discriminatory analyses of the orebodies

Addressing the issue of finding proxy classifications for ore deposits has been one of the main targets of recent research focused on trace element analyses of magnetite. Several authors have proposed discriminatory diagrams that consider the incorporation of trace elements into the magnetite structure and cover a wide range of metallogenic conditions. The Al + Mn+ Ca vs Ti + V from Dupuis and Beaudoin (2011) and later reinterpretations from Nadoll et al. (2014; 2015) are one of the discriminatory diagrams that are applied to skarn deposits forming in different tectonic and temporal settings (Xie et al., 2017; Sun et al., 2020; Zhang et al., 2020; Dong et al., 2021; Peng et al., 2021; Yan et al., 2021). These diagrams combine elements which are known to be easily incorporated into magnetite as a function of temperature (x axis) and by fluid-rock interactions (y-axis). **Figure 4.7a** shows the plot of all the data acquired throughout this research, showing that most of the magnetite, independently of being classified as Mag I or Mag II, plots in the skarn field from Dupuis and Beaudoin (2011). An Al / (Zn + Co) vs Cu / (Si + Ca) diagram could be useful, however, the application of such discriminatory diagram is not possible since Cu was mostly below or close to the LOD of the equipment (**Appendix F**). Nevertheless, several other discriminatory criteria were applied to the magnetite chemistry.

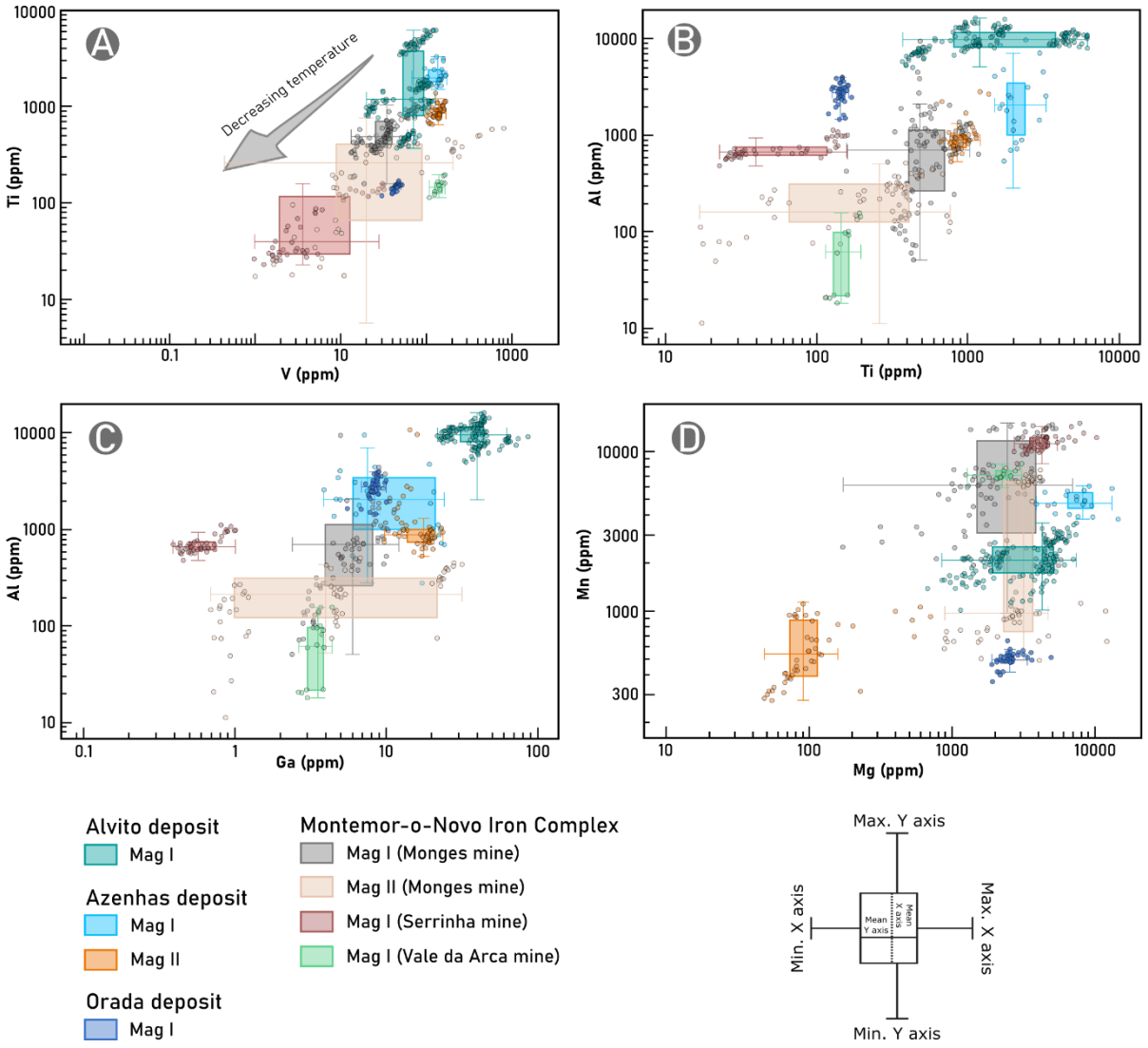

Figure 4.6 Binary scatterplots of LA-ICP-MS data for selected trace elements analyzed in magnetite from the selected deposits and following the color code displayed in Figure 4. The plot includes the data from Maia et al. (2022a). (A) Ti vs V plot in which a progressive depletion is observed from the skarn deposits to the deposits comprised in the MIC. Since the incorporation of Ti and V in magnetite structure is controlled by the temperature of the system, their concentration in magnetite can suggest different temperatures at the time of magnetite deposition (marked by the grey arrow). (B) Al vs. Ti scatterplot. (C) Al vs. Ga scatterplot. (D) Mn vs. Mg scatterplot revealing a positive correlation. LA-ICP-MS trace element data to the Discriminant diagrams.

Regarding the Al + Mn vs. Ti + V diagram, one can conclude that this diagram is not useful for the discrimination of magnetite in the studied deposits of the MIC (**Fig. 4.7a**), if considering that the MIC deposits derive from volcanogenic-hydrothermal. Furthermore, a clear misfit of Mag II from the Azenhas deposit is observed, plotting in the field of Iron Oxide Copper-Gold deposits. However, the fields defined by Nadoll et al. (2015) in a graph of the same type (**Fig. 4.7b**) better reflect the composition of OMZ skarn deposits.

Nickel and chromium have different partitioning behaviors in both magmatic and hydrothermal fluids and their ratios have been proposed as discriminators for igneous and hydrothermal

magnetites (Dare et al., 2014). In Figure 7C the Ti versus Ni/Cr plot is displayed; the results indicate that MIC deposits, Alvito, and Azenhas-Orada magnetite have Ni/Cr ratios higher than one, which is indicative of magnetite derived from a hydrothermal source. Nevertheless, several outliers are observed in magnetite from the Alvito deposit, which fall in the magmatic field (Ni/Cr < 1) and could be indicative of partial crystallization directly from a magmatic source.

To better discriminate the studied deposits, the Co vs Zn plot is proposed (**Fig. 4.7d**), and the data acquired throughout this study is compared to literature data for magnetite from skarn deposits and other low-temperature hydrothermal deposits (Dare et al., 2014; Nadoll et al., 2015; Hu et al., 2017; Araújo et al., 2019; Liu et al., 2019; Peng et al., 2021). Both elements are found at higher concentrations in magnetite from skarn deposits and other high-temperature deposits, and their incorporation in magnetite can be influenced by the presence of sulfides (Hu et al., 2017). The proposed plot shows great results for the discrimination of skarn deposits from other hydrothermal ore deposits, in both our data and the gathered data from the literature (red and blue shaded areas; Dare et al., 2014; Hu et al., 2017; Araújo et al., 2019; Liu et al., 2019; Peng et al., 2021). Following these results two major fields are proposed for the Co vs Zn plot, the “Skarn deposits field” and the “Other hydrothermal deposits” field, contributing to the discrimination of magnetite formed in different metallogenic settings. **Figure 4.7d** shows that both Mag I and Mag II from the Alvito and Azenhas-Orada deposits have Co and Zn contents compatible with magnetite from skarn deposits collected in the literature. On the other hand, the magnetite from the MIC deposits shows values close to those of magnetite from low-temperature deposits (**Fig. 4.7d**).

4.5.3 Principal Component Analysis

Another successful approach to discriminate the orebodies using geochemical data is to apply a multivariate statistical approach that can deal with large datasets, such as the Principal Components Analysis (PCA) (Canil et al., 2016; Makvandi et al., 2016a; 2016b; 2021). The PCA has been applied to the large LA-ICP-MS dataset and revealed to be successful in discriminating magnetite types based on their trace element composition.

For this study, PCA was performed in two separate datasets: i) magnetites from the Montemor-o-Novo Iron Complex, and ii) magnetites from the Alvito and Azenhas-Orada deposits. For this exploratory analysis, the zComposition package (Palarea-Albaladejo & Martín-Fernandez, 2015) was used in the R software environment. Using the built-in ZPattern function all elements showing more than 40% of the data below the LOD were rejected. Following this criterion Ca, Sc, Co, Ni, Cu, Hf, and Pb were excluded from the MIC dataset,

and Ca and Cu from the skarn deposit dataset from Azenhas and Alvito from Maia et al. (2022a).

The PCA of the MIC dataset revealed that for all the magnetite types, the first three principal components (PC1, PC2, and PC3) explain 30.2 %, 24.2 %, and 9.9 % (**Fig. 4.8a, b**), respectively. The cumulative explanation of PC1-PC2-PC3 is 64.3%, which indicates that they are representative of the MIC magnetite dataset. The plot of PC1-PC2 (Fig. 8A) shows a horizontal clustering along the PC1 axis, discriminating between magnetite from the Serrinha deposit and the remaining deposits (Monges and Vale da Arca). PC1-PC2 plot indicates that most magnetite composition is discriminated by the elements that explain PC1, such as Sn, Mg, Mn, Mo, Zr and W at the positive PC1 component of the plot, and Ti, V, Ge, Ga, and Cr at the negative PC1 component. The vertical clustering of elements, that is observed along the PC2 axis, discriminates the first generation (Mag I) from the second-generation magnetite (Mag II) from the Monges deposit. The elements that seem to better discriminate Mag I are seen at the positive PC2 component (Si, Zn), and Mag II at the negative PC2 component (Nb, Ta, Al). Vale da Arca magnetite composition shows a dispersion along the PC2 axis in the PC1-PC2 plot (**Fig. 4.8a**), therefore the identification of the elements that better discriminate this type of magnetite could not be identified.

The PC1-PC3 plot reveals that magnetite from the MIC has extremely variable trace element compositions, overlapping in some cases (**Fig. 4.8b**). In this case, a horizontal clustering of elements along the PC1 axis is still observed which discriminate the Serrinha deposit magnetite, as seen in PC1-PC2 plot. In the plot of PC1-PC3 the clustering along PC3 axis is not so well observed, nevertheless clustering of Vale da Arca magnetite is seen at the negative PC3 component, mainly influenced by Ta, Nb, and Zn concentrations.

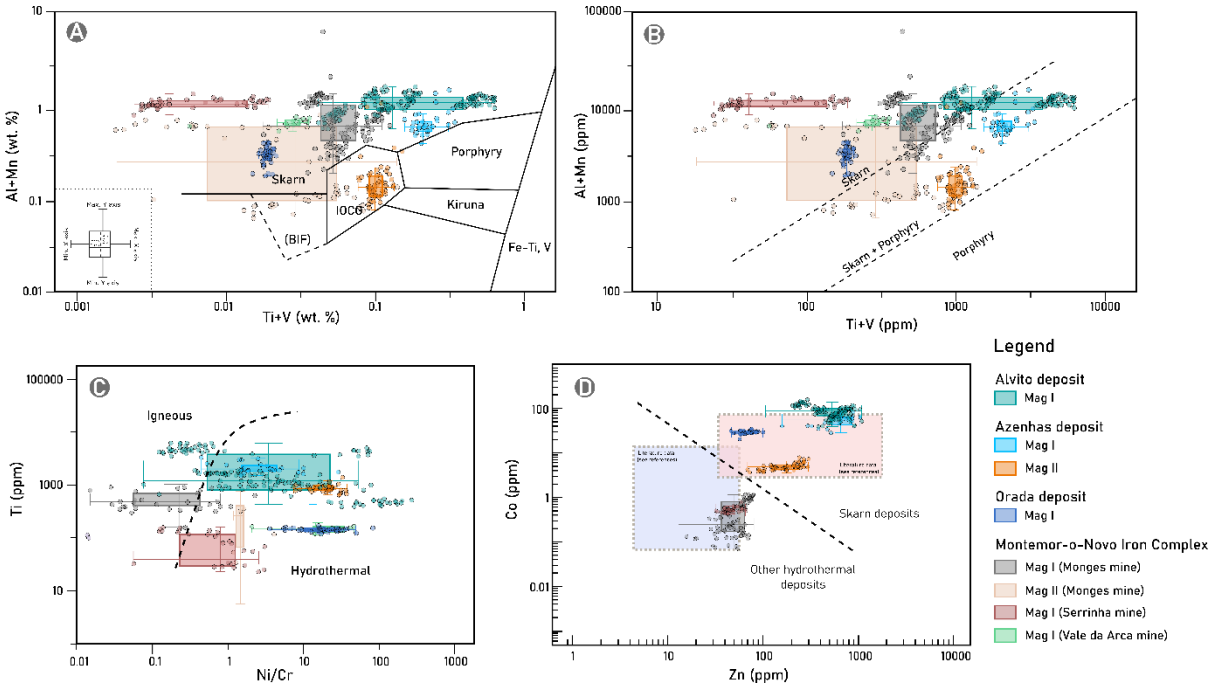

Figure 4.7 LA-ICP-MS trace element data of magnetite from the selected deposits applied to the Discriminant diagrams. The plot includes the data from Maia et al. (2022a). (A) Al + Mn vs. Ti + V discriminant diagram with the boundaries defined by Dupuis and Beaudoin (2011). (B) Reinterpretation of the Al+Mn vs. Ti+V diagram by Nadoll et al. (2015). (C) Ti vs. Ni/Cr ratio discriminant diagram for igneous and hydrothermal magnetite (after Dare et al., 2014). (D) Co vs. Zn scatterplot proposed for the discrimination between magnetite from skarn deposits and those from other hydrothermal origins. The data from this research is compared to literature data to corroborate the discrimination and to define the fields proposed in the plot. The red shaded area in the plot represents the limits of the LA-ICP-MS literature data for magnetite from skarn deposits (Hu et al., 2017; Liu et al., 2019; Peng et al., 2021) and high-temperature magnetite (Dare et al., 2014). The blue shaded area corresponds to the LA-ICP-MS literature data for magnetite from Banded Iron Formation deposits (Araújo et al., 2019) and other low-temperature hydrothermal deposits (Dare et al., 2014).

For the skarn deposits dataset, PCA showed that PC1, PC2, and PC3 could explain 38 %, 13.4 %, and 11.3 % of the data, respectively (**Fig. 4.9a and b**). Clustering of the data is observed along the PC1 axis, which strongly explains most of the variability of the data and is mainly influenced by As, Ti, V, and Si in the positive axis and by high field strength elements (HFSE) such as Nb, Zr, Hf, and Ta in the negative axis.

In the PC1-PC2 plot, a clear distinction is observed between Alvito and Azenhas-Orada deposits, and between Mag I and Mag II (**Fig. 4.9a**). The Alvito samples are influenced by Al, Co, and most of the analyzed HFSE, then followed by the Mag I from the Orada-Azenhas deposits. Differences are registered between Orada Mag I and Azenhas Mag I, with Azenhas magnetite composition being extremely influenced by elements such as Mo, Mn, and Zn. A clear distinction is observed in the Azenhas Mag II, which plot in the complete opposite axis from Alvito and Orada magnetites. The PC1-PC3 plot (**Fig. 4.9b**) reinforces the differences

between Mag I and Mag II from the Fe skarn deposits and marks the similarities between Mag I from both skarn deposits.

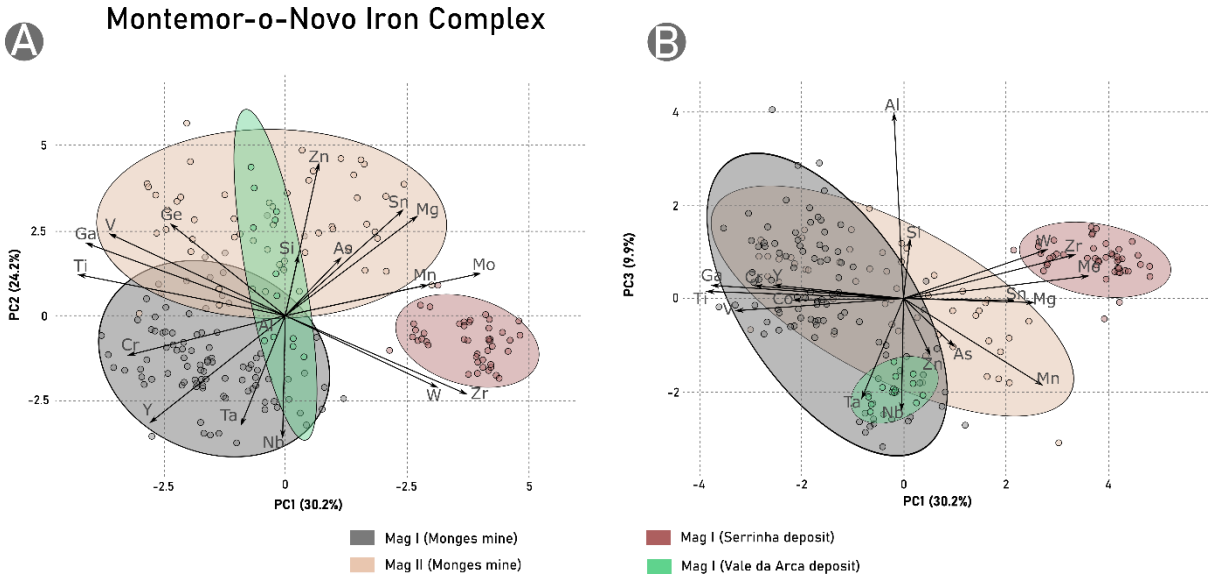

Figure 4.8 Biplot of PC1-PC2 (left site) and PC1-PC3 (right side) clusters, correspondent to the LA-ICP-MS data from the analysis of magnetite from the selected MIC deposits.

4.5.4 Proxies for temperature constraints

A robust approach to the constraint of temperature should focus on the multitude of temperature-dependent elements compatible with magnetite structure. Hence several geochemical criteria were applied to the trace element contents of magnetite.

4.5.4.1 Trace element profiles

A comprehensive overview of magnetite trace element composition can be achieved using the Dare et al. (2014) multielement variation diagram proposal. These plots are key to compare the trace element profiles of magnetite, normalized to the bulk continental crust (Rudnick and Gao, 2003), from the Alvito and Azenhas-Orada skarn deposits to the contrasting volcanogenic-hydrothermal MIC deposits (**Fig. 4.10**). Furthermore, trace element profiles were compared to literature data from low-temperature hydrothermal, high-temperature hydrothermal magnetite, and magmatic magnetite (Dare et al., 2014; Knipping et al., 2015) used as a petrogenetic indicator and a relative method to constrain the temperature settings related to the deposition of each magnetite type.

The trace element profiles from the Alvito Mag I overlap with the high-temperature hydrothermal magnetite (yellow shaded profile in **Fig. 4.10a**) and display a close correlation

with the magmatic magnetite profiles from the literature (Dare et al., 2014), influenced by the enrichment in T-dependent elements such as Sn and Ga (Kamvong et al., 2007), and high field strength elements (Ta, Nb). Higher concentration of such elements is usually found in magmatic-hydrothermal systems, which are associated with higher temperatures of formation (Kamvong et al., 2007; Dare et al., 2014; Nadoll et al., 2015), corroborating the influence of the gabbro-diorite emplacement on the mineralizing processes (Maia et al., 2022a).

It is noteworthy that the Azenhas-Orada Mag I trace element pattern (**Fig. 4.10b**) also fits in the high-temperature hydrothermal magnetite profile, which agrees with the model attributed to these deposits. Magnetite II from the Azenhas deposit reveals a trace element profile depleted in most elements when compared to first generation magnetite indicating a low-temperature hydrothermal origin (Nadoll et al., 2012; Dare et al., 2014; Knipping et al., 2015). The depleted concentrations in T-dependent elements such as Al, Ga, Ti, and HFSE are a common feature of all types of magnetite from the MIC hydrothermal deposits (**Fig. 4.10c, d**). Additionally, a marked depletion in Co is found in this magnetite type, which is a remarkable difference from the skarn deposits (**Fig. 4.10a, b**).

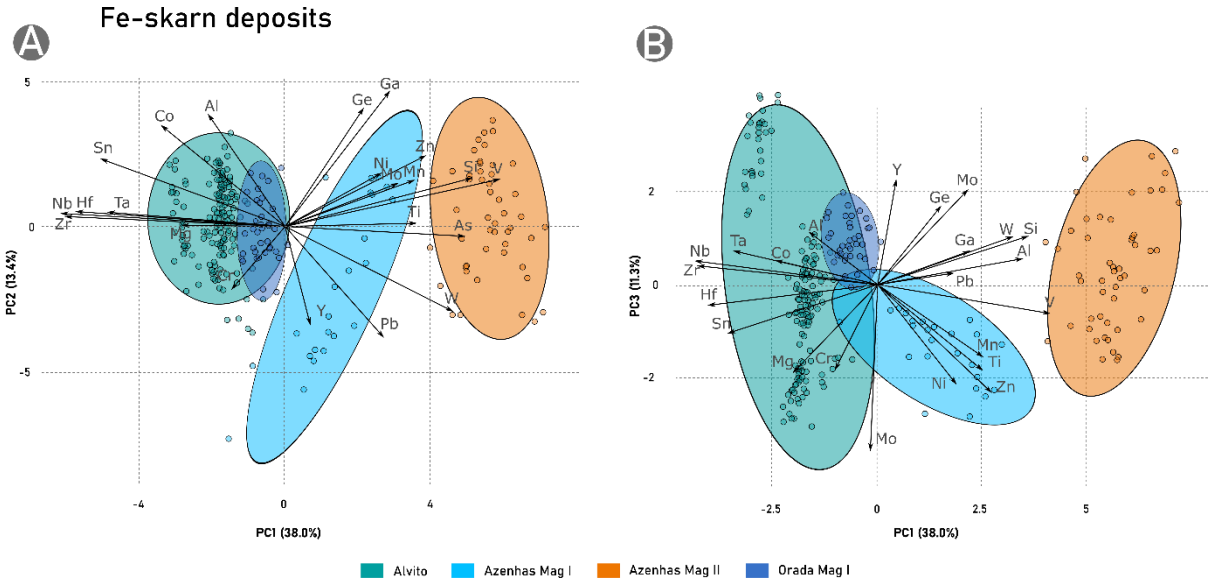

Figure 4.9 Biplot of PC1-PC2 (left site) and PC1-PC3 (right side) clusters, correspondent to the LA-ICP-MS data from the analysis of magnetite from the Alvito and Azenhas-Orada deposits. The plot includes the data from Maia et al. (2022a).

4.5.4.2 High field strength elements

Several authors have examined the influence of temperature on the mobility of HFSE – Nb, Ta, Hf, Zr - (e.g. Nielsen and Beard, 2000; Jiang et al., 2005; Dare et al., 2014; Cheng et al., 2019) and have concluded that their analysis can provide valuable information regarding the temperature and transporting solutions of ores. HFSE are relatively incompatible with

magnetite structure with the higher concentrations of these elements being found in magnetite directly crystallized from a melt (igneous magnetite - Dare et al., 2012). HFSE are relatively immobile under magmatic-hydrothermal regimes, although several geochemical conditions can contribute to their mobility in such systems (Jiang et al., 2005). For this reason, the concentrations of HFSE in magnetite were compared to other elements to identify: i) other possible T-dependent elements; ii) propose new discriminant criteria for low-temperature and high-temperature magnetite by comparing the magnetite from skarn deposits to the presumably lower temperature magnetite from the MIC deposits, and iii) contribute for a robust differentiation of the iron ores from SW Iberia and provide new insights on the ore-forming mechanisms.

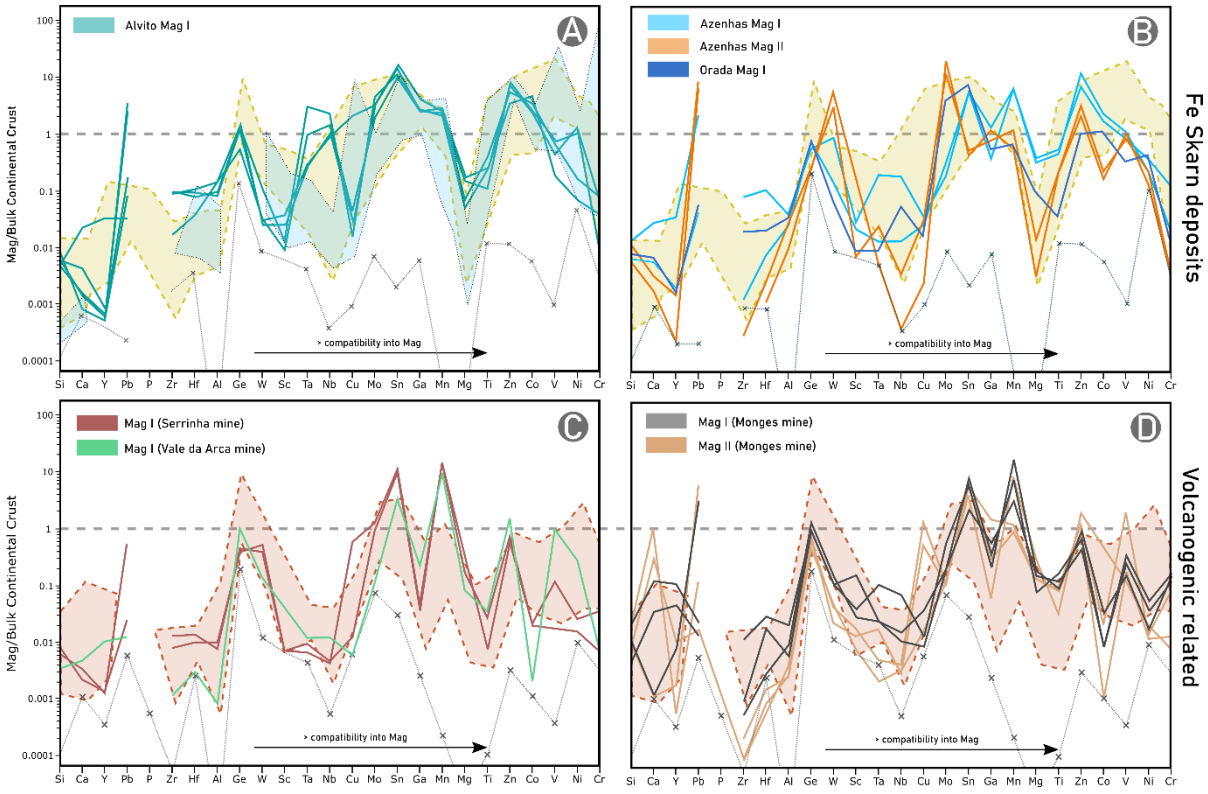

Figure 4.10 Trace element variation diagrams of the magnetite LA-ICP-MS data normalized to the Bulk Continental Crust values (Rudnick and Gao, 2003). Obtained analyses were compared to literature data for low-temperature hydrothermal magnetite (red dashed profile), high-temperature hydrothermal magnetite (yellow dashed profile) and magmatic magnetite (blue dashed profile; after Dare et al., 2014; Knipping et al., 2015). The limits of detection are represented in the plots by the small-spaced dashed grey lines. The data from the MIC deposits were divided into two plots for clarification. (A) Trace element variation plot of the data from the Alvito deposit (adapted from Maia et al., 2022a). (B) Trace element variation plot of the Mag I and Mag II data from the Azenhas deposit (adapted from (Maia et al., 2022a). (C) Trace element variation plot of the data from the primary magnetite from the MIC Serrinha and Vale da Arca deposits. (D) Trace element variation plot of the data from the primary magnetite from the MIC Monges deposits.

Figure 4.11a shows a plot of Nb vs. Zr that displays a positive correlation (R2= 0.63) between both elements and reveals a trend of decrease in HFSE from the skarn deposits Mag I (Alvito ≥ Azenhas ≈ Orada) to the MIC deposits Mag I and Mag II. Strong evidence for Zr and Nb being strongly controlled by temperature is found when looking at the Azenhas Mag II, which plot at the lowest Zr and Nb concentrations and contrasts to Mag I results from the Azenhas-Orada deposits. Such evidence corroborates that Azenhas Mag II is related to low-temperature processes, as previously suggested by the trace element pattern (**Fig 4.10b**).
These results support the discussion from Maia et al. (2022a) which applied the Canil and Lacourse (2020) magnetite geothermometer and gathered temperatures ranging from 676ºC to 689ºC for magnetite from the Alvito deposit; 765ºC to 773ºC for Mag I, and 408 ºC to 429 ºC for Mag II from the Azenhas deposit. Magnetite geothermometer ($T_{Mg\text{-}Mag}$) applied to MIC magnetites revealed average temperatures as follows: 646 ºC for Monges Mag I; 665 ºC for Monges Mag II; 715 ºC for Mag I from Serrinha, and 638 ºC for Mag I from Vale da Arca. The geothermometer showed consistent estimations when applied to magnetite chemistry from other authors (Salgueiro, 2011), revealing average temperatures of 609 ºC for Mag I. Such temperatures are much higher than those of hydrothermal fluids enrolled in SEDEX-VMS systems which suggests that, if considering a primary volcanogenic origin, the ores from the MIC deposit were affected by late metamorphic events that promoted recrystallization of the ores and are imprinted in the final magnetite composition, previously recognized by other authors (Salgueiro, 2011). Although the estimations derived from magnetite geothermometer should be interpreted with care for systems where magnetite did not derive from a silicate liquid (Canil and Lacourse, 2020), such as the study cases presented through this work, these authors (Canil and Lacourse, 2020) have gathered consistent data for hydrothermal magnetite from skarn and porphyry deposits.

As shown in **Figure 4.10**, the contents of Co are contrasting between the magnetite from skarn and volcanogenic-hydrothermal deposits. Comparing the Co concentrations to Nb/Ti ratios (**Fig. 4.11b**) suggests that cobalt is likely incorporated as a function of temperature, with magnetite from skarn deposits showing Co concentration > 1ppm, and < 1ppm in the deposits formed under lower temperatures. A temperature trend is proposed for the studied magnetite from skarn deposits (**Fig. 4.11b**). The relation between Co and HFSE, such as Zr and Nb (**Fig. 4.11c, d**), indicates that, for the studied cases, the magnetites with a higher concentration of Co also exhibit higher HFSE concentrations suggesting a magmatic-hydrothermal origin.

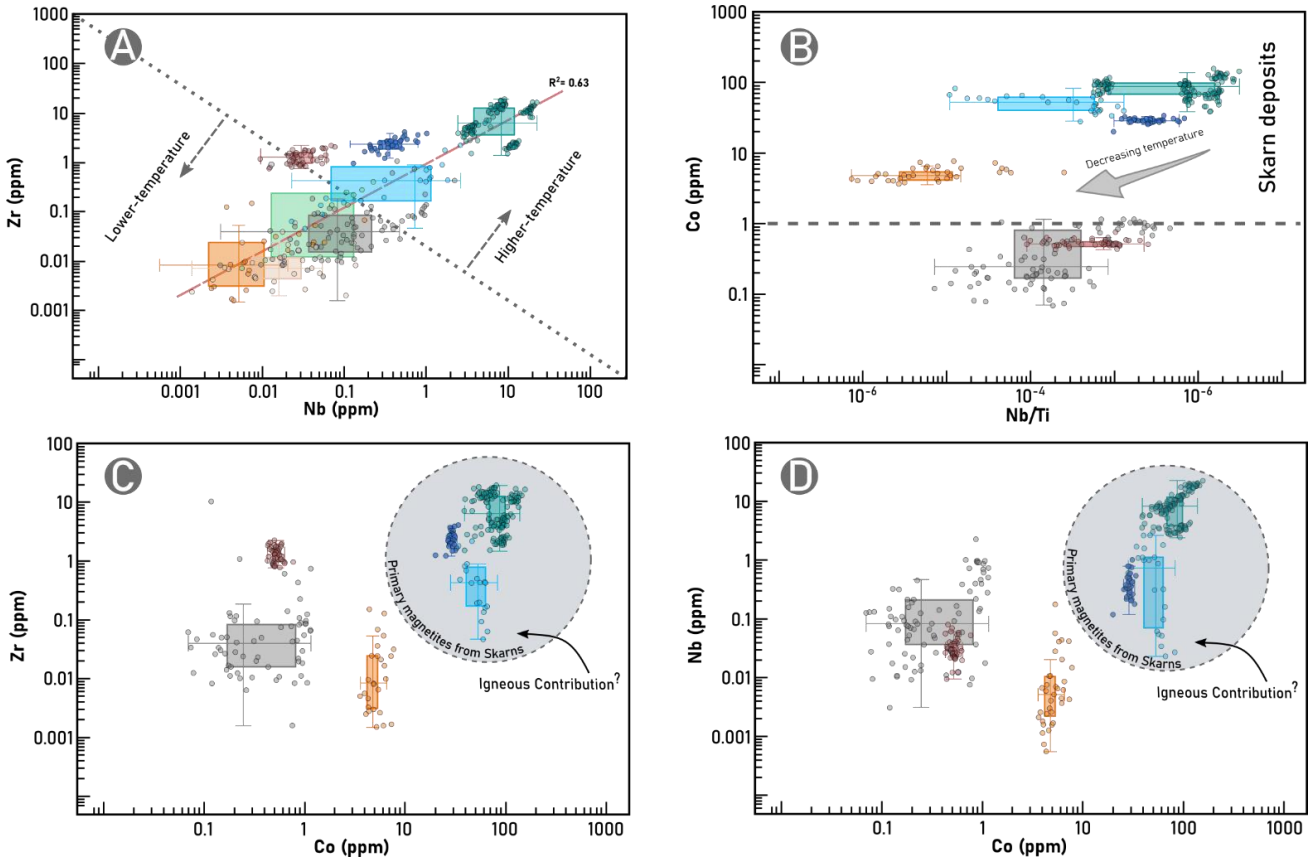

Figure 4.11 Inspection of HFSE and Co concentrations, analyzed in magnetites, as discriminant elements for the studied deposits including the data from Maia et al. (2022a). (A) Zr vs Nb scatterplot. Note the progressive decrease in the concentration of these HFSE from the skarn deposits towards the MIC deposits. Such trend indicates a positive correlation between Zr and Nb and a progressive decrease of temperature at the time of ore deposition. (B) Co vs Nb/Ti ratio plot, proposed as discrimination between the high-temperature Alvito and Azenhas-Orada skarn deposits and the low-temperature volcanogenic MIC deposits. (C) Zr vs Co scatterplot with a clear differentiation of primary magnetite from the Alvito and Azenhas-Orada skarn deposits. Such differentiation could indicate an igneous/magmatic contribution of fluids and heat to the system and corroborates the idea that for the studied skarn deposits, Co incorporation is temperature controlled. (D) Nb vs Co scatterplot, showing the same behavior as seen in Figure 4.11c.

4.5.5 Oxygen isotopes and the origin of the orebodies

Magnetite oxygen isotope ($\delta^{18}O$) signatures can provide valuable information regarding the ore sources by helping to identify the origin of the fluids involved in the transport of the ores and in constraining the fractionation processes imposed by fluid-rock interactions.

4.5.5.1 Montemor-o-Novo Iron Complex

Considering the hypothesis of a SEDEX-VMS continuum model to the Montemor-o-Novo Iron Complex (Salgueiro, 2011) the metallogeny of the deposits would be directly linked to seafloor hydrothermal venting systems (Shanks, 2013), and therefore seawater influx should be an important contribution for metal transport and deposition. Considering this metallogenic hypothesis, the inherited $\delta^{18}O$ signatures would reflect the lighter signatures of seawater. The $\delta^{18}O$ signatures of magnetite (**Table 4.5** and **Fig. 4.12**) deviate greatly from what was expected for magnetite derived from SEDEX-VMS ore fluids which should, as previously stated, exhibit lower $\delta^{18}O$ values (-2 ‰ to 3.5‰; Shanks, 2013). Particularly heavier signatures were obtained for Mag I from Monges deposit (7.7 ‰ – 9.0 ‰) and the results from the primary ores from the Serrinha deposit agree with those of Mag I from Monges deposit (**Fig. 4.12**). The much lighter $\delta^{18}O$ values of Mag I from the Vale da Arca deposit (4.3 ‰) suggest different fractionation processes than those from the remaining MIC deposits. These $\delta^{18}O$ values could be justified by the influence of late low-temperature hydrothermal fluids responsible for the precipitation of porous sphalerite-rich magnetite at the rims of texturally and chemically homogeneous magnetite crystals (**Fig. 4.2G**), imposing significant changes to the primary $\delta^{18}O$ signatures of magnetite.

4.5.5.2 Alvito

The $\delta^{18}O$ values (**Table 4.5)** of Mag I from Alvito (10.1 ‰ – 10.6 ‰) are higher than those attributed to magmatic fluids (**Fig. 4.12**) and considerably lower than those typical of Cambrian carbonates (Peters et al., 2019). In skarn deposits, the $\delta^{18}O$ signatures has been recognized to shift due to extensive magmatic-hydrothermal fluid interaction with surrounding carbonate-rich rocks, which can be high ^{18}O reservoirs (Hoefs, 2018). The reaction between a low ^{18}O fluid and a high ^{18}O rock can lead to a progressive shift towards higher ^{18}O signatures, resulting in heavier $\delta^{18}O$ signatures in magnetite (Rose et al., 1985; Xie et al., 2017), which can explain the values obtained in the analysis of Alvito magnetite. This hypothesis is supported by the metallogenic settings in which the Alvito skarn deposit has formed suggesting that the $\delta^{18}O$ signatures found in magnetite derive from the reaction of a magmatic-hydrothermal fluid with the dolomite-calcite country-rock.

4.5.5.3 Azenhas-Orada

Magnetites from the Azenhas and Orada orebodies revealed $\delta^{18}O$ signatures in a narrow range (4.0 ‰ – 5.6 ‰; **Fig. 4.12**) reinforcing the interpretation of both deposits sharing a single/similar source. The $\delta^{18}O$ values are in the range of those found in skarn deposits in which a strong contribution of magmatic fluids has been identified (Xie et al., 2017; Morris and Canil, 2020; Dong et al., 2021; Tornos et al., 2021).

The magnetite from Alvito and Azenhas-Orada Fe skarn deposits show $\delta^{18}O$ signatures compatible with those obtained in the analysis of magnetite from other skarn deposits from OMZ, such as the Monchi (6.0 ‰ – 7.5 ‰) and Cala (3 ‰ – 5 ‰) skarn ores (Tornos et al., 2021), which have been interpreted as reflecting the contribution of magmatic-hydrothermal fluids to ore transport and deposition. The lighter $\delta^{18}O$ values in Azenhas-Orada magnetite could indicate that the orebodies might have formed through inputs of magmatic-derived hydrothermal fluids with little contribution from host rock, corroborating previous discussions (Maia et al., 2022a).

4.5.6 Metallogenic implications for the genesis of iron ore deposits in SW Iberia

4.5.6.1 Montemor-o-Novo Iron Complex

The deposits from the Montemor-o-Novo Iron Complex raise several questions regarding their genetic model. They have been early classified as skarn deposits (Andrade et al., 1949), related to metasomatic processes triggered by the emplacement of granitic bodies, although no clear relation between the ore bodies and a granitic suite was ever found. For this reason and considering the geological settings and host rocks of the mineralization, later interpretations have attributed a continuous transition between a SEDEX and VMS model for the deposits of the MIC (Salgueiro, 2011; Mateus et al., 2013). Chemical composition of magnetite from the MIC deposits plot in the skarn field of the Al + Mn vs Ti + V diagrams (**Fig. 4.7b**), however, when plotted on the Co vs Zn diagram their composition shows affinities with magnetites from other low temperature hydrothermal deposits (**Fig. 4.7c**; **Fig. 4.10c and d**; **Fig. 4.11a and b**). When comparing the geochemical data of magnetite from the MIC with magnetite from the skarn deposits, clear distinctions also exist, namely the lower content in Co and Zn, magnetite trace element pattern and $\delta^{18}O$ signatures falling within the magmatic water range. Considering the gathered data and the tectonic settings in which the MIC deposits occur, it is plausible that their genesis could be associated with volcanogenic processes. Nevertheless, magnetite texture and chemistry indicate that regional metamorphic events had promoted a strong overprinting effect on the ores. Considering that amphiboles

are associated with the magnetite and have developed in the marbles, under a metamorphic regime that reached the amphibolitic facies, such conditions are consistent with magnetite recrystallization during regional metamorphism. Our data agrees with prior considerations from Salgueiro (2011), which have suggested that magnetite recrystallization should have occurred at temperatures higher than 550 ºC. Additionally, accessory sphalerite mineralization was identified in the Vale da Arca orebodies, which can be a good indication for the generation of Zn mineralization at the MIC area and justify the lower temperatures and much lighter $\delta^{18}O$ values (4.3 ‰) of magnetite.

4.5.6.2 Alvito deposit

The gathered data is evidence for a clear relation between the emplacement of CAGD and the genesis of the Alvito deposit through the metasomatic reaction between a magmatic fluid and the carbonate host-rocks, with magnetite ores being hosted in a typical skarn mineral assemblage accompanied by diopside-hedenbergite pyroxene. Nevertheless, there is still space for some debate on whether all magnetite crystallized from a magmatic-hydrothermal fluid, and therefore high-temperature hydrothermal magnetite, or if there could have been a crystallization directly from the magma, which would classify the magnetite as igneous. The fact that the Alvito magnetite displays higher concentrations of HFSE (**Fig. 4.11a**), allied with the geological settings of the deposit; the presence of (Co)-rich pentlandite in the ore assemblage and high Co contents of magnetite (Ave. 86.4 ppm); the abundance of oxyexsolution, commonly found in magmatic magnetite (Huang & Beaudoin, 2019), can indicate towards a magmatic origin for the ores with magnetite being directly derived from a melt (Huang et al., 2019). But one can argue contrarily, since titanium rich oxyexsolutions, although much more common in magmatic magnetite, are also found in high-temperature hydrothermal magnetite (Wu et al., 2019), such as those from Fe skarn deposits (Hu et al., 2015), and to which magnetite shows a compatible trace element profile (**Fig. 4.10a**). Furthermore, the high contents of HFSE could be present as impurities (Nadoll et al., 2014) in the oxyexsolutions found in Alvito Mag I. Nevertheless, most of the discriminant criteria applied to the magnetite chemistry shows that Alvito magnetite has affinity to hydrothermal systems (**Fig. 4.7c**) and Co and Zn concentrations are coherent to those found in skarn deposits from the literature (**Fig. 4.7d**). It is therefore suggested that, considering the gathered data and subsequent discussion, Fe mineralization from the Alvito skarn deposit derived from a magmatic-hydrothermal system, and that although ^{18}O signatures of magnetite are higher than those usually found in skarn deposits (Xie et al., 2017; Morris and Canil, 2020; Dong et al., 2021; Tornos et al., 2021) they could be reflecting the extent of fluid-rock interactions, by means of metassomatism, between a lighter 18O signature fluid derived from a magmatic

source, the CAGD intrusion, and a heavier ^{18}O signature host-rock, such as the host-rock marbles.

Additionally, the high contents of Co, allied to the presence of Ni-Co sulfides suggests that the magmatic source is prone to generate other types of ore deposits, and therefore the Alvito area could be an interesting prospect for future mineral exploration (Maia et al., 2022a).

4.5.6.3 Azenhas-Orada deposit

At the Azenhas-Orada deposits, two magnetite types (Mag I and Mag II) were distinguished by their textural features, which is clearly supported by their chemistry (e.g. **Fig. 4.6b and d**). Although a magmatic contribution can be debatable, since evidence for an intrusion compatible with the mineralization is not known in the area (Maia et al., 2022a), it becomes evident that their composition is comparable to magnetite I from the Alvito deposit (**Fig. 4.7d**). However, important differences exist, such as the lower concentrations of HFSE, Co, and other temperature-dependent elements. Trace element concentrations of magnetite I from both the Azenhas and Orada deposits share several features (**Fig. 4.9a and b**), which corroborates the idea that although they are spatially separated orebodies, they may share the same fluid and metal source.

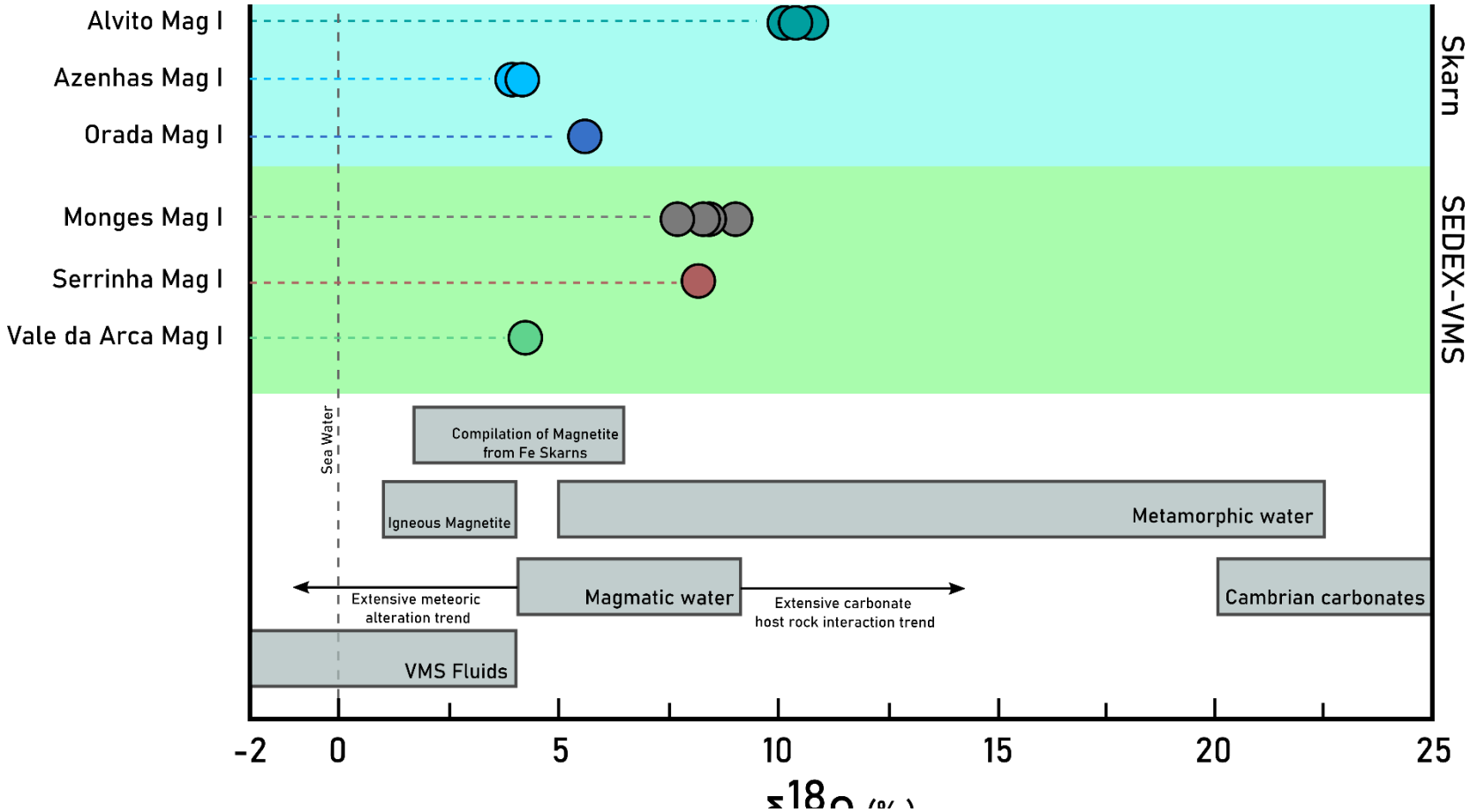

Figure 4.12 Distribution of δ18O isotope results from the analysis of selected magnetite samples representative of the studied orebodies, compared to literature 18O signatures of different ore-fluids, Cambrian carbonates, and magnetite (Shanks, 2013; Hoefs, 2018; Peters et al., 2019; Troll et al., 2019).

4.6 Conclusions

Our research suggests that magnetite LA-ICP-MS trace element analysis is a powerful method for the characterization of ore-forming processes. The acquired data is useful in discriminating magnetite formed in different metallogenic settings, and thus provides new insights on the genesis of these types of ore deposits in SW Iberia, such as:

- Magnetite from the MIC (Montemor-o-Novo Iron Complex) deposits is hardly discriminated from the studied skarn deposits (Alvito and Azenhas-Orada) if only using the Al + Mn vs. Ti + V diagrams. Nevertheless, several other discriminatory indexes have been proposed, such as the Co and Zn scatterplot (**Fig. 4.7d**), in which magnetite from the skarn deposits are clearly differentiated by their high contents in Co and Zn (**Table 4.1 and 4.2**).
- •Magnetite trace element compositions showed to be valuable in contributing to the discussion on the dubious origin attributed to the MIC deposits. It is suggested that the Variscan metamorphic regime (greenschist-amphibolitic facies) played a major role in overprinting the initial chemical and textural features of the ores as supported by the variable $\delta^{18}O$ signatures and the magnetite temperature estimations.
- The comparison of our data to literature magnetite analysis led us to propose that the Co vs Zn plot can be used to discriminate between magnetite from skarn deposits and magnetite from other deposits of hydrothermal origin.
- This research outlines that the inspection of HFSE such as Nb and Zr is key to differentiate the fluid temperature of the fluids associated with ore deposition (**Fig. 4.11a**), particularly in skarn deposits. Oxygen isotope signatures of magnetite from the Alvito deposit suggest that magnetite crystallized from a magmatic-derived hydrothermal fluid (lighter $\delta^{18}O$ signatures) hat has extensively interacted with the carbonate host rocks (heavier $\delta^{18}O$ signatures), reinforcing the role of magmatic fluids upon ore deposition.
- Furthermore, the magnetite from the Azenhas-Orada Fe skarn deposit revealed $\delta^{18}O$ signatures that correlate to those of Fe skarn magnetite from the literature. The clear identification of the mineralization source is still an unresolved problem and could favor further isotopic analysis of magnetite (e.g. Fe and Sm-Nd isotopes).

Chapter References

Andrade, A., Silva, J.M., Arruda, C.R., Gameiro, J.C.S., 1949. Minas de Ferro de Montemor-o-Novo. Serviço de Fomento Mineiro, v. 15, p. 125

Apalategui, O., Eguiluz, L., and Quesada, C., 1990. Ossa-Morena Zone: Structure. In: Martinez E and Dallmeyer RD (Eds.) Pre-Mesozoic Geology of Iberia, Springer Verlag, p. 280-291.

Araújo, A., 1995. Estrutura de uma Geotransversal entre Brinches e Mourão (Zona de Ossa-Morena). Implicações na evolução geodinâmica da margem Sudoeste do Terreno Autóctone Ibérico. PhD Thesis, Univ. Évora, Portugal, 200p.

Araújo, A., Fonseca, P., Munhá, J., Moita, P., Pedro, J., and Ribeiro, A., 2005. The Moura Phyllonitic Complex: An Accretionary Complex related with obduction in the Southern Iberia Variscan Suture. Geodinamica Acta, v. 18(5), p. 375-388.

Araújo, J.C.S., and Lobato, L.M., 2019. Depositional model for banded iron formation host to gold in the Archean Rio das Velhas greenstone belt, Brazil, based on geochemistry and LA-ICPMS magnetite analyses. Journal of South American Earth Sciences, v. 97, 102205. https://doi.org/10.1016/j.jsames.2019.05.021

Armbruster, T., Bonazzi, P., Akasaka, M., Bermanec, V., Chopin, C., Gieré, R., Heuss-Assbichler, S., Liebsher, A., Menchetti, S., Pan, Y., and Pasero, M., 2006. Recommended nomenclature of epidote-group minerals. European Journal of Mineralogy, v. 18, p.551-567. https://doi.org/10.1127/0935-1221/2006/0018-0551

Ayupova, N.R., Novoselov, K.A., Maslennikov, V., Melekestseva, I.Y., Hollis, S.P., Artemyev, D.A., and Tessalina, S.G., 2020. The formation of magnetite ores of the Glubochenskoe deposit, Turgai iron belt, Russia. new structural, mineralogical, geochemical, and isotopic constraints: Mineralium Deposita, v.56, 103-123. https://doi.org/10.1007/s00126-020-00994-6

Barroso, M., Mateus, A., Figueiras, J., Martins, R., and Oliveira, V., 2003. Mineralogy and geochemical characteristics of different superimposed mineralisations at the Enfermarias prospect (Moura, Portugal). VI Congresso Nacional de Geologia, Lisboa (Portugal), Ciências da Terra (UNL), Lisboa, n.º esp. V, CD-ROM, F9-F12.

Canil, D., Grondahl, C., Lacourse, T., and Pisiak, L.K., 2016. Trace elements in magnetite from porphyry Cu–Mo–Au deposits in British Columbia, Canada. Ore Geology Reviews, v. 72, p. 1116-1128. http://dx.doi.org/10.1016/j.oregeorev.2015.10.007

Canil, D., and Lacourse, T., 2020. Geothermometry using minor and trace elements in igneous and hydrothermal magnetite. Chemical Geology, v. 541, 119576. https://doi.org/10.1016/j.chemgeo.2020.119576

Carvalho, D., 1971. Observações sobre os jazigos de ferro da área Pedrógão-Orada. I Congresso Hispano – Luso – Americano de Geologia Económica, Madrid – Lisboa, v.1, p. 519-537.

Carvalhosa, A.B., and Zbyszewski, G., 1971. Carta Geológica de Portugal à escala 1: 50 000: Folha 40-C Viana do Alentejo. Direção Geral de Minas e Serviços Geológicos.

Carriedo, J., Tornos, F., Chiaradia, M., and Galindo, C., 2021. A genetic link between albitic magmas and IOCG mineralization in the Ossa Morena Zone (SW Iberia). Journal of Iberian Geology, v. 47, p. 85-119. https://doi.org/10.1007/s41513-021-00162-3

Chen, W., Ying, Y.-C., Bai, T., Zhang, J.-J., Jiang, S.-Y., Zhao, K.-D., Shin, D., and Kynicky, J., 2019. In situ major and trace element analysis of magnetite from carbonatite related complexes: Implications for petrogenesis and ore genesis. Ore Geology Reviews, v.107, p. 30-40. https://doi.org/10.1016/j.oregeorev.2019.01.029

Chichorro, M., Pereira, M.F., Díaz-Azpiroz, M., Williams, I.S., Fernández, C., Pin, C., and Silva, J.B., 2008. Cambrian ensialic rift-related magmatism in the Ossa-Morena Zone (Évora–Aracena metamorphic belt, SW Iberian Massif): Sm–Nd isotopes and SHRIMP zircon U–Th–Pb geochronology. Tectonophysics, v. 461, p. 91-113. https://doi.org/10.1016/j.tecto.2008.01.008

Childress, T., Simon, A.C., Reich, M., Barra, F., Bilenker, L.D., La Cruz, N.L., Bindeman, I.N., and Ovalle, T.J., 2020. Triple Oxygen (δ18O, Δ17O), Hydrogen (δ2H), and Iron (δ56Fe) Stable Isotope Signatures Indicate a Silicate Magma Source and Magmatic-Hydrothermal Genesis for Magnetite Orebodies at El Laco, Chile. Economic Geology, v. 115, p. 1519-1536. https://doi.org/10.5382/econgeo.4760

Codeço, M.S., Weis, P., Trumbull, R.B., Hinsberg, V.H., Pinto, F., Lecumberri-Sanchez, P., and Schleicher, A.M., 2021. The imprint of hydrothermal fluids on trace-element contents in white mica and tourmaline from the Panasqueira W–Sn–Cu deposit, Portugal. Mineralium Deposita, v. 56, p. 481-508. https://doi.org/10.1007/s00126-020-00984-8

Cook, N., Ciobanu, C.L., George, L., Zhu, Z.-Y., Wade, B., and Ehrig, K., 2016. Trace Element Analysis of Minerals in Magmatic-Hydrothermal Ores by Laser Ablation Inductively-Coupled Plasma Mass Spectrometry: Approaches and Opportunities: Minerals, v. 6, 111. https://doi.org/10.3390/min6040111

Dare, S.A.S., Barnes, S.-J., Beaudoin, G., Méric, J., Boutroy, E., and Potvin-Doucet, C., 2014. Trace elements in magnetite as petrogenetic indicators. Mineralium Deposita, v. 49, p. 785-796. https://doi.org/10.1007/s00126-014-0529-0

Dias da Silva, Í., Pereira, M.F., Silva, J.B., and Gama, C., 2018. Time-space distribution of silicic plutonism in a gneiss dome of the Iberian Variscan Belt: The Évora Massif (Ossa-Morena Zone, Portugal). Tectonophysics, v. 747, p. 298-317. https://doi.org/10.1016/j.tecto.2018.10.015

Dias R., Moreira N., Ribeiro A., and Basile C., 2017. Late Variscan Deformation in the Iberian Peninsula; A late feature in the Laurasia-Gondwana Dextral Collision. International Journal of Earth Sciences (Geol Rundsch), v. 106(2), p. 549-567. https://doi.org/10.1007/s00531-016-1409-x

Diéz Fernández, R., Arenas, R., Pereira, M.F., Sánchez-Martínez, S., Albert, R., Parra, L.-M.M., Rubio Pascual, F.-J., and Matas, J., 2016. Tectonic evolution of Variscan Iberia: Gondwana–Laurussia collision revisited. Earth-Science Reviews, v. 162, p. 269-292. http://dx.doi.org/10.1016/j.earscirev.2016.08.002

Dong, R., Wang, He, Li, W., Yan, Q.-H., and Zhang, X., 2021. The geology, magnetite geochemistry, and oxygen isotopic composition of the Akesayi skarn iron deposit, Western Kunlun Orogenic Belt, Xinjiang, northwest China: Implications for ore genesis. Ore Geology Reviews, v. 130, 103854. https://doi.org/10.1016/j.oregeorev.2020.103854

Duan, C., Li, Y., Mao, J., Hou, K., Wang, C., Yang, B., Wang, Q., and Li, W., 2019. Ore formation at the Washan iron oxide–apatite deposit in the Ningwu Ore District, eastern China: Insights from in situ LA-ICP-MS magnetite trace element geochemistry. Ore Geology Reviews, v. 112, 103064. https://doi.org/10.1016/j.oregeorev.2019.103064

Dupuis, C., and Beaudoin, G., 2011. Discriminant diagrams for iron oxide trace element fingerprinting of mineral deposit types. Mineralium Deposita, v. 46, p. 319-335. https://doi.org/10.1007/s00126-011-0334-y

Eguiluz, L., Gil Ibarguchi, J. I., Abalos B., and Apraiz, A., 2000. Superposed Hercynian and Cadomian orogenic cycles in the Ossa-Morena Zone and related areas of the Iberian Massif. Geological Society of America Bulletin, v. 112(9), p. 1398-1413.

Farias, P., Gallastegui, G., González Lodeiro, F., Marquínez, J., Martin Parra, L., Martínez Catalán, J., Paolo Macia, J., and Rodriguez Fernandez, L., 1987. Aportaciones al conocimiento de la litoestratigrafia y estrutura de Galiza Central. Memória, Fac. Ciênc. Univ. Porto v. 1, p. 411-431.

Ghazi, J.M., Harris, C., Rahgoshay, M., and Moazzen, M., 2019. Combined igneous and hydrothermal source for the Kiruna-type Bafq magnetite-apatite deposit in Central Iran; trace element and oxygen isotope studies of magnetite. Ore Geology Reviews, v. 105, p. 590-604. https://doi.org/10.1016/j.oregeorev.2019.01.006

Goínhas, A.C., and Martins, L.M.P., 1986. Área metalífera de Montemor-o-Novo – Casa Branca (Baixo Alentejo, Portugal). Estudo, Notas e Trabalhos, v. 28, p. 119-148.

Gomes, E.M.C., and Fonseca, P.E., 2006. Eventos metamórfico/metassomáticos tardi-variscos na região de Alvito (Alentejo, sul de Portugal). Cadernos Xeológicos de Laxe, v.31, p. 67-85. ISSN: 0213 – 4497

Guillong, M., Hametner, K., Reusser, E., Wilson, S.A., and Günther, D., 2005. Preliminary Characterisation of New Glass Reference Materials (GSA-1G, GSC-1G, GSD-1G and GSE-1G) by Laser Ablation-Inductively Coupled Plasma-Mass Spectrometry Using 193 nm, 213 nm and 266 nm Wavelengths. Geostandards and Geoanalytical Research, v. 29(3), p. 315-331. https://doi.org/10.1111/j.1751-908X.2005.tb00903.x

Gomes, E.M.C., 2000. Metamorfismo de rochas carbonatadas siliciosas da região de Alvito (Alentejo, Sul de Portugal). PhD Thesis, Universidade de Coimbra, pp. 240.

Gomes, E.M.C., and Fonseca, P.E., 2006. Eventos metamórfico/metassomáticos tardi-variscos na região de Alvito (Alentejo, sul de Portugal). Cadernos Xeológicos de Laxe, v.31, p. 67-85. ISSN: 0213 – 4497

Hoefs, J., 2018. Stable isotope geochemistry, Eight edition, 460 pp. https://doi.org/10.1007/978-3-319-78527-1

Hu, H., Lentz, D., Li, J.-W., McCarron, T., Zhao, X.-F., and Hall, D., 2015. Reequilibration processes in magnetite from iron skarn deposits. Economic Geology, v.110, pp. 1-8. https://doi.org/10.2113/econgeo.110.1.1

Hu, X., Chen, H., Zhao, L., Han, J., and Xia, X., 2017. Magnetite geochemistry of the Longqiao and Tieshan Fe–(Cu) deposits in the Middle-Lower Yangtze River Belt: Implications for deposit type and ore genesis. Ore Geology Reviews, v. 89, p. 822-835. http://dx.doi.org/10.1016/j.oregeorev.2017.07.019

Huang, X.-W., and Beaudoin, G., 2019. Textures and chemical and compositions of magnetite from Iron Oxide Copper-Gold (IOCG) and Kiruna-type Iron Oxide Apatite (IOA) deposits and their implications for ore genesis and magnetite classification schemes. Economic Geology, v.114, p. 953-979. https://doi.org/10.5382/econgeo.4651

Huang, X.-W., and Beaudoin, G., 2021. Nanoinclusions in zoned magnetite from the Sossego IOCG deposit, Carajás, Brazil: Implication for mineral zoning and magnetite origin discrimination. Ore Geology Reviews, v. 139, 104453. https://doi.org/10.1016/j.oregeorev.2021.104453

Huang, X.-W., Sappin, A.-A., Boutroy, É., Beaudoin, G., and Makvandi, S., 2019. Trace element composition of igneous and hydrothermal magnetite from porphyry deposits: Relationship to deposit subtypes and magmatic affinity. Economic Geology, v. 114(5), p. 917-952. https://doi.org/10.5382/econgeo.4648

Jesus, A.P., Mateus, A., Munhá, J.M., Tassinari, C.C.G., Bento dos Santos, T., and Benoit, M., 2016. Evidence for underplating in the genesis of the Variscan synorogenic Beja Layered Gabbroic Sequence (Portugal) and related mesocratic rocks. Tectonophysics, v. 683, p. 148-171. http://dx.doi.org/10.1016/j.tecto.2016.06.001

Jesus, A.P., Mateus, A., Benoit, M., Tassinari, C.C.G., and Bento dos Santos, T., 2020. The timing of sulfide segregation in a Variscan synorogenic gabbroic layered intrusion (Beja, Portugal): Implications for Ni-Cu-PGE exploration in orogenic settings. Ore Geology Reviews, v.126, 103767. https://doi.org/10.1016/j.oregeorev.2020.103767

Jiang, S.-Y., Wang, C.-R., Xu, X.-S., and Zhao, K.-D., 2005. Mobility of high field strength elements (HFSE) in magmatic-, metamorphic-, and submarine-hydrothermal systems. Physics and Chemistry of the Earth, v. 30, p. 1020-1029. https://doi.org/10.1016/j.pce.2004.11.004

Jochum, K.P., Willbold, M., Raczek, I., Stoll, B., and Herwig, K., 2005. Chemical Characterisation of the USGS Reference Glasses GSA-1G, GSC-1G, GSD-1G, GSE-1G, BCR-2G, BHVO-2G and BIR-1G Using EPMA, ID-TIMS, ID-ICP-MS and LA-ICP-MS. Geostandards and Geoanalytical Research, v. 29(3), p. 285.302. https://doi.org/10.1111/j.1751-908X.2005.tb00901.x

Jochum, K.P., Weis, U., Stoll, B., Kuzmin, D., Yang, Q., Raczek, I., Jacob, D.E., Stracke, A., Birbaum, K., Frick, D.A., Günther, D., and Enzweiler, J., 2011. Determination of reference values for NIST SRM 610-617 glasses following ISO guidelines. Geostandards and Geoanalytical Research, v. 35, p. 397–429. https://doi.org/10.1111/j.1751-908X.2011.00120.x

Johnson, C.A., Day, W.C., and Rye, R.O., 2016. Oxygen, Hydrogen, Sulfur, and Carbon Isotopes in the Pea Ridge Magnetite-Apatite Deposit, Southeast Missouri, and Sulfur Isotope Comparisons to Other Iron Deposits in the Region. Economic Geology, v. 111, p. 2017-2032. https://doi.org/10.2113/econgeo.111.8.2017

Julivert, M., Fontboté, J.M., Ribeiro, A., and Conde, L., 1972. Mapa Tectónico de La Península Ibérica y Baleares (Tectonic Map of the Iberian Peninsula and Balearían Ilands). IGME-SPI, Instituto Geológico y Minero de España, Madrid 113.

Kamvong T, Zaw K, and Siegele, R., 2007. PIXE/PIGE microanalysis of trace elements in hydrothermal magnetite and exploration significance: a pilot study. 15th Australian Conference on Nuclear and Complementary Techniques of Analysis and 9th Vacuum Society of Australia Congress. University of Melbourne, Melbourne.

Knipping, J.L., Bilenker, L.D., Simon, A.C., Reich, M., Barra, F., Deditius, A.P., Wälle, M., Heinrich, C.A., Holtz, F., and Munizaga, R., 2015. Trace elements in magnetite from massive iron oxide-apatite deposits indicate a combined formation by igneous and magmatic-hydrothermal processes. Geochimica et Cosmochimica Acta, v. 171, p. 15-38. http://dx.doi.org/10.1016/j.gca.2015.08.010

Leake, B.E., Wooley, A.R., Arps, C.E.S, Birch, W.D., Gilbert, M.C., Grice, J.D., Hawthorne, F.C., Kato, A., Kisch, H.J., Krivovichev, V.G., Linhout, K., Laird, J., Mandarino, J., Maresch, W.V., Nickel, E.H., Schumacher, J.C., Stepenson, N.C.N., Whittaker, E.J.W., Youzhi, G., 1997. Nomenclature of Amphiboles: Report of the Subcommittee on Amphiboles of the International Mineralogical Association Commission on New Minerals and Mineral Names. Mineralogical Magazine, v. 61, p. 295-321.

Liu, Y., Fan, Y., Zhou, T., Xiao, X., White, N.C., Thompson, J., Hong, H., and Zhang, L., 2019. Geochemical characteristics of magnetite in Longqiao skarn iron deposit in the Middle-Lower Yangtze Metallogenic Belt, Eastern China. Mineralium Deposita, v. 54, p. 1229-1242. https://doi.org/10.1007/s00126-019-00871-x

Maia, M., Moreira, N., Vicente, S., Mirão, J., Noronha, F., and Nogueira, P., 2020. Multi-Stage Fluid System Responsible for Ore Deposition in the Ossa-Morena Zone (Portugal). Constraints in Cu-Ore Deposits Formation: Geology of Ore Deposits, v. 62(6), p. 508-534. https://doi.org/10.1134/S1075701520060094

Maia, M., Barrulas, P., Nogueira, P., Mirão, J., and Noronha, F., 2022a. In situ LA-ICP-MS trace element analysis of magnetite as a vector towards mineral exploration: A comparative case study of Fe-skarn deposits from SW Iberia (Ossa-Morena Zone). Journal of Geochemical Exploration, v. 234, 106941. https://doi.org/10.1016/j.gexplo.2021.106941

Maia, M., Roseiro, J., Nogueira, P., Noronha, F., Fuertes.Fuente, M., Cepedal, A., and Mirão, J., 2022b. New insights on the Escoural Orogenic gold district (Ossa-Morena Zone, SW Iberia): Geochemistry, fluid inclusions and stable isotope constraints from the Monfurado gold prospect. Ore Geology Reviews, v. 142, 104736. https://doi.org/10.1016/j.oregeorev.2022.104736

Makvandi, S., Ghasemzadeh-Barvarz, M., Beaudoin, G., Grunsky, E.C., McClenaghan, M.B., and Duchesne, C., 2016a. Principal component analysis of magnetite composition from volcanogenic massive sulfide deposits: Case studies from the Izok Lake (Nunavut, Canada) and Halfmile Lake (New Brunswick, Canada) deposits. Ore Geology Reviews, v. 72, p. 60-85. http://dx.doi.org/10.1016/j.oregeorev.2015.06.023

Makvandi, S., Ghasemzadeh-Barvarz, M., Beaudoin, G., Grunsky, E.C., McClenaghan, M.B., Duchesne, C., and Boutroy, E.C., 2016b. Partial least squares-discriminant analysis of trace element compositions of magnetite from various VMS deposit subtypes: Application to mineral exploration. Ore Geology Reviews, v.78, p. 388-408. http://dx.doi.org/10.1016/j.oregeorev.2016.04.014

Makvandi, S., Huang, X., Beaudoin, G., Quirt, D., Ledru, P., and Fayek, M., 2021. Trace element signatures in hematite and goethite associated with the Kiggavik–Andrew Lake structural trend U deposits (Nunavut, Canada). Mineralium Deposita, v. 56, p. 509-535. https://doi.org/10.1007/s00126-020-00980-y

Marimoto, N., Fabried, J., Ferguson, A.K., Ginzburg, I.V., Ross, M., Seifert, F.A., Zussman, J., Aoki, K., and Gottardi, G., 1988. Nomenclature of Pyroxenes. Mineralogy and Petrology, v. 39, p. 55-76. https://doi.org/10.1007/BF01226262

Martins, R., Mateus, A., Figueiras, J., Barroso, M., Oliveira, V. 2003. Post-metamorphic evolution of the Lower Cambrian section at Enfermarias (Moura, Portugal): its record and metallogenic implications. VI Congresso Nacional de Geologia, Lisboa (Portugal), Ciências da Terra (UNL), Lisboa, n.º esp. V, CD-ROM, B60-B63.

Mateus, A., Araújo, A., Gonçalves, M.A., and Matos, J., 2005. Variscan overthrusting, fluid flow and genesis of magnetite ore-bodies at the Azenhas area (Pedrógão, Ossa-Morena Zona, SE Portugal). Boletín Geológico y Minero, v.116(1), p. 3-22. ISSN 0366-0176.

Mateus, A., Munhá, J., Inverno, C., Matos, J.X., Martins, L., Oliveira, D., Jesus, A., and Salgueiro, R., 2013. Mineralizações no sector português da Zona de Ossa-Morena. In: R. Dias, A. Araújo, P. Terrinha, J.C. Kullberg (Eds.). Geologia de Portugal, v. 1, p. 577-619, Lisboa: Escolar Editora.

Matte, P., 2001. The Variscan collage and orogeny (480–290 Ma) and the tectonic definition of the Armorica microplate: a review. Terra Nova, v. 13(2), p. 122-128. https://doi.org/10.1046/j.1365-3121.2001.00327.x

Meinert, L.D., Dipple, G.M., Nicolescu, S., 2005. World skarn deposits. In: Economic Geology 100th Anniversary Volume, pp. 299–336. https://doi.org/10.5382/AV100.11

Meng, Y., Hu, Ruizhong, Huang, X., and Gao, J., 2017. Germanium in Magnetite: A Preliminary Review. Acta Geologica Sinica, v. 91, p. 711-729. https://doi.org/10.1111/1755-6724.13127

Moita P., Santos J.F., Pereira and M.F., 2009. Layered granitoids: interaction between continental crust recycling processes and mantle-derived magmatism: examples from the Évora Massif (Ossa–Morena Zone, southwest Iberia, Portugal). Lithos, v. 111, p. 125–141. https://doi.org/10.1016/j.lithos.2009.02.009

Moita P., Santos J.F., Pereira M.F., Costa M.M., and Corfu F., 2015. The quartz-dioritic Hospitais intrusion (SW Iberian Massif) and its mafic microgranular enclaves — Evidence for mineral clustering. Lithos v. 224-225, p. 78-100. https://doi.org/10.1016/j.lithos.2015.02.012

Moreira, N., Romão, J., Dias, R., Ribeiro, A., Pedro, J., 2019. The Finisterra-Léon-Mid German Cristalline Rise Domain; Proposal of a New Terrane in the Variscan Chain. In: Quesada, C., Oliveira, J. (eds) The Geology of Iberia: A Geodynamic Approach. Regional Geology Reviews. Springer, Cham. https://doi.org/10.1007/978-3-030-10519-8_7

Morris, R. and Canil, D., 2021. Cryptic magmatic skarn of the MerryWidow deposit, Vancouver Island (NTS 092L): Geoscience BC Summary of Activities 2020. Minerals, Geoscience BC, Report 2021-01, p. 47–54.

Nadoll, P., and Koenig, A.E., 2011. LA-ICP-MS of magnetite: methods and reference materials. Journal of Analytical Atomic Spectrometry, v. 26, p. 1872-1877. https://doi.org/10.1039/C1JA10105F

Nadoll, P., Mauk, J.L., Hayes, T.S., Koenig, A.E., and Box, S.E., 2012. Geochemistry of Magnetite from Hydrothermal Ore Deposits and Host Rocks of the Mesoproterozoic Belt Supergroup, United States. Economic Geology, v. 107, p. 1275-1292. https://doi.org/10.2113/econgeo.107.6.1275

Nadoll, P., Angerer, T., Mauk, J.L., French, D., and Walshe, J., 2014. The chemistry of hydrothermal magnetite: A review. Ore Geology Reviews: v. 61, p. 1-32. http://dx.doi.org/10.1016/j.oregeorev.2013.12.013

Nadoll, P., Mauk, J.L., Leveille, R.A., and Koenig, A.E., 2015. Geochemistry of magnetite from porphyry Cu and skarn deposits in the southwestern United States. Mineralium Deposita v. 50, p. 493–515. https://doi.org/10.1007/s00126-014-0539-y

Nielsen, R.L., and Beard, J.S., 2000. Magnetite–melt HFSE partitioning. Chemical Geology, v. 164, p. 21-34. https://doi.org/10.1016/S0009-2541(99)00139-4

Nyström, J.O., Billström, K., Henríquez, F., Fallick, A.E., and Naslund, R., 2008. Oxygen isotope composition of magnetite in iron ores of the Kiruna type in Chile and Sweden. GFF, v. 130, p. 177-188. https://doi.org/10.1080/11035890809452771

Oliveira, J.T., Oliveira, V., and Piçarra, J.M., 1991. Traços gerais da evolução tectono-estratigráfica da Zona de Ossa Morena, em Portugal: síntese crítica do estado actual dos conhecimentos. Comunicações dos Serviços Geológicos de Portugal, v. 77, p. 3-26.

Palarea-Albaladejo, J., and Martín-Fernández, J.A., 2015. zCompositions — R package for multivariate imputation of left-censored data under a compositional approach. Chemometrics and Intelligent Laboratory Systems, v.143, p. 85-96. http://dx.doi.org/10.1016/j.chemolab.2015.02.019

Palma, G., Reich, M., Barra, F., Ovalle, J.T., del Real, I., and Simon, A.C., 2021. Thermal evolution of Andean iron oxide–apatite (IOA) deposits as revealed by magnetite thermometry. Scientific Reports, v. 11, 18424. https://doi.org/10.1038/s41598-021-97883-3

Pedro, J., Araújo, A., Fonseca, P., Tassinari, C., and Ribeiro, A., 2010. Geochemistey and U-Pb zircon age of the internal Ossa-Morena Zone ophiolite sequences. A remnant of Rheic ocean in SW Iberia: Ofioliti, v. 35(2), p. 117-130. https://doi.org/10.4454/ofioliti.v35i2.390

Peng, H.-J, Hou, L., Sun, C., Zou, H., Wang, T.-R, and Ma, Z.-Z., 2021. Geochemistry of magnetite from the Hongniu–Hongshan Cu skarn deposit in Yunnan Province, SW China. Ore Geology Reviews, v.134, 104237. https://doi.org/10.1016/j.oregeorev.2021.104237

Pereira, M.F., Silva, J.B., and Chichorro, M., 2003. Internal Structure of the Évora High-grade Terrains and the Montemor-o-Novo Shear Zone (Ossa-Morena Zone, Portugal). Geogaceta, v.33, p.79-82.

Pereira, M.F., Silva, J.B., Chichorro, M., Moita, P., Santos, J.F., Apraiz, A., and Ribeiro, C., 2007. Crustal growth and deformational processes in the northern Gondwana margin: Constraints from the Évora Massif (Ossa-Morena zone, southwest Iberia, Portugal). Special Paper 423. The Evolution of the Rheic Ocean: From Avalonian-Cadomian Active Margin to Alleghenian-Variscan Collision, p. 333–358. https://doi.org/10.1130/2007.2423(16)

Pereira, M.F., Chichorro, M., Moita, P., Santos, J.F., Solá, A.M.R., Williams, I.S., Silva, J.B., and Armstrong, R.A., 2015. The multistage crystallization of zircon in calc-alkaline granitoids: U–Pb age constraints on the timing of Variscan tectonic activity in SW Iberia. International Journal of Earth Sciences, v. 104, p. 1167-1183. https://doi.org/10.1007/s00531-015-1149-3

Pereira, M.F., Gutíerrez-Alonso, G., Mourphy, J.B., Drost, K., Gama, C., and Silva J.B., 2017. Birth and demise of the Rheic Ocean magmatic arc(s): Combined U–Pb and Hf isotope analyses in detrital zircon from SW Iberia siliciclastic strata. Lithos, v. 278-281, p. 383-399. http://dx.doi.org/10.1016/j.lithos.2017.02.009

Peters, S.M, Alibabaie, N., Pack, A., McKibbin, S.J., Raeisi, D., Nayebi, N., Torab, F., Ireland, T., and Lehmann, B., 2019. Triple oxygen isotope variations in magnetite from iron-oxide deposits, central Iran, record magmatic

fluid interaction with evaporite and carbonate host rocks. Geology, v. 48, p. 211-215. https://doi.org/10.1130/G47858Y.1

Pin, C., Fonseca, P.E., Paquette, J.-L., Castro, P., and Matte, P., 2008. The ca. 350 Ma Beja Igneous Complex: a record of transcurrent slab break-off in the Southern Iberia Variscan Belt?. Tectonophysics, v. 461, p. 356–377. https://doi.org/10.1016/j.tecto.2008.06.001

Pisiak, L.K., Canil, D., Lacourse, T., Plouffe, A., and Ferbey, T., 2017. Magnetite as an Indicator Mineral in the Exploration of Porphyry Deposits: A Case Study in Till near the Mount Polley Cu-Au Deposit, British Columbia, Canada. Economic Geology, v. 112, p. 919-940. https://doi.org/10.2113/econgeo.112.4.919

Quesada, C., Fonseca, P.E., Munhá, J., Oliveira, J., and Ribeiro, A., 1994. The Beja-Acebuches Ophiolite (Southern Iberian Variscan fold belt). geologic characterization and geodynamic significance: Boletin Geologico y Minero, v. 105, p. 3–44.

Ribeiro A., Munhá J., Dias R., Mateus A., Pereira E., Ribeiro L., Fonseca P., Araújo A., Oliveira O., Romão J., Chaminé H., Coke C., and Pedro, J.C., 2007. Geodynamic evolution of the SW Europe Variscides. Tectononics 26:TC6009. https://doi.org/10.1029/2006TC002058

Ribeiro, A., Munhá, J., Fonseca, P.E., Araújo, A., Pedro, J.C., Mateus, A., Tassinari, C., Machado, G., and Jesus, A., 2010. Variscan ophiolite belts in the Ossa-Morena Zone (Southwest Iberia): Geological characterization and geodynamic significance. Gondwana Research, v. 17, p. 408-421. https://doi.org/10.1016/j.gr.2009.09.005

Rodriguez-Mustafa, M.A., Simon A.C., del Real I., Thompson, J.F.H., Bilenker, L.D., Barra, F., Bindeman, I., and Cadwell, D., 2020. A Continuum from Iron Oxide Copper-Gold to Iron Oxide-Apatite Deposits: Evidence from Fe and O Stable Isotopes and Trace Element Chemistry of Magnetite. Economic Geology, v. 115, p. 1443-1459. https://doi.org/10.5382/econgeo.4752

Rojo-Pérez, E., Fuenlabrada, J.M., Linnemann, U., Arenas, R., Martínez, S.S., Fernández, R.D., Parra, L.M.M., Matas, J., Andonaegui, P., and Fernández-Suárez, J., 2021. Geochemistry and Sm–Nd isotopic sources of Late Ediacaran siliciclastic series in the Ossa–Morena Complex: Iberian–Bohemian correlations. International Journal of Earth Sciences, v. 110, p. 467-485. https://doi.org/10.1007/s00531-020-01963-0

Rose, A.W., Herrick, D.C., and Deines, P., 1985. An Oxygen and Sulfur Isotope Study of Skarn-Type Magnetite Deposits of the Cornwall Type, Southeastern Pennsylvania. Economic Geology, v. 80, p. 418-443. https://doi.org/10.2113/gsecongeo.80.2.418

Rudnick, R.L., and Gao, S., 2003. The composition of continental crust Eds: Heinrich D. Holland, Karl K. Turekian. Treatise on Geochemistry, Pergamon, 2003, p. 1–64. https://doi.org/10.1016/B0-08-043751-6/03016-4.

Salgueiro, R., 2011. Caracterização e génese das mineralizações de magnetite – sulfuretos em Monges (Santiago do Escoural, Montemor-o-Novo) e ensaio comparativo com as suas congéneres em Orada-Vale de Pães (Serpa-Vidigueira). PhD Thesis, Univ. Lisboa, 524 p.

Salgueiro, R., Mateus, A., and Inverno, C., 2010. Caracterização e génese do skarn ferrífero de Orada (Zona de Ossa-Morena). E-Terra, v. 20(3).

Salgueiro, R., Mateus, A, and Inverno, C., 2012. Mineralizações de magnetite e sulfuretos de monges (Santiago do Escoural, Montemor-o-Novo), Vale de Pães (Cuba-Vidigueira) e Orada (Pedrógão, Serpa): Síntese de ensaio comparativo. Boletim de Minas, v. 47(1), p. 27-30.

Sánchez-García, T., Chichorro, M., Solá, A.R., Álvaro, J.J., Díez-Montes, A., Bellido, F., Ribeiro, M.L., Quesada, C., Lopes, J.C., Dias da Silva, Í., González-Clavijo, E., Gómez Barreiro, J., and López-Carmona, A., 2019. The Cambrian-Early Ordovician Rift Stage in the Gondwanan Units of the Iberian Massif. In: Quesada, C. & Oliveira J.T. (Eds) The Geology of Iberia: A Geodynamic Approach, Vol. 2. The Variscan Cycle. Springer Nature, Switzerland, p. 27-74. https://doi.org/10.1007/978-3-030-10519-8

Sciuba, M., and Beaudoin, G., 2021. Texture and Trace Element Composition of Rutile in Orogenic Gold Deposits. Economic Geology, v. 116, p. 1865-1892. https://doi.org/10.5382/econgeo.4857

Serviço de Fomento Mineiro, 1960. Carta Geológica e Mineira da Região de Santiago do Escoural (Montemor-o-Novo) à escala 1:5000.

Serviços de Fomento Mineiro, 1965. Carta Geológica da Região de Pedrõgão-Orada à escala 1:10 000.

Shanks, W.C., 2013. Stable Isotope Geochemistry of Mineral Deposits, Eds: Heinrich D. Holland, Karl K. Turekian, Treatise on Geochemistry, Elsevier, p. 59-85. http://dx.doi.org/10.1016/B978-0-08-095975-7.01103-7

Silva, J.B., Araújo, A.A., and Fonseca, P., 1988. Novos elementos sobre cartografia geológica de uma área a leste de Santiago do Escoural (Montemor- o - Novo). Departamento de Geologia da Faculdade de Ciências de Lisboa, 10 p.

Simancas, J.F., 2019. Variscan Cycle. In: Quesada C., Oliveira J. (Eds) The Geology of Iberia: A Geodynamic Approach. Regional Geology Reviews. Springer, Cham. https://doi.org/10.1007/978-3-030-10519-8_1

Steadman, J.A., Large, R.R., Olin, P.H., Danyushevsky, L.V., Meffre, S., Huston, D., Fabris, A., Lisitsin, A., and Wells, T., 2021. Pyrite trace element behavior in magmatic-hydrothermal environments: An LA-ICPMS imaging study. Ore Geology Reviews, v. 128, 103878. https://doi.org/10.1016/j.oregeorev.2020.103878

Sun, G., Zeng, Q., Zhouf, L., Wang, Y., and Chen, P., 2020. Trace element contents and in situ sulfur isotope analyses of pyrite in the Baiyun gold deposit, NE China: Implication for the genesis of intrusion related gold deposits. Ore Geology Reviews, v. 118, 103330. https://doi.org/10.1016/j.oregeorev.2020.103330

Taylor, H.P., 1968. The oxygen isotope geochemistry of igneous rocks. Contrib. Mineral. Petrol., v. 19, p. 1–71.

Taylor, H.P., 1974. The application of oxygen and hydrogen isotope studies to problems of hydrothermal alteration and ore deposition. Economic Geology, v. 69, p. 843-883. https://doi.org/10.2113/gsecongeo.69.6.843

Tornos, F., Inverno, C.M.C., Casquet, C., Mateus, A., Ortiz, G., and Oliveira, V., 2004. The metallogenic evolution of the Ossa-Morena Zone. Journal of Iberian Geology, v. 30, p. 143-181.

Tornos, F., Galindo, C., Casquet, C., Pevida, L.R., Martínez, C., Martínez, E., Velasco, F., and Iriondo, A., 2006. The Aguablanca Ni–(Cu) sulfide deposit, SW Spain: geologic and geochemical controls and the relationship with a midcrustal layered mafic complex. Mineralium Deposita, v. 41, p. 737–769. https://doi.org/10.1007/s00126-006-0090-6

Tornos, F., Galindo, C., Darbyshire, F., Casquet, C., and Noble, S.R., 2021. Isotope geochemistry, age, and origin of the magnetite-vonsenite mineralization of the Monchi Mine, SW Iberia. Journal of Iberian Geology, v. 47, p. 64-84. https://doi.org/10.1007/s41513-020-00159-4

Troll, V.R., Weis, F.A., Jonsson, E., Andersson, U.B., Majidi, S.A., Hogdahl, K., Harris, C., Millet, M.-A., Chinnasamy, S.S., Koojiman, E., and Nilsoon K.P., 2019. Global Fe–O isotope correlation reveals magmatic origin of Kiruna-type apatite-iron-oxide ores. Nature Communications, v. 10, 1712. https://doi.org/10.1038/s41467-019-09244-4

Velasco, F., and Amigó, J.M., 1981. Mineralogy and origin of the skarn from Cala (Huelva, Spain). Economic Geology, v. 76, p. 719-727. https://doi.org/10.2113/gsecongeo.76.3.719

Xie, Q., Zhang, Z., Hou, T., Jin, Z., and Santosh, M., 2017. Geochemistry and oxygen isotope composition of magnetite from the Zhangmatun deposit, North China Craton: Implications for the magmatic-hydrothermal evolution of Cornwall-type iron mineralization. Ore Geology Reviews, v. 88, p. 57-70. https://doi.org/10.1016/j.oregeorev.2017.04.014

Yan, H., Tian, J., Yu, D., Di, J., Li, J., and Liu, Z., 2021. Hydrothermal origin of the Naojiao Fe deposit in Lingxiang district, Eastern China: Evidence from in-situ LA-ICP-MS magnetite trace element analysis. Solid Earth Sciences, v. 6, p. 268-282. https://doi.org/10.1016/j.sesci.2021.06.004

Yuan, K., Lee, S.S., Cha, Wonsuk, Ulvestad, A., Kim, H., Abdilla, B., Sturchio, N.C., and Fenter, P., 2019. Oxidation induced strain and defects in magnetite crystals. Nature Communications, v. 10, 703. https://doi.org/10.1038/s41467-019-08470-0

Wu, C., Chen, H., Hong, W., Li, D., Liang, P., Fang, J., Zhang, L., and Lai, C., 2019. Magnetite chemistry and implications for the magmatic-hydrothermal ore-forming process: An example from the Devonian Yuleken porphyry Cu system, NW China. Chemical Geology, v. 522, p. 1-15. https://doi.org/10.1016/j.chemgeo.2019.04.022

Zhang, Y., Hollings, P., Shao, Y., Li, D., Chen, H., and Li, H., 2020. Magnetite texture and trace-element geochemistry fingerprint of pulsed mineralization in the Xinqiao Cu-Fe-Au deposit, Eastern China. American Mineralogist, v. 105, p. 1712-1723. https://doi.org/10.2138/am-2020-7414

Chapter 5

A machine learning approach to the classification of ore deposits: Random Forest classification of in-situ LA-ICP-MS trace element analysis of magnetite

To be submitted.

Co-authors:

Pedro Nogueira

Pedro Barrulas

José Mirão

Fernando Noronha

Abstract

The Ossa-Morena Zone (SW Iberia) hosts several iron deposits which display the potential for future mineral exploration projects, both in Portugal and Spain. In this work we explore extensive mineral geochemistry results using a machine learning approach to assess the potential of using Random Forest for the classification of magnetites from SEDEX-VMS (Montemor-o-Novo Iron Complex) and Skarn deposits (Alvito, Azenhas, and Orada), based on LA-ICP-MS trace element analyses.

Four different Random Forest models were designed: i) Model 1 corresponds to a two-category classification (Skarn vs. Volcanogenic-Exhalative) using randomly selected analysis from the dataset for the Random Forest classifier training; ii) Model 2 is a four-category classification that considers four types of magnetites: Primary Volcanogenic, Secondary Volcanogenic, Primary Skarn, and Secondary Skarn, using the same Random Forest classifier training dataset used in Model 1; iii) Model 3 is a five-category classification that uses the fields defined in the conventional Al + Mn + Ca (wt. %) vs Ti + V (wt. %) scatterplot widely used in the classification of magnetite trace element data. In this last case the training dataset was constructed using literature data from deposits which are represented in the discriminant fields of this conventional diagram (Skarn; IOCG; IOA; Porphyry; BIF); iv) Model 4 is a two-category classification (Skarn vs VMS) Random Forest classifier that uses literature data from skarn and VMS magnetite as the training dataset.

Models 1 and 4 were the ones that showed better accuracies in the Random Forest Confusion Matrix, suggesting that using more than two-categories for the classification of data should be carefully considered. In Model 1, 100 % of the analyses of volcanogenic-exhalative magnetite were classified as so, and 67.2 % of the skarn magnetite analysis of the testing dataset were also correctly classified.

Model 4 was the one that provided more information regarding the classification of the ore deposits by applying Random Forest classification of the magnetite data. This model was not trained using random analyses from the testing dataset, contrariwise literature data was used so that bias was avoided. Using this model, 100 % of the magnetite from the volcanogenic-exhalative deposits from the Montemor-o-Novo Iron Complex was classified as VMS, and 65 % of the skarn deposits magnetite was correctly classified as Skarn.

Applying a Random Forest classification to magnetite chemistry has proven to be a good approach for the classification of ore deposits, which is essential to define robust geological models that can be applied in mineral exploration.

Keywords: Machine Learning; Random Forest; LA-ICP-MS; Geochemistry; Magnetite

5.1 Introduction

One of the most challenging tasks in ore deposit exploration is the definition of suitable metallogenic models, based on a multitude of sources of data. The definition of such models in the early stages of exploration is an important time and money saver, and strongly relies on an early consistent classification of the ore deposit. With such goals in mind, magnetite trace element data have been proficiently used in the classification of ore deposits during recent years (e.g. Chen et al., 2019; Liu et al., 2019; Ayupova et al., 2020; Qi et al., 2021). Magnetite is one of the most common minerals in deposits formed in different metallogenic setting (e.g. IOA, Skarn, IOCG, Porphyry, VMS). Therefore, its composition has been found to provide valuable information to constrain the conditions and mechanisms related to ore deposition, which can ultimately allow to distinguish between barren and mineralized areas.

The determination of magnetite trace element composition by laser ablation-inductively coupled plasma-mass spectrometry (LA-ICP-MS) has proven to contribute to the correct classification of ore deposits using conventional discriminatory diagrams (Dupuis and Beaudoin, 2011; Dare et al., 2014; Nadoll et al., 2014; 2015). Nevertheless, the chemical analysis of magnetite often ends in large datasets with numerous variables, constituting a challenge for data analysis of the results.

The application of supervised classification methods, such as Random Forest (RF), to the trace element composition of magnetite is increasingly used to classify ore deposits (e.g. Hong et al., 2021; Bédard et al., 2022). Other data mining methods, such as Principal Component Analysis (PCA), have provided good results in many cases (Makvandi et al., 2016a; Canil et al., 2016; Maia et al., 2022a). As pointed out by O´Brien et al. (2015), RF classification, and other machine learning approaches to explore geochemical data are not often used as an auxiliary method in mineral exploration although the results may be extremely valuable (Gregory et al., 2019; Zhong et al., 2021).

The use of RF for the classification of magnetite trace element data presents an enormous advantage when compared to conventional biplot classification. Random Forest facilitates the classification of multi-dimensional datasets (e.g. multiple element analyses), which allow for a more robust inspection of data and, consequently, more robust geological models.

In this work, RF classification is tested on a large dataset of magnetite trace element analysis published in Maia et al. (2022a) and Maia et al. (subm.). The analyses from these works were performed in magnetites from three volcanogenic-exhalative deposits (i.e. Monges, Vale da Arca, Serrinha) that belong to the Montemor-o-Novo Iron Complex (MIC), as well as in three Fe-skarn deposits (i.e. Alvito, Azenhas, and Orada) from the Ossa-Morena Zone (SW Iberia). For this work four RF models have been tested to classify over 470 LA-ICP-MS magnetite analyses. Moreover, when available, magnetite data from the literature has also

been used to train the RF classifiers. The classification was compared to the conventional classification diagrams (Dupuis and Beaudoin, 2011; Nadoll et al., 2014, 2015) and the combination of both methods revealed great advantages in the correct classification of ore deposits.

5.2 Geologic settings of the selected deposits

For the present study, magnetite data (Maia et al., 2022a; Maia et al., subm.) from a total of six iron deposits located at the SW of Ossa-Morena Zone (**Fig. 5.1a**; Julivert et al., 1972; Farias et al., 1987) have been inspected. The selected deposits are located in the Montemor-o-Novo – Ficalho metallogenic province (Mateus et al., 2013), a subdivision of the Évora-Aracena belt (Tornos et al., 2004).

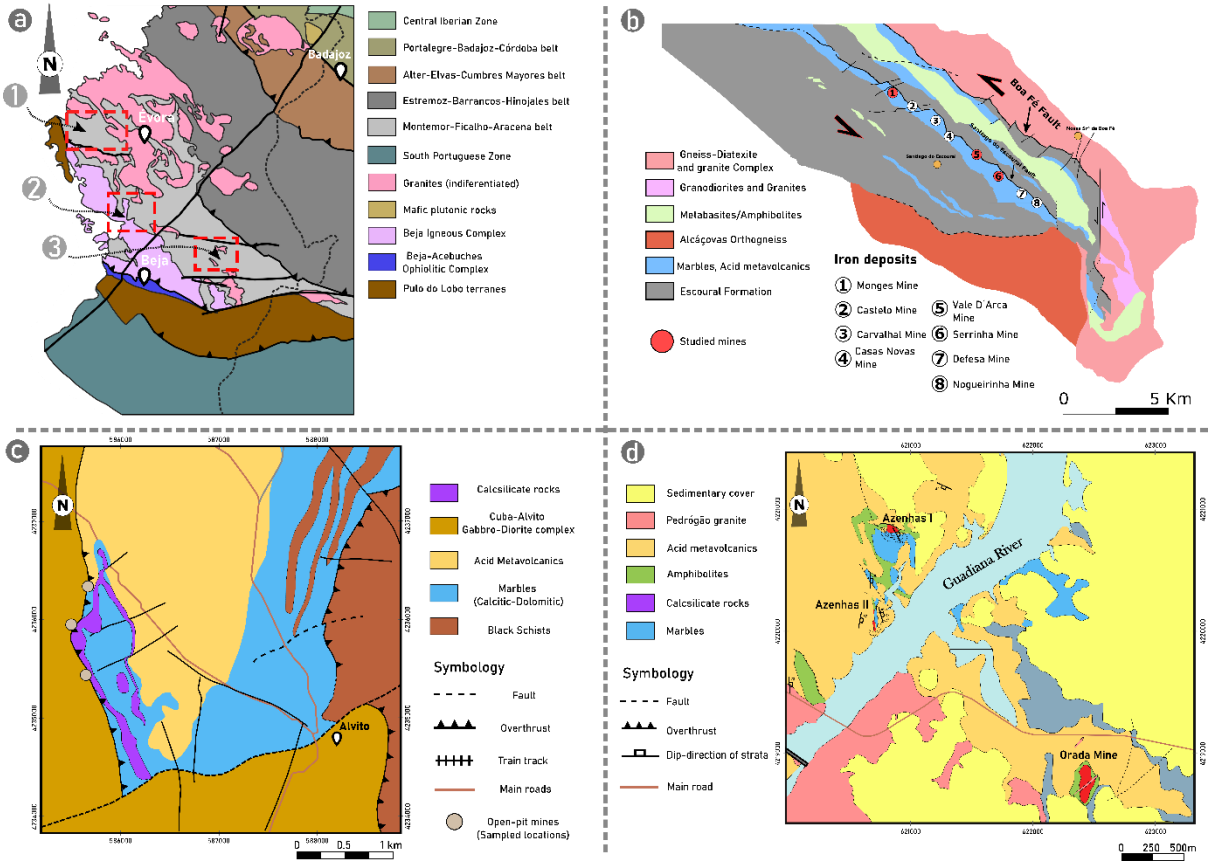

Figure 5.1. Geological mapping of the selected deposits for this study. a. Representative geotectonic arrangement of Ossa-Morena Zone (Julivert et al., 1972) with location of the Fe deposits selected for this study (red rectangles; adapted from Jesus et al., 2020; Maia et al., 2022). b. Geological map of the Montemor-o-Novo Shear Zone (adapted from Chichorro, 2006; Maia et al., 2022b) with the location of the main iron deposits that integrate the Montemor-o-Novo Iron Complex (Andrade et al., 1949; Goínhas and Martins, 1986). The circles filled in red represent the deposits selected for this study. c. Geological map of the Alvito area (adapted from Carvalhosa and Zbyszewski, 1971; Gomes, 2000; Gomes and Fonseca, 2006; Maia et al., 2022) with representation of the open-pit mining location in which magnetite samples were collected and further examined by LA-ICP-MS (Maia et al.,

2022). d. Geological map of the Azenhas (Azenhas I and Azenhas II) and Orada deposits (adapted from Serviço de Fomento Mineiro, 1965; Maia et al., submm.).

5.2.1 Montemor-o-Novo Iron Complex

Three of the selected deposits, Monges, Vale da Arca, and Serrinha deposits, belong to the volcanogenic-exhalative Montemor-o-Novo Iron Complex (MIC; Maia et al., subm. The MIC comprises several iron deposits (**Fig. 5.1b**), many of which were mined during the early 20th century, and their main metallogenic input is associated with a early-middle Cambrian intracontinental rifting stage (Variscan cycle; Ribeiro et al., 2007). The iron ores are mainly hosted by calcite-dolomite rocks from the Monfurado Formation (Chichorro, 2006), which were metasomatized in the late-stages of the Variscan cycle by means of fluid circulation promoted by the Montemor-o-Novo Shear Zone activity (Pereira et al., 2003, 2006, 2007). The host-rocks of the iron ores often display mineral assemblages and textures typical of metasomatized domains, with the iron ores being surrounded by amphibole and pyroxene (**Fig. 5.2a** and **5.2b**). Recent works have proposed a combined volcanogenic-exhalative (SEDEX-VMS) origin for the MIC deposits (Salgueiro, 2011), with ore deposition being associated with the input of hydrothermal fluids during the early stages of oceanization of the Rheic, by means of seafloor hydrothermal venting systems. Two magnetite types were mainly identified in the MIC deposits orebodies, classified as first-generation magnetite (Mag I) and second-generation magnetite (Mag II).

5.2.2 Alvito deposit

The Alvito deposit (**Fig. 5.1c**) is an Fe-skarn deposit associated with the emplacement of a gabbro-diorite suite, that is part of the Beja Igneous Complex (**Fig. 5.1a**). The emplacement of this magmatic body started at 350 Ma ± 5 Ma (Pin et al., 2008), and in the Alvito area it contacts with carbonate rocks and generates an exoskarn that hosts most of the massive magnetite. The ore deposition is attributed to the retrograde stages of metassomatism (Maia et al., 2022a), and magnetite is accompanied by a diopside-hedenbergite rich matrix (**Fig. 5.2c**).

5.2.3 Azenhas- Orada deposits

The Azenhas-Orada deposits (**Fig. 5.1d**) are a complex of iron orebodies in which mining took place up until the second half of the 20th century. The massive orebodies are mostly hosted in metasomatized allochthonous amphibolites (Tornos et al., 2004; Mateus et al., 2005; Araújo et al., 2005) which are tectonically imbricated over Cambrian carbonates. The genesis of these

deposits has been previously discussed, with authors attributing their genesis to a prolonged thermal gradient associated with the tectonic imbrication. This tectonic arrangement is thought to have favored the deposition of magnetite related with the metassomatism of the amphibolites. Recently, magnetite trace element analysis revealed that the genesis of these deposits might be associated with higher temperature processes (Maia et al., 2022a). Although first generation magnetite ores (Mag I) are mainly found hosted in the amphibolites (**Fig. 5.2d**), they also occur in banded sections within the carbonate rocks at the Azenhas deposit (**Fig. 5.2e**). Second generation magnetite has been described for the Azenhas deposit (Azenhas Mag II) and is found in thin veinlets within epidote-rich rocks and is assumed as a result of later hydrothermal processes.

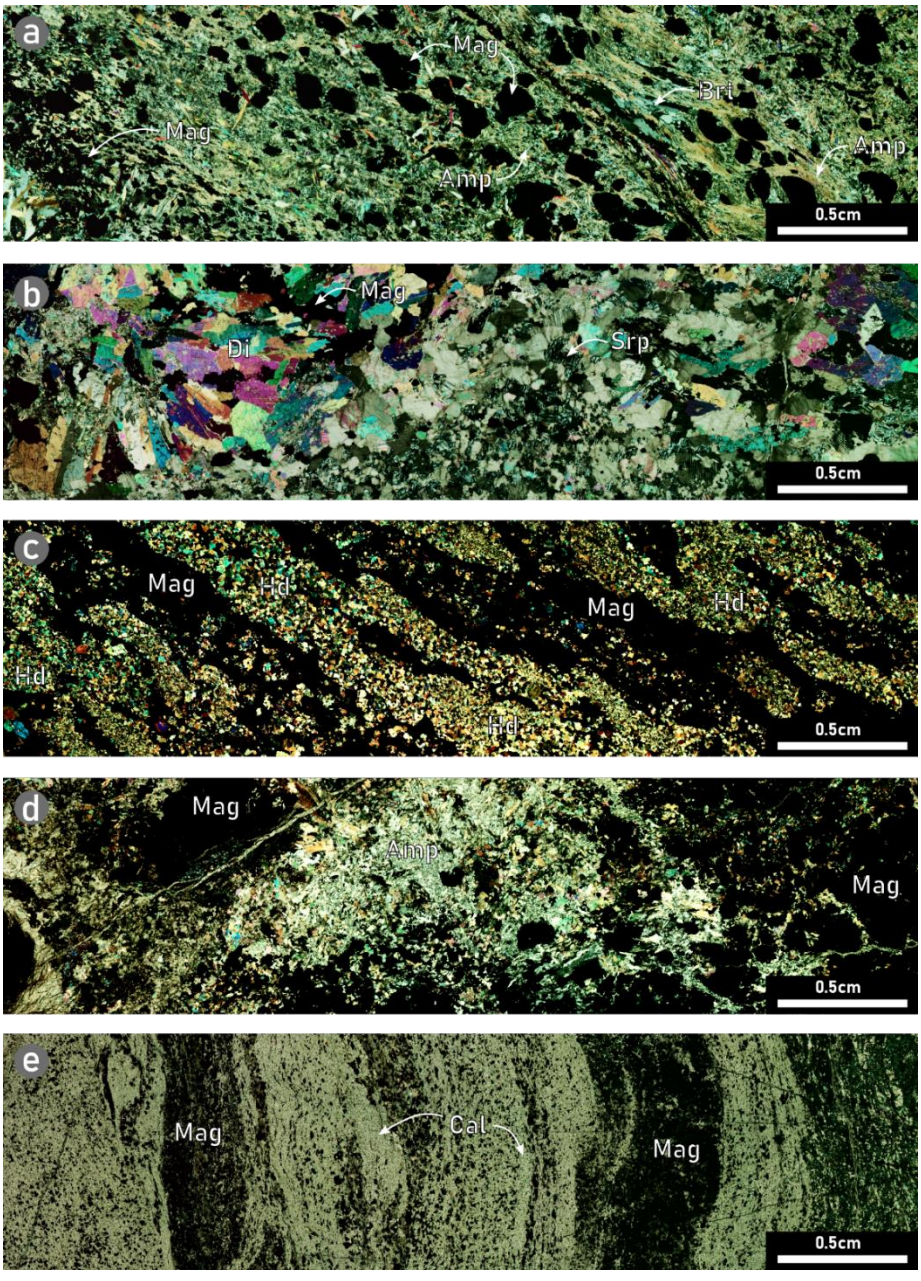

Figure 5.2. Microphotography of representative mineral assemblages and textures described for the orebodies of the MIC, Alvito, and Azenhas deposits. a. Cross polarized light (CPL) microphotography of primary magnetite (Mag) disseminated in a highly metasomatized marble from the Monges deposit, with amphiboles (Amp) surrounding magnetite. b. CPL microphotography of a marble from the Vale da Arca deposit with disseminated primary magnetite, in which calcite and serpentine (Srp) are observed and diopside (Di) seems to have formed in association with magnetite c. CPL microphotography representative of the mineral assemblages found in the orebodies of the Alvito skarn deposit, with massive magnetite in clear association with hedenbergite (Hd). d. CPL microphotography of the mineral assemblages associated with the massive magnetite bodies of the Azenhas skarn deposit in which magnetite has developed in an amphibole rich matrix. e. CPL microphotography of the banded fine grained magnetite crystals found in the marbles from the Azenhas skarn deposit.

5.3 Methods and data source

5.3.1 Magnetite trace element data

Herein the Random Forest supervised classification method is applied to the data gathered in previous works (Maia et al., 2022a; Maia et al., subm.), with the goal of inspecting the validity of this approach in the classification of ore deposits from OMZ by using magnetite trace element composition.

Trace element data of magnetite from OMZ deposits is inspected throughout this works, including volcanogenic-exhalative ore bodies from the Montemor-o-Novo Iron Complex (MIC) and the ore bodies of the Alvito, Azenhas, and Orada skarn deposits. Previous works were able to identify textural and geochemical features that allowed for discriminate different magnetite generations and define criteria for the discrimination of the ore-forming processes. For complete analytical conditions please refer to Maia et al. (2022a).

Additionally, literature data were used as the training dataset in some of the proposed RF models, which include LA-ICP-MS analyses of magnetite from Banded Iron Formation (BIF) deposits (Araújo et al., 2019), Iron-Oxide Copper and Gold (IOCG) deposits (Wang et al., 2020), Porphyry-type deposits (Huang et al., 2019), Kiruna-type Iron Oxide Apatite (IOA) deposits (La Cruz et al., 2020), skarn deposits (Hu et al., 2017), and volcanogenic massive sulfide from the Izok Lake VMS (Makvandi, 2015; Makvandi et al., 2016a; 2016b). Equal number of analyses from each deposit was considered for the preparation of the training dataset and a statistical summary is provided in **Table 5.1**.

5.3.2 Random Forest classification

Random Forest (Breiman, 2001) is a supervised classification algorithm that uses a wide number of decision trees (herein we used a minimum of 500, by default), to classify data. In

this work, Random Forest was processed in the R environment by using the *randomForest* package (Liaw and Wiener, 2002) in combination with the *caret* package.

Prior to classification, three tasks of major importance have been dealt with, i) pre-processing of the testing dataset to perform substitution of missing values (NA) which result from elements with values below LOD; ii) inspect the variable importance on the testing dataset for the selection of the elements to be used in the RF models.; and iii) delineation of RF models and selection of the training dataset.

5.3.2.1 Pre-processing of testing datasets

As previously referred, the testing dataset used in this study was gathered from other works (Maia et al., 2022a; Maia et al., subm.) which thoroughly discussed LA-ICP-MS analysis of magnetite from Fe deposits from the OMZ (**Fig. 5.1a**). One of the biggest issues with dealing with wide geochemical datasets is the presence of missing values (censored values), which are usually associated with the detection limits of the equipment used for the analysis. To circumvent this limitation, the substitution of censored data was performed using the *zCompositions* package (Palarea-Albaladejo and Martín-Fernandez, 2015) in R-programming language environment. This package allows the inspection of the censored values using the *zPatterns* function so that the variables with over 40 % missing values can be excluded from the dataset (Hron et al., 2010). The remaining dataset (< 40 % missing values) moves on for substitution of censored data which considers the limits of detection of each variable, i.e. chemical element, using an input based on log-ratio Expectation-Maximisation (EM) algorithm through the *lrEM* function in the *zCompositions* package (Palarea-Albaladejo and Martín-Fernandez, 2015).

5.3.2.2 Variable importance

In order to perform robust RF models, the contribution of the variables in a particular dataset needs to be inspected. The element importance is the result of the contribution of each element and is given by the mean decrease in Gini index.

The dataset was divided according to the deposit to which each magnetite analysis corresponded; therefore, two datasets were used separately, one composed of analysis in magnetite from the MIC volcanogenic-exhalative deposits with 208 entries (magnetite analyses), and the other with the analysis performed in magnetite from the Alvito, Azenhas, and Orada skarn deposits with 265 entries.

Element importance was inspected separately in both datasets, showing that Ti, Mn, Ga, Zn, V, Al, Mg, Sn, Mo, Zr, and Y are the elements that most influence the RF classification in the volcanogenic-magnetite, whereas Ti, Mn, Ga, Zn, V, Al, Mg, Sn, Mo, Zr, Nb, Co, Hf, Ta, and Ni were the elements with a higher importance in the case of the magnetite dataset from skarn deposits (**Fig. 5.3**). The volcanogenic-exhalative and skarn deposits dataset does not have the same number of variables since some elements from each dataset had to be removed due to the high percentage (> 40%) of missing values revealed by *zPatterns*. **Figure 5.3** shows the variable importance plots for the elements inspected in both datasets, where the bars with grey dashed borders represent the elements that were selected to integrate the testing and training datasets used in the RF classifiers (Ti, Mn, Ga, Zn, Al, Mg, Zr, Nb, Co, Ta, Ni).

The element selection not only relied on the variable importance scores but also on the fact that magnetite from the skarn deposits is discriminated by their higher concentrations of high-field strength elements (e.g., Nb, Zr, Hf, and Ta; Maia et al., 2022a).

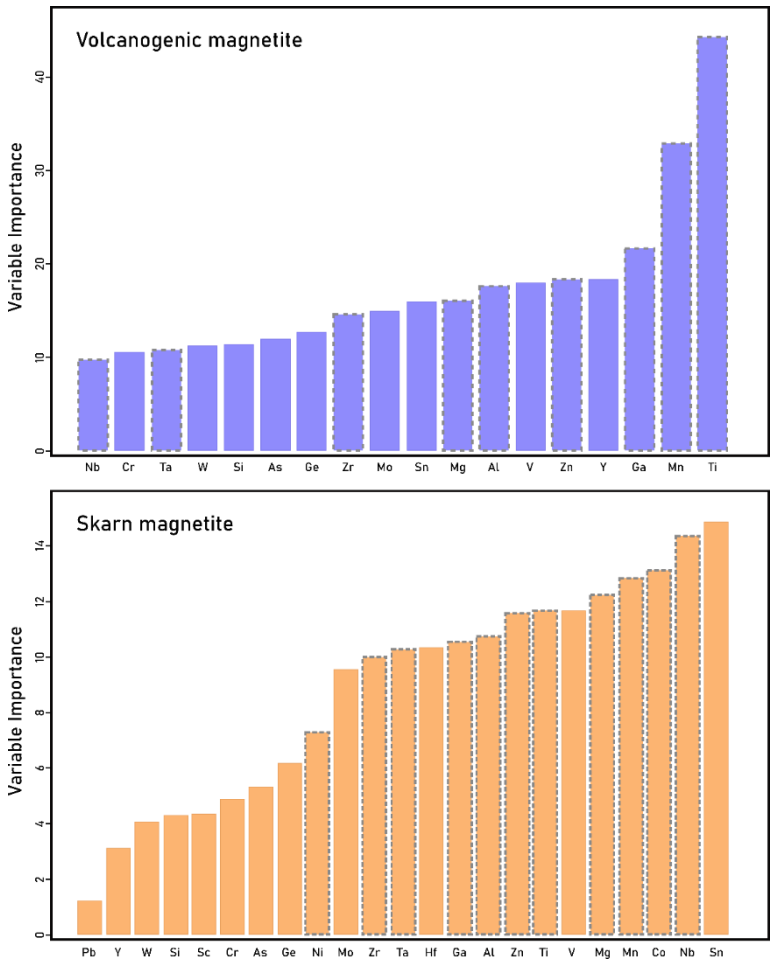

Figure 5.3. Variable importance plot of the LA-ICP-MS trace element data for the volcanogenic magnetite from the MIC deposits (histogram at the top) and magnetite from the Alvito, Azenhas, and Orada skarn deposits (histogram at the bottom).

5.3.2.3 Model construction

Following the selection of elements that integrate the testing dataset, with over 470 magnetite analyses, four model approaches were adopted for magnetite classification.

1) Model 1 considers the discrimination according two main categories, Skarn and Volcanogenic-Exhalative. For this model, the training dataset was constructed using magnetite analysis from the complete dataset. To avoid any classification bias, the same number of magnetite analysis from skarn deposits and the volcanogenic-exhalative deposits was provided to the training dataset. The training dataset was then composed of 30 analyses of each category.
2) Model 2 was performed contemplating four categories that were chosen considering the magnetite types described for both deposit types, as follows: First and second generation volcanogenic-exhalative magnetite (Mag I and Mag II), and first and second-generation skarn magnetite (Mag I and Mag II). The testing dataset that was used for this model is the same as the one used in the former model, but the training dataset was constructed based on an equal number of analyses from each magnetite type.
3) Model 3 was performed considering five categories (Skarn, BIF, IOCG, IOA, and Porphyry) that were selected to meet the main fields defined in the Al + Mn vs Ti + V magnetite discriminatory diagram (Dupuis and Beaudoin, 2011; Nadoll et al., 2014; 2015). The goal of this model was to inspect the accuracy of magnetite classification using literature data as the training dataset and compare the results of the RF classifier with those obtained by the conventional discrimination diagrams. The literature data (**Table 5.1**) chosen for this model was the one described in detail in section 4.2.2. Random Forest classifier was performed in the complete dataset of magnetite from the volcanogenic-exhalative MIC deposits and the Alvito, Azenhas, and Orada skarn deposits. The elements selected for the previous models had to be adjusted once most of the literature data did not simultaneously include all the elements analyzed in the testing dataset. Therefore, the elements selected for this RF model were Mg, Al, Ti, Mn, Co, Ni, Zn, and Ga.
4) Model 4 was performed using two categories to distinguish between skarn and volcanogenic massive sulfides (VMS) deposits, and literature data of both deposit types were used in the training dataset. This model mainly aimed in characterizing the affinity between the trace element composition of magnetites from the debatably classified SEDEX-VMS MIC deposits and data from other VMS deposits. The elements selected for this model followed the same criteria applied in Model 3. The training dataset was constructed using literature VMS data (**Table 5.1**).

The criteria to consider a correct classification of the deposits was adopted from Gregory et al. (2019). Therefore, accuracies above 65 % are considered as a correct classification, between 55 % and 65 % inconclusive and below 35 % are deemed as incorrect.

Table 5.1. Summary statistics of the literature LA-ICP-MS magnetite trace element data used in the training datasets of Ramdom Forest Model 3 and Model 4.

Reference	Hu et al., 2017				Araújo et al., 2019				Wang et al., 2020				Huang et al., 2019				La Cruz et al., 2020				Makvandi, 2016			
Deposit type	Skarn				BIF				IOCG				Porphyry				IOA				VMS			
	Min.	Max.	Average	σ	Min.	Max.	Average	σ	Min.	Max.	Average	σ	Min.	Max.	Average	σ	Min.	Max.	Average	σ	Min.	Max.	Average	σ
Mg	3041.8	5905.8	4364.4	871.2	1466.1	2736.9	1938.1	382.6	5.9	240.0	69.4	62.9	36.1	1060.0	259.5	272.3	503.0	11320.0	8311.6	2644.5	9.0	1490.0	157.1	330.0
Al	4232.5	10062.6	7371.1	1638.4	0.0	364.3	234.7	93.7	154.0	437.0	343.1	97.7	305.0	1690.0	1033.7	489.8	7.1	110.0	39.1	33.1	66.0	3690.0	1109.0	1246.5
Ti	859.4	1554.7	1216.3	207.9	52.8	97.5	79.3	11.3	41.0	130.0	65.5	21.3	252.0	1980.0	769.9	399.5	5.6	22.0	9.9	5.4	21.0	3670.0	602.0	856.6
Mn	1315.4	6329.6	2407.8	1052.0	2.7	35.8	14.9	9.2	18.9	188.0	65.5	46.8	462.0	2740.0	1296.3	565.0	57.1	374.0	247.9	129.3	203.0	1929.0	801.1	574.7
Co	43.4	70.5	54.3	8.4	2.3	3.1	2.7	0.3	80.5	95.3	89.3	4.0	4.6	71.8	33.5	24.9	60.5	153.0	115.2	21.6	0.9	64.0	18.6	17.2
Ni	6.7	10.4	8.3	1.0	0.0	11.1	6.6	3.1	106.0	174.0	141.9	22.7	16.3	51.6	33.4	10.9	175.0	253.0	227.0	21.8	0.0	93.0	20.8	27.9
Zn	144.9	604.2	269.4	126.8	30.4	60.7	44.6	9.2	4.6	12.2	7.1	2.5	61.3	930.0	436.1	236.1	15.6	56.9	39.5	13.7	2.0	1036.0	151.7	214.8
Ga	10.5	31.6	23.3	6.3	1.5	4.6	2.7	1.0	9.3	16.6	13.3	2.0	14.3	99.4	48.4	30.2	0.5	1.5	0.7	0.4	2.7	176.7	50.0	45.8

5.4 Results and Discussion

5.4.1 Trace element composition of magnetite

Distinguishing features between magnetite from the studied deposits have been described by examining textural characteristics, trace element contents, and oxygen isotope signatures, and have been pointed out in detail by Maia et al. (2022a) and Maia et al. (subm.).

The trace element analysis of the magnetite from the volcanogenic-exhalative MIC deposits revealed that their geochemical signature is contrastingly different to that of magnetite from skarn deposits. Magnetite from the MIC has a lower concentration in most trace elements, and specific differences are found when inspecting the contents in HFSE, which are usually found in magnetites formed under magmatic-hydrothermal conditions (Nadoll et al., 2015). The petrogenetic discrimination (Dare et al., 2014) suggests that magnetite from volcanogenic-exhalative MIC deposits have trace element profiles that closely overlap those gathered from low-temperature hydrothermal magnetite. Furthermore, the Co vs. Zn discriminant diagram proposed by Maia et al. (subm.) shows that magnetite I from the MIC deposits plot close to the field of other low-temperature hydrothermal deposits, which was constructed using literature data such as BIF magnetite formed under the influence of fluids inputted by hydrothermal vents (Araújo et al., 2019). When inspecting the concentrations of the variables selected to integrate the datasets for RF classification (Mg, Al, Ti, Mn, Co, Ni, Zn, Ga, Zr, Nb, Ta) using a radar plot (**Fig. 5.4**) we concluded that Mn, Al and Mg are the ones that show higher concentrations in magnetite from the MIC deposits (Monges, Serrinha, and Vale da Arca). Radar representation of geochemical data is a visual method for data comparison. In the presented case (**Fig. 5.4**) it is shown that magnetite from the MIC deposits share similar trace element profiles and therefore have similar compositions.

Magnetite I from the studied skarn deposits (Alvito, Azenhas, Orada) show concentrations of temperature-dependent elements (e.g. Sn, Ga, and HFSE) higher than those found in magnetites from the MIC. Higher contents of Zn, Ni, and Co have been found in this magnetite type which might be a good geochemical proxy for adjacent ores. Nevertheless, great metallogenic differences exist between the Alvito deposit and the Azenhas-Orada deposits. In the case of Alvito the primary ores were formed by the metassomatic reaction of magmatic-hydrothermal fluids, promoted by the emplacement of a gabbro-diorite suite, with the carbonate country-rocks. The geochemistry of magnetite records the conditions of ore formation, with magnetite displaying a trace element profile consistent with those from high-temperature hydrothermal magnetite (Knipping et al., 2015). Principal component analysis of trace element data indicated that the concentration of elements such as Nb, Zr, Hf, and Ta clearly discriminate magnetite I from the skarn deposits (Maia et al., 2022a).

The origin of the Azenhas and Orada deposits is complex and although the most accepted model is of a skarn deposit formed by metasomatic reaction within the host amphibolites, several evidence suggest a distinctive genesis, involving processes with temperatures above 700ºC (Maia et al., 2022a), much higher than previously modelled (Mateus et al., 2005). A second magnetite generation (Magnetite II) from skarn deposits was only described for the Azenhas deposit and in this case trace element contents are much lower than those found in magnetite I, suggesting that magnetite II is associated to lower-temperature processes as suggested by the similar trace element profile to that of low-temperature magnetite (Maia et al., 2022a).

The radar plot from **figure 5.4** shows that the composition of magnetite I from the skarn deposits (Alvito, Azenhas, and Orada) is similar in what concerns the contents of the elements selected for the RF classification. Such similitude is evidenced by the shapes and profiles of the radar, which clearly contrast with those from the magnetite I of the MIC deposit.

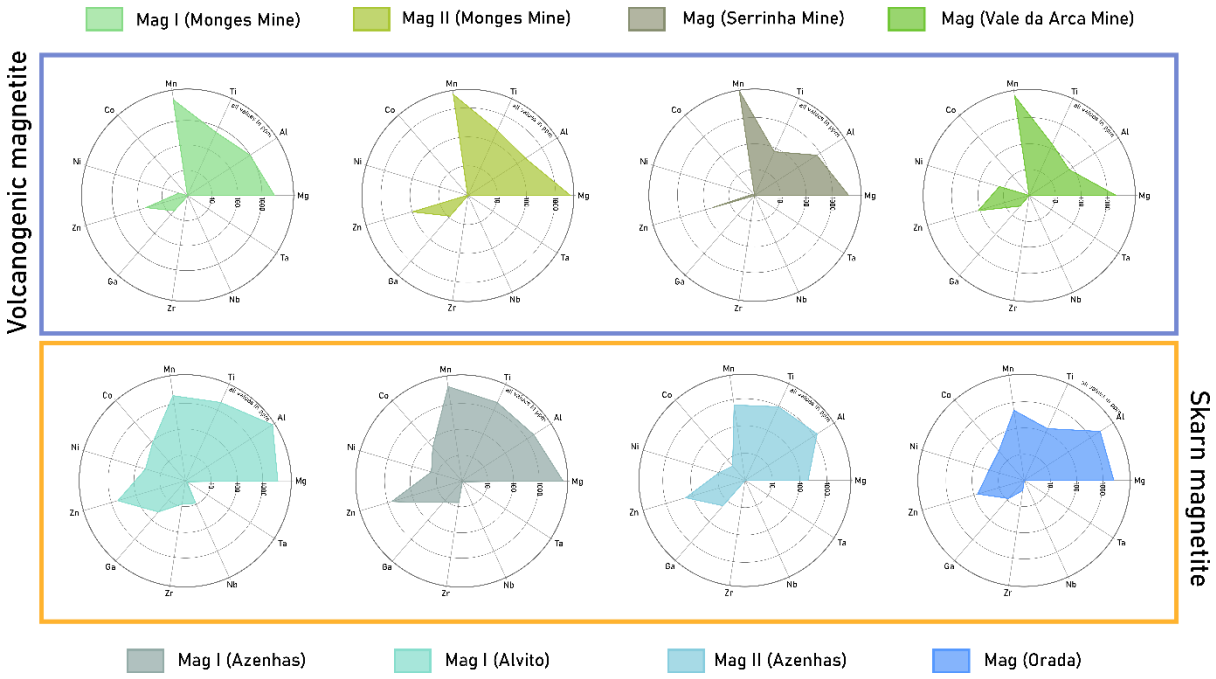

Figure 5.4. Radar plot of the trace element contents of magnetites from the MIC volcanogenic-exhalative deposits (Monges, Vale da Arca, and Serrinha) and the Alvito, Azenhas, and Orada skarn deposits. Trace element content is displayed according to magnetite origin and type and only the concentrations of the elements selected to integrate the testing and training dataset are displayed.

5.4.2 Conventional magnetite discrimination

The use of magnetite trace element concentrations for the discrimination and classification of ore deposits has been widely applied in low-temperature and high-temperature systems (Dare

et al., 2014; Canil et al., 2016; Duan et al., 2019; Huang et al., 2019; Peng et al., 2021), with results that prove to be valuable in the definition of geological models that can be applied in mineral exploration, as well as in identifying anomalous trace element contents that could suggest ore sources enriched in other metals.

Dupuis and Nadoll (2011) presented a thorough revision of EPMA magnetite trace element composition as a method to the classification of ore deposits. They have proposed several discriminant diagrams that can be applied in a wide range of metallogenic settings, from low-temperature to high-temperature deposits. One of the most widely applied diagrams is the Al + Mn + Ca (wt. %) vs. Ti + V (wt. %), which can aid in the discrimination of magnetite from BIF, IOCG, Porphyry, Kiruna IOA, Skarn, and Fe-Ti-V deposits. This diagram was later reinterpreted by Nadoll et al. (2014) and Nadoll et al. (2015) with new and more sensitive LA-ICP-MS analysis.

5.4.2.1 Classification of the testing dataset – Magnetites from Ossa-Morena Zone deposits

The trace element data of magnetite (over 470 analysis) from the selected iron deposits of OMZ which integrate the testing dataset, were plotted in the conventional Al + Mn (ppm) + Ti + V (ppm) discriminatory diagram (**Fig. 5.5a and 5.5b**). The discrimination of magnetite from volcanogenic-exhalative MIC deposits using such diagram is not possible since there is no specific field for such metallogenic settings. Nevertheless, the magnetite data from the MIC mostly scatters between the skarn and the BIF fields (**Fig. 5.5a and 5.5b**). The most recent works by Maia et al. (subm.) have found trace element contents and $\delta^{18}O$ signatures of magnetite (7.7 ‰ – 9.0 ‰) that support the possibility for extensive metamorphic overprinting of the primary ores.

This conventional discrimination shows that magnetite I from the skarn deposits of Alvito, Azenhas, and Orada plot inside the field of skarn deposits defined by Dupuis and Beaudoin (2011), and therefore good discrimination can be inferred. On the contrary, magnetite II from the Azenhas skarn deposit plots within the IOCG field (**Fig. 5.5a**) and, therefore, is inadequately classified in terms of the geology of the area. Thus, we prefer to use the fields in the Al + Mn (ppm) vs. Ti + V (ppm) diagram by Nadoll et al. (2015) (**Fig. 5.5b**), since fields for skarn deposits are much more inclusive, especially regarding the Mg, Al, Ti, and V concentrations.

5.4.2.2 Classification of the literature training dataset

The training dataset, used in the previously described RF Model 3 and Model 4, contains literature data from BIF, IOCG, Porphyry, Skarn, Kiruna-type IOA (**Table 5.1**), and VMS and was also plotted in the conventional Al+ Mn (wt. %) + V + Ti (wt. %) discriminatory diagram (**Fig. 5.5c**) as a method of confirming their classification for future comparison with the Random Forest classifier results. Exceptionally, the VMS data was not plotted in this diagram since it does not have a field dedicated to such kind of deposits.

The BIF deposits data was gathered from Araújo et al. (2019) that studies magnetite from several Algoma-type BIF deposits within the Quadrilátero Ferrífero (Brazil). The BIF magnetite analysis used in the training dataset are from hydrothermal magnetite associated with carbonates from the Campo Grande deposit, and plot just outside of the BIF field (**Fig. 5.5c**), which was interpreted because of its early-hydrothermal origin (Araújo et al., 2019). The choice of this magnetite type was particularly important since such relation to hydrothermal-venting systems and post-deposition alteration processes could be closest to what is found in the magnetite from the MIC deposits.

The IOCG magnetite data included in the literature dataset was obtained from Wang et al. (2020), which performed analysis of magnetite from the debatably classified Dahongshan deposits (SW China) that plot just outside of the IOCG field from **figure 5.5c**.

Trace element data of magnetite from the Butte Cu-Mo porphyry deposit (Huang et al., 2019) scatters along the IOCG and Porphyry field in the plot from **Figure 5.5c**, which supports its use for comparison between conventional discrimination using x-y scatterplots and Random Forest.

Magnetite data from the skarn deposits was collected from Hu et al. (2017), which performed analysis in magnetite from the Longqiao Fe-Skarn deposit (SE China), plotting within the skarn field in the Al + Mn (ppm) vs. Ti + V (ppm) diagram (**Fig. 5.5c**)

The data from IOA deposits corresponds to analysis performed in magnetite from the Laco Norte orebodies (La Cruz et al., 2019) at the El Laco deposit (Chile), and plots outside of the Kiruna type deposits (**Fig. 5.5c**) but are consistent with other results for this deposit (Dupuis and Beaudoin, 2011).

5.4.3 Random Forest classification

5.4.3.1 Model 1

The results for the deposit classification using self-data as the training dataset can be found in **Table 5.2**. The predictiveness accuracy of RF classification was of 100 % for the analysis of magnetite from the MIC deposits, which are here referred to as volcanogenic for

simplification. An estimated accuracy of 67.2 % was obtained for the analysis of magnetite from the skarn deposits. The close inspection of the results indicates that most (32.8 %) of the misclassification in the skarn magnetite analysis is found in magnetite II of the Azenhas deposit. Nevertheless, the overall accuracy can be interpreted as a correct classification of the deposits.

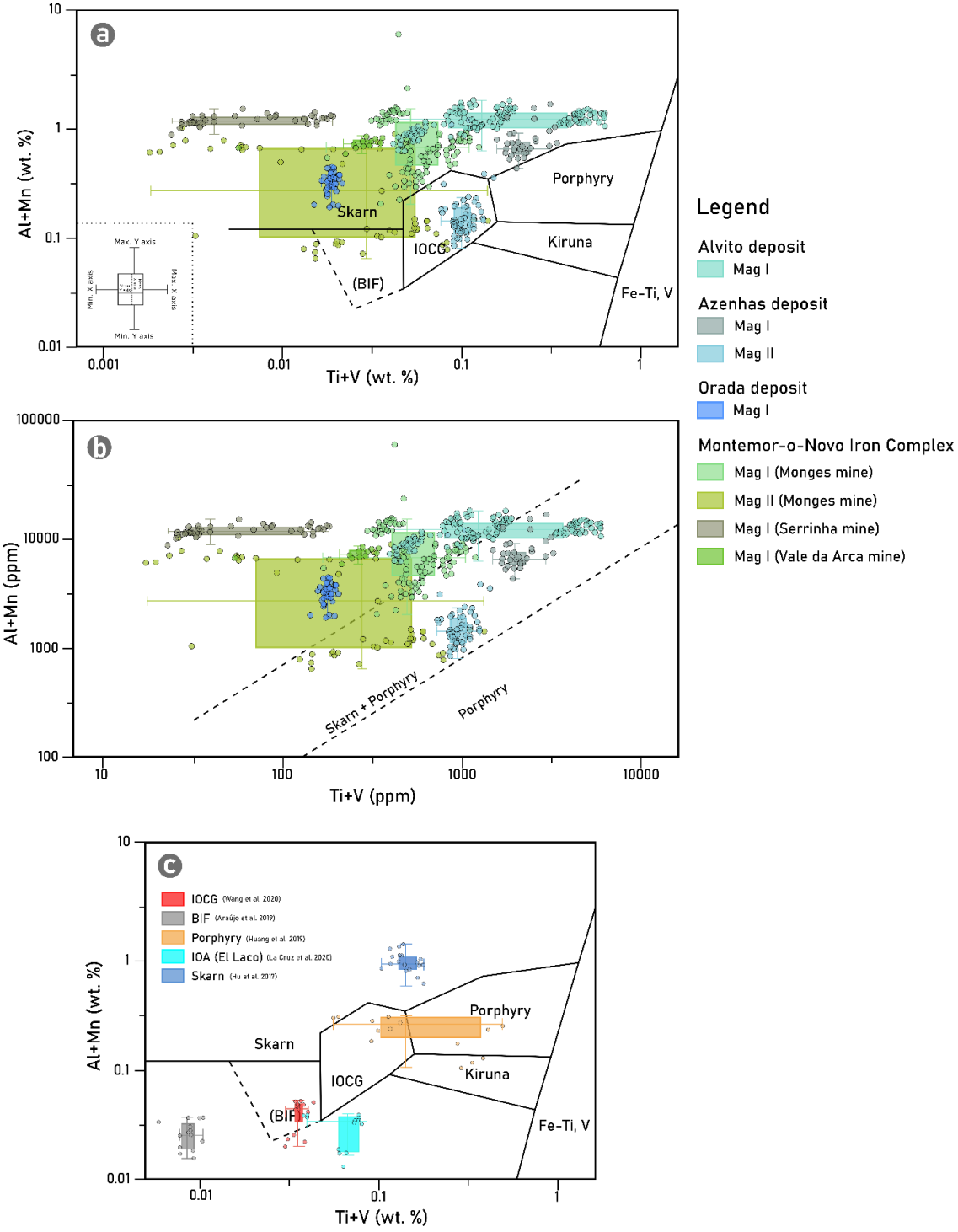

Figure 5.5. Discriminant scatterplots (Dupuis and Beaudoin, 2011; Nadoll et al., 2015) applied to the testing dataset (a and b) and training dataset (c).

5.4.3.2 Model 2

The RF classification results based on four categories for the classification of magnetite types can be found in **Table 5.3**, and an example of a decision tree based on the four-category classification presented in Model 2 is shown in **Figure 5.6**. The classification of magnetite I from the Alvito deposit showed accuracies of 85.6 %, with the RF classifying them as Primary Skarn magnetite. Contrarily to Model 1, this RF classifier showed better results in classifying the magnetite I and II from the Azenhas deposit, with an accuracy of 100 %. Magnetite from the Orada deposit is not classified as primary skarn magnetite (**Table 5.3**).

Monges magnetite I was correctly classified as a primary magnetite, with an accuracy of 74.5 % and with 25 out of the 98 magnetite analysis being classified as not primary volcanogenic magnetite. The Monges magnetite II (Monges Mag II) was inconclusive (between 55 % and 65 %), with 22 of the 53 analyses being classified as primary magnetite.

Magnetite I of the Serrinha deposit were mostly correctly classified as primary volcanogenic magnetite, although 15 of the 45 analyses were not classified as primary. Vale da Arca magnetite was classified as secondary volcanogenic, which might suggest a reinterpretation of prior classification (Maia et al., subm.) should be done, and further analysis should be carried.

Table 5.2. Confusion Matrix of Random Forest classification results from Model 1 dedicated to the classification of the magnetite analyses according to the deposit type.

Actual	Predicted			
	Volcanogenic	Skarn	Sum	% correct
Volcanogenic	208		208	100
Skarn	87	178	265	67.17
Sum	295	178	473	

5.4.3.3 Model 3

The results of the deposit classification using literature data as the training dataset are shown in the confusion matrix of **Table 5.4**. Excellent results were gathered in the classification of magnetite I from the Alvito deposit, with an accuracy of 98.7 %. On the other hand, magnetite from the Azenhas deposit showed much lower accuracies (54.5 %), and therefore their classification is considered inconclusive. The trace element concentration in magnetite from the Azenhas deposit shows affinities to the Porphyry magnetite used in the training dataset which resulted in an incorrect classification. Such results are aligned to the misclassification

gathered in the discriminant diagram of **Figure 5.5**. In the case of the Orada magnetite I, only 6 of the 35 analyses present in the dataset were correctly classified as Skarn, leading to an accuracy of 17.1 %.

In the case of the analyses of magnetite from the MIC deposits, 83 % (171 out of 208) were classified as BIF. This classification suggests that magnetite from the MIC orebodies show more similarities with the BIF magnetite analyses used in the training dataset (Araújo et al., 2019).

Table 5.3. Confusion Matrix of Random Forest classification results from Model 2 dedicated to the classification of the magnetite analyses according to the magnetite type.

Actual Magnetite Type by deposit	Predicted Magnetite Type					
	Primary Skarn	Secondary Skarn	Primary Volcanogenic	Secondary Volcanogenic	Sum	% correct
Alvito Mag I	136	22	1		159	85.6
Azenhas Mag I	22				22	100
Azenhas Mag II		49			49	100
Orada Mag I		35			35	0
Monges Mag I			73	25	98	74.5
Monges Mag II			22	31	53	58.5
Serrinha Mag I			30	15	45	66.7
Vale da Arca Mag I				12	12	0
Sum	158	106	126	83	473	

5.4.3.4 Model 4

To address the difficult classification of the MIC deposits, which are currently interpreted as a SEDEX-VMS deposit (Salgueiro, 2011; Salgueiro et al., 2012), it was necessary to apply a RF classifier model that used VMS magnetite LA-ICP-MS trace element data (Makvandi, 2015) in the training dataset coupled with LA-CIP-MS data of magnetite from skarn deposits (Hu et al., 2017). The accuracy classification of magnetite I from the Alvito and Azenhas skarn deposits (**Table 5.5**) were of 93.7 % and 100 %, respectively, and are considered as a correct classification. Once again, the classification of magnetite II from the Azenhas skarn deposit

and magnetite I from the Orada skarn deposit were mostly misclassified as VMS deposits magnetite. This misclassification can be a result of the lower trace element contents when compared to the remaining magnetite I from skarns (**Fig. 5.4**).

The classification of magnetite from the MIC deposits was incredibly accurate when using VMS magnetite data as the training dataset (**Table 5.5**). These results suggest that, in fact, MIC deposits share affinities with VMS deposits worldwide. This model showed the most accurate results from the classification of magnetites from the MIC deposit.

Table 5.4. Confusion Matrix of Random Forest classification results from Model 3 dedicated to the classification of the magnetite analyses according to deposit type using literature data as the training dataset.

Actual Magnetite Type by deposit	Predicted Deposit Type						
	Skarn	BIF	IOCG	IOA	Porphyry	Sum	% accuracy
Alvito Mag I	157			1	1	159	98.7
Azenhas Mag I	12				10	22	54.5
Azenhas Mag II	2				47	49	4.1
Orada Mag I	6	4			25	35	17.1
Monges Mag I	7	79			12	98	N.A.*
Monges Mag II		39			14	53	N.A.
Serrinha Mag I		45				45	N.A.
Vale da Arca Mag I		8			4	12	N.A.
Sum	184	175		1	113	473	

5.5 Conclusions

The results of our study validate the use of Random Forest for the classification of large datasets of magnetite trace element data. The conventional discriminatory diagrams have been used successfully to some extent, as previously referred, but the accuracy of RF classifier is quantifiable, whereas quantifying the conventional x-y scatterplot results in the classification of ore deposits is not so easy. Nevertheless, their use is encouraged allied with a more robust inspection of the geochemical data using Random Forest for the classification

of ore deposits. Furthermore, the use of this kind of classification should never be dissociated from the use of other data mining methods (e.g. Principal Component Analysis).

Additionally, the results from this research suggests that:

i) The training dataset must be robust enough so that a correct classification of the testing dataset is performed. There is necessary pre-processing of the data to evaluate which is the variable importance in the RF model so that a decision can be made regarding the elements that must be excluded from the training dataset, as well as a robust method for the substitution of missing values;

ii) Several external factors may influence the correct classification of magnetite, such as the effect of long metamorphic overprinting of the primary trace element composition. The gathered data suggests that this is the case of magnetites from the volcanogenic-exhalative MIC deposits, in which primary ores were subjected to long fluid circulation promoted by the regionally expressive Montemor-o-Novo Shear Zone;

iii) The use of more than 2 categories should be carefully evaluated since the use of many classification categories will lead to bigger misclassification in the confusion matrix, as expressed in Model 2 and Model 3 (**Table 5.3** and **Table 5.4**);

iv) The RF classifier from Model 1 and Model 2, using the elements Mg, Al, Ti, Mn, Co, Ni, Zn, Ga, Zr, Nb, Ta, correctly classified the investigated magnetite trace element dataset. With Model 1, a total accuracy of 100 % and 67.2 % was gathered for the classification of the magnetite from the MIC volcanogenic-exhalative deposits and the magnetites from the skarn deposits, respectively. Model 2 resulted in a total accuracy of 66.5 % (103/155) for the classification of magnetite I from the MIC deposits as volcanogenic-exhalative, and of 72.2% (158/216) for the classification of magnetite I from the skarn deposits as a skarn magnetite (Alvito, Azenhas, and Orada);

v) The use of literature data as the training dataset of RF classifier proved to be a good approach for the classification of ore deposits using LA-ICP-MS magnetite trace element data, as shown by the results from Model 3 and Model 4 (**Table 5.4** and **Table 5.5**). Model 3 was envisioned so that the training dataset considered data from deposits formed in metallogenic systems that met the fields defined in the Al + Mn + Ca (wt. %) vs Ti + V (wt. %) diagram (Dupuis and Beaudoin, 2011) so that a comparison between both classification methods could be done. Random Forest classifier showed high accuracies in the discrimination of magnetite I from the Alvito skarn deposit (98.7 %). We have considered the classification of magnetite from the MIC deposits to be not applicable (**Table 5.4**) using this model since these deposits are classified as SEDEX-VMS and such field is not considered in the Al + Mn (wt. %) vs. Ti + V (wt. %) diagram (**Fig. 5.5**), and therefore were not considered in the training dataset. Nevertheless, interesting interpretations can derive from the classification of most magnetite

from the MIC deposits as having a trace element composition with affinities to the magnetite composition from BIF deposits.

Table 5.5. Confusion Matrix of Random Forest classification results from Model 5 dedicated to the classification of the magnetite analyses according to deposit type using literature data as the training dataset.

Actual deposit type	Actual magnetite type	Predicted deposit type			
		Skarn	VMS	Sum	% accuracy
Skarn	Alvito Mag I	149	10	159	93.7
	Azenhas Mag I	22		22	100
	Azenhas Mag II	1	48	49	2.0
	Orada Mag I		35	35	0
SEDEX-VMS	Monges Mag I	2	96	98	97.9
	Monges Mag II		53	53	100
	Serrinha Mag I		45	45	100
	Vale da Arca Mag I		12	12	100
	Sum	174	299	473	

It is not possible to interpret geochemistry results without the complete metallogenic conditions of the deposit, and although the formation of magnetite from the MIC is not related to conditions involved in the formation of BIF deposits, its primary genesis is associated with volcanogenic-exhalative systems during the rifting stages of the Variscan cycle, which to some extents are also associated with the Algoma-type BIF deposits from Araújo et al. (2019) used in the training dataset.

The two-category Model 4 was the one that showed the best results in classifying the volcanogenic-exhalative deposits from the MIC (Monges, Vale da Arca, and Serrinha) and the skarn deposits (Alvito, Azenhas, and Orada) from the Ossa-Morena Zone. The training dataset from this model contemplated magnetite trace element data from VMS (Makvandi, 2016) and skarn deposits (Hu et al., 2017), with Random Forest classifying approximately 100 % of the magnetite analyses from the MIC deposits as being VMS, and 65 % of the skarn magnetite analyses from OMZ as being Skarn (**Table 5.5**). The misclassification of magnetite II from the Azenhas and magnetite I from the Orada deposit is a clear result of the lower trace element contents found in those magnetite. In the Azenhas deposit the magnetite II is interpreted as a late remobilization of primary ores (Maia et al., 2022a), which may lead to a depletion in trace element contents. The case of the magnetite from the Orada deposit should be further investigated, with a more thorough sampling of the orebodies.

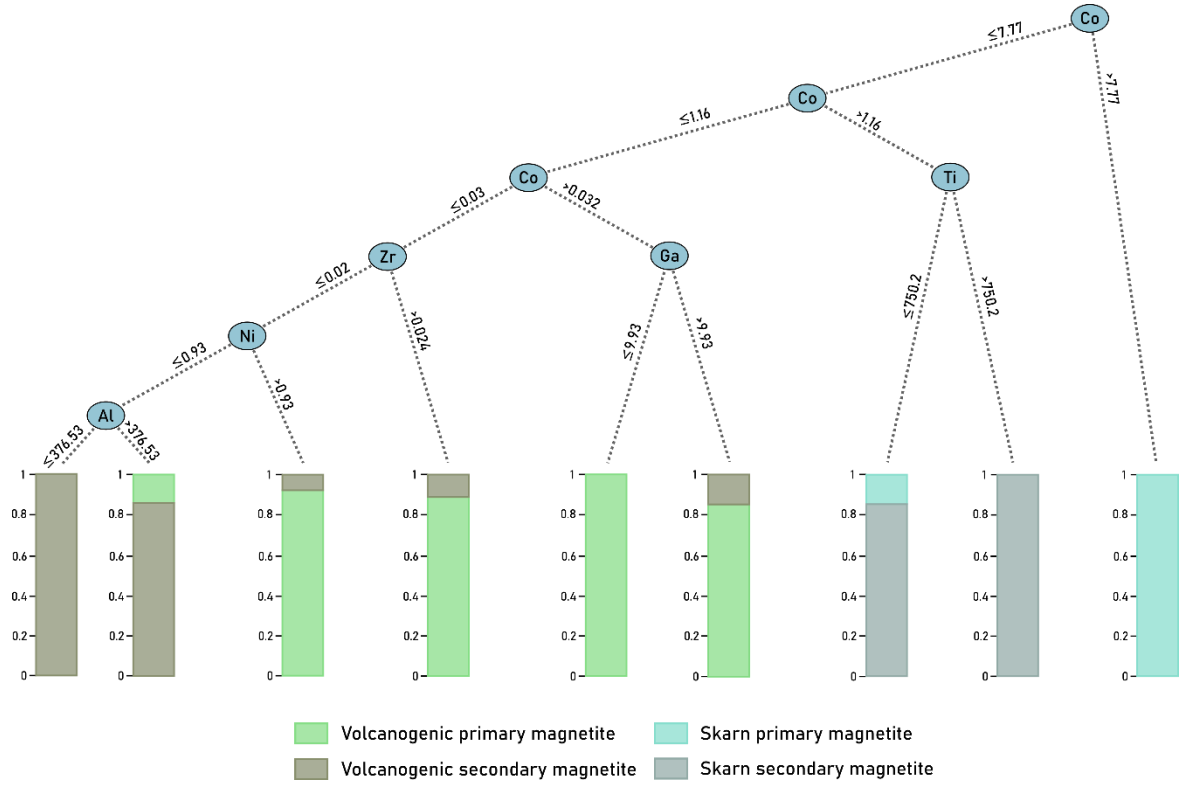

Figure 5.6. Classification tree for the four-category Random Forest Model 2 applied to the discrimination of the magnetite type according to the two deposit types studied in this study.

Chapter References

Andrade, A., Silva, J.M., Arruda, C.R., Gameiro, J.C.S., 1949, Minas de Ferro de Montemor-o-Novo: Serviço de Fomento Mineiro, v. 15, p. 125

Araújo, A., Fonseca, P., Munhá, J., Moita, P., Pedro, J., Ribeiro, A., 2005. The Moura Phyllonitic

Complex: An Accretionary Complex related with obduction in the Southern Iberia Variscan Suture. Geodinamica Acta, v.18(5), pp. 375-388.

Araújo, J.C.S., and Lobato, L.M., 2019, Depositional model for banded iron formation host to gold in the Archean Rio das Velhas greenstone belt, Brazil, based on geochemistry and LA-ICPMS magnetite analyses. Journal of South American Earth Sciences, v. 97, 102205. https://doi.org/10.1016/j.jsames.2019.05.021

Ayupova, N.R., Novoselov, K.A., Maslennikov, V., Melekestseva, I.Y., Hollis, S.P., Artemyev, D.A., and Tessalina, S.G., 2020. The formation of magnetite ores of the Glubochenskoe deposit, Turgai iron belt, Russia: new structural, mineralogical, geochemical, and isotopic constraints. Mineralium Deposita, v.56, pp. 103-123. https://doi.org/10.1007/s00126-020-00994-6

Bédard, E., De Bronac de Vazelhes, V., and Beaudoin, G., 2022. Performance of predictive supervised classification models of trace elements in magnetite for mineral exploration. Journal of Geochemical Exploration. https://doi.org/10.1016/j.gexplo.2022.106959

Breiman, L., 2001. Random Forests. Machine Learning, v. 45, pp. 5–32. https://doi.org/10.1023/A:1010933404324

Canil, D., Grondahl, C., Lacourse, T., and Pisiak, L.K., 2016. Trace elements in magnetite from porphyry Cu–Mo–Au deposits in British Columbia, Canada. Ore Geology Reviews, v.72, pp. 1116-1128. http://dx.doi.org/10.1016/j.oregeorev.2015.10.007

Carvalhosa, A.B., and Zbyszewski, G., 1971, Carta Geológica de Portugal à escala 1: 50 000: Folha 40-C Viana do Alentejo: Direção Geral de Minas e Serviços Geológicos.

Chen, W., Ying, Y.-C., Bai, T., Zhang, J.-J., Jiang, S.-Y., Zhao, K.-D., Shin, D., and Kynicky, J., 2019. In situ major and trace element analysis of magnetite from carbonatite related complexes: Implications for petrogenesis and ore genesis. Ore Geology Reviews, v.107, pp. 30-40. https://doi.org/10.1016/j.oregeorev.2019.01.029

Chichorro, M., 2006. A evolução tectónica da Zona de Cisalhamento de Montemor-o-Novo (Sudoeste da Zona de Ossa-Morena – Área de Santiago do Escoural – Cabrela). PhD Thesis, University of Évora, p. 569.

Dare, S.A.S., Barnes, S.-J., Beaudoin, G., Méric, J., Boutroy, E., and Potvin-Doucet, C., 2014. Trace elements in magnetite as petrogenetic indicators. Mineralium Deposita, v.49, pp. 785-796. https://doi.org/10.1007/s00126-014-0529-0

Duan, C., Li, Y., Mao, J., Hou, K., Wang, C., Yang, B., Wang, Q., and Li, W., 2019. Ore formation at the Washan iron oxide–apatite deposit in the Ningwu Ore District, eastern China: Insights from in situ LA-ICP-MS

magnetite trace element geochemistry. Ore Geology Reviews, v.112, 103064. https://doi.org/10.1016/j.oregeorev.2019.103064

Dupuis, C., and Beaudoin, G., 2011. Discriminant diagrams for iron oxide trace element fingerprinting of mineral deposit types. Mineralium Deposita, v. 46, pp. 319-335. https://doi.org/10.1007/s00126-011-0334-y

Farias, P., Gallastegui, G., González Lodeiro, F., Marquínez, J., Martin Parra, L., Martínez Catalán, J., Paolo Macia, J., and Rodriguez Fernandez, L., 1987, Aportaciones al conocimiento de la litoestratigrafia y estrutura de Galiza Central: Memória, Fac. Ciênc. Univ. Porto v. 1, pp. 411-431.

Goínhas, A.C., and Martins, L.M.P., 1986. Área metalífera de Montemor-o-Novo – Casa Branca (Baixo Alentejo, Portugal). Estudo, Notas e Trabalhos, v. 28, pp. 119-148.

Gomes, E.M.C., 2000. Metamorfismo de rochas carbonatadas siliciosas da região de Alvito (Alentejo, Sul de Portugal). PhD Thesis, University of Coimbra, 240 p..

Gomes, E.M.C., and Fonseca, P.E., 2006. Eventos metamórfico/metassomáticos tardi-variscos na região de Alvito (Alentejo, sul de Portugal). Cadernos Xeológicos de Laxe, v.31, pp. 67-85. ISSN: 0213 – 4497

Gregory, D.D., Cracknell, M.J., Large, R.R., McGoldrick, P., Kunh, S., Maslennikov, V.V., Baker, M.J., Fox, N., Belousov, I., Figueroa, M.C., Steadman, J.A., Fabris, A.J., and Lyons, T.W., 2019. Distinguishing Ore Deposit Type and Barren Sedimentary Pyrite Using Laser Ablation-Inductively Coupled Plasma-Mass Spectrometry Trace Element Data and Statistical Analysis of Large Data Sets. Economic Geology, v. 114(4), pp. 771-786. https://doi.org/10.5382/econgeo.4654

Guillong, M., Hametner, K., Reusser, E., Wilson, S.A., and Günther, D., 2005. Preliminary Characterisation of New Glass Reference Materials (GSA-1G, GSC-1G, GSD-1G and GSE-1G) by Laser Ablation-Inductively Coupled Plasma-Mass Spectrometry Using 193 nm, 213 nm and 266 nm Wavelengths. Geostandards and Geoanalytical Research, v. 29(3), pp. 315-331. https://doi.org/10.1111/j.1751-908X.2005.tb00903.x

Hong, S., Zuo, R., Juang, X., and Xiong, Y., 2021. Distinguishing IOCG and IOA deposits via random forest algorithm based on magnetite composition. Journal of Geochemical Exploration, v. 230, 106859. https://doi.org/10.1016/j.gexplo.2021.106859

Hron, K., Templ, M., and Filzmoser, P., 2010. Imputation of missing values for compositional data using classical and robust methods. Computational Statistics and Data Analysis, v. 54, pp. 3095-3107. https://doi.org/10.1016/j.csda.2009.11.023

Hu, X., Chen, H., Zhao, L., Han, J., and Xia, X., 2017. Magnetite geochemistry of the Longqiao and Tieshan Fe–(Cu) deposits in the Middle-Lower Yangtze River Belt: Implications for deposit type and ore genesis. Ore Geology Reviews, v.89, p. 822-835. http://dx.doi.org/10.1016/j.oregeorev.2017.07.019

Huang, X.-W., Sappin, A.-A., Boutroy, É., Beaudoin, G., and Makvandi, S., 2019. Trace element composition of igneous and hydrothermal magnetite from porphyry deposits: Relationship to deposit subtypes and magmatic affinity. Economic Geology, v.114(5), pp. 917-952. https://doi.org/10.5382/econgeo.4648

Jesus, A.P., Mateus, A., Benoit, M., Tassinari, C.C.G., and Bento dos Santos, T., 2020. The timing of sulfide segregation in a Variscan synorogenic gabbroic layered intrusion (Beja, Portugal): Implications for Ni-Cu-PGE

exploration in orogenic settings. Ore Geology Reviews, v.126, 103767. https://doi.org/10.1016/j.oregeorev.2020.103767

Jochum, K.P., Willbold, M., Raczek, I., Stoll, B., and Herwig, K., 2005. Chemical Characterisation of the USGS Reference Glasses GSA-1G, GSC-1G, GSD-1G, GSE-1G, BCR-2G, BHVO-2G and BIR-1G Using EPMA, ID-TIMS, ID-ICP-MS and LA-ICP-MS. Geostandards and Geoanalytical Research, v. 29(3), pp. 285.302. https://doi.org/10.1111/j.1751-908X.2005.tb00901.x

Julivert, M., Fontboté, J.M., Ribeiro, A., and Conde, L., 1972, Mapa Tectónico de La Península Ibérica y Baleares (Tectonic Map of the Iberian Peninsula and Balearían Ilands): IGME-SPI, Instituto Geológico y Minero de España, Madrid 113.

Knipping, J.L., Bilenker, L.D., Simon, A.C., Reich, M., Barra, F., Deditius, A.P., Wälle, M., Heinrich, C.A., Holtz, F., and Munizaga, R., 2015. Trace elements in magnetite from massive iron oxide-apatite deposits indicate a combined formation by igneous and magmatic-hydrothermal processes. Geochimica et Cosmochimica Acta, v.171, pp. 15-38. http://dx.doi.org/10.1016/j.gca.2015.08.010

La Cruz, N.L., Ovalle, J.T., Simon, A.C., Konecke, B.A., Barra, F., Reich, M., Leisen, M., and Childress, T.M., 2020. The Geochemistry of Magnetite and Apatite from the El Laco Iron Oxide-Apatite Deposit, Chile: Implications for Ore Genesis. Economic Geology, v. 115, pp. 1461-1491. https://doi.org/10.5382/econgeo.4753

Liu, Y., Fan, Y., Zhou, T., Xiao, X., White, N.C., Thompson, J., Hong, H., and Zhang, L., 2019. Geochemical characteristics of magnetite in Longqiao skarn iron deposit in the Middle-Lower Yangtze Metallogenic Belt, Eastern China. Mineralium Deposita, v.54, pp. 1229-1242. https://doi.org/10.1007/s00126-019-00871-x

Liaw, A., and Wiener, M., 2002. Classification and regression by randomForest. R News, v. 2, pp. 18–22.

Maia, M., Barrulas, P., Nogueira, P., Mirão, J., and Noronha, F., 2022a. In situ LA-ICP-MS trace element analysis of magnetite as a vector towards mineral exploration: A comparative case study of Fe-skarn deposits from SW Iberia (Ossa-Morena Zone). Journal of Geochemical Exploration, v. 234, 106941. https://doi.org/10.1016/j.gexplo.2021.106941

Maia, M., Roseiro, J., Nogueira, P., Noronha, F., Fuertes.Fuente, M., Cepedal, A., and Mirão, J., 2022b. New insights on the Escoural Orogenic gold district (Ossa-Morena Zone, SW Iberia): Geochemistry, fluid inclusions and stable isotope constraints from the Monfurado gold prospect. Ore Geology Reviews, v. 142, 104736. https://doi.org/10.1016/j.oregeorev.2022.104736

Makvandi, S., 2015. Indicator mineral exploration methodologies for VMS deposits using geochemistry and physical characteristics of magnetite. PhD Thesis, Université Laval, 235 p.

Makvandi, S., Ghasemzadeh-Barvarz, M., Beaudoin, G., Grunsky, E.C., McClenaghan, M.B., and Duchesne, C., 2016a. Principal component analysis of magnetite composition from volcanogenic massive sulfide deposits: Case studies from the Izok Lake (Nunavut, Canada) and Halfmile Lake (New Brunswick, Canada) deposits. Ore Geology Reviews, v. 72, pp. 60-85. http://dx.doi.org/10.1016/j.oregeorev.2015.06.023

Makvandi, S., 2015. Indicator mineral exploration methodologies for VMS deposits using geochemistry and physical characteristics of magnetite. PhD Thesis, Université Laval, 235 p.

Makvandi, S., Ghasemzadeh-Barvarz, M., Beaudoin, G., Grunsky, E.C., McClenaghan, M.B., Duchesne, C., and Boutroy, E.C., 2016b. Partial least squares-discriminant analysis of trace element compositions of magnetite from various VMS deposit subtypes: Application to mineral exploration. Ore Geology Reviews, v.78, pp. 388-408. http://dx.doi.org/10.1016/j.oregeorev.2016.04.014

Mateus, A., Araújo, A., Gonçalves, M.A., and Matos, J., 2005, Variscan overthrusting, fluid flow and genesis of magnetite ore-bodies at the Azenhas area (Pedrógão, Ossa-Morena Zona, SE Portugal). Boletín Geológico y Minero, v.116(1), pp. 3-22. ISSN 0366-0176.

Mateus, A., Munhá, J., Inverno, C., Matos, J.X., Martins, L., Oliveira, D., Jesus, A., and Salgueiro, R., 2013, Mineralizações no sector português da Zona de Ossa-Morena. In: R. Dias, A. Araújo, P. Terrinha, J.C. Kullberg (Eds.), Geologia de Portugal, v.1, pp. 577-619, Lisboa: Escolar Editora.

Nadoll, P., and Koenig, A.E., 2011. LA-ICP-MS of magnetite: methods and reference materials. Journal of Analytical Atomic Spectrometry, v. 26, pp. 1872-1877. DOI: 10.1039/c1ja10105f

Nadoll, P., Angerer, T., Mauk, J.L., French, D., and Walshe, J., 2014. The chemistry of hydrothermal magnetite: A review. Ore Geology Reviews, v. 61, pp. 1-32. http://dx.doi.org/10.1016/j.oregeorev.2013.12.013

Nadoll, P., Mauk, J.L., Leveille, R.A., and Koenig, A.E., 2015. Geochemistry of magnetite from porphyry Cu and skarn deposits in the southwestern United States. Mineralium Deposita, v.50, pp. 493-515. https://doi.org/10.1007/s00126-014-0539-y

O´Brien, J.J., Spry, P.G., Nettleton, D., Xu, R., and Teale, G.S., 2015. Using Random Forests to distinguish gahnite compositions as an exploration guide to Broken Hill-type Pb–Zn–Ag deposits in the Broken Hill domain, Australia. Journal of Geochemical Exploration, v. 149, pp. 74-86. http://dx.doi.org/10.1016/j.gexplo.2014.11.010

Palarea-Albaladejo, J., and Martín-Fernández, J.A., 2015. zCompositions — R package for multivariate imputation of left-censored data under a compositional approach. Chemometrics and Intelligent Laboratory Systems, v.143, pp. 85-96. http://dx.doi.org/10.1016/j.chemolab.2015.02.019

Peng, H.-J, Hou, L., Sun, C., Zou, H., Wang, T.-R, and Ma, Z.-Z., 2021. Geochemistry of magnetite from the Hongniu–Hongshan Cu skarn deposit in Yunnan Province, SW China. Ore Geology Reviews, v.134, 104237. https://doi.org/10.1016/j.oregeorev.2021.104237

Pereira, M.F., Silva, J.B., and Chichorro, M., 2003. Internal Structure of the Évora High-grade Terrains and the Montemor-o-Novo Shear Zone (Ossa-Morena Zone, Portugal), Geogaceta, v.33, pp.79-82.

Pereira, M. F., Chichorro, M., Linnemann, U., Eguiluz, L., and Silva, J. B., 2006. Inherited arc signature in Ediacaran and Early Cambrian basins of the Ossa-Morena zone (Iberian Massif, Portugal): paleogeographic link with European and North African Cadomian correlatives. Precambrian Research, v. 144(3-4), pp. 297-315. https://doi.org/10.1016/j.precamres.2005.11.011

Pereira, M. F., Silva, J. B., Chichorro, M., Moita, P., Santos, J. F., Apraiz, A., and Ribeiro, C., 2007. Crustal growth and deformational processes in the northern Gondwana margin: Constraints from the Évora Massif (Ossa-Morena zone, southwest Iberia, Portugal). Special Paper 423: The Evolution of the Rheic Ocean: From

Avalonian-Cadomian Active Margin to Alleghenian-Variscan Collision, pp. 333–358. https://doi.org/10.1130/2007.2423(16)

Pin, C., Fonseca, P.E., Paquette, J.-L., Castro, P., and Matte, P., 2008. The ca. 350 Ma Beja Igneous Complex: a record of transcurrent slab break-off in the Southern Iberia Variscan Belt? Tectonophysics, v.461, pp. 356–377. https://doi.org/10.1016/j.tecto.2008.06.001

Qi, Y., Hu, R., Gao, J., Gao, W., and Gong, H., 2021. Trace element characteristics of magnetite: Constraints on the genesis of the Lengshuikeng Ag–Pb–Zn deposit, China. Ore Geology Reviews, v.129, 103943. https://doi.org/10.1016/j.oregeorev.2020.103943

Salgueiro, R., 2011, Caracterização e génese das mineralizações de magnetite – sulfuretos em Monges (Santiago do Escoural, Montemor-o-Novo) e ensaio comparativo com as suas congéneres em Orada-Vale de Pães (Serpa-Vidigueira). PhD Thesis, University of Lisbon, 524 p.

Salgueiro, R., Mateus, A, and Inverno, C., 2012. Mineralizações de magnetite e sulfuretos de monges (Santiago do Escoural, Montemor-o-Novo), Vale de Pães (Cuba-Vidigueira) e Orada (Pedrógão, Serpa): Síntese de ensaio comparativo: Boletim de Minas, v.47(1), pp. 27-30.

Serviços de Fomento Mineiro, 1965. Carta Geológica da Região de Pedrõgão-Orada à escala 1:10 000.

Ribeiro A., Munhá J., Dias R., Mateus A., Pereira E., Ribeiro L., Fonseca P., Araújo A., Oliveira O., Romão J., Chaminé H., Coke C., and Pedro, J.C., 2007. Geodynamic evolution of the SW Europe Variscides. Tectononics 26:TC6009. https://doi.org/10.1029/2006TC002058

Tornos, F., Inverno, C.M.C., Casquet, C., Mateus, A., Ortiz, G., and Oliveira, V., 2004. The metallogenic evolution of the Ossa-Morena Zone. Journal of Iberian Geology, v. 30, pp. 143-181.

Wang, Y.-J., Zhu, W.-G., Huang, H.-Q., Bai, Z.-J., Zhong, H., Yao, J.-H., and Fan, H.-P., 2020. Geochemistry of magnetite from the giant Paleoproterozoic Dahongshan Fe-Cu deposit, SW China: Constraints on nature of ore-forming fluids and depositional setting. Ore Geology Reviews, v. 118, 103361. https://doi.org/10.1016/j.oregeorev.2020.103361

Zhong, R., Deng, Y., Li, W., Nanyushevsky, L.V., Cracknell, M.J., Belousov, I., Chen, Y., and Li, L., 2021. Revealing the multi-stage ore-forming history of a mineral deposit using pyrite geochemistry and machine learning-based data interpretation. Ore Geology Reviews, v. 133, 104079. https://doi.org/10.1016/j.oregeorev.2021.104079

Chapter 6

Geodiversity assessment through the Évora – Montemor-o-Novo region: On the scope of valorising the mining heritage of the Ossa-Morena Zone (SW Iberia, Portugal)

Geoheritage, v. 14, 90.

https://doi.org/10.1007/s12371-022-00728-2

Co-authors:

Pedro Nogueira

José Mirão

Fernando Noronha

Abstract

The SW of Iberia registers diverse examples of mining remnants from activities that ceased during the 20th century, namely in the Ossa-Morena Zone. Such activities exposed outcrops that make part of the mining heritage of the Alentejo province (Portugal), and examples of that are found throughout the Évora – Montemor-o-Novo region at the ancient Montemor-o-Novo iron mines. The area, comprised within the *Évora Massif*, besides displaying an important mining and quarrying heritage, also exhibits important geomorphological, structural, and lithological features that are key to understand the geodynamic evolution of the Variscan Orogeny at the SW of Iberia.

This work intends to evaluate the geodiversity throughout the region and propose routes that integrate geodiversity features along with the mining heritage of the ancient mines from the Montemor-o-Novo iron district. Furthermore, the region is characterised by immense cultural, historical and archaeological assets that together with the geodiversity of the region have efficiently been used for scientific and formal and informal educational purposes.

Mining heritage can contribute to the understanding of the role of mineral resources on the past, present, and future of society as we know it. The proposal herein disclosed although intending to promote geoconservation strategies regarding the mineral resources of Ossa-Morena Zone does not aim to make exploration and mining unfeasible in these locations. On the contrary, this work intends to promote strategies in which industry and geoheritage can work together on the knowledge transfer to society, contributing to the geological literacy.

Keywords: SW Iberia; Ossa-Morena Zone; Mining heritage; Geodiversity assessment.

6.1 Introduction

Society, as we know it, emerged and has been shaped by the necessity of life quality enhancement, and with it the indissociable increasing need for mineral resources. To achieve such goals the pursuit for raw materials, many of which provided by mineral deposits, has promoted human migrations and territorial occupation throughout history, such as the well-known Punic and Roman occupancy of the Iberian Peninsula which is an uttermost example of mineral resources exploration and mining. Diverse examples of Roman occupation are found in the Iberian territory, mainly in what concerned gold and tin exploration. Remnants of the Roman mining activities can be found throughout Iberia, with some of those sites having been studied for their geological, educational, and scientific value, such as the Tresminas, Valongo and Castromil Roman gold mines in NW Portugal (e.g. Lima et al 2010; Fonte et al 2017; Cruz et al 2018), and the Las Médulas Roman Gold Mines in NW Spain (e.g. Matías and Llamas 2021). This intricate relation between mineral resources, historical, cultural and archaeological heritage should be considered in a geodiversity assessment and geoconservation strategy, since they could be used to widen the audience range to these geodiversity sites. The Évora – Montemor-o-Novo region is one of the regions that can benefit from such a strategy as it comprises a complex geological evolution which is key to reconstruct the geodynamic evolution of Iberia through the Cadomian and Variscan orogenies. The geological complexity is allied with the fact that human settlements in the area go back as far as the Palaeolithic, and due to the metallogenic characteristics of the region it has also been the target of iron exploitation during Roman times. The iron mining history continues up to the 20th century, marking an important era of industrial development. Furthermore, the potential for future exploration still exists, particularly at the *Escoural* area, which has been the target for several research and exploration projects focusing on gold mineralisation (Ribeiro et al 1993; Inverno 2001; Maia et al 2022).

Throughout this work the assessment of 10 locations with the potential for geodiversity and geosite classification is provided. We intended to propose a geodiversity route between Évora and Montemor-o-Novo municipalities that focuses on the relevant mining heritage of the Montemor-o-Novo ancient iron mines area.

These mining areas are located in the vicinity of the Santiago do Escoural Village, at approximately 13 km west of the Évora municipality, classified by UNESCO as a World Heritage City since 1986.

Some of the locations described throughout this work have already been considered for previous geoconservation strategies, and two of them are already catalogued as geosites, such as the *Herdade Monte das Flores* quarry (Brilha et al 2008, 2010) and the *Escoural* caves (Brilha et al 2008, 2010; Brilha and Pereira 2020). Unfortunately, the potential of the region is

still not fully taken advantage of, lacking the existence of a common framework for geodiversity between both municipalities.

The work here presented is motivated by the necessity of increasing the awareness about mineral resources usage and their applications to every-day life, and their importance in achieving the 2030 Sustainable Development Goals proposed by the United Nations Organization, as well as in developing a consistent strategy for the beneficiation of geodiversity of mining heritage in the geotectonic Ossa-Morena Zone, with an integrative approach that considers other geological, cultural and historical heritage sites. Through the last decades efforts have led to the definition of the Geosite Frameworks of Portugal (Brilha et al 2005, 2008, 2010). Unfortunately, the mining areas of Ossa-Morena Zone were not considered, with exception to framework xxviii) Gold Mineralizations (Brilha et al., 2008), applicable to all Portuguese territory. Nevertheless, several crucial frameworks for Geoconservation in Ossa-Morena Zone have been defined, such as the framework iv) Silurian of the Portuguese Ossa-Morena Zone and xxiv) Pre-Mesozoic granitoids (Brilha et al., 2008).

Despite mining heritage usually being left out of the Geological Heritage and Geosite definition umbrella (Brilha 2016), several authors argue in favour of its consideration (López-García et al 2011; Prosser et al 2018; Mazadiego et al 2019; Gioncada et al 2019), as it should be considered an important part of those definitions as mining heritage provides sites with proven scientific and educational values (Hellqvist 2019), and such is the case of the Montemor-o-Novo ancient iron mines.

6.2 The geology of the Ossa-Morena Zone

The SW border of the Iberian Massif is the outermost terrane of the European Variscides, which separates the tectonostratigraphic terranes of Ossa-Morena Zone (OMZ) and South Portuguese Zone (SPZ) (Julivert et al 1972; Farias et al 1987). The geodynamic evolution of OMZ is conditioned by the Rheic Ocean opening and closure, part of the Variscan Cycle (Ribeiro et al. 2007; 2010) and which can be simplistically framed in the light of the Wilson cycle (Wilson et al. 2019) as follows: Stage 1) early stages of continental rifting at northern Gondwana (Middle Cambrian) mark the beginning of the Variscides evolution that will significantly overprint structures from a previous orogeny (Cadomian Orogeny); Stage 2) Rheic Ocean opening (500 – 470 Ma.) marking the detachment of Avalonia from Gondwana; Stage 3) The achievement of a mature passive margin when Rheic becomes a wide ocean (Ribeiro et al. 2007); Stage 4/5) Beginning of the compressional regime and oceanic crust subduction under the Gondwana terrain (425 – 410 Ma.); Stage 5) As compression continues the Avalonia – Gondwana approximation culminates in an oblique collision (390 – 370 Ma.) that marks the beginning of the continental orogen, the suture of this collision is preserved by

the contact between OMZ and SPZ; Stage 6) The final stages of the Variscan Orogeny are achieved by dextral transpression between Avalonia and Gondwana (aprox. 290 Ma.; Ribeiro et al. 2007).

The OMZ is limited at NE by the *Tomar-Badajóz-Córdoba shear zone*, which is interpreted as a Cadomian suture between the OMZ terrains and Central Iberian Zone (CIZ) latter reactivated during the Variscan Orogeny as a transpressive shear-zone (Ribeiro et al 2010; Araújo et al 2013). The SW limit, between OMZ and SPZ, is materialised by the *Beja-Acebuches Ophiolitic Complex*, which corresponds to an obducted oceanic crustal fragment during Rheic closure (Ribeiro et al 2010), and by the *Beja Igneous Complex* which marks the emplacement of mafic to intermediate magmatic bodies (Jesus et al 2020).

The basement of OMZ is characterised by a thick Neoproterozoic metasedimentary sequence that results from the dismantlement of a Cadomian magmatic arc, referred as *Série Negra* in Iberia.

The Rheic closure marks the beginning of intense tectonism with metamorphic conditions being ubiquitously kept at the greenschist and amphibolitic facies. The compressional regime led to the oblique collision between Avalonia and Gondwana (390 Ma – 390 Ma; Ribeiro et al 2007) triggering the thrusting of autochthonous and allochthonous terrains over the metasedimentary basement in the inner domains of Iberia (Araújo 1995; Ribeiro et al 2010). Such events are promoted by the transcurrent collision between Avalonia and Gondwana, which also marks the beginning of several tectono-metamorphic and magmatic events, such as those that form the *Évora Massif*.

6.2.1 The Évora Massif

The complexity and geological heterogeneity of the region are expressed by the wide and extensive *Évora Massif* terrains, situated between Évora and Montemor-o-Novo municipalities. The *Évora Massif* is located at the NW of the *Montemor-Ficalho sector* (Oliveira et al 1991, Araújo 1995), which correspond to the *Évora-Beja-Aracena* domains (Chacón et al 1983; Apalagueti et al 1990) and marks the suture of a continental collision (Ribeiro et al 2007, 2010). The *Évora Massif* was internally subdivided into three main metamorphic domains: i) the *Montemor-o-Novo Shear Zone* (MNSZ), ii) the *high-grade metamorphic terrains*, and iii) the *Évora mid-grade metamorphic terrains* (Pereira et al 2003, 2006, 2007; Chichorro 2006; Moita et al 2009; Moita 2007; Dias da Silva et al 2018). The *Évora Massif*, particularly the high-grade metamorphic terrains, are evidence of the complex geodynamic context of the SW of OMZ, with reflections of the transcurrent continental collisional stages controlling the intense WNW-ESE deformation and the calc-alkaline magmatic activity throughout the suture zone. This magmatic activity is interpreted as being triggered by oceanic

plate subduction during the Rheic Ocean closure and subsequent slab break-off mechanisms, leading to the emplacement of several calc-alkaline plutons during Early-Carboniferous (e.g. *Beja Igneous Complex*; Jesus et al 2016, 2020). Throughout the *Évora Massif* evidence for such activity is materialised at the high-grade metamorphic terrains, where the Hospitais tonalite and the *Alto the São Bento* granitic suites have been emplaced.

i) The *Montemor-o-Novo Shear Zone* (MNSZ) is part of the hanging-wall of the *Évora Massif*, and corresponds to a NW-SE deformation corridor, developed during the late-collisional stages of the Variscan orogeny, in which the metamorphic conditions were sustained in the greenschist to amphibolic facies. MNSZ displays a lithostratigraphy highly controlled by the left-lateral movement and affects three main units, as follows: 1) A Neoproterozoic metasedimentary sequence, locally referred as *Escoural Formation* (560-550 Ma; Chichorro 2006), mainly composed of mica-schists, paragneiss and local amphibolite intercalations. 2) A carbonate unit of Cambrian ages (*Monfurado Formation*), ubiquitous throughout the Ossa-Morena Zone, which was locally divided into two main units (Chichorro 2006): a lower unit displaying abundant acid metavolcanic rocks with rhyolite-rhyodacite affinities (522 ± 5 Ma; Chichorro 2006; Chichorro et al 2008) emplaced within the carbonate units and interpreted to mark intense rift-related volcanic events (Sánchez-Garcia et al 2003, 2019; Chichorro 2006); and a upper unit corresponding to a gradual transition to less altered and coarse-grained marbles, and marking the transition to basic volcanism, locally evidenced by the amphibolites interbedding. 3) At the top of the *Monfurado Formation*, the ubiquitous presence of amphibolites and metabasites, locally called *Carvalhal Formation* (Carvalhosa 1983; Carvalhosa and Zbyszweski 1994), suggest that during the Upper Cambrian – Ordovician? the basic volcanic events intensified, latter metamorphosed into the greenschist and amphibolitic facies.

ii) The high-grade metamorphic terrains of the (**Fig. 6.1b**) correspond to a 15-20km belt composed by the *Gneiss-Migmatite Complex* (GMC; Carvalhosa and Zbyszewski 1994) and intruded by several magmatic complexes (tonalites and granites) targeted for several geochemical and geochronological studies (Chichorro 2006; Moita 2007; Moita et al 2009, 2015; Pereira et al 2007, 2015; Dias da Silva et al 2018). These studies focused on the genesis of some of the intrusive magmatic bodies (*Hospitais Tonalite Massif* and *Alto de São Bento Granitic Suite*), as well as in identifying the complex conditions in which migmatization occurred at the *Gneiss-Migmatite Complex* (e.g. Migmatites at the Almansor River).

This complex corresponds to a diatexitic-anatetic migmatite complex which, at the contact with the *Hospitais Tonalite Massif*, displays an extremely heterogeneous structure with individualisation of several migmatization textures such as diatexites and metatexites and amphibole-rich restites with geochemical signatures that suggest crustal anatexy of the

Neoproterozoic metasediments. The ages for GMC were constrained around 341 Ma (Pereira et al 2015), indicating that migmatization events should slightly precede the elongated WNW-ESE *Hospitais TonaliteMassif* installation with 337-336 Ma. and characterised by ubiquitous medium to coarse-grained tonalite, which displays sparse mafic enclaves with diorite affinity (Moita, 2007; Moita et al 2015).

The *Alto de São Bento Granitic Suite* is a suite of plutonic rocks characterised by two-mica leucogranite and porphyritic granites with mafic enclaves, similar to the ones described for the *Hospitais Tonalite Massif* (Moita et al 2015) and with ages around 336.7 Ma ± 3.2 Ma (Pereira et al 2015). The leucogranites are strongly peraluminous with calc-alkaline signatures coherent with the geodynamic settings that triggered magmatism in the SW of OMZ. The porphyritic granites are characterised by large crystals of alkali-feldspar, with sparse large mafic enclaves and by several pegmatitic-veins (Moita et al 2009).

iii) The Évora mid-grade metamorphic terrains is part of the hanging-wall at the NE of the *Évora massif* (Pereira et al., 2015; Dias da Silva et al., 2018) and corresponds to a wide sector affected by amphibolitic facies metamorphism and composed of metasedimentary rocks (schists, amphibolites) and gneisses, intruded by the *Divor* and the *Pavia* Carboniferous plutons (Dias da Silva et al., 2018).

The research here presented focus on the *Montemor-o-Novo Shear Zone* terrains, which comprise a complex metallogenic setting responsible for the formation of several iron and gold deposits, some of which part of the Montemor-o-Novo iron mining district.

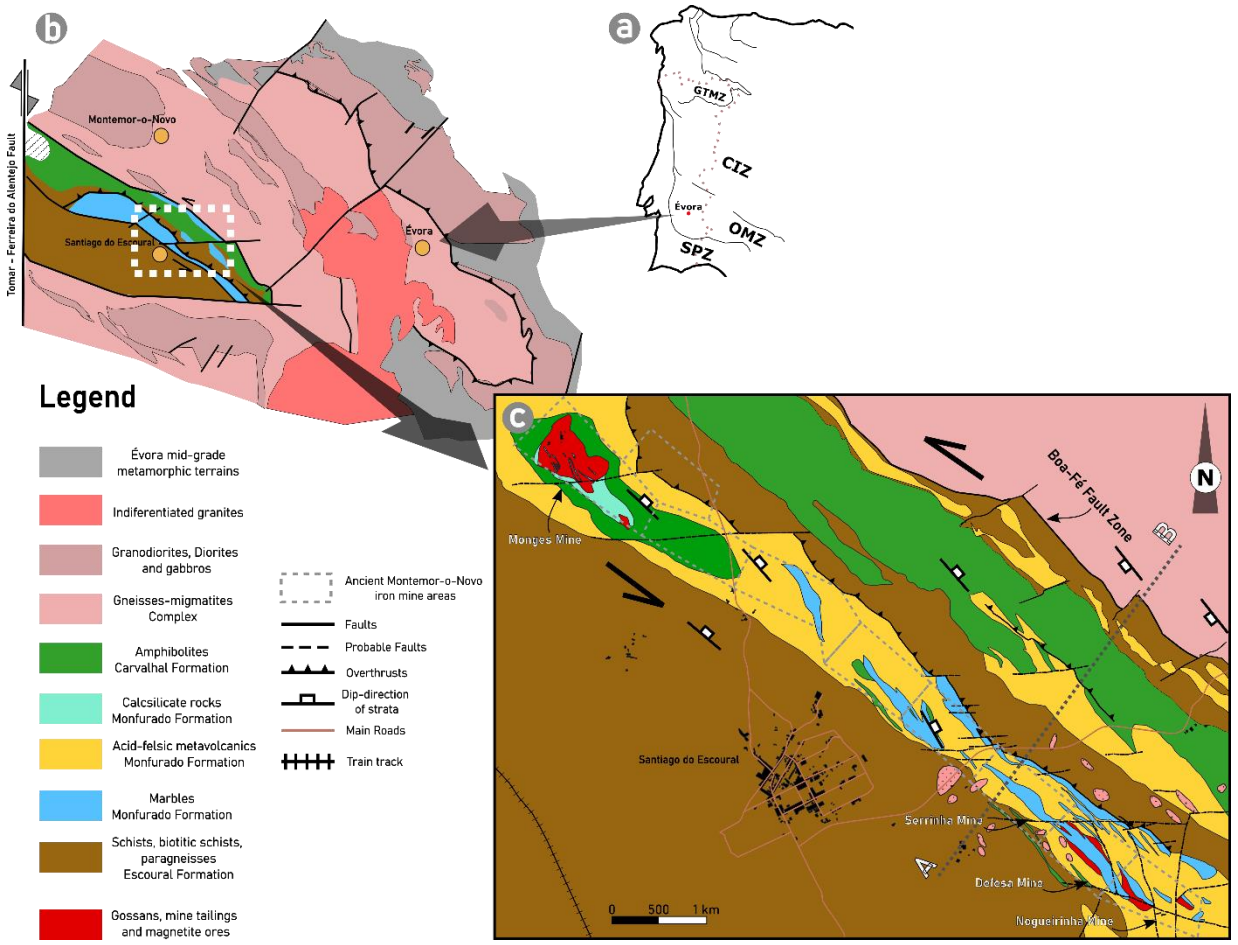

Figure 6.1 (a) Contextualization of the study area within the Ossa-Morena Zone and the Iberian Massif. (b) Simplified geological map of the Évora Massif terrains (adapted after Pereira et al 2003, 2015; Moita et al 2009). (c) Geological map of the Santiago do Escoural area and Montemor-o-Novo iron mining district (Andrade et al 1949), with delimitation of the mining areas (grey dashed rectangles). The map results from the reinterpretation and adaptation from seven Geological-Mining Maps at the scale 1: 5000 (nº0/-126; nº0/-124; nº-2/-122; nº-2/-124; nº-4/-122; nº-6/-120; nº-6/-122 - Serviço de Fomento Mineiro 1960) and from previous geological mapping works (Silva et al 1988; Chichorro 2006).

6.3 The Montemor-o-Novo iron mining district

The ancient mines from the Montemor-o-Novo iron district (**Fig. 2.1**) are located at the SW of the Ossa-Morena Zone, close to the Montemor-o-Novo municipality, which gives the name to the mining complex, and to the Santiago do Escoural village, in the Monfurado Mountain range (441 meters). Evidence for human occupation in the area dates back to the Palaeolithic age based on wall paintings and artefacts (100 000 bC – 10 000 bC; Silva et al 2017), and therefore, the use of mineral resources (including for the pigments used on the wall paintings) for human well-being is assumed to have occurred in the area from those times up to the Roman occupation of Iberia, later succeeded by modern mining in the 20th century.

Such a long mining history has produced not only landscape transformations (e.g., the presence of mine tailings and open pits), but also the cultural and historical heritage of the region. Examples of this are recognised in the toponymy of the Monfurado Mountain and the Santiago do Escoural village. The name of the mountain range (*Monfurado*) derives from the agglomeration of *Monte* (=range/small mountain) *Furado* (=bored/excavated/with cavities), owing its name to the ubiquitous excavations seen throughout the mountain which are attributed to Roman mining works. Another explanation for this name could be related to the karst morphologies associated with the limestones and marbles of the Monfurado range, such as the ones observed at the Escoural Caves (see section 4.). The Monfurado range corresponds to an area protected under the "Natura 2000" network, considered as a Special Conservation Zone aiming to protect and preserve important natural habitats.

The Santiago do *Escoural* village name is considered to have its origin related to the iron exploration and beneficiation during Roman times. The *Escoural* name could have derived from *Escorial,* which means "a field of slag", due to the findings of several tailings of slag through the area considered to have been produced during Roman iron mining works.

Long after the Roman occupation the Montemor-o-Novo area was the target for iron exploitation through ten concessions along a 10 km NW-SE belt (**Fig. 6.1c**), in which open-pit and to a lesser extent underground mining was carried out from 1865 until 1929 (Andrade et al 1949).

6.3.1 Ore deposit geology

The geodynamic evolution of the SW Iberian Variscides sustained conditions suitable for the formation of ore deposits associated with rift-related submarine volcanism during the opening of the Rheic Ocean

Example of such metallogenic systems is the Montemor-o-Novo iron deposits (Salgueiro 2011; Salgueiro et al 2012; Mateus et al 2013), to which a classification as SEDEX and VMS deposits were attributed due to their geological settings at the presumable time of formation and ore assemblage, mainly constituted by massive magnetite bodies and massive sulfide layers (Maia et al 2022). Sedimentary exhalative (SEDEX) deposits are formed near seafloor submarine hydrothermal vents that promote the precipitation of metals (Cu, Pb, Zn) in stratiform bodies, usually hosted by shales and siltstones. The conditions that lead to SEDEX deposits formation are intrinsically related to rift-related events, in which rifting promotes the formation of hydrothermal vents that leach metals from the surrounding host rocks (Hannington 2021; Wilkinson 2014).

The Volcanogenic massive sulfide (VMS) term refers to deposits formed in a submarine environment near large episodes of submarine volcanisms many times triggered during the rifting stages of an orogen. The VMS deposits are usually rich in base metals (Cu, Zn, Pb), and found in massive sulfide lenses composed of more than 60 % of sulfides (Hannington 2014), mostly pyrite and pyrrhotite.

The iron ores from the Montemor-o-Novo deposits are mainly hosted as massive lenticules in the Monfurado Formation marbles, although disseminated and massive magnetite is also found at depth (intersected by drill cores; Maia et al 2022). The host carbonate units display intense amphibole development close to the ore horizons, which is in some cases the reflection of the metamorphism in the greenschist to amphibolitic facies. The relation of the iron ores and the host rocks has led to the interpretation that consider them as being syngenetic and therefore magnetite formation should be contemporaneous of the Cambrian sedimentary carbonate formation.

The continental orogen stage of the Variscan Orogeny (390 Ma – 370 Ma: Ribeiro et al., 2007) promoted the formation of several deposits related to such geodynamic context, such as the Escoural Orogenic gold deposits (Ribeiro et al 1993; Inverno 2001; Maia et al 2022) found near the study area. These deposits mainly occur in the vicinity of the *Boa-Fé* fault, within the MNSZ, and are hosted in quartz veins crosscutting the Escoural Formation metasedimentary succession, in which gold-arsenopyrite-loellingite-maldonite assemblages have been identified. Gold mineralisation is structurally controlled by the Variscan MNSZ activity (356 – 322 Ma; Pereira et al 2015), with vein development mainly associated with a brittle-ductile transition. The spatial relation between the iron ores and gold mineralisation has been discussed in recent works (Maia et al 2022).

6.4 Geodiversity Assessment

The insufficient geological literacy, particularly in Portugal, is in part due to the inappropriate and unproportionally teaching of geology through middle and high school, when compared to other natural sciences (Reis et al 2014). This inefficiency leads to a deficient awareness to the role of mineral resources in society. This becomes a problem when it is necessary to grasp environmentally responsible exploration and mining projects, leading to problems with local communities and therefore in acquiring the necessary social license to operate. Geologists have their share in this problem, since normally it is quite difficult to deconstruct some of the concepts of geology (*sensu lato*), and particularly the ones related to exploration and mining, to a non-specialised public. For this, the assessment of geodiversity and mining heritage by cataloguing and promoting the scientific and educational value of key locations is of major importance.

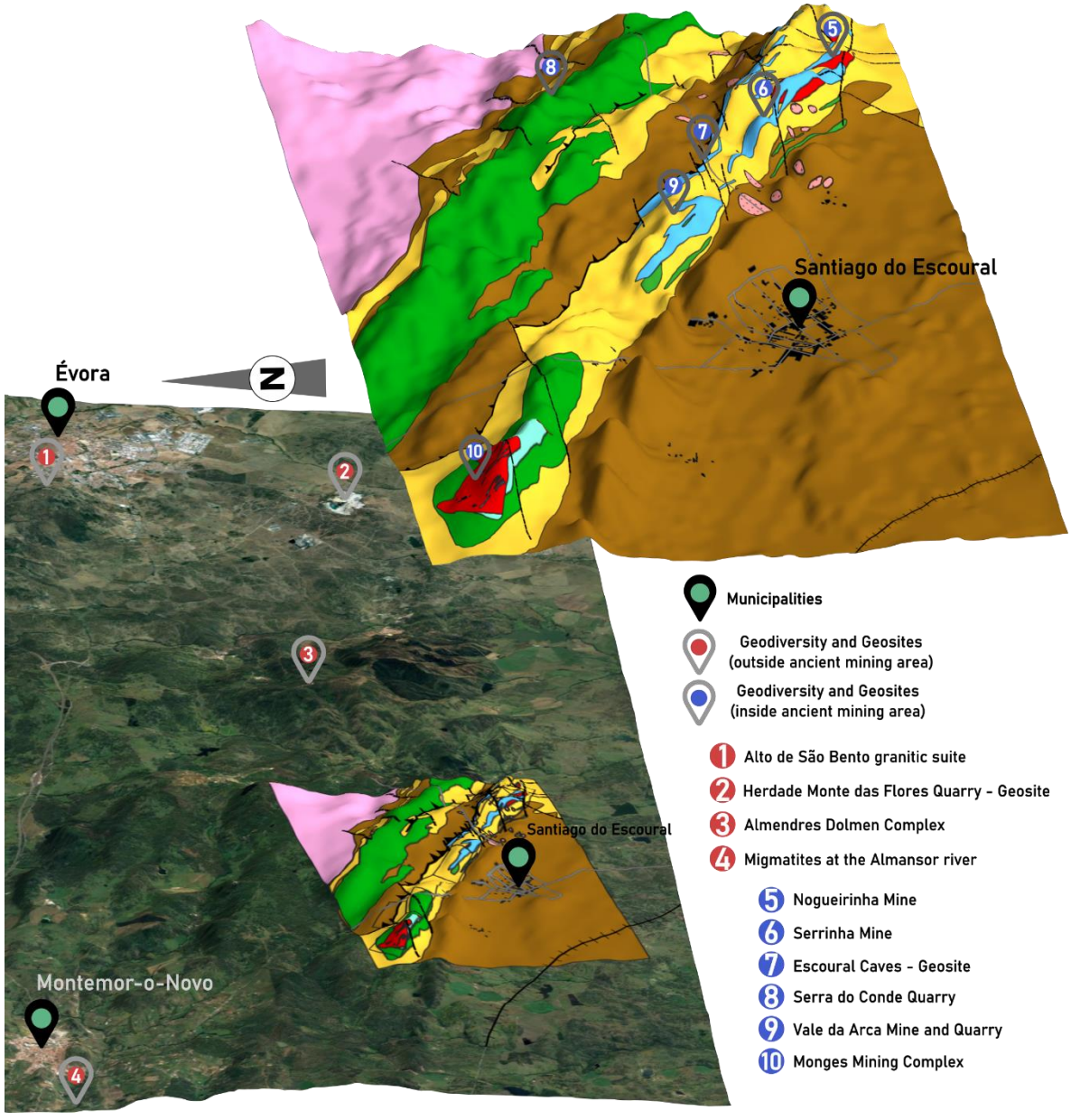

Figure 6.2 (previous page). Digital Elevation Model projection using QGIS (plugin QGIS2ThreeJS) with the overlap of the Geological map of the Santiago do Escoural area (shown in Figure 1). Location of the Évora and Montemor-o-Novo municipalities is provided, as well as the selected locations for the presented geodiversity assessment.

The Évora – Montemor-o-Novo districts comprise attractive and didactic geosites and geodiversity sites that display a strong relationship with several cultural and historical values of the region that could, and should, be used in informal and formal teaching activities focusing on the local and regional geology. A total of ten sites, both outside and inside the ancient iron mining area (**Fig. 6.2**), are outlined as being able to integrate a geological and cultural route between Évora and Montemor-o-Novo (**Fig. 6.2**). Limelight will be focussed on the mining heritage located in the Montemor-o-Novo municipality, near the Santiago do Escoural village, since geodiversity characterisation and assessment within these areas raises more concerns in terms of geoconservation due to the rapid deterioration of some of the mining heritage sites.

The description of geodiversity is herein addressed both for the outside and inside of the ancient Montemor-o-Novo mining district, aiming to propose a geodiversity route that interlinks the Évora and Montemor-o-Novo municipalities. A qualitative assessment (Brilha 2016, Brilha et al 2018) of individual potential location is provided through the next sections, as well as a tentative quantitative assessment of Geodiversity regarding the Scientific (SV), Educational (EV) and Touristic values (TV) of the locations proposed to integrate the geodiversity route, allied with the degradation risk assessment following the criteria defined by Brilha (2016). The quantitative assessment results can be consulted in **Appendix A**. A score from 1 to 4, is attributed to each site selected to integrate the geodiversity route, with exception of the *Almendres Dolmen Complex* since it does not meet the criteria to be considered a geodiversity location Nevertheless, the *Almendres Dolmen Complex* was most probably constructed using local granitic stones, and due to its significant archaeological and cultural heritage is herein considered as an important asset for the route. The numbering of the sites is shown in accordance to **Figure 6.2** and does not represent the sequence of visitation for the potential geodiversity route (see section 6.). The list of the sites both inside and outside of the ancient mining area can be found in **Table 6.1**.

Table 6.1. Identification of the sites selected to integrate the geodiversity assessment with identification of owner, legal protection, accessibility, key features, and framework.

Site Name	GPS	Owner	Legal Protection	Accessibility	Key features	Framework (if applicable)*
Alto de São Bento granitic suite	38.580910; -7.937558	Public	-	Paved road (easy)	Évora Massif granitic facies	Pre-Mesozoic Granitoids
Herdade Monte das Flores quarry	38.524725; -7.954017	Private	Geosite	Paved road (easy)	Évora Massif granitic facies	Pre-Mesozoic Granitoids
Almendres Dolmen Complex	38.557508; -8.061331	Public	National Monument	Dirt road (easy)	95 monoliths from the Neolithic period, made using the local Évora granites	-
Migmatites at the Almansor river	38.645783; -8.229458	Public	-	Paved road – by foot (medium)	Impressive outcrop of the Évora Massif Gneiss-Migmatite Complex	Pre-Mesozoic Granitoids
Nogueirinha mine	38.530739; -8.124066	Private	-	By foot (hard)	Mining heritage; Mine tailings	-
Serrinha mine	38.538831; -8.136711	Private	-	By foot (hard)	Mining heritage; Ore bodies outcrops; Mine tailings	-
Escoural caves	38.543636; -8.1377728	Public	Geosite - National Monument	Paved road (easy)	Karst cave with evidence of Palaeolithic occupation	Karst Systems of Portugal
Serra do Conde quarry	38.555941; -8.131335	Private	-	By foot (medium)	Impressive amphibolite outcrops	-
Vale da Arca mine and quarry	38.548015; -8.146171	Private	-	Paved road (easy)	Monfurado Formation outcropts	-
Monges mining complex	38.573301; -8.193995	Private	-	By foot (medium)	Mining heritage; Ore bodies outcrops	-

6.4.1 Geodiversity and geosites outside the ancient mining area

6.4.1.1 Alto de São Bento granitic suite (Ancient Quarry)

The *Alto de São Bento* area is a geomorphological feature of the Évora landscape, located at around 3 km from the city centre, and corresponds to an elevation (aprox. 360 m) that contrast with the surrounding characteristic Alentejo plains. At the area, outcrops of two-mica leucogranite and porphyritic granites (**Fig. 6.3a**) were exposed by quarrying activities during the 20th century and are now accessible to the public. The contrasting altitude of Alto de São Bento with the surrounding landscape was an important factor for the settlement of several windmills used for seed processing.

The geological, biological and cultural assets of the area are currently musealized (Brilha & Carvalho 2010) by the Évora municipality, which developed a museum that offers several educational and touristic activities, allied with the fact that the *Alto de São Bento* area offers one of the most beautiful sight-seeing sceneries over the Évora UNESCO city (**Fig. 6.3b**).

Several geological features are displayed at the outcrop, such as the ubiquitous course-grained porphyritic granite with abundant K-feldspar phenocrysts which display concentric zoning (**Fig. 6.3a**) and a medium grained two-mica leucogranite. The porphyritic granite facies also exhibit large mafic enclaves of igneous material (biotite-rich; **Fig 6.3a**) that put in evidence fractional crystallisation processes (Moita et al 2009).

Considering the described characteristics, it is evident that the substantive scientific, educational and even touristic values of the area, with scores of 3.1, 3.3 and 2.9 respectively, flag it as a potential geosites location, benefiting from the musealization and conservation already developed in the area. Furthermore, the Alto de São Bento granitic suite could easily be integrated in the Pre-Mesozoic Granitoids framework of the Portuguese Geosite Inventory (PGI; Brilha et al 2005, 2008, 2010), and for this reason this site is herein considered a mandatory geodiversity stop in the geodiversity route proposed through section 6.

6.4.1.2 Herdade Monte das Flores Quarry

The *Monte das Flores Quarry* is an example of geodiversity in the Évora Municipality, located at circa 6 km from the city centre, it is part of the PGI framed on the Pre-Mesozoic Granitoids (Brilha et al 2008, 2010) and publicised on the ProGEO – Portugal website. The quarry is located at the Évora Massif, and extraction is devoted to the Évora granite/ granodiorite facies for industrial uses (Industrial rocks). The quarry was classified as a geosite due to its geological, economic, cultural, archaeological, and educative value. The most relevant

features are associated to the use of the Évora granites as building-stones from the Megalithic period until the present days. Evidence of that is the *Almendres Dolmen Complex* (see next section).

Figure 6.3. Main geodiversity and landscape features from the Geodiversity and Geosites excluding the mining heritage and located around the Évora and Montemor-o-Novo municipalities. **(a)** Representative photography of the Porphyritic Granite facies of the Alto de São Bento granitic suite, with characteristic K-feldspar phenocrysts commonly showing concentric zoning (zoomed-in photo also shown); large biotitic enclaves and thin pegmatitic veins (photo from the authors). **(b)** Scenery over the Évora UNESCO City at the Alto de São Bento Area (photo from the authors). **(c)** Drone imagery over the Almendres Dolmen Complex (photo from the authors). **(d.)** Overview of the migmatite outcrop at the Almansor riverbed (photo from the authors). **(e.)** Example of the diatexite, metatexite and restite structures individualized in the Gneiss-Migmatite Complex at the Almansor river (photo from the authors). **(f.)** Photography showing geological features characteristic of the karst system inside of the Escoural Cave. This photography is a courtesy from the Direção Regional de Cultura do Alentejo (DRCA; Regional Direction of Alentejo´s Culture).

6.4.1.3 Almendres Dolmen Complex

The *Almendres Dolmen Complex* corresponds to a cromlech archeologic structure located at circa 7 km of the UNESCO Évora city and is composed of 95 Neolithic granitic monoliths (**Fig. 6.3c**), arranged in a circle. The site was classified as a National Monument in 2015, and besides being an example of archaeological heritage, the geological aspects of the monument, like the nature of the rock utilized in the construction, can also be used for educational purposes.

Although the *Almendres Dolmen Complex* does not fit the criteria for geological heritage, if inserted in the geodiversity route, this site could be used as an example of the societal and cultural evolution associated with the use of geological resources. This monument is part of the Megalithic Route, promoted by the Évora Municipality, and although tourists intensely visit the area, it lacks proper interpretative communication, better road access, infrastructures, and visitation circuits.

6.4.1.4 Migmatites at the Almansor river

The Almansor area corresponds to an outcrop that displays the perfect conditions for the observation of the high-grade metamorphic terrains from the Variscan *Gneiss-Migmatite Complex*, part of the *Évora Massif*.

The area is located along the left and right margins of the Almansor river that contours the Montemor-o-Novo municipality (ca. 2 km from the city centre). At the outcrop scale several petrogenetic features have been individualised by several authors, such as diatexites, weakly foliated granitoids and trondhjemitic veins (Moita et al 2009). The high-grade metamorphic terrains register the effects of intense migmatization of the metasedimentary country rocks (Escoural Formation), in which partial fusion (crustal anatexy) is evidenced by the presence of diatexites, metatexites, restites and numerous mafic enclaves observed through the area, revealing variable fusion rates.

The diatexites-metatexites mark the migmatization flow (**Fig. 6.3d**) commonly exhibiting centimetric to metric restites of metamorphic origin (Moita 2007; Moita et al 2009), possibly reflecting metasedimentary host rock blocks, from the Escoural formation, that did not undergo total fusion and in which pre-migmatization textures are sometimes preserved (**Fig. 6.3e**).

The diatexites and metatexites are composed of leucosome and melanosome components (**Fig. 6.3e**) and the relation between the GMC and the adjacent *Hospitais Tonalite Massif* is evidenced by the weakly-foliated granitoids present in the area (Moita et al 2009).

As gathered from the previous description, and reinforced by the SV, EV and TV scores (**Appendix A**) of 3.6, 3.1, and 2.65, respectively, it is here suggested that the area has the

potential to be classified as a geosite framed in the Pre-Mezosoic Framework of the PGI Inventory (Brilha et al 2008 2010). Furthermore, there has been a previous proposition for the creation of two Eco-trails through the Almansor river margins (Dias da Silva et al 2006), which contemplates the geological, cultural and landscape characteristics of the area. The geoconservation strategies that could possibly be implemented should focus on the implementation of interpretative centres focusing on the representative and rare geological processes displayed through the outcrops. Besides the proposals from other authors, we believe that contemplating this site in a geodiversity route is extremely important in interpreting regional geological settings.

6.4.2 Geodiversity and geosites inside the ancient mining area

6.4.2.1 Nogueirinha and Serrinha mine

The *Nogueirinha* and *Serrinha* mines were two of the main open-pit exploitation areas corresponding to two of the 10 mining concessions part of the ancient Montemor-o-Novo iron district (**Fig. 6.1**). Both mines are located approximately at 26 km and 21 km from Évora and Montemor-o-Novo municipalities, respectively. Mining activities were sustained from 1876 until 1929, and the total amount of exploited iron ores are estimated at around 137 406 tons (Andrade et al 1949), which at the face of current societal supply and demand is considered insignificant.

Currently, the open-pit mining areas are abandoned and have not been the target of any geoconservation proposals. They are both located inside private owned lands, although access is usually granted for educational and scientific purposes. From a visitation point of view these proposed locations are the ones that raise more concerns regarding security and accessibility to the outcrops, but nevertheless field work is possible.

Remnants of the ancient mining works are ubiquitously denounced by large volumes of tailings in both *Nogueirinha* and *Serrinha* mines. At the *Serrinha* mining area, the access to the outcrop is easier, and primary magnetite ± primary pyrite mineralisation can be observed.

The quantitative assessment of both locations revealed SV; EV and TV of 1.75/1.9, 2.2/2.2 and 2.2/2.2 respectively.

6.4.2.2 Escoural cave

The *Escoural caves* is a geosite framed in the "*Karst Systems of Portugal*" classified by the PGI (Brilha et al 2008, 2010; Brilha and Pereira 2020) and corresponds to a typical carbonate karst system, located at approximately 15 km from the Montemor-o-Novo municipality (**Fig. 6.2**). The cave was accidentally discovered in 1963 during quarrying works in the area, which

focused operations on marble extraction for ornamental purposes. The marbles belong to the Cambrian Monfurado Formation (Chichorro 2006). Allied with the karst other geological features are identified, such as stalactites and stalagmites (**Fig. 6.3f**).

Besides the described geological features, that classify the *Escoural cave* as a geosite, carvings and paintings found on the cave walls demonstrate that the karst system was used as a shelter for human settlements since the Palaeolithic (Silva et al 2017). The discovery of these findings has classified the cave as a national monument due to its major archaeological value.

Hence, the *Escoural cave* has been the aim of several conservation interventions and academic research in a wide range of scientific fields (e.g. Caldeira et al 2021). Visitation is currently possible, although prior booking with the Montemor-o-Novo municipality is mandatory. The guided tour through the small cave takes approximately 30 minutes and can be organised in groups of up to 10 persons (pre-COVID). Although the cave displays interesting geodiversity features, the visitation currently only focuses on the pre-historic archaeological features of the monument. The geodiversity quantitative assessment of the *Escoural cave* revealed SV, EV and TV scores of 3.1, 3.3 and 3.25 respectively, supporting the geological significance of the monument. We believe that since the area is already classified as a geosite, the guided tour in the *Escoural cave* should also focus on the geological features of the karst system, and if so, should integrate the herein suggested geodiversity route.

6.4.2.3 Serra do Conde Quarry

The *Serra do Conde* area corresponds to a differential erosion relief (439 m) part of the Monfurado Mountain range, located at approximately 23 km from Évora and 21 km from the Montemor-o-Novo municipalities.

At the *Serra do Conde* area outcrops of amphibolites from the *Carvalhal Formation* (**Fig. 6.1; Fig. 6.4a**) occurring in the core of a synclinal structure can be observed (**Fig. 6.4c;** Chichorro 2006). The amphibolites display a nematoblastic texture and two main metamorphic-deformation fabrics can be seen. One parallel to an S_0 foliation with a N325º direction and sub-vertical dipping, strongly marked by the development of epidote (**Fig. 6.4b**). Primary foliation is transposed by a generally folded S_1 mylonitization (N145º direction; **Fig. 6.4b**). The rock quality and weak fracturing fomented the extraction of several blocks as ornamental stone, and therefore the outcrops at the Serra do Conde area were exposed by the quarrying activity.

The area contributed to scientific research that focused on the interpretation of the regional and structural geological settings (Chichorro 2006) reinforcing the scientific value

score of 3.2 (**Appendix A**). Access to the area can be done by foot or by SUV through an earth road (approximately 1.5 km from the nearest paved road). The described characteristics of the *Serra do Conde Quarry* resulted in EV and TV scores of 1.95 and 2.05 respectively, although we believe that the educational value is far greater than the touristic value.

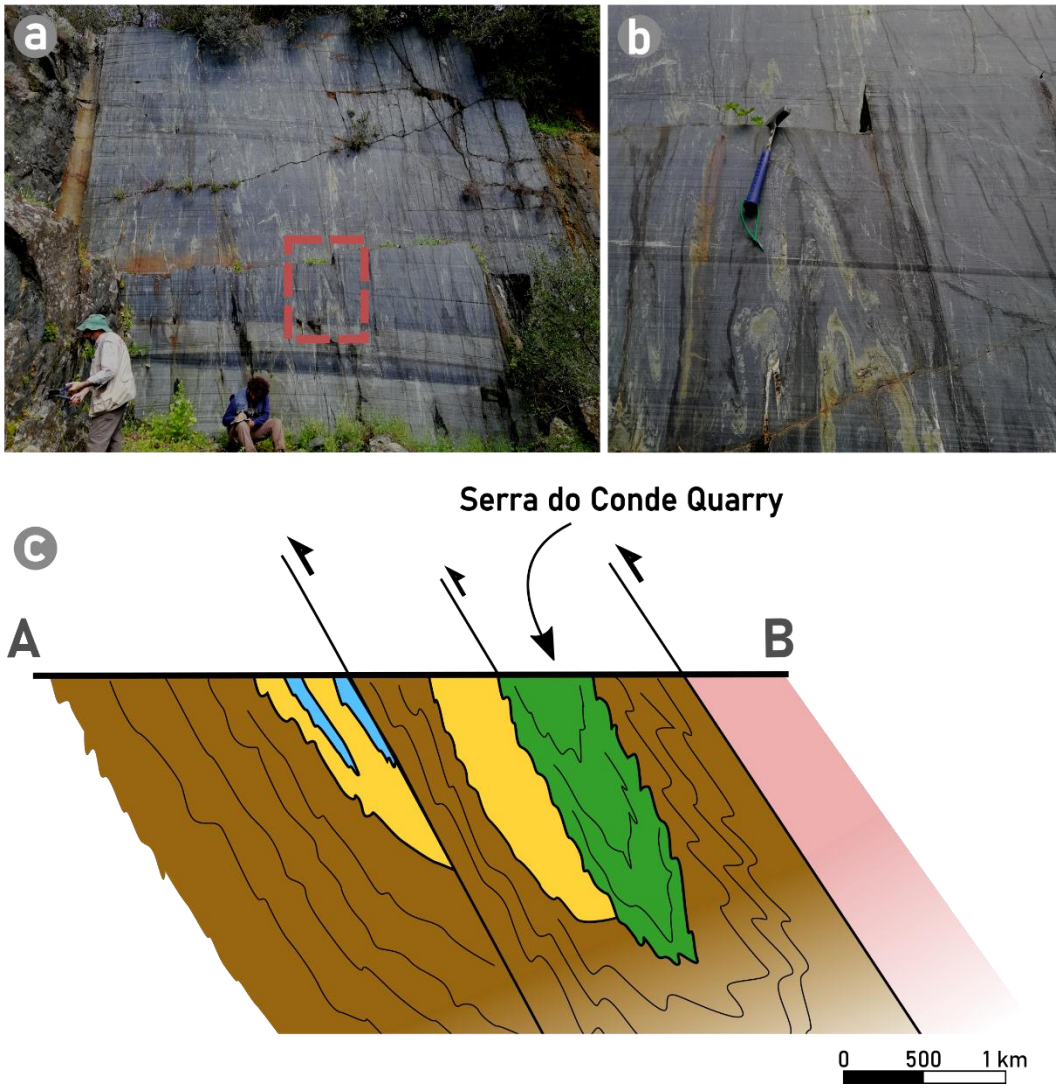

Figure 6.4. Serra do Conde Quarry representative features and A-B cross section shown in Figure 1. **(a)** Wall of the front of quarry exploration in which exceptional outcrops of the green-amphibolites of the Carvalhal Formation are observed (photo from the authors). **(b)** Close-up photography of the Carvalhal Formation amphibolites at the Serra do Conde Quarry, with clear Epidote development marks the S0 foliation, later folded and marking a second stage of deformation (S1) (photo from the authors). **(c)** A-B cross section representative of the Serra do Conde area. The A-B profile is shown in Figure 1 (adapted from Silva 2013).

6.4.2.4 Vale da Arca Mine

Vale da Arca Mine is located at circa 16 km and 25 km from the Montemor-o-Novo and Évora municipality and contributed with a minor amount of ore production to the overall tonnage of the Montemor-o-Novo iron district, although concrete numbers are not known (Andrade et al 1949). The mine was abandoned during the early 20th century, although it was latter used for quarrying activities that focused on the extraction of the marbles. The quarry is presently abandoned, but both the mining and quarrying activities exposed outcrops that allow for the characterisation of geodiversity features related to the geodynamic and structural settings of the MNSZ.

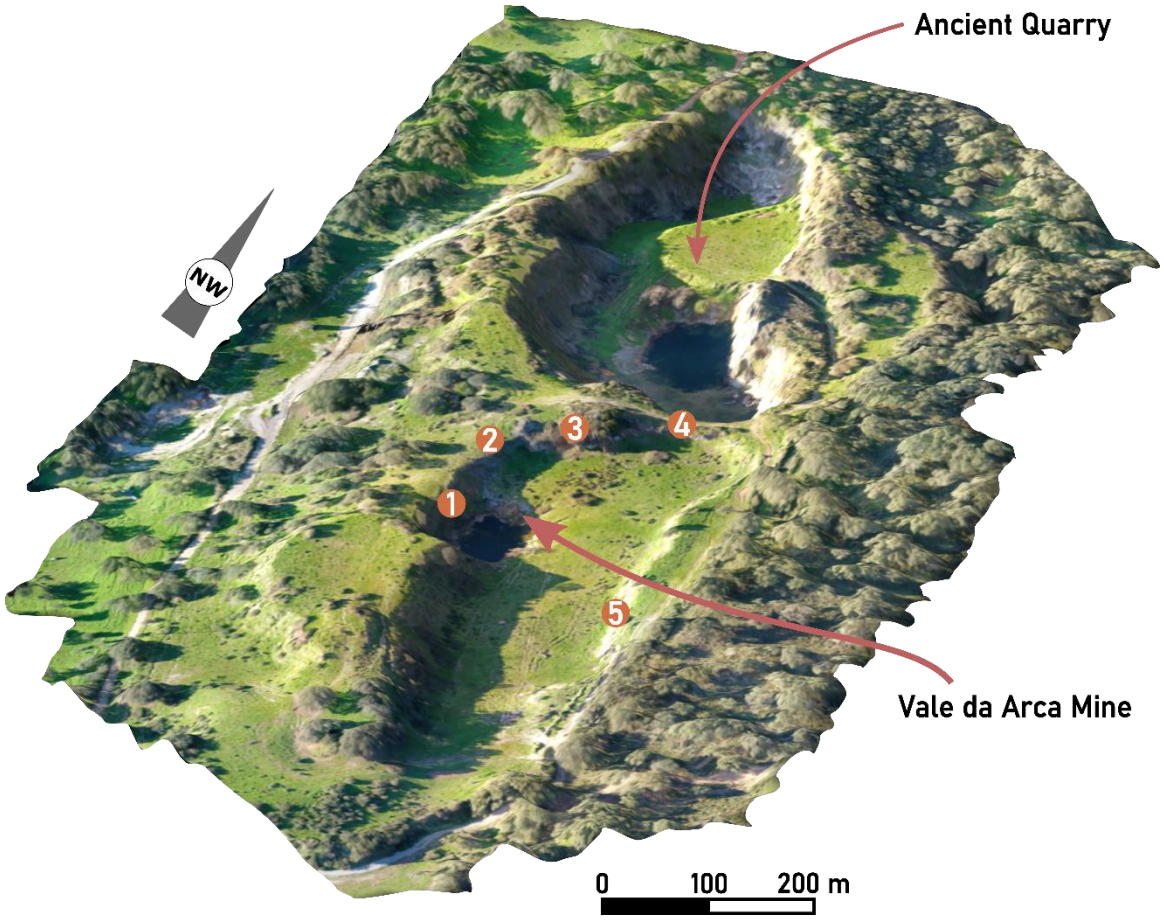

Figure 6.5. Digital elevation model with overlapped ortophotomaps of the Vale da Arca Mine area, which is the result of drone aerial imaging and latter 2.5D model construction using QGIS plugin QGIS2ThreeJS. The pinpoints on the model correspond to locations where several geodiversity features can be observed. These locations are described throughout the manuscript.

For the present work the Digital Elevation Model (DEM) was constructed using drone imagery collection in the Vale da Arca area (**Fig. 6.5**), and five geological features of the

outcrops are outlined (**Fig. 6.5**): 1) Observation marbles with olivine and disseminated magnetite ± pyrite mineralisation. This lithotype belongs to the *Monfurado Formation* marbles and here it is possible to understand that the disseminated textures and low tonnage were probably the reasons why the mine was abandoned; 2) Boudinage structures of a silicious layer interbedded within the olivine marbles (**Fig. 6.6a**) resulting from the different mechanical/rheological competence between the marbles, with a ductile behaviour, and the silicious layer which has a brittle behaviour, generated due to the overall NW-SE deformation associated to the MNSZ activity. Boudinage structures such as chocolate tablet boudinage and inter-boudin (**Fig. 6.6c**) and necking structures (**Fig. 6.6d**) are observed in this site; 3) At the area, beds of massive pyrite ± magnetite layers can be observed (**Fig. 6.6b**) and usually exhibit surficial oxidation (**Fig. 6.6b**). These beds are over thrusted (N355º; 40ºE) by pristine course-grained marble lithotype, which correspond to point 4 in **Figure 6.5**; 5) The upper unit of the *Monfurado Formation* marks the initial stages of Cambrian basic volcanism, with abundant intercalations of metavolcanic coarse-grained rocks, which can be observed in this point. These rocks exhibit large crystals of amphibole, epidote and feldspar (**Fig. 6.6e**).

The pin-pointed geological features (**Fig. 6.2**) show the relevance of these outcrops for a possible geodiversity route, which favour the accessibility conditions of the *Vale da Arca Mine*. The SV, EV and TV scores (2.1, 2.5, 2.4; **Appendix A**) reinforce the proposition of the *Vale da Arca* area as a geosite that would easily be integrated in a geodiversity route.

Ongoing research focusing on trace element composition of magnetite (Maia et al. *in prep.*) found evidence for the deposition of sphalerite (ZnS) along late stages of magnetite deposition. The textures found on magnetite crystals indicate that sphalerite is associated with the porous rims (**Fig. 6.6f**), where they occur as inclusions along with pyrite (**Fig. 6.6g** – green Zn distribution). Such findings might be good indications for future mineral exploration in the area, which should not be constrained by future geoconservation strategy because the mining potential of the area should be an ally of the use of the area for scientific, formal and informal education activities.

6.4.2.5 Monges Mining Complex

The *Monges Mining Complex* correspond to the biggest mining works part of the Montemor-o-Novo iron district. The area is located approximately 10 km from the Montemor-o-Novo and 35 km from the Évora cities. Mining works were mostly performed in open pit, although locally underground mining was adopted, with ore production estimated around 206 783 tons, which correspond to 60% of the iron production in the sector (Andrade et al 1949).

The *Monges* mine (Monges = Monks) owe its name to the existence of an Abbey (**Fig. 6.7a**) which construction dates to 1738 and served hermit monks that inhabited the Abbey

until 1834. After the abandonment, and with the discovery of the iron ores, the Abbey was used to lodge many of the miners that worked at the mine site (Andrade et al 1949). Currently, the beautiful building is in ruins (**Fig. 6.7a**) due to an unfortunate lack of architectonic conservation strategies.

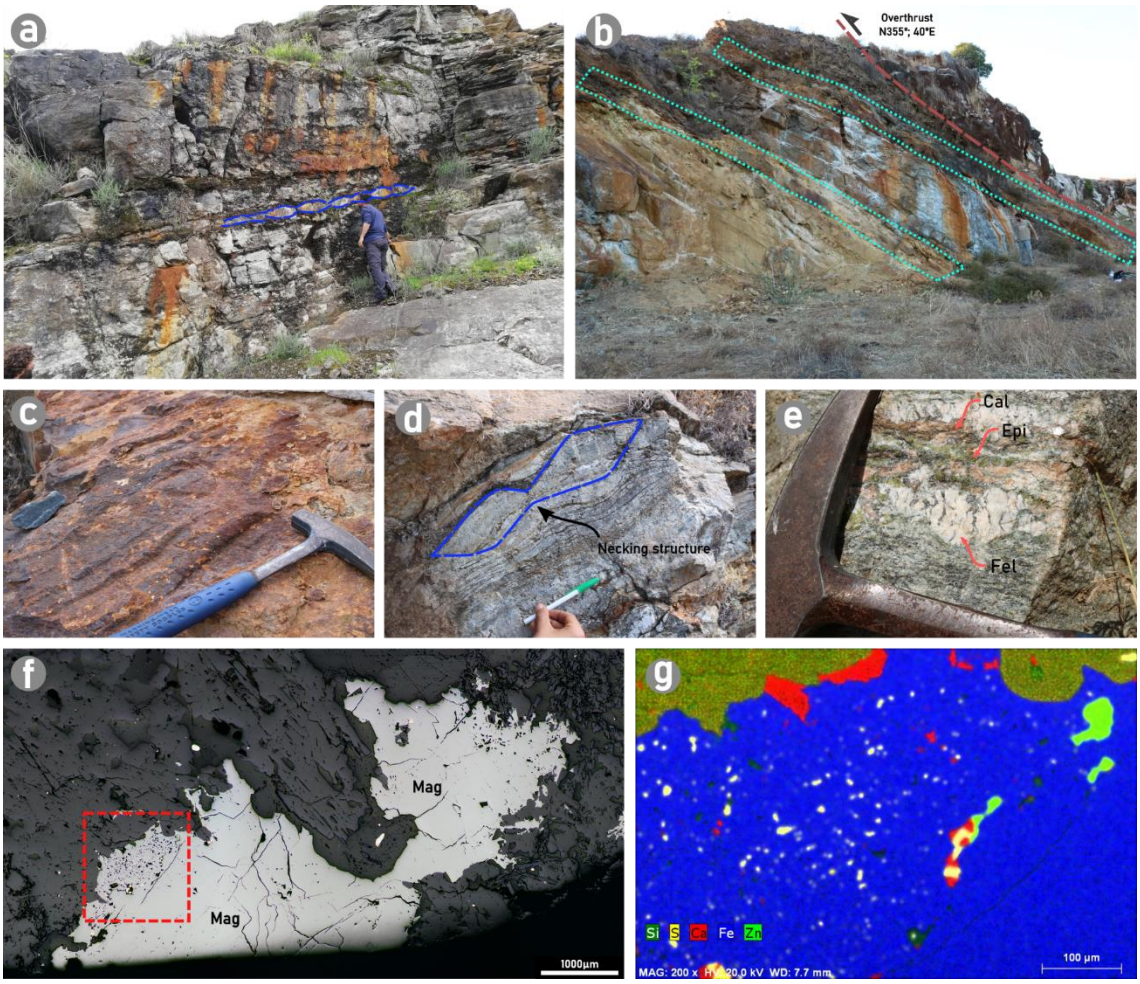

Figure 6.6. Main geodiversity features of the Vale da Arca Mine. **(a)** Boudinage of a siliceous bedding parallel to the surrounding marbles at the Vale da Arca area. The boudains mark the main deformation direction (NNW-SSE) (photo from the authors). **(b)** Inter-boudain structures observed in the marble units (photo from the authors). **(c)** Necking boudinage structures observed in the marble units and marking the deformation direction (photo from the authors). **(e)** Close-up photography of a metavolcanic intercalation on the marble units, where individualization of large feldspar, epidote, amphibole and calcite crystals is possible (photo from the authors). **(f)** Photomicrograph of a cross-section prepared from the magnetite ore bodies of the Vale da Arca mine, with porous rims (red rectangle) (photo from the authors). **(g)** Electron Dispersive Spectroscopy mapping showing Si, S, Ca, Fe and Zn distribution of the section shown in the red rectangle from (f). The SEM-EDS mapping allowed to identify the mineral phases observed in the porous rims of the magnetite crystals.

The remnant open-pit mining activities are currently dominated by intense vegetation which outlines nature restoration promoted by natural processes combined with human

abandonment. Even though access is difficult, at the area large mine tailings can be observed, as well as *in-situ* ore bodies. As previously described, mining activities in the region are thought to date back to the Roman period, and at the time iron ores were found due to the intense leaching capping (gossan zone) that are an evidence of intense iron-oxide surficial alteration (**Fig. 6.7c**).

The massive ore bodies are mainly constituted by magnetite (± pyrite ± chalcopyrite) and perfect crystallisation of magnetite is ubiquitously observed (**Fig. 6.7b**). The effects of pyrite exposure to atmospheric conditions are observed at the outcrop scale, and the oxidation of pyrite results in sulphates and native sulphur formation, denounced by its characteristic yellow colour (**Fig. 6.7d**). Microscopic examination of magnetite samples collected at the *Monges* open pits (**Fig. 6.7e and f**) revealed euhedral magnetite crystals with porous textures and homogenous chemical compositions (**Fig. 6.7f**), but with sparse silicate inclusions.

The examination of the *Monges Mining Complex* indicates that this is one of the prime examples of mining heritage in the region and is herein proposed to integrate the Portuguese geosites list, although a framework that considers the mining heritage of Ossa-Morena Zone would have to be proposed. This proposition is supported by the obtained SV and EV quantitative assessments (**Appendix A**). Although some accessibility conditioning is identified, such as the access by an earth road and by foot, the area also displays the necessary conditions for a trekking route, taking advantage of the Monfurado Mountain habitats and characteristic vegetation (*Quercus Suber*).

6.5 Proven educational value

Proven educational and scientific value of the Évora – Montemor-o-Novo region is recognised by the many scientific papers (e.g. Moita et al 2009, 2015; Chichorro et al 2008; Salgueiro 2011; Pereira et al 2003; 2006, 2015; Dias da Silva et al 2018; Maia et al 2022.) and educational activities continuously being developed, both addressing the lithological and metallogenic diversity of the area.

Most of the educational activities carried out through the area are dedicated to geology bachelor and master's degree students, and one of the reasons why this is continuously done is the proximity to the University of Évora. During the last four years, the dynamization of several activities in the area was done by the project "ZOM3D: 3D Metallogenic Modelling of the Ossa-Morena Zone – Valorisation of the mineral resources of Alentejo" (from now on referred as ZOM3D) and by the Geoscience Department of the University of Évora.

The activities were targeted to a geoscientific audience, and examples of that were the 2018 Spring Course and the recent 2021 accredited field course devoted to the upgrading of geological concepts targeted to professors from the basic and high-school education levels.

Additionally, the Montemor-o-Novo iron district were the theme for a geoscience communication and divulgation webserie, promoted by the ZOM3D project and targeted to a Portuguese non-specialised audience. The webseries are dedicated to the iron deposits of the Fe-Zn-(Pb) *Montemor-Ficalho belt*, with special dedication to the mining heritage of the Montemor-o-Novo ancient iron mines. This webserie is composed of five episodes with lengths between the 3 to 5 minutes, promoting the use of virtual teaching resources inside the classroom. The videos were scientifically revised by the researchers of the ZOM3D project and are currently allocated in the ZOM3D project YouTube channel (https://www.youtube.com/c/ZOM3D/videos), in which several other webseries dedicated to other geological concepts and mineral resources of Ossa-Morena Zone can be found.

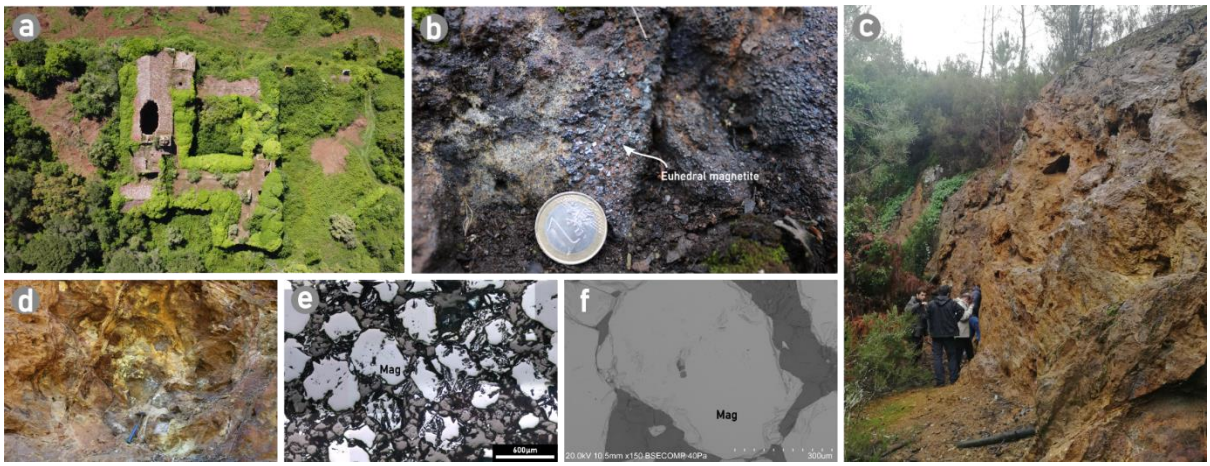

Figure 6.7. Main geodiversity features of the Monges Mining Complex. **(a)** Abbey at the Monges Mine, which gives the name to the mine and was used to lodge the miners (drone photo from the authors). **(b)** Euhedral crystals of magnetite on massive magnetite ore bodies, which are observed at the outcrops of the open pits at the Monges area (photo from the authors). **(c)** Example of one of the open-pit mining area at the Monges Mine (photo from the authors). **(d)** Oxidation processes of the magnetite-pyrite ores (photo from the authors). **(e)** Photomicrograph of a cross-section prepared from the magnetite ore bodies. **(f.)** Identification of micrometric inclusions by backscattered electron imagery.

6.6 Geodiversity Route between Évora and Montemor-o-Novo

The proposal of a geodiversity route between Évora and Montemor-o-Novo municipalities was conceptualised to take advantage of several sites that have already proved their geological value, some already having been classified as geological heritage (e.g. *Escoural Cave*), and aiming for the beneficiation of the Alentejo mineral resources, in particular the mining heritage of the region (Montemor-o-Novo ancient iron mines).

This geodiversity route would serve as a geological link between the two municipalities, tightening their relationship and reinforcing that geology has no administrative borders. The

qualitative and quantitative assessment of geodiversity reveals a great potential for geoconservation purposes of some of the sites, particularly the Alto de São Bento granitic suite; *Serra do Conde quarry* and *Monges Mining Complex* which display the best scores for considering them key-locations of geodiversity in the Évora – Montemor-o-Novo transect and are therefore proposed to be classified as Geosites.

Besides the geological aspects of the Geodiversity Route, it also displays additional important archaeological and cultural features that enrich its intrinsic value, such as the proximity to the UNESCO World Heritage Évora City. From another perspective, the geological diversity of the route covers several fields of Earth Sciences, from mineral resources to structural geology, and geological ages, from the Neoproterozoic up to the Carboniferous. Such features offer the possibility to travel through different stages of the evolution of the Iberian Variscan belt, presenting it at the light of the Wilson Cycle, and therefore immensely favourable for educational and scientific purposes. The proximity to the University of Évora and its state-of-the-art institutes (Institute of Earth Sciences - ICT; HERCULES Laboratory) are key factors for the viability of this route, to which the scientific know-how of these institutions could provide unique inputs.

As described, some of the locations are currently used as educational and touristic attractions (e.g. *Almendres Dolmen Complex*; *Escoural cave*), and were intervened by conservation strategies (e.g. *Alto de São Bento*), but their state of conservation is debatable and their touristic and economic beneficiation seems to fall a short from their true potential. For this reason, the geodiversity promotion proposed in this work could favour both the reinforcement of investment in the already classified areas and the beginning of a regional geoconservation strategy focusing on the Montemor-o-Novo ancient iron mining area.

The proposal shown in **Figure 6.8** displays a possible arrangement for the Geodiversity Route, starting from the Évora city, where several remnants of Arabic and Roman occupation can be visited (e.g., Roman Temple). Two routes are proposed for the Geodiversity Route, and as previously referred these could be adapted for public who has a geological background and for those who do not. The proposal suggests the following visitation route: 1 – *Alto de São Bento* granitic suite (**Fig. 6.3a and b**); 2 – Herdade Monte das Flores Quarry (Geosite); 3 – *Almendres Dolmen Complex* (**Fig. 6.3c**); 4 – *Nogueirinha Mine*; 5 – *Serrinha Mine*; 6 – *Escoural cave*s (Geosite; **Fig. 6.3f**); 7 – *Serra do Conde quarry* (**Fig. 6.4**); 8 – *Vale da Arca Mine* (**Fig. 6.6**); 9 – *Monges Mining Complex* (**Fig. 6.7**); 10 – *Migmatites at the Almansor river* (**Fig. 6.3d and e**). Nevertheless, some of the proposed locations have aspects that could be detractors of a possible beneficiation for touristic and even educational uses of this route, such as: the difficulty to access some of the locations (e.g. *Nogueirinha* and *Serrinha* mines; *Serra do Conde* quarry); private property location (e.g. *Herdade Monte das Flores* quarry) and safety issues related to ancient mining areas. Such questions could be addressed with protocols

between the municipalities and landowners for the use of private access roads to the geodiversity sites, as well as the common geoconservation strategy of the sites.

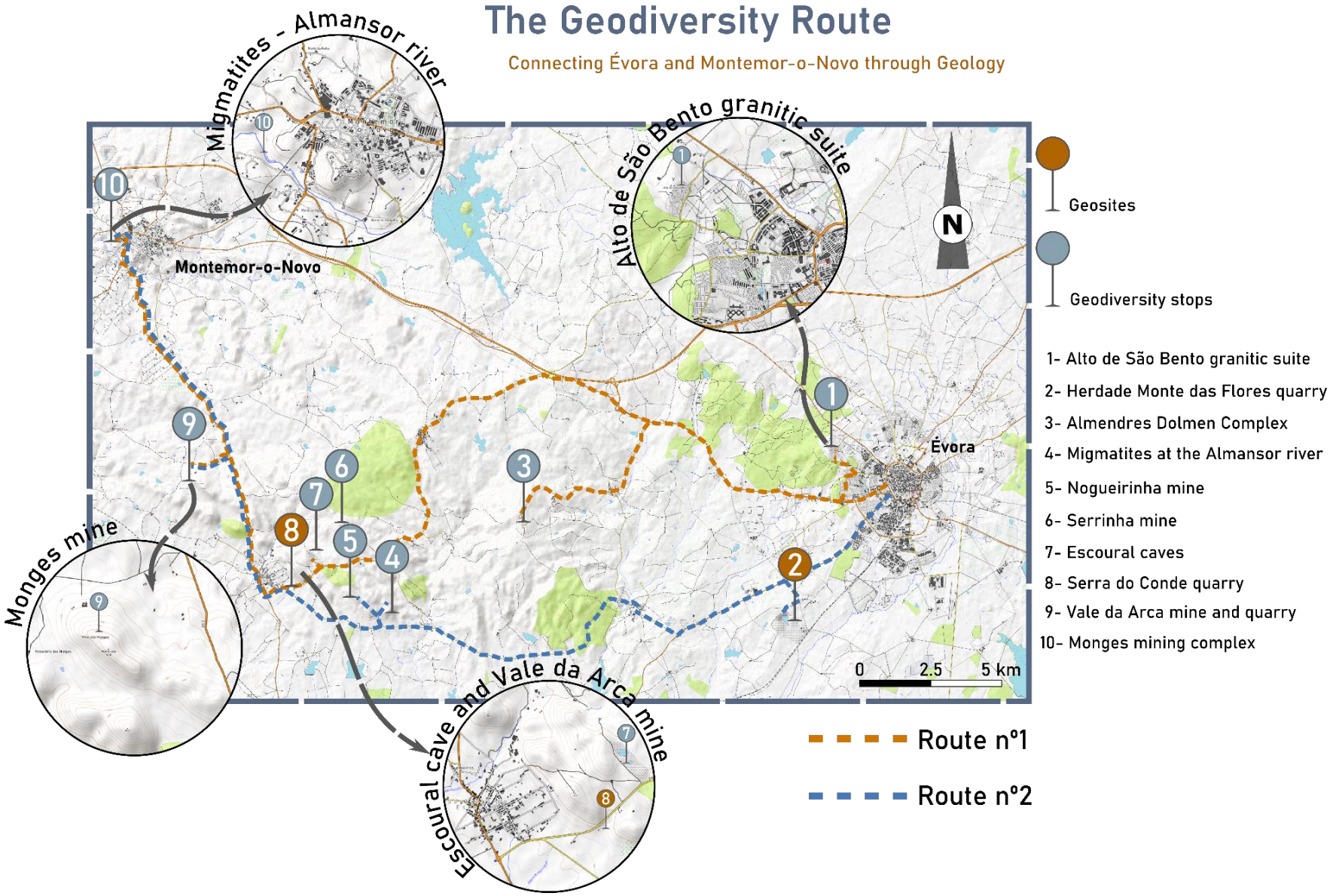
The Geodiversity Route
Connecting Évora and Montemor-o-Novo through Geology
Migmatites - Almansor river
Alto de São Bento granitic suite
Montemor-o-Novo
Évora
Monges mine
Escoural cave and Vale da Arca mine
N
0
2.5
5 km
Geosites
Geodiversity stops
1- Alto de São Bento granitic suite
2- Herdade Monte das Flores quarry
3- Almendres Dolmen Complex
4- Migmatites at the Almansor river
5- Nogueirinha mine
6- Serrinha mine
7- Escoural caves
8- Serra do Conde quarry
9- Vale da Arca mine and quarry
10- Monges mining complex
Route nº1
Route nº2

Figure 6.8. (previous page). Proposal of geodiversity routes between the Évora and Montemor-o-Novo Municipalities. The proposed routes are idealized to create a Geodivertisy "Bridge" between these two historical cities. The marked locations correspond to the geodiversity sites and geosites described throughout the manuscript; the base map was constructed from QGIS using the Ortophotomap from Open Street View.

6.7 Conclusions

There are still many efforts to be done in what concerns the beneficiation and geoconservation of mining and quarrying heritage in Alentejo, particularly in the Ossa-Morena Zone, aiming for the use of such geosites in proper geoscience communication and awareness of the importance of mining on the economic and social development of society.

In many of the mining areas of the Ossa-Morena Zone, such as the Montemor-o-Novo ancient iron mines (**Fig. 6.1**), beneficiation could provide assets for local communities by the means of geotourism, with the proposition of geotouristic routes that could combine geodiversity, mining history, history, and other cultural assets (e.g., archaeological).

Many of the geodiversity sites and mining heritage, besides their geological value, display landscape sceneries that complement their significance and can attract more public to the sites, increasing the possibility of geoscience communication being effectively delivered.

As previously stated, mining is usually perceived by the public as only being connected to negative key-factors, such as, acid mine drainage, landscape degradations, and therefore tends to be demonised. Such negative opinion is undeniably related to ancient mining, in which exploitation was performed under lax environmental regulation and with insufficient or absent oversight. Even though current regulations are strict, at least for Portuguese sites, the public perception is stained by the poor examples. This brings us to one of the major problems that present exploration and mining projects face, the social license to operate, and such can only be achieved through effective and attractive geoscience communication strategies, transparency of the exploration and mining projects, and by involving the local communities in the projects. Geodiversity assessment can be a powerful ally in the awareness for the necessity and importance of mining for the society. On the reverse, mining and quarrying works can be powerful allies of geodiversity and geoconservation, as they expose geological features that would otherwise be inaccessible (Prosser 2018).

We believe that the geodiversity assessment herein presented for the Geodiversity Route between the Évora and Montemor-o-Novo municipalities should not be used as an argument to detain future exploration, mining, and quarrying projects, on the other hand we propose that in the future such projects could provide fruitful cooperation for the catalogue of important geological features, and by fomenting scientific and educational activities and further promoting the bridges between academia-industry-society. In sum, the existence of a territorial

geoconservation strategy interplayed with responsible mining of mineral resources does and cannot mean the unfeasibility of future exploration, mining, and quarrying projects.

Chapter References

Andrade, A., Silva, J.M., Arruda, C.R, and Gameiro, J.C.S., 1949. Minas de Ferro de Montemor-o-Novo. Serviço de Fomento Mineiro, v. 15, p. 125.

Apalategui, O., Eguiluz, L., and Quesada, C., 1990. Ossa-Morena Zone: Structure. In: Martinez E and Dallmeyer RD (Eds.) Pre-Mesozoic Geology of Iberia, Springer Verlag, p. 280-291.

Araújo, A., 1995. Estrutura de uma geotransversal entre Brinches e Mourão (Zona Ossa Morena): Implicações na evolução geodinâmica da margem SW do terreno Autóctone Ibérico. PhD thesis Universidade de Évora, 200 p. (in Portuguese with English abstract)

Araújo, A., Piçarra de Almeida, J., Borrego, J. Pedro, J. and Oliveira, T., 2013. As regiões central e sul da Zona de Ossa-Morena. In: Dias R, Araújo A, Terrinha P, Kullberg JC (Eds), Geologia de Portugal, Volume 1, Escolar Editora, pp 509-549.

Brilha, J., Andrade, C., Azerêdo, A., Barriga, F.J.A.S., Cachão, M., Couto, H., Cunha, P.P., Crispim, J.A., Dantas, P., Duarte, L.V., Freitas, M.C., Granja, H.M., Henriques, M.H., Henriques, P., Lopes, L., Madeira, J., Matos, J.M.X., Noronha, F., Pais, J., Piçarra, J., Ramalho, M.M., Relvas, J.M.R.S., Ribeiro, A., Santos, A., Santos, A., Santos, V.F., and Terrinha, P., 2005. Definition of the Portuguese frameworks with international relevance as an input for the European geological heritage characterisation. Episodes, v. 28, p. 177-186. https://doi.org/10.18814/epiiugs/2005/v28i3/004

Brilha, J., Barriga, F., Cachão, M., Couto, M.H., Dias, R., Henriques, M.H., Kullberg, J.C., Medina, J., Moura, D., Nunes, J.C,, Pereira, D., Pereira, P., Prada, S., and Sá, A., 2008. Geological heritage inventory in Portugal: implementing geological frameworks. 5th International ProGEO Symposium Proceedings. 93 pp.

Brilha, J., and Galopim de Carvalho, A.M., 2010. Geoconservação em Portugal: uma introdução. In: Cotelo Neiva J.M., Ribeiro, A., Mendes, V. L., Noronha, F., Magalhães Ramalho, M., (eds) Ciências Geológicas: Ensino, Investigação e sua História. Associação Portuguesa de Geólogos, Volume II, p. 435–441.

Brilha, J., Alcalá, L., Almeida, A., and Araújo, A., et al 2010. O inventário nacional do património geológico: abordagem metodológica e resultados. e-Terra 18.

Brilha, J., 2016. Inventory and Quantitative Assessment of Geosites and Geodiversity Sites: a Review. Geoheritage, v. 8, p. 119-134. https://doi.org/10.1007/s12371-014-0139-3

Brilha, J., Gray, M., Pereira, D.I., and Pereira, P., 2018. Geodiversity: An integrative review as a contribution to the sustainable management of the whole of nature. Environmental Science and Policy, v. 86, p. 19-28. https://doi.org/10.1016/j.envsci.2018.05.001

Brilha, J., Pereira, P., 2020. Geoconservation in Portugal with Emphasis on the Geomorphological Heritage. In: Vieira, G., Zêzere, J.L., Mora, C., (Eds): Landscapes and Landforms of Portugal, World Geomorphological Landscapes, p. 307-314. https://doi.org/10.1007/978-3-319-03641-0

Caldeira, A.T., Schiavon, N., Mauran, G., Salvador, C., Rosado, T., Mirão, J., and Candeias, A., 2021. On the Biodiversity and Biodeteriogenic Activity of Microbial Communities Present in the Hypogenic Environment of the Escoural Cave, Alentejo, Portugal. Coatings, v. 11, 209. https://doi.org/10.3390/coatings11020209

Carvalhosa, A., 1983. Esquema geológico do Maciço de Évora. Comunicações dos Serviços Geológicos de Portugal, v.69(2), p. 201-208.

Carvalhosa, A., and Zbyszewski, G., 1994. Carta Geológica de Portugal, Notícia Explicativa da Folha 35-D (Montemor-o-Novo), Instituto Geológico e Mineiro, 1:50 000.

Chacón, J., Oliveira, V., Ribeiro, A., and Oliveira, J.T., 1983. La estructura de la Zona de Ossa Morena. Libro Jubilar J. M. Rios – Geologia de España, Tomo I (eds) Comba, J.A. (Coord). Instituto Geológico y Minero de España, Madrid, p. 490-504.

Chichorro, M., 2006. A evolução tectónica da Zona de Cisalhamento de Montemor-o-Novo (Sudoeste da Zona de Ossa-Morena – Área de Santiago do Escoural – Cabrela). PhD Thesis, University of Évora, p.569, (in Portuguese with English abstract).

Chichorro, M., Pereira, M.F., Díaz-Azpiroz, M., Williams, I.S., Fernández, C., Pin, C., and Silva, J.B., 2008. Cambrian ensialic rift-related magmatism in the Ossa-Morena Zone (Évora–Aracena metamorphic belt, SW Iberian Massif): Sm–Nd isotopes and SHRIMP zircon U–Th–Pb geochronology. Tectonophysics, v. 461, p. 91-113. https://doi.org/10.1016/j.tecto.2008.01.008

Cruz, C., Noronha, F., Santos, P., Mortensen, J.K., Lima, A., 2018. Supergene gold enrichment in the Castromil-Serra da Quinta gold deposit, NW Portugal. Mineralogical Magazine, v. 82, p. 307-320. https://doi.org/10.1180/minmag.2017.081.063

Dias da Silva, Í., Pinto, A.J., Mattioli, M., and Da Silva, J.C., 2006. Avaliação do Património Geológico no Rio Almansor (Montemor-o-Novo): Proposta de Classificação e de Protecção. VII Congresso Nacional de Geologia Proceedings, v. 1, p. 981-984.

Dias da Silva, Í., Pereira, M.F., Silva, J.B., and Gama, C., 2018. Time-space distribution of silicic plutonism in a gneiss dome of the Iberian Variscan Belt: The Évora Massif (Ossa-Morena Zone, Portugal). Tectonophysics, 747, 298-317. https://doi.org/10.1016/j.tecto.2018.10.015

Farias, P., Gallastegui, G., González Lodeiro, F., Marquínez, J., Martin Parra, L., Martínez Catalán, J., Paolo Macia, J., and Rodriguez Fernandez, L., 1987. Aportaciones al conocimiento de la litoestratigrafia y estrutura de Galiza Central. Memória, Fac. Ciênc. Univ. Porto v. 1, p. 411-431.

Fonte, J., Lima, A., Matías Rodríguez, R., Gonçalves, J.A., and Leal, S., 2017. Novas evidências de mineração aurífera no Alto Vale do Tâmega (Montalegre e Boticas, Norte de Portugal). Estudos do Quaternário, v. 17, p. 45-55. https://doi.org/10.30893/eq.v0i17.160

Gioncada, A., Pitzalis, E., Cioni, R., Fulignati, P., Lezzerini, M., Mundula, F., and Funedda, A., 2019. The Volcanic and Mining Geoheritage of San Pietro Island (Sulcis, Sardinia, Italy): the Potential for Geosite Valorization. Geoheritage, v. 11, p. 1567-1581. https://doi.org/10.1007/s12371-019-00418-6

Hannington, M.D., 2014. Volcanogenic Massive Sulfide Deposits. In: Holland, H.D., and Turekian, K.K., (Eds) Treatise on Geochemistry (Second Edition), Elsevier, p.463-488. http://dx.doi.org/10.1016/B978-0-08-095975-7.01120-7

Hannington, M.D., 2021. VMS and SEDEX Deposits. In: Alderton D, Elias S (eds) Encyclopedia of Geology (Second Edition), p. 867 – 876. https://doi.org/10.1016/B978-0-08-102908-4.00075-8

Hellqvist, M., 2019. Teaching Sustainability in Geoscience Field Education at Falun Mine World Heritage Site in Sweden. Geoheritage, v. 11, p. 1785-1798. https://doi.org/10.1007/s12371-019-00387-w

Inverno, C.M.C., 2001. Comparison between orogenic (or mesothermal) gold deposits and intrusion-related gold deposits. Some extrapolation to Portugal. Cadernos Lab. Xeolóxico de Laxe, v.36, p.99-156 (in Portuguese with English abstract).

Jesus, A.P., Mateus, A., Munhá, J.M., Tassinari, C.C.G., Bento dos Santos, T., and Benoit, M., 2016. Evidence for underplating in the genesis of the Variscan synorogenic Beja Layered Gabbroic Sequence (Portugal) and related mesocratic rocks. Tectonophysics, v. 683, p. 148-171. http://dx.doi.org/10.1016/j.tecto.2016.06.001

Jesus, A.P., Mateus, A., Benoit, M., Tassinari, C.C.G., and Bento dos Santos, T., 2020. The timing of sulfide segregation in a Variscan synorogenic gabbroic layered intrusion (Beja, Portugal): Implications for Ni-Cu-PGE exploration in orogenic settings. Ore Geology Reviews, v.126, 103767. https://doi.org/10.1016/j.oregeorev.2020.103767

Julivert, M., Fontboté, J.M., Ribeiro, A., and Nabais Conde, L.E., 1972. Mapa Tectónico de la Península Ibérica y Baleares. Scale 1:1.000.000. IGME.

Lima, A., Vasconcelos, C., Félix, N., Barros, J., and Mendonça, A., 2010. Field trip activity in an ancient gold mine: scientific literacy in informal education. Public Understanding of Science, v. 19(3), p. 322-334. https://doi.org/10.1177/0963662509104725

López-García, J.A., Oyarzun, R., Andrés, S.L., and Martínez, J.I.M., 2011. Scientific, Educational, and Environmental Considerations Regarding Mine Sites and Geoheritage: A Perspective from SE Spain. Geoheritage, v. 3, p. 267-275. https://doi.org/10.1007/s12371-011-0040-2

Maia, M., Roseiro, J., Nogueira, P., Noronha, F., Fuertes.Fuente, M., Cepedal, A., and Mirão, J., 2022. New insights on the Escoural Orogenic gold district (Ossa-Morena Zone, SW Iberia): Geochemistry, fluid inclusions and stable isotope constraints from the Monfurado gold prospect. Ore Geology Reviews, v. 132, 104736. https://doi.org/10.1016/j.oregeorev.2022.104736

Mateus, A., Munhá, J., Inverno, C., Matos, J.X., Martins, L., Oliveira, D., Jesus, A., and Salgueiro, R., 2013. Mineralizações no sector português da Zona de Ossa-Morena. In R. Dias, A. Araújo, P. Terrinha, J.C. Kullberg (Eds.), Geologia de Portugal (p. 577-619, v.1). Lisboa: Escolar Editora.

Matías, R., and Llamas, B., 2021. Roman Gold Mining at “Las Miédolas” (NW Spain): Lidar and Photo Interpretation in the Analysis of “Peines” System. Geoheritage. https://doi.org/10.1007/s12371-021-00555-x

Mazadiego, L.F., Llamas, B., de Górgolas, C.R., Pous, J., and Puche, O., 2019. The Contingent Valuation Method Applied to the Mining Heritage of Extremadura (Spain). Geoheritage, v. 11, p. 665-679. https://doi.org/10.1007/s12371-018-0319-7

Moita, P., 2007. Granitoides no SW da Zona de Ossa-Morena (Montemor-o-Novo - Evora). Petrogénese e processos geodinâmicos. Dissertation Thesis, University of Évora, 351 p.

Moita, P., Santos, J.F., and Pereira, M.F., 2009. Layered granitoids: interaction between continental crust recycling processes and mantle-derived magmatism: examples from the Évora Massif (Ossa–Morena Zone, southwest Iberia, Portugal). Lithos 111,125–141. https://doi.org/10.1016/j.lithos.2009.02.009

Moita, P., Santos, J.F., Pereira, M.F., Costa, M.M., and Corfu, F., 2015. The quartz-dioritic Hospitais intrusion (SW Iberian Massif) and its mafic microgranular enclaves — Evidence for mineral clustering. Lithos, v. 224-225, p. 78-100. https://doi.org/10.1016/j.lithos.2015.02.012

Oliveira, J.T., Oliveira, V., and Piçarra, J.M., 1991. Traços gerais da evolução tectono-estratigráfica da Zona de Ossa Morena, em Portugal: síntese crítica do estado actual dos conhecimentos. Comum. Serv. Geol, Port., v.77, p.3-26.

Pereira, M.F., Silva, J.B., and Chichorro, M., 2003. Internal Structure of the Évora High-grade Terrains and the Montemor-o-Novo Shear Zone (Ossa-Morena Zone, Portugal), Geogaceta, v.33, p.79-82.

Pereira, M. F., Chichorro, M., Linnemann, U., Eguiluz, L., and Silva, J. B., 2006. Inherited arc signature in Ediacaran and Early Cambrian basins of the Ossa-Morena zone (Iberian Massif, Portugal): paleogeographic link with European and North African Cadomian correlatives. Precambrian Research, v. 144(3-4), p. 297-315. https://doi.org/10.1016/j.precamres.2005.11.011

Pereira, M. F., Silva, J. B., Chichorro, M., Moita, P., Santos, J. F., Apraiz, A., and Ribeiro, C., 2007. Crustal growth and deformational processes in the northern Gondwana margin: Constraints from the Évora Massif (Ossa-Morena zone, southwest Iberia, Portugal). Special Paper 423: The Evolution of the Rheic Ocean: From Avalonian-Cadomian Active Margin to Alleghenian-Variscan Collision, 333–358. https://doi.org/10.1130/2007.2423(16).

Pereira, M.F., Chichorro, M., Moita, P., Santos, J.F., Solá, A.M.R., Williams, I.S., and Silva, J.B., 2015. The multistage crystallization of zircon in calc-alkaline granitoids: U–Pb age constraints on the timing of Variscan tectonic activity in SW Iberia. International Journal of Earth Sciences, v. 104, p. 1167 – 1183. https://doi.org/10.1007/s00531-015-1149-3

Prosser, C.D., 2018. Geoconservation, Quarrying and Mining: Opportunities and Challenges Illustrated Through Working in Partnership with the Mineral Extraction Industry in England. Geoheritage, v. 10, p. 259-270. https://doi.org/10.1007/s12371-016-0206-z

Reis, J., Póvoa, L., Barriga, F.J.A.S., Lopes, C., Santos, V.F., Ribeiro, B., Cascalho, J., and Pinto, A., 2014. Science Education in a Museum: Enhancing Earth Sciences Literacy as a Way to Enhance Public Awareness of Geological Heritage. Geoheritage, v. 6, p. 217 – 223. https://doi.org/.1007/s12371-014-0105-0

Ribeiro, A., Munhá, J., Dias, R., Mateus, A., Pereira, E., Ribeiro, L., Fonseca, P., Araújo, A., Oliveira, O., Romão, J., Chaminé, H., Coke, C., and Pedro, J.C., 2007. Geodynamic evolution of the SW Europe Variscides. Tectonophysics, v.26, TC6009. https://doi.org/10.1029/2006TC002058

Ribeiro, A., Munhá, J., Fonseca, P.E., Araújo, A., Pedro, J.C., Mateus, A., Tassinari, C., Machado, G., and Jesus, A., 2010. Variscan ophiolite belts in the Ossa-Morena Zone (Southwest Iberia): Geological characterization

and geodynamic significance. Gondwana Research, v.17, p. 408-421. https://doi.org/10.1016/j.gr.2009.09.005

Ribeiro, C., Mateus, A., and Barriga, F., 1993. Gold mineralization of the Escoural area (Montemor, Évora, Portugal): a progress report. Comun. XII Reun. Geol. Oeste Penins., v.1, p.215-226.

Salgueiro, R., 2011. Caracterização e génese das mineralizações de magnetite – sulfuretos em Monges (Santiago do Escoural, Montemor-o-Novo) e ensaio comparativo com as suas congéneres em Orada-Vale de Pães (Serpa-Vidigueira). PhD Thesis, Univ. Lisboa, 524 p., (in Portuguese with English abstract).

Salgueiro, R., Mateus, A, and Inverno, C., 2012. Mineralizações de magnetite e sulfuretos de monges (Santiago do Escoural, Montemor-o-Novo), Vale de Pães (Cuba-Vidigueira) e Orada (Pedrógão, Serpa): Síntese de ensaio comparativo. Boletim de Minas, v. 47(1), p. 27-30.

Sánchez-Garcia, T., Bellindo, F., and Quesada, C., 2003. Geodynamic setting and geochemical signatures of Cambrian-Ordovician rift-related igneous rocks (Ossa-Morena Zone, SW Iberia). Tectonophysics 365, p.233-255. https://doi.org/10.1016/S0040-1951(03)00024-6

Sánchez-García, T., Chichorro, M., Solá, A.R., Álvaro, J.J., Díez-Montes, A., Bellido, F., Ribeiro, M.L., Quesada, C., Lopes, J.C., Dias da Silva, Í., González-Clavijo, E., Gómez Barreiro, J., and López-Carmona, A., 2019. The Cambrian-Early Ordovician Rift Stage in the Gondwanan Units of the Iberian Massif. In: Quesada, C. & Oliveira J.T. (Eds) The Geology of Iberia: A Geodynamic Approach, Vol. 2: The Variscan Cycle. Springer Nature, Switzerland, p.27-74. https://doi.org/10.1007/978-3-030-10519-8

Silva, A.F., 2013. Uma Integração e Reinterpretação do Atual Conhecimento sobre a Geologia da Região de Nossa Senhora da Boa Fé (Évora) – Santiago do Escoural (Montemor-o-Novo) e a sua Relação com as Mineralizações Auríferas. Boletim de Minas, v. 48, p. 15-44.

Silva, A.C., Mauran, G., Rosado, T., Mirão, J., Candeias, A., Carpetudo, C., and Caldeira, A.T., 2017. A arte rupestre da gruta do Escoural – Novos dados analíticos sobre a pintura paleolítica. In: Arqueologia de Portugal, eds. José Morais Arnaud and Andrea Martins. Associação Portuguesa de Geólogos, p. 1003 – 1019.

Silva, J.B., Araújo, A.A., and Fonseca, P., 1988 Novos elementos sobre cartografia geológica de uma área a leste de Santiago do Escoural (Montemor- o - Novo): Departamento de Geologia da Faculdade de Ciências de Lisboa, 10 p.

Wilkinson, J.J., 2014. Sediment-Hosted Zinc–Lead Mineralization: Processes and Perspectives. In: Holland, HD & Turekian KK (Eds) Treatise on Geochemistry (Second Edition), Elsevier, p. 219-249. http://dx.doi.org/10.1016/B978-0-08-095975-7.01109-8

Wilson, R.W., Houseman, G.A., Buiter, S.J.H., Mccaffrey, K.J.W., Doré, A.G., 2019. Fifty Years of the Wilson Cycle Concept. In Wilson, R.W., Houseman, G.A., Mccaffrey, K.J.W., Doré, A.G., Buiter, S.J.H., (eds) Plate Tectonics. Geological Society, London, Special Publications, 470. https://doi.org/10.1144/SP470-2019-58

“The more assumptions you make the less you learn from Nature.”

Professor Larryn Diamond (ECROFI 2017)

Chapter 7

Conclusions

7.1 General concluding remarks

Chapter 2

The concluding remarks from this chapter focus on the provided valuable new information regarding the mechanisms behind ore deposition in one of the most complex mineral deposits from the Escoural gold district, the Monfurado gold prospect. It concluded that gold transport was promoted by initially reduced metamorphic fluids, in complexes such as $Au(HS)_2^-$. Gold, at the Monfurado prospect, is mainly hosted in massive sulfide layers predominantly composed of pyrrhotite, but it is also found hosted in thin veins cross-cutting acid metavolcanic rocks. Its deposition has been promoted by the change of the fluid redox conditions due to the interaction between a metamorphic fluid and the magnetite-rich carbonate host-rocks, promoting sulfidation processes that resulted in magnetite-pyrrhotite alteration.

This evidence is extremely important to vector future mineral exploration in the area. As the gold deposition was assisted by the interaction between the transporting fluid and the magnetite host-rocks and since the Escoural district area is also characterised by numerous iron deposits, this type of sulfidation reaction might have occurred in other unknown prospects. The presence of these gold-bearing massive sulfide layers could be used as a lithological guide horizon for the mineral exploration works, and future drilling in the area should assess if this kind of approach is viable for other locations within the Escoural gold district.

Chapter 3

Magnetite chemistry, particularly LA-ICP-MS trace element analysis, proved to be a powerful method to discriminate the mechanisms behind ore deposition in distinct skarn systems, such as the Alvito and Azenhas Fe deposits. As thoroughly discussed in Chapter 3, these deposits have been previously the target of geochemical and mineralogical studies focusing on the genesis of the Fe skarn orebodies, and in the Azenhas case previous EPMA trace element data were available from the literature.

This PhD, particularly this chapter, defines the physic-chemical conditions associated with the origin of these deposits, providing evidence that corroborate the previously published models, or propose alternative models. Our results have found evidence that clearly associates the genesis of the Fe orebodies from Alvito with the installation of the Cuba-Alvito Gabbro-Diorite Complex, with temperature estimations of magnetite crystallisation close to those modelled for the plutonic complex.

In the case of the Azenhas deposit, the genesis of this Fe skarn deposit is controversial, with the previous research pointing towards a reactive skarn promoted by

successive thrusting events and iron ores being hosted in a highly metasomatized amphibolite unit. The trace element composition of primary magnetite has revealed that the genesis of the orebodies is associated to higher temperatures (ca. 770 ºC) than those previously modelled. Furthermore, magnetite shows high concentrations of Zn, which suggests that the hydrothermal fluids were enriched in other metals. The textural and chemical characterization of the ores, combined with a thorough geological mapping and host-rock petrography and geochemistry allowed to propose an alternative model for the genesis of this Fe skarn deposit. Our model suggests that iron was introduced in the system in much earlier times, possibly associated with the mafic volcanism that generated the protoliths of the amphibolites. The iron ores are hosted in a metavolcanic unit belonging to the Moura-Ficalho phyllonitic complex, an allochthonous unit interpreted as an accretionary prism with evidence of the imbrication of several ophiolite fragments. The amalgamation of this complex was generated during the collisional stages of the Variscan orogeny with the generation of several thrusting events, such as the ones observed in the Azenhas deposit. Field evidence suggest that the Variscan thrusts were important for the remobilisation and reconcentration of the iron ores.

Comparing between such different skarn systems (Azenhas vs Alvito) can be extremely difficult. Nevertheless, it is believed that the objective of constraining ore deposition in the Fe deposits of OMZ is particularly important, even more when both deposits are found in the same metallogenic belt.

Chapter 4

This chapter is the extension of the research from Chapter 3, with the characterisation of iron ore deposits from the OMZ being widened throughout the Montemor-o-Novo – Ficalho metallogenic belt to the Montemor-o-Novo Iron Complex, particularly to three orebodies from the MIC. Furthermore, this work also presents the first characterisation of the $\delta^{18}O$ isotopic signature of magnetite from iron ore deposits in Portugal, and the LA-ICP-MS trace element analyses of magnetite are also widened to the Orada orebodies, which belong to the Azenhas-Orada deposits.

The results show that combining the trace element analyses of magnetite with the oxygen isotope signature benefits the understanding of the ore sources and the physical and chemical mechanisms of ore deposition. This approach was particularly important for the characterization of the iron ores from the MIC deposits, once the superposition of latter events (deformation; reprecipitation; remobilization) imposed by the intense activity and fluid circulation in the Montemor-o-Novo Shear Zone, has overprinted most of the primary features of the ores.

Conventional classification diagrams, such as the Al + Mn vs Ti + V, were applied to trace element in magnetites of the MIC deposits. The results show that they are hardly discriminated from the skarn magnetites. Other criteria were further applied to their discrimination, with the trace element profiles pointing toward an affinity with a low-temperature hydrothermal origin. The manuscript that makes part of this chapter presents a proposal of a Co vs Zn discrimination diagram that is successful in discriminating skarn magnetite from magnetite formed in other low-temperature ore systems, such as BIF. The $\delta^{18}O$ signatures of magnetite from the MIC are variable, with heavy signatures being found in the Monges area and lower values being found at the Vale da Arca mine. The lower values from Vale da Arca (4.3 ‰) are closer to what is expected for a magmatic provenance. Nevertheless, these results contrast with the heavier signatures found in primary magnetites from the remaining MIC deposits (7.7 ‰ – 9.0 ‰), suggesting that late fluid-rock interactions had an overprinting effect on the oxygen isotope signature of magnetite, which is also corroborated by the trace element contents and textural characterisation.

Magnetite from the Alvito and Azenhas-Orada deposit are quite well discriminated by the conventional diagrams (Al + Mn vs Ti + V), and display a Ni/Cr ratio that indicates a non-igneous origin. The trace element profiles of primary magnetites from these deposits show an affinity to high-temperature magnetite, which clearly discriminate them from the MIC magnetite. This principal component analysis applied to the skarn magnetite highlights that high-field strength elements, such as Nb, Zr, Hf and Ta, are key elements to discriminate primary magnetite from skarns.

In what concerns the $\delta^{18}O$ signatures of the Alvito magnetite, they display a heavier signature than those typically found in skarn magnetites derived from modified magmatic fluids. Such deviation reveals the strong interaction between the magmatic fluids, derived from the Gabbro-Diorite suite, and the carbonate host-rocks (marbles and dolomites. This explanation is plausible since most mineralisation is found in an exoskarn, hosted in strongly metasomatized carbonates.

The $\delta^{18}O$ signatures of magnetite from the Azenhas-Orada deposits come to fuel the discussion regarding the genesis of these deposits. The range of signatures found in these magnetites (4.0 ‰ - 5.6 ‰) are consistent to literature data on oxygen isotope signatures of magnetite from skarns and suggest a magmatic-hydrothermal source. Further analysis should be carried out, particularly in the isotopic regimes, as proposed in the future research direction section.

The mineral chemistry is information for the characterisation and discrimination of mineral deposits. The high-sensitive methods (LA-ICP-MS and EPMA) used throughout this work are a great advantage in quantifying the trace element contents of magnetite, enlightening the mechanisms of their incorporation in the structure of the minerals (i.e. magnetite).

These geochemical datasets have long been used in traditional discriminant diagrams to classify ore deposits. Since these datasets are usually long and with numerous variables their visualisation and handling can be quite tricky and time-consuming. This chapter applies a machine learning algorithm (Random Forest) to the classification of ore deposits by using the results gathered from the *in-situ* LA-ICP-MS trace element analyses of magnetite, presented in Chapter 4 and Chapter 5. The results shown in this chapter are encouraging and serve an additional exploratory data-driven method for the characterisation of the ore deposits studied in this PhD thesis.

The application of Random Forest classifiers, using multiple categories, to the magnetite data proved to be a good approach for the classification of iron ore deposits from OMZ. The data examination using this machine learning algorithm revealed that magnetites from the Montemor-o-Novo Iron Complex (MIC) are classified as VMS when using VMS magnetite literature data as the training dataset. Such results indicate that magnetite from the MIC has trace element concentrations similar to other magnetites found in VMS deposits (Makvandi, 2015), which corroborates the previous classification of the deposits from the MIC as a SEDEX-VMS continuum model (Salgueiro et al., 2012; Salgueiro, 2011).

The classification of magnetite trace element data from the Alvito and Azenhas skarn deposit was also extremely accurate when using literature data of magnetite from Fe skarn deposits as the training dataset (Hu et al., 2017). These results highlight that although both deposits are skarns formed from completely different processes, they share similar trace element contents to other worldwide skarn deposits. The classification of secondary magnetite from the Azenhas deposit and magnetite from the Orada deposit showed poor classification results, as shown in the confusion matrix from Chapter 5, which is justified due to the lower concentration of trace elements, closer to the trace element contents found in the magnetites from the MIC. Further analyses of secondary ores from the Azenhas deposit and primary ores from the Orada orebody should be carried out, although the access to the Orada mine is extremely difficult and dangerous and drill core samples should be preferred.

Chapter 6

The work presented in this chapter provides a geodiversity deliverable that is accessible, representative, and could beneficiate the local economic activity and foster the geotourism in this ancient mining area. The proposed geological route integrates the mining heritaqe of the Montemor-o-Novo – Évora transect. It is an attempt to value the raw material potential of this area, and the whole Alentejo province, by implementing formal and informal educational and geotourism activities that use these routes. As previously stated, throughout this PhD thesis, one of the main goals was to valorise the mineral resources and ore deposits of the Ossa-Morena Zone by providing new insights on the genesis of the iron and gold deposits and presenting geochemical proxies for future mineral exploration. This approach can provide the population with the "best tools" to scrutinise the mineral exploration and mining activities, and to fully understand the importance of mineral resources, and adjacent industries, to the societal, economic, and technological development, minerals take part of everything in our daily life.

The conclusions derived from Chapter 6 are more of a discussion regarding the role of geoheritage in the mining and exploration industries, and on how the geological diversity can contribute to the geological literacy and to a change in the public opinion regarding these industries, hence contributing to the Social License to Operate.

7.2 Future research directions

This PhD thesis is a major output of a project on mineral resources, economic geology, and the ore deposits geology, which aimed to provide new criteria for the classification of ore deposits and in the identification of geochemical proxies that could be used in vectoring for future mineral exploration in the Ossa-Morena Zone, at the SW of Iberia. The work intends to answer several questions, as disclosed in the introductory chapters. It provided many answers and raised more questions and ideas that could, and should, be addressed in future research.

The following research guidelines are presented to instigate future research focusing on the ore deposits of Ossa-Morena Zone and valorising the mineral raw materials of Alentejo, which can be an important player in future metal supply in Portugal and Europe as mineral exploration and mining move onto smaller and local exploration in an effort of diminishing the environmental impacts and reduce the operational costs.

1. Extend the study of gold transport and deposition mechanisms to the remaining gold deposits from the Escoural gold district by applying a similar research approach to that

adopted for the characterisation of the mineralisation types from the Monfurado gold deposit (see Chapter 3).

2. Explore the hypothesis for the study of alluvial gold particles as a method for mineral exploration and as an indicator for hypogene mineralisation in the Escoural gold district area.

3. Replicate the chemical and textural characterisation of magnetite for the iron deposits from the Spanish counterpart of Ossa-Morena Zone, such as the Monchi, Colmenar, and Cala deposits (Velasco and Amigó, 1981; Carriedo et al., 2006; 2021; Tornos et al., 2002; 2021). Integrate the data of in-situ LA-ICP-MS trace element analysis of magnetite from OMZ deposits in a database to fingerprint the mechanisms behind ore deposition and evaluate the similarities between metallogenic provinces.

4. Analysis of magnetite isotope composition, such as Sm-Nd and Fe (Cliff and Rickard, 1992; Gallindo et al., 1995; Zhang and Zuo, 2014; Zhang et al., 2015; Troll et al., 2019), which would contribute with age estimations for the mineralising episodes and could clarify some of the doubts regarding the timing of ore deposition in the cases of the Montemor-o-Novo Iron Complex deposits and the Azenhas-Orada skarn deposits.

5. Could a more widespread compositional database be effective to identify potential ore deposits and commodities? To answer this question the approach adopted throughout this thesis, particularly the trace element analysis of magnetite, could be applied to the study of major deposits in Portugal, such as the VMS deposits from the Iberian Pyrite Belt (e.g. Neves-Corvo and Aljustrel).

Chapter References

Carriedo, J., Tornos, F., Velasco, F., and Terrón, A., 2006. Mineralizaciones de magnetita asociadas a skarns y bandas de cizalla: La mina de Cala (Huelva). Geogaceta, v.40, p. 235-238. ISSN: 0213683X

Carriedo, J., Tornos, F., Chiaradia, M., and Galindo, C., 2021. A genetic link between albitic magmas and IOCG mineralization in the Ossa Morena Zone (SW Iberia). Journal of Iberian Geology. https://doi.org/10.1007/s41513-021-00162-3

Cliff, R.A., and Rickard, D., 1992. Isotope systematics of the Kiruna magnetite ores, Sweden: Part 2. Evidence for a secondary event 400 m.y. after ore formation. Economic Geology, v. 87, p. 1121-1129. https://doi.org/10.2113/gsecongeo.87.4.1121

Galindo, C., Casquet, C., Darbyshire, F., Tornos, F., and Cuervo, S., 1995. Sm-Nd isotope geochemistry and dating of magnetites: A case study from na Fe district in the SW of Spain. Proceedings of the third bienal SGA Meeting, Prague (Czech Republic), 1995, p. 41-43.

Hu, X., Chen, H., Zhao, L., Han, J., and Xia, X., 2017. Magnetite geochemistry of the Longqiao and Tieshan Fe–(Cu) deposits in the Middle-Lower Yangtze River Belt: Implications for deposit type and ore genesis. Ore Geology Reviews, v.89, p. 822-835. http://dx.doi.org/10.1016/j.oregeorev.2017.07.019

Makvandi, S., 2015. Indicator mineral exploration methodologies for VMS deposits using geochemistry and physical characteristics of magnetite. PhD Thesis, Université Laval, 235 p.

Tornos, F., Galindo, C., Darbyshire, F., Casquet, C., and Noble, S.R., 2021. Isotope geochemistry, age, and origin of the magnetite-vonsenite mineralization of the Monchi Mine, SW Iberia. Journal of Iberian Geology, v. 47, p. 64-84. https://doi.org/10.1007/s41513-020-00159-4

Salgueiro, R., 2011, Caracterização e génese das mineralizações de magnetite – sulfuretos em Monges (Santiago do Escoural, Montemor-o-Novo) e ensaio comparativo com as suas congéneres em Orada-Vale de Pães (Serpa-Vidigueira). PhD Thesis, University of Lisbon, 524 p.

Salgueiro, R., Mateus, A, and Inverno, C., 2012. Mineralizações de magnetite e sulfuretos de monges (Santiago do Escoural, Montemor-o-Novo), Vale de Pães (Cuba-Vidigueira) e Orada (Pedrógão, Serpa): Síntese de ensaio comparativo: Boletim de Minas, v.47(1), pp. 27-30.

Troll, V.R., Weis, F.A., Jonsson, E., Andersson, U.B., Majidi, S.A., Hogdahl, K., Harris, C., Millet, M.-A., Chinnasamy, S.S., Koojiman, E., and Nilsoon K.P., 2019. Global Fe–O isotope correlation reveals magmatic

origin of Kiruna-type apatite-iron-oxide ores. Nature Communications, v. 10, 1712. https://doi.org/10.1038/s41467-019-09244-4

Velasco, F., and Amigó, J.M., 1981. Mineralogy and origin of the skarn from Cala (Huelva, Spain). Economic Geology, v. 76, p. 719-727. https://doi.org/10.2113/gsecongeo.76.3.719

Zhang, Z., and Zuo, R., 2014. Sr–Nd–Pb isotope systematics of magnetite: Implications for the genesis of Makeng Fe deposit, southern China. Ore Geology Reviews, v. 57, p. 53-60. http://dx.doi.org/10.1016/j.oregeorev.2013.09.009

Zhang, Z., Zuo, R., and Cheng, Q., 2015. The mineralization age of the Makeng Fe deposit, South China: implications from U–Pb and Sm–Nd geochronology. International Journal of Earth Sciences, v. 104, p. 663-682. https://doi.org/10.1007/s00531-014-1096-4

Appendices

Appendix A

Complete scores for the quantitative geodiversity assessment

Appendix A-1. – Scientific Values scores according to Brilha et al. (2016).

Site	A (30%)	B(20%)	C (5%)	D (15%)	E (5%)	F (15%)	G (10%)	Total
São Bento	4	1	4	4	4	2	4	3.1
Monte das Flores	2	0	1	4	1	4	2	2.1
Almansor	4	2	4	4	4	4	4	3.6
Nogueirinha	2	1	2	1	4	2	2	1.75
Serrinha	2	1	2	2	4	2	2	1.9
Escoural	4	2	2	4	2	4	1	3.1
Serra do Conde	4	2	2	4	2	4	2	3.2
Vale da Arca	2	1	2	4	2	2	2	2.1
Monges	4	2	4	1	4	2	2	2.65

Appendix A-2. – Educational Values scores according to Brilha et al. (2016).

Site	A (10%)	B (10%)	C (5%)	D (10%)	E (5%)	F (5%)	G (5%)	H (5%)	I (5%)	J (10%)	K (20%)	L (10%)	Total
São Bento	3	3	4	4	4	1	4	1	2	4	4	3	3.3
Monte das Flores	2	3	2	4	4	1	4	0	1	3	4	3	2.9
Almansor	4	3	4	2	4	1	4	0	3	4	3	4	3.1
Nogueirinha	4	1	2	2	4	1	4	0	3	1	2	3	2.2
Serrinha	4	1	2	2	4	1	4	0	3	1	2	3	2.2
Escoural	4	4	4	4	4	1	4	2	3	4	3	2	3.3
Serra do Conde	3	1	2	2	4	1	4	0	2	2	1	3	1.95
Vale da Arca	3	3	4	2	4	1	4	0	2	3	2	3	2.55
Monges	3	1	4	2	4	1	4	0	3	2	2	3	2.3

Appendix A-3. – Touristic Values scores according to Brilha et al. (2016).

Site	A (10%)	B (10%)	C (5%)	D (10%)	E (5%)	F (5%)	G (5%)	H (15%)	I (10%)	J (5%)	K (10%)	L (5%)	M (5%)	Total
Alto de São Bento	3	3	4	4	4	1	4	1	2	4	4	2	4	2.9
Monte das Flores	2	3	2	4	4	1	4	0	1	3	3	2	4	2.3
Almansor	4	3	4	2	4	1	4	0	3	4	3	2	4	2.65
Nogueirinha	4	1	2	2	4	1	4	0	3	1	3	2	4	2.2
Serrinha	4	1	2	2	4	1	4	0	3	1	3	2	4	2.2
Escoural	4	4	4	4	4	1	4	2	3	4	3	2	4	3.25
Serra do Conde	3	1	2	2	4	1	4	0	2	2	3	2	4	2.05
Vale da Arca	3	3	4	2	4	1	4	0	2	3	3	2	4	2.4
Monges	3	1	4	2	4	1	4	0	3	2	3	2	4	2.25

Appendix A-4. – Degradation risk assessment according to Brilha et al. (2016).

Site	A (35%)	B (20%)	C (20%)	D (15%)	E (10%)	Total
São Bento	2	2	4	3	1	2.45
Monte das Flores	4	4	1	3	1	2.95
Almansor	2	1	2	1	1	1.55
Nogueirinha	3	0	1	1	1	1.5
Serrinha	3	0	1	1	1	1.5
Escoural	2	0	1	4	1	1.6
Serra do Conde	1	0	1	0	1	0.65
Vale da Arca	2	1	2	3	1	1.85
Monges	2	0	2	0	1	1.2

Appendix B

Sampling and sample information: Coordinates, type of sample, and analytical methods applied to each sample

Sample Ref	004-1	004-2	004-3	004-4	004-5	004-6	004-7	004-8	004-9
Ore Deposit	Monfurado prospect	Monfurado prospect	Monfurado prospect	Monfurado prospect	Monfurado prospect	Monfurado prospect	Monfurado prospect	Monfurado prospect	Monfurado prospect
Litostratigraphic unit	Marbles	Amphibolic schists	Calcsilicate rocks	Marbles	Calcsilicate rocks	Acid metavolcanic	Biotitic micaschists	Acid metavolcanic	Acid metavolcanic
Mineralization	Barren	Barren	Py	Py	Py	Barren	Py	Py	Py
Coordinates:									
x	4269325	4269325	4269325	4269325	4269325	4269325	4269325	4269325	4269325
y	571048	571048	571048	571048	571048	571048	571048	571048	571048
Depth	15.91-16.06	27.44-27.69	28.45-28.06	29.1-29.28	30.6-30.75	32.45-32.67	41.75-42.05	43.67-43.61	44.8-45
Petrography	✓	✓	✓		✓	✓	✓	✓	✓
Whole rock geoch.									
EPMA		✓					✓		
LA-ICP-MS									
Fluid Inc.									
SEM-EDX									
Oxygen isotopes									
Sulfur isotopes									

Sample Ref	004-10	004-11	004-12	004-13	004-14	005-1	005-2	005-3	005-4
Ore Deposit	Monfurado prospect	Monfurado prospect	Monfurado prospect	Monfurado prospect	Monfurado prospect	Monfurado prospect	Monfurado prospect	Monfurado prospect	Monfurado prospect
Litostratigraphic unit	Calcsilicate rocks	Calcsilicate rocks	Marbles	Marbles	Marbles	Amphibolic schists	Amphibolic schists	Amphibolic schists	Amphibolic schists
Mineralization	Py + Po	Massive sulphides	Py	Py	Py	Barren	Barren	Barren	Py
Coordinates:									
x	4269325	4269325	4269325	4269325	4269325	4269366	4269366	4269366	4269366
y	571048	571048	571048	571048	571048	571080	571080	571080	571080
Depth	48.65-48.95	49.2-49.4	49.88-50.06	50.58-50.83	54.0-54.04	18.5-18.8	20.95-21.25	21.7-21.92	22.58-22.7
Petrography	✓	✓	✓	✓	✓	✓	✓	✓	✓
Whole rock geoch.									
EPMA	✓	✓	✓	✓				✓	
LA-ICP-MS	✓		✓						
Fluid Inc.									✓
SEM-EDX	✓	✓			✓				
Oxygen isotopes									
Sulfur isotopes		✓			✓				

Sample Ref	005-5	005-6	005-7	005-8	005-9	005-10	005-11	005-12	005-13
Ore Deposit	Monfurado prospect	Monfurado prospect	Monfurado prospect	Monfurado prospect	Monfurado prospect	Monfurado prospect	Monfurado prospect	Monfurado prospect	Monfurado prospect
Litostratigraphic unit	Amphibolic schists	Amphibolic schists	Marbles	Marbles	Calcsilicate rocks	Calcsilicate rocks	Marbles	Marbles	Calcsilicate rocks
Mineralization	Barren	Barren	Barren	Barren	Barren	Barren	Barren	Barren	Py
Coordinates:									
x	4269366	4269366	4269366	4269366	4269366	4269366	4269366	4269366	4269366
y	571080	571080	571080	571080	571080	571080	571080	571080	571080
Depth	23.8-24.1	26.5-26.9	29.8-30.05	32.42-32.66	33.39-33.59	34.61-34.84	37.26-37.46	40.45-40.75	43.75-73.95
Petrography	✓	✓	✓	✓	✓	✓	✓	✓	✓
Whole rock geoch.									
EPMA									
LA-ICP-MS									
Fluid Inc.		✓							
SEM-EDX									
Oxygen isotopes									
Sulfur isotopes									

Sample Ref	005-14	005-15	005-16	005-17	005-18	005-19	005-20	005-21	005-22
Ore Deposit	Monfurado prospect	Monfurado prospect	Monfurado prospect	Monfurado prospect	Monfurado prospect	Monfurado prospect	Monfurado prospect	Monfurado prospect	Monfurado prospect
Litostratigraphic unit	Marbles	Calcsilicate rocks	Marbles	Marbles	Marbles	Marbles	Calcsilicate rocks	Marbles	Amphibolic schists
Mineralization	Barren	Barren	Barren	Mag	Mag	Mag+Py	Mag+Py	Py	Py
Coordinates:									
x	4269366	4269366	4269366	4269366	4269366	4269366	4269366	4269366	4269366
y	571080	571080	571080	571080	571080	571080	571080	571080	571080
Depth	44.95-45.25	58.05-58.35	62.0-62.25	62.7-63.1	63.85-64.2	65.07-65.34	65.55-65.8	66.17-66.37	67.85-68
Petrography	✓	✓	✓	✓	✓	✓	✓	✓	✓
Whole rock geoch.									
EPMA				✓			✓	✓	
LA-ICP-MS							✓	✓	
Fluid Inc.									✓
SEM-EDX				✓			✓	✓	
Oxygen isotopes				✓				✓	
Sulfur isotopes									

Sample Ref	005-23	005-24	005-25	005-26	005-27	005-28	005-29	005-30	005-31
Ore Deposit	Monfurado prospect	Monfurado prospect	Monfurado prospect	Monfurado prospect	Monfurado prospect	Monfurado prospect	Monfurado prospect	Monfurado prospect	Monfurado prospect
Litostratigraphic unit	Acid metavolcanic	Acid metavolcanic	Biotitic micaschists	Biotitic micaschists	Biotitic micaschists	Calcsilicate rocks	Calcsilicate rocks	Calcsilicate rocks	Calcsilicate rocks
Mineralization	Barren	Barren	Barren	Barren	Barren	Barren	Barren	Py + Po + Ccp	Massive sulphides
Coordinates:									
x	4269366	4269366	4269366	4269366	4269366	4269366	4269366	4269366	4269366
y	571080	571080	571080	571080	571080	571080	571080	571080	571080
Depth	69.47-69.67	67.85-68	69.47-69.67	70.82-71.07	71.96-72.16	72.25-72.4	81.2-81.5	83.25-83.52	83.98-84.28
Petrography	✓	✓	✓	✓	✓	✓	✓	✓	✓
Whole rock geoch.									
EPMA								✓	✓
LA-ICP-MS									✓
Fluid Inc.		✓		✓	✓				
SEM-EDX								✓	✓
Oxygen isotopes									
Sulfur isotopes								✓	✓

Sample Ref	005-32	005-33	005-34	005-35	006-1	006-2	006-3	006-4	006-5
Ore Deposit	Monfurado prospect	Monfurado prospect	Monfurado prospect	Monfurado prospect	Monfurado prospect	Monfurado prospect	Monfurado prospect	Monfurado prospect	Monfurado prospect
Litostratigraphic unit	Calcsilicate rocks	Calcsilicate rocks	Marbles	Marbles	Acid metavolcanic	Acid metavolcanic	Acid metavolcanic	Acid metavolcanic	Acid metavolcanic
Mineralization	Massive sulphides	Py + Po + Ccp	Py + Po + Ccp	Py + Po + Ccp	Barren	Barren	Barren	Barren	Barren
Coordinates:									
x	4269366	4269366	4269366	4269366	4269396	4269396	4269396	4269396	4269396
y	571080	571080	571080	571080	570967	570967	570967	570967	570967
Depth	86.89-87.14	89.3-89.45	90.3-90.55	90.9-91.1	27.92-28.2	28.17-28.42	28.67-28.87	30.67-30.97	32.75-33.0
Petrography	✓	✓	✓	✓	✓	✓	✓	✓	✓
Whole rock geoch.					✓				
EPMA	✓								
LA-ICP-MS									
Fluid Inc.					✓	✓	✓	✓	
SEM-EDX	✓		✓						
Oxygen isotopes									
Sulfur isotopes	✓								

Sample Ref	006-6	006-7	006-8	006-9	006-10	006-11	006-12	006-13	006-14
Ore Deposit	Monfurado prospect	Monfurado prospect	Monfurado prospect	Monfurado prospect	Monfurado prospect	Monfurado prospect	Monfurado prospect	Monfurado prospect	Monfurado prospect
Litostratigraphic unit	Acid metavolcanic	Acid metavolcanic	Acid metavolcanic	Calcsilicate rocks	Calcsilicate rocks	Marbles	Marbles	Marbles	Marbles
Mineralization	Barren	Py	Barren	Barren	Py	Py	Py	Py	Py
Coordinates:									
x	4269396	4269396	4269396	4269396	4269396	4269396	4269396	4269396	4269396
y	570967	570967	570967	570967	570967	570967	570967	570967	570967
Depth	33.87-33.98	35.2-35.45	36.08-36.23	37.57-37.74	38.18-38.4	38.87-39.04	40.0-40.25	41.33-41.53	42.2-42.47
Petrography	✓	✓	✓	✓	✓	✓	✓	✓	✓
Whole rock geoch.									
EPMA									
LA-ICP-MS									
Fluid Inc.							✓		
SEM-EDX									
Oxygen isotopes									
Sulfur isotopes									

Sample Ref	006-15	006-16	006-17	006-18	006-19	006-20	006-21	006-22	006-23
Ore Deposit	Monfurado prospect	Monfurado prospect	Monfurado prospect	Monfurado prospect	Monfurado prospect	Monfurado prospect	Monfurado prospect	Monfurado prospect	Monfurado prospect
Litostratigraphic unit	Marbles	Marbles	Marbles	Calcsilicate rocks	Calcsilicate rocks	Marbles	Marbles	Marbles	Marbles
Mineralization	Barren	Py	Py	Py	Py	Barren	Barren	Barren	Py
Coordinates:									
x	4269396	4269396	4269396	4269396	4269396	4269396	4269396	4269396	4269396
y	570967	570967	570967	570967	570967	570967	570967	570967	570967
Depth	43.17-43.44	45.08-45.28	47.17-47.39	50.26-50.46	50.66-50.83	52.03-52.22	53.27-53.42	55.0-55.27	56.07-56.37
Petrography	✓	✓	✓	✓	✓	✓	✓	✓	✓
Whole rock geoch.									
EPMA									
LA-ICP-MS									
Fluid Inc.								✓	
SEM-EDX									
Oxygen isotopes									
Sulfur isotopes									

Sample Ref	006-24	006-25	007-1	007-2	007-3	007-4	007-5	007-6	007-7
Ore Deposit	Monfurado prospect	Monfurado prospect	Monfurado prospect	Monfurado prospect	Monfurado prospect	Monfurado prospect	Monfurado prospect	Monfurado prospect	Monfurado prospect
Litostratigraphic unit	Calcsilicate rocks	Calcsilicate rocks	Amphibolic schists	Marbles	Calcsilicate rocks	Amphibolic schists	Acid metavolcanic	Acid metavolcanic	Acid metavolcanic
Mineralization	Barren	Barren	Py	Py	Barren	Barren	Barren	Barren	Barren
Coordinates:									
x	4269396	4269396	4269403	4269403	4269403	4269403	4269403	4269403	4269403
y	570967	570967	571115	571115	571115	571115	571115	571115	571115
Depth	58.86-59.06	60.5-60.67	58.1-58.3	61.15-61.3	89.7-90.1	93.8-94.0	94.56-94.76	95.2-95.4	97.68-97.88
Petrography	✓	✓	✓	✓	✓	✓	✓	✓	✓
Whole rock geoch.		✓							
EPMA				✓					
LA-ICP-MS									
Fluid Inc.							✓		✓
SEM-EDX									
Oxygen isotopes									
Sulfur isotopes									

Sample Ref	007-8	007-9	007-10	007-11	007-12	007-13	007-14	007-15	007-16
Ore Deposit	Monfurado prospect	Monfurado prospect	Monfurado prospect	Monfurado prospect	Monfurado prospect	Monfurado prospect	Monfurado prospect	Monfurado prospect	Monfurado prospect
Litostratigraphic unit	Acid metavolcanic	Acid metavolcanic	Acid metavolcanic	Amphibolic schists	Calcsilicate rocks	Marbles	Calcsilicate rocks	Calcsilicate rocks	Calcsilicate rocks
Mineralization	Barren	Py	Py + Au	Py + Po	Massive sulphides	Massive sulphides	Barren	Barren	Barren
Coordinates:									
x	4269403	4269403	4269403	4269403	4269403	4269403	4269403	4269403	4269403
y	571115	571115	571115	571115	571115	571115	571115	571115	571115
Depth	105.2-105.3	106.45-106.57	107.35-107.55	109.23-109.35	109.82-110.02	110.18-110.48	110.63-110.8	112.94-113.19	115.0-115.3
Petrography	✓	✓	✓	✓	✓	✓	✓	✓	✓
Whole rock geoch.									
EPMA	✓		✓				✓	✓	
LA-ICP-MS									
Fluid Inc.	✓								
SEM-EDX			✓				✓	✓	
Oxygen isotopes									
Sulfur isotopes			✓					✓	

Sample Ref	007-17	007-18	007-19	007-20	007-21	008-1	008-2	008-3	008-4
Ore Deposit	Monfurado prospect	Monfurado prospect	Monfurado prospect	Monfurado prospect	Monfurado prospect	Monfurado prospect	Monfurado prospect	Monfurado prospect	Monfurado prospect
Litostratigraphic unit	Calcsilicate rocks	Calcsilicate rocks	Calcsilicate rocks	Calcsilicate rocks	Calcsilicate rocks	Acid metavolcanic	Acid metavolcanic	Marbles	Marbles
Mineralization	Py	Py	Massive Py	Barren	Massive arsenopyrite	Barren	Barren	Barren	Barren
Coordinates:									
x	4269403	4269403	4269403	4269403	4269403	4269435	4269435	4269435	4269435
y	571115	571115	571115	571115	571115	571010	571010	571010	571010
Depth	115.76-115.99	119.54-119.87	120.45-120.7	121.6-121.9	122.6-123.05	80.07-80.37	82.22-82.52	84.62-84.82	87.0-87.32
Petrography	✓	✓	✓	✓	✓	✓	✓	✓	✓
Whole rock geoch.						✓	✓		
EPMA					✓				
LA-ICP-MS									
Fluid Inc.									
SEM-EDX			✓		✓				
Oxygen isotopes									
Sulfur isotopes			✓		✓				

Sample Ref	008-5	008-6	008-7	008-8	008-9	008-10	008-11	008-12	008-13
Ore Deposit	Monfurado prospect	Monfurado prospect	Monfurado prospect	Monfurado prospect	Monfurado prospect	Monfurado prospect	Monfurado prospect	Monfurado prospect	Monfurado prospect
Litostratigraphic unit	Marbles	Marbles	Marbles	Calcsilicate rocks	Calcsilicate rocks	Calcsilicate rocks	Calcsilicate rocks	Calcsilicate rocks	Calcsilicate rocks
Mineralization	Barren	Barren	Py	Barren	Py	Py	Py	Py	Barren
Coordinates:									
x	4269435	4269435	4269435	4269435	4269435	4269435	4269435	4269435	4269435
y	571010	571010	571010	571010	571010	571010	571010	571010	571010
Depth	88.82-89.0	91.93-92.23	92.73-93.0	94.8-95.0	96.4-96.65	97.0-97.25	100.1-100.3	100.8-101.02	103.6-103.8
Petrography	✓	✓	✓	✓	✓	✓	✓	✓	✓
Whole rock geoch.									
EPMA									
LA-ICP-MS									
Fluid Inc.									
SEM-EDX									
Oxygen isotopes									
Sulfur isotopes									

Sample Ref	008-14	008-15	008-16	008-17	008-18	010-1	010-2	010-3	010-4
Ore Deposit	Monfurado prospect	Monfurado prospect	Monfurado prospect	Monfurado prospect	Monfurado prospect	Monfurado prospect	Monfurado prospect	Monfurado prospect	Monfurado prospect
Litostratigraphic unit	Calcsilicate rocks	Calcsilicate rocks	Calcsilicate rocks	Calcsilicate rocks	Calcsilicate rocks	Calcsilicate rocks	Marbles	Marbles	Calcsilicate rocks
Mineralization	Barren	Py +Mag	Barren	Barren	Barren	Po + Py + Mag	Py + Po	Py	Py
Coordinates:									
x	4269435	4269435	4269435	4269435	4269435	4269373	4269373	4269373	4269373
y	571010	571010	571010	571010	571010	571086	571086	571086	571086
Depth	106.15-106.35	108.14-108.46	110.76-110.96	113.48-113.82	114.52-114.72	74.7-75.37	75.86-76.21	76.31-76.41	78.37-78.5
Petrography	✓	✓	✓	✓	✓	✓	✓	✓	✓
Whole rock geoch.							✓		
EPMA									
LA-ICP-MS									
Fluid Inc.									
SEM-EDX									
Oxygen isotopes									
Sulfur isotopes									

Sample Ref	012-1	012-2	012-3	012-4	012-5	012-6	012-7	012-8	012-9
Ore Deposit	Monfurado prospect	Monfurado prospect	Monfurado prospect	Monfurado prospect	Monfurado prospect	Monfurado prospect	Monfurado prospect	Monfurado prospect	Monfurado prospect
Litostratigraphic unit	Amphibolic schists	Amphibolic schists	Amphibolic schists	Amphibolic schists	Amphibolic schists	Amphibolic schists	Amphibolic schists	Amphibolic schists	Amphibolic schists
Mineralization	Barren	Barren	Barren	Barren	Barren	Barren	Barren	Barren	Barren
Coordinates:									
x	4269432	4269432	4269432	4269432	4269432	4269432	4269432	4269432	4269432
y	571154	571154	571154	571154	571154	571154	571154	571154	571154
Depth	47.7-47.9	49.0-49.2	51.15-51.35	52.05-52.25	53.07-53.22	55.05-55.35	59.15-59.30	62.75-62.90	66.3-69.45
Petrography	✓	✓	✓	✓	✓	✓	✓	✓	✓
Whole rock geoch.									✓
EPMA									
LA-ICP-MS									
Fluid Inc.									
SEM-EDX									
Oxygen isotopes									
Sulfur isotopes									

Sample Ref	012-10	012-11	012-12	012-13	012-14	012-15	012-16	012-17	012-18
Ore Deposit	Monfurado prospect	Monfurado prospect	Monfurado prospect	Monfurado prospect	Monfurado prospect	Monfurado prospect	Monfurado prospect	Monfurado prospect	Monfurado prospect
Litostratigraphic unit	Amphibolic schists	Amphibolic schists	Amphibolic schists	Calcsilicate rocks	Calcsilicate rocks	Calcsilicate rocks	Calcsilicate rocks	Calcsilicate rocks	Marbles
Mineralization	Py	Py	Py	Py	Barren	Barren	Barren	Barren	Barren
Coordinates:									
x	4269432	4269432	4269432	4269432	4269432	4269432	4269432	4269432	4269432
y	571154	571154	571154	571154	571154	571154	571154	571154	571154
Depth	67.96-68.10	69.30-69.45	71.45-71.65	74.80-75.05	94.98-95.30	96.80-97.10	98.55-98.75	103.05-103.35	109.40-109.80
Petrography	✓	✓	✓	✓	✓	✓	✓	✓	✓
Whole rock geoch.					✓		✓		
EPMA									
LA-ICP-MS									
Fluid Inc.	✓	✓		✓					
SEM-EDX									
Oxygen isotopes									
Sulfur isotopes									

Sample Ref	012-19	MNG 1	MNG 2	SER 1	MV 1	MV 2	MV 3	MV 4	MV 5
Ore Deposit	Monfurado prospect	Monges	Monges	Serrinha	Vale da Arca	Vale da Arca	Vale da Arca	Vale da Arca	Vale da Arca
Lithology	Marbles	Massive ore horizon	Massive ore horizon	Massive ore horizon	Calcsilicate rocks	Calcsilicate rocks	Calcsilicate rocks	Calcsilicate rocks	Calcsilicate rocks
Mineralization	Mag	Mag	Mag	Mag	Py + Mag	Py + Mag	Py + Mag	Py + Mag	Py
Coordinates:									
x	4269432	4269661.98	4269661.98	4265896.68	4266803	4266803	4266787	4266815	4266875
y	571154	570312.86	570312.86	575304.79	574499	574499	574512	574495	574482
Depth	124.29-124.59	Outcrop	Outcrop	Outcrop	Outcrop	Outcrop	Outcrop	Outcrop	Outcrop
Petrography	✓	✓	✓	✓	✓	✓	✓	✓	✓
Whole rock geoch.					✓	✓	✓	✓	✓
EPMA							✓		
LA-ICP-MS		✓	✓	✓			✓		
Fluid Inc.									
SEM-EDX		✓	✓	✓	✓	✓	✓		
Oxygen isotopes		✓		✓				✓	
Sulfur isotopes									

Sample Ref	MV 6	MV 7	AL 1	AL 2	AL 3	AL 4	AL 5	AL 6	AL 7
Ore Deposit	Vale da Arca	Vale da Arca	Alvito	Alvito	Alvito	Alvito	Alvito	Alvito	Alvito
Litostratigraphic unit	Basic metavolcanic	Calcsilicate rocks	Calcsilicate rocks	Diorite	Massive ore horizons	Calcsilicate rocks	Marbles	Massive ore horizons	Marbles
Mineralization	Barren	Barren	Barren	Barren	Mag	Barren	Barren	Mag	Barren
Coordinates:									
x	4266777	4266862	4236458.48	4236458.48	4236458.48	4236458.48	4236458.48	4236458.48	4236458.48
y	574637	574474	585589.64	585589.64	585589.64	585589.64	585589.64	585589.64	585589.64
Depth	Outcrop	Outcrop	Outcrop	Outcrop	Outcrop	Outcrop	Outcrop	Outcrop	Outcrop
Petrography	✓	✓	✓	✓	✓	✓	✓	✓	✓
Whole rock geoch.	✓	✓	✓	✓	✓	✓	✓	✓	✓
EPMA	✓					✓		✓	
LA-ICP-MS									
Fluid Inc.									
SEM-EDX					✓			✓	
Oxygen isotopes									
Sulfur isotopes									

Sample Ref	AL 8	AL 9	AL 10	AL 11	AL 12	AL 13	AL 14	AL 15	AL 16
Ore Deposit	Alvito	Alvito	Alvito	Alvito	Alvito	Alvito	Alvito	Alvito	Alvito
Litostratigraphic unit	Massive ore horizons	Felsic metavolcanic rocks	Massive ore horizons	Massive ore horizons	Skarn	Skarn	Diorite	Felsic metavolcanic rocks	Marbles
Mineralization	Mag	Barren	Mag	Mag	Barren	Barren	Barren	Barren	Barren
Coordinates:									
x	4235374.94	4235374.94	4235374.94	4235374.94	4235374.94	4235374.94	4235374.94	4235374.94	4235374.94
y	585548.26	585548.26	585548.26	585548.26	585548.26	585548.26	585548.26	585548.26	585548.26
Depth	Outcrop	Outcrop	Outcrop	Outcrop	Outcrop	Outcrop	Outcrop	Outcrop	Outcrop
Petrography	✓	✓	✓	✓	✓	✓	✓	✓	✓
Whole rock geoch.	✓	✓	✓		✓	✓	✓	✓	✓
EPMA	✓	✓					✓		
LA-ICP-MS	✓		✓						
Fluid Inc.									
SEM-EDX	✓		✓						
Oxygen isotopes									
Sulfur isotopes									

Sample Ref	AL 17	AL 18	AL 19	AL 20	AL 21	AL 22	AL 30	AL 31	AL 33
Ore Deposit	Alvito	Alvito	Alvito	Alvito	Alvito	Alvito	Alvito	Alvito	Alvito
Litostratigraphic unit	Diorite	Massive ore horizons	Massive ore horizons	Massive ore horizons	Marbles	Marbles	Felsic metavolcanic rocks	Skarn	Dacite
Mineralization		Mag	Mag	Mag	Mag	Mag	Barren		Barren
Coordinates:									
x	4235770.42	4235770.42	4235770.42	4236269.25	4236269.25	4236282	4235627.44	4236357.23	4236357.23
y	585482.31	585482.31	585482.31	585640.64	585640.64	585679	586543.37	585669.45	585669.45
Depth	Outcrop	Outcrop	Outcrop	Outcrop	Outcrop	Outcrop	Outcrop	Outcrop	Outcrop
Petrography	✓	✓	✓	✓	✓	✓			
Whole rock geoch.	✓		✓	✓	✓	✓	✓		✓
EPMA	✓		✓	✓					
LA-ICP-MS			✓	✓					
Fluid Inc.									
SEM-EDX			✓	✓					
Oxygen isotopes			✓	✓					
Sulfur isotopes									

Sample Ref	AL 34	AZ 1	AZ 2	AZ 3	AZ 4	AZ 5	AZ 6	AZ 7	AZ 8
Ore Deposit	Alvito	Azenhas	Azenhas	Azenhas	Azenhas	Azenhas	Azenhas	Azenhas	Azenhas
Litostratigraphic unit	Diorite	Felsic metavolcanic rocks	Felsic metavolcanic rocks	Mineralized amphibolite	Skarn	Skarn	Mineralized amphibolite	Mineralized amphibolite	Mineralized amphibolite
Mineralization	Barren	Barren	Barren	Mag	Mag	Mag	Mag	Mag	Mag
Coordinates:									
x	4236281.69	4220842.38	4220836.87	4220838.97	4220829.84	4220836.45	4220838.48	4220838.48	4220811.85
y	585662.38	620820.94	620823.66	620815.73	620798.34	620795.61	620782.43	620782.43	620782.82
Depth	Outcrop	Outcrop	Outcrop	Outcrop	Outcrop	Outcrop	Outcrop	Outcrop	Outcrop
Petrography	✓	✓	✓	✓	✓	✓	✓	✓	✓
Whole rock geoch.	✓	✓	✓		✓	✓	✓	✓	✓
EPMA		✓			✓			✓	✓
LA-ICP-MS					✓			✓	✓
Fluid Inc.									
SEM-EDX					✓				✓
Oxygen isotopes									✓
Sulfur isotopes									

Sample Ref	AZ 9	AZ 10	AZ 11	AZ 12	ORA 1	ORA 2
Ore Deposit	Azenhas	Azenhas	Azenhas	Azenhas	Orada	Orada
Litostratigraphic unit	Marbles	Marbles	Mineralized amphibolite	Skarn	Massive magnetite	Massive magnetite
Mineralization			Mag	Barren		
Coordinates:						
x	4220816.30	4220820.95	4220844.73	4220833.36	4218753	4218753
y	620783.63	620797.59	620755.16	620803.64	622166	622166
Depth	Outcrop	Outcrop	Outcrop	Outcrop	Outcrop	Outcrop
Petrography	✓	✓	✓	✓	✓	✓
Whole rock geoch.	✓	✓	✓			
EPMA						
LA-ICP-MS						✓
Fluid Inc.						
SEM-EDX			✓			
Oxygen isotopes						
Sulfur isotopes						

Appendix C

Microthermometry results for the fluid inclusion study of samples from the Monfurado gold prospect

Appendix C-1. – Complete microthermometry results for the Lw1 fluid inclusions

Sample	IF Ref.	Host	Te	Tm_{ice}	Th_{total}	Td	Homogenization (L,V)	eq.w(NaCl)	x(NaCl)	Vm	p	VL at SLV	P (Mpa)
M6-1.1	Z1_1	Tourmaline	-	-1.2	420	-	L	2.07	0.01	42.05	0.43	42.90	27.63
M6-1.1	Z1_2	Tourmaline	-24.8	-1	420	-	L	1.74	-	-	-	-	-
M6-1.1	Z1_3	Tourmaline	-	-16.4	420	-	L	19.76	0.07	27.83	0.75	65.41	29.80
M6-1.1	Z1_4	Tourmaline	-	-1	425	-	L	1.74	-	-	-	-	-
M6-1.1	Z1_5	Tourmaline	-	-6	420	-	L	9.21	0.03	32.55	0.59	55.50	32.39
M6-1.1	Z2_1	Tourmaline	-	-0.5	460	-	L	0.88	-	-	-	-	-
M6-1.1	Z2_2	Tourmaline	-	-1.8	460	-	L	3.06	-	-	-	-	-
M6-1.1	Z2_3	Tourmaline	-	-2	460	-	L	3.39	-	-	-	-	-
M6-12.2	Z1_1	Tremolite	-	-11.3	-	309	L	15.27	0.05	23.37	0.86	77.57	8.87
M6-12.2	Z1_2	Tremolite	-	-11.6	-	309	L	15.57	0.05	23.34	0.86	77.67	8.85
M6-12.2	Z2_1	Baryte	-	-21.2	-	-	L	23.18	0.09	21.91	0.98	83.44	4.95
M6-12.2	Z2_2	Baryte	-	-18.8	274	-	L	21.54	0.08	21.95	0.96	83.08	5.03
M6-12.2	Z2_3	Baryte	-	-3.7	274	309	L	6.01	0.02	24.51	0.77	73.62	9.43
M6-12.2	Z3_1	Tremolite	-	-6.4	305	-	L	9.73	0.03	23.77	0.81	76.00	8.73
M6-12.2	Z3_2	Tremolite	-	-2.3	270	-	L	3.87	0.01	22.94	0.81	78.63	5.39
M6-12.2	Z3_4	Tremolite	-	-10	330	-	L	13.94	0.05	24.36	0.82	74.34	11.81
M6-12.2	Z3_7	Tremolite	-	-7.4	315.3	-	L	10.98	0.04	24.08	0.81	-	9.96
M6-12.2	Z3_8	Tremolite	-	-10.1	305	-	L	14.04	0.05	23.33	0.86	77.64	8.47
M6-12.2	Z3_9	Tremolite	-	-6.8	315	-	L	10.24	0.03	24.16	0.80	74.80	9.97
M6-12.2	Z4_1	Tremolite	-18.4	-1.5	265	-	L	2.57	0.01	22.88	0.80	78.85	5.02
M6-12.2	Z4_2	Tremolite	-	-2.4	194.5	-	L	4.03	0.01	20.53	0.90	87.90	1.35
M6-12.2	Z4_3	Tremolite	-34.4	-19.5	239.5	-	L	22.03	0.08	21.14	1.01	86.32	2.80
M6-12.2	Z4_4	Tremolite	-	-16.6	256.4	-	L	19.92	0.07	21.57	0.97	84.41	3.84
M6-12.2	Z4_5	Tremolite	-	-8.3	305	-	L	12.05	0.04	23.52	0.84	76.92	8.59
M6-12.2	Z4_6	Tremolite	-	-8.3	320	-	L	12.05	0.04	24.15	0.81	74.89	10.52

Appendix C-2. – Complete microthermometry results for the Lw2 fluid inclusions

Sample	IF Ref.	Host	Te	Tm_{ice}	Th_{total}	Td	Homogenization (L,V)	eq.w(NaCl)	x(NaCl)	Vm	p	VL at SLV	P (Mpa)
M5-27.3b	Z2_2	Quartz	-25.6	-3.2	249.1	-	L	5.26	0.02	22.03	0.85	81.91	3.80
M5-27.3b	Z2_3	Quartz	-24.11	-3.2	234	-	L	5.26	0.02	21.54	0.87	83.76	2.92
M5-27.2b	Z1_1	Quartz	-25	-6.2	216.7	-	L	9.47	0.03	20.90	0.92	86.45	2.05
M5-27.2b	Z1_2	Quartz	-25.2	-6.5	240.2	-	L	9.86	0.03	21.50	0.90	84.06	3.16
M5-27.2b	Z1_3	Quartz	-25.2	-6.3	250	-	L	9.59895	0.03	21.79	0.89	82.92	3.75
M5-27.2b	Z1_4	Quartz	-27.1	-6.4	220.1	-	L	9.73	0.03	20.97	0.92	86.15	2.18
M5-27.2b	Z1_7	Quartz	-24.4	-6.5	232.8	-	L	9.86	0.03	21.29	0.91	84.85	2.77
M5-27.2b	Z1_11	Quartz	-25.6	-6.5	233.8	-	L	9.86	0.03	21.32	0.91	84.75	2.82
M6-2.2	Z1_1	Quartz	-	-6.5	209.5	-	L	9.86	0.03	20.72	0.93	87.22	1.77
M6-2.2	Z1_2	Quartz	-	-6.5	214	-	L	9.86	0.03	20.82	0.93	86.78	1.93
M6-2.2	Z1_4	Quartz	-	-1.8	213.7	-	L	3.06	0.01	21.06	0.87	85.64	2.01
M6-2.2	Z1_5	Quartz	-	-2.9	213	-	L	4.8	0.02	20.97	0.89	86.05	1.96
M6-2.2	Z1_6	Quartz	-	-3	225	-	L	4.96	0.02	21.29	0.88	84.74	2.47
M6-2.2	Z1_7	Quartz	-	-2	242.7	-	L	3.39	0.01	21.95	0.84	82.19	3.44
M6-2.2	Z1_8	Quartz	-	-2	205	-	L	3.39	0.01	20.81	0.89	86.68	1.69
M6-2.2	Z1_9	Quartz	-	-1.6	204.5	-	L	2.74	0.01	20.83	0.88	86.62	1.68
M6-2.2	Z2_10	Quartz	-31	-6.1	201.5	-	L	9.34	0.03	20.55	0.94	87.92	1.51
M6-2.2	Z2_14	Quartz	-	-2.5	186.8	-	L	4.18	0.01	20.34	0.91	88.70	1.14
M6-2.2	Z3_3	Quartz	-	-2.5	257.5	-	L	4.18	0.01	22.41	0.83	80.49	4.40
M6-2.2	Z4_1	Quartz	-	-1.9	148.9	-	L	3.23	0.01	19.58	0.94	92.16	0.45
M6-2.2	Z4_2	Quartz	-	-1.9	148	-	L	3.23	0.01	19.56	0.94	92.24	0.44
M6-2.2	Z4_3	Quartz	-	-3	180.6	-	L	4.96	0.02	20.18	0.92	89.40	0.98
M6-2.2	Z4_4	Quartz	-	-2.3	206.5	-	L	3.87	0.01	20.83	0.89	86.60	1.73
M6-3.2	Z1_1	Quartz	-	-8.9	235.2	-	L	12.73	0.04	21.25	0.93	85.14	2.83
M6-3.2	Z1_2	Quartz	-	-9.3	253.2	-	L	13.18	0.04	21.71	0.91	83.36	3.86
M6-3.2	Z1_4	Quartz	-	-8.8	198.2	-	L	12.62	0.04	20.42	0.97	88.62	1.37
M6-3.2	Z1_5	Quartz	-	-5.4	215	-	L	8.41	0.03	20.89	0.92	86.45	1.99
M6-3.2	Z1_6	Quartz	-	-5.8	240.6	-	L	8.95	0.03	21.55	0.89	83.82	3.20

Appendix C-2. – Continuation of previous table

M6-3.2	Z2_1	Quartz	-	-8	230	-	L	11.7	0.04	21.16	0.93	85.48	2.59
M6-3.2	Z2_2	Quartz	-	-8	226	-	L	11.7	0.04	21.06	0.93	85.88	2.40
M6-3.2	Z2_3	Quartz	-25	-5.4	223.3	-	L	8.41	0.03	21.10	0.91	85.59	2.34
M6-3.2	Z2_4	Quartz	-	-8	243	-	L	11.7	0.04	21.49	0.91	84.14	3.28
M6-3.2	Z2_5	Quartz	-	-8.5	222.8	-	L	12.28	0.04	20.97	0.94	86.29	2.25
M6-3.2	Z2_6	Quartz	-	-8.6	230	-	L	12.39	0.04	21.14	0.93	85.60	2.58
M6-3.2	Z2_7	Quartz	-	-8.9	206	-	L	12.73	0.43	20.58	0.96	87.93	1.61
M6-3.2	Z2_8	Quartz	-	-8.9	237.6	-	L	12.73	0.04	21.32	0.93	84.89	2.95
M6-3.2	Z2_9	Quartz	-	-9.1	229.5	-	L	12.96	0.04	21.11	0.94	85.74	2.54
M6-3.2	Z2_10	Quartz	-	-8.8	227.5	-	L	12.62	0.04	21.07	0.94	85.88	2.45
M6-3.2	Z2_11	Quartz	-	-9.1	241.6	-	L	12.96	0.04	21.41	0.92	84.53	3.16
M6-4.1	Z1_2	Quartz	-40.9	-8	227.5	-	L	1.7	0.04	21.10	0.93	85.73	2.47
M6-4.1	Z1_3	Quartz	-46.4	-8.3	176	-	L	12.05	0.04	12.05	0.98	90.47	0.83
M6-4.1	Z1_4	Quartz	-33.4	-2.9	176.8	-	L	4.8	0.02	20.10	0.93	89.74	0.90
M6-4.1	Z1_5	Quartz	-39.4	-2.9	181.3	-	L	4.8	0.02	20.20	0.92	89.31	1.00
M6-4.1	Z1_6	Quartz	-47.4	-6.7	176	-	L	10.11	0.03	20.01	0.97	90.30	0.85
M6-4.1	Z1_7	Quartz	-41.4	-7.7	227.5	-	L	11.34	0.04	21.11	0.93	85.67	2.48
M6-4.1	Z1_8	Quartz	-48.4	-8.2	214.4	-	L	11.93	0.04	20.78	0.94	87.04	1.92
M6-4.1	Z1_9	Quartz	-	-2.7	183	-	L	4.49	0.01	20.25	0.92	89.11	1.04
M6-4.1	Z1_10	Quartz	-	-2.4	180	-	L	4.03	0.01	20.19	0.92	89.35	0.98
M6-4.1	Z1_11	Quartz	-32.4	-2.3	172.4	-	L	3.87	0.01	20.30	0.92	90.07	0.82
M6-4.1	Z1_12	Quartz	-	-2.3	175.7	-	L	3.87	0.01	20.10	0.92	89.75	0.88
M6-4.1	Z1_13	Quartz	-42.9	-5	220	-	L	7.86	0.03	21.03	0.91	85.84	2.21
M6-4.1	Z1_14	Quartz	-	-4.3	187.3	-	L	6.88	0.02	20.29	0.93	88.97	1.13
M6-4.1	Z1_15	Quartz	-	-2.3	187.3	-	L	3.87	0.01	20.36	0.91	88.61	1.15
M6-4.1	Z1_16	Quartz	-	-2.2	182.7	-	L	3.71	0.01	20.26	0.91	89.05	1.04
M6-4.1	Z1_17	Quartz	-	-2.3	182.8	-	L	3.87	0.01	20.26	0.91	89.06	1.04
M6-4.1	Z1_18	Quartz	-	-1.8	180	-	L	3.06	0.01	20.21	0.91	89.24	0.98
M6-4.1	Z2_1	Quartz	-	-3.6	200.3	-	L	5.86	0.02	20.61	0.91	87.56	1.51

Appendix C-2. – Continuation of previous table

M6-4.1	Z2_2	Quartz	-41.9	-3.7	200.3	-	L	6.01	0.02	20.60	0.91	87.59	1.50
M6-4.1	Z2_3	Quartz	-	-3.6	196.5	-	L	5.86	0.02	20.52	0.92	87.95	1.39
M6-4.1	Z2_4	Quartz	-27.4	-5.7	233.5	-	L	8.81	0.03	21.35	0.90	84.58	2.82
M6-4.1	Z3_1	Quartz	-49.4	-9.7	226.7	-	L	13.62	0.05	21.02	0.95	86.12	2.40
M6-4.1	Z3_2	Quartz	-39.4	-9.6	197.8	-	L	13.51	0.05	20.40	0.97	88.75	1.34
M6-4.1	Z3_4	Quartz	-	-3.7	196.7	-	L	6.01	0.02	20.52	0.92	87.95	1.39
M6-4.2	Z4_1	Quartz	-	-10	240	-	L	13.94	0.05	21.34	0.93	84.87	3.05
M6-4.3	Z4_2	Quartz	-33	-21.2	240	-	L	25.78685	0.10	21.11	1.04	86.89	2.70
M6-4.4	Z4_3	Quartz	-	-21.1	242	-	L	23.11	0.08	21.18	1.01	86.28	2.90
M6-4.5	Z4_4	Quartz	-	-21.2	241.6	-	L	23.18	0.09	21.17	1.01	86.33	2.87
M6-4.6	Z4_5	Quartz	-27.4	-7.4	246	-	L	10.98	0.04	21.61	0.90	83.67	3.47
M6-4.1	Z4_6	Quartz	-	-5.5	271	-	L	8.55	0.03	22.54	0.85	80.12	5.33
M6-4.1	Z5_9	Quartz	-27.4	-2.7	240	270	L	4.49	0.01	21.78	0.85	82.84	3.26
M6-4.1	Z5_13	Quartz	-25	-7	242	270	L	10.49	0.03	21.52	0.90	84.00	3.25
M6-4.1	Z5_14	Quartz	-25	-7	242	-	L	10.49	0.03	21.52	0.90	84.00	3.25
M6-4.1	Z5_15	Quartz	-	-5.3	252.8	-	L	8.28	0.03	21.95	0.87	82.27	3.97
M6-4.1	Z5_16	Quartz	-	-5.5	262.7	-	L	8.28	0.03	22.25	0.86	81.15	4.67
M6-4.1	Z5_18	Quartz	-25.4	-6.1	241	-	L	9.34	0.03	21.54	0.89	83.86	3.22
M6-4.1	Z5_19	Quartz	-25.4	-6.3	241	-	L	9.6	0.03	21.53	0.90	83.92	3.21
M6-4.1	Z5_20	Quartz	-25.4	-21.2	241	-	L	23.18	0.09	21.16	1.01	86.38	2.84
M6-4.1	Z5_23	Quartz	-34.4	-10.3	254.3	-	L	14.25	0.05	21.70	0.92	83.48	3.90
M6-4.1	Z5_24	Quartz	-34.2	-10.3	252.8	-	L	14.25	0.05	21.66	0.92	83.63	3.80
M6-4.1	Z5_25	Quartz	-34.4	-3.5	252.8	-	L	5.71	0.02	22.12	0.85	81.58	4.04
M6-22.1	Z1_1	Quartz	-	-2.3	270	-	L	3.87	0.01	22.94	0.81	78.63	5.39
M6-22.1	Z1_2	Quartz	-20.8	-3.5	315	-	L	5.71	0.02	24.91	0.75	72.45	10.25
M6-22.1	Z1_3	Quartz	-	-3	218	-	L	4.96	0.02	21.10	0.88	85.53	2.17
M6-22.1	Z1_4	Quartz	-	-3.4	227	-	L	5.56	0.02	21.32	0.88	84.64	2.56
M6-22.1	Z1_5	Quartz	-	-3.1	258	-	L	5.11	0.02	22.35	0.84	80.72	4.42
M6-22.1	Z1_6	Quartz	-	-2.6	221	-	L	4.34	0.01	21.21	0.88	85.06	2.30

Appendix C-2. – Continuation of previous table

M6-22.1	Z1_7	Quartz	-	-2.6	206	-	L	4.34	0.01	20.80	0.89	86.73	1.71
M6-23.1	Z1_2	Quartz	-	-1.1	236	-	L	1.91	0.01	21.83	0.84	82.64	3.08
M7-7.1	Z2_2	Quartz	-25.9	-7.1	300	-	L	10.61	0.04	23.46	0.83	77.04	8.09
M7-7.1	Z2_4	Quartz	-26	-8.2	235.4	-	L	11.931	0.04	21.29	0.92	84.97	2.86
M7-7.1	Z2_5	Quartz	-	-8.1	226	-	L	11.81	0.04	21.06	0.93	85.90	2.40
M7-7.4	Z1_6	Quartz	-23.2	-6.7	208.1	-	L	10.11	0.03	20.68	0.94	87.39	1.71
M12.5.2	Z1_1	Quartz	-	-1.8	162.9	-	L	3.06	0.01	19.85	0.93	90.89	0.65
M12.5.2	Z1_2	Quartz	-	-2.7	230.6	-	L	4.49	0.01	21.48	0.87	83.98	2.75
M12.5.2	Z1_3	Quartz	-	-2.2	165	-	L	3.71	0.01	19.88	0.93	90.75	0.68
M12.5.2	Z1_4	Quartz	-	-1.7	154	-	L	2.9	0.01	19.68	0.93	91.69	0.52
M12.5.2	Z1_5	Quartz	-	-3.9	207.4	-	L	6.3	0.02	20.77	0.91	86.90	1.74
M12.5.2	Z1_6	Quartz	-	-4	163	-	L	6.45	0.02	19.80	0.95	91.14	0.64
M12.5.2	Z2_1	Quartz	-	-4.1	235.8	-	L	6.59	0.02	21.52	0.88	83.85	2.99
M12.5.2	Z2_2	Quartz	-	-4.8	235.8	-	L	7.59	0.02	21.47	0.85	84.07	2.97
M12.5.2	Z2_3	Quartz	-	-3.4	260	-	L	5.56	0.02	22.39	0.84	80.60	4.55
M12.5.2	Z2_4	Quartz	-	-3.1	259	-	L	5.11	0.02	22.39	0.83	80.59	4.49
M12.5.2	Z2_5	Quartz	-	-2.8	197	-	L	4.65	0.01	20.57	0.91	87.73	1.42
M12.5.2	Z2_6	Quartz	-	-2.1	177.4	-	L	3.55	0.01	20.14	0.92	89.55	0.92
M12.5.2	Z2_7	Quartz	-	-2.2	187	-	L	3.71	0.01	20.36	0.91	88.62	1.15
M12.5.2	Z2_8	Quartz	-	-2.3	197.5	-	L	3.87	0.01	20.60	0.90	87.56	1.44
M12.5.2	Z3_1	Quartz	-	-3.7	215	-	L	6.01	0.02	20.97	0.90	86.05	2.03
M12.5.2	Z3_3	Quartz	-	-4.7	189	-	L	7.45	0.02	20.31	0.94	88.88	1.17
M12.5.2	Z3_4	Quartz	-	-3.6	314	-	L	5.86	0.02	24.82	0.76	72.71	10.10
M12.5.2	Z3_5	Quartz	-	-2.8	295	-	L	4.65	0.01	24.00	0.78	75.18	7.90
M12.6.1	Z1_1	Quartz	-	-2.6	219	-	L	4.34	0.01	21.15	0.88	85.29	2.22
M12.6.1	Z1_2	Quartz	-	-2.7	285	-	L	4.49	0.01	23.53	0.79	76.67	6.75
M12.6.1	Z1_3	Quartz	-	-2.6	187	-	L	4.34	0.01	20.34	0.91	88.70	1.14
M12.6.1	Z1_4	Quartz	-21.6	-2.5	210	-	L	4.8	0.01	20.91	0.89	86.26	1.86
M12.6.1	Z1_5	Quartz	-	-3	288	-	L	4.96	0.02	23.61	0.79	76.42	7.04

Appendix C-2. – Continuation of previous table

M12.6.1	Z1_6	Quartz	-10.2	-2.9	236	-	L	4.8	0.02	21.63	0.86	83.41	3.03
M12.6.1	Z1_7	Quartz	-	-3.3	221	-	L	5.41	0.02	21.16	0.88	85.28	2.29
M12.6.1	Z1_8	Quartz	-22.8	-6.9	228	-	L	10.36	0.03	21.15	0.92	85.45	2.52
M12.6.1	Z1_9	Quartz	-25	-5	230.3	-	L	7.86	0.03	21.31	0.89	84.74	2.68
M12.6.1	Z1_10	Quartz	-25	-5	270	-	L	7.86	0.03	22.56	0.84	80.03	5.27
M12.6.1	Z2_11	Quartz	-	-2.9	250	-	L	4.8	0.02	22.09	0.84	81.67	3.87
M12.6.1	Z2_12	Quartz	-	-3.3	247.8	-	L	5.41	0.02	21.97	0.85	82.12	3.71
M12.6.1	Z2_13	Quartz	-	-6.2	262.5	-	L	9.47	0.03	22.19	0.87	81.43	4.62
M12.6.1	Z2_14	Quartz	-	-4	231	-	L	6.45	0.02	21.39	0.88	84.37	2.74
M12.6.1	Z2_15	Quartz	-15	-4.7	263	-	L	7.45	0.02	22.34	0.85	80.79	4.72
M12.6.1	Z2_16	Quartz	-21	-3.3	220	-	L	5.41	0.02	21.13	0.89	85.39	2.24
M12.6.1	Z3_1	Quartz	-26.5	-4	220	-	L	6.45	0.02	21.09	0.89	85.59	2.23
M12.6.1	Z3_2	Quartz	-26.5	-4.1	201	-	L	6.59	0.02	20.60	0.92	87.60	1.52
M12.6.1	Z3_3	Quartz	-	-4	290	-	L	6.45	0.02	23.51	0.80	76.77	7.19
M12.6.1	Z3_4	Quartz	-27	-4.2	217	-	L	6.74	0.02	21.00	0.90	85.96	2.10
M12.6.1	Z3_5	Quartz	-27	-4.1	220	-	L	6.59	0.02	21.08	0.90	85.62	2.23
M12.6.1	Z3_6	Quartz	-23	-4	262.7	-	L	6.45	0.02	22.41	0.84	80.53	4.73
M12.6.1	Z3_7	Quartz	-25	-3.9	230	-	L	6.3	0.02	21.37	0.88	84.45	2.69
M12.6.1	Z4_1	Quartz	-	-3.2	230	-	L	5.26	0.02	21.42	0.87	84.22	2.71
M12.6.1	Z4_2	Quartz	-	-3.2	220.7	-	L	5.26	0.02	21.16	0.88	85.29	2.28
M12.6.1	Z4_3	Quartz	-22.7	-4.7	224.7	-	L	7.45	0.02	21.17	0.90	85.27	2.42
M12.6.1	Z4_4	Quartz	-21	-6	235	-	L	9.21	0.03	21.38	0.90	84.49	2.89
M12.6.1	Z4_5	Quartz	-	-3.3	232.9	-	L	5.41	0.02	21.50	0.87	83.92	2.86
M12.6.1	Z4_6	Quartz	-21.2	-3.2	218.1	-	L	5.26	0.02	21.09	0.89	85.57	2.16
M12.6.1	Z4_7	Quartz	-20.5	-3.1	224.5	-	L	5.11	0.02	21.27	0.88	84.83	2.45
M12.6.1	Z4_8	Quartz	-23	-3.1	203.2	-	L	5.11	0.02	20.70	0.90	87.15	1.61
M12.6.1	Z4_9	Quartz	-22.5	-3.2	265	-	L	5.26	0.02	22.60	0.83	79.84	4.94
M12.6.1	Z4_10	Quartz	-22.7	-3.2	217.1	-	L	5.26	0.02	21.06	0.89	85.69	2.12
M12.6.1	Z5_12	Quartz	-	-1	203.4	-	L	1.74	0.01	20.84	0.87	86.56	1.65

Appendix C-2. – Continuation of previous table

M12.6.1	Z5_13	Quartz	-22.4	-3.4	201.9	-	L	5.56	0.02	20.66	0.91	87.36	1.56
M12.6.1	Z5_14	Quartz	-21.8	-3	202	-	L	4.96	0.02	20.68	0.90	87.25	1.57
M12.6.1	Z5_15	Quartz	-21.1	-3.3	210	-	L	5.41	0.02	20.90	0.90	86.48	1.84
M12.6.1	Z5_16	Quartz	-21.7	-3.3	260	-	L	5.41	0.02	22.40	0.84	80.56	4.55
M12.6.1	Z5_17	Quartz	-21.7	-3.3	248.8	-	L	5.41	0.02	22.01	0.85	81.99	3.78
M12.6.1	Z5_18	Quartz	-21.7	-3.2	237.7	-	L	5.26	0.02	21.66	0.86	83.32	3.12
M12.6.1	Z6_1	Quartz	-	-3.8	182	-	L	6.16	0.02	20.19	0.93	89.39	1.01
M12.6.1	Z6_2	Quartz	-24.7	-5.8	135	-	L	8.95	0.03	19.31	0.99	93.52	0.29
M12.6.1	Z6_3	Quartz	-	-5	220	-	L	7.86	0.03	21.03	0.91	85.84	2.21
M12-10.1	Z1_1	Quartz	-20.7	-1.8	229.6	-	L	3.06	0.01	21.54	0.85	83.76	2.73
M12-10.1	Z1_2	Quartz	-20.7	-1.8	224.4	-	L	3.06	0.01	21.38	0.86	84.39	2.48
M12-10.1	Z1_3	Quartz	-20.7	-1.8	223.4	-	L	3.06	0.01	213478.00	0.86	84.51	2.43
M12-10.1	Z2_2	Quartz	-	-2.2	245.5	-	L	3.71	0.01	22.02	0.84	81.93	3.61
M12-10.1	Z2_3	Quartz	-	-5.8	195	-	L	8.95	0.03	20.41	0.94	88.48	1.31
M12-10.1	Z2_5	Quartz	-	-2.3	142.2	-	L	3.87	0.01	19.45	0.95	92.76	0.37
M12-10.1	Z2_7	Quartz	-24.7	-2.2	263.6	-	L	3.71	0.01	22.70	0.81	79.48	4.87
M12-10.1	Z2_9	Quartz	-	-4.7	205	-	L	7.45	0.02	20.68	0.92	87.32	1.64
M12-10.1	Z2_10	Quartz	-18.7	-3.6	245.5	-	L	5.86	0.02	21.87	0.86	82.52	3.56
M12-10.1	Z2_11	Quartz	-	-2.3	292.2	-	L	3.87	0.01	23.98	0.77	75.23	7.53
M12-10.1	Z2_12	Quartz	-17.9	-4.4	236	-	L	7.02	0.02	21.51	0.88	83.92	2.99
M12-10.1	Z3_1	Quartz	-	-3.1	198.6	-	L	5.11	0.02	20.59	0.91	87.63	1.46
M12-10.1	Z3_2	Quartz	-24.1	-3.9	202.8	-	L	6.3	0.02	20.66	0.91	87.37	1.58
M12-10.1	Z3_3	Quartz	-	-4.2	187.1	-	L	6.74	0.02	20.29	0.93	88.97	1.12
M12-10.1	Z4_1	Quartz	-	-2.6	230	-	L	4.34	0.01	21.47	0.86	84.01	2.73
M12-10.1	Z4_2	Quartz	-	-2.5	219	-	L	4.18	0.01	21.16	0.88	85.26	2.22
M12-10.1	Z4_3	Quartz	-	-8.7	250	-	L	12.51	0.04	21.65	0.91	83.56	3.68
M12-10.1	Z4_4	Quartz	-	-2.6	281	-	L	4.34	0.01	23.37	0.79	77.20	6.37
M12-10.1	Z5_1	Quartz	-	-3.1	308.6	-	L	5.11	0.02	24.65	0.76	73.19	9.46
M12-10.1	Z5_2	Quartz	-	-4.2	327	-	L	6.74	0.02	25.42	0.74	71.02	11.93

Appendix C-2. – Continuation of previous table

M12-10.1	Z5_3	Quartz	-	-4	280	-	L	6.45	0.02	23.08	0.82	78.20	6.20
M12-10.1	Z5_4	Quartz	-	-6.3	280	-	L	9.6	0.03	22.78	0.85	79.30	6.08
M12-11.2	Z1_1	Quartz	-	-1.7	306.5	-	L	2.9	0.01	24.99	0.74	72.19	9.27
M12-11.2	Z1_2	Quartz	-21.8	-4.1	310	-	L	6.59	0.02	24.46	0.77	73.78	9.53
M12-11.2	Z1_3	Quartz	-24.8	-3.4	219.8	-	L	5.56	0.02	21.12	0.89	85.44	2.23
M12-11.2	Z1_4	Quartz	-25.1	-3.4	220	-	L	5.56	0.02	21.12	0.89	85.42	2.24
M12-11.2	Z2_1	Quartz	-	-3.3	235	-	L	5.41	0.02	21.57	0.87	83.67	2.97
M12-11.2	Z2_2	Quartz	-	-3.7	238.1	-	L	6.01	0.02	21.63	0.87	83.45	3.12
M12-11.2	Z2_3	Quartz	-24.7	-4	231.6	-	L	6.45	0.02	21.41	0.88	84.30	2.77
M12-11.2	Z2_4	Quartz	-22.5	-4	238.5	-	L	6.45	0.02	21.61	0.87	83.50	3.14
M12-11.2	Z2_5	Quartz	-25.9	-3.7	238.6	-	L	6.01	0.02	21.64	0.87	83.39	3.15
M12-11.2	Z2_6	Quartz	-	-3.4	226.7	-	L	5.56	0.02	21.31	0.88	84.67	2.54
M12-11.2	Z3_1	Quartz	-24.7	-3.2	297.7	-	L	5.26	0.02	24.04	0.78	75.06	8.09
M12-11.2	Z3_2	Quartz	-26	-3.3	250	-	L	5.41	0.02	22.05	0.85	81.84	3.86
M12-11.2	Z3_3	Quartz	-25.7	-3.4	224.4	-	L	5.56	0.02	21.25	0.88	84.93	2.44
M12-11.2	Z3_4	Quartz	-	-3.3	287.3	-	L	5.41	0.02	23.52	0.80	76.73	6.95
M12-11.2	Z3_5	Quartz	-26.5	-21.4	382	-	L	23.18	0.09	25.41	0.85	71.95	19.65
M12-11.2	Z3_6	Quartz	-24.1	-3.4	307	-	L	5.56	0.02	24.48	0.77	73.71	9.20
M12-11.2	Z3_7	Quartz	-	-3.6	221.8	-	L	5.86	0.02	21.46	0.89	85.28	2.32
M12-11.2	Z3_8	Quartz	-25.7	-4.1	295	-	L	6.59	0.02	23.72	0.80	76.10	7.72
M12-11.2	Z4_1	Quartz	-25.5	-4.3	250	-	L	6.88	0.02	21.95	0.86	82.24	3.82
M12-11.2	Z4_2	Quartz	-	-5.6	290	-	L	8.68	0.03	23.25	0.82	77.66	7.10
M12-11.2	Z4_3	Quartz	-27	-4.6	247.8	-	L	7.31	0.02	21.85	0.87	82.62	3.67
M12-11.2	Z4_4	Quartz	-22.7	-4.6	236.6	-	L	7.31	0.02	21.51	0.88	83.92	3.02
M12-11.2	Z4_5	Quartz	-27.7	-4.9	236.7	-	L	7.73	0.03	21.49	0.89	84.00	3.01
M12-11.2	Z4_6	Quartz	-27.7	-3.3	235	-	L	5.41	0.02	21.57	0.87	83.67	2.97
M12-11.2	Z4_7	Quartz	-27.7	-5.6	240	-	L	8.68	0.03	21.54	0.89	83.83	3.17
M12-11.2	Z4_8	Quartz	-26.8	-4.2	245	-	L	6.74	0.02	21.80	0.87	82.81	3.51
M12-11.2	Z5_1	Quartz	-26.5	-3.4	196.8	-	L	5.56	0.02	20.53	0.91	87.88	1.40

Appendix C-2. – Continuation of previous table

M12-11.2	Z5_2	Quartz	-	-3.7	186	-	L	6.01	0.02	20.28	0.93	89.00	1.10
M12-11.2	Z5_3	Quartz	-26.7	-3.7	205	-	L	6.01	0.02	20.72	0.91	87.10	1.66
M12-11.2	Z5_4	Quartz	-23.3	-3.9	274.1	-	L	6.3	0.02	22.86	0.82	78.97	5.67
M12-11.2	Z6_2	Quartz	-24.7	-2.8	265.5	-	L	4.65	0.01	22.68	0.82	79.56	5.00
M12-11.2	Z7_1	Quartz	-26.7	-4	150	-	L	6.45	0.02	19.57	0.96	92.24	0.45
M12-11.2	Z7_2	Quartz	-	-4.6	198.5	-	L	7.31	0.02	20.53	0.92	87.94	1.43
M12-11.2	Z7_3	Quartz	-33.7	-4.3	208.9	-	L	6.88	0.02	20.79	0.91	86.84	1.78
M12-11.2	Z7_4	Quartz	-34.8	-11.3	193.2	-	L	15.27	0.05	20.29	0.99	89.34	1.20
M12-11.2	Z7_5	Quartz	-34.8	-5.2	182.1	-	L	8.14	0.03	20.16	0.95	89.59	0.99
M12-11.2	Z7_6	Quartz	-	-4.5	178	-	L	7.17	0.02	20.09	0.94	89.87	0.91
M12-11.2	Z7_7	Quartz	-	-4.4	158.1	-	L	7.02	0.02	19.71	0.96	91.60	0.56
M12-13.2	Z1_4	Quartz	-33.7	-3.2	252.7	-	L	5.26	0.02	22.15	0.84	81.46	4.04
M12-13.2	Z1_5	Quartz	-	-3.1	176	252.7	L	5.11	0.02	20.08	0.93	89.85	0.88
M12-13.2	Z1_6	Quartz	-38.7	-9.4	143.7	-	L	13.29	0.05	19.45	1.02	93.05	0.36
M12-13.2	Z2_5	Quartz	-25.5	-7	231.4	-	L	10.49	0.03	21.23	0.91	85.12	2.68
M12-13.2	Z3_1	Quartz	-32.7	-9.8	125.4	-	L	13.72	0.05	19.19	1.04	94.34	0.21
M12-13.2	Z3_2	Quartz	-31.7	-6.9	291.2	-	L	10.36	0.03	23.14	0.84	78.12	7.14
M12-13.2	Z3_3	Quartz	-29.7	-7.6	187.2	-	L	11.22	0.04	20.22	0.97	89.44	1.09
M12-13.2	Z3_4	Quartz	-28.3	-7.2	231.4	-	L	10.72	0.04	21.22	0.92	85.16	2.68
M12-13.2	Z3_5	Quartz	-34.7	-5.4	180	-	L	8.41	0.03	20.11	0.95	89.80	0.94
M12-13.2	Z3_6	Quartz	-27.7	-11.2	180	-	L	15.17	0.05	20.05	1.00	90.40	0.89
M12-13.2	Z3_7	Quartz	-	-3.9	279	-	L	6.3	0.02	23.05	0.82	78.29	6.11
M12-13.2	Z4_1	Quartz	-24.7	-4.6	223.2	246.5	L	7.31	0.02	21.14	0.90	85.40	2.35
M12-13.2	Z4_2	Quartz	-24.7	-4.9	253.2	-	L	7.73	0.03	22.00	0.87	82.08	4.01
M12-13.2	Z4_3	Quartz	-27.7	-6.5	273.2	-	L	9.86	0.03	22.52	0.86	80.24	5.47
M12-13.2	Z5_1	Quartz	-32.7	-4.5	212.1	-	L	7.17	0.02	20.86	0.91	86.55	1.90
M12-13.2	Z5_2	Quartz	-32.7	-4.8	267.3	-	L	7.59	0.02	22.49	0.85	80.29	5.06
M12-13.2	Z5_3	Quartz	-29.8	-4.7	257.2	-	L	7.45	0.02	22.15	0.86	81.52	4.30
M12-13.2	Z5_4	Quartz	-24.3	-4.6	197.8	-	L	7.31	0.02	20.51	0.93	88.01	1.41

Appendix C-2. – Continuation of previous table

M12-13.2	Z5_6	Quartz	-	-4.6	235	-	L	7.31	0.02	21.47	0.88	84.10	2.93
M12-13.2	Z5_7	Quartz	-30.6	-4.5	229.3	-	L	7.17	0.02	21.31	0.89	84.71	2.64
M12-13.2	Z5_8	Quartz	-28.7	-4.5	250	-	L	7.17	0.02	21.93	0.86	82.32	3.81
M12-13.2	Z5_9	Quartz	-28.7	-4.5	244.2	-	L	7.17	0.02	21.75	0.87	83.01	3.45

Appendix C-3. – Complete microthermometry results for the Lc-w fluid inclusions

Sample	IF Ref.	Host	Tm_{CO2}	Te	Tm_{ice}	Tm_{cla}	Th_{CO2}	Homogenization (L,V)
M12-13.2	Z1_1	Quartz	-56.8	-	-	-	18.6	L
M12-13.2	Z1_2	Quartz	-56.8				0	L
M12-13.2	Z1_3	Quartz	-56.9				5.7	L
M12-13.2	Z1_7	Quartz	-57.7		-4.5	5.2	13.9	L
M12-13.2	Z2_1	Quartz	-56.9		-14.3		24.6	L
M12-13.2	Z2_2	Quartz	-57.2				13.7	L
M12-13.2	Z2_3	Quartz	-57.2		-8.8		9.6	L
M12-13.2	Z2_4	Quartz	-57.1				0.9	L
M12-13.2	Z2_6	Quartz	-57.3		-6		18	L
M12-13.2	Z2_7	Quartz	-57		-9	-	15.4	L
M12-13.2	Z2_8	Quartz	-57.8	-	-9	-	10.5	L
M12-13.2	Z2_9	Quartz	-57.5	-	-	-	2.1	L
M12-13.2	Z2_10	Quartz	-57.4	-	-	-	5	L
M12-13.2	Z3_4	Quartz	-57.6	-25.9	-4.8	-	12.8	L
M12-13.2	Z3_5	Quartz	-58.2	-24.3	-4.8	-	9.8	L
M12-13.2	Z3_6	Quartz	-58.6	-	-4.5	-	6.9	L
M12-13.2	Z4_5	Quartz	-58.1	-	-	-	3.9	L

Appendix C-4. – Complete microthermometry results for the LVCH4 fluid inclusions

Sample	IF Ref.	Host	Tm_{ice}	Th_{CH4}	Flw	Homogenization (L,V)	Vm	D	Int. Pressure(Mpa) @20ºC	Ph
M5-27.3b	Z1_1	Quartz	-	-138.3	5	L	38.77	0.42	155.77	0.49
M5-27.3b	Z1_2	Quartz	-	-138.1	5	L	38.80	0.42	155.18	0.49
M5-27.3b	Z1_3	Quartz	-	-138.7	5	V	310.10	0.06	1.14	0.47
M5-27.3b	Z1_4	Quartz	-	-138	5	V	308.46	0.06	1.18	0.49
M5-27.3b	Z1_5	Quartz	-	-137.4	5	V	307.03	0.06	1.21	0.51
M5-27.3b	Z1_6	Quartz	-	-137.4	5	V	307.03	0.06	1.21	0.51
M5-27.3b	Z2_4	Quartz	-7	-136.3	5	L	39.09	0.42	149.96	0.54
M5-27.3b	Z2_5	Quartz	-5	-137.8	5	V	307.98	0.06	1.19	0.50
M5-27.3b	Z2_6	Quartz	-	-141.3	5	L	38.32	0.42	164.71	0.41
M5-27.3b	Z2_7	Quartz	-1	-137	5	V	306.07	0.06	1.24	0.52
M5-27.3b	Z2_8	Quartz	-	-137.1	5	V	306.31	0.06	1.23	0.52
M5-27.2b	Z1_5	Quartz	-2.2	-142.7	5	L	38.11	0.43	168.97	0.38
M5-27.2b	Z1_6	Quartz	-6.2	-141.8	5	L	38.24	0.43	166.22	0.40
M5-27.2b	Z1_9	Quartz	-	-142.3	5	L	38.17	0.43	167.75	0.39
M5-27.2b	Z1_10	Quartz	-	-142.3	5	L	38.17	0.43	167.75	0.39
M5-27.2b	Z1_12	Quartz	-	-142.8	5	L	38.09	0.43	169.28	0.37
M5-27.2b	Z1_13	Quartz	-	-143.5	5	L	37.99	0.43	171.43	0.36
M7-7.1	Z1_1	Quartz	-0.9	-141	5	L	38.36	0.42	163.80	0.42
M7-7.4	Z1_1	Quartz	-	-141	5	V	315.27	0.06	1.01	0.42
M7-7.4	Z1_2	Quartz	-	-140	5	V	313.06	0.06	1.06	0.44
M7-7.4	Z1_3	Quartz	-	-136	5	V	303.62	0.06	1.30	0.55
M7-7.4	Z1_4	Quartz	-	-137.3	5	V	306.79	0.06	1.22	0.51
M7-7.4	Z2_1	Quartz	-	-139.7	5	V	312.38	0.06	1.08	0.45

Appendix D

Complete results of whole rock geochemistry

Appendix D-1. – Whole-rock geochemistry of samples from the Montemor-o-Novo area

	Drillcore samples from the Monges mine area – Monfurado gold prospect									
Sample		1	2	3	4	5	6	7	8	9
	LOD*	M12@66m Paragneiss	M8@80m Acid Metavolcanics	M8@83m Acid Metavolcanics	M6@28m Acid Metavolcanics	Acid Metavolcanics (outcrop)	M10@76m Marble	M6@60m Calcsilicate rock	M12@95m Intermediate Metavolcanics	M12@98m Basic Metavolcanics
wt. %										
SiO_2	0.01	70.5	76.4	72.6	73.3	75.3	3.56	6.88	60.8	49.1
Al_2O_3	0.01	12.8	13.55	12.85	13.2	13.75	0.08	1.51	16.75	14.3
Fe_2O_3	0.01	4.58	1.35	4.35	1.66	0.64	6.07	3.35	5.01	5.09
CaO	0.01	0.58	1.1	1.19	0.56	0.96	29.3	36.8	5.94	17.4
MgO	0.01	2.83	0.41	1.77	1.87	1.07	18.3	10.95	1.47	2.49
Na_2O	0.01	2.83	6.42	5.49	1.58	7.59	0.02	0.14	3.22	1.52
K_2O	0.01	0.86	0.55	0.6	5.77	0.17	0.01	0.35	4.08	2.81
<LOD Cr_2O_3	0.002	0.006	<0.002	0.003	0.002	0.006	<LOD	<LOD	0.011	0.011
TiO_2	0.01	0.39	0.22	0.41	0.29	0.48	<LOD	<LOD	0.68	0.57
MnO	0.01	0.01	<LOD	0.02	0.01	0.02	0.52	0.41	0.07	0.12
P_2O_5	0.01	0.11	0.13	0.13	0.1	0.07	0.02	0.05	0.15	0.13
SrO	0.01	<LOD	0.01	0.01	<LOD	<LOD	0.01	0.03	0.01	0.03
BaO	0.01	0.03	0.05	0.07	0.13	0.01	0.07	0.02	0.09	0.08
LOI	0.01	2.69	1.44	2.39	1.6	0.72	38.3	36	2.01	5.36
Total		98.22	101.63	101.88	100.07	100.79	96.26	96.58	100.29	99.01
	LOD									
ppm										
Ba	0.5	282	393	593	1130	46.2	584	659	823	686
Sr	0.1	91.1	240	210	50.9	87.8	181	212	230	352
Rb	0.2	31.5	13	12.3	126	6.2	0.6	65.9	122.5	91.7
Cs	0.01	0.48	0.44	0.53	1.72	0.09	0.12	1.1	1.77	1.37
V	5	102	11	33	21	78	7	23	110	124
Co	1	11	5	6	1	1	<LOD	<LOD	8	5
Ni	1	19	2	5	3	7	<LOD	<LOD	27	34
Cr	10	50	20	20	20	50	<LOD	<LOD	90	90
Zr	2	117	249	265	215	193	5	120	177	179
Hf	0.1	3.5	7.4	7.8	7	5.4	0.2	3.7	5.2	5.3
Nb	0.1	5.8	5.8	9.3	9.6	9.5	<LOD	5.4	12.8	10.4
Ta	0.1	0.5	0.6	0.9	1.1	0.6	0.1	0.7	0.9	0.8
Ga	0.1	18.2	15.1	17	19.1	15.1	0.7	10.7	21.5	21.7
Tl	0.02	<10	<LOD	<LOD	<10	<10	<10	<LOD	<LOD	<LOD
Li	10	10	<LOD	<LOD	10	<10	<10	<LOD	<LOD	<LOD
Cd	0.5	<0.5	<LOD	<LOD	<0.5	<0.5	<0.5	<LOD	<LOD	<LOD
Mo	1	2	<LOD	<LOD	1	1	2	<LOD	<LOD	1
Sn	1	12	3	5	9	6	<LOD	5	3	6
W	1	6	2	3	5	4	1	5	3	3
Ag	0.5	<LOD	<LOD	<LOD	<0.5	<0.5	<0.5	1.8	<LOD	<LOD
As	0.1	<LOD	<LOD	<LOD	12	8	7	10	<LOD	<LOD
Pb	2	<LOD	<LOD	<LOD	10	3	3	8	6	8
Zn	2	6	16	11	10	18	16	20	15	20
Cu	1	1	27	79	4	6	17	11	25	8
Th	0.05	3.94	16.4	14.35	17	7.78	<LOD	8.56	10.95	9.58
U	0.05	1.65	5.88	6.13	9.52	4.72	0.13	5.04	3.88	3.46
Y	0.1	16.6	27.4	21.2	39.3	23.7	1.7	22.4	30.6	29.6
Sc	1	11	1	8	5	8	<LOD	4	15	14
La	0.1	11.8	5.3	11.7	37.7	10.1	1.9	21.2	39.7	34.6
Ce	0.1	24.2	14	27.8	78.9	19	2.9	44.8	81.8	74.5
Pr	0.02	2.65	1.98	3.4	9.14	3.35	0.29	5.14	8.97	8.34
Nd	0.1	10.2	9.2	14.8	33.8	14.2	1.4	19.2	32.5	31.9
Sm	0.03	1.85	3.1	3.3	7.01	4.11	0.38	3.92	5.76	5.91
Eu	0.02	0.84	0.49	0.52	0.57	0.33	0.25	0.61	1.08	1.19
Gd	0.05	2.26	3.63	3.13	6.86	3.52	0.46	3.67	5.05	5.84
Tb	0.01	0.45	0.7	0.53	1.15	0.67	0.07	0.59	0.85	0.87
Dy	0.05	3	5.21	3.48	7.09	4.28	0.36	3.87	5.5	5.43
Ho	0.01	0.61	1.09	0.81	1.49	0.82	0.05	0.79	1.16	1.14
Er	0.03	1.84	3.07	2.38	4.25	2.61	0.14	2.52	3.33	3.09
Tm	0.01	0.28	0.45	0.38	0.61	0.38	0.02	0.33	0.54	0.46
Yb	0.03	1.77	2.96	2.6	3.93	2.78	0.16	2.09	3.34	2.87
Lu	0.01	0.23	0.41	0.39	0.57	0.44	<0.01	0.3	0.49	0.41

Appendix D-1. – Continuation of the previous table

	Samples collected at the Vale da Arca mine							
Sample		MV1	MV2	MV3	MV4	MV5	MV6	MV 7
	LOD*	M12@66m Paragneiss	M8@80m Acid Metavolcanics	M8@83m Acid Metavolcanics	M6@28m Acid Metavolcanics	Acid Metavolcanics (outcrop)	M10@76m Marble	M6@60m Calcsilicate rock
wt. %								
SiO_2	0.01	49.1	12.05	15	39.6	14.8	16.1	40.7
Al_2O_3	0.01	14.3	1.3	0.51	0.2	0.54	4.5	10.45
Fe_2O_3	0.01	5.09	8.61	5.2	7.73	4.94	22	3.06
CaO	0.01	17.4	28.2	30.5	24.3	30.9	19.05	21.5
MgO	0.01	2.49	16.15	16.95	16.45	17.3	8.55	2.16
Na_2O	0.01	1.52	0.02	0.01	0.04	0.02	0.04	1.19
K_2O	0.01	2.81	0.19	0.09	0.03	0.02	1.85	5.04
Cr_2O_3	0.002	0.011	<LOD	<LOD	<LOD	<LOD	<LOD	0.004
TiO_2	0.01	0.57	0.06	0.01	0.01	0.02	0.07	0.41
MnO	0.01	0.12	0.41	0.56	0.57	0.51	0.58	0.09
P_2O_5	0.01	0.13	0.41	0.15	0.02	0.09	0.05	0.1
SrO	0.01	0.03	<LOD	<LOD	<LOD	<LOD	<LOD	0.01
BaO	0.01	0.08	0.02	0.25	0.01	0.01	0.44	0.06
LOI	0.01	5.36	24.5	28.5	4.66	28.4	7.54	13.5
Total		99.01	91.92	97.73	93.62	97.55	80.77	98.27
	LOD							
ppm								
Ba	0.5	153.5	1940	84	85.2	2990	503	62.4
Sr	0.1	81.2	89.8	58.4	82.8	92.2	175	72.7
Rb	0.2	5.4	6.8	1.6	0.9	51	89.2	0.5
Cs	0.01	1.57	4.42	0.56	0.91	4.02	1.86	0.24
V	5	33	14	18	15	17	34	7
Co	1	6	<LOD	5	<LOD	<LOD	3	<LOD
Ni	1	9	3	5	9	12	17	11
Cr	10	20	20	130	10	180	30	10
Zr	2	13	6	<LOD	<LOD	54	205	9
Hf	0.1	0.5	0.2	<LOD	<LOD	2.1	5.9	0.2
Nb	0.1	0.8	0.2	<LOD	<LOD	1.3	5.8	0.4
Ta	0.1	0.1	0.1	<LOD	<LOD	0.3	0.4	<LOD
Ga	0.1	2.8	1.8	<LOD	<LOD	6.8	11.4	0.8
Tl	0.02	<LOD	<LOD	<LOD	<LOD	<LOD	<10	<LOD
Li	10	<LOD	<LOD	<LOD	<LOD	<LOD	10	<LOD
Cd	0.5	<LOD	<LOD	<LOD	<LOD	<LOD	<0.5	<LOD
Mo	1	13	<LOD	<LOD	<LOD	<LOD	<1	<LOD
Sn	1	1	<LOD	<LOD	<LOD	<LOD	2	<LOD
W	1	8	6	9	2	6	1	2
Ag	0.5	<LOD	<LOD	<0.5	2.5	1.4	<LOD	0.8
As	0.1	14	11	7	10	30	8	5
Pb	2	3	7	3	2	6	11	3
Zn	2	9	17	17	7	35	45	6
Cu	1	12	13	13	9	34	<LOD	10
Th	0.05	1.71	0.33	0.09	0.13	7.19	5.19	0.12
U	0.05	6.2	4.28	1.52	2.06	4.38	0.66	2.02
Y	0.1	14.3	8.5	5.5	8.3	16	22.7	7.2
Sc	1	2	1	<LOD	1	2	8	1
La	0.1	5.1	5.1	2.9	4.6	11.3	22.5	7.5
Ce	0.1	12.5	11.1	6.3	9.5	21.6	46.8	15.1
Pr	0.02	1.79	1.33	0.79	1.17	2.49	5.8	1.9
Nd	0.1	8.1	6	3.7	5.1	8.8	22.4	7.7
Sm	0.03	2.36	1.63	0.87	1.4	2.29	4.3	1.7
Eu	0.02	0.69	0.78	0.38	0.71	1.05	0.92	0.78
Gd	0.05	2.9	1.81	1.03	1.61	2.71	3.92	1.83
Tb	0.01	0.43	0.27	0.15	0.25	0.45	0.63	0.25
Dy	0.05	2.49	1.66	0.85	1.44	2.7	4.4	1.53
Ho	0.01	0.45	0.28	0.16	0.24	0.55	0.88	0.27
Er	0.03	1.17	0.77	0.45	0.77	1.51	2.72	0.64
Tm	0.01	0.18	0.09	0.06	0.1	0.22	0.37	0.11
Yb	0.03	0.98	0.41	0.3	0.47	1.38	2.42	0.46
Lu	0.01	0.11	0.05	0.03	0.05	0.21	0.37	0.05

Appendix D-2. – Whole-rock geochemistry of samples from the Alvito area

Sample Reference	AL 2	AL 14	AL 17	AL 34	AL 9	AL 15	AL 29	AL 30
Lithology	Diorites				Felsic Metavolcanic rocks			
wt. %								
SiO_2	58.3	50.3	55.1	55.4	75.8	68.5	77.7	78.1
Al_2O_3	17.85	15.25	16.85	16.75	13.55	15.4	11.5	11.6
Fe_2O_3	6.81	6.44	8.06	5.22	0.28	3.45	1.19	1.21
CaO	6.06	5.62	8.2	6.38	1.27	2.01	0.03	0.04
MgO	3.22	3.07	4.18	6.5	0.15	0.99	0.23	0.24
Na_2O	3.64	3.53	4.14	3.81	3.61	4.29	0.15	0.15
K_2O	1.06	0.95	0.77	2.18	4.54	2.1	6.39	6.49
Cr_2O_3	0.002	0.005	0.002	0.026	<0.002	0.002	<0.002	<0.002
TiO_2	0.88	0.86	1.6	0.58	0.11	0.38	0.13	0.13
MnO	0.1	0.11	0.14	0.11	0.01	0.06	<0.01	<0.01
P_2O_5	0.14	0.15	0.21	0.08	0.07	0.1	0.01	0.01
SrO	0.02	0.02	0.04	0.03	0.01	0.02	<0.01	<0.01
BaO	0.02	0.04	0.05	0.1	0.16	0.08	0.08	0.08
LOI	1.91	1.72	1.2	2.95	0.64	1.69	1.61	1.68
Total	100.01	88.07	100.54	100.12	100.2	99.07	99.02	99.73
ppm								
Ba	225	417	475	989	1455	770	676	693
Sr	378	313	418	343	208	257	83.5	82.8
Rb	48.1	34.9	21.1	60.6	87.6	52.4	179.5	184
Cs	2.69	0.7	0.81	190	0.57	0.4	10	10
V	167	139	233	106	12	39	<5	<5
Co	16	20	23	24	1	4	<1	1
Ni	<1	17	5	83	<1	1	4	5
Cr	10	50	30	190	10	20	10	10
Zr	148	195	75	75	94	252	254	251
Hf	4	5	2.3	2.4	3.4	6.4	8.8	8.6
Nb	6.3	7.6	6.4	4.1	8.4	8.1	15.3	15.7
Ta	0.6	0.7	0.5	0.4	1.3	0.7	1.1	1
Ga	20.2	19.9	19.3	18.1	16.6	18.1	23.3	22.6
Tl	<10	<10	10	<10	<10	10	<10	<10
Li	10	10	<10	20	<10	10	20	20
Cd	<0.5	<0.5	<0.5	<0.5	<0.5	<0.5	<0.5	<0.5
Mo	<1	<1	1	<1	<1	1	1	1
Sn	2	2	1	1	2	1	3	3
W	1	1	2	2	<1	6	5	5
Ag	<0.5	<0.5	<0.5	<0.5	<0.5	<0.5	<0.5	<0.5
As	5	<5	7	<5	<5	<5	<5	<5
Pb	<2	6	7	2	5	3	3	2
Zn	51	65	63	40	3	40	6	6
Cu	<1	18	18	2	1	<1	4	5
Th	2.7	4.97	3.49	4.83	11	11.7	14.3	15.05
U	1.05	1.81	1.23	1.05	3.48	3.5	2.74	2.73
Y	25.9	26.7	25.9	17.1	20.6	27.7	67.5	69.8
Sc	16	19	26	24	2	8	4	4
La	11.9	22.1	19.1	7.6	9.1	44.7	62.3	62.1
Ce	27.9	45	39.4	16.2	26.6	88.5	105.5	105
Pr	4.03	5.61	5.13	2.02	3.81	9.88	10.45	10.15
Nd	17.1	22.5	21.1	9.6	14.4	34.4	37	36.8
Sm	4.2	4.8	4.7	2.41	3.28	6.54	6.2	6.2
Eu	1.02	1.53	1.32	0.53	0.34	1.09	0.28	0.23
Gd	4.38	4.83	4.74	2.79	2.94	5.39	7.23	7.32
Tb	0.79	0.81	0.83	0.44	0.52	0.79	1.39	1.46
Dy	4.96	5.11	4.84	3.29	3.53	5.02	10.7	11.15
Ho	1.02	1.02	1.02	0.66	0.7	0.96	2.35	2.46
Er	2.97	2.83	2.92	1.85	2.33	3.02	7.3	7.4
Tm	0.45	0.46	0.44	0.28	0.35	0.49	0.97	1.05
Yb	2.74	2.75	2.51	1.76	2.44	2.98	6.39	6.73
Lu	0.45	0.45	0.38	0.28	0.35	0.48	0.96	1

Appendix D-2. – Continuation of the previous table

Sample Reference	AL 5	AL 7	AL 16	AL 21	AL 22	AL 1	AL 4	AL 31
Lithology	Marbles					Calcsilicate		
SiO_2	5.78	2.1	1.26	0.52	1.24	44.3	41.3	40
Al_2O_3	0.17	0.45	0.17	0.11	0.43	20.8	21.2	1.17
Fe_2O_3	0.14	3.06	0.17	1.87	1.66	7.18	9.33	19.9
CaO	54	31.1	53.1	33.4	31.3	16.95	7.69	21.8
MgO	0.77	19.2	2.08	19.45	19.05	2.68	8.87	5.76
Na_2O	0.02	0.01	0.02	0.01	0.01	0.44	0.56	0.17
K_2O	0.08	<0.01	0.07	<0.01	0.01	2.86	3.23	0.05
Cr_2O_3	<0.002	<0.002	<0.002	<0.002	<0.002	0.01	0.005	<0.002
TiO_2	0.01	0.03	0.01	<0.01	0.03	0.77	0.83	0.04
MnO	0.09	0.52	0.08	0.43	0.42	0.26	1.24	0.83
P_2O_5	<0.01	<0.01	<0.01	<0.01	<0.01	0.18	0.17	0.02
SrO	0.02	<0.01	0.01	0.01	<0.01	0.02	0.01	<0.01
BaO	0.02	<0.01	<0.01	<0.01	<0.01	0.08	0.11	0.01
LOI	38.5	43	42.7	42.8	44.6	3.73	6.07	9.06
Total	99.6	99.47	99.67	98.6	98.75	100.26	100.62	98.81
ppm								
Ba	159.5	7.2	16.7	17	14.4	681	954	46.9
Sr	276	64	146.5	109.5	94.1	249	248	90.4
Rb	3	0.4	3	0.3	0.4	145	180.5	0.6
Cs	0.12	0.03	0.2	0.03	0.08	8.17	8.08	10
V	13	16	8	7	10	44	88	12
Co	<1	<1	<1	<1	<1	15	7	28
Ni	9	3	7	3	3	9	11	11
Cr	10	10	10	60	10	70	30	10
Zr	15	14	6	8	8	299	136	12
Hf	0.2	0.4	<0.2	0.2	0.2	8.1	3.8	0.3
Nb	<0.2	0.4	<0.2	0.3	0.4	13.8	7.5	0.6
Ta	0.1	0.1	0.1	<0.1	0.1	0.8	0.5	<0.1
Ga	0.7	1.3	0.4	0.7	1.2	23	18.2	3.7
Tl	<10	<10	<10	<10	<10	<10	<10	<10
Li	<10	<10	<10	<10	<10	110	80	<10
Cd	<0.5	<0.5	<0.5	<0.5	<0.5	<0.5	<0.5	2.1
Mo	1	1	1	1	<1	1	<1	<1
Sn	<1	1	<1	<1	<1	13	23	6
W	<1	1	<1	2	1	16	2	1
Ag	<0.5	<0.5	<0.5	<0.5	<0.5	<0.5	<0.5	<0.5
As	<5	<5	<5	6	5	<5	<5	<5
Pb	<2	9	3	3	<2	7	10	<2
Zn	5	21	6	16	12	109	53	78
Cu	<1	22	<1	2	<1	1	<1	<1
Th	0.1	<0.05	0.14	0.08	0.29	17.15	3.57	0.33
U	1.84	0.06	0.81	0.06	0.47	4.76	2.61	0.31
Y	0.6	0.9	1.2	0.6	0.7	39.4	21.2	1
Sc	<1	<1	<1	<1	<1	10	12	1
La	0.7	0.9	1.6	1	0.8	101	10.1	0.5
Ce	1.3	1.6	2.8	1.5	1.7	162	25.7	0.8
Pr	0.13	0.18	0.34	0.16	0.2	16.1	3.53	0.12
Nd	0.5	0.6	1.1	0.6	0.9	51.5	14.7	0.4
Sm	0.11	0.19	0.3	0.17	0.11	8.89	3.41	0.08
Eu	<0.03	0.03	0.04	<0.03	0.03	1.05	0.92	0.02
Gd	0.1	0.13	0.16	0.15	0.14	7.82	3.7	0.15
Tb	<0.01	0.02	0.03	0.01	0.01	1.23	0.59	0.02
Dy	0.05	0.1	0.15	<0.05	0.08	7.64	4.04	0.12
Ho	0.01	0.03	0.02	0.01	0.02	1.53	0.8	0.04
Er	<0.03	0.07	0.09	0.04	0.05	4.55	2.54	0.13
Tm	0.03	0.03	0.03	0.03	0.03	0.65	0.42	0.03
Yb	0.03	0.11	0.05	0.03	0.1	3.85	2.57	0.17
Lu	<0.01	0.01	<0.01			0.6	0.37	0.02

Appendix D-2. – Continuation of the previous table

Sample Reference	AL 3	AL 6	AL 8	AL 10	AL 19	AL 20
Lithology	Magnetite ores					
SiO_2	17.85	31.2	44.7	42.5	31.6	18.3
Al_2O_3	0.52	0.16	2.62	4.95	4.24	0.91
Fe_2O_3	54.8	36.9	22.6	29.3	46.5	48.8
CaO	0.09	1.39	21.2	15.45	13.4	2.68
MgO	22.2	28.2	9.67	3.8	4.6	21.3
Na_2O	0.02	0.02	0.12	0.44	0.2	0.01
K_2O	<0.01	<0.01	0.07	0.71	0.29	0.01
Cr_2O_3	<0.002	<0.002	<0.002	0.003	<0.002	<0.002
TiO_2	0.02	0.01	0.03	0.15	0.04	0.07
MnO	0.3	0.72	0.3	0.58	0.24	0.22
P_2O_5	0.01	0.11	<0.01	0.52	<0.01	0.01
SrO	<0.01	<0.01	<0.01	<0.01	<0.01	<0.01
BaO	<0.01	<0.01	<0.01	0.01	0.01	<0.01
LOI	4.65	1.9	0.13	0.33	-0.41	8.66
Total	100.46	100.61	101.44	98.74	100.71	100.97
ppm						
Ba	3.3	8.2	11.3	114	127.5	2.6
Sr	1.1	2.5	18	47.9	40.2	11.6
Rb	0.3	0.8	1	3.9	11.3	0.3
Cs	0.02	0.12	0.18	0.48	0.34	0.03
V	11	9	11	25	17	23
Co	63	146	39	41	83	63
Ni	5	179	3	15	4	43
Cr	10	10	10	130	20	20
Zr	11	7	40	68	40	21
Hf	0.2	<0.2	1.7	2.6	2	0.6
Nb	4	1	3	6.9	6.9	5.2
Ta	0.1	0.1	0.1	0.5	1.1	0.2
Ga	3.1	6.1	8	13.9	19.7	17.9
Tl	<10	<10	<10	<10	<10	<10
Li	<10	<10	10	<10	10	<10
Cd	<0.5	<0.5	0.8	0.5	<0.5	<0.5
Mo	3	1	<1	1	2	<1
Sn	32	4	12	27	11	26
W	1	6	<1	4	2	6
Ag	<0.5	<0.5	<0.5	<0.5	<0.5	<0.5
As	<5	5	<5	7	<5	5
Pb	<2	<2	3	<2	3	6
Zn	222	257	110	130	86	236
Cu	4	353	3	86	1	23
Th	0.07	0.77	0.25	20.2	2.1	0.09
U	0.29	0.24	0.33	2.5	1.34	0.1
Y	0.2	3.3	5.6	19.1	47.2	1
Sc	<1	1	2	4	1	1
La	0.2	3.7	6	29.6	10.6	1.4
Ce	0.1	7.5	20	66.8	33.8	2.2
Pr	<0.03	0.85	3	8.08	5.23	0.24
Nd	0.1	3	10.7	28.4	22.7	0.8
Sm	<0.03	0.51	1.69	4.29	5.73	0.13
Eu	<0.03	<0.03	0.2	0.68	0.26	<0.03
Gd	<0.05	0.44	1.18	3.46	6.62	0.12
Tb	<0.01	0.06	0.19	0.53	1.31	0.01
Dy	<0.05	0.42	1.17	3.32	8.43	0.1
Ho	<0.01	0.13	0.22	0.68	1.78	0.02
Er	0.04	0.66	0.69	2.16	5.69	0.11
Tm	0.03	0.2	0.13	0.32	0.95	0.05
Yb	0.1	2.2	0.57	1.84	6.28	0.26
Lu	0.02	0.71	0.1	0.25	0.89	0.05

Appendix D-3. – Whole-rock geochemistry of samples from the Azenhas area

Sample Reference	AZ 1	AZ 2	AZ 5	AZ 6	AZ 7	AZ 9	AZ 10	AZ 4	AZ 12	AZ 8	AZ 11
Lithology	Felsic Metavolcanic rocks		Marbles and caclsilicate rocks					Metassomatized amphibolites		Magnetite ores	
wt. %											
SiO_2	71.9	77.7	55.5	11.6	11.8	8.75	9.46	49.7	48.2	18.65	11.8
Al_2O_3	13.9	12.3	16.3	0.98	1.78	1.21	1.27	9.83	10.8	1.88	0.57
Fe_2O_3	2.07	1.45	1.02	4.3	6.25	5.41	2.81	10.3	10.55	59.3	21
CaO	1.19	0.32	9.51	39.9	28.9	41.1	41.3	17.3	17.9	3.03	17.65
MgO	0.46	0.7	0.45	7.19	16.85	9.39	9.55	7.52	6.36	15.15	21.1
Na_2O	7.64	6.74	8.89	0.03	0.03	0.02	0.02	3.04	2.81	0.03	0.02
K_2O	0.09	0.04	0.06	<0.01	<0.01	<0.01	<0.01	0.02	0.02	0.01	<0.01
TiO_2	0.65	0.22	0.17	0.04	0.09	0.06	0.06	0.37	0.37	0.18	0.01
MnO	0.04	0.02	0.05	0.39	0.83	0.43	0.36	0.21	0.2	0.6	0.64
P_2O_5	0.12	0.02	0.03	0.02	0.02	0.01	0.02	0.17	0.11	0.01	<0.01
LOI	0.91	0.73	6.73	34.4	33.4	32.9	34.3	1.69	2.23	2.34	27.2
Total	98.97	100.24	98.74	98.86	99.96	99.3	99.16	100.18	99.59	101.18	99.99
ppm											
Ba	225	417	53.8	8.8	4.1	10.5	13.9	31.9	22.6	9.1	7.2
Sr	378	313	282	220	147	245	215	322	392	6.9	52.4
Rb	48.1	34.9	1.2	0.2	0.2	<0.2	0.2	0.8	0.5	0.2	0.2
Cs	2.69	0.7	0.13	0.09	0.11	0.02	0.06	0.09	<10	0.13	0.07
V	167	139	7	27	23	21	17	28	14	98	28
Co	16	20	<1	1	3	3	<1	3	5	56	56
Ni	<1	17	<1	5	6	11	11	6	6	8	4
Cr	10	50	10	20	20	20	20	10	<10	20	10
Zr	148	195	164	11	17	16	20	155	156	7	4
Hf	4	5	5.6	0.4	0.6	0.6	0.6	4.8	4.5	0.3	0.2
Nb	6.3	7.6	5.2	0.8	1.2	1.1	1.2	6.5	5.6	0.7	0.6
Ta	0.6	0.7	0.5	0.1	0.2	0.1	0.2	0.4	0.1	0.1	<0.1
Ga	20.2	19.9	9	1.8	3.1	2.2	2.4	14.9	16.7	12.8	1.8
Tl	<10	<10	<10	<10	<10	<10	<10	<10	<10	<10	<10
Li	10	10	<10	10	10	<10	<10	20	20	<10	<10
Cd	<0.5	<0.5	0.7	<0.5	0.7	0.5	<0.5	<0.5	1.2	<0.5	<0.5
Mo	<1	<1	2	<1	1	1	1	1	<1	<1	1
Sn	2	2	3	1	2	1	1	7	7	6	12
W	1	1	2	1	2	2	1	1	1	5	2
Ag	<0.5	<0.5	<0.5	<0.5	<0.5	<0.5	<0.5	<0.5	<0.5	<0.5	<0.5
As	5	<5	<5	10	6	8	<5	8	8	<5	255
Pb	<2	6	16	8	5	11	8	12	20	<2	2
Zn	51	65	32	217	601	99	53	139	119	590	421
Cu	<1	18	932	3	8	4	3	1	1	1	1
Th	2.7	4.97	9.9	0.63	0.98	0.8	0.88	2.91	2.54	0.1	0.08
U	1.05	1.81	1.48	3.17	3.43	2.58	3.34	2.4	2.97	0.24	0.65
Y	25.9	26.7	11.6	2.5	6.1	3.9	4.7	21.6	27.3	2.5	4.2
Sc	16	19	3	1	2	1	1	9	9	1	<1
La	11.9	22.1	0.7	3.2	5.7	3.3	3.3	7.8	8.7	1.2	14.5
Ce	27.9	45	2.2	6.1	12.6	6.8	6.6	24.1	23.9	3.3	30.5
Pr	4.03	5.61	0.42	0.69	1.43	0.77	0.75	3	3.08	0.38	3.03
Nd	17.1	22.5	2.1	2.6	5.5	3.3	3	10.2	11	1.5	9.3
Sm	4.2	4.8	0.82	0.48	0.93	0.71	0.73	2.03	2.6	0.29	1.19
Eu	1.02	1.53	0.2	0.32	0.37	0.17	0.13	1.62	2.63	0.12	0.5
Gd	4.38	4.83	1.03	0.42	0.92	0.64	0.86	2.82	3.74	0.24	0.86
Tb	0.79	0.81	0.26	0.05	0.13	0.09	0.11	0.5	0.62	0.04	0.11
Dy	4.96	5.11	1.87	0.37	0.88	0.66	0.77	3.6	4.56	0.37	0.71
Ho	1.02	1.02	0.39	0.07	0.19	0.1	0.14	0.78	0.99	0.07	0.11
Er	2.97	2.83	1.38	0.23	0.61	0.39	0.41	2.41	3.33	0.26	0.36
Tm	0.45	0.46	0.27	0.03	0.08	0.04	0.06	0.36	0.46	0.06	0.05
Yb	2.74	2.75	1.8	0.18	0.54	0.29	0.28	2.48	2.77	0.45	0.35
Lu	0.45	0.45	0.3	0.01	0.07	0.03	0.03	0.36	0.42	0.1	0.03

Appendix E

Complete EPMA raw results

Appendix E-1.

Complete results of EPMA analysis of sulfides, gold, magnetite and silicates from the Montemor-o-Novo area

Appendix E-1.1. – EPMA raw results of silicates from the Montemor-o-Novo area – Plagioclase and alkali feldspars from samples of the Monges mine (drill core samples)

Sample	**005-3.4b**					**007-1.3b**							
Lithotype	Paragneiss – Escoural Fm.					Basic metavolcanic rocks							
Analysis Ref.	Z1 P2	Z1 P3	Z1 P5	Z1 P6	Z1 P7	Z1 P1	Z1 P2	Z1 P3	Z1 P4	Z1 P5	Z1 P6	Z1 P7	Z1 P8
Element (wt. %)													
SiO_2	63.99	63.82	61.01	63.99	64.21	63.99	64.63	64.10	65.07	63.71	63.63	64.37	63.95
TiO_2										0.03			
Al_2O_3	18.88	19.14	17.88	18.67	18.90	18.55	18.85	18.83	18.82	18.69	18.54	19.09	19.19
FeO	0.07									0.06			
CaO			2.43		0.03	0.03	0.00	0.01	0.00	0.03	0.07	0.01	0.03
Na_2O	0.73	0.25	0.41	0.35	0.36	0.28	0.78	0.68	0.74	0.87	0.28	0.65	0.32
K_2O	16.00	16.78	15.35	16.37	16.50	16.85	15.91	16.02	15.88	15.55	16.46	16.08	16.60
BaO	0.41	0.51	0.45	0.50	0.20	0.29	0.33	0.53	0.45	0.71	0.45	0.55	0.33
Total	100.08	100.50	97.53	99.88	100.19	99.99	100.51	100.17	100.96	99.64	99.43	100.75	100.42
Formula (32O)													
Si	11.87	11.83	11.71	11.91	11.89	11.91	11.91	11.88	11.94	11.88	11.90	11.86	11.84
Ti													
Al	4.13	4.18	4.05	4.09	4.12	4.07	4.10	4.11	4.07	4.11	4.09	4.15	4.19
Fe(ii)	0.01		0.01							0.01			
Ca			0.50		0.01	0.01	0.00	0.00	0.00	0.01	0.01	0.00	0.01
Na	0.26	0.09	0.15	0.12	0.13	0.10	0.28	0.24	0.26	0.32	0.10	0.23	0.11
K	3.79	3.97	3.76	3.88	3.90	4.00	3.74	3.79	3.72	3.70	3.93	3.78	3.92
Ba	0.03	0.04	0.03	0.04	0.01	0.02	0.02	0.04	0.03	0.05	0.03	0.04	0.02
Total	20.09	20.11	20.21	20.05	20.06	20.11	20.05	20.07	20.02	20.07	20.07	20.07	20.09
An (%)	0.03	0.04	11.34	0.09	0.14	0.16	0.00	0.05	0.00	0.14	0.33	0.02	0.15
Ab (%)	6.50	2.23	3.49	3.10	3.22	2.45	6.90	6.02	6.64	7.84	2.55	5.78	2.82
Or (%)	93.47	97.73	85.18	96.80	96.64	97.39	93.10	93.93	93.36	92.03	97.12	94.20	97.03

Sample	**007-8.1b**										
Lithotype	Quartz – Feldspar – Chlorite veins in acid metavolcanic rocks										
Analysis Ref.	Z1 P1	Z1 P2	Z1 P3	Z1 P4	Z1 P5	Z1 P6	Z1 P7	Z1 P8	Z1 P9	Z1 P12	Z1 P13
Element (wt. %)											
SiO_2	67.55	63.38	67.14	67.48	66.52	66.60	67.20	67.50	67.23	67.08	66.90
TiO_2											
Al_2O_3	20.90	19.39	20.39	20.54	21.06	19.87	21.20	20.69	21.20	20.77	20.82
FeO		0.08					0.05				
CaO	0.74	0.15	1.00	0.53	1.30	0.47	1.32	1.06	1.16	0.83	0.74
Na_2O	11.17	2.29	11.09	10.92	10.74	7.87	10.53	10.74	10.70	11.08	9.83
K_2O	0.13	12.86	0.16	0.33	0.09	4.48	0.13	0.13	0.19	0.17	1.31
BaO		1.73									
Total	100.49	99.88	99.78	99.80	99.71	99.28	100.43	100.11	100.48	99.93	99.60
Formula (32O)											
Si	11.76	11.76	11.79	11.82	11.69	11.88	11.71	11.79	11.71	11.75	11.78
Ti											
Al	4.29	4.24	4.22	4.24	4.36	4.18	4.35	4.26	4.35	4.29	4.32
Fe(ii)		0.01					0.01				
Ca	0.14	0.03	0.19	0.10	0.24	0.09	0.25	0.20	0.22	0.16	0.14
Na	3.77	0.83	3.77	3.71	3.66	2.72	3.56	3.64	3.61	3.76	3.35
K	0.03	3.05	0.03	0.07	0.02	1.02	0.03	0.03	0.04	0.04	0.29
Ba		0.13									
Total	19.99	20.05	20.01	19.95	19.97	19.90	19.91	19.91	19.94	20.00	19.89
An (%)	3.49	0.76	4.69	2.58	6.23	2.32	6.42	5.11	5.61	3.94	3.70
Ab (%)	95.76	21.16	94.43	95.52	93.25	71.06	92.84	94.15	93.30	95.13	88.54
Or (%)	0.76	78.07	0.87	1.90	0.52	26.61	0.75	0.73	1.09	0.93	7.76

Appendix E-1.1. – EPMA results of silicates from the Montemor-o-Novo area – Plagioclase and alkali feldspars from samples of the Vale da Arca mine (outcrop samples)

Sample	**MV 6**								
Lithotype	Basic metavolcanic rocks								
Analysis Ref.	Z1 P1	Z1 P2	Z1 P3	Z1 P4	Z1 P5	Z1 P6	Z1 P7	Z1 P8	Z1 P9
Element (wt. %)									
SiO_2	63.67	64.03	64.78	63.68	63.51	68.08	63.67	63.68	63.76
TiO_2									
Al_2O_3	18.42	18.55	18.88	18.81	18.76	20.40	18.84	18.55	18.81
FeO									
CaO						0.13			0.06
Na_2O	0.28	0.34	1.84	0.56	0.61	11.03	0.65	0.39	0.24
K_2O	16.58	16.46	14.82	16.32	16.38	0.20	16.17	16.59	16.69
BaO	0.26	0.31	0.17	0.31	0.27		0.23	0.22	0.32
Total	99.21	99.69	100.48	99.68	99.53	99.85	99.56	99.44	99.87
Formula (32O)									
Si	11.92	11.92	11.90	11.87	11.86	11.89	11.87	11.90	11.87
Ti									
Al	4.07	4.07	4.09	4.13	4.13	4.20	4.14	4.09	4.13
Fe(ii)						0.01			
Ca						0.02			0.01
Na	0.10	0.12	0.66	0.20	0.22	3.74	0.23	0.14	0.09
K	3.96	3.91	3.47	3.88	3.90	0.04	3.84	3.96	3.96
Ba	0.02	0.02	0.01	0.02	0.02	19.90	0.02	0.02	0.02
Total	20.08	20.05	20.12	20.11	20.13		20.10	20.11	20.09
An (%)	0.02	0.07	0.02			0.62		0.05	0.28
Ab (%)	2.53	3.02	15.88	4.99	5.34	98.21	5.73	3.48	2.11
Or (%)	97.45	96.91	84.11	95.01	94.66	1.18	94.27	96.46	97.61

Appendix E-1.1. – EPMA results of silicates from the Montemor-o-Novo area – Amphibole analysis from samples of the Monges mine (drill core samples)

Sample	**004-2.5a**								**004-13.3b**					
Lithotype	Basic metavolcanic rocks								Amphiboles accompanying sulphides hosted in marbles					
Analysis Ref.	Z1 P3	Z1 P4	Z1 P5	Z1 P6	Z1 P7	Z12 P8	Z1 P9	Z1 P10	Z1 P1	Z1 P2	Z1 P3	Z1 P4	Z1 P5	Z1 P6
Element (wt. %)														
SiO_2	46.2806	42.7669	45.939	60.4248	42.9358	49.0517	37.2347	52.0446	57.8335	57.669	57.6788	57.1227	57.8751	57.3601
Al_2O_3	11.0822	12.026	10.0645	24.7026	14.1037	7.518	26.5815	4.6495	0.0207	0.1155	0.2184	0.106	0.303	0.3606
MnO	0.3704	0.2713	0.2681		0.2149	0.2959	0.0615	0.238	0.3585	0.2996	0.3149	0.2587	0.3789	0.2551
FeO	12.881	15.9971	14.3324	0.5178	14.1777	12.2254	2.5287	10.9473	3.4854	3.9088	5.0138	6.6862	4.3461	5.484
MgO	11.6062	9.6894	11.9021	0.0826	10.439	14.1835	3.3002	15.1849	21.2755	21.7361	20.5964	19.3976	21.1557	20.6812
CaO	10.6327	11.2624	11.6821	5.1724	11.6201	11.3203	22.9755	12.2252	12.7858	12.8965	12.8387	12.8432	12.8203	12.4204
Na_2O	1.6516	1.9586	1.4268	8.429	1.7026	1.2549		0.8036		0.0514	0.0371	0.0503	0.064	0.0894
K_2O	0.2580	0.3580	0.2395	0.1313	0.4129	0.1744		0.1018					0.0485	
Total	94.7627	94.3297	95.8545	99.4605	95.6067	96.0241	92.7104	96.1949	95.7594	96.6769	96.6981	96.4647	96.9916	96.6508
T														
Si	6.892	6.58	6.839	7.77	6.444	7.166	5.589	7.561	8.093	8.022	8.054	8.062	8.038	8.026
Al	1.108	1.42	1.161	0.23	1.556	0.834	2.411	0.439						
T (total)	8	8	8	8	8	8	8	8	8.093	8.022	8.054	8.062	8.038	8.026
C														
Al	0.837	0.761	0.604	3.513	0.939	0.461	2.292	0.357	0.003	0.019	0.036	0.018	0.05	0.059
Fe^{3+}	0.225	0.136	0.246		0.143	0.28		0.019			0.002			
Mn^{2+}							0.008	0.024	0.042	0.019	0.037	0.031	0.045	
Fe^{2+}	1.362	1.881	1.509	0.056	1.583	1.17	0.317	1.311	0.408	0.455	0.584	0.789	0.505	0.627
Mg	2.576	2.223	2.641	0.016	2.336	3.089	0.739	3.289	4.438	4.508	4.288	4.081	4.38	4.314
C (total)	5	5.001	5	3.585	5.001	5	3.356	5	4.891	5.001	4.947	4.919	4.98	5
B														
Mn^{2+}	0.047	0.035	0.034		0.027	0.037		0.005		0.017				0.03
Fe^{2+}	0.017	0.042	0.03		0.054	0.044								0.015
Ca	1.696	1.857	1.863	0.713	1.869	1.772	2	1.903	1.917	1.922	1.921	1.942	1.908	1.862
Na	0.239	0.066	0.073	1.287	0.05	0.148		0.092	0.005	0.014	0.01	0.014	0.017	0.024
B (total)	1.999	2	2	2	2	2.001	2	2	1.922	1.953	1.931	1.956	1.925	1.931
A														
Na	0.237	0.518	0.339	0.814	0.445	0.208	0.01	0.135						
K	0.049	0.07	0.045	0.022	0.079	0.033	0.005	0.019					0.009	
A (total)	0.286	0.588	0.384	0.836	0.524	0.241	1.71	0.154	0	0	0	0	0.009	0

Sample	004-13.3b							005-30.8a						
Lithotype	Amphiboles accompanying sulphides hosted in marbles							Amphiboles accompanying sulphides hosted in marbles						
Analysis Ref.	Z1 P7	Z1 P8	Z1 P9	Z1 P10	Z1 P11	Z1 P12	Z1 P13	Z1 P1	Z1 P2	Z1 P3	Z1 P4	Z1 P5	Z1 P6	Z1 P7
Element (wt. %)														
SiO_2	57.6585	57.1355	57.3724	57.7393	56.7996	57.8979	57.9445	56.1107	56.8213	56.5153	56.4883	55.4171	56.3902	54.9607
Al_2O_3	0.2112	0.3594	0.1425	0.1359	0.4144	0.1681	0.0608	0.9737	0.3179	1.0723	0.8454	1.394	1.2157	2.2211
MnO	0.3882	0.2372	0.2383	0.2942	0.1674	0.3293	0.3074	0.1721	0.1535	0.1214	0.0796	0.1607	0.0947	0.0932
FeO	3.9479	5.3864	5.1751	4.4013	6.8177	3.3655	3.0422	5.9992	5.0878	6.0995	4.7582	6.7749	6.5937	5.3394
MgO	21.5419	20.6978	21.015	21.2536	19.736	21.857	21.8428	20.4204	20.7341	19.3144	20.3007	18.6543	18.9522	19.7492
CaO	13.1048	12.5031	12.6693	12.5915	12.3324	12.8477	12.964	12.7217	12.781	12.4828	12.8196	11.9179	12.4016	13.0262
Na_2O		0.1859	0.0544	0.0687	0.1405	0.0874		0.0897	0.0761	0.1499	0.1381	0.2826	0.2066	0.3155
K_2O		0.0561				0.0429		0.0714	0.0209	0.0436	0.0344	0.0958	0.0519	0.0993
Total	96.8525	96.5614	96.667	96.4845	96.408	96.5958	96.1617	96.5589	95.9926	95.7992	95.4643	94.6973	95.9066	95.8046
T														
Si	8.012	8.009	8.023	8.054	8.017	8.039	8.063	7.896	8.004	8.001	7.987	7.965	7.991	7.795
Al								0.104			0.013	0.035	0.009	0.205
T (total)	8.012	8.009	8.023	8.054	8.017	8.039	8.063	8	8.004	8.001	8	8	8	8
C														
Al	0.035	0.059	0.023	0.022	0.069	0.028	0.01	0.058	0.053	0.179	0.128	0.202	0.194	0.167
Fe^{3+}								0.035						
Mn^{2+}	0.044			0.035		0.039	0.036			0.015	0.01		0.011	0.011
Fe^{2+}	0.459	0.615	0.596	0.513	0.778	0.391	0.354	0.623	0.593	0.722	0.563	0.801	0.781	0.633
Mg	4.462	4.325	4.381	4.419	4.153	4.524	4.531	4.284	4.354	4.076	4.279	3.997	4.004	4.176
C (total)	5	4.999	5	4.989	5	4.982	4.931	5	5	4.992	4.98	5	4.99	4.987
B														
Mn^{2+}	0.001	0.028	0.028		0.02			0.021	0.018			0.02		
Fe^{2+}		0.016	0.009		0.027			0.048	0.006			0.013		
Ca	1.951	1.878	1.898	1.882	1.865	1.911	1.933	1.918	1.929	1.893	1.942	1.835	1.883	1.98
Na	0.015	0.051	0.015	0.019	0.038	0.024	0.009	0.013	0.021	0.041	0.038	0.079	0.057	0.02
B (total)	1.967	1.973	1.95	1.901	1.95	1.935	1.942	2	1.974	1.934	1.98	1.947	1.94	2
A														
Na								0.011						0.066
K		0.01				0.008		0.013	0.004	0.008	0.006	0.018	0.009	0.018
A (total)	0	0.01	0	0	0	0.008	0	0.024	0.004	0.008	0.006	0.018	0.009	0.084

Sample	005-30.8a			005-32.1a							
Lithotype	Amphiboles accompanying sulphides hosted in marbles			Amphiboles accompanying sulphides hosted in marbles							
Analysis Ref.	Z1 P8	Z1 P9	Z1 P10	Z1 P1	Z1 P2	Z12 P3	Z1 P4	Z1 P5	Z1 P6	Z1 P7	Z1 P8
Element (wt. %)											
SiO_2	57.6585	57.1355	57.3724	62.66	63.03	58.69	58.38	62.60	57.21	62.04	58.17
Al_2O_3	0.2112	0.3594	0.1425	0.13	0.13	0.16	0.28	0.23	0.60	0.19	0.22
MnO	0.3882	0.2372	0.2383	0.02	0.05	0.78	0.13		0.15	0.03	0.14
FeO	3.9479	5.3864	5.1751	1.44	1.23	8.17	2.69	1.71	4.01	1.84	2.44
MgO	21.5419	20.6978	21.015	29.34	29.53	26.87	22.29	29.76	21.59	29.84	23.12
CaO	13.1048	12.5031	12.6693		0.02	1.90	12.44	0.04	12.29	0.04	12.63
Na_2O		0.1859	0.0544	0.07	0.10	0.08	0.10	0.06	0.19	0.08	0.12
K_2O		0.0561									0.16
Total	96.8525	96.5614	96.667	93.66	94.09	96.65	96.32	94.40	96.04	94.07	97.00
T											
Si	8.012	8.009	8.023	8.45	8.45	8.07	8.08	8.40	8.00	8.37	8.01
Al									0.00		
T (total)	8.012	8.009	8.023	8.45	8.45	8.07	8.08	8.40	8.00	8.37	8.01
C											
Al	0.035	0.059	0.023	0.02	0.02	0.03	0.05	0.04	0.10	0.03	0.04
Fe^{3+}											
Mn^{2+}	0.044						0.02				
Fe^{2+}	0.459	0.615	0.596				0.31		0.40		0.22
Mg	4.462	4.325	4.381	4.98	4.98	4.98	4.60	4.96	4.50	4.97	4.74
C (total)	5	4.999	5	5.00	5.00	5.00	4.97	5.00	5.00	5.00	5.00
B											
Mn^{2+}	0.001	0.028	0.028	0.00	0.01	0.09			0.02	0.00	0.02
Fe^{2+}		0.016	0.009	0.16	0.14	0.94		0.19	0.07	0.21	0.06
Ca	1.951	1.878	1.898	0.00	0.00	0.28	1.84	0.01	1.84	0.01	1.86
Na	0.015	0.051	0.015	0.02	0.03	0.02	0.03	0.02	0.05	0.02	0.03
B (total)	1.967	1.973	1.95	1.10	1.10	1.86	1.87	1.20	1.98	1.27	1.97
A											
Na											
K		0.01									0.03
A (total)	0	0.01	0	0.00	0.00	0.00	0.00	0.00	0.00	0.00	0.03

Sample	**007-14.2a**											
Lithotype	Amphiboles accompanying sulphides hosted in marbles											
Analysis Ref.	Z1 P1	Z1 P2	Z1 P3	Z1 P4	Z1 P5	Z1 P6	Z1 P7	Z1 P8	Z1 P9	Z1 P10	Z1 P11	Z1 P12
Element (wt. %)												
SiO_2	57.99	56.43	57.06	56.93	56.70	56.19	57.87	57.31	57.26	56.30	57.30	56.84
Al_2O_3	0.81	0.58	0.49	0.53	0.59	0.64	0.71	0.23	0.46	0.62	0.56	0.36
MnO	0.13	0.11	0.13	0.17	0.19	0.10	0.12	0.13	0.20	0.15	0.14	0.15
FeO	3.10	8.11	7.84	7.41	6.63	8.06	2.86	6.96	7.29	7.81	5.63	6.89
MgO	22.52	19.41	19.26	18.60	19.98	18.44	21.92	19.28	19.81	19.33	20.88	20.16
CaO	13.10	12.16	12.32	12.45	12.47	12.26	13.05	12.64	12.14	12.41	12.49	12.61
Na_2O	0.12	0.23	0.19	0.16	0.18	0.18	0.19	0.12	0.11	0.14	0.14	0.11
K_2O	0.04	0.01	0.05	0.04	0.03	0.02	0.04	0.03	0.02	0.04	0.03	0.03
Total	97.81	97.05	97.33	96.29	96.76	95.89	96.76	96.70	97.29	96.81	97.18	97.15
T												
Si	7.95	7.96	8.01	8.06	7.98	8.02	8.00	8.07	8.02	7.96	7.98	7.98
Al	0.06	0.04			0.02					0.04	0.02	0.03
T (total)	8.00	8.00	8.01	8.06	8.00	8.02	8.00	8.07	8.02	8.00	8.00	8.00
C												
Al	0.08	0.06	0.08	0.09	0.07	0.11	0.12	0.04	0.08	0.07	0.08	0.04
Fe^{3+}	0.00	0.03								0.00		0.01
Mn^{2+}				0.02		0.01	0.02	0.02				
Fe^{2+}	0.32	0.84	0.89	0.88	0.74	0.96	0.33	0.82	0.79	0.86	0.59	0.74
Mg	4.60	4.08	4.03	3.93	4.19	3.92	4.52	4.05	4.14	4.08	4.34	4.22
C (total)	5.00	5.00	5.00	4.91	5.00	5.00	4.98	4.92	5.00	5.00	5.00	5.00
B												
Mn^{2+}	0.02	0.01	0.02		0.02	0.01			0.02	0.02	0.02	0.02
Fe^{2+}	0.03	0.09	0.03		0.05				0.06	0.06	0.07	0.06
Ca	1.92	1.84	1.85	1.89	1.88	1.88	1.93	1.91	1.82	1.88	1.86	1.90
Na	0.03	0.05	0.05	0.04	0.05	0.05	0.05	0.03	0.03	0.04	0.04	0.03
B (total)	2.00	2.00	1.95	1.93	2.00	1.93	1.98	1.94	1.94	2.00	1.99	2.00
A												
Na	0.00	0.01								0.00		0.00
K	0.01	0.00	0.01	0.01	0.01	0.00	0.01	0.01	0.00	0.01	0.01	0.01
A (total)	0.01	0.01	0.01	0.01	0.01	0.00	0.01	0.01	0.00	0.01	0.01	0.01

Sample	**007-15.6a**					
Lithotype	Amphiboles accompanying sulphides hosted in marbles					
Analysis Ref.	Z1 P1	Z1 P2	Z1 P3	Z1 P4	Z1 P5	Z1 P6
Element (wt. %)						
SiO_2	56.5426	58.2678	57.5344	57.3947	58.5905	57.4165
Al_2O_3	0.5128	0.2485	0.1181	0.7895	0.177	0.0247
MnO	0.1869	0.47	0.5866	0.1609	0.2393	0.6486
FeO	6.9713	3.4676	5.4664	6.1322	3.0615	4.0766
MgO	19.5939	23.0386	20.7381	20.2471	23.0224	21.2701
CaO	12.6608	11.4986	12.0754	12.5456	12.4874	12.0893
Na_2O	0.0923	0.0684	0.1188	0.2347	0.0841	0.054
K_2O	0.0256	0.0168	0.0205	0.0305	0.0112	0.0105
Total	96.5862	97.0763	96.6583	97.5352	97.6734	95.5903
T						
Si	7.985	8.024	8.053	7.985	8.019	8.074
Al	0.015			0.015		
T (total)	8	8.024	8.053	8	8.019	8.074
C						
Al	0.071	0.04	0.019	0.114	0.029	0.004
Fe^{3+}						
Mn^{2+}			0.014			0.057
Fe^{2+}	0.804	0.23	0.64	0.686	0.274	0.479
Mg	4.125	4.73	4.327	4.199	4.697	4.459
C (total)	5	5	5	4.999	5	4.999
B						
Mn^{2+}	0.022	0.055	0.056	0.019	0.028	0.02
Fe^{2+}	0.019	0.169		0.027	0.076	
Ca	1.916	1.697	1.811	1.87	1.831	1.822
Na	0.025	0.018	0.032	0.063	0.022	0.015
B (total)	1.982	1.939	1.899	1.979	1.957	1.857
A						
Na						
K	0.005	0.003	0.004	0.005	0.002	0.002
A (total)	0.005	0.003	0.004	0.005	0.002	0.002

Sample	MV 6			
Lithotype	Basic metavolcanic rocks			
Analysis Ref.	Z2 P9	Z2 P10	Z2 P11	Z2 P12
Element (wt. %)				
SiO_2	54.281	51.5422	52.0643	44.6917
Al_2O_3	1.0576	5.2306	2.8864	8.9347
MnO	0.2791	0.2078	0.2109	0.2017
FeO	14.1083	14.6642	14.4615	18.2681
MgO	14.0067	12.4836	13.8491	9.5477
CaO	12.519	11.1449	12.2493	11.7336
Na_2O	0.2024	0.7637	0.502	1.1282
K_2O	0.0604	0.4277	0.1937	0.8414
Total	96.5145	96.4647	96.4172	95.3471
T				
Si	7.952	7.575	7.67	6.86
Al	0.048	0.425	0.33	1.14
T (total)	8	8	8	8
C				
Al	0.135	0.481	0.171	0.477
Fe^{3+}		0.05	0.072	0.238
Mn^{2+}	0.035		0.006	
Fe^{2+}	1.729	1.735	1.71	2.101
Mg	3.059	2.735	3.041	2.185
C (total)	4.958	5.001	5	5.001
B				
Mn^{2+}		0.026	0.02	0.026
Fe^{2+}		0.018		0.006
Ca	1.965	1.755	1.933	1.93
Na	0.035	0.201	0.046	0.038
B (total)	2	2	1.999	2
A				
Na	0.023	0.016	0.097	0.298
K	0.011	0.08	0.036	0.165
A (total)	0.034	0.096	0.133	0.463

Appendix E-1.1. – EPMA results of silicates from the Montemor-o-Novo area – Analysis of pyroxene from samples of the Vale da Arca mine (outcrop samples)

Sample	**MV 6**							
Lithotype								
Analysis Ref.	Z1 P3	Z1 P4	Z1 P5	Z1 P6	Z1 P7	Z1 P8	Z1 P9	Z1 P10
Element (wt. %)								
SiO_2	47.57	55.22	55.44	54.25	46.93	54.69	55.29	45.90
TiO_2		0.13	0.20	0.26		0.09	0.12	
Al_2O_3	3.45	0.45	0.66	0.55	3.87	0.14	0.11	4.45
FeO	16.11	0.93	2.34	1.19	18.83	0.84	1.04	19.87
MnO	0.38	0.38	0.56	0.60	0.30	0.49	0.51	0.34
MgO	6.72	17.13	15.78	16.90	5.03	17.25	17.34	4.11
CaO	22.90	25.35	25.05	25.46	22.66	25.43	25.31	22.65
Na_2O	0.08		0.05		0.15			0.08
Total	97.21	99.59	100.07	99.19	97.76	98.92	99.72	97.39
Formula (6O)								
Si	1.91	2.01	2.01	1.99	1.89	2.00	2.01	1.87
Al	0.09	0.00	-0.01	0.01	0.11	0.00	-0.01	0.13
Al	0.07	0.02	0.04	0.01	0.08	0.01	0.01	0.09
Fe(iii)	0.04				0.06			0.07
Ti	0.00	0.00	0.01	0.01		0.00	0.00	0.00
Fe(ii)	0.50	0.03	0.07	0.04	0.58	0.03	0.03	0.60
Mn	0.01	0.01	0.02	0.02	0.01	0.02	0.02	0.01
Mg	0.40	0.93	0.85	0.92	0.30	0.94	0.94	0.25
Ca	0.98	0.99	0.97	1.00	0.98	1.00	0.98	0.99
Na	0.01	0.00	0.00		0.01			0.01
Total	4.01	3.99	3.97	3.99	4.02	3.99	3.99	4.02

Appendix E-1.1. – EPMA results of silicates from the Montemor-o-Novo area – Chlorite analysis from samples of the Monges mine (drill core samples)

Sample	007-10.2b												
Lithotype	Quartz-Chlorite-Pyrite-(Gold) veins hosted in acid metavolcanic rocks												
Analysis Ref.	Z1 P1	Z1 P2	Z1 P3	Z1 P4	Z1 P5	Z1 P6	Z1 P7	Z2 P2	Z2 P3	Z2 P4	Z2 P5	Z2 P6	Z2 P7
Element (wt. %)	28.6128	28.9234	29.2504	29.2670	28.6511	28.8453	28.5808	28.8713	28.9323	27.4695	27.4127	27.9711	28.98
SiO_2	0.0060	0.0383	0.0360	0.0154	0.1603	0.0656	0.0641	0	0	0	0.0047	0.0173	0.0014
TiO_2	17.3527	17.3579	18.0663	17.9453	17.6390	17.5229	17.2781	17.6055	17.6602	17.1702	17.3395	18.9824	17.697
Al_2O_3	20.1371	19.4837	20.1980	20.1584	19.8665	19.9532	20.6889	22.7401	21.7921	26.8663	25.95	19.5246	23.2243
FeO	0.2168	0.1631	0.1870	0.2490	0.2331	0.2571	0.1951	0.2301	0.2379	0.1728	0.1793	0.2403	0.2056
MnO	17.8441	17.8572	18.3259	19.1092	18.3073	18.2430	18.2423	16.5602	16.8316	13.5692	14.3642	18.2429	16.706
MgO	0.1201	0.1607	0.1491	0.0998	0.1504	0.1331	0.1413	0.1297	0.165	0.1337	0.1037	0.0708	0.178
CaO	0.0744	0.0412	0.0386	0.0493	0.0137	0.0233	0.0259	0.0282	0.0616	0.0276	0.041	0	0.0226
Na_2O	0.0818	0.0592	0.0420	0.0310	0.0289	0.0238	0.0234	0.0266	0.0462	0.0552	0.0213	0.0236	0.0151
K_2O	84.4458	84.0847	86.2933	86.9244	85.0503	85.0673	85.2399	86.1917	85.7269	85.4645	85.4164	85.0730	87.0300
Total													
Z	3.06	3.08	3.04	3.05	3.04	3.04	3.02	3.06	3.08	3.02	3.00	2.94	3.04
Si	0.94	0.92	0.96	0.95	0.96	0.96	0.98	0.94	0.92	0.98	1.00	10594.00	0.96
Al^{IV}	4.00	4.00	4.00	4.00	4.00	4.00	4.00	4.00	4.00	4.00	4.00	4.00	4.00
Total (IV)													
R	1.25	1.28	1.27	1.16	1.22	1.22	1.19	1.24	1.28	1.26	1.23	1.25	1.21
Al^{VI}	0.00	0.00	0.00	0.00	0.00	0.00	0.00	0.00	0.00	0.00	0.00	0.00	0.00
Ti	0.00	0.00	0.00	0.00	0.00	0.00	0.00	0.00	0.00	0.00	0.00	0.00	0.00
Cr	0.00	0.00	0.00	0.00	0.00	0.00	0.00	0.00	0.00	0.00	0.00	0.00	0.00
Fe^{3+}	1.83	1.75	1.76	1.76	1.73	1.73	1.81	2.01	1.93	2.43	2.33	1.73	2.09
Fe^{2+}	0.00	0.00	0.00	0.00	0.00	0.00	0.00	0.00	0.00	0.00	0.00	0.00	0.00
Mn	2.77	2.79	2.82	2.98	2.92	2.92	2.90	2.60	2.62	2.17	2.32	2.92	2.59
Mg	5.85	5.82	5.84	5.90	5.87	5.87	5.89	5.85	5.82	5.86	5.88	5.90	5.88
Total (VI)	9.85	9.82	9.84	9.90	9.87	9.87	9.89	9.85	9.82	9.86	9.88	9.90	9.88
Total													
	0.40	0.39	0.38	0.37	0.37	0.37	0.38	0.44	0.42	0.53	0.50	0.37	0.45
Fe/(Fe + Mg)	4.60	4.54	4.57	4.74	4.64	4.64	4.71	4.61	4.55	4.60	4.65	4.65	4.67
Mg + Fe	0.60	0.61	0.62	0.63	0.63	0.63	0.62	0.56	0.58	0.47	0.50	0.63	0.55
Mg/(Mg+Fe)	18.73	18.94	19.06	17.87	18.56	18.56	18.36	18.68	18.89	19.12	18.95	19.57	18.47
Al-chl (%)	33.90	33.16	32.74	31.60	31.71	31.71	32.46	36.84	36.13	43.89	41.57	30.93	37.54
Fe-chl (%)	47.37	47.91	48.21	50.53	49.72	49.72	49.18	44.48	44.98	36.99	39.48	49.50	43.99
Mg-chl (%)	28.6128	28.9234	29.2504	29.2670	28.6511	28.8453	28.5808	28.8713	28.9323	27.4695	27.4127	27.9711	28.98

Sample	007-10.2b			007-8.1b	
Lithotype	Quartz-Chlorite-Fespar-(gold) veins hosted in acid metavolcanic rocks				
Analysis Ref.	Z1 P8	Z1 92	Z1 P10	Z1 P10	Z1 P11
Element (wt. %)	28.6128	28.9234	29.2504	29.2670	28.6511
SiO_2	0.0060	0.0383	0.0360	0.0154	0.1603
TiO_2	17.3527	17.3579	18.0663	17.9453	17.6390
Al_2O_3	20.1371	19.4837	20.1980	20.1584	19.8665
FeO	0.2168	0.1631	0.1870	0.2490	0.2331
MnO	17.8441	17.8572	18.3259	19.1092	18.3073
MgO	0.1201	0.1607	0.1491	0.0998	0.1504
CaO	0.0744	0.0412	0.0386	0.0493	0.0137
Na_2O	0.0818	0.0592	0.0420	0.0310	0.0289
K_2O	84.4458	84.0847	86.2933	86.9244	85.0503
Total					
Z	3.06	3.08	3.04	3.05	3.04
Si	0.94	0.92	0.96	0.95	0.96
Al^{IV}	4.00	4.00	4.00	4.00	4.00
Total (IV)					
R	1.25	1.28	1.27	1.16	1.22
Al^{VI}	0.00	0.00	0.00	0.00	0.00
Ti	0.00	0.00	0.00	0.00	0.00
Cr	0.00	0.00	0.00	0.00	0.00
Fe^{3+}	1.83	1.75	1.76	1.76	1.73
Fe^{2+}	0.00	0.00	0.00	0.00	0.00
Mn	2.77	2.79	2.82	2.98	2.92
Mg	5.85	5.82	5.84	5.90	5.87
Total (VI)	9.85	9.82	9.84	9.90	9.87
Total					
	0.40	0.39	0.38	0.37	0.37
Fe/(Fe + Mg)	4.60	4.54	4.57	4.74	4.64
Mg + Fe	0.60	0.61	0.62	0.63	0.63
Mg/(Mg+Fe)	18.73	18.94	19.06	17.87	18.56
Al-chl (%)	33.90	33.16	32.74	31.60	31.71
Fe-chl (%)	47.37	47.91	48.21	50.53	49.72
Mg-chl (%)	28.6128	28.9234	29.2504	29.2670	28.6511

Appendix E-1.1. – EPMA results of silicates from the Montemor-o-Novo area – Tourmaline analysis from samples of the Monges mine (drill core samples)

Sample	**004-7.5a**										
Lithotype	Quartz – Tourmaline veins hosted in acid metavolcanic rocks										
Analysis Ref.	Z1 P1	Z1 P2	Z1 P3	Z1 P4	Z1 P5	Z1 P6	Z1 P7	Z1 P8	Z1 P9	Z1 P12	Z1 P13
Crystal spot	Rim	Core	Rim	Core	Rim	Rim	Core	Core	Rim	Core	Core
Element (wt. %)											
SiO_2	37.41	37.80	37.54	37.46	37.07	37.21	36.54	37.58	36.91	37.64	37.42
TiO_2	0.52	0.20	0.42	0.24	1.42	1.38	1.52	0.24	0.48	0.25	0.25
Al_2O_3	30.94	31.72	31.27	31.12	29.04	29.01	27.05	32.04	30.28	31.86	30.04
FeO	4.36	3.64	4.40	5.60	4.79	4.59	7.94	3.80	5.23	3.43	5.55
MgO	9.28	8.95	9.00	8.78	8.86	9.38	8.54	8.65	8.76	8.82	8.52
CaO	0.36	0.20	0.30	0.24	0.90	0.96	1.06	0.34	0.57	0.32	0.23
Na_2O	2.31	2.34	2.42	2.54	2.20	2.38	2.22	2.68	2.47	2.58	2.49
Total	85.18	84.86	85.35	85.98	84.27	84.90	84.86	85.32	84.70	84.90	84.50
Formula (29 O)											
B	3.00	3.00	3.00	3.00	3.00	3.00	3.00	3.00	3.00	3.00	3.00
Si	6.09	6.14	6.10	6.09	6.14	6.12	6.14	6.09	6.09	6.11	6.18
Ti	0.06	0.02	0.05	0.03	0.18	0.17	0.19	0.03	0.06	0.03	0.03
Al	5.94	6.07	5.99	5.96	5.67	5.63	5.36	6.12	5.89	6.10	5.85
Fe(ii)	0.59	0.49	0.60	0.76	0.66	0.63	1.12	0.51	0.72	0.47	0.77
Mn	0.00	0.00	0.00	0.00	0.00	0.00	0.00	0.00	0.00	0.00	0.00
Mg	2.25	2.17	2.18	2.13	2.19	2.30	2.14	2.09	2.16	2.14	2.10
Ca	0.06	0.04	0.05	0.04	0.16	0.17	0.19	0.06	0.10	0.06	0.04
Na	0.73	0.74	0.76	0.80	0.71	0.76	0.72	0.84	0.79	0.81	0.80
Total	18.74	18.67	18.73	18.80	18.70	18.78	18.85	18.74	18.80	18.71	18.76

Appendix E-1.1. – EPMA results of silicates from the Montemor-o-Novo area – Epidote analysis from samples of the Vale da Arca mine (outcrop samples)

Sample	**AZ 4.3**							
Analysis Ref.	Z2 P1	Z2 P2	Z2 P3	Z2 P4	Z2 P5	Z2 P6	Z2 P7	Z2 P8
Element (wt. %)								
SiO_2	37.63	37.34	37.13	37.46	37.16	36.89	38.00	37.24
TiO_2	0.04	0.15	0.04	0.07	0.07	0.28	0.09	0.06
Al_2O_3	22.89	22.86	22.04	22.76	20.87	21.56	21.65	21.46
Fe_2O_3	13.69	14.32	15.42	14.31	16.21	15.52	15.54	15.43
MnO						0.13		
MgO	0.11							
CaO	22.72	23.11	22.94	23.06	22.77	22.86	23.01	22.90
P_2O_5	0.29	0.20	0.32	0.23	0.28	0.25	0.27	0.37
Total	97.38	97.99	97.89	97.89	97.36	97.50	98.57	97.46
Formula (12.5O)								
Si	3.23	3.21	3.23	3.22	3.27	3.23	3.28	3.26
Ti	0.00	0.01	0.00	0.00	0.00	0.02	0.01	0.00
Al	2.32	2.31	2.26	2.31	2.17	2.22	2.20	2.21
Fe(iii)	0.44	0.46	0.50	0.46	0.54	0.51	0.50	0.51
Mn	0.00	0.00	0.00	0.00	0.00	0.01	0.00	0.00
Mg	0.01	0.00	0.00	0.00	0.00	0.00	0.00	0.00
Ca	2.09	2.13	2.14	2.12	2.15	2.14	2.12	2.15
P	0.01	0.01	0.01	0.01	0.01	0.01	0.01	0.01
Total	8.11	8.13	8.14	8.12	8.14	8.14	8.12	8.13

Appendix E-1.2. – EPMA results of sulfides from the Montemor-o-Novo area – Pyrite analysis from samples of the Monges mine (drill core samples)

Analysis Reference	**Pyrite Type**	**S**	**As**	**Fe**	**Total**
LOD (ppm)		1295	1734	493	
007-10.3b_z1_py1	Py B	53.6719	0.7049	44.9461	99.3381
007-10.3b_z1_py3	Py B	53.9694	<LOD	45.4805	99.6196
007-10.3b_z1_py4	Py B	53.7607	0.5037	44.9693	99.2379
007-10.3b_z1_py5	Py B	53.8797	<LOD	45.6681	99.7112
007-10.3b_z1_py6	Py B	53.4803	0.6723	44.8196	98.9722
007-10.3b_z1_py7	Py B	53.4870	0.6817	44.8876	99.0563
007-10.3b_z1_py8	Py B	53.6943	0.5908	45.1036	99.3887
007-10.3b_z1_py9	Py B	53.4205	0.6416	45.0608	99.1229
007-10.3b_z1_py10	Py B	53.8066	<LOD	45.7537	99.6862
007-10.3b_z1_py11	Py B	53.4614	0.5421	45.2163	99.2340
007-10.3b_z1_py12	Py B	53.8482	<LOD	45.8754	99.8182
007-10.3b_z1_py13	Py B	53.7573	0.4624	45.2429	99.4711
007-10.3b_z1_py14	Py B	53.7675	0.5150	45.1194	99.4080
007-10.3b_z1_py15	Py B	53.7559	0.5308	45.3847	99.7018
007-10.3b_z1_py16	Py B	53.9322	<LOD	45.6771	99.7110
007-10.3b_z1_py17	Py B	53.7608	0.6856	45.0266	99.4873
007-10.3b_z1_py18	Py B	53.7220	0.2737	45.4800	99.4885
007-10.3b_z2_py1	Py B	53.7722	0.3352	45.4827	99.6072
007-10.3b_z2_py2	Py B	53.9753	0.3719	45.1108	99.4580
007-10.3b_z2_py3	Py B	53.3146	0.6359	45.1126	99.0630
007-10.3b_z2_py4	Py B	53.7808	0.2344	45.5494	99.5751

Analysis Reference	**Pyrite Type**	**S**	**As**	**Fe**	**Total**
LOD (ppm)		1295	1734	493	
007-10.3b_z2_py5	Py B	54.1453	0.2216	45.6775	100.0542
007-10.3b_z2_py6	Py B	53.8154	0.3760	45.4717	99.6631
007-10.3b_z2_py7	Py B	53.6274	0.3299	45.3341	99.2984
007-10.3b_z2_py8	Py B	53.9211	0.3018	45.4668	99.6897
007-10.3b_z2_py9	Py B	53.9126	<LOD	45.4360	99.4361
007-10.3b_z2_py10	Py B	53.8502	0.2257	45.5156	99.5915
007-10.3b_z2_py11	Py B	54.1436	0.2123	45.8570	100.2182
007-10.3b_z2_py12	Py B	53.8907	0.2449	45.6105	99.7461
007-10.3b_z2_py13	Py B	54.1938	0.2397	45.5633	99.9968
007-10.3b_z2_py14	Py B	54.1120	0.1773	45.1887	99.4780
007-10.3b_z2_py15	Py B	53.8509	0.2228	46.1137	100.1873
005-32.4b_z2_py_p1	Py A	53.5624	0.2035	45.6132	99.3884
005-32.4b_z2_py_p2	Py A	53.6972	<LOD	45.4948	99.3162
005-32.4b_z2_py_p3	Py A	53.9175	<LOD	45.3951	99.4236
005-32.4b_z2_py_p4	Py A	53.7439	<LOD	45.2853	99.1872
005-32.4b_z2_py_p5	Py A	54.0023	<LOD	45.2999	99.3896
005-32.4b_z2_py_p6	Py A	53.6792	<LOD	45.2355	99.0772

Appendix E-1.2. – EPMA results of sulfides from the Montemor-o-Novo area – Arsenopyrite analysis from samples of the Monges mine (drill core samples)

Analysis Reference	**Arsenopyrite Type**	**S (wt. %)**	**As (wt. %)**	**Fe (wt. %)**	**Total**
LOD (ppm)		1273	1834	490	
007-21.8a_z2_asp1	Apy B	23.7159	41.3508	35.0653	100.1320
007-21.8a_z2_asp2	Apy B	24.9316	39.9747	35.3567	100.2630
007-21.8a_z2_asp3	Apy B	23.6304	40.8719	34.8850	99.3873
007-21.8a_z2_asp4	Apy B	24.7386	40.0332	35.4336	100.2054
007-21.8a_z2_asp5	Apy B	23.6556	40.8850	34.9184	99.4590
007-21.8a_z2_asp6	Apy B	25.1485	39.7032	35.6343	100.4860
007-21.8a_z2_asp7	Apy B	23.3654	41.7615	35.0682	100.1951
007-21.8a_z2_asp8	Apy B	23.8432	41.0464	35.0655	99.9551
007-21.8a_z2_asp9	Apy B	23.7056	41.1404	35.3474	100.1934
007-21.8a_z2_asp10	Apy B	25.0778	39.8623	35.4517	100.3918
007-21.8a_z2_asp11	Apy B	23.5077	40.9776	35.0587	99.5440
007-21.8a_z2_asp12	Apy B	23.7246	40.7849	35.0191	99.5286
007-21.8a_z2_asp13	Apy B	23.5994	41.4987	34.9310	100.0291
007-21.8a_z2_asp14	Apy B	23.6907	41.4840	34.9929	100.1676
007-21.8a_z2_asp15	Apy B	23.8134	41.1155	35.0323	99.9612
007-21.8a_z2_asp16	Apy B	23.6900	41.2458	35.0571	99.9929
007-21.8a_z2_asp17	Apy B	24.3562	40.6443	35.3860	100.3865
007-21.8a_z2_asp18	Apy B	23.7373	41.0737	35.2040	100.0150
007-21.8a_z2_asp19	Apy B	24.2313	40.7779	35.3015	100.3107
007-21.8a_z2_asp20	Apy B	23.9031	40.9147	34.9441	99.7619
007-21.8a_z1_asp1	Apy B	23.6861	40.8818	34.8120	99.3799

Analysis Reference	**Arsenopyrite Type**	**S (wt. %)**	**As (wt. %)**	**Fe (wt. %)**	**Total**
LOD (ppm)		1273	1834	490	
007-21.8a_z1_asp2	Apy B	23.8544	40.5050	35.0846	99.4440
007-21.8a_z1_asp3	Apy B	24.0244	40.8557	35.0861	99.9662
007-21.8a_z1_asp4	Apy B	23.5700	41.1224	34.9187	99.6111
007-21.8a_z1_asp5	Apy B	23.6738	40.8348	34.9978	99.5064
007-21.8a_z1_asp6	Apy B	23.5764	41.0386	34.7854	99.4004
007-21.8a_z1_asp7	Apy B	23.3623	41.1578	34.8841	99.4042
007-21.8a_z1_asp8	Apy B	23.2587	41.7566	34.8784	99.8937
007-21.8a_z1_asp9	Apy B	23.5672	40.9363	34.9969	99.5004
007-21.8a_z1_asp10	Apy B	23.6235	40.9921	35.1321	99.7477
007-21.8a_z1_asp11	Apy B	23.9450	40.6096	35.0191	99.5737
007-21.8a_z1_asp12	Apy B	23.4394	41.4008	34.8910	99.7312
007-21.8a_z1_asp13	Apy B	23.7220	41.1232	35.0816	99.9268
007-21.8a_z1_asp14	Apy B	24.5412	40.0351	35.3296	99.9059
007-21.8a_z1_asp15	Apy B	23.6424	41.2952	35.0004	99.9380
007-21.8a_z1_asp16	Apy B	23.1435	41.6470	34.8095	99.6000
007-21.8a_z1_asp17	Apy B	23.5632	40.8585	35.0508	99.4725
007-21.8a_z1_asp18	Apy B	23.5344	40.4477	34.9181	98.9002
007-21.8a_z1_asp19	Apy B	24.2261	40.3170	35.1194	99.6625
007-21.8a_z1_asp20	Apy B	23.9848	41.2623	35.0012	100.2483
005-31.3b_z1_asp_p1	Apy A	23.1200	40.4393	35.6231	99.1824
005-31.3b_z1_asp_p2	Apy A	24.2394	40.0491	36.1946	100.4831

Analysis Reference	**Arsenopyrite Type**	**S (wt. %)**	**As (wt. %)**	**Fe (wt. %)**	**Total**
LOD (ppm)		1273	1834	490	
005-31.3b_z1_asp_p3	Apy A	23.2691	41.2561	35.7738	100.2990
005-31.3b_z1_asp_p4	Apy A	23.2094	40.9321	35.5773	99.7188
005-31.3b_z1_asp_p5	Apy A	23.6401	40.6887	35.9843	100.3131
005-31.3b_z1_asp_p6	Apy A	23.3508	41.1530	35.6901	100.1939
005-31.3b_z1_asp_p7	Apy A	23.4536	40.8874	35.7478	100.0888
005-31.3b_z1_asp_p8	Apy A	23.4499	40.8247	35.6106	99.8852
005-31.3b_z1_asp_p9	Apy A	23.7302	40.7464	35.8422	100.3188
005-31.3b_z1_asp_p10	Apy A	23.5964	40.7490	35.7919	100.1373
005-31.3b_z1_asp_p11	Apy A	23.6841	40.9370	35.8631	100.4842
005-31.3b_z1_asp_p12	Apy A	23.4227	41.3259	35.7334	100.4820
005-31.3b_z1_asp_p13	Apy A	22.9736	41.2787	35.7163	99.9686
005-31.3b_z1_asp_p14	Apy A	23.9145	40.4734	35.7839	100.1718
005-31.3b_z1_asp_p15	Apy A	23.6702	41.2076	35.8077	100.6855
005-31.3b_z1_asp_p16	Apy A	23.3941	41.3654	35.9428	100.7023
005-31.3b_z1_asp_p17	Apy A	23.6423	41.2452	36.0662	100.9537
005-31.3b_z1_asp_p18	Apy A	23.7916	40.4061	35.8678	100.0655
005-31.3b_z2_asp_p3	Apy A	23.4685	41.5522	35.5472	100.5679
005-31.3b_z2_asp_p2	Apy A	23.6496	41.2141	35.6011	100.4648
005-31.3b_z2_asp_p1	Apy A	23.2123	39.7159	35.1645	98.0927
005-31.3b_z2_asp_p4	Apy A	23.0612	41.6658	35.5643	100.2913
005-31.3b_z2_asp_p5	Apy A	23.4016	40.9695	35.5506	99.9217

Analysis Reference	**Arsenopyrite Type**	**S (wt. %)**	**As (wt. %)**	**Fe (wt. %)**	**Total**
LOD (ppm)		1273	1834	490	
005-31.3b_z2_asp_p6	Apy A	23.3151	40.6263	35.6051	99.5465
005-31.3b_z2_asp_p7	Apy A	23.7373	40.6556	35.5068	99.8997
005-31.3b_z2_asp_p9	Apy A	30.7598	33.0137	37.8130	101.5865
005-31.3b_z2_asp_p10	Apy A	22.7110	42.4552	35.2492	100.4154
005-31.3b_z2_asp_p8	Apy A	23.5467	41.9176	35.3754	100.8397
005-31.3b_z2_asp_p11	Apy A	23.7789	41.4945	35.2072	100.4806
005-31.3b_z2_asp_p12	Apy A	23.1777	42.0650	35.2451	100.4878
005-31.3b_z2_asp_p14	Apy A	23.6303	41.6693	34.8099	100.1095
005-31.3b_z2_asp_p13	Apy A	23.7725	41.9984	35.1982	100.9691
005-31.3b_z3_asp_p10	Apy A	23.2860	42.4707	34.3091	100.0658
005-31.3b_z3_asp_p7	Apy A	22.7950	42.7241	34.4976	100.0167
005-31.3b_z3_asp_p9	Apy A	23.1730	41.5974	34.5319	99.3023
005-31.3b_z3_asp_p8	Apy A	23.4290	41.0336	34.1424	98.6050
005-31.3b_z3_asp_p6	Apy A	23.1052	42.4706	34.3944	99.9702
005-31.3b_z3_asp_p4	Apy A	23.0896	42.8843	35.3529	101.3268
005-31.3b_z3_asp_p3	Apy A	22.9430	42.6434	35.1427	100.7291
005-31.3b_z3_asp_p5	Apy A	22.9637	41.6323	34.9024	99.4984
005-31.3b_z3_asp_p2	Apy A	22.7234	42.9235	34.4195	100.0664
005-31.3b_z3_asp_p1	Apy A	22.2999	43.0548	34.5276	99.8823
005-31.3b_z3_asp_p11	Apy A	23.4159	42.1543	34.2522	99.8224
005-31.3b_z3_asp_p12	Apy A	23.5493	42.6148	34.2595	100.4236

Analysis Reference	**Arsenopyrite Type**	**S (wt. %)**	**As (wt. %)**	**Fe (wt. %)**	**Total**
LOD (ppm)		1273	1834	490	
005-31.3b_z3_asp_p13	Apy A	23.1549	42.1455	34.0853	99.3857
005-31.3b_z3_asp_p14	Apy A	23.3074	41.2684	32.7996	97.3754
005-31.3b_z3_asp_p15	Apy A	23.3980	42.2318	34.2830	99.9128
005-31.3b_z3_asp_p16	Apy A	23.7290	41.9050	34.1310	99.7650
005-31.3b_z3_asp_p18	Apy A	23.6065	41.6979	33.7853	99.0897
005-31.3b_z3_asp_p18	Apy A	23.6966	41.8095	34.1480	99.6541
005-31.3b_z3_asp_p17	Apy A	23.6170	38.1451	31.8523	93.6144
005-32.4b_z1_asp_p1	Apy A	23.2786	42.3525	34.6212	100.2523
005-32.4b_z1_asp_p2	Apy A	23.3010	42.8057	34.2267	100.3334
005-32.4b_z1_asp_p3	Apy A	23.2138	43.0604	34.2977	100.5719
005-32.4b_z1_asp_p4	Apy A	23.3975	42.8514	34.3154	100.5643
005-32.4b_z1_asp_p5	Apy A	22.9417	42.1501	34.0607	99.1525
005-32.4b_z1_asp_p6	Apy A	22.7143	42.6621	34.6957	100.0721
005-32.4b_z1_asp_p7	Apy A	22.8740	42.4504	34.7770	100.1014
005-32.4b_z1_asp_p9	Apy A	23.0314	42.7844	34.6485	100.4643
005-32.4b_z1_asp_p10	Apy A	22.8425	42.8674	34.8536	100.5635
005-32.4b_z1_asp_p8	Apy A	23.3722	41.7081	34.7964	99.8767
005-32.4b_z1_asp_p11	Apy A	23.3847	41.6360	34.6754	99.6961
005-32.4b_z2_asp_p1	Apy A	23.3359	41.3793	34.561	99.2762
005-32.4b_z2_asp_p2	Apy A	23.4396	41.5298	34.8313	99.8007
005-32.4b_z2_asp_p3	Apy A	23.591	41.0087	34.6275	99.2272

Analysis Reference	**Arsenopyrite Type**	**S (wt. %)**	**As (wt. %)**	**Fe (wt. %)**	**Total**
LOD (ppm)		1273	1834	490	
005-32.4b_z2_asp_p4	Apy A	23.8591	40.9182	34.8964	99.6737
005-32.4b_z2_asp_p5	Apy A	23.6326	41.0821	34.6693	99.3840
005-32.4b_z2_asp_p6	Apy A	23.8024	40.7174	34.6656	99.1854
007-14.1a2_z1_asp_p1	Apy A	20.05	34.9397	31.4239	86.4136
007-14.1a2_z1_asp_p2	Apy A	20.0839	34.2972	31.2581	85.6392
007-14.1a2_z1_asp_p3	Apy A	19.6689	35.4989	31.3003	86.4681
007-14.1a2_z1_asp_p4	Apy A	46.5706	0.1214	39.7919	86.4839
007-14.1a2_z1_asp_p5	Apy A	46.6976	0.1039	39.5089	86.3104
004-11.1b_z1_asp_p1	Apy A	23.5335	41.8504	34.7077	100.0916
004-11.1b_z1_asp_p2	Apy A	23.5308	41.8558	35.1537	100.5403
004-11.1b_z1_asp_p3	Apy A	22.9054	42.2885	35.2997	100.4936
004-11.1b_z1_asp_p4	Apy A	23.1806	42.0717	34.2129	99.4652
004-11.1b_z1_asp_p5	Apy A	23.4197	41.7238	34.4726	99.6161
004-11.1b_z1_asp_p20	Apy A	22.9017	42.3039	34.9174	100.1230
004-11.1b_z1_asp_p9	Apy A	23.4057	42.0851	35.0054	100.4962
004-11.1b_z1_asp_p12	Apy A	23.6611	41.8674	34.3283	99.8568
004-11.1b_z1_asp_p17	Apy A	23.2194	42.1133	34.5386	99.8713
004-11.1b_z1_asp_p18	Apy A	23.5642	42.0075	34.8127	100.3844
004-11.1b_z1_asp_p10	Apy A	23.3816	41.5448	34.3735	99.2999
004-11.1b_z1_asp_p11	Apy A	23.5126	41.4520	34.5198	99.4844

004-11.1b_z1_asp_p14	Apy A	23.2769	42.0382	34.4781	99.7932
Analysis Reference	**Arsenopyrite Type**	**S (wt. %)**	**As (wt. %)**	**Fe (wt. %)**	**Total**
LOD (ppm)		1273	1834	490	
004-11.1b_z1_asp_p13	Apy A	23.7378	41.7150	34.7572	100.2100
004-11.1b_z1_asp_p16	Apy A	23.7687	41.3224	34.7420	99.8331
004-11.1b_z1_asp_p19	Apy A	23.3371	41.8438	34.7000	99.8809
004-11.1b_z1_asp_p15	Apy A	23.2720	42.2789	34.8378	100.3887
004-11.1b_z1_asp_p7	Apy A	23.5209	41.5281	34.8652	99.9142
004-11.1b_z1_asp_p6	Apy A	23.4587	41.7342	34.5215	99.7144
004-11.1b_z1_asp_p8	Apy A	23.3911	41.6753	35.0417	100.1081
005-32.4c_z1_asp_p1	Apy A	23.7635	41.1500	35.2179	100.1314
005-32.4c_z1_asp_p2	Apy A	23.7748	41.3372	35.2571	100.3691
005-32.4c_z1_asp_p3	Apy A	23.6152	41.0789	35.1783	99.8724
005-32.4c_z1_asp_p4	Apy A	23.6867	41.0982	35.1655	99.9504
005-32.4c_z1_asp_p5	Apy A	23.5983	40.8639	35.1402	99.6024
005-32.4c_z1_asp_p6	Apy A	23.6813	40.9575	35.3362	99.9750
005-32.4c_z1_asp_p7	Apy A	24.0768	40.4312	35.3784	99.8864
005-32.4c_z1_asp_p8	Apy A	23.9801	40.6006	35.0726	99.6533
005-32.4c_z1_asp_p9	Apy A	23.6049	40.9614	35.1058	99.6721
005-32.4c_z1_asp_p12	Apy A	23.5764	40.7649	35.0309	99.3722
005-32.4c_z1_asp_p11	Apy A	23.8386	41.1296	35.2250	100.1932
005-32.4c_z1_asp_p10	Apy A	23.6603	41.1198	35.0393	99.8194
005-32.4c_z2_asp_p76	Apy A	23.6486	40.7663	35.4214	99.8363
005-32.4c_z2_asp_p77	Apy A	24.0467	40.0899	35.5751	99.7117

Analysis Reference	**Arsenopyrite Type**	**S (wt. %)**	**As (wt. %)**	**Fe (wt. %)**	**Total**
LOD (ppm)		1273	1834	490	
005-32.4c_z2_asp_p78	Apy A	24.0757	31.4657	34.5609	90.1023
005-32.4c_z2_asp_p79	Apy A	23.2640	40.2414	35.2227	98.7281
005-32.4c_z2_asp_p74	Apy A	24.0783	40.9241	35.5356	100.5380
005-32.4c_z2_asp_p75	Apy A	23.3925	41.7677	35.2209	100.3811
005-32.4c_z2_asp_p73	Apy A	23.4914	41.1590	35.1963	99.8467
005-32.4c_z2_asp_p70	Apy A	23.4673	41.7525	34.9952	100.2150
005-32.4c_z2_asp_p71	Apy A	23.4402	41.5805	35.2696	100.2903
005-32.4c_z2_asp_p72	Apy A	23.3249	41.5350	35.5909	100.4508
005-32.4c_z2_asp_p88	Apy A	20.9009	36.4371	30.5526	87.8906
005-32.4c_z2_asp_p89	Apy A	23.4652	42.0404	34.2791	99.7847
005-32.4c_z2_asp_p87	Apy A	23.2970	41.7908	34.4465	99.5343
005-32.4c_z2_asp_p85	Apy A	23.6233	41.8263	34.6005	100.0501
005-32.4c_z2_asp_p86	Apy A	23.9259	41.1160	34.9989	100.0408
005-32.4c_z2_asp_p40	Apy A	22.8510	41.3258	35.5849	99.7617
005-32.4c_z2_asp_p41	Apy A	23.0835	41.1619	35.6039	99.8493
005-32.4c_z2_asp_p39	Apy A	23.2699	40.7125	35.6021	99.5845
005-32.4c_z2_asp_p38	Apy A	22.9960	41.3076	35.4787	99.7823

Appendix E-1.2. – EPMA results of gold from the Montemor-o-Novo area – Gold analysis from samples of the Monges mine (drill core samples)

Mineralization Type		**Type i)**				**Type ii)**		
Mode of occurence		**Filling Apy A fractures**			**Free particles**	**Filling Py B fractures**		
(wt. %)	**LOD (ppm)**	**1**	**2**	**3**	**4**	**5**	**6**	**7**
Au	5554	85.5623	86.2867	86.2194	91.8017	80.5427	82.8970	82.1758
Ag	861	13.5587	13.2686	13.1482	7.0838	18.6811	16.8268	17.4702
Fe	498	0.1247	0.1644	b.d.l.	0.1572	0.2442	0.1242	0.116
Cu	360	0.0368	b.d.l.	b.d.l.	b.d.l.	b.d.l.	b.d.l.	b.d.l.
Se	731	b.d.l.	b.d.l.	b.d.l.	b.d.l.	b.d.l.	b.d.l.	b.d.l.
Te	388	b.d.l.	b.d.l.	b.d.l.	b.d.l.	b.d.l.	b.d.l.	b.d.l.
Bi	1463	b.d.l.	b.d.l.	b.d.l.	b.d.l.	b.d.l.	b.d.l.	b.d.l.
Hg	3886	b.d.l.	b.d.l.	b.d.l.	b.d.l.	b.d.l.	b.d.l.	b.d.l.
Total		99.3163	99.8263	99.5365	99.1189	99.6290	99.9311	99.8498
Fineness	-	863	867	868	928	812	831	825

Appendix E-1.3. – EPMA results of magnetite from the Montemor-o-Novo area – Magnetite analysis from samples of the Monges mine (drill core samples)

Analysis Code	Deposit	Ore body	Sample Type	Magnetite type	Mg	Al	Si	Ca	Ti	Fe	Cr	Mn	Ni	V	Co	Zn	O	Total
005-20.3a_z2.2_mag_p1	MIC	Monges	Drill Core	Mag I	0.29	0.22	0.57	0.02	0.04	69.46	<LOD	0.20	<LOD	<LOD	<LOD	<LOD	19.62	90.44
005-20.3a_z2.2_mag_p2	MIC	Monges	Drill Core	Mag I	<LOD	<LOD	0.13	0.04	0.05	71.62	<LOD	0.13	<LOD	<LOD	<LOD	<LOD	19.39	91.39
005-20.3a_z2.2_mag_p3	MIC	Monges	Drill Core	Mag I	<LOD	0.03	0.09	0.02	0.03	71.59	<LOD	0.05	<LOD	<LOD	<LOD	<LOD	19.27	91.12
005-20.3a_z2.2_mag_p4	MIC	Monges	Drill Core	Mag I	<LOD	0.11	0.58	0.03	0.05	70.07	<LOD	0.15	<LOD	<LOD	<LOD	<LOD	19.49	90.48
005-20.3a_z2.2_mag_p5	MIC	Monges	Drill Core	Mag I	<LOD	0.04	0.06	0.06	0.04	70.36	<LOD	0.24	<LOD	<LOD	<LOD	<LOD	19.02	89.88
005-20.3a_z2.2_mag_p6	MIC	Monges	Drill Core	Mag I	<LOD	<LOD	0.05	0.03	0.03	71.37	<LOD	0.11	<LOD	<LOD	<LOD	<LOD	19.36	91.01
005-20.3a_z2.2_mag_p7	MIC	Monges	Drill Core	Mag I	0.39	0.36	0.94	0.04	0.04	68.48	<LOD	0.16	<LOD	<LOD	<LOD	<LOD	20.03	90.49
005-20.3a_z2.2_mag_p8	MIC	Monges	Drill Core	Mag I	0.07	0.10	0.24	0.02	0.04	70.51	<LOD	0.24	<LOD	<LOD	<LOD	<LOD	19.30	90.53
005-20.3a_z2.2_mag_p9	MIC	Monges	Drill Core	Mag I	<LOD	0.04	0.04	<LOD	0.04	70.97	<LOD	0.29	<LOD	<LOD	<LOD	<LOD	19.10	90.50
005-20.3a_z2.2_mag_p10	MIC	Monges	Drill Core	Mag I	0.25	0.25	0.64	0.05	0.04	69.13	<LOD	0.12	<LOD	<LOD	<LOD	<LOD	19.65	90.14
005-20.3a_z2.2_mag_p11	MIC	Monges	Drill Core	Mag I	0.19	0.27	1.15	0.06	0.06	68.35	<LOD	0.14	<LOD	<LOD	<LOD	<LOD	20.06	90.31
005-20.3a_z2.2_mag_p12	MIC	Monges	Drill Core	Mag I	<LOD	0.08	0.34	<LOD	0.04	70.78	<LOD	0.11	<LOD	<LOD	<LOD	<LOD	19.42	90.82
005-20.3a_z2.2_mag_p13	MIC	Monges	Drill Core	Mag I	0.15	0.16	0.54	0.04	0.04	69.69	<LOD	0.11	<LOD	<LOD	<LOD	<LOD	19.49	90.22
005-20.3a_z2.2_mag_p14	MIC	Monges	Drill Core	Mag I	<LOD	0.03	0.44	<LOD	0.04	70.65	<LOD	0.23	<LOD	<LOD	<LOD	<LOD	19.56	90.98
005-20.3a_z2.2_mag_p15	MIC	Monges	Drill Core	Mag I	0.23	0.24	0.69	0.04	0.05	69.31	<LOD	0.11	<LOD	<LOD	<LOD	<LOD	19.71	90.38
005-20.3a_z2.2_mag_p16	MIC	Monges	Drill Core	Mag I	<LOD	0.05	0.13	0.02	0.04	70.87	<LOD	0.30	<LOD	<LOD	<LOD	<LOD	19.21	90.66
005-20.3a_z2.2_mag_p17	MIC	Monges	Drill Core	Mag I	<LOD	0.04	0.02	0.02	0.04	71.18	<LOD	0.25	<LOD	<LOD	<LOD	<LOD	19.16	90.73
005-20.3a_z2.2_mag_p18	MIC	Monges	Drill Core	Mag I	0.15	0.11	0.56	0.04	0.03	70.28	<LOD	0.08	<LOD	<LOD	<LOD	<LOD	19.71	91.00
005-20.3a_z2.2_mag_p19	MIC	Monges	Drill Core	Mag I	<LOD	0.04	0.18	<LOD	0.04	71.25	<LOD	0.27	<LOD	<LOD	<LOD	<LOD	19.34	91.15
005-20.3a_z2.2_mag_p20	MIC	Monges	Drill Core	Mag I	0.19	0.28	0.52	0.04	0.05	69.49	<LOD	0.14	<LOD	<LOD	<LOD	<LOD	19.60	90.32

005-20.3a_z2.2_mag_p21	MIC	Monges	Drill Core	Mag I	0.09	0.11	0.87	0.07	0.06	69.16	<LOD	0.15	<LOD	<LOD	<LOD	<LOD	19.84	90.36
005-20.3a_z2_mag_p1	MIC	Monges	Drill Core	Mag I	0.06	0.07	0.33	0.05	0.05	70.35	<LOD	0.05	<LOD	<LOD	<LOD	<LOD	19.34	90.30
005-20.3a_z2_mag_p2	MIC	Monges	Drill Core	Mag I	<LOD	0.07	0.16	0.02	0.05	71.09	<LOD	0.13	<LOD	<LOD	<LOD	<LOD	19.30	90.85

Analysis Code	Deposit	Ore body	Sample Type	Magnetite type	Mg	Al	Si	Ca	Ti	Fe	Cr	Mn	Ni	V	Co	Zn	O	Total
005-20.3a_z2_mag_p3	MIC	Monges	Drill Core	Mag I	<LOD	<LOD	0.04	0.06	0.04	71.18	<LOD	0.21	<LOD	<LOD	<LOD	<LOD	19.19	90.79
005-20.3a_z2_mag_p4	MIC	Monges	Drill Core	Mag I	<LOD	0.05	0.09	0.03	0.05	70.55	<LOD	0.22	<LOD	<LOD	<LOD	<LOD	19.08	90.08
005-20.3a_z2_mag_p5	MIC	Monges	Drill Core	Mag I	0.07	0.11	0.27	0.06	0.05	70.87	<LOD	0.13	<LOD	<LOD	<LOD	<LOD	19.65	91.24
005-20.3a_z2_mag_p6	MIC	Monges	Drill Core	Mag I	<LOD	0.03	0.03	0.03	0.05	70.98	<LOD	0.23	<LOD	<LOD	<LOD	<LOD	19.11	90.47
005-20.3a_z2_mag_p7	MIC	Monges	Drill Core	Mag I	0.07	0.08	0.23	0.05	0.05	70.99	<LOD	0.17	<LOD	<LOD	<LOD	<LOD	19.65	91.29
005-20.3a_z2_mag_p8	MIC	Monges	Drill Core	Mag I	<LOD	0.04	0.03	<LOD	0.05	71.26	<LOD	0.16	<LOD	<LOD	<LOD	<LOD	19.16	90.73
005-20.3a_z2_mag_p9	MIC	Monges	Drill Core	Mag I	<LOD	0.06	0.03	0.02	0.05	71.54	<LOD	0.30	<LOD	<LOD	<LOD	<LOD	19.34	91.39
005-20.3a_z2_mag_p10	MIC	Monges	Drill Core	Mag I	<LOD	0.08	0.56	<LOD	0.06	70.21	<LOD	0.28	<LOD	<LOD	<LOD	<LOD	19.57	90.85
005-20.3a_z2_mag_p11	MIC	Monges	Drill Core	Mag I	<LOD	0.06	0.34	0.03	0.05	70.64	<LOD	0.30	<LOD	<LOD	<LOD	<LOD	19.43	90.86
005-20.3a_z2_mag_p12	MIC	Monges	Drill Core	Mag I	0.10	0.11	0.34	0.02	0.04	70.35	<LOD	0.13	<LOD	<LOD	<LOD	<LOD	19.39	90.51
005-20.3a_z2_mag_p13	MIC	Monges	Drill Core	Mag I	<LOD	0.05	0.03	<LOD	0.05	71.09	<LOD	0.32	<LOD	<LOD	<LOD	<LOD	19.17	90.74
005-20.3a_z2_mag_p14	MIC	Monges	Drill Core	Mag I	<LOD	0.10	0.08	0.03	0.05	70.07	<LOD	0.30	<LOD	<LOD	<LOD	<LOD	18.99	89.65
005-20.3a_z2_mag_p15	MIC	Monges	Drill Core	Mag I	<LOD	0.09	0.56	0.05	0.06	70.36	<LOD	0.28	<LOD	<LOD	<LOD	<LOD	19.66	91.11
005-20.3a_z2_mag_p16	MIC	Monges	Drill Core	Mag I	<LOD	0.05	0.43	0.02	0.05	70.73	<LOD	0.30	<LOD	<LOD	<LOD	<LOD	19.50	91.11
005-20.3a_z2_mag_p20	MIC	Monges	Drill Core	Mag I	<LOD	0.07	0.03	<LOD	0.04	71.32	<LOD	0.25	<LOD	<LOD	<LOD	<LOD	19.25	91.00
005-20.3a_z2_mag_p19	MIC	Monges	Drill Core	Mag I	<LOD	0.07	0.05	0.03	0.04	70.15	<LOD	0.30	<LOD	<LOD	<LOD	<LOD	18.94	89.64
005-20.3a_z2_mag_p18	MIC	Monges	Drill Core	Mag I	0.13	0.18	0.68	0.03	0.05	69.62	<LOD	0.18	<LOD	<LOD	<LOD	<LOD	19.76	90.65
005-20.3a_z2_mag_p17	MIC	Monges	Drill Core	Mag I	<LOD	0.06	0.03	0.03	0.05	71.04	<LOD	0.27	<LOD	<LOD	<LOD	<LOD	19.27	90.76
005-21.2b_z1_mag_p1	MIC	Monges	Drill Core	Mag I	0.05	0.05	0.14	<LOD	0.07	66.55	<LOD	0.40	<LOD	<LOD	<LOD	<LOD	18.22	85.53
005-21.2b_z1_mag_p2	MIC	Monges	Drill Core	Mag I	<LOD	<LOD	<LOD	<LOD	0.05	67.07	<LOD	0.29	<LOD	<LOD	<LOD	<LOD	18.28	85.78
005-21.2b_z1_mag_p3	MIC	Monges	Drill Core	Mag I	<LOD	0.05	<LOD	<LOD	0.06	67.45	<LOD	0.36	<LOD	<LOD	<LOD	<LOD	18.33	86.30
005-21.2b_z1_mag_p4	MIC	Monges	Drill Core	Mag I	0.06	0.06	0.14	<LOD	0.07	67.29	<LOD	0.11	<LOD	<LOD	<LOD	<LOD	18.36	86.10
005-21.2b_z1_mag_p6	MIC	Monges	Drill Core	Mag I	0.08	0.04	0.05	0.02	0.07	66.67	<LOD	0.48	<LOD	<LOD	<LOD	<LOD	18.20	85.60

Analysis Code	Deposit	Ore body	Sample Type	Magnetite type	Mg	Al	Si	Ca	Ti	Fe	Cr	Mn	Ni	V	Co	Zn	O	Total
005-21.2b_z1_mag_p5	MIC	Monges	Drill Core	Mag I	0.06	0.06	0.07	<LOD	0.06	66.96	<LOD	0.30	<LOD	<LOD	<LOD	<LOD	18.24	85.78
005-21.2b_z1_mag_p7	MIC	Monges	Drill Core	Mag I	<LOD	0.07	0.03	<LOD	0.02	65.88	<LOD	0.42	<LOD	<LOD	<LOD	<LOD	17.89	84.35
005-21.2b_z1_mag_p9	MIC	Monges	Drill Core	Mag I	<LOD	0.03	<LOD	<LOD	0.04	67.96	<LOD	0.40	<LOD	<LOD	<LOD	<LOD	19.00	87.49
005-21.2b_z1_mag_p10	MIC	Monges	Drill Core	Mag I	<LOD	0.07	0.03	<LOD	0.04	68.62	<LOD	0.30	<LOD	<LOD	<LOD	<LOD	18.65	87.78
005-21.2b_z1_mag_p11	MIC	Monges	Drill Core	Mag I	0.13	0.06	0.28	<LOD	0.04	66.99	<LOD	0.10	<LOD	<LOD	<LOD	<LOD	18.42	86.03
005-21.2b_z1_mag_p17	MIC	Monges	Drill Core	Mag I	<LOD	0.04	0.04	0.10	0.03	67.80	<LOD	0.31	<LOD	<LOD	<LOD	<LOD	18.86	87.21
005-21.2b_z1_mag_p15	MIC	Monges	Drill Core	Mag I	<LOD	0.06	0.07	0.06	0.04	68.09	<LOD	0.10	<LOD	<LOD	<LOD	<LOD	18.52	86.95
005-21.2b_z2_mag_p41	MIC	Monges	Drill Core	Mag I	<LOD	0.05	0.05	<LOD	0.08	66.61	<LOD	0.50	<LOD	<LOD	<LOD	<LOD	18.16	85.52
005-21.2b_z2_mag_p47	MIC	Monges	Drill Core	Mag I	0.08	0.07	0.08	<LOD	0.09	66.84	<LOD	0.52	<LOD	<LOD	<LOD	<LOD	18.31	86.04
005-21.2b_z2_mag_p53	MIC	Monges	Drill Core	Mag I	0.06	0.09	0.04	<LOD	0.09	67.86	<LOD	0.51	<LOD	<LOD	<LOD	<LOD	18.54	87.20
005-21.2b_z2_mag_p57	MIC	Monges	Drill Core	Mag I	<LOD	0.11	<LOD	<LOD	0.09	67.84	<LOD	0.56	<LOD	<LOD	<LOD	<LOD	18.52	87.20
005-21.2b_z2_mag_p75	MIC	Monges	Drill Core	Mag I	0.05	0.03	0.10	<LOD	0.07	69.12	<LOD	0.50	<LOD	<LOD	<LOD	<LOD	18.88	88.84
005-21.2b_z2_mag_p77	MIC	Monges	Drill Core	Mag I	0.08	0.03	0.18	<LOD	0.08	68.92	<LOD	0.44	<LOD	<LOD	<LOD	<LOD	18.94	88.72
005-21.2b_z2_mag_p89	MIC	Monges	Drill Core	Mag I	0.06	0.10	0.20	<LOD	0.08	69.61	<LOD	0.18	<LOD	<LOD	<LOD	<LOD	19.08	89.32
005-21.2b_z2_mag_p70	MIC	Monges	Drill Core	Mag I	0.06	0.13	0.03	<LOD	0.09	68.69	<LOD	0.39	<LOD	<LOD	<LOD	<LOD	18.76	88.18
005-21.2b_z2_mag_p80	MIC	Monges	Drill Core	Mag I	0.05	0.12	0.06	<LOD	0.09	68.31	<LOD	0.24	<LOD	<LOD	<LOD	<LOD	18.65	87.58
005-21.2b_z2_mag_p87	MIC	Monges	Drill Core	Mag I	0.22	0.09	0.40	<LOD	0.07	67.67	<LOD	0.51	<LOD	<LOD	<LOD	<LOD	18.98	87.96
005-21.2b_z2_mag_p100	MIC	Monges	Drill Core	Mag I	<LOD	<LOD	0.02	<LOD	0.08	67.55	<LOD	0.43	<LOD	<LOD	<LOD	<LOD	18.32	86.45
005-21.2b_z2_mag_p97	MIC	Monges	Drill Core	Mag I	<LOD	0.03	0.03	<LOD	0.07	67.82	<LOD	0.46	<LOD	<LOD	<LOD	<LOD	18.41	86.85
005-21.2b_z2_mag_p61	MIC	Monges	Drill Core	Mag I	<LOD	0.12	0.03	<LOD	0.09	67.39	<LOD	0.53	<LOD	<LOD	<LOD	<LOD	18.41	86.63
005-21.2b_z2_mag_p91	MIC	Monges	Drill Core	Mag I	0.26	0.18	0.49	<LOD	0.07	68.16	<LOD	0.27	<LOD	<LOD	<LOD	<LOD	19.24	88.69
005-21.2b_z2_mag_p92	MIC	Monges	Drill Core	Mag I	0.14	0.05	0.28	<LOD	0.07	68.54	<LOD	0.15	<LOD	<LOD	<LOD	<LOD	18.89	88.15
005-21.2b_z2_mag_p93	MIC	Monges	Drill Core	Mag I	0.08	0.06	0.10	<LOD	0.07	67.41	<LOD	0.28	<LOD	<LOD	<LOD	<LOD	18.36	86.38

Analysis Code	Deposit	Ore body	Sample Type	Magnetite type	Mg	Al	Si	Ca	Ti	Fe	Cr	Mn	Ni	V	Co	Zn	O	Total
005-21.2b_z2_mag_p94	MIC	Monges	Drill Core	Mag I	<LOD	<LOD	0.02	<LOD	0.07	67.40	<LOD	0.44	<LOD	<LOD	<LOD	<LOD	18.27	86.28
005-17.3a_z2_mag_p1	MIC	Monges	Drill Core	Mag I	0.35	<LOD	0.18	<LOD	0.04	69.45	<LOD	1.17	<LOD	<LOD	<LOD	0.06	19.36	90.63
005-17.3a_z1_mag_p2	MIC	Monges	Drill Core	Mag I	0.57	0.04	0.32	<LOD	0.04	68.72	<LOD	1.18	<LOD	<LOD	<LOD	0.06	19.48	90.44
005-17.3a_z1_mag_p3	MIC	Monges	Drill Core	Mag I	0.18	<LOD	0.03	<LOD	0.04	69.58	<LOD	1.22	<LOD	<LOD	<LOD	0.07	19.11	90.27
005-17.3a_z1_mag_p4	MIC	Monges	Drill Core	Mag I	0.20	<LOD	0.04	<LOD	0.04	69.31	<LOD	1.24	<LOD	<LOD	<LOD	0.07	19.04	89.96
005-17.3a_z2_mag_p5	MIC	Monges	Drill Core	Mag I	0.56	0.05	0.34	<LOD	0.04	68.78	<LOD	1.16	<LOD	<LOD	<LOD	0.07	19.52	90.53
005-17.3a_z2_mag_p6	MIC	Monges	Drill Core	Mag I	0.36	<LOD	0.09	<LOD	0.03	69.69	<LOD	1.21	<LOD	<LOD	<LOD	0.07	19.33	90.80
005-17.3a_z2_mag_p7	MIC	Monges	Drill Core	Mag I	0.61	0.03	0.37	<LOD	0.03	68.57	<LOD	1.16	<LOD	<LOD	<LOD	0.07	19.51	90.38
005-17.3a_z2_mag_p8	MIC	Monges	Drill Core	Mag I	0.27	<LOD	0.04	<LOD	0.04	69.76	<LOD	1.20	<LOD	<LOD	<LOD	0.05	19.24	90.64
005-17.3a_z2_mag_p9	MIC	Monges	Drill Core	Mag I	0.36	<LOD	0.02	<LOD	0.03	69.40	<LOD	1.18	<LOD	<LOD	<LOD	0.06	19.17	90.26
005-17.3a_z2_mag_p10	MIC	Monges	Drill Core	Mag I	0.34	<LOD	0.02	<LOD	0.04	69.63	<LOD	1.11	<LOD	<LOD	<LOD	0.08	19.20	90.44
005-17.3a_z2_mag_p11	MIC	Monges	Drill Core	Mag I	0.27	<LOD	0.02	<LOD	0.04	69.46	<LOD	1.18	<LOD	<LOD	<LOD	0.07	19.14	90.20
005-17.3a_z2_mag_p12	MIC	Monges	Drill Core	Mag I	0.35	<LOD	0.06	<LOD	0.04	69.41	<LOD	1.16	<LOD	<LOD	<LOD	0.08	19.21	90.31
005-17.3a_z2_mag_p13	MIC	Monges	Drill Core	Mag I	0.32	<LOD	0.03	<LOD	0.04	69.63	<LOD	1.14	<LOD	<LOD	<LOD	0.07	19.20	90.45
005-17.3a_z2_mag_p14	MIC	Monges	Drill Core	Mag I	0.37	<LOD	0.12	<LOD	0.04	69.29	<LOD	1.14	<LOD	<LOD	<LOD	0.06	19.26	90.33
005-17.3a_z2_mag_p15	MIC	Monges	Drill Core	Mag I	0.34	<LOD	0.18	<LOD	0.04	68.93	<LOD	1.16	<LOD	<LOD	<LOD	0.07	19.19	89.94
005-17.3a_z1_mag_p1	MIC	Monges	Drill Core	Mag I	0.33	<LOD	0.15	<LOD	0.04	69.48	<LOD	1.09	<LOD	<LOD	<LOD	0.05	19.28	90.44
005-17.3a_z1_mag_p2	MIC	Monges	Drill Core	Mag I	0.29	0.04	0.07	<LOD	0.03	69.86	<LOD	1.10	<LOD	<LOD	<LOD	0.05	19.29	90.74
005-17.3a_z1_mag_p3	MIC	Monges	Drill Core	Mag I	0.26	<LOD	<LOD	0.02	0.04	70.05	<LOD	1.12	<LOD	<LOD	<LOD	0.06	19.26	90.85
005-17.3a_z1_mag_p4	MIC	Monges	Drill Core	Mag I	0.25	<LOD	0.15	<LOD	0.03	69.99	<LOD	1.12	<LOD	<LOD	<LOD	0.06	19.37	91.02
005-17.3a_z1_mag_p5	MIC	Monges	Drill Core	Mag I	0.10	<LOD	0.02	0.02	0.05	70.32	<LOD	1.14	<LOD	<LOD	<LOD	0.06	19.24	90.97
005-17.3a_z1_mag_p6	MIC	Monges	Drill Core	Mag I	0.06	<LOD	0.02	<LOD	0.04	70.21	<LOD	1.06	<LOD	<LOD	<LOD	0.05	19.13	90.61
005-17.3a_z1_mag_p7	MIC	Monges	Drill Core	Mag I	0.13	<LOD	0.16	<LOD	0.04	69.72	<LOD	1.08	<LOD	<LOD	<LOD	0.07	19.23	90.46

Analysis Code	Deposit	Ore body	Sample Type	Magnetite type	Mg	Al	Si	Ca	Ti	Fe	Cr	Mn	Ni	V	Co	Zn	O	Total
005-17.3a_z1_mag_p8	MIC	Monges	Drill Core	Mag I	0.15	0.03	0.02	0.03	0.03	70.50	<LOD	1.17	<LOD	<LOD	<LOD	0.04	19.33	91.31
005-17.3a_z1_mag_p9	MIC	Monges	Drill Core	Mag I	0.20	<LOD	0.13	<LOD	0.03	70.18	<LOD	1.20	<LOD	<LOD	<LOD	0.05	19.39	91.21
005-17.3a_z1_mag_p10	MIC	Monges	Drill Core	Mag I	0.14	<LOD	0.05	<LOD	0.03	70.65	<LOD	1.18	<LOD	<LOD	<LOD	0.06	19.37	91.52
005-17.3a_z1_mag_p11	MIC	Monges	Drill Core	Mag I	0.15	<LOD	<LOD	0.02	0.03	70.64	<LOD	1.15	<LOD	<LOD	<LOD	0.05	19.35	91.42
005-17.3a_z1_mag_p12	MIC	Monges	Drill Core	Mag I	0.24	<LOD	0.02	0.02	0.04	70.06	<LOD	1.16	<LOD	<LOD	<LOD	0.04	19.25	90.87
005-17.3a_z1_mag_p13	MIC	Monges	Drill Core	Mag I	0.19	0.03	0.03	<LOD	0.03	70.14	<LOD	1.24	<LOD	<LOD	<LOD	0.06	19.30	91.05
005-17.3a_z1_mag_p14	MIC	Monges	Drill Core	Mag I	0.28	<LOD	0.08	<LOD	0.03	69.66	<LOD	1.20	<LOD	<LOD	<LOD	0.06	19.27	90.63
005-17.3a_z1_mag_p15	MIC	Monges	Drill Core	Mag I	0.21	<LOD	0.02	<LOD	0.04	69.74	<LOD	1.22	<LOD	<LOD	<LOD	0.05	19.17	90.51
005-17.3a_z1_mag_p16	MIC	Monges	Drill Core	Mag I	0.18	0.04	<LOD	<LOD	0.04	70.03	<LOD	1.22	<LOD	<LOD	<LOD	0.05	19.23	90.79
005-17.3a_z1_mag_p17	MIC	Monges	Drill Core	Mag I	0.24	0.03	0.02	<LOD	0.04	69.55	<LOD	1.20	<LOD	<LOD	<LOD	0.06	19.16	90.34
005-17.3a_z1_mag_p18	MIC	Monges	Drill Core	Mag I	0.19	0.03	0.02	<LOD	0.03	70.49	<LOD	1.14	<LOD	<LOD	<LOD	0.07	19.37	91.40
005-17.3a_z1_mag_p22	MIC	Monges	Drill Core	Mag I	0.29	<LOD	0.02	<LOD	0.04	70.07	<LOD	1.16	<LOD	<LOD	<LOD	0.05	19.30	90.97
005-17.3a_z1_mag_p21	MIC	Monges	Drill Core	Mag I	0.29	<LOD	0.16	<LOD	0.04	69.86	<LOD	1.03	<LOD	<LOD	<LOD	0.06	19.36	90.81
005-17.3a_z1_mag_p20	MIC	Monges	Drill Core	Mag I	0.33	<LOD	0.11	0.03	0.04	69.70	<LOD	1.11	<LOD	<LOD	<LOD	0.04	19.32	90.72
005-17.3a_z1_mag_p19	MIC	Monges	Drill Core	Mag I	0.19	<LOD	<LOD	<LOD	0.04	70.32	<LOD	1.19	<LOD	<LOD	<LOD	0.05	19.28	91.13
004-10.2a_z1_mag_p1	MIC	Monges	Drill Core	Mag II	0.06	<LOD	<LOD	<LOD	0.07	71.29	<LOD	0.03	<LOD	<LOD	<LOD	<LOD	19.15	90.67
004-10.2a_z1_mag_p2	MIC	Monges	Drill Core	Mag II	0.10	<LOD	<LOD	0.03	0.03	71.22	<LOD	0.07	<LOD	<LOD	<LOD	<LOD	19.16	90.65
004-10.2a_z1_mag_p3	MIC	Monges	Drill Core	Mag II	0.15	0.04	<LOD	<LOD	0.03	71.05	<LOD	0.07	<LOD	<LOD	<LOD	<LOD	19.13	90.48
004-10.2a_z1_mag_p4	MIC	Monges	Drill Core	Mag II	<LOD	<LOD	0.02	<LOD	0.07	71.09	<LOD	0.06	<LOD	<LOD	<LOD	<LOD	19.09	90.41
004-10.2a_z1_mag_p5	MIC	Monges	Drill Core	Mag II	0.06	<LOD	<LOD	<LOD	0.07	71.03	<LOD	0.05	<LOD	<LOD	<LOD	<LOD	19.07	90.32
004-10.2a_z1_mag_p6	MIC	Monges	Drill Core	Mag II	0.12	0.04	<LOD	0.02	0.03	71.03	<LOD	0.04	<LOD	<LOD	<LOD	<LOD	19.11	90.41
004-10.2a_z1_mag_p7	MIC	Monges	Drill Core	Mag II	0.14	0.03	<LOD	<LOD	0.02	70.86	<LOD	0.05	<LOD	<LOD	<LOD	<LOD	19.06	90.21
004-10.2a_z1_mag_p8	MIC	Monges	Drill Core	Mag II	<LOD	<LOD	<LOD	0.03	0.08	71.05	<LOD	0.06	<LOD	<LOD	<LOD	<LOD	19.09	90.40

Analysis Code	Deposit	Ore body	Sample Type	Magnetite type	Mg	Al	Si	Ca	Ti	Fe	Cr	Mn	Ni	V	Co	Zn	O	Total
004-10.2a_z1_mag_p9	MIC	Monges	Drill Core	Mag II	0.13	0.04	<LOD	<LOD	0.05	71.23	<LOD	0.06	<LOD	<LOD	<LOD	<LOD	19.22	90.78
004-10.2a_z1_mag_p10	MIC	Monges	Drill Core	Mag II	0.11	0.03	<LOD	0.02	0.02	71.04	<LOD	0.08	<LOD	<LOD	<LOD	<LOD	19.15	90.46
004-10.2a_z1_mag_p11	MIC	Monges	Drill Core	Mag II	0.10	<LOD	<LOD	0.02	0.03	70.83	<LOD	0.05	<LOD	<LOD	<LOD	<LOD	19.12	90.20
004-10.2a_z1_mag_p12	MIC	Monges	Drill Core	Mag II	0.11	0.03	<LOD	<LOD	0.03	71.23	<LOD	0.03	<LOD	<LOD	<LOD	<LOD	19.20	90.70
004-10.2a_z1_mag_p13	MIC	Monges	Drill Core	Mag II	0.12	<LOD	<LOD	0.10	0.02	70.89	<LOD	0.05	<LOD	<LOD	<LOD	<LOD	19.12	90.33
004-10.2a_z1_mag_p14	MIC	Monges	Drill Core	Mag II	0.06	<LOD	<LOD	0.04	0.02	70.98	<LOD	0.06	<LOD	<LOD	<LOD	<LOD	19.03	90.22
004-10.2a_z1_mag_p15	MIC	Monges	Drill Core	Mag II	0.07	<LOD	<LOD	0.04	0.02	70.99	<LOD	0.06	<LOD	<LOD	<LOD	<LOD	19.05	90.26
004-10.2a_z1_mag_p16	MIC	Monges	Drill Core	Mag II	<LOD	<LOD	0.02	0.04	<LOD	71.10	<LOD	0.06	<LOD	<LOD	<LOD	<LOD	19.06	90.37
004-10.2a_z1_mag_p17	MIC	Monges	Drill Core	Mag II	0.07	<LOD	0.03	0.04	0.01	71.10	<LOD	0.05	<LOD	<LOD	<LOD	<LOD	19.15	90.50
004-10.2a_z1_mag_p18	MIC	Monges	Drill Core	Mag II	<LOD	<LOD	<LOD	0.05	0.02	71.24	<LOD	0.05	<LOD	<LOD	<LOD	<LOD	19.20	90.65
005-20.3a_z1_mag_p1	MIC	Monges	Drill Core	Mag II	<LOD	<LOD	0.25	0.02	0.02	70.29	<LOD	0.13	<LOD	<LOD	<LOD	<LOD	19.12	89.86
005-20.3a_z1_mag_p2	MIC	Monges	Drill Core	Mag II	0.07	0.08	0.55	0.14	0.05	67.83	<LOD	0.21	<LOD	<LOD	<LOD	<LOD	18.96	87.90
005-20.3a_z1_mag_p3	MIC	Monges	Drill Core	Mag II	<LOD	0.05	0.06	0.04	0.04	70.56	<LOD	0.22	<LOD	<LOD	<LOD	<LOD	19.07	90.09
005-20.3a_z1_mag_p4	MIC	Monges	Drill Core	Mag II	<LOD	0.06	0.06	0.02	0.04	70.71	<LOD	0.30	<LOD	<LOD	<LOD	<LOD	19.13	90.37
005-20.3a_z1_mag_p5	MIC	Monges	Drill Core	Mag II	<LOD	0.05	0.15	0.02	0.04	70.15	<LOD	0.08	<LOD	<LOD	<LOD	<LOD	19.07	89.60
005-20.3a_z1_mag_p6	MIC	Monges	Drill Core	Mag II	0.88	0.46	1.76	0.10	0.04	63.82	<LOD	0.22	<LOD	<LOD	<LOD	<LOD	20.00	87.28
005-20.3a_z1_mag_p7	MIC	Monges	Drill Core	Mag II	0.28	0.14	0.78	0.08	0.04	67.67	<LOD	0.19	<LOD	<LOD	<LOD	<LOD	19.34	88.57
005-20.3a_z1_mag_p8	MIC	Monges	Drill Core	Mag II	0.69	0.24	0.52	0.07	0.04	67.38	<LOD	0.26	<LOD	<LOD	<LOD	<LOD	19.29	88.48
005-20.3a_z1_mag_p10	MIC	Monges	Drill Core	Mag II	<LOD	0.03	0.07	0.02	0.04	70.72	<LOD	0.30	<LOD	<LOD	<LOD	<LOD	19.13	90.37
005-20.3a_z1_mag_p11	MIC	Monges	Drill Core	Mag II	0.42	0.18	0.59	0.06	0.03	68.08	<LOD	0.15	<LOD	<LOD	<LOD	<LOD	19.32	88.86
005-20.3a_z1_mag_p13	MIC	Monges	Drill Core	Mag II	<LOD	0.03	<LOD	0.02	0.04	70.48	<LOD	0.27	<LOD	<LOD	<LOD	<LOD	18.94	89.81
005-20.3a_z1_mag_p12	MIC	Monges	Drill Core	Mag II	<LOD	0.04	0.02	<LOD	0.05	70.97	<LOD	0.19	<LOD	<LOD	<LOD	<LOD	19.08	90.38
005-20.3a_z1_mag_p14	MIC	Monges	Drill Core	Mag II	<LOD	0.03	0.27	0.03	0.04	69.95	<LOD	0.17	<LOD	<LOD	<LOD	<LOD	19.09	89.63

Analysis Code	Deposit	Ore body	Sample Type	Magnetite type	Mg	Al	Si	Ca	Ti	Fe	Cr	Mn	Ni	V	Co	Zn	O	Total
005-20.3a_z1_mag_p15	MIC	Monges	Drill Core	Mag II	0.17	0.09	0.46	0.30	0.05	64.33	<LOD	0.07	<LOD	<LOD	<LOD	<LOD	17.92	83.40
005-20.3a_z1_mag_p16	MIC	Monges	Drill Core	Mag II	<LOD	<LOD	0.02	0.03	0.04	70.51	<LOD	0.25	<LOD	<LOD	<LOD	<LOD	18.96	89.84
005-20.3a_z1_mag_p17	MIC	Monges	Drill Core	Mag II	<LOD	<LOD	0.34	0.04	0.03	69.91	<LOD	0.21	<LOD	<LOD	<LOD	<LOD	19.15	89.73
005-20.3a_z1_mag_p19	MIC	Monges	Drill Core	Mag II	<LOD	0.03	0.02	0.03	0.04	70.65	<LOD	0.30	<LOD	<LOD	<LOD	<LOD	19.04	90.16
005-31.4b_z1_mag_p1	MIC	Monges	Drill Core	Mag II	0.14	0.04	<LOD	<LOD	0.03	71.52	<LOD	0.08	<LOD	<LOD	<LOD	<LOD	19.28	91.15
005-31.4b_z1_mag_p2	MIC	Monges	Drill Core	Mag II	0.17	0.04	<LOD	<LOD	0.04	71.50	<LOD	0.08	<LOD	<LOD	<LOD	<LOD	19.28	91.19
005-31.4b_z1_mag_p3	MIC	Monges	Drill Core	Mag II	0.19	0.03	<LOD	<LOD	0.03	71.87	<LOD	0.09	<LOD	<LOD	<LOD	<LOD	19.40	91.66
005-31.4b_z1_mag_p5	MIC	Monges	Drill Core	Mag II	0.21	0.03	<LOD	<LOD	0.04	71.52	<LOD	0.08	<LOD	<LOD	<LOD	<LOD	19.30	91.23
005-31.4b_z1_mag_p6	MIC	Monges	Drill Core	Mag II	0.20	0.05	<LOD	<LOD	0.03	71.58	<LOD	0.08	<LOD	<LOD	<LOD	<LOD	19.33	91.32
005-31.4b_z1_mag_p7	MIC	Monges	Drill Core	Mag II	0.22	0.03	<LOD	<LOD	0.04	71.32	<LOD	0.09	<LOD	<LOD	<LOD	<LOD	19.29	91.09
005-31.4b_z1_mag_p8	MIC	Monges	Drill Core	Mag II	0.21	0.03	<LOD	<LOD	0.05	71.06	<LOD	0.08	<LOD	<LOD	<LOD	<LOD	19.19	90.71
005-31.4b_z1_mag_p9	MIC	Monges	Drill Core	Mag II	0.22	0.05	<LOD	<LOD	0.06	71.31	<LOD	0.09	<LOD	<LOD	<LOD	<LOD	19.30	91.13
005-31.4b_z1_mag_p10	MIC	Monges	Drill Core	Mag II	0.23	0.03	0.03	0.02	0.04	71.39	<LOD	0.09	<LOD	<LOD	<LOD	<LOD	19.29	91.15
005-31.4b_z1_mag_p12	MIC	Monges	Drill Core	Mag II	0.11	0.03	<LOD	<LOD	<LOD	71.77	<LOD	0.08	<LOD	<LOD	<LOD	<LOD	19.28	91.32
005-31.4b_z1_mag_p11	MIC	Monges	Drill Core	Mag II	0.17	0.04	<LOD	<LOD	0.02	72.13	<LOD	0.08	<LOD	<LOD	<LOD	<LOD	19.47	91.99
005-31.4b_z1_mag_p13	MIC	Monges	Drill Core	Mag II	0.19	0.04	<LOD	<LOD	0.03	71.46	<LOD	0.08	<LOD	<LOD	<LOD	<LOD	19.27	91.11
005-31.4b_z1_mag_p19	MIC	Monges	Drill Core	Mag II	0.21	0.04	<LOD	<LOD	0.05	71.28	<LOD	0.10	<LOD	0.07	<LOD	<LOD	19.30	91.09
005-31.4b_z1_mag_p18	MIC	Monges	Drill Core	Mag II	0.22	0.05	0.02	<LOD	0.04	71.70	<LOD	0.09	<LOD	<LOD	<LOD	<LOD	19.43	91.64
005-31.4b_z1_mag_p14	MIC	Monges	Drill Core	Mag II	0.20	0.05	0.09	<LOD	0.03	71.39	<LOD	0.11	<LOD	<LOD	<LOD	<LOD	19.36	91.27
005-31.4b_z1_mag_p15	MIC	Monges	Drill Core	Mag II	0.19	0.05	0.02	<LOD	0.03	71.39	<LOD	0.09	<LOD	<LOD	<LOD	<LOD	19.29	91.10
005-31.4b_z1_mag_p16	MIC	Monges	Drill Core	Mag II	0.19	0.04	<LOD	<LOD	0.02	71.71	<LOD	0.09	<LOD	<LOD	<LOD	<LOD	19.35	91.47
005-31.4b_z1_mag_p17	MIC	Monges	Drill Core	Mag II	0.43	0.03	0.44	<LOD	0.02	70.09	<LOD	0.08	<LOD	<LOD	<LOD	<LOD	19.54	90.71
005-31.4b_z1_mag_p20	MIC	Monges	Drill Core	Mag II	0.18	0.05	<LOD	<LOD	0.06	71.31	<LOD	0.07	<LOD	0.08	<LOD	<LOD	19.29	91.09

Analysis Code	Deposit	Ore body	Sample Type	Magnetite type	Mg	Al	Si	Ca	Ti	Fe	Cr	Mn	Ni	V	Co	Zn	O	Total
005-31.4b_z1_mag_p21	MIC	Monges	Drill Core	Mag II	0.25	0.05	<LOD	<LOD	0.05	70.93	<LOD	0.09	<LOD	<LOD	<LOD	<LOD	19.19	90.63
005-31.4b_z1_mag_p22	MIC	Monges	Drill Core	Mag II	0.23	0.06	<LOD	<LOD	0.03	71.45	<LOD	0.08	<LOD	<LOD	<LOD	<LOD	19.30	91.19
005-31.4b_z1_mag_p23	MIC	Monges	Drill Core	Mag II	0.23	0.04	<LOD	<LOD	0.03	71.69	<LOD	0.10	<LOD	<LOD	<LOD	<LOD	19.37	91.51
005-31.4b_z1_mag_p24	MIC	Monges	Drill Core	Mag II	0.17	0.03	<LOD	<LOD	<LOD	71.50	<LOD	0.07	<LOD	<LOD	<LOD	<LOD	19.24	91.04
005-31.4b_z1_mag_p25	MIC	Monges	Drill Core	Mag II	0.19	<LOD	<LOD	<LOD	0.02	71.82	<LOD	0.08	<LOD	<LOD	<LOD	<LOD	19.36	91.57
005-31.4b_z1_mag_p26	MIC	Monges	Drill Core	Mag II	0.22	0.03	<LOD	<LOD	0.03	71.47	<LOD	0.09	<LOD	<LOD	<LOD	<LOD	19.29	91.16
005-31.4b_z1_mag_p27	MIC	Monges	Drill Core	Mag II	0.22	0.03	<LOD	<LOD	0.03	71.92	<LOD	0.09	<LOD	<LOD	<LOD	<LOD	19.42	91.75
005-31.4b_z1_mag_p28	MIC	Monges	Drill Core	Mag II	0.20	0.04	<LOD	<LOD	0.03	71.44	<LOD	0.10	<LOD	<LOD	<LOD	<LOD	19.30	91.17
005-31.4b_z1_mag_p29	MIC	Monges	Drill Core	Mag II	0.19	0.05	<LOD	<LOD	0.03	71.53	<LOD	0.09	<LOD	<LOD	<LOD	<LOD	19.32	91.26
005-31.4b_z1_mag_p30	MIC	Monges	Drill Core	Mag II	0.19	0.05	0.02	<LOD	0.03	71.71	<LOD	0.08	<LOD	<LOD	<LOD	<LOD	19.38	91.52
005-31.4b_z1_mag_p31	MIC	Monges	Drill Core	Mag II	0.24	0.03	<LOD	<LOD	0.03	71.29	<LOD	0.09	<LOD	<LOD	<LOD	<LOD	19.24	90.96
005-31.4b_z1_mag_p32	MIC	Monges	Drill Core	Mag II	0.23	0.03	<LOD	<LOD	0.03	72.08	<LOD	0.08	<LOD	<LOD	<LOD	<LOD	19.49	92.00
005-31.4b_z1_mag_p33	MIC	Monges	Drill Core	Mag II	0.23	<LOD	<LOD	<LOD	<LOD	72.25	<LOD	0.08	<LOD	<LOD	<LOD	<LOD	19.48	92.07
004-12.3b_z1_mag_p1	MIC	Monges	Drill Core	Mag II	0.25	<LOD	<LOD	0.05	<LOD	70.97	<LOD	0.58	<LOD	<LOD	<LOD	<LOD	19.27	91.17
004-12.3b_z1_mag_p2	MIC	Monges	Drill Core	Mag II	0.19	<LOD	<LOD	0.03	<LOD	71.44	<LOD	0.62	<LOD	<LOD	<LOD	<LOD	19.36	91.67
004-12.3b_z1_mag_p3	MIC	Monges	Drill Core	Mag II	0.15	<LOD	<LOD	0.05	0.01	71.05	<LOD	0.57	<LOD	<LOD	<LOD	<LOD	19.26	91.12
004-12.3b_z1_mag_p4	MIC	Monges	Drill Core	Mag II	0.18	<LOD	<LOD	0.06	<LOD	71.47	<LOD	0.60	<LOD	<LOD	<LOD	<LOD	19.41	91.76
004-12.3b_z1_mag_p5	MIC	Monges	Drill Core	Mag II	0.21	<LOD	<LOD	0.02	<LOD	70.93	<LOD	0.61	<LOD	<LOD	<LOD	<LOD	19.26	91.10
004-12.3b_z1_mag_p6	MIC	Monges	Drill Core	Mag II	0.25	<LOD	<LOD	<LOD	0.03	70.91	<LOD	0.61	<LOD	<LOD	<LOD	<LOD	19.30	91.17
004-12.3b_z1_mag_p7	MIC	Monges	Drill Core	Mag II	0.22	<LOD	<LOD	<LOD	0.03	71.46	<LOD	0.62	<LOD	<LOD	<LOD	<LOD	19.41	91.78
004-12.3b_z1_mag_p8	MIC	Monges	Drill Core	Mag II	0.22	<LOD	<LOD	<LOD	0.04	70.60	<LOD	0.60	<LOD	<LOD	<LOD	<LOD	19.18	90.70
004-12.3b_z1_mag_p9	MIC	Monges	Drill Core	Mag II	0.21	<LOD	<LOD	0.03	0.01	70.92	<LOD	0.60	<LOD	<LOD	<LOD	<LOD	19.23	91.01
004-12.3b_z1_mag_p11	MIC	Monges	Drill Core	Mag II	0.30	<LOD	<LOD	<LOD	0.03	70.81	<LOD	0.58	<LOD	<LOD	<LOD	<LOD	19.27	91.03

Analysis Code	Deposit	Ore body	Sample Type	Magnetite type	Mg	Al	Si	Ca	Ti	Fe	Cr	Mn	Ni	V	Co	Zn	O	Total
004-12.3b_z1_mag_p12	MIC	Monges	Drill Core	Mag II	0.24	<LOD	<LOD	<LOD	0.03	71.18	<LOD	0.62	<LOD	<LOD	<LOD	<LOD	19.38	91.54
004-12.3b_z1_mag_p13	MIC	Monges	Drill Core	Mag II	0.28	0.03	<LOD	<LOD	0.02	71.14	<LOD	0.61	<LOD	<LOD	<LOD	<LOD	19.36	91.46
004-12.3b_z1_mag_p14	MIC	Monges	Drill Core	Mag II	0.22	<LOD	<LOD	<LOD	0.04	71.04	<LOD	0.59	<LOD	<LOD	<LOD	<LOD	19.33	91.29
004-12.3b_z1_mag_p15	MIC	Monges	Drill Core	Mag II	0.30	<LOD	<LOD	<LOD	0.04	71.23	<LOD	0.59	<LOD	<LOD	<LOD	<LOD	19.41	91.63
004-12.3b_z1_mag_p16	MIC	Monges	Drill Core	Mag II	0.25	<LOD	<LOD	<LOD	0.02	71.55	<LOD	0.57	<LOD	<LOD	<LOD	<LOD	19.44	91.87
004-12.3b_z1_mag_p17	MIC	Monges	Drill Core	Mag II	0.22	<LOD	<LOD	0.02	0.01	71.06	<LOD	0.62	<LOD	<LOD	<LOD	<LOD	19.29	91.25
004-12.3b_z1_mag_p18	MIC	Monges	Drill Core	Mag II	0.19	<LOD	<LOD	0.09	<LOD	71.45	<LOD	0.61	<LOD	<LOD	<LOD	<LOD	19.44	91.83
004-12.3b_z1_mag_p19	MIC	Monges	Drill Core	Mag II	0.15	<LOD	<LOD	0.02	<LOD	71.66	<LOD	0.42	<LOD	<LOD	<LOD	<LOD	19.37	91.69
004-12.3b_z1_mag_p20	MIC	Monges	Drill Core	Mag II	0.23	<LOD	<LOD	0.12	0.02	71.22	<LOD	0.59	<LOD	<LOD	<LOD	<LOD	19.39	91.60
004-12.3b_z1_mag_p21	MIC	Monges	Drill Core	Mag II	0.31	<LOD	<LOD	<LOD	0.04	70.91	<LOD	0.61	<LOD	<LOD	<LOD	<LOD	19.34	91.28
004-12.3b_z1_mag_p22	MIC	Monges	Drill Core	Mag II	0.22	<LOD	<LOD	<LOD	0.02	71.32	<LOD	0.56	<LOD	<LOD	<LOD	<LOD	19.35	91.52
004-12.3b_z1_mag_p23	MIC	Monges	Drill Core	Mag II	0.21	<LOD	<LOD	0.03	<LOD	71.11	<LOD	0.61	<LOD	<LOD	<LOD	<LOD	19.29	91.28
004-12.3b_z1_mag_p24	MIC	Monges	Drill Core	Mag II	0.29	<LOD	<LOD	<LOD	0.02	71.36	<LOD	0.54	<LOD	<LOD	<LOD	<LOD	19.40	91.69
004-12.3b_z1_mag_p25	MIC	Monges	Drill Core	Mag II	0.24	<LOD	<LOD	<LOD	0.03	71.09	<LOD	0.60	<LOD	<LOD	<LOD	<LOD	19.33	91.35
004-12.3b_z1_mag_p26	MIC	Monges	Drill Core	Mag II	0.29	<LOD	0.02	0.02	0.02	71.27	<LOD	0.60	<LOD	<LOD	<LOD	<LOD	19.44	91.73
004-12.3b_z1_mag_p27	MIC	Monges	Drill Core	Mag II	0.29	<LOD	<LOD	<LOD	0.02	71.29	<LOD	0.58	<LOD	<LOD	<LOD	0.03	19.40	91.64
004-12.3b_z1_mag_p28	MIC	Monges	Drill Core	Mag II	0.29	<LOD	<LOD	0.02	<LOD	71.29	<LOD	0.55	<LOD	<LOD	<LOD	<LOD	19.40	91.59
004-12.3b_z1_mag_p29	MIC	Monges	Drill Core	Mag II	0.26	0.03	<LOD	<LOD	0.01	71.11	<LOD	0.56	<LOD	<LOD	<LOD	<LOD	19.36	91.39
004-12.3b_z1_mag_p30	MIC	Monges	Drill Core	Mag II	0.23	<LOD	<LOD	0.51	<LOD	70.34	<LOD	0.44	<LOD	<LOD	<LOD	<LOD	19.25	90.82
004-12.3b_z1_mag_p31	MIC	Monges	Drill Core	Mag II	0.28	<LOD	<LOD	<LOD	0.01	71.22	<LOD	0.58	<LOD	<LOD	<LOD	<LOD	19.39	91.54
004-12.3b_z1_mag_p32	MIC	Monges	Drill Core	Mag II	0.26	<LOD	<LOD	<LOD	0.02	71.29	<LOD	0.56	<LOD	<LOD	<LOD	<LOD	19.39	91.59
004-12.3b_z1_mag_p33	MIC	Monges	Drill Core	Mag II	0.26	<LOD	<LOD	<LOD	<LOD	70.86	<LOD	0.56	<LOD	<LOD	<LOD	<LOD	19.27	91.04
004-12.3b_z1_mag_p34	MIC	Monges	Drill Core	Mag II	0.27	<LOD	<LOD	<LOD	<LOD	70.75	<LOD	0.56	<LOD	<LOD	<LOD	<LOD	19.22	90.85

Analysis Code	Deposit	Ore body	Sample Type	Magnetite type	Mg	Al	Si	Ca	Ti	Fe	Cr	Mn	Ni	V	Co	Zn	O	Total
004-12.3b_z1_mag_p35	MIC	Monges	Drill Core	Mag II	0.17	<LOD	<LOD	0.02	0.01	71.05	<LOD	0.59	<LOD	<LOD	<LOD	<LOD	19.28	91.20
004-12.3b_z1_mag_p36	MIC	Monges	Drill Core	Mag II	0.22	<LOD	<LOD	<LOD	<LOD	71.30	<LOD	0.58	<LOD	<LOD	<LOD	<LOD	19.33	91.48
004-12.3b_z1_mag_p37	MIC	Monges	Drill Core	Mag II	0.17	<LOD	<LOD	<LOD	0.02	70.99	<LOD	0.58	<LOD	<LOD	<LOD	<LOD	19.26	91.10
004-12.3b_z1_mag_p38	MIC	Monges	Drill Core	Mag II	0.24	<LOD	<LOD	<LOD	<LOD	70.99	<LOD	0.58	<LOD	<LOD	<LOD	<LOD	19.27	91.14
004-12.3b_z1_mag_p39	MIC	Monges	Drill Core	Mag II	0.17	<LOD	0.02	0.04	<LOD	71.26	<LOD	0.59	<LOD	<LOD	<LOD	<LOD	19.34	91.45
004-12.3b_z1_mag_p40	MIC	Monges	Drill Core	Mag II	0.20	<LOD	<LOD	0.03	<LOD	71.45	<LOD	0.58	<LOD	<LOD	<LOD	<LOD	19.39	91.70
004-12.3b_z1_mag_p41	MIC	Monges	Drill Core	Mag II	0.21	<LOD	<LOD	0.02	<LOD	71.47	<LOD	0.55	<LOD	<LOD	<LOD	<LOD	19.39	91.70
004-12.3b_z1_mag_p42	MIC	Monges	Drill Core	Mag II	0.23	<LOD	0.03	0.02	<LOD	71.53	<LOD	0.53	<LOD	<LOD	<LOD	<LOD	19.43	91.79
004-12.3b_z1_mag_p43	MIC	Monges	Drill Core	Mag II	0.23	<LOD	<LOD	<LOD	<LOD	71.22	<LOD	0.58	<LOD	<LOD	<LOD	<LOD	19.33	91.40
004-12.3b_z1_mag_p44	MIC	Monges	Drill Core	Mag II	0.22	<LOD	<LOD	0.05	<LOD	71.08	<LOD	0.56	<LOD	<LOD	<LOD	<LOD	19.28	91.23
004-12.3b_z1_mag_p45	MIC	Monges	Drill Core	Mag II	0.15	<LOD	<LOD	0.09	<LOD	71.47	<LOD	0.55	<LOD	<LOD	<LOD	<LOD	19.38	91.70
004-12.3b_z1_mag_p52	MIC	Monges	Drill Core	Mag II	0.19	<LOD	<LOD	0.06	<LOD	71.27	<LOD	0.54	<LOD	<LOD	<LOD	<LOD	19.35	91.44
004-12.3b_z1_mag_p46	MIC	Monges	Drill Core	Mag II	0.18	<LOD	<LOD	0.12	<LOD	71.43	<LOD	0.42	<LOD	<LOD	<LOD	<LOD	19.35	91.54
004-12.3b_z1_mag_p47	MIC	Monges	Drill Core	Mag II	0.15	<LOD	0.04	0.05	<LOD	71.29	<LOD	0.49	<LOD	<LOD	<LOD	<LOD	19.37	91.46
004-12.3b_z1_mag_p48	MIC	Monges	Drill Core	Mag II	0.23	<LOD	<LOD	0.08	<LOD	71.21	<LOD	0.59	<LOD	<LOD	<LOD	<LOD	19.38	91.55
004-12.3b_z1_mag_p49	MIC	Monges	Drill Core	Mag II	0.16	<LOD	<LOD	1.01	<LOD	69.76	<LOD	0.47	<LOD	<LOD	<LOD	0.10	19.31	90.86
004-12.3b_z1_mag_p50	MIC	Monges	Drill Core	Mag II	0.23	<LOD	<LOD	0.03	<LOD	71.40	<LOD	0.60	<LOD	<LOD	<LOD	<LOD	19.40	91.69
004-12.3b_z1_mag_p51	MIC	Monges	Drill Core	Mag II	0.20	<LOD	<LOD	0.07	0.02	71.31	<LOD	0.61	<LOD	<LOD	<LOD	<LOD	19.42	91.69
004-12.3b_z1_mag_p53	MIC	Monges	Drill Core	Mag II	0.21	<LOD	<LOD	0.03	<LOD	71.26	<LOD	0.60	<LOD	<LOD	<LOD	<LOD	19.36	91.52
004-12.3b_z1_mag_p54	MIC	Monges	Drill Core	Mag II	0.18	<LOD	<LOD	0.10	<LOD	70.95	<LOD	0.61	<LOD	<LOD	<LOD	<LOD	19.30	91.18
MV3_z1_mag_p1	MIC	Vale da Arca	Outcrop	Mag I	0.12	<LOD	<LOD	0.02	<LOD	71.09	<LOD	0.60	0.13	<LOD	<LOD	<LOD	19.26	91.25
MV3_z1_mag_p2	MIC	Vale da Arca	Outcrop	Mag I	0.13	<LOD	0.07	0.07	<LOD	70.65	<LOD	0.55	<LOD	<LOD	<LOD	<LOD	19.21	90.74
MV3_z1_mag_p4	MIC	Vale da Arca	Outcrop	Mag I	0.21	<LOD	0.21	0.04	0.03	70.60	<LOD	0.63	<LOD	<LOD	<LOD	<LOD	19.42	91.18

Analysis Code	Deposit	Ore body	Sample Type	Magnetite type	Mg	Al	Si	Ca	Ti	Fe	Cr	Mn	Ni	V	Co	Zn	O	Total
MV3_z1_mag_p5	MIC	Vale da Arca	Outcrop	Mag I	0.19	<LOD	0.20	0.04	0.02	70.49	<LOD	0.62	<LOD	<LOD	<LOD	<LOD	19.37	90.97
MV3_z1_mag_p3	MIC	Vale da Arca	Outcrop	Mag I	0.18	<LOD	<LOD	0.03	<LOD	70.22	<LOD	0.60	<LOD	<LOD	<LOD	<LOD	19.07	90.19
MV3_z1_mag_p7	MIC	Vale da Arca	Outcrop	Mag I	0.18	<LOD	<LOD	0.04	0.02	70.22	<LOD	0.58	0.14	<LOD	<LOD	<LOD	19.06	90.25
MV3_z1_mag_p6	MIC	Vale da Arca	Outcrop	Mag I	0.14	<LOD	<LOD	<LOD	0.02	70.95	<LOD	0.61	0.11	<LOD	<LOD	<LOD	19.24	91.11
MV3_z1_mag_p8	MIC	Vale da Arca	Outcrop	Mag I	0.11	<LOD	0.03	0.02	0.02	70.97	<LOD	0.63	<LOD	<LOD	<LOD	<LOD	19.25	91.06
MV3_z1_mag_p9	MIC	Vale da Arca	Outcrop	Mag I	0.15	<LOD	<LOD	0.03	<LOD	70.87	<LOD	0.62	0.12	<LOD	<LOD	<LOD	19.23	91.05
MV3_z1_mag_p10	MIC	Vale da Arca	Outcrop	Mag I	0.20	<LOD	0.16	0.05	0.01	70.67	<LOD	0.73	<LOD	<LOD	<LOD	<LOD	19.42	91.30
MV3_z1_mag_p11	MIC	Vale da Arca	Outcrop	Mag I	0.20	<LOD	0.13	<LOD	<LOD	70.95	<LOD	0.69	<LOD	<LOD	<LOD	<LOD	19.45	91.50
MV3_z1_mag_p12	MIC	Vale da Arca	Outcrop	Mag I	0.22	<LOD	0.12	0.02	0.02	70.94	<LOD	0.64	<LOD	<LOD	<LOD	<LOD	19.41	91.39
MV3_z1_mag_p13	MIC	Vale da Arca	Outcrop	Mag I	0.18	<LOD	<LOD	<LOD	0.01	71.01	<LOD	0.65	<LOD	<LOD	<LOD	<LOD	19.29	91.21
MV3_z1_mag_p14	MIC	Vale da Arca	Outcrop	Mag I	0.17	<LOD	<LOD	0.02	<LOD	71.04	<LOD	0.65	<LOD	<LOD	<LOD	<LOD	19.27	91.20
MV3_z1_mag_p15	MIC	Vale da Arca	Outcrop	Mag I	0.16	<LOD	0.03	<LOD	0.01	70.99	<LOD	0.67	<LOD	<LOD	<LOD	<LOD	19.27	91.17
MV3_z1_mag_p16	MIC	Vale da Arca	Outcrop	Mag I	0.17	<LOD	0.03	<LOD	<LOD	70.91	<LOD	0.62	<LOD	<LOD	<LOD	<LOD	19.26	91.04
MV3_z1_mag_p17	MIC	Vale da Arca	Outcrop	Mag I	0.15	<LOD	0.03	<LOD	<LOD	70.68	<LOD	0.61	<LOD	<LOD	<LOD	<LOD	19.20	90.77
MV3_z1_mag_p18	MIC	Vale da Arca	Outcrop	Mag I	0.17	<LOD	0.03	<LOD	<LOD	70.66	<LOD	0.65	<LOD	<LOD	<LOD	<LOD	19.22	90.84
MV3_z1_mag_p19	MIC	Vale da Arca	Outcrop	Mag I	0.15	<LOD	<LOD	<LOD	<LOD	70.84	<LOD	0.63	0.16	<LOD	<LOD	<LOD	19.24	91.06

Appendix E-2.

Complete results of EPMA silicates and magnetite from the Alvito deposit

Appendix E-2.1. – EPMA results of silicates from the Alvito area - EPMA results for plagioclase and alkali feldspars

Sample	**AL 9**													
Analysis Ref.	Z1 P1	Z1 P2	Z1 P3	Z1 P4	Z1 P5	Z1 P6	Z1 P7	Z2 P1	Z2 P2	Z2 P3	Z2 P4	Z2 P5	Z2 P6	Z2 P7
Element (wt. %)														
SiO_2	63.06	61.15	59.83	61.25	63.93	63.55	64.99	61.76	61.35	63.13	62.74	61.97	63.19	61.17
TiO_2	0.00	0.00	0.00	0.00	0.00	0.00	0.00	0.00	0.00	0.00	0.00	0.00	0.00	0.00
Al_2O_3	23.38	24.81	25.77	24.07	22.84	18.47	19.20	24.42	24.68	23.17	24.08	23.89	23.38	24.30
FeO	0.06	0.06	0.00	0.06	0.00	0.05	0.00	0.00	0.06	0.00	0.06	0.06	0.00	0.00
CaO	3.79	5.40	6.68	5.37	3.49	0.03	0.11	5.05	5.05	3.71	4.36	4.51	3.87	5.31
Na_2O	9.03	7.75	7.47	8.10	8.92	0.61	4.70	8.40	8.05	9.13	8.81	8.97	9.40	8.29
K_2O	0.38	0.46	0.23	0.43	0.46	16.11	10.24	0.50	0.46	0.34	0.39	0.16	0.27	0.46
BaO	0.00	0.00	0.00	0.00	0.00	0.41	0.49	0.00	0.00	0.00	0.00	0.00	0.00	0.00
Total	99.70	99.62	99.99	99.27	99.63	99.25	99.73	100.13	99.65	99.49	100.44	99.55	100.11	99.53
Formula (32O)														
Si	11.18	10.88	10.65	10.95	11.31	11.90	11.86	10.94	10.91	11.21	11.06	11.02	11.16	10.91
Ti														
Al	4.88	5.20	5.41	5.07	4.76	4.08	4.13	5.10	5.17	4.85	5.00	5.01	4.87	5.11
Fe(ii)	0.01	0.01		0.01		0.01			0.01	0.01	0.01	0.01	0.01	
Ca	0.72	1.03	1.27	1.03	0.66	0.01	0.02	0.96	0.96	0.71	0.82	0.86	0.73	1.01
Na	3.10	2.67	2.58	2.81	3.06	0.22	1.66	2.89	2.78	3.14	3.01	3.09	3.22	2.87
K	0.09	0.10	0.05	0.10	0.10	3.85	2.38	0.11	0.10	0.08	0.09	0.04	0.06	0.10
Ba						0.03	0.04							
Total	19.98	19.90	19.96	19.96	19.89	20.09	20.10	20.01	19.94	19.98	19.99	20.03	20.04	20.02
An (%)	18.43	27.03	32.63	26.16	17.31	0.17	0.51	24.21	25.03	17.98	21.00	21.54	18.27	25.44
Ab (%)	79.39	70.23	66.02	71.36	80.00	5.41	40.89	72.95	72.24	80.03	76.76	77.58	80.20	71.93
Or (%)	2.18	2.74	1.36	2.49	2.69	94.42	58.60	2.84	2.73	1.99	2.24	0.88	1.52	2.63

Appendix E-2.1. – EPMA results of silicates from the Alvito area - EPMA results for plagioclase and alkali feldspars

Sample	AL 14							AL 17				
Analysis Ref.	Z1 P1	Z1 P2	Z1 P3	Z1 P4	Z1 P5	Z1 P6	Z1 P7	Z2 P1	Z2 P2	Z2 P3	Z2 P4	Z2 P5
Element (wt. %)												
SiO_2	57.61	56.99	58.36	57.42	56.43	57.10	57.60	60.10	58.84	58.76	61.29	58.88
TiO_2	0.03			0.03	0.04	0.03	0.05				0.07	
Al_2O_3	26.68	27.31	26.72	26.92	27.55	27.24	26.88	25.80	26.66	26.44	24.06	26.00
FeO	0.16	0.17	0.14	0.18	0.11	0.27	0.16	0.06		0.10	0.06	0.12
CaO	8.19	8.26	8.16	7.73	8.46	8.26	7.92	6.88	7.77	7.48	5.08	7.54
Na_2O	6.58	6.47	6.42	6.73	6.45	6.54	6.61	7.29	6.72	6.81	6.44	7.01
K_2O	0.33	0.39	0.35	0.45	0.22	0.36	0.33	0.37	0.31	0.36	3.22	0.33
BaO												
Total	99.58	99.60	100.14	99.45	99.25	99.81	99.55	100.50	100.30	99.95	100.21	99.88
Formula (32O)												
Si	10.36	10.26	10.42	10.34	10.19	10.26	10.35	10.65	10.47	10.49	10.96	10.53
Ti												
Al	5.65	5.79	5.62	5.71	5.86	5.77	5.69	5.39	5.59	5.56	5.07	5.48
Fe(ii)	0.02	0.03	0.02	0.03	0.02	0.04	0.02	0.01	0.00	0.02	0.01	0.02
Ca	1.58	1.59	1.56	1.49	1.64	1.59	1.52	1.31	1.48	1.43	0.97	1.44
Na	2.29	2.26	2.22	2.35	2.26	2.28	2.30	2.50	2.32	2.36	2.23	2.43
K	0.08	0.09	0.08	0.10	0.05	0.08	0.08	0.08	0.07	0.08	0.73	0.08
Ba												
Total	19.99	20.02	19.92	20.03	20.02	20.03	19.98	19.95	19.93	19.94	19.98	19.98
An (%)	39.98	40.41	40.41	37.82	41.48	40.25	39.04	33.55	38.26	36.95	24.70	36.57
Ab (%)	58.09	57.30	57.54	59.58	57.22	57.65	59.02	64.30	59.93	60.92	56.68	61.52
Or (%)	1.93	2.29	2.05	2.60	1.30	2.10	1.94	2.15	1.81	2.13	18.63	1.91

Appendix E-2.1. – EPMA results of silicates from the Alvito area - EPMA results for amphiboles (Diorites – CAGD)

Sample	AL 17													
Analysis Ref.	Z1 P6	Z1 P7	Z1 P8	Z1 P9	Z2 P1	Z2 P2	Z2 P3	Z2 P4	Z2 P5	Z2 P6	Z2 P7	Z2 P8	Z2 P9	Z2 P10
Element (wt. %)														
SiO_2	47.5408	48.9674	48.4112	48.1908	48.1527	48.0637	48.7291	48.0651	47.4626	47.5161	47.6513	47.0436	49.1527	48.4642
Al_2O_3	6.2076	5.567	6.3501	6.1975	5.7546	6.0075	5.3881	5.9045	6.5449	6.1014	6.276	6.2752	5.4395	5.5888
MnO	0.3484	0.3635	0.3046	0.3326	0.3041	0.239	0.2902	0.2724	0.3739	0.3417	0.2976	0.3416	0.2571	0.2909
FeO	16.5363	16.4711	15.6544	16.5251	16.7728	16.0861	16.1509	16.6592	16.5677	16.9135	16.6515	16.5872	15.7603	16.0617
MgO	11.3771	11.5929	10.8448	11.3056	11.1335	11.6418	11.8817	11.4192	10.9594	10.7492	10.7839	11.1037	11.5886	11.5797
CaO	11.2434	11.0279	11.1444	11.1886	11.1412	11.6448	11.4553	11.2993	11.1977	11.3388	11.226	11.1536	11.4689	11.2916
Na_2O	0.9307	0.9533	0.7179	0.9208	0.8825	0.6479	0.7724	0.8691	0.8664	0.7621	0.9101	0.9131	0.4658	0.7414
K_2O	0.5705	0.4100	0.5293	0.5219	0.5062	0.5389	0.4900	0.5012	0.6036	0.5686	0.5566	0.5186	0.4160	0.5166
Total	94.7548	95.3531	93.9567	95.1829	94.6476	94.8697	95.1577	94.99	94.5762	94.2914	94.353	93.9366	94.5489	94.5349
T														
Si	7.229	7.364	7.382	7.281	7.327	7.281	7.352	7.284	7.234	7.281	7.286	7.22	7.436	7.357
Al	0.771	0.636	0.618	0.719	0.673	0.719	0.648	0.716	0.766	0.719	0.714	0.78	0.564	0.643
T (total)	8	8	8	8	8	8	8	8	8	8	8	8	8	8
C														
Al	0.342	0.351	0.524	0.385	0.359	0.354	0.31	0.339	0.409	0.383	0.417	0.355	0.406	0.357
Fe^{3+}	0.242	0.238	0.087	0.217	0.205	0.188	0.2	0.227	0.208	0.176	0.153	0.243	0.129	0.188
Mn^{2+}			0.015											
Fe^{2+}	1.837	1.812	1.909	1.852	1.91	1.829	1.817	1.855	1.893	1.986	1.972	1.86	1.851	1.835
Mg	2.579	2.599	2.465	2.546	2.526	2.629	2.672	2.58	2.49	2.455	2.458	2.541	2.614	2.62
C (total)	5	5	5	5	5	5	4.999	5.001	5	5	5	4.999	5	5
B														
Mn^{2+}	0.045	0.046	0.025	0.043	0.039	0.031	0.037	0.035	0.048	0.044	0.039	0.044	0.033	0.037
Fe^{2+}	0.024	0.022		0.019	0.019	0.021	0.02	0.03	0.011	0.006	0.005	0.025	0.014	0.016
Ca	1.832	1.777	1.821	1.811	1.816	1.89	1.852	1.835	1.829	1.862	1.839	1.834	1.859	1.837
Na	0.099	0.155	0.154	0.127	0.125	0.059	0.091	0.101	0.112	0.088	0.117	0.096	0.094	0.11
B (total)	2	2	2	2	1.999	2.001	2	2.001	2	2	2	1.999	2	2
A														
Na	0.175	0.123	0.058	0.143	0.135	0.132	0.135	0.155	0.144	0.138	0.152	0.175	0.042	0.108
K	0.111	0.079	0.103	0.101	0.098	0.104	0.094	0.097	0.117	0.111	0.109	0.102	0.08	0.1

A (total)	0.286	0.202	0.161	0.244	0.233	0.236	0.229	0.252	0.261	0.249	0.261	0.277	0.122	0.208

Appendix E-2.1. – EPMA results of silicates from the Alvito area - EPMA results for pyroxene (exoskarn)

Sample	**AL 19**												
Analysis Ref.	Z1 P1	Z1 P2	Z1 P3	Z1 P4	Z1 P5	Z1 P6	Z1 P7	Z1 P8	Z1 P9	Z1 P10	Z1 P11	Z1 P12	Z1 P13
Element (wt. %)													
SiO_2	47.57	55.22	55.44	54.25	46.93	54.69	55.29	45.90	54.45	47.48	47.43	47.64	47.48
TiO_2		0.13	0.20	0.26		0.09	0.12		0.03				
Al_2O_3	3.45	0.45	0.66	0.55	3.87	0.14	0.11	4.45	0.71	3.59	3.10	2.73	3.36
FeO	16.11	0.93	2.34	1.19	18.83	0.84	1.04	19.87	1.61	18.16	18.52	18.80	19.15
MnO	0.38	0.38	0.56	0.60	0.30	0.49	0.51	0.34	0.52	0.33	0.35	0.31	0.33
MgO	6.72	17.13	15.78	16.90	5.03	17.25	17.34	4.11	16.28	5.34	5.44	5.37	5.48
CaO	22.90	25.35	25.05	25.46	22.66	25.43	25.31	22.65	25.34	22.40	22.40	22.46	22.53
Na_2O	0.08		0.05		0.15			0.08		0.14	0.10	0.18	0.14
Total	97.21	99.59	100.07	99.19	97.76	98.92	99.72	97.39	98.94	97.43	97.34	97.50	98.45
Formula (6O)													
Si	1.91	2.01	2.01	1.99	1.89	2.00	2.01	1.87	2.00	1.91	1.92	1.93	1.90
Al	0.09	0.00	-0.01	0.01	0.11	0.00	-0.01	0.13	0.00	0.09	0.08	0.07	0.10
Al	0.07	0.02	0.04	0.01	0.08	0.01	0.01	0.09	0.03	0.08	0.07	0.06	0.06
Fe(iii)	0.04				0.06			0.07		0.02	0.03	0.05	0.06
Ti	0.00	0.00	0.01	0.01		0.00	0.00	0.00	0.00				0.00
Fe(ii)	0.50	0.03	0.07	0.04	0.58	0.03	0.03	0.60	0.05	0.59	0.59	0.59	0.57
Mn	0.01	0.01	0.02	0.02	0.01	0.02	0.02	0.01	0.02	0.01	0.01	0.01	0.01
Mg	0.40	0.93	0.85	0.92	0.30	0.94	0.94	0.25	0.89	0.32	0.33	0.32	0.33
Ca	0.98	0.99	0.97	1.00	0.98	1.00	0.98	0.99	1.00	0.97	0.97	0.97	0.97
Na	0.01	0.00	0.00		0.01			0.01		0.01	0.01	0.01	0.01
Total	4.01	3.99	3.97	3.99	4.02	3.99	3.99	4.02	3.98	4.01	4.01	4.01	4.02

Appendix E-2.1. – EPMA results of silicates from the Alvito area - EPMA results for chlorite (diorite - CAGD)

Sample	AL 14		
Analysis Ref.	Z1 P8	Z1 P9	Z1 P10
Element (wt. %)			
SiO_2	26.8760	26.4089	25.3515
TiO_2	0.1641	0.0608	0.0573
Al_2O_3	18.1520	18.2499	19.3486
FeO	27.2774	27.4028	25.8884
MnO	0.3004	0.3114	0.3286
MgO	12.9969	12.5758	12.3510
CaO	0.1019	0.1073	0.1194
Na_2O	0.0723	0.0668	0.0176
K_2O	0.0327	0.0348	0.0234
Total	85.9737	85.2185	83.4858
Z			
Si	2.93	2.93	2.86
Al^{IV}	1.07	1.07	1.14
Total (IV)	4.00	4.00	4.00
R			
Al^{VI}	1.32	1.32	1.42
Ti	0.00	0.00	0.00
Cr	0.00	0.00	0.00
Fe^{3+}	0.00	0.00	0.00
Fe^{2+}	2.54	2.54	2.39
Mn	0.00	0.00	0.00
Mg	2.02	2.02	2.05
Total (VI)	5.88	5.88	5.86
Total	9.88	9.88	9.86
Fe/(Fe + Mg)	0.56	0.56	0.54
Mg + Fe	4.56	4.56	4.44
Mg/(Mg+Fe)	0.44	0.44	0.46
Al-chl (%)	20.33	20.33	21.86
Fe-chl (%)	45.38	45.38	43.22
Mg-chl (%)	34.29	34.29	34.92

Appendix E-2.1. – EPMA results of silicates from the Alvito area - EPMA results for vesuvianite (calcsilicate nodules)

Sample	**AL 19**										
Analysis Ref.	Z1 P1	Z1 P2	Z1 P3	Z1 P4	Z1 P5	Z1 P6	Z1 P7	Z1 P8	Z1 P9	Z1 P10	Z1 P11
Element (wt. %)											
SiO_2	38.09	37.61	38.13	37.74	38.47	37.82	37.57	37.94	38.28	37.57	38.08
TiO_2	0.01	0.03	0.00	0.17	0.25	0.15	0.05	0.07	0.27	0.09	0.10
Al_2O_3	27.11	27.24	27.95	27.24	27.73	26.82	27.63	25.97	27.47	25.93	26.36
FeO	8.18	8.12	7.43	7.61	7.26	8.65	7.89	8.35	6.90	8.62	8.62
MnO	0.33	0.42	0.42	0.04	0.06	0.06	0.34	0.06	0.07	0.06	0.06
MgO	0.08	0.07	0.16	0.18	0.16	0.06	0.13	0.00	0.21	0.08	0.00
CaO	22.65	22.90	22.58	23.75	23.38	23.38	22.66	23.37	23.50	23.13	23.17
Total	96.46	96.39	96.68	96.73	97.31	96.94	96.28	95.76	96.71	95.49	96.38
Formula (78 Anions)											
Si	19.09	18.90	18.98	18.87	19.02	18.95	18.86	19.22	19.04	19.12	19.16
Ti	0.01	0.01	0.00	0.06	0.09	0.06	0.02	0.02	0.10	0.03	0.04
Al	16.01	16.13	16.40	16.05	16.16	15.83	16.34	15.51	16.10	15.55	15.64
Fe(ii)	3.43	3.41	3.09	3.18	3.00	3.62	3.31	3.54	2.87	3.67	3.63
Mn	0.14	0.18	0.18	0.02	0.02	0.03	0.15	0.03	0.03	0.03	0.02
Mg	0.06	0.05	0.12	0.14	0.12	0.04	0.10	0.00	0.15	0.06	0.00
Ca	12.16	12.33	12.05	12.73	12.38	12.55	12.18	12.69	12.52	12.61	12.49
Total	50.90	51.02	50.82	51.04	50.81	51.08	50.96	51.00	50.81	51.07	50.98

Appendix E-2.2. – EPMA results of magnetite from the Alvito deposit

Analysis Code	Deposit	Sample Type	Magnetite type	Mg	Al	Si	Ca	Ti	Fe	Cr	Mn	Ni	V	Co	Zn	O	Total
AL20_z1_mag_p33	Alvito	Outcrop	Mag I	1.70	1.08	<LOD	<LOD	0.10	67.61	<LOD	0.20	<LOD	<LOD	<LOD	0.04	20.25	91.00
AL20_z1_mag_p1	Alvito	Outcrop	Mag I	1.49	0.76	<LOD	0.04	0.08	67.53	<LOD	0.22	<LOD	<LOD	<LOD	0.04	19.80	89.97
AL20_z1_mag_p2	Alvito	Outcrop	Mag I	1.55	0.89	<LOD	<LOD	0.10	67.34	<LOD	0.21	<LOD	<LOD	<LOD	0.04	19.94	90.12
AL20_z1_mag_p3	Alvito	Outcrop	Mag I	1.70	0.94	<LOD	<LOD	0.09	67.62	<LOD	0.22	<LOD	<LOD	<LOD	0.03	20.11	90.73
AL20_z1_mag_p4	Alvito	Outcrop	Mag I	1.70	1.23	<LOD	<LOD	0.09	67.22	<LOD	0.21	<LOD	<LOD	<LOD	0.03	20.28	90.78
AL20_z1_mag_p5	Alvito	Outcrop	Mag I	1.64	1.05	<LOD	<LOD	0.10	67.48	<LOD	0.20	<LOD	<LOD	<LOD	0.04	20.18	90.76
AL20_z1_mag_p6	Alvito	Outcrop	Mag I	1.66	1.04	<LOD	<LOD	0.09	67.55	<LOD	0.20	<LOD	<LOD	<LOD	0.03	20.19	90.80
AL20_z1_mag_p7	Alvito	Outcrop	Mag I	1.80	1.04	<LOD	<LOD	0.09	67.45	<LOD	0.21	<LOD	<LOD	<LOD	0.04	20.25	90.91
AL20_z1_mag_p8	Alvito	Outcrop	Mag I	1.77	1.14	<LOD	<LOD	0.09	67.06	<LOD	0.22	<LOD	<LOD	<LOD	0.03	20.21	90.55
AL20_z1_mag_p9	Alvito	Outcrop	Mag I	1.57	0.77	<LOD	<LOD	0.08	67.86	<LOD	0.21	<LOD	<LOD	<LOD	0.03	19.96	90.50
AL20_z1_mag_p10	Alvito	Outcrop	Mag I	1.54	0.87	<LOD	<LOD	0.09	67.93	<LOD	0.22	<LOD	<LOD	<LOD	0.05	20.06	90.77
AL20_z1_mag_p11	Alvito	Outcrop	Mag I	1.73	0.90	<LOD	<LOD	0.09	67.67	<LOD	0.21	<LOD	<LOD	<LOD	0.04	20.13	90.78
AL20_z1_mag_p12	Alvito	Outcrop	Mag I	1.77	1.26	<LOD	<LOD	0.10	67.10	<LOD	0.21	<LOD	<LOD	<LOD	0.04	20.35	90.88
AL20_z1_mag_p13	Alvito	Outcrop	Mag I	1.46	0.93	0.02	<LOD	0.10	67.99	<LOD	0.21	<LOD	<LOD	<LOD	0.03	20.11	90.91
AL20_z1_mag_p14	Alvito	Outcrop	Mag I	1.78	1.17	<LOD	<LOD	0.09	67.35	<LOD	0.20	<LOD	<LOD	<LOD	0.03	20.31	90.97
AL20_z1_mag_p15	Alvito	Outcrop	Mag I	1.81	1.13	<LOD	<LOD	0.09	67.52	<LOD	0.22	<LOD	<LOD	<LOD	0.04	20.36	91.21
AL20_z1_mag_p16	Alvito	Outcrop	Mag I	1.72	1.27	<LOD	<LOD	0.08	67.01	<LOD	0.22	<LOD	<LOD	<LOD	0.04	20.28	90.66
AL20_z1_mag_p17	Alvito	Outcrop	Mag I	1.75	1.28	<LOD	<LOD	0.10	67.80	<LOD	0.23	<LOD	<LOD	<LOD	0.03	20.54	91.76
AL20_z1_mag_p18	Alvito	Outcrop	Mag I	1.68	1.08	<LOD	<LOD	0.09	67.56	<LOD	0.21	<LOD	<LOD	<LOD	0.03	20.25	90.96
AL20_z1_mag_p19	Alvito	Outcrop	Mag I	1.74	1.13	<LOD	<LOD	0.09	67.26	<LOD	0.20	<LOD	<LOD	<LOD	0.04	20.24	90.76
AL20_z1_mag_p20	Alvito	Outcrop	Mag I	1.45	0.71	<LOD	<LOD	0.09	68.12	<LOD	0.21	<LOD	<LOD	<LOD	0.03	19.90	90.56
AL20_z1_mag_p21	Alvito	Outcrop	Mag I	1.50	0.86	<LOD	<LOD	0.08	67.87	<LOD	0.20	<LOD	<LOD	<LOD	<LOD	20.02	90.64
AL20_z1_mag_p23	Alvito	Outcrop	Mag I	1.51	1.00	<LOD	<LOD	0.08	67.65	<LOD	0.21	<LOD	<LOD	<LOD	0.04	20.08	90.62

Analysis Code	Deposit	Sample Type	Magnetite type	Mg	Al	Si	Ca	Ti	Fe	Cr	Mn	Ni	V	Co	Zn	O	Total
AL20_z1_mag_p22	Alvito	Outcrop	Mag I	1.50	1.03	<LOD	<LOD	0.09	67.55	<LOD	0.22	<LOD	<LOD	<LOD	0.04	20.07	90.56
AL20_z1_mag_p24	Alvito	Outcrop	Mag I	1.78	0.97	<LOD	0.02	0.08	66.86	<LOD	0.20	<LOD	<LOD	<LOD	0.04	20.01	89.98
AL20_z1_mag_p25	Alvito	Outcrop	Mag I	1.53	0.90	<LOD	<LOD	0.09	68.13	<LOD	0.22	<LOD	<LOD	<LOD	<LOD	20.11	91.02
AL20_z1_mag_p26	Alvito	Outcrop	Mag I	1.51	1.07	<LOD	0.02	0.08	67.19	<LOD	0.20	<LOD	<LOD	<LOD	0.03	20.02	90.16
AL20_z1_mag_p27	Alvito	Outcrop	Mag I	1.57	1.12	<LOD	<LOD	0.09	67.43	<LOD	0.20	<LOD	<LOD	<LOD	0.03	20.14	90.61
AL20_z1_mag_p28	Alvito	Outcrop	Mag I	1.76	1.02	<LOD	<LOD	0.09	67.40	<LOD	0.21	<LOD	<LOD	<LOD	0.03	20.20	90.80
AL20_z1_mag_p29	Alvito	Outcrop	Mag I	1.72	1.37	<LOD	<LOD	0.09	67.42	<LOD	0.22	<LOD	<LOD	<LOD	0.05	20.48	91.38
AL20_z1_mag_p30	Alvito	Outcrop	Mag I	1.64	1.14	<LOD	<LOD	0.09	67.40	<LOD	0.22	<LOD	<LOD	<LOD	0.04	20.22	90.77
AL20_z1_mag_p31	Alvito	Outcrop	Mag I	1.64	1.07	<LOD	<LOD	0.09	67.81	<LOD	0.21	<LOD	<LOD	<LOD	0.03	20.28	91.19
AL20_z1_mag_p32	Alvito	Outcrop	Mag I	1.66	1.17	<LOD	<LOD	0.08	67.32	<LOD	0.21	<LOD	<LOD	<LOD	0.04	20.22	90.73
AL20_z1_mag_p34	Alvito	Outcrop	Mag I	1.54	1.07	<LOD	<LOD	0.08	67.84	<LOD	0.21	<LOD	<LOD	<LOD	0.03	20.20	90.99
AL20_z1_mag_p35	Alvito	Outcrop	Mag I	1.59	0.86	<LOD	<LOD	0.08	67.71	<LOD	0.22	<LOD	<LOD	<LOD	0.03	20.03	90.56
AL20_z1_mag_p36	Alvito	Outcrop	Mag I	1.60	1.09	<LOD	<LOD	0.08	67.46	<LOD	0.20	<LOD	<LOD	<LOD	0.04	20.16	90.67
AL20_z1_mag_p37	Alvito	Outcrop	Mag I	1.49	1.12	<LOD	<LOD	0.09	67.63	<LOD	0.21	<LOD	<LOD	<LOD	0.04	20.15	90.74
AL20_z1_mag_p38	Alvito	Outcrop	Mag I	1.62	1.03	<LOD	<LOD	0.08	67.50	<LOD	0.22	<LOD	<LOD	<LOD	0.03	20.13	90.65
AL20_z1_mag_p39	Alvito	Outcrop	Mag I	1.58	1.03	<LOD	<LOD	0.09	67.71	<LOD	0.22	<LOD	<LOD	<LOD	0.04	20.18	90.90
AL20_z1_mag_p40	Alvito	Outcrop	Mag I	1.73	1.16	<LOD	<LOD	0.09	67.30	<LOD	0.20	<LOD	<LOD	<LOD	0.03	20.27	90.82
AL20_z1_mag_p41	Alvito	Outcrop	Mag I	1.62	0.98	<LOD	<LOD	0.09	67.50	<LOD	0.22	<LOD	<LOD	<LOD	0.04	20.10	90.59
AL20_z1_mag_p42	Alvito	Outcrop	Mag I	1.59	1.01	<LOD	<LOD	0.09	67.75	<LOD	0.20	<LOD	<LOD	<LOD	0.03	20.15	90.85
AL19_z1_mag_p1	Alvito	Outcrop	Mag I	0.10	1.21	0.04	<LOD	0.07	70.94	<LOD	0.14	<LOD	<LOD	<LOD	0.03	20.20	92.73
AL19_z1_mag_p22	Alvito	Outcrop	Mag I	0.10	1.13	0.10	0.06	0.09	71.04	<LOD	0.13	<LOD	<LOD	<LOD	0.04	20.28	92.97
AL19_z1_mag_p23	Alvito	Outcrop	Mag I	0.06	0.98	0.03	0.05	0.07	71.51	<LOD	0.13	<LOD	<LOD	<LOD	0.03	20.17	93.06
AL19_z1_mag_p2	Alvito	Outcrop	Mag I	0.11	1.17	0.02	0.04	0.08	70.94	<LOD	0.13	<LOD	<LOD	<LOD	0.03	20.21	92.75

Analysis Code	Deposit	Sample Type	Magnetite type	Mg	Al	Si	Ca	Ti	Fe	Cr	Mn	Ni	V	Co	Zn	O	Total
AL19_z1_mag_p24	Alvito	Outcrop	Mag I	0.12	1.43	0.02	<LOD	0.07	70.82	<LOD	0.14	<LOD	<LOD	<LOD	0.05	20.38	93.05
AL19_z1_mag_p4	Alvito	Outcrop	Mag I	0.08	1.40	0.04	<LOD	0.09	71.74	<LOD	0.15	<LOD	<LOD	<LOD	0.04	20.62	94.21
AL19_z1_mag_p25	Alvito	Outcrop	Mag I	0.15	1.32	0.11	0.06	0.07	70.65	<LOD	0.16	<LOD	<LOD	<LOD	<LOD	20.37	92.93
AL19_z1_mag_p5	Alvito	Outcrop	Mag I	0.10	1.38	0.04	<LOD	0.09	70.75	<LOD	0.15	<LOD	<LOD	<LOD	0.05	20.31	92.86
AL19_z1_mag_p6	Alvito	Outcrop	Mag I	0.07	1.70	0.03	<LOD	0.09	70.31	<LOD	0.10	<LOD	<LOD	<LOD	0.04	20.44	92.80
AL19_z1_mag_p7	Alvito	Outcrop	Mag I	0.09	1.41	0.05	<LOD	0.08	70.38	<LOD	0.16	<LOD	<LOD	<LOD	0.03	20.25	92.47
AL19_z1_mag_p20	Alvito	Outcrop	Mag I	0.10	1.45	0.06	<LOD	0.08	70.35	<LOD	0.13	<LOD	<LOD	<LOD	0.06	20.32	92.58
AL19_z1_mag_p8	Alvito	Outcrop	Mag I	0.06	1.43	0.04	<LOD	0.07	70.84	<LOD	0.15	<LOD	<LOD	<LOD	0.04	20.38	93.05
AL19_z1_mag_p19	Alvito	Outcrop	Mag I	0.10	1.41	0.04	0.02	0.09	70.70	<LOD	0.15	<LOD	<LOD	<LOD	0.04	20.36	92.93
AL19_z1_mag_p18	Alvito	Outcrop	Mag I	0.07	1.29	0.09	0.04	0.09	70.55	<LOD	0.16	<LOD	<LOD	<LOD	0.04	20.27	92.64
AL19_z1_mag_p13	Alvito	Outcrop	Mag I	0.06	0.94	0.02	<LOD	0.08	71.66	<LOD	0.14	<LOD	<LOD	<LOD	0.04	20.17	93.17
AL19_z1_mag_p14	Alvito	Outcrop	Mag I	0.11	1.51	0.06	0.04	0.09	70.90	<LOD	0.15	<LOD	<LOD	<LOD	0.04	20.54	93.46
AL19_z1_mag_p15	Alvito	Outcrop	Mag I	0.36	1.46	0.60	0.35	0.10	69.28	<LOD	0.15	<LOD	<LOD	<LOD	0.04	20.94	93.27
AL19_z1_mag_p16	Alvito	Outcrop	Mag I	0.09	1.04	0.03	<LOD	0.09	71.43	<LOD	0.12	<LOD	<LOD	<LOD	0.03	20.18	93.03
AL19_z1_mag_p17	Alvito	Outcrop	Mag I	0.07	1.41	0.03	<LOD	0.08	71.48	<LOD	0.14	<LOD	<LOD	<LOD	0.04	20.50	93.76
AL19_z1_mag_p9	Alvito	Outcrop	Mag I	0.12	1.77	0.03	<LOD	0.09	70.00	<LOD	0.17	<LOD	<LOD	<LOD	0.04	20.47	92.73
AL19_z1_mag_p21	Alvito	Outcrop	Mag I	0.12	1.37	0.03	<LOD	0.09	71.08	<LOD	0.14	<LOD	<LOD	<LOD	0.04	20.41	93.29
AL19_z1_mag_p12	Alvito	Outcrop	Mag I	0.10	1.61	0.03	<LOD	0.09	70.61	<LOD	0.16	<LOD	<LOD	<LOD	<LOD	20.50	93.17
AL19_z1_mag_p10	Alvito	Outcrop	Mag I	0.14	1.47	0.04	<LOD	0.09	70.95	<LOD	0.14	<LOD	<LOD	<LOD	0.04	20.49	93.40
AL19_z1_mag_p11	Alvito	Outcrop	Mag I	0.13	1.63	0.04	<LOD	0.09	70.89	<LOD	0.15	<LOD	<LOD	<LOD	0.05	20.65	93.69
AL8_z1_mag_p1	Alvito	Outcrop	Mag I	0.14	0.60	0.29	0.02	0.10	69.40	<LOD	0.11	<LOD	<LOD	<LOD	<LOD	19.57	90.26
AL8_z1_mag_p2	Alvito	Outcrop	Mag I	0.13	1.43	0.03	<LOD	0.14	69.21	<LOD	0.20	<LOD	<LOD	<LOD	<LOD	19.99	91.16
AL8_z1_mag_p3	Alvito	Outcrop	Mag I	0.12	1.15	0.04	<LOD	0.11	69.77	<LOD	0.15	<LOD	<LOD	<LOD	<LOD	19.88	91.26

Analysis Code	Deposit	Sample Type	Magnetite type	Mg	Al	Si	Ca	Ti	Fe	Cr	Mn	Ni	V	Co	Zn	O	Total
AL8_z1_mag_p4	Alvito	Outcrop	Mag I	0.10	1.19	0.04	<LOD	0.20	69.53	<LOD	0.19	<LOD	<LOD	<LOD	<LOD	19.92	91.21
AL8_z1_mag_p5	Alvito	Outcrop	Mag I	0.16	1.52	0.06	<LOD	0.18	68.83	<LOD	0.21	<LOD	<LOD	<LOD	<LOD	20.06	91.05
AL8_z1_mag_p6	Alvito	Outcrop	Mag I	0.13	1.48	0.04	<LOD	0.12	68.93	<LOD	0.18	<LOD	<LOD	<LOD	0.03	19.96	90.88
AL8_z1_mag_p7	Alvito	Outcrop	Mag I	0.06	1.11	0.03	<LOD	0.16	69.85	<LOD	0.16	<LOD	<LOD	<LOD	<LOD	19.85	91.26
AL8_z1_mag_p11	Alvito	Outcrop	Mag I	0.11	1.43	0.03	<LOD	0.11	69.17	<LOD	0.18	<LOD	<LOD	<LOD	<LOD	19.96	91.01
AL8_z1_mag_p10	Alvito	Outcrop	Mag I	0.14	1.52	0.03	<LOD	0.10	68.84	<LOD	0.18	<LOD	<LOD	<LOD	<LOD	19.94	90.78
AL8_z1_mag_p9	Alvito	Outcrop	Mag I	0.11	1.24	0.03	<LOD	0.17	69.45	<LOD	0.18	<LOD	<LOD	<LOD	0.03	19.92	91.15
AL8_z1_mag_p8	Alvito	Outcrop	Mag I	0.07	1.32	0.04	<LOD	0.14	69.65	<LOD	0.19	<LOD	<LOD	<LOD	<LOD	19.98	91.42
AL8_z1_mag_p12	Alvito	Outcrop	Mag I	0.10	1.08	0.04	<LOD	0.11	69.93	<LOD	0.16	<LOD	<LOD	<LOD	<LOD	19.85	91.31
AL8_z1_mag_p13	Alvito	Outcrop	Mag I	0.07	1.00	0.04	<LOD	0.10	70.12	<LOD	0.16	<LOD	<LOD	<LOD	0.03	19.80	91.35
AL8_z1_mag_p14	Alvito	Outcrop	Mag I	0.10	0.98	0.04	<LOD	0.13	69.86	<LOD	0.15	<LOD	<LOD	<LOD	<LOD	19.75	91.05
AL6.2_z2_mag_p1	Alvito	Outcrop	Mag I	0.29	0.94	0.04	0.02	0.04	70.23	<LOD	0.16	<LOD	<LOD	<LOD	0.07	19.91	91.71
AL6.2_z2_mag_p2	Alvito	Outcrop	Mag I	0.26	0.94	0.02	<LOD	0.05	70.25	<LOD	0.13	<LOD	<LOD	<LOD	0.09	19.85	91.59
AL6.2_z2_mag_p3	Alvito	Outcrop	Mag I	0.33	1.02	0.04	<LOD	0.04	70.47	<LOD	0.13	<LOD	<LOD	<LOD	0.08	20.05	92.18
AL6.2_z2_mag_p4	Alvito	Outcrop	Mag I	0.24	0.87	0.03	<LOD	0.05	71.15	<LOD	0.13	<LOD	<LOD	<LOD	0.06	20.06	92.67
AL6.2_z2_mag_p5	Alvito	Outcrop	Mag I	0.37	0.95	0.03	<LOD	0.04	70.19	<LOD	0.16	<LOD	<LOD	<LOD	0.08	19.95	91.81
AL6.2_z2_mag_p6	Alvito	Outcrop	Mag I	0.37	0.91	0.04	<LOD	0.05	70.18	<LOD	0.16	<LOD	<LOD	<LOD	0.06	19.90	91.68
AL6.2_z2_mag_p7	Alvito	Outcrop	Mag I	0.30	0.88	0.04	<LOD	0.04	70.34	<LOD	0.17	<LOD	<LOD	<LOD	0.06	19.87	91.71
AL6.2_z2_mag_p8	Alvito	Outcrop	Mag I	0.34	0.85	0.04	<LOD	0.05	70.54	<LOD	0.15	<LOD	<LOD	<LOD	0.06	19.93	91.97
AL6.2_z2_mag_p9	Alvito	Outcrop	Mag I	0.33	0.80	0.04	<LOD	0.04	70.79	<LOD	0.17	<LOD	<LOD	<LOD	0.06	19.95	92.20
AL6.2_z2_mag_p10	Alvito	Outcrop	Mag I	0.36	0.95	0.03	<LOD	0.05	70.10	<LOD	0.17	<LOD	<LOD	<LOD	0.06	19.90	91.62
AL6.2_z2_mag_p11	Alvito	Outcrop	Mag I	0.33	0.81	0.03	<LOD	0.05	70.33	<LOD	0.16	<LOD	<LOD	<LOD	0.06	19.82	91.63
AL6.2_z2_mag_p12	Alvito	Outcrop	Mag I	0.21	0.65	0.04	0.02	0.05	71.32	<LOD	0.13	<LOD	<LOD	<LOD	0.07	19.90	92.41

Analysis Code	Deposit	Sample Type	Magnetite type	Mg	Al	Si	Ca	Ti	Fe	Cr	Mn	Ni	V	Co	Zn	O	Total
AL6.2_z2_mag_p13	Alvito	Outcrop	Mag I	0.26	0.70	0.04	0.02	0.05	70.89	<LOD	0.17	<LOD	<LOD	<LOD	0.06	19.85	92.04
AL6.2_z2_mag_p14	Alvito	Outcrop	Mag I	0.30	0.82	0.04	<LOD	0.04	70.66	<LOD	0.16	<LOD	<LOD	<LOD	0.06	19.90	91.99
AL6.2_z2_mag_p15	Alvito	Outcrop	Mag I	0.27	0.63	0.02	<LOD	0.05	70.59	<LOD	0.18	<LOD	<LOD	<LOD	0.06	19.71	91.55
AL6.2_z2_mag_p16	Alvito	Outcrop	Mag I	0.28	0.80	0.03	<LOD	0.05	70.46	<LOD	0.17	<LOD	<LOD	<LOD	0.06	19.83	91.73
AL6.2_z2_mag_p17	Alvito	Outcrop	Mag I	0.39	1.01	0.04	<LOD	0.04	70.21	<LOD	0.19	<LOD	<LOD	<LOD	0.07	20.02	91.97
AL6.2_z2_mag_p18	Alvito	Outcrop	Mag I	0.33	0.96	0.03	<LOD	0.04	70.37	<LOD	0.19	<LOD	<LOD	<LOD	0.06	19.97	91.98
AL6.2_z2_mag_p19	Alvito	Outcrop	Mag I	0.34	0.92	0.03	<LOD	0.04	70.67	<LOD	0.18	<LOD	<LOD	<LOD	0.06	20.02	92.27
AL6.2_z2_mag_p20	Alvito	Outcrop	Mag I	0.31	1.02	0.04	<LOD	0.04	70.16	<LOD	0.18	<LOD	<LOD	<LOD	0.06	19.97	91.82
AL6.2_z2_mag_p21	Alvito	Outcrop	Mag I	0.30	0.88	0.04	<LOD	0.05	70.69	<LOD	0.17	<LOD	<LOD	<LOD	0.07	19.98	92.20
AL6.2_z2_mag_p22	Alvito	Outcrop	Mag I	0.31	0.88	0.03	<LOD	0.04	70.18	<LOD	0.18	<LOD	<LOD	<LOD	0.04	19.82	91.52
AL6.2_z2_mag_p23	Alvito	Outcrop	Mag I	0.28	0.82	0.03	<LOD	0.05	70.38	<LOD	0.18	<LOD	<LOD	<LOD	0.05	19.85	91.66
AL6.2_z2_mag_p24	Alvito	Outcrop	Mag I	0.32	0.99	0.03	<LOD	0.04	70.10	<LOD	0.18	<LOD	<LOD	<LOD	0.07	19.96	91.74
AL6.2_z1_mag_p1	Alvito	Outcrop	Mag I	<LOD	<LOD	0.02	<LOD	<LOD	71.93	<LOD	0.07	<LOD	<LOD	<LOD	<LOD	19.23	91.28
AL6.2_z1_mag_p2	Alvito	Outcrop	Mag I	<LOD	<LOD	0.04	<LOD	<LOD	71.84	<LOD	0.09	<LOD	<LOD	<LOD	<LOD	19.30	91.37
AL6.2_z1_mag_p3	Alvito	Outcrop	Mag I	<LOD	<LOD	0.10	<LOD	<LOD	71.23	<LOD	0.07	0.14	<LOD	<LOD	0.03	19.34	90.93
AL6.2_z1_mag_p4	Alvito	Outcrop	Mag I	0.05	<LOD	0.06	<LOD	<LOD	71.65	<LOD	0.05	0.06	<LOD	<LOD	<LOD	19.29	91.20

Appendix E-3.

Complete results of EPMA silicates and magnetite from the Azenhas deposit

Appendix E-3.1. – EPMA results of silicates from the Azenhas area - EPMA results for plagioclase and alkali feldspars (metavolcanic rocks)

Sample	**AZ 1.1**							
Analysis Ref.	Z1 P1	Z1 P2	Z1 P3	Z1 P4	Z1 P5	Z1 P6	Z1 P7	Z2 P8
Element (wt. %)								
SiO_2	68.33	68.63	68.68	67.88	68.13	68.56	66.78	66.94
TiO_2	<LOD	<LOD	<LOD	<LOD	<LOD	<LOD	<LOD	<LOD
Al_2O_3	20.07	20.04	19.58	19.74	19.98	20.43	19.81	20.16
FeO	<LOD	<LOD	0.07	<LOD	0.06	0.06	2.41	0.23
CaO	0.21	0.16	0.15	0.29	0.24	0.27	0.75	0.72
Na_2O	11.40	11.37	11.37	11.33	11.46	11.36	10.29	10.97
K_2O	0.05	0.04	0.04	0.05	0.06	0.18	0.19	0.04
BaO								
Total	100.07	100.25	99.89	99.28	99.94	100.87	100.22	99.07
Formula (32O)								
Si	11.92	11.94	11.99	11.94	11.91	11.88	11.77	11.82
Ti	0.0	0.0	0.0	0.0	0.0	0.0	0.0	0.0
Al	4.13	4.11	4.03	4.09	4.12	4.17	4.12	4.20
Fe(ii)	0.0	0.0	0.01	0.0	0.01	0.01	0.36	0.03
Ca	0.04	0.03	0.03	0.05	0.05	0.05	0.14	0.14
Na	3.85	3.83	3.85	3.86	3.89	3.81	3.52	3.76
K	0.01	0.01	0.01	0.01	0.01	0.04	0.04	0.01
Ba								
Total	19.95	19.92	19.92	19.96	19.98	19.96	19.95	19.96
An (%)	1.02	0.78	0.70	1.37	1.15	1.30	3.82	3.51
Ab (%)	98.70	98.96	99.04	98.35	98.52	97.69	95.01	96.23
Or (%)	0.29	0.25	0.26	0.28	0.33	1.00	1.17	0.26

Appendix E-3.1. – EPMA results of silicates from the Azenhas area - EPMA results for amphibole feldspars (calcsilicate rocks)

Sample	AZ 4.3				AZ 8.1					
Analysis Ref.	Z1 P1	Z1 P2	Z1 P3	Z1 P4	Z1 P5	Z2 P1	Z2 P2	Z2 P3	Z2 P4	Z2 P5
Element (wt. %)										
SiO_2	52.3594	48.9368	52.3889	52.8652	57.7768	58.7048	58.5817	58.6643	58.5644	59.048
Al_2O_3	3.7487	6.5178	4.0324	3.6699	0.1693			0.0311	0.2162	0.0336
MnO	0.3367	0.327	0.3287	0.3473	0.419	0.5858	0.5242	0.5619	0.3834	0.4495
FeO	7.404	9.4645	7.2181	7.9482	1.8031	1.6498	1.6754	1.4574	2.0569	1.387
MgO	18.1406	16.5583	18.5797	18.5374	23.5951	23.1251	22.9868	23.3292	22.7313	23.263
CaO	12.0656	11.6783	12.155	12.0474	12.5318	12.8989	12.7755	13.0815	12.7144	13.1105
Na_2O	1.5301	2.1405	1.614	1.4013					0.132	
K_2O	0.3305	0.1658	0.1873	0.1873		0.0717	0.0515			
Total	95.9156	95.789	96.5041	97.004	96.2951	97.0361	96.5951	97.1254	96.7986	97.2916
T										
Si	7.544	7.15	7.486	7.516	7.985	8.053	8.067	8.038	8.056	8.062
Al	0.456	0.85	0.514	0.484	0.015					
T (total)	8	8	8	8	8	8.053	8.067	8.038	8.056	8.062
C										
Al	0.181	0.272	0.166	0.131	0.013			0.005	0.035	0.005
Fe^{3+}	0.039	0.133	0.092	0.167	0.01					
Mn^{2+}	0.03		0.014			0.068	0.061	0.063	0.045	0.052
Fe^{2+}	0.853	0.988	0.771	0.773	0.115	0.189	0.193	0.167	0.237	0.158
Mg	3.897	3.607	3.958	3.929	4.862	4.729	4.719	4.765	4.662	4.735
C (total)	5	5	5.001	5	5	4.986	4.973	5	4.979	4.95
B										
Mn^{2+}	0.011	0.04	0.026	0.042	0.049			0.002		
Fe^{2+}		0.035		0.006	0.083					
Ca	1.863	1.828	1.861	1.835	1.856	1.896	1.885	1.92	1.874	1.918
Na	0.126	0.096	0.113	0.117	0.012	0.008	0.006		0.035	0.008
B (total)	2	1.999	2	2	2	1.904	1.891	1.922	1.909	1.926
A										
Na	0.301	0.51	0.334	0.269	0.003					
K	0.061	0.031	0.034	0.034		0.013	0.009			
A (total)	0.362	0.541	0.368	0.303	0.003	0.013	0.009	0	0	0

Appendix E-3.1. – EPMA results of silicates from the Azenhas area - EPMA results for epidote (skarn)

Sample	AZ 4.3													
Analysis Ref.	Z1 P4	Z1 P5	Z1 P6	Z1 P7	Z1 P8	Z1 P9	Z2 P1	Z2 P2	Z2 P3	Z2 P4	Z2 P5	Z2 P6	Z2 P7	Z2 P8
Element (wt. %)														
SiO_2	37.60	37.81	36.78	37.82	37.84	37.54	37.35	37.37	37.83	37.32	37.48	37.34	37.86	37.56
TiO_2	0.19	0.19	0.03	0.01	0.08	0.09	0.19	0.17	0.12	0.07	0.16	0.12	0.12	0.07
Al_2O_3	24.00	24.20	20.54	23.26	24.54	23.64	22.92	23.09	23.27	22.97	23.84	23.13	23.72	23.70
Fe_2O_3	11.71	12.01	15.32	13.14	11.58	13.50	12.79	13.37	12.88	13.74	13.10	14.04	13.33	12.92
MnO						0.50	0.27	0.25	0.24	0.13	0.28	0.13	0.33	
MgO														
CaO	23.12	23.22	22.74	23.21	23.30	22.62	23.00	22.88	22.81	23.05	22.80	23.03	22.87	23.54
P_2O_5	0.27	0.28	0.28	0.27	0.26	0.30	0.20	0.31	0.35	0.32	0.24	0.27	0.26	0.32
Total	96.89	97.72	95.68	97.70	97.61	98.19	96.71	97.45	97.51	97.61	97.90	98.06	98.50	98.11
Formula (12.5O)														
Si	3.19	3.19	3.28	3.22	3.18	3.20	3.21	3.21	3.23	3.21	3.19	3.20	3.20	3.19
Ti	0.01	0.01	0.00	0.00	0.01	0.01	0.01	0.01	0.01	0.00	0.01	0.01	0.01	0.00
Al	2.40	2.41	2.16	2.34	2.43	2.37	2.32	2.34	2.34	2.33	2.39	2.34	2.37	2.37
Fe(iii)	0.37	0.38	0.51	0.42	0.37	0.43	0.41	0.43	0.41	0.44	0.42	0.45	0.42	0.41
Mn	0.00	0.00	0.00	0.00	0.00	0.04	0.02	0.02	0.02	0.01	0.02	0.01	0.02	0.00
Mg	0.00	0.00	0.00	0.00	0.00	0.00	0.00	0.00	0.00	0.00	0.00	0.00	0.00	0.00
Ca	2.10	2.10	2.17	2.12	2.10	2.06	2.12	2.10	2.08	2.12	2.08	2.11	2.07	2.14
P	0.01	0.01	0.01	0.01	0.01	0.01	0.01	0.01	0.01	0.01	0.01	0.01	0.01	0.01
Total	8.09	8.10	8.14	8.11	8.09	8.11	8.11	8.11	8.10	8.12	8.11	8.13	8.11	8.12

Appendix E-3.2. – EPMA results of magnetite from the Azenhas deposit

Analysis Code	Deposit	Ore Bodie	Sample Type	Magnetite type	Mg	Al	Si	Ca	Ti	Fe	Cr	Mn	Ni	V	Co	Zn	O	Total
AZ8.1_z1_mag_p1	Azenhas-Orada	Azenhas	Outcrop	Mag I	0.37	<LOD	<LOD	<LOD	0.18	70.92	<LOD	0.39	<LOD	<LOD	<LOD	0.13	19.50	91.57
AZ8.1_z1_mag_p2	Azenhas-Orada	Azenhas	Outcrop	Mag I	0.36	<LOD	0.02	<LOD	0.18	71.06	<LOD	0.35	<LOD	<LOD	<LOD	0.12	19.50	91.64
AZ8.1_z1_mag_p4	Azenhas-Orada	Azenhas	Outcrop	Mag I	0.34	<LOD	<LOD	<LOD	0.18	71.44	<LOD	0.41	<LOD	<LOD	<LOD	0.13	19.61	92.17
AZ8.1_z1_mag_p3	Azenhas-Orada	Azenhas	Outcrop	Mag I	0.37	<LOD	<LOD	<LOD	0.19	71.14	<LOD	0.38	<LOD	<LOD	<LOD	0.15	19.56	91.86
AZ8.1_z1_mag_p5	Azenhas-Orada	Azenhas	Outcrop	Mag I	0.34	0.03	0.02	<LOD	0.20	70.65	<LOD	0.40	<LOD	<LOD	<LOD	0.13	19.43	91.26
AZ8.1_z1_mag_p6	Azenhas-Orada	Azenhas	Outcrop	Mag I	0.34	<LOD	<LOD	<LOD	0.18	71.09	<LOD	0.38	<LOD	<LOD	<LOD	0.12	19.50	91.70
AZ8.1_z1_mag_p7	Azenhas-Orada	Azenhas	Outcrop	Mag I	0.36	<LOD	0.02	<LOD	0.17	70.52	<LOD	0.37	<LOD	<LOD	<LOD	0.11	19.35	90.92
AZ8.1_z1_mag_p8	Azenhas-Orada	Azenhas	Outcrop	Mag I	0.36	0.06	0.02	0.04	0.21	70.95	<LOD	0.41	<LOD	<LOD	<LOD	0.14	19.61	91.82
AZ8.1_z1_mag_p9	Azenhas-Orada	Azenhas	Outcrop	Mag I	0.39	0.07	<LOD	<LOD	0.20	70.41	<LOD	0.39	<LOD	<LOD	<LOD	0.13	19.40	91.02
AZ8.1_z1_mag_p10	Azenhas-Orada	Azenhas	Outcrop	Mag I	0.37	0.14	0.02	<LOD	0.19	70.86	<LOD	0.41	<LOD	<LOD	<LOD	0.13	19.61	91.79
AZ8.1_z1_mag_p11	Azenhas-Orada	Azenhas	Outcrop	Mag I	0.47	0.07	0.07	<LOD	0.20	70.89	<LOD	0.40	<LOD	<LOD	<LOD	0.12	19.66	91.89
AZ8.1_z1_mag_p12	Azenhas-Orada	Azenhas	Outcrop	Mag I	0.33	0.05	0.02	<LOD	0.20	71.32	<LOD	0.38	<LOD	<LOD	<LOD	0.12	19.61	92.06
AZ8.1_z1_mag_p13	Azenhas-Orada	Azenhas	Outcrop	Mag I	0.34	0.13	0.02	<LOD	0.19	70.71	<LOD	0.43	<LOD	<LOD	<LOD	0.13	19.56	91.53
AZ8.1_z1_mag_p14	Azenhas-Orada	Azenhas	Outcrop	Mag I	0.34	0.12	<LOD	<LOD	0.19	70.72	<LOD	0.39	<LOD	<LOD	<LOD	0.12	19.50	91.42
AZ8.1_z1_mag_p15	Azenhas-Orada	Azenhas	Outcrop	Mag I	0.33	0.03	<LOD	<LOD	0.21	71.07	<LOD	0.39	<LOD	<LOD	<LOD	0.13	19.54	91.74
AZ8.1_z1_mag_p16	Azenhas-Orada	Azenhas	Outcrop	Mag I	0.57	0.16	0.57	0.08	0.15	67.77	<LOD	1.02	<LOD	<LOD	<LOD	0.14	19.67	90.15
AZ8.1_z1_mag_p18	Azenhas-Orada	Azenhas	Outcrop	Mag I	0.37	0.06	<LOD	<LOD	0.18	71.16	<LOD	0.41	<LOD	<LOD	<LOD	0.12	19.57	91.90
AZ8.1_z1_mag_p17	Azenhas-Orada	Azenhas	Outcrop	Mag I	0.35	0.06	0.03	<LOD	0.19	70.68	<LOD	0.38	<LOD	<LOD	<LOD	0.15	19.47	91.32
AZ8.1_z1_mag_p19	Azenhas-Orada	Azenhas	Outcrop	Mag I	0.37	0.06	<LOD	<LOD	0.17	70.92	<LOD	0.41	<LOD	<LOD	<LOD	0.12	19.52	91.61
AZ8.1_z1_mag_p20	Azenhas-Orada	Azenhas	Outcrop	Mag I	0.39	0.08	<LOD	<LOD	0.20	70.94	<LOD	0.41	<LOD	<LOD	<LOD	0.12	19.59	91.81
AZ8.1_z1_mag_p21	Azenhas-Orada	Azenhas	Outcrop	Mag I	0.84	0.24	0.41	<LOD	0.18	68.90	<LOD	0.40	<LOD	<LOD	<LOD	0.13	19.87	90.99
AZ8.1_z1_mag_p22	Azenhas-Orada	Azenhas	Outcrop	Mag I	0.41	0.11	0.02	<LOD	0.19	70.86	<LOD	0.42	<LOD	<LOD	<LOD	0.14	19.61	91.78
AZ8.1_z1_mag_p23	Azenhas-Orada	Azenhas	Outcrop	Mag I	0.38	<LOD	<LOD	<LOD	0.21	70.99	<LOD	0.38	<LOD	<LOD	<LOD	0.12	19.51	91.65

Analysis Code	Deposit	Ore Bodie	Sample Type	Magnetite type	Mg	Al	Si	Ca	Ti	Fe	Cr	Mn	Ni	V	Co	Zn	O	Total
AZ8.1_z1_mag_p24	Azenhas-Orada	Azenhas	Outcrop	Mag I	0.40	0.08	0.02	<LOD	0.20	70.37	<LOD	0.41	<LOD	<LOD	<LOD	0.13	19.44	91.10
AZ8.1_z1_mag_p25	Azenhas-Orada	Azenhas	Outcrop	Mag I	0.37	0.06	0.03	<LOD	0.18	70.95	<LOD	0.39	<LOD	<LOD	<LOD	0.12	19.54	91.69
AZ8.1_z1_mag_p26	Azenhas-Orada	Azenhas	Outcrop	Mag I	0.38	0.04	<LOD	<LOD	0.18	71.07	<LOD	0.42	<LOD	<LOD	<LOD	0.13	19.55	91.82
AZ8.1_z1_mag_p27	Azenhas-Orada	Azenhas	Outcrop	Mag I	0.40	0.09	<LOD	<LOD	0.19	70.47	<LOD	0.42	<LOD	<LOD	<LOD	0.13	19.47	91.22
AZ8.1_z1_mag_p28	Azenhas-Orada	Azenhas	Outcrop	Mag I	0.35	0.06	0.02	<LOD	0.18	71.09	<LOD	0.38	<LOD	<LOD	<LOD	0.14	19.56	91.79
AZ8.1_z1_mag_p29	Azenhas-Orada	Azenhas	Outcrop	Mag I	0.38	0.07	<LOD	<LOD	0.19	70.52	<LOD	0.42	<LOD	<LOD	<LOD	0.14	19.44	91.21
AZ8.1_z1_mag_p30	Azenhas-Orada	Azenhas	Outcrop	Mag I	0.38	<LOD	0.02	<LOD	0.16	71.19	<LOD	0.33	<LOD	<LOD	<LOD	0.11	19.50	91.71
AZ7.4_z1_mag_p1	Azenhas-Orada	Azenhas	Outcrop	Mag I	0.49	0.14	0.21	0.06	0.32	69.38	<LOD	0.52	<LOD	<LOD	<LOD	<LOD	19.69	90.84
AZ7.4_z1_mag_p2	Azenhas-Orada	Azenhas	Outcrop	Mag I	0.33	0.03	0.11	0.28	0.25	69.90	<LOD	0.46	<LOD	<LOD	<LOD	0.04	19.87	91.28
AZ7.4_z1_mag_p3	Azenhas-Orada	Azenhas	Outcrop	Mag I	2.45	0.73	1.35	0.04	0.16	64.21	<LOD	0.48	<LOD	<LOD	<LOD	0.03	21.43	90.89
AZ7.4_z1_mag_p4	Azenhas-Orada	Azenhas	Outcrop	Mag I	0.26	0.04	0.07	0.11	0.30	70.13	<LOD	0.56	<LOD	<LOD	<LOD	0.04	19.55	91.11
AZ7.4_z1_mag_p5	Azenhas-Orada	Azenhas	Outcrop	Mag I	0.46	0.16	0.21	0.06	0.26	69.56	<LOD	0.41	<LOD	<LOD	<LOD	0.05	19.62	90.80
AZ7.4_z1_mag_p6	Azenhas-Orada	Azenhas	Outcrop	Mag I	0.21	0.05	0.04	<LOD	0.26	70.71	<LOD	0.41	<LOD	<LOD	<LOD	0.06	19.47	91.22
AZ7.4_z1_mag_p7	Azenhas-Orada	Azenhas	Outcrop	Mag I	0.40	0.14	0.17	0.04	0.27	69.67	<LOD	0.48	<LOD	<LOD	<LOD	0.05	19.68	90.92
AZ7.4_z1_mag_p8	Azenhas-Orada	Azenhas	Outcrop	Mag I	0.29	0.03	0.04	0.29	0.24	69.67	<LOD	0.45	<LOD	<LOD	<LOD	0.05	19.40	90.46
AZ7.4_z1_mag_p9	Azenhas-Orada	Azenhas	Outcrop	Mag I	0.16	0.03	<LOD	0.05	0.24	70.62	<LOD	0.42	<LOD	<LOD	<LOD	0.05	19.36	90.95
AZ7.4_z1_mag_p10	Azenhas-Orada	Azenhas	Outcrop	Mag I	0.25	0.07	0.03	0.02	0.23	70.16	<LOD	0.40	<LOD	<LOD	<LOD	0.05	19.30	90.52
AZ7.4_z1_mag_p26	Azenhas-Orada	Azenhas	Outcrop	Mag I	0.58	0.19	0.26	0.03	0.27	68.76	<LOD	0.47	<LOD	<LOD	<LOD	0.04	19.56	90.20
AZ7.4_z1_mag_p11	Azenhas-Orada	Azenhas	Outcrop	Mag I	3.13	1.11	1.61	<LOD	0.20	63.10	<LOD	0.38	<LOD	<LOD	<LOD	0.05	21.88	91.50
AZ7.4_z1_mag_p12	Azenhas-Orada	Azenhas	Outcrop	Mag I	0.78	0.28	0.32	<LOD	0.21	68.93	<LOD	0.39	<LOD	<LOD	<LOD	0.04	19.90	90.86
AZ7.4_z1_mag_p13	Azenhas-Orada	Azenhas	Outcrop	Mag I	0.90	0.33	0.45	0.71	0.22	67.24	<LOD	0.43	<LOD	<LOD	<LOD	0.05	19.84	90.17
AZ7.4_z1_mag_p14	Azenhas-Orada	Azenhas	Outcrop	Mag I	0.22	0.04	0.03	0.03	0.22	70.24	<LOD	0.44	<LOD	<LOD	<LOD	0.05	19.27	90.55
AZ7.4_z1_mag_p15	Azenhas-Orada	Azenhas	Outcrop	Mag I	2.61	0.82	1.33	0.04	0.21	64.96	<LOD	0.38	<LOD	<LOD	<LOD	0.04	21.50	91.90

Analysis Code	Deposit	Ore Bodie	Sample Type	Magnetite type	Mg	Al	Si	Ca	Ti	Fe	Cr	Mn	Ni	V	Co	Zn	O	Total
AZ7.4_z1_mag_p16	Azenhas-Orada	Azenhas	Outcrop	Mag I	0.48	0.17	0.20	<LOD	0.24	69.39	<LOD	0.42	<LOD	<LOD	<LOD	0.04	19.64	90.60
AZ7.4_z1_mag_p17	Azenhas-Orada	Azenhas	Outcrop	Mag I	2.16	0.44	1.27	0.02	0.20	65.01	<LOD	0.39	<LOD	<LOD	<LOD	0.04	20.88	90.43
AZ7.4_z1_mag_p19	Azenhas-Orada	Azenhas	Outcrop	Mag I	0.71	0.22	0.40	0.84	0.27	67.18	<LOD	0.43	<LOD	<LOD	<LOD	0.04	19.67	89.77
AZ7.4_z1_mag_p20	Azenhas-Orada	Azenhas	Outcrop	Mag I	0.75	0.22	0.55	0.64	0.27	66.84	<LOD	0.48	<LOD	<LOD	<LOD	0.04	19.84	89.68
AZ7.4_z1_mag_p21	Azenhas-Orada	Azenhas	Outcrop	Mag I	2.53	0.86	1.70	0.04	0.14	63.20	<LOD	0.43	<LOD	<LOD	<LOD	<LOD	21.76	90.71
AZ7.4_z1_mag_p22	Azenhas-Orada	Azenhas	Outcrop	Mag I	3.54	1.16	1.73	0.03	0.21	62.37	<LOD	0.39	<LOD	<LOD	<LOD	0.05	22.30	91.78
AZ7.4_z1_mag_p24	Azenhas-Orada	Azenhas	Outcrop	Mag I	0.40	0.08	0.20	0.03	0.25	69.44	<LOD	0.47	<LOD	<LOD	<LOD	0.05	19.42	90.35
AZ7.4_z1_mag_p25	Azenhas-Orada	Azenhas	Outcrop	Mag I	0.28	0.07	0.09	<LOD	0.24	70.38	<LOD	0.44	<LOD	<LOD	<LOD	0.06	19.45	91.02
AZ7.4_z1_mag_p27	Azenhas-Orada	Azenhas	Outcrop	Mag I	0.22	0.07	0.04	0.04	0.22	70.34	<LOD	0.43	<LOD	<LOD	<LOD	0.04	19.32	90.73
AZ7.4_z1_mag_p28	Azenhas-Orada	Azenhas	Outcrop	Mag I	0.60	0.23	0.31	0.04	0.24	69.17	<LOD	0.42	<LOD	<LOD	<LOD	0.04	19.72	90.80
AZ7.4_z1_mag_p29	Azenhas-Orada	Azenhas	Outcrop	Mag I	0.34	0.12	0.08	<LOD	0.23	69.83	<LOD	0.43	<LOD	<LOD	<LOD	0.04	19.35	90.45
AZ7.4_z1_mag_p30	Azenhas-Orada	Azenhas	Outcrop	Mag I	0.53	0.20	0.27	0.04	0.35	69.01	<LOD	0.46	<LOD	<LOD	<LOD	0.05	19.68	90.61
AZ7.4_z1_mag_p31	Azenhas-Orada	Azenhas	Outcrop	Mag I	0.73	0.21	0.36	0.04	0.29	68.61	<LOD	0.43	<LOD	<LOD	<LOD	0.05	19.73	90.47
AZ7.4_z1_mag_p32	Azenhas-Orada	Azenhas	Outcrop	Mag I	0.60	0.23	0.35	0.03	0.42	68.45	<LOD	0.49	<LOD	<LOD	<LOD	0.05	19.71	90.36
AZ7.4_z1_mag_p33	Azenhas-Orada	Azenhas	Outcrop	Mag I	0.36	0.09	0.08	0.08	0.34	69.85	<LOD	0.47	<LOD	<LOD	<LOD	0.07	19.49	90.83
AZ7.4_z1_mag_p34	Azenhas-Orada	Azenhas	Outcrop	Mag I	0.25	0.06	0.07	0.15	0.28	69.82	<LOD	0.42	<LOD	<LOD	<LOD	0.06	19.45	90.57
AZ7.4_z1_mag_p35	Azenhas-Orada	Azenhas	Outcrop	Mag I	0.21	0.05	0.07	0.20	0.28	70.37	<LOD	0.47	<LOD	<LOD	<LOD	0.04	19.76	91.45
AZ7.4_z1_mag_p36	Azenhas-Orada	Azenhas	Outcrop	Mag I	0.25	0.10	0.07	<LOD	0.29	70.15	<LOD	0.49	<LOD	<LOD	<LOD	0.04	19.40	90.80
AZ7.4_z1_mag_p37	Azenhas-Orada	Azenhas	Outcrop	Mag I	0.32	0.07	0.09	0.03	0.27	69.98	<LOD	0.46	<LOD	<LOD	<LOD	0.05	19.40	90.67
AZ7.4_z1_mag_p38	Azenhas-Orada	Azenhas	Outcrop	Mag I	0.17	<LOD	0.04	0.08	0.28	69.92	<LOD	0.47	<LOD	<LOD	<LOD	0.04	19.22	90.26
AZ7.4_z1_mag_p39	Azenhas-Orada	Azenhas	Outcrop	Mag I	0.42	0.15	0.17	<LOD	0.30	69.39	<LOD	0.50	<LOD	<LOD	<LOD	0.07	19.51	90.53
AZ7.4_z1_mag_p40	Azenhas-Orada	Azenhas	Outcrop	Mag I	0.92	0.41	0.50	0.04	0.22	67.50	<LOD	0.46	<LOD	<LOD	<LOD	0.03	19.84	89.96
AZ7.4_z1_mag_p41	Azenhas-Orada	Azenhas	Outcrop	Mag I	0.49	0.16	0.24	<LOD	0.22	69.69	<LOD	0.44	<LOD	<LOD	<LOD	0.05	19.65	90.97

Analysis Code	Deposit	Ore Bodie	Sample Type	Magnetite type	Mg	Al	Si	Ca	Ti	Fe	Cr	Mn	Ni	V	Co	Zn	O	Total
AZ7.4_z1_mag_p42	Azenhas-Orada	Azenhas	Outcrop	Mag I	0.13	<LOD	0.02	0.03	0.21	70.78	<LOD	0.44	<LOD	<LOD	<LOD	0.04	19.35	91.07
AZ7.4_z1_mag_p43	Azenhas-Orada	Azenhas	Outcrop	Mag I	0.40	0.12	0.35	<LOD	0.22	69.20	<LOD	0.47	<LOD	<LOD	<LOD	0.05	19.55	90.40
AZ7.4_z1_mag_p44	Azenhas-Orada	Azenhas	Outcrop	Mag I	0.55	0.17	0.21	<LOD	0.24	69.69	<LOD	0.46	<LOD	<LOD	<LOD	0.04	19.67	91.09
AZ7.4_z1_mag_p45	Azenhas-Orada	Azenhas	Outcrop	Mag I	1.43	0.42	0.68	<LOD	0.46	66.61	<LOD	0.66	<LOD	<LOD	<LOD	<LOD	20.33	90.65
AZ7.4_z1_mag_p46	Azenhas-Orada	Azenhas	Outcrop	Mag I	0.29	0.04	0.21	0.08	0.16	69.67	<LOD	0.44	<LOD	<LOD	<LOD	0.04	19.36	90.31
AZ7.4_z1_mag_p47	Azenhas-Orada	Azenhas	Outcrop	Mag I	0.24	0.06	0.22	0.02	0.14	69.58	<LOD	0.43	<LOD	<LOD	<LOD	0.03	19.27	90.03
AZ7.4_z1_mag_p48	Azenhas-Orada	Azenhas	Outcrop	Mag I	0.17	0.03	0.02	0.12	0.15	70.49	<LOD	0.44	<LOD	<LOD	<LOD	0.03	19.26	90.73
AZ7.4_z1_mag_p49	Azenhas-Orada	Azenhas	Outcrop	Mag I	0.21	0.07	0.04	<LOD	0.20	70.58	<LOD	0.49	<LOD	<LOD	<LOD	<LOD	19.46	91.12
AZ7.4_z1_mag_p50	Azenhas-Orada	Azenhas	Outcrop	Mag I	0.23	<LOD	0.04	0.10	0.19	70.31	<LOD	0.47	<LOD	<LOD	<LOD	<LOD	19.42	90.83
AZ7.4_z1_mag_p51	Azenhas-Orada	Azenhas	Outcrop	Mag I	0.22	0.03	0.04	0.02	0.18	70.36	<LOD	0.46	<LOD	<LOD	<LOD	0.21	19.33	90.86
AZ7.4_z1_mag_p52	Azenhas-Orada	Azenhas	Outcrop	Mag I	0.63	0.22	0.35	0.13	0.21	68.65	<LOD	0.49	<LOD	<LOD	<LOD	0.04	19.67	90.40
AZ7.4_z1_mag_p53	Azenhas-Orada	Azenhas	Outcrop	Mag I	0.70	0.25	0.36	2.31	0.19	63.98	<LOD	0.48	<LOD	<LOD	<LOD	<LOD	19.29	87.64
AZ7.4_z1_mag_p54	Azenhas-Orada	Azenhas	Outcrop	Mag I	0.40	0.14	0.21	0.10	0.21	69.35	<LOD	0.52	<LOD	<LOD	<LOD	<LOD	19.47	90.42
AZ7.4_z1_mag_p55	Azenhas-Orada	Azenhas	Outcrop	Mag I	0.53	0.21	0.29	0.03	0.25	68.96	<LOD	0.54	<LOD	<LOD	<LOD	0.03	19.62	90.51
AZ7.4_z1_mag_p56	Azenhas-Orada	Azenhas	Outcrop	Mag I	0.27	0.08	0.08	0.03	0.23	69.80	<LOD	0.53	<LOD	<LOD	<LOD	<LOD	19.30	90.33
AZ7.4_z1_mag_p57	Azenhas-Orada	Azenhas	Outcrop	Mag I	0.38	0.14	0.10	0.02	0.20	69.78	<LOD	0.54	<LOD	<LOD	<LOD	<LOD	19.54	90.72
AZ7.4_z1_mag_p58	Azenhas-Orada	Azenhas	Outcrop	Mag I	0.46	0.20	0.19	<LOD	0.20	69.58	<LOD	0.54	<LOD	<LOD	<LOD	<LOD	19.56	90.76
AZ7.4_z1_mag_p59	Azenhas-Orada	Azenhas	Outcrop	Mag I	0.46	0.16	0.17	0.04	0.20	69.62	<LOD	0.51	<LOD	<LOD	<LOD	<LOD	19.56	90.74
AZ7.4_z1_mag_p60	Azenhas-Orada	Azenhas	Outcrop	Mag I	0.41	0.14	0.17	<LOD	0.19	69.65	<LOD	0.52	<LOD	<LOD	<LOD	0.06	19.49	90.68
AZ7.4_z1_mag_p61	Azenhas-Orada	Azenhas	Outcrop	Mag I	0.42	0.20	0.19	0.02	0.20	69.32	<LOD	0.56	<LOD	<LOD	<LOD	0.04	19.49	90.47
AZ7.4_z1_mag_p62	Azenhas-Orada	Azenhas	Outcrop	Mag I	0.24	0.05	<LOD	<LOD	0.21	70.71	<LOD	0.53	<LOD	<LOD	<LOD	0.03	19.43	91.26
AZ7.4_z1_mag_p63	Azenhas-Orada	Azenhas	Outcrop	Mag I	0.18	<LOD	0.06	0.04	0.20	70.06	<LOD	0.46	<LOD	<LOD	<LOD	<LOD	19.26	90.33
AZ7.4_z1_mag_p64	Azenhas-Orada	Azenhas	Outcrop	Mag I	0.23	<LOD	0.04	0.07	0.17	70.41	<LOD	0.47	<LOD	<LOD	<LOD	0.03	19.33	90.82

Analysis Code	Deposit	Ore Bodie	Sample Type	Magnetite type	Mg	Al	Si	Ca	Ti	Fe	Cr	Mn	Ni	V	Co	Zn	O	Total
AZ7.4_z1_mag_p65	Azenhas-Orada	Azenhas	Outcrop	Mag I	0.18	0.04	0.07	0.03	0.16	70.72	<LOD	0.44	<LOD	<LOD	<LOD	0.04	19.37	91.08
AZ7.4_z1_mag_p66	Azenhas-Orada	Azenhas	Outcrop	Mag I	0.20	0.04	0.05	0.28	0.15	69.80	<LOD	0.45	<LOD	<LOD	<LOD	0.05	19.20	90.25
AZ7.4_z1_mag_p67	Azenhas-Orada	Azenhas	Outcrop	Mag I	0.38	0.14	0.14	0.03	0.17	69.33	<LOD	0.49	<LOD	<LOD	<LOD	0.05	19.31	90.07
AZ7.4_z1_mag_p68	Azenhas-Orada	Azenhas	Outcrop	Mag I	0.19	0.09	0.04	<LOD	0.15	70.36	<LOD	0.52	<LOD	<LOD	<LOD	0.05	19.30	90.73
AZ7.4_z1_mag_p69	Azenhas-Orada	Azenhas	Outcrop	Mag I	0.46	0.17	0.17	<LOD	0.14	69.50	<LOD	0.52	<LOD	<LOD	<LOD	0.06	19.51	90.56
AZ7.4_z1_mag_p70	Azenhas-Orada	Azenhas	Outcrop	Mag I	0.37	0.10	0.11	<LOD	0.13	69.51	<LOD	0.55	<LOD	<LOD	<LOD	0.07	19.28	90.16
AZ7.4_z1_mag_p71	Azenhas-Orada	Azenhas	Outcrop	Mag I	0.21	0.03	0.08	0.03	0.13	69.96	<LOD	0.56	<LOD	<LOD	<LOD	0.06	19.25	90.36
AZ7.4_z1_mag_p72	Azenhas-Orada	Azenhas	Outcrop	Mag I	0.67	0.26	0.37	0.16	0.13	68.59	<LOD	0.47	<LOD	<LOD	<LOD	0.04	19.68	90.38
AZ7.4_z1_mag_p73	Azenhas-Orada	Azenhas	Outcrop	Mag I	0.22	<LOD	0.04	0.05	0.12	70.34	<LOD	0.45	<LOD	<LOD	<LOD	0.05	19.23	90.54
AZ7.4_z1_mag_p77	Azenhas-Orada	Azenhas	Outcrop	Mag I	1.02	0.34	0.58	0.08	0.10	67.42	<LOD	0.48	<LOD	<LOD	<LOD	0.03	19.86	89.94
AZ7.4_z1_mag_p75	Azenhas-Orada	Azenhas	Outcrop	Mag I	0.22	0.05	0.07	0.07	0.12	69.92	<LOD	0.54	<LOD	<LOD	<LOD	0.05	19.20	90.25
AZ7.4_z1_mag_p77	Azenhas-Orada	Azenhas	Outcrop	Mag I	0.23	0.05	0.06	0.04	0.12	70.19	<LOD	0.50	<LOD	<LOD	<LOD	0.05	19.23	90.48
AZ7.4_z1_mag_p76	Azenhas-Orada	Azenhas	Outcrop	Mag I	0.21	0.07	0.03	<LOD	0.11	70.20	<LOD	0.48	<LOD	<LOD	<LOD	0.04	19.20	90.39
AZ7.4_z1_mag_p78	Azenhas-Orada	Azenhas	Outcrop	Mag I	0.26	0.08	0.08	0.02	0.12	70.26	<LOD	0.48	<LOD	<LOD	<LOD	0.06	19.33	90.70
AZ4.3_z1_mag_p5	Azenhas-Orada	Azenhas	Outcrop	Mag II	<LOD	0.07	<LOD	0.05	0.08	71.96	<LOD	0.06	<LOD	<LOD	<LOD	<LOD	19.37	91.64
AZ4.3_z1_mag_p6	Azenhas-Orada	Azenhas	Outcrop	Mag II	<LOD	0.46	0.91	0.04	0.11	69.58	<LOD	0.07	<LOD	<LOD	<LOD	<LOD	20.36	91.58
AZ4.3_z1_mag_p7	Azenhas-Orada	Azenhas	Outcrop	Mag II	<LOD	0.09	0.03	0.02	0.08	71.68	<LOD	0.05	<LOD	<LOD	<LOD	<LOD	19.51	91.52
AZ4.3_z1_mag_p8	Azenhas-Orada	Azenhas	Outcrop	Mag II	<LOD	0.08	0.02	0.02	0.08	72.14	<LOD	0.07	<LOD	<LOD	<LOD	<LOD	19.44	91.88
AZ4.3_z1_mag_p9	Azenhas-Orada	Azenhas	Outcrop	Mag II	<LOD	0.06	0.05	0.05	0.07	71.51	<LOD	0.06	<LOD	<LOD	<LOD	<LOD	19.32	91.16
AZ4.3_z1_mag_p10	Azenhas-Orada	Azenhas	Outcrop	Mag II	<LOD	0.08	0.11	<LOD	0.08	72.08	<LOD	0.05	<LOD	<LOD	<LOD	<LOD	19.54	92.02
AZ4.3_z1_mag_p11	Azenhas-Orada	Azenhas	Outcrop	Mag II	<LOD	0.11	0.11	0.13	0.09	71.92	<LOD	0.07	<LOD	<LOD	<LOD	<LOD	19.82	92.30
AZ4.3_z1_mag_p12	Azenhas-Orada	Azenhas	Outcrop	Mag II	<LOD	0.11	0.07	<LOD	0.10	71.85	<LOD	0.06	<LOD	<LOD	<LOD	<LOD	19.50	91.74
AZ4.3_z1_mag_p13	Azenhas-Orada	Azenhas	Outcrop	Mag II	<LOD	0.08	0.02	0.02	0.10	72.13	<LOD	0.08	<LOD	<LOD	<LOD	<LOD	19.54	91.99

Analysis Code	Deposit	Ore Bodie	Sample Type	Magnetite type	Mg	Al	Si	Ca	Ti	Fe	Cr	Mn	Ni	V	Co	Zn	O	Total
AZ4.3_z1_mag_p14	Azenhas-Orada	Azenhas	Outcrop	Mag II	<LOD	0.07	0.03	0.04	0.07	71.88	<LOD	0.07	<LOD	<LOD	<LOD	<LOD	19.70	91.93
AZ4.3_z1_mag_p15	Azenhas-Orada	Azenhas	Outcrop	Mag II	<LOD	0.11	0.11	<LOD	0.08	71.55	<LOD	0.07	<LOD	<LOD	<LOD	0.03	19.49	91.47
AZ4.3_z1_mag_p16	Azenhas-Orada	Azenhas	Outcrop	Mag II	<LOD	0.08	0.04	0.02	0.08	72.03	<LOD	0.09	<LOD	<LOD	<LOD	<LOD	19.99	92.35
AZ4.3_z1_mag_p17	Azenhas-Orada	Azenhas	Outcrop	Mag II	<LOD	0.06	<LOD	<LOD	0.07	72.06	<LOD	0.08	<LOD	<LOD	<LOD	<LOD	19.57	91.89
AZ4.3_z1_mag_p19	Azenhas-Orada	Azenhas	Outcrop	Mag II	<LOD	0.06	0.02	0.03	0.08	71.91	<LOD	0.09	<LOD	<LOD	<LOD	<LOD	19.96	92.17
AZ4.3_z1_mag_p20	Azenhas-Orada	Azenhas	Outcrop	Mag II	<LOD	0.12	0.20	0.10	0.10	71.22	<LOD	0.09	<LOD	<LOD	<LOD	<LOD	19.62	91.53
AZ4.3_z1_mag_p21	Azenhas-Orada	Azenhas	Outcrop	Mag II	<LOD	0.11	<LOD	<LOD	0.09	72.42	<LOD	0.07	<LOD	<LOD	<LOD	<LOD	19.56	92.32
AZ4.3_z1_mag_p24	Azenhas-Orada	Azenhas	Outcrop	Mag II	<LOD	0.09	0.03	0.08	0.09	71.77	<LOD	0.10	<LOD	<LOD	<LOD	<LOD	19.76	91.92
AZ4.3_z1_mag_p25	Azenhas-Orada	Azenhas	Outcrop	Mag II	<LOD	0.07	<LOD	0.03	0.08	71.98	<LOD	0.09	<LOD	<LOD	<LOD	<LOD	19.40	91.74
AZ4.3_z1_mag_p23	Azenhas-Orada	Azenhas	Outcrop	Mag II	<LOD	0.10	0.03	0.02	0.09	71.82	<LOD	0.10	<LOD	<LOD	<LOD	<LOD	19.42	91.59
AZ4.3_z1_mag_p22	Azenhas-Orada	Azenhas	Outcrop	Mag II	<LOD	0.08	<LOD	0.03	0.08	72.01	<LOD	0.08	<LOD	<LOD	<LOD	<LOD	19.53	91.85
AZ4.3_z1_mag_p26	Azenhas-Orada	Azenhas	Outcrop	Mag II	<LOD	0.07	<LOD	<LOD	0.07	72.02	<LOD	0.09	<LOD	<LOD	<LOD	<LOD	19.57	91.88
AZ4.3_z1_mag_p27	Azenhas-Orada	Azenhas	Outcrop	Mag II	<LOD	0.09	0.03	0.02	0.10	71.20	<LOD	0.09	<LOD	<LOD	<LOD	<LOD	19.25	90.83
AZ4.3_z1_mag_p28	Azenhas-Orada	Azenhas	Outcrop	Mag II	<LOD	0.10	0.02	<LOD	0.06	71.63	<LOD	0.06	<LOD	<LOD	<LOD	<LOD	19.28	91.21
AZ4.3_z1_mag_p29	Azenhas-Orada	Azenhas	Outcrop	Mag II	<LOD	0.10	<LOD	<LOD	0.08	71.63	<LOD	0.06	<LOD	<LOD	<LOD	<LOD	19.30	91.23
AZ4.3_z1_mag_p30	Azenhas-Orada	Azenhas	Outcrop	Mag II	<LOD	0.12	<LOD	<LOD	0.08	71.48	<LOD	0.08	<LOD	<LOD	<LOD	0.03	19.30	91.18
AZ4.3_z1_mag_p31	Azenhas-Orada	Azenhas	Outcrop	Mag II	<LOD	0.12	<LOD	<LOD	0.08	72.29	<LOD	0.09	<LOD	<LOD	<LOD	<LOD	19.48	92.12
AZ4.3_z1_mag_p33	Azenhas-Orada	Azenhas	Outcrop	Mag II	<LOD	0.11	<LOD	<LOD	0.07	71.91	<LOD	0.05	<LOD	<LOD	<LOD	<LOD	19.36	91.59
AZ4.3_z1_mag_p32	Azenhas-Orada	Azenhas	Outcrop	Mag II	<LOD	0.12	0.05	<LOD	0.07	71.71	<LOD	0.07	<LOD	<LOD	<LOD	0.03	19.37	91.47
AZ4.3_z1_mag_p34	Azenhas-Orada	Azenhas	Outcrop	Mag II	<LOD	0.12	0.02	<LOD	0.07	71.23	<LOD	0.07	<LOD	<LOD	<LOD	0.04	19.21	90.80
AZ4.3_z1_mag_p35	Azenhas-Orada	Azenhas	Outcrop	Mag II	<LOD	0.10	<LOD	<LOD	0.07	71.74	<LOD	0.08	<LOD	<LOD	<LOD	<LOD	19.33	91.39
AZ4.3_z1_mag_p36	Azenhas-Orada	Azenhas	Outcrop	Mag II	<LOD	0.07	<LOD	<LOD	0.07	71.61	<LOD	0.08	<LOD	<LOD	<LOD	<LOD	19.26	91.14
AZ4.3_z1_mag_p37	Azenhas-Orada	Azenhas	Outcrop	Mag II	<LOD	0.11	0.02	<LOD	0.07	71.64	<LOD	0.08	<LOD	<LOD	<LOD	<LOD	19.29	91.26

Analysis Code	Deposit	Ore Bodie	Sample Type	Magnetite type	Mg	Al	Si	Ca	Ti	Fe	Cr	Mn	Ni	V	Co	Zn	O	Total
AZ4.3_z1_mag_p38	Azenhas-Orada	Azenhas	Outcrop	Mag II	<LOD	0.13	<LOD	<LOD	0.07	71.50	<LOD	0.08	<LOD	<LOD	<LOD	<LOD	19.25	91.08
AZ4.3_z1_mag_p39	Azenhas-Orada	Azenhas	Outcrop	Mag II	<LOD	0.10	<LOD	<LOD	0.07	71.48	<LOD	0.06	<LOD	<LOD	<LOD	<LOD	19.21	90.96
AZ4.3_z1_mag_p40	Azenhas-Orada	Azenhas	Outcrop	Mag II	<LOD	0.09	0.02	0.03	0.08	72.15	<LOD	0.08	<LOD	<LOD	<LOD	<LOD	19.67	92.16
AZ4.3_z1_mag_p41	Azenhas-Orada	Azenhas	Outcrop	Mag II	<LOD	0.10	0.02	<LOD	0.07	71.60	<LOD	0.09	<LOD	<LOD	<LOD	<LOD	19.29	91.23
AZ4.3_z1_mag_p42	Azenhas-Orada	Azenhas	Outcrop	Mag II	<LOD	0.11	0.02	<LOD	0.07	71.70	<LOD	0.09	<LOD	<LOD	<LOD	<LOD	19.32	91.37
AZ4.3_z1_mag_p43	Azenhas-Orada	Azenhas	Outcrop	Mag II	<LOD	0.10	0.02	<LOD	0.07	71.58	<LOD	0.06	<LOD	<LOD	<LOD	<LOD	19.30	91.17
AZ4.3_z1_mag_p44	Azenhas-Orada	Azenhas	Outcrop	Mag II	<LOD	0.08	<LOD	<LOD	0.06	71.72	<LOD	0.07	<LOD	<LOD	<LOD	<LOD	19.26	91.25
AZ4.3_z1_mag_p45	Azenhas-Orada	Azenhas	Outcrop	Mag II	<LOD	0.09	<LOD	0.02	0.07	71.86	<LOD	0.08	<LOD	<LOD	<LOD	<LOD	19.35	91.54
AZ4.3_z1_mag_p46	Azenhas-Orada	Azenhas	Outcrop	Mag II	<LOD	0.12	<LOD	<LOD	0.07	71.46	<LOD	0.07	<LOD	<LOD	<LOD	<LOD	19.24	91.04
AZ4.3_z1_mag_p47	Azenhas-Orada	Azenhas	Outcrop	Mag II	<LOD	0.13	<LOD	0.02	0.07	71.77	<LOD	0.09	<LOD	<LOD	<LOD	<LOD	19.34	91.47
AZ4.3_z1_mag_p48	Azenhas-Orada	Azenhas	Outcrop	Mag II	<LOD	0.10	<LOD	<LOD	0.08	71.40	<LOD	0.09	<LOD	<LOD	<LOD	<LOD	19.21	90.94
AZ4.3_z1_mag_p49	Azenhas-Orada	Azenhas	Outcrop	Mag II	<LOD	0.09	<LOD	<LOD	0.07	72.03	<LOD	0.08	<LOD	<LOD	<LOD	<LOD	19.40	91.77
AZ4.3_z1_mag_p50	Azenhas-Orada	Azenhas	Outcrop	Mag II	<LOD	0.10	<LOD	<LOD	0.07	72.19	<LOD	0.10	<LOD	<LOD	<LOD	<LOD	19.44	91.99
AZ4.3_z1_mag_p51	Azenhas-Orada	Azenhas	Outcrop	Mag II	<LOD	0.15	<LOD	<LOD	0.08	71.12	<LOD	0.08	<LOD	<LOD	<LOD	<LOD	19.16	90.63
AZ4.3_z1_mag_p52	Azenhas-Orada	Azenhas	Outcrop	Mag II	0.07	0.10	0.29	0.14	0.08	71.02	<LOD	0.09	<LOD	<LOD	<LOD	<LOD	19.53	91.35
AZ4.3_z1_mag_p53	Azenhas-Orada	Azenhas	Outcrop	Mag II	<LOD	0.11	<LOD	<LOD	0.07	71.55	<LOD	0.09	<LOD	<LOD	<LOD	<LOD	19.27	91.15
AZ4.3_z1_mag_p54	Azenhas-Orada	Azenhas	Outcrop	Mag II	<LOD	0.12	<LOD	<LOD	0.07	71.60	<LOD	0.09	<LOD	<LOD	<LOD	<LOD	19.31	91.30
AZ4.3_z1_mag_p55	Azenhas-Orada	Azenhas	Outcrop	Mag II	<LOD	0.11	<LOD	<LOD	0.08	72.16	<LOD	0.09	<LOD	<LOD	<LOD	<LOD	19.48	92.04
AZ4.3_z1_mag_p56	Azenhas-Orada	Azenhas	Outcrop	Mag II	<LOD	0.12	<LOD	<LOD	0.07	71.69	<LOD	0.10	<LOD	<LOD	<LOD	<LOD	19.32	91.34
AZ4.3_z1_mag_p57	Azenhas-Orada	Azenhas	Outcrop	Mag II	<LOD	0.07	<LOD	<LOD	0.08	72.11	<LOD	0.08	<LOD	<LOD	<LOD	<LOD	19.38	91.77
AZ4.3_z1_mag_p58	Azenhas-Orada	Azenhas	Outcrop	Mag II	<LOD	0.10	<LOD	<LOD	0.08	72.17	<LOD	0.08	<LOD	<LOD	<LOD	<LOD	19.44	91.93
AZ4.3_z1_mag_p59	Azenhas-Orada	Azenhas	Outcrop	Mag II	<LOD	0.11	<LOD	<LOD	0.09	71.60	<LOD	0.08	<LOD	<LOD	<LOD	<LOD	19.28	91.19
AZ4.3_z1_mag_p60	Azenhas-Orada	Azenhas	Outcrop	Mag II	<LOD	0.10	<LOD	<LOD	0.10	71.65	<LOD	0.07	<LOD	<LOD	<LOD	<LOD	19.31	91.30

Analysis Code	Deposit	Ore Bodie	Sample Type	Magnetite type	Mg	Al	Si	Ca	Ti	Fe	Cr	Mn	Ni	V	Co	Zn	O	Total
AZ4.3_z1_mag_p61	Azenhas-Orada	Azenhas	Outcrop	Mag II	<LOD	0.08	0.02	<LOD	0.10	71.80	<LOD	0.06	<LOD	<LOD	<LOD	<LOD	19.33	91.43
AZ4.3_z1_mag_p62	Azenhas-Orada	Azenhas	Outcrop	Mag II	<LOD	0.10	0.03	<LOD	0.09	71.64	<LOD	0.08	<LOD	<LOD	<LOD	<LOD	19.29	91.25
AZ4.3_z1_mag_p63	Azenhas-Orada	Azenhas	Outcrop	Mag II	<LOD	0.09	<LOD	<LOD	0.09	71.98	<LOD	0.06	<LOD	<LOD	<LOD	<LOD	19.37	91.65
AZ4.3_z1_mag_p64	Azenhas-Orada	Azenhas	Outcrop	Mag II	<LOD	0.10	<LOD	<LOD	0.09	71.86	<LOD	0.08	<LOD	<LOD	<LOD	<LOD	19.33	91.51
AZ4.3_z1_mag_p65	Azenhas-Orada	Azenhas	Outcrop	Mag II	<LOD	0.10	<LOD	<LOD	0.10	71.87	<LOD	0.06	<LOD	<LOD	<LOD	<LOD	19.37	91.57
AZ4.3_z1_mag_p66	Azenhas-Orada	Azenhas	Outcrop	Mag II	<LOD	0.10	<LOD	<LOD	0.10	71.44	<LOD	0.07	<LOD	<LOD	<LOD	0.03	19.27	91.08
AZ4.3_z1_mag_p67	Azenhas-Orada	Azenhas	Outcrop	Mag II	<LOD	0.08	<LOD	0.04	0.09	71.75	<LOD	0.08	<LOD	<LOD	<LOD	<LOD	19.46	91.52
AZ4.3_z1_mag_p68	Azenhas-Orada	Azenhas	Outcrop	Mag II	<LOD	0.11	0.10	0.06	0.10	71.14	<LOD	0.08	<LOD	<LOD	<LOD	<LOD	19.31	90.98
AZ4.3_z1_mag_p69	Azenhas-Orada	Azenhas	Outcrop	Mag II	<LOD	0.09	<LOD	0.02	0.09	71.43	<LOD	0.07	<LOD	<LOD	<LOD	<LOD	19.25	91.03
AZ4.3_z1_mag_p70	Azenhas-Orada	Azenhas	Outcrop	Mag II	<LOD	0.08	0.07	0.04	0.12	71.47	<LOD	0.06	<LOD	<LOD	<LOD	<LOD	19.33	91.22
AZ4.3_z1_mag_p71	Azenhas-Orada	Azenhas	Outcrop	Mag II	<LOD	0.07	<LOD	<LOD	0.09	71.43	<LOD	0.06	<LOD	<LOD	<LOD	<LOD	19.20	90.90
AZ4.3_z1_mag_p72	Azenhas-Orada	Azenhas	Outcrop	Mag II	<LOD	0.10	<LOD	0.02	0.09	71.47	<LOD	0.08	<LOD	<LOD	<LOD	<LOD	19.27	91.09
AZ4.3_z1_mag_p73	Azenhas-Orada	Azenhas	Outcrop	Mag II	<LOD	0.12	<LOD	0.08	0.08	71.16	<LOD	0.08	<LOD	<LOD	<LOD	<LOD	19.40	90.95
AZ4.3_z1_mag_p74	Azenhas-Orada	Azenhas	Outcrop	Mag II	<LOD	0.10	0.02	0.02	0.08	71.69	<LOD	0.07	<LOD	<LOD	<LOD	<LOD	19.77	91.80
AZ4.3_z1_mag_p75	Azenhas-Orada	Azenhas	Outcrop	Mag II	<LOD	0.10	<LOD	0.02	0.08	71.40	<LOD	0.09	<LOD	<LOD	<LOD	<LOD	19.20	90.91
AZ4.3_z1_mag_p76	Azenhas-Orada	Azenhas	Outcrop	Mag II	<LOD	0.09	0.02	<LOD	0.08	71.56	<LOD	0.07	<LOD	<LOD	<LOD	<LOD	19.25	91.10
AZ4.3_z1_mag_p77	Azenhas-Orada	Azenhas	Outcrop	Mag II	<LOD	0.10	<LOD	<LOD	0.08	71.33	<LOD	0.08	<LOD	<LOD	<LOD	<LOD	19.17	90.81
AZ4.3_z1_mag_p78	Azenhas-Orada	Azenhas	Outcrop	Mag II	<LOD	0.08	<LOD	<LOD	0.09	71.73	<LOD	0.09	<LOD	<LOD	<LOD	<LOD	19.30	91.34
AZ4.3_z1_mag_p79	Azenhas-Orada	Azenhas	Outcrop	Mag II	<LOD	0.11	<LOD	<LOD	0.08	71.84	<LOD	0.08	<LOD	<LOD	<LOD	<LOD	19.41	91.61

Appendix F

Complete LA-ICP-MS raw results

Appendix F-1.

Average LOD, accuracy and precision for the analysis of the reference materials used throughout LA-ICP-MS analysis

		External Standard					Quality Controls									
		GSE-1G					BCR-2G					GSC-1G				
Element	**Avg. LOD**	**Total Avg.**	**Avg. Total Recovery**	**Avg. Total Accuracy**	**Avg. Total Stdev.**	**Avg. Total precision (%)**	**Total Avg.**	**Avg. Total Recovery**	**Avg. Total Accuracy**	**Avg. Total Stdev.**	**Avg. Total precision (%)**	**Total Avg.**	**Avg. Total Recovery**	**Avg. Total Accuracy**	**Avg. Total Stdev.**	**Avg. Total precision (%)**
Mg24	0.514	21053.025	100.253	-0.253	779.105	3.699	20595.365	94.641	5.359	693.731	3.349	21304.254	98.124	1.876	1150.348	5.316
Al27	0.406	68965.484	100.241	-0.241	2573.715	3.730	68410.297	95.161	4.839	2453.865	3.553	70392.261	98.589	1.411	3705.292	5.168
Si28	61.340	251708.010	100.282	-0.282	10293.949	4.087	252105.178	99.649	0.351	10524.674	4.129	248270.256	103.231	-3.231	13161.540	5.196
Ca42	57.802	53099.382	100.188	-0.188	1591.167	2.995	50917.646	99.976	0.024	1988.562	3.847	52175.251	102.910	-2.910	2148.338	4.094
Sc45	0.152	530.726	100.137	-0.137	13.823	2.604	33.564	102.211	-2.211	1.112	3.285	5.599	103.684	-3.684	0.262	4.721
Ti49	0.429	450.663	100.147	-0.147	15.527	3.445	13954.167	98.774	1.226	477.264	3.386	8755.132	106.770	-6.770	458.510	5.148
V51	0.049	440.632	100.144	-0.144	12.521	2.841	438.194	103.459	-3.459	12.182	2.757	5.564	103.030	-3.030	0.320	5.659
Cr52	0.389	400.875	100.219	-0.219	11.326	2.822	16.659	97.874	2.126	0.447	2.684	10.380	100.776	-0.776	0.583	5.601
Mn55	0.170	590.698	100.118	-0.118	10.507	1.778	1555.248	102.420	-2.420	23.206	1.479	186.324	105.866	-5.866	6.931	3.681
Fe57	9.570	98699.845	100.000	0.000	0.011	0.000	96504.241	99.983	0.017	0.011	0.000	105714.300	99.730	0.270	0.011	0.000
Co59	0.030	380.453	100.119	-0.119	7.826	2.057	37.207	97.851	2.149	0.827	2.210	6.024	102.105	-2.105	0.268	4.363
Ni62	0.865	440.410	100.093	-0.093	12.217	2.773	12.387	95.290	4.710	0.724	5.889	21.133	100.635	-0.635	1.718	8.056
Cu65	0.167	380.376	100.099	-0.099	9.956	2.616	17.215	80.048	19.952	0.584	3.450	16.525	103.283	-3.283	1.788	10.836
Zn66	0.225	460.402	100.087	-0.087	12.917	2.805	141.684	114.853	-14.853	4.481	3.079	12.806	100.835	-0.835	0.785	5.978
Ga71	0.039	490.994	100.203	-0.203	12.844	2.614	20.371	87.081	12.919	0.460	2.280	9.763	97.634	2.366	0.497	4.975
Ge73	0.252	320.474	100.148	-0.148	9.438	2.944	1.649	112.519	-12.519	0.225	13.340	3.676	91.894	8.106	0.324	8.691
As75	0.255	260.749	100.288	-0.288	11.656	4.468	1.012	#DIV/0!	#DIV/0!	0.174	16.608	3.523	110.082	-10.082	0.300	8.389
Y89	0.006	411.182	100.288	-0.288	11.454	2.783	32.897	93.537	6.463	0.831	2.529	4.474	93.206	6.794	0.213	4.707
Zr90	0.007	410.636	100.155	-0.155	10.042	2.444	181.230	98.190	1.810	4.317	2.372	6.437	94.659	5.341	0.317	4.877
Nb93	0.004	420.903	100.215	-0.215	11.879	2.820	11.548	91.797	8.203	0.311	2.706	4.497	99.940	0.060	0.214	4.691

Mo97	0.057	390.801	100.205	-0.205	11.836	3.027	262.281	96.886	3.114	5.979	2.279	4.534	98.556	1.444	0.343	7.444
Sn118	0.050	280.600	100.214	-0.214	7.522	2.678	1.749	63.404	36.596	0.090	5.424	3.645	68.768	31.232	0.228	6.155
La139	0.004	392.934	100.238	-0.238	10.433	2.653	24.641	99.957	0.043	0.677	2.742	4.386	100.601	-0.601	0.186	4.198
Ce140	0.003	415.179	100.285	-0.285	11.880	2.858	52.057	97.588	2.412	1.450	2.781	4.702	101.781	-1.781	0.226	4.752
Pr141	0.003	461.267	100.275	-0.275	13.809	2.991	6.464	96.465	3.535	0.190	2.936	4.769	99.351	0.649	0.202	4.188
Nd146	0.019	454.350	100.298	-0.298	14.798	3.252	28.398	98.152	1.848	0.851	2.982	4.812	101.952	-1.952	0.256	5.247
Sm147	0.018	489.499	100.307	-0.307	15.319	3.125	6.503	98.824	1.176	0.236	3.616	5.103	102.058	-2.058	0.340	6.561
Eu153	0.008	411.010	100.246	-0.246	12.230	2.973	1.961	100.439	-0.439	0.074	3.725	4.399	99.984	0.016	0.179	4.029
Gd157	0.041	515.043	100.203	-0.203	14.430	2.800	6.740	101.276	-1.276	0.252	3.709	5.311	100.392	-0.392	0.281	5.258
Tb159	0.003	481.633	100.340	-0.340	14.426	2.990	0.974	95.500	4.500	0.040	4.085	4.937	96.795	3.205	0.240	4.845
Dy163	0.011	525.218	100.232	-0.232	15.549	2.957	6.268	97.286	2.714	0.237	3.780	5.422	100.218	-0.218	0.265	4.879
Ho165	0.003	502.258	100.251	-0.251	14.675	2.919	1.247	98.210	1.790	0.049	3.922	5.030	98.634	1.366	0.249	4.924
Er166	0.008	605.156	101.707	-1.707	56.362	9.275	3.581	96.450	3.550	0.177	4.932	3.716	99.892	0.108	0.285	7.562
Tm169	0.003	501.587	100.317	-0.317	15.104	3.007	0.486	95.319	4.681	0.022	4.515	5.037	96.857	3.143	0.264	5.221
Yb172	0.014	521.309	100.252	-0.252	14.132	2.707	3.344	98.894	1.106	0.187	5.589	5.302	100.225	-0.225	0.286	5.383
Lu175	0.003	519.478	100.285	-0.285	14.968	2.876	0.488	96.798	3.202	0.024	5.010	5.280	99.065	0.935	0.235	4.434
Hf178	0.011	395.870	100.220	-0.220	11.390	2.874	4.736	98.097	1.903	0.184	3.885	4.250	98.826	1.174	0.234	5.458
Ta181	0.003	391.143	100.293	-0.293	12.694	3.241	0.680	85.784	14.216	0.031	4.616	4.179	94.986	5.014	0.225	5.347
W182	0.014	431.062	100.247	-0.247	13.122	3.039	0.527	106.269	-6.269	0.047	8.925	4.686	104.138	-4.138	0.251	5.250
Pb208	0.063	378.998	100.264	-0.264	12.509	3.296	10.264	92.725	7.275	0.331	3.258	14.107	100.765	-0.765	0.720	5.023
Th232	0.010	382.192	100.577	-0.577	17.629	4.605	5.766	97.836	2.164	0.206	3.594	3.766	89.675	10.325	0.276	7.388
U238	0.004	421.419	100.338	-0.338	13.951	3.306	1.711	101.565	-1.565	0.061	3.554	4.653	98.998	1.002	0.224	4.778

Appendix F-2.

Complete results of the LA-ICP-MS analysis of magnetite from the Montemor-o-Novo iron deposits

Appendix F-2.1. – LA-ICP-MS ray results of drill core samples of magnetite fom Montemor-o-Novo iron mines – Monges Mine (the unfilled spaces in the following tables correspond to values below the limits of detection of the equipment).

Sample	005.20.3a								
Analysis	1	2	3	4	5	6	7	8	9
Element (ppm)	Primary Magnetite (Mag I)								
Mg	315.58	1732.61	7596.08	5788.1	1838.4	322.08	3868.58	1229.35	1260.08
Al	520.02	1484.65	4410	3789.68	1418.31	433.98	2679.95	804.95	806.04
Si	483.59	5905.61	17633.14	12752.91	7479.08	3095.8	9468.11	4734.42	5266.33
Ca		173.2	634.06	304.04	316.83				
Sc									
Ti	458.71	572.79	465.33	482.87	431.15	476.98	477.33	516.81	394.4
V	37.55	42.89	33.75	33.46	33.65	35.07	34.97	34.67	33.49
Cr	14.72	7.43	10.58	6.26	52.43	4.7	12.19	33.59	2.53
Mn	3365.58	3441.98	1802.71	2084.59	2623.98	2696.3	2105.04	2951.13	2132.31
Fe	758803.31	758803.31	758803.31	758803.31	758803.3	758803.31	758803.31	758803.3	758803.3
Co									
Ni				4.56	1.54	1.38		1.97	2
Cu									
Zn	43.19	49	19.34	24.53	33.5	39.74	38.72	31.84	27.95
Ga	10.06	11.18	8.95	9.86	8.29	9.58	9.6	8.85	9.64
Ge	1.41	1.15	0.79	1.29	1.31	0.81	1.4	1.28	1.04
As		0.89				0.92			0.91
Y	0.0708	0.403	1.796	0.649	0.359	0.115	0.697	0.395	0.293
Zr	0.0266	0.0388	0.091	0.0066	0.0107	0.0148	0.086	0.185	0.0097
Nb	0.0071	0.068	0.0428		0.0134	0.0233	0.058	0.0407	0.0189
Mo							0.139		
Sn	1.5	2.16	2.33	1.91	1.25	1.46	3.06	2.34	2.23
Hf		0.0148							
Ta	0.006	0.0104	0.0167		0.0219	0.006	0.0195	0.0441	0.0047
W		0.101	0.116	0.089	0.039	0.084	0.06	0.021	0.041
Pb		0.123	0.174			0.223		0.594	
Th	0.0036	0.0021	0.005			0.009	0.0025	0.0092	0.0028
U	0.0077	0.085	0.428	0.167	0.146	0.0306	0.071	0.049	0.0533

Sample	005.20.3a								
Analysis	10	11	12	13	14	15	16	17	18
Element (ppm)	Primary Magnetite (Mag I)								
Mg	3750.29	2416.92	172.17	1405.88	611.62	2107.96	567.21	1040.9	2677.84
Al	1868.71	1862.38	434.6	1034.1	954.59	1949.47	1013.89	1090.27	1684.86
Si	11801.96	6343.17	2285.06	5279.21	3105.81	6927.39	2109.6	5137.8	7025.5
Ca	732.53								
Sc									
Ti	364.33	603.67	449.41	617.11	594.76	563.05	594.31	547.64	564.71
V	29.82	39.4	29.49	37.05	39.33	35.62	37.49	35.21	38.24
Cr	2.92	18	14.34	15.36	29.61	8.77	11.75	31.85	34.31
Mn	1922.08	2749.85	2504.88	1924.79	3047.38	1849.64	3367.04	2488.13	1617.73
Fe	758803.31	763301.56	763301.56	763301.63	768102.9	768103	768103	768103.1	768103
Co		0.346	0.186	0.185	0.526	0.316	0.435	0.339	0.13
Ni									
Cu									
Zn	23.11	35.12	36.84	36.6	39.62	32.02	39.61	36.23	15.82
Ga	8.96	12.17	7.78	9.63	10.34	10.58	10.09	9.19	8.21
Ge	1.17	1.13	0.75	1.58	0.76	0.97	1.03	1.18	1.54
As	1.83			0.84	0.88	1.02		0.68	0.56
Y	0.799	0.691	0.0957	0.538	0.222	0.88	0.159	0.373	0.698
Zr	0.051	0.023		0.0159	0.0094	0.044	0.0158	0.094	0.026
Nb	0.0518	0.0266	0.052	0.161	0.093	0.082	0.011	0.0472	0.324
Mo		0.226		0.261					
Sn	2.9	3.09	3.8	3.08	7.55	5.86	9.03	2.42	1.95
Hf		0.016						0.0031	
Ta	0.0104	0.0045	0.0095	0.0185	0.0344	0.0147	0.0025	0.0071	0.0237
W	0.132	0.021		0.161	0.031	0.117	0.0195	0.046	0.524
Pb	0.164								
Th	0.0113	0.0237	0.0024	0.0279	0.0017	0.002	0.0025	0.004	0.0038
U	0.114	0.181	0.022	0.396	0.0036	0.0065	0.015	0.029	0.176

Sample	005.20.3a								
Analysis	19	20	21	22	23	24	25	26	27
Element (ppm)	Primary Magnetite (Mag I)								
Mg	3294.66	2652.43	2780.87	2487.22	1587.23	5557.4	777.34	1899.21	1207.89
Al	2080.62	1641.01	1973.88	1596.91	1225.93	1123.15	756.49	1174.33	847.15
Si	11746.29	7799.47	7946.52	7246.93	4281.4	17912.18	3143.02	7450.8	5051.61
Ca	447.79	176.56	1055.38	242.35	496.43	5232.18			
Sc									
Ti	620.02	520.15	470.9	499.23	445.76	462.17	520.94	522.88	538.9
V	35.36	35.57	32.62	36.22	31.88	33.2	34.03	33.66	35.74
Cr	7.8	23.93	42.17	20.5	8.56	5.53	14.92	9.81	16.79
Mn	2477.23	1175.99	1306.52	2136.47	2088.31	1922.72	2123.4	2133.58	3146.76
Fe	768103	768102.9	768102.9	768102.9	768102.9	768102.9	768102.9	768102.9	768102.9
Co	0.15	0.118	0.118	0.211	0.081		0.169	0.075	0.217
Ni		1.74							
Cu			1.63						
Zn	31.2	19.63	20.41	33.49	30.06	20.05	35.27	31.53	41.43
Ga	10.56	8.91	8.16	11.36	8.58	8.33	8.8	9.93	9.55
Ge	1.68	0.93	1.25	2.11	1.02	1.2	1.07	1.12	0.81
As	2.67			0.52			0.79	1.22	
Y	1.128	1.077	0.891	0.437	0.338	3.98	0.272	0.42	0.155
Zr	0.05	10.49	26.96	0.117		0.078	0.0141	0.034	0.0124
Nb	0.313	0.076	0.15	0.0669	0.0095	0.126	0.092	0.131	0.09
Mo	0.09	0.165				0.122			
Sn	2.59	2.5	1.72	1.89	2.84	5.22	3.05	2.81	2.19
Hf		0.325	0.518				0.014	0.0061	0.007
Ta	0.0424	0.0156		0.0107	0.0041	0.0087	0.0184	0.0053	0.0182
W	0.374	0.049	0.122	0.0169	0.032	0.04		0.288	0.038
Pb			0.215				0.089		
Th	0.0206	0.063	0.0159	0.0055	0.0041	0.0105	0.0031	0.0053	
U	0.356	1.168	0.719	0.18	0.193	0.293	0.064	0.095	0.06

Sample	005.21.2b								
Analysis	1	2	3	4	5	6	7	8	9
Element (ppm)	Primary Magnetite (Mag I)								
Mg	1731.05	804.7	1291.05	2632.86	938.58	1587.08	2589.37	2901.76	1634.17
Al	438.08	196.01	464.42	710.52	420.13	516.16	1140.04	1068.7	378.23
Si	698.55	1018.56	1469.45	2730.66	1316.25	2829.24	4419.1	3941.85	1754.19
Ca				1728.92	83.24	6010.46			
Sc		0.59	0.47		0.219	1.04		0.69	
Ti	592.88	573.07	650.68	708.36	157.86	296.4	422.23	329.2	485.11
V	31.02	16.82	35.82	39.99	18.75	15.18	26.91	24.8	32.58
Cr	6.11		18.97	21.37	42.89	60.85	9.94	7.65	7.16
Mn	5135.35	5372.71	6121.9	6596.78	5018.78	5391.34	1074.36	965.55	7335.53
Fe	766348.6	766348.5	766348.5	766348.5	766348.6	766348.5	766348.6	766348.6	766348.6
Co	0.194	0.118	0.265	0.183					0.182
Ni		2.66			11.56	3.24	5.7	2.97	
Cu							0.236		
Zn	28.74	32.77	48.57	45.04	37.7	43.04	18.75	13.06	54.94
Ga	5.25	5.02	6.67	7.07	4.03	5.13	4.64	3.97	6.54
Ge	1.43	0.91	1.14	2.17	0.89	2.08	1.67	1.21	1.61
As				2.94	1.81	3.03			1.49
Y	0.494	0.162	0.29	0.706	0.355	4.04	1.245	1.287	0.414
Zr			0.0064	0.114	0.0049	0.074	0.024	0.0318	0.011
Nb	0.07	0.0374	0.0361	0.076	0.0563	0.225	0.092	0.131	0.044
Mo								0.131	
Sn	11.03	13.87	12.04	13.37	5.51	15.56	11.67	10.26	14.39
Hf	0.013			0.0103	0.0034		0.0039		
Ta	0.0074		0.0125	0.0104	0.0103	0.0427	0.0078	0.0094	0.0123
W	0.0057	0.092		0.082	0.127	0.53	0.29	0.213	0.037
Pb				0.289	0.089	0.184			
Th		0.0059	0.0019			0.0144			0.0083
U	0.0123		0.0376	0.0292	0.0097	0.062	0.02	0.0275	0.0404

Sample	005.21.2b								
Analysis	10	11	12	13	14	15	16	17	18
Element (ppm)	Primary Magnetite (Mag I)								
Mg	1382.07	1408.6	997.75	1151.28	3213.37	1508.33	1930.35	2809.16	1324.72
Al	415.5	775.82	493.41	261.81	1097.83	691.94	984.64	699.63	356.99
Si	1625.29	1580.51	1313.92	995.96	3640.31	1077.73	1562.86	3633.17	1756.54
Ca								1541.13	
Sc	0.79	0.35	0.4			0.35	0.83	0.87	
Ti	700.72	481.26	703.28	431.81	611.08	424.08	489	712.27	468.51
V	35.42	32.49	35.35	27.7	39.82	33.03	35.85	34.62	21.63
Cr	5.97	12.72	5.54	4.26	3.11	2.76	1.58	5.96	3.92
Mn	6629.99	4525.66	6267.93	6001.02	5391.36	6152.78	6577.32	6576.41	4008.16
Fe	766348.6	766348.6	766348.6	766348.6	766348.6	766348.6	766348.6	766348.6	766348.6
Co	0.637	0.246	0.797	0.121	0.559	0.197	0.172	0.375	0.329
Ni	2.37								
Cu									
Zn	57.5	43.73	41.61	47.37	55.33	50.21	58.97	44.67	27.55
Ga	5.99	6.11	6.33	6.11	7.06	6.18	6.2	7.12	3.89
Ge	1.89	1.69	0.84	1.24	1.64	1.96	2.14	0.98	0.72
As					1.58			3.42	0.81
Y	0.464	0.162	0.09	0.085	1.84	0.103	0.213	1.307	0.496
Zr			0.0084	0.0082				0.049	0.0199
Nb	0.059	0.0132	0.0097	0.0031	0.165	0.0092	0.0151	0.139	0.0524
Mo		0.097	0.182	0.21		0.146			
Sn	12.22	14.73	13.16	15.09	15.64	14.1	15.95	14.08	9.17
Hf		0.0028							
Ta	0.0172	0.0032	0.0016	0.0033	0.0381			0.0179	0.011
W	0.169	0.132	0.044	0.015	0.131		0.081	0.118	0.023
Pb									
Th	0.0058	0.0049			0.0048			0.027	0.0046
U	0.038	0.0079	0.0053		0.092	0.007	0.0057	0.127	0.0182

Sample	005.21.2b								
Analysis	19	20	21	22	23	24	25	26	27
Element (ppm)	Primary Magnetite (Mag I)								
Mg	4261.36	1035.4	2477.15	1247.84	4162.21	3438.44	1470.7	1640.9	1803.02
Al	1356.49	493.97	718.48	629.92	1110.65	1314.64	1201.11	1282.71	1284.73
Si	6280.02	1444.61	4036.65	1742.6	4958.49	4152.72	1557.5	1528.82	1740.18
Ca	191.21								
Sc			0.8		0.74	0.6	0.46	0.65	1
Ti	882.07	622.98	692.71	835.83	965.55	1032.74	920.62	988.72	985.71
V	36.82	45.49	39.28	49.47	70.62	75.69	68.26	81.74	79.83
Cr	11.84	0.67	26.53	4.38	10.08	58.74	123.57	18.11	28.47
Mn	3281.44	5676.61	5121.81	7131.29	6493.38	6387.33	7845.41	7679.96	8270.91
Fe	766348.6	766452.9	766452.9	766452.9	766452.9	766452.9	766452.9	766452.9	766452.9
Co	0.227		0.07		0.139	0.161	0.141	0.212	0.205
Ni	2.56	1.53							
Cu									
Zn	44.45	54.81	54.15	54.02	59.06	63.57	71.81	49.51	58.94
Ga	6.86	5.06	4.49	6.66	5.82	6.46	6.9	5.99	7
Ge	1.67	1.29	2.04	1.3	2.07	3.31	2.89	4.93	2.96
As					4.33	5.2			
Y	1.523	0.398	1.081	1.448	1.69	1.367		0.207	0.066
Zr	1.074		0.062	0.0148	0.033	0.027		0.041	0.028
Nb	0.444	0.0493	0.128	0.071	0.098	0.109	0.0104	0.0127	0.0221
Mo				0.138		0.103			0.178
Sn	14.45	11.63	12.61	12.82	15.41	15.89	16.33	17.68	21.4
Hf			0.0085	0.0155					
Ta	0.05	0.0126	0.0195	0.0163	0.0411	0.0252	0.018	0.0163	
W	1.29	0.097	0.179	0.103			0.05	0.137	
Pb									
Th	0.037	0.0043		0.0296	0.0027			0.005	
U	0.219	0.0372	0.04	0.04	0.0089	0.0135		0.038	0.0036

Sample	005.21.2b								
Analysis	29	29	30	31	32	33	34	35	36
Element (ppm)	Primary Magnetite (Mag I)								
Mg	2077.47	3603.54	1856.3	4292.57	1429.68	6919	1766.02	1815.85	3560.15
Al	936.35	1123.07	701.32	1188.92	1037.22	2007.22	804.49	851.54	884.93
Si	2587.83	4356.73	2507.44	5335.73	1671.29	8625.49	2209.52	1092.29	4340.42
Ca									
Sc	0.62	0.76		0.93	0.53	0.41	0.68	0.53	0.43
Ti	821.77	904.42	817.81	892.68	909.32	762.05	912.53	462.95	1032.68
V	62.14	72.14	60.48	62.95	66.14	60.25	77.66	35.14	71.57
Cr	3.99	11.97	2.28	59.37	86.29	8.79	9.06		26.39
Mn	5897.34	7824.08	6047.7	6600.02	6971.46	4410.24	7262.28	6919.2	7434.39
Fe	766452.9	766452.9	766452.9	766452.9	766452.8	766452.9	766452.9	766348.6	766452.9
Co	0.302	0.243	0.208	0.2	0.128	0.124	0.117	0.143	
Ni		3.16			2.43			2.28	
Cu									
Zn	54.53	65.3	45.57	61.73	52.12	41.42	69.83	64.34	61.67
Ga	5.79	7.04	5.63	6.94	5.88	5.52	6.41	6.86	6.13
Ge	1.93	3.47	0.76	2.91	2.51	2.25	1.07	2.31	1.39
As	1.16	4.69	0.96	2.97		3.84	1.21		2.77
Y	0.365	1.379	0.397	2.78	0.148	2.37	0.592	0.093	1.59
Zr	0.0104	0.0237		0.098		0.056			0.0339
Nb	0.065	0.124	0.212	0.189	0.0177	0.11	0.081	0.0111	0.165
Mo	0.16		0.138	0.166					
Sn	14.88	16.08	15.22	16.92	13.85	15.01	14.89	16.07	15.77
Hf		0.0148		0.024					
Ta	0.0109	0.0129	0.0258	0.0301		0.0162	0.0137		0.0174
W	0.072	0.052	0.685	0.076	0.047	0.107	0.018	0.054	0.041
Pb		0.098			0.089	0.101	0.148	0.104	
Th	0.0024	0.0022				0.0125			0.0064
U	0.0313	0.06	0.0163	0.047	0.032	0.092	0.0098	0.0072	0.057

Sample	005.21.2b							
Analysis	37	38	39	40	41	42	43	44
Element (ppm)	Primary Magnetite (Mag I)							
Mg	1031.85	1628.36	4671.05	1871.07	2886.22	1988.08	2081.33	1540.93
Al	241.52	543.77	1090.09	615.52	711.47	515.11	1064.11	624.45
Si	1354.08	2382.03	5972.03	2751.1	4242.21	3030.05	2047.37	2588.98
Ca				91.53				
Sc	0.4		1.11	0.56	0.92	0.38	0.73	0.55
Ti	816.54	797.61	834.55	762.84	867.49	781.45	927.02	1179.45
V	60.13	58.71	69.44	62.41	73.81	57.41	57.04	67.98
Cr	78.48	105.3	10.74	21.71	4.22	7.43	18.01	14.76
Mn	7680.11	4063	4585.21	5114.07	5469.16	4669.53	6772.67	6214.57
Fe	766452.9	766453	766452.9	766452.9	766452.9	766452.9	766453	766452.9
Co	0.248	0.17	0.18	0.229	0.176	0.084	0.079	0.147
Ni		1.58		1.3	2.57	3.16		
Cu								
Zn	47.14	32.97	39.59	44.78	39.9	43.48	52.65	61.56
Ga	5.06	4.84	6.16	5.96	6.51	5.03	5.47	5.41
Ge	0.92	0.94	1.48	1.25		0.9	1.71	1.14
As			2.83	0.54	1.33	1.12	0.53	
Y	0.205	0.396	3	0.524	0.723	1.33	0.235	0.497
Zr		0.051	0.129	0.0103	0.0163	0.047	0.0124	0.03
Nb	0.016	0.0251	0.215	0.083	0.079	0.132	0.0273	0.065
Mo	0.197	0.27	0.093	0.105	0.153			
Sn	12.7	13.19	13.8	12.06	15.39	11.83	10.26	15.92
Hf								
Ta	0.0037		0.0281	0.0083	0.0118	0.0217		0.0123
W	0.0086	0.09	0.134	0.049	0.172	0.1	0.086	0.081
Pb			0.134				0.255	
Th			0.0267	0.0037		0.0102	0.0022	
U		0.0212	0.16	0.0142	0.041	0.0074	0.0318	0.053

Sample	005.17.3a									
Analysis	1	2	3	4	5	6	7	8	9	10
Element (ppm)	Primary Magnetite (Mag I)									
Mg	5334.95	6042.78	7823.5	3775.72	2852.62	2571.96	1349.01	1823.58	1949.99	2027.79
Al	305.18	271.58	210.45	106.29	127.36	99.63	50.35	72.12	59.2	70.75
Si	4186.71	6137.33	5638.58	4568.23	4858.35	5430.61	4431.93	4557.86	4320.99	4278.1
Ca										
Sc	1.058	1.115	1.27	0.637	0.813	0.838	0.453	0.626	0.698	0.466
Ti	348.27	334.73	413.4	319.71	331.41	384.67	439.13	434.59	426.14	454.7
V	14.34	13.51	15.74	14.78	13.31	15.78	16.39	17.82	18.18	17.08
Cr	3.9	3.79	17.07	2.03	3.85	27.26	1.36	11		4.8
Mn	13917.35	10581.9	15064.85	12320.7	12066.94	14442.84	13808.06	13569.74	14083.43	13839.86
Fe	758608.8	758608.7	758608.8	758608.8	758608.7	758608.8	758608.8	758608.8	758608.8	758608.8
Co	0.993	0.904	1.159	0.875	0.739	0.962	0.758	0.758	0.952	0.633
Ni	0.66	0.88		1.4		1.12		1.26		
Cu										0.209
Zn	74.98	72.46	79.85	65.56	63.77	72.07	59.3	70.88	74.03	66.54
Ga	3.95	3.86	4.74	3.3	2.92	3.4	2.4	2.86	3.02	2.66
Ge	0.98	1.4	1.2	1.21	0.693	0.8	1.03	0.76	0.66	0.59
As	0.743	0.39	0.609	1.1	0.515	0.659	0.186	0.277	0.321	0.61
Y	0.109	0.26	0.175	0.159	0.139	0.0589		0.0513	0.0565	0.182
Zr	0.0546	0.227	0.747	0.0839	0.0769	0.0292	0.0016	0.0424	0.0183	0.616
Nb	0.397	0.985	0.724	0.959	0.719	0.471	0.0076	0.295	0.147	0.384
Mo	0.128	0.084	5.1	5.63	0.092	0.067	0.076	0.089	0.06	0.361
Sn	9.97	8.88	11.57	9.43	9.11	10.56	10.41	10.5	10.64	9.91
Hf	0.0088		0.013	0.0098	0.0095	0.291	0.0024	0.0036	0.0279	0.0256
Ta	0.0344	0.0789	0.0574	0.0907	0.0749	0.0526	0.00175	0.0329	0.0143	0.0381
W	0.149	0.345	0.0155	0.142	0.069	0.0142	0.0099	0.0155	0.0247	0.204
Pb	0.253	0.222	1.82	676.69	0.187	0.119	0.164	0.217	0.198	0.143
Th	0.0035	0.097	0.0194	0.0166	0.005		0.00097		0.0245	0.0207
U	0.0501	0.206	0.228	0.265	0.162	0.0684	0.00051	0.0684	0.075	0.109

Sample	005.17.3a								
Analysis	11	12	13	14	15	16	17	18	19
Element (ppm)	Primary Magnetite (Mag I)								
Mg	4168.63	2905.69	4523.01	3166.62	5072.13	3258.34	4756.01	5024.52	3941.63
Al	188.36	141.84	226.46	134.78	255.69	112.11	245.16	311.74	128.39
Si	5278.22	3542.64	6372.73	4399.43	6562.74	3951.3	5924.08	6425.23	3902.4
Ca			46.39					53.88	
Sc	0.812	0.82	0.955	0.979	0.785	0.823	1.039	0.831	0.858
Ti	350.68	365.84	394.55	391.09	391.23	358.88	380.98	398.44	349.45
V	22.83	25.79	20.81	22.49	23.83	25.29	25.32	26.72	23.37
Cr	15.47	1.75		27.53	31.6	45.11	41.66	45.26	30.72
Mn	11048.85	12213.52	14142.09	14866.78	13918.6	13287.9	14657.55	14751.51	13207.12
Fe	755400	755400	755400.1	755400.1	755400.1	755400	755400	755400	755400.1
Co	0.683	0.561	0.585	1.143	0.889	0.846	1.02	1.031	0.931
Ni		0.75	0.71						1.14
Cu	1.102	0.319							0.07
Zn	58.96	60.46	64.78	70.98	77.76	62.77	75.94	73.56	74.48
Ga	3.06	3.03	3.1	3.59	3.67	3.33	3.68	4.47	3.36
Ge	0.65	6.6	0.87	0.85	1.12	0.71	0.74	1.04	0.87
As	0.61	0.241	1.27	0.346	1.38	0.409	1.23	1.34	0.412
Y	0.195	0.137	0.424	0.0674	0.211	0.0415	0.128	0.074	0.125
Zr	0.142	0.0106	0.0745	0.0644	0.11	0.0439	0.0846	0.086	0.011
Nb	1.012	0.0535	0.124	0.502	0.893	0.399	0.68	0.615	0.133
Mo	0.067	0.119	0.069	0.062	0.083	0.051	0.071	0.111	0.085
Sn	8.97	9.24	9.75	10.66	10.14	9.96	11.73	11.91	9.14
Hf	0.0147	0.0012	0.869	0.009	0.0103	0.0106	0.0079	0.0163	0.0029
Ta	0.0817	0.0063	0.0095	0.0696	0.0577	0.0421	0.0422	0.0401	0.018
W	0.0272	0.282	0.101	0.0399	0.213	0.0129	0.0122		0.127
Pb	0.123	0.15	0.106	0.135	5.12	0.361	0.176	0.156	0.196
Th	0.0037	0.00046	0.0157	0.0049	0.0041	0.00042		0.0022	
U	0.114	0.0082	0.0571	0.094	0.0806	0.0519	0.0618	0.0395	0.0261

Sample	005.17.3a						
Analysis	20	21	22	23	24	25	26
Element (ppm)	Primary Magnetite (Mag I)						
Mg	4095.47	3694.09	3819.62	4368.68	4532.79	5945.98	3953.95
Al	94.48	81.07	105.66	161.65	153.96	313.14	137.54
Si	3675.27	4553.8	4375.73	6027.85	6934.58	8017.43	5001.84
Ca							65.04
Sc	0.802	0.816	0.817	0.949	0.891	0.911	1.006
Ti	354.26	390.55	331.32	380.94	463.53	396.68	362.14
V	24.43	28.24	26.53	24.74	35.91	31.12	28.43
Cr	1.64	1.22	25.71	60.26	24.67	28.9	14.08
Mn	12475.74	14602.46	11672.26	11800.33	13989.26	11829.82	12169.18
Fe	755400	755400	755400	755400	755400	755400	755399.9
Co	0.864	1.069	0.867	1.026	1.059	1.143	0.922
Ni	0.64	1.32			1.41	1.25	0.85
Cu			0.102				
Zn	64.46	79.04	67.59	62.98	77.81	65.96	64.55
Ga	3.31	3.77	2.84	3.25	3.71	3.46	2.86
Ge	1.21	0.74	0.81	0.797	0.94	0.79	0.8
As	0.137	0.149	0.41	1.07	0.8	0.353	1.1
Y	0.0088	0.0254	0.0283	0.174	0.139	0.228	0.138
Zr	0.0217	0.0084	0.0198	0.096	0.125	0.0674	0.0881
Nb	0.0371	0.0178	0.217	0.873	0.946	0.28	0.902
Mo	0.19	0.118	0.084	0.086	0.088	0.068	0.049
Sn	9.17	11.47	9.34	9.29	11.2	10.27	10.26
Hf			0.162	0.0083			0.0099
Ta	0.0077	0.00037	0.82	0.0436	0.0845	0.0241	0.0611
W		0.051	0.162	0.0141	0.0189	0.121	0.112
Pb	292.85	0.154	0.096	3.49	0.267	0.127	29.93
Th		0.00154	0.669	0.0037	0.0031	0.0339	0.00039
U	0.0072		1.73	0.098	0.15	0.105	0.0825

Sample	005.31.4b								
Analysis	1	2	3	4	5	6	7	8	9
Element (ppm)	Secondary Magnetite (Mag II)								
Mg	2554.59	2311.97	2642.91	11868.4	2391.61	2629.47	2960.19	2711.41	3052.79
Al	278.39	292.74	388.25	396.11	317.58	261.55	303.67	311.67	414.97
Si	4528.98	3599.57	4392.38	19047.95	3907.78	4390.01	4423.02	3635.01	5336.46
Ca									
Sc	0.247	0.21	0.275	0.305	0.329	0.303	0.296	0.198	0.61
Ti	383.01	361.68	500.56	423.11	339.61	205.89	294.18	350.21	496.81
V	260.58	204.3	404.47	218.81	204.09	88.85	102.73	213.45	427.31
Cr	1.39	0.51	7.39	11.44	32.87	32.9	3.58	3.31	7.05
Mn	902.57	884.83	936.51	992.99	887.44	913.89	849.21	841.02	999.21
Fe	771320.2	771320.1	771320.1	771320.1	771320.1	771320.2	771320.1	771320.1	771320.1
Co			0.562						
Ni		0.83							
Cu				0.128	42.69				
Zn	73.96	90.29	101.31	96.56	85.03	58	76.87	81.56	103.59
Ga	20.05	22.28	24.76	25.05	22.77	22.88	23.04	23.36	27.89
Ge	0.73	0.73	0.84	1.42	0.94	0.95	0.96	0.95	0.95
As	2.64	0.41	1.62	2.01	0.57	1.53	0.22	0.346	0.31
Y	0.0153	0.00055	0.0027	0.092		0.0046		0.00167	
Zr	0.0123		0.0092					0.0044	
Nb	0.0187		0.0076	0.0314	0.00168	0.0146	0.0019	0.0083	
Mo	0.087	0.051			0.076	0.065	0.133	0.071	0.083
Sn	7.59	10.66	10.09	10.51	10.76	8.02	11.73	10.49	10.44
Hf					0.0015	0.0016			
Ta	0.0045	0.00047	0.0014	0.0034	0.0025				0.006
W			0.0069		0.002				
Pb	0.159	0.091	0.173	0.137	0.084	0.156			0.142
Th	0.0022			0.01		0.00132			
U	0.0446		0.0063	0.063	0.0025	0.0097		0.0035	

Sample	005.31.4b					
Analysis	10	11	12	13	14	15
Element (ppm)	Secondary Magnetite (Mag II)					
Mg	4081.94	2869.93	2777.12	3870.92	7896.22	2923.43
Al	448.62	434.65	378.6	363.72	309.67	74.36
Si	5443.42	4607.41	4893.45	7572.16	12462.62	3644.56
Ca				36.57	68.79	
Sc	0.263	0.277	0.331	0.43	0.183	0.166
Ti	589.78	580.61	455.98	351.96	304.79	26.46
V	811.95	590.38	179.55	200.97	242.27	6.03
Cr	53.87	10.44	0.49	0.5	6.51	0.58
Mn	966	1008.12	1015.3	958.42	1114.02	940.69
Fe	771320.1	771320.1	771320.1	771320.1	771320.1	771320.1
Co						
Ni						
Cu	0.414					
Zn	92.55	102.54	97.25	93.6	90.67	69.45
Ga	28.12	31.67	25.67	24.1	23.9	21.77
Ge	1.42	1.4	1.26	1.92	0.89	0.41
As	5.36	0.61	0.79	0.92	24.58	1.94
Y	0.0269		0.0412	0.119	0.065	0.0135
Zr		0.0068			0.0231	
Nb	0.055	0.0039	0.0083	0.0182	0.131	0.0086
Mo	0.114	0.06	0.055	0.126	0.127	0.065
Sn	9.24	10.49	11.5	10.09	9.76	8.64
Hf	0.0038					
Ta	0.07			0.0034	0.0207	
W	0.064		0.0085	0.027	0.029	
Pb	0.594		0.18	0.294	0.619	813.92
Th	0.0015		0.0012	0.0016	0.0308	
U	0.07		0.0091	0.0365	0.246	0.0162

Sample	004.10.2a								
Analysis	1	2	3	4	5	6	7	8	9
Element (ppm)	Secondary Magnetite (Mag II)								
Mg	1574.63	1768.22	912.59	924.3	1591.41	1521.53	892.76	2070.4	1503.71
Al	394.44	244.28	123.66	98.99	217.38	237.62	144.14	376.53	202.3
Si	3654.25	2987.87	3524.71	2956.59	3140.32	3472.75	2924.92	3468.47	2666.09
Ca							52.31		
Sc							0.15		
Ti	680.82	318.88	768.03	755.84	261.97	189.81	728.56	500.42	193.97
V	41.99	20.07	59.56	72.91	19.69	14.61	51.26	26.16	8.04
Cr	11.54	0.48	1.23	1.17	2.36	0.54	4.25		0.35
Mn	656.4	782.39	740.48	636.08	498.75	636.35	674.63	689.23	733.25
Fe	773875.3	773875.3	773875.3	773875.3	773875.3	773875.3	773875.3	773875.3	773875.3
Co									
Ni		0.7							
Cu	0.059				2.82	0.2		0.171	0.095
Zn	66.66	67.97	68.14	57.2	37.69	56.84	60.14	58.59	66.39
Ga	4.32	4.54	4.72	4.75	4.5	4.96	4.67	5.37	4.78
Ge	0.42	0.32	0.38	0.38	0.53	0.67	0.37	0.71	
As	43.85	1.17	0.87	0.84	0.54	0.8	1.55	6.15	0.59
Y	0.0174			0.0035	0.0127	0.0108	0.009	0.0148	
Zr	0.0121	0.0047			0.0074	0.0025		0.0038	0.0043
Nb	0.0511	0.0081		0.00139	0.0035	0.0134	0.0073	0.0142	0.0025
Mo	0.112	0.136	0.124	0.107	0.123	0.075	0.093	0.061	0.074
Sn	9.9	11.3	11.16	10.05	7.45	10.31	9.93	11.93	10.57
Hf			0.0032	0.0033	0.0051		0.0041		0.004
Ta	0.0028			0.00095			0.00039	0.0022	
W		0.0023	0.0117	0.169	0.0073	0.0146			0.0028
Pb	0.147	0.082	0.087	0.081	0.302		0.088		
Th							0.0021		
U	0.0011		0.00128	0.0046	0.0214	0.00133			

Sample	004.10.2a							
Analysis	10	11	13	13	14	15	16	17
Element (ppm)	Secondary Magnetite (Mag II)							
Mg	12062.75	4028.13	1142.74	1753.04	884.33	1028.1	4072.47	4694.37
Al	504.28	372.62	133.02	139.89	73.94	109.3	256.15	212.05
Si	24264.88	7381.86	3196.2	4507.65	2986.58	3298	8563.55	5950.96
Ca	7893.95	1741.4					142.65	3956.3
Sc	0.263		0.09					
Ti	389.27	331.24	186.7	186.43	143.93	120.24	144.88	205.43
V	37.04	25.71	14.19	13.31	9.08	11.65	8.36	10.13
Cr	3.8	1.23	0.51	0.62	0.5	0.35		0.55
Mn	640.89	644.4	755.91	757.39	578.41	644.33	488.41	693.33
Fe	773875.3	773875.3	773875.3	773875.3	773875.3	773875.3	773875.3	773875.2
Co					0.0216			0.032
Ni								
Cu	0.91	0.208		0.174		0.075		0.214
Zn	50.16	52.68	78.52	63.8	44.01	56.25	44.8	61.34
Ga	6.72	5.95	5.13	4.6	4.36	4.62	4.33	5.37
Ge	1.03	0.98		0.31	0.246	0.44	1.64	0.86
As	7.37	3.85	2.3	0.96	0.88	0.85	1.08	3.13
Y	0.882	0.108	0.022	0.0193		0.0056	0.091	0.2
Zr	0.06	0.0191	0.0027		0.0057	0.0083	0.0119	0.0212
Nb	0.0249	0.0456	0.0336	0.0238	0.0506	0.139	0.0161	0.0206
Mo	0.05	0.114	0.105	0.081	0.108	0.098	0.055	0.095
Sn	10.07	10.95	9.99	9.9	9.19	10.13	9.8	9.5
Hf					0.0013		0.0026	
Ta		0.0018	0.00053			0.00122	0.0017	
W	0.08	0.096	0.0053	0.048		0.078	0.07	0.035
Pb	0.89	0.145	0.178	0.092		0.347	0.08	0.092
Th	0.0071	0.0024					0.002	0.0027
U	0.099	0.0386	0.0204	0.0066		0.00056	0.073	0.0119

Sample	004.12.3b								
Analysis	1	2	3	4	5	6	7	8	9
Element (ppm)	Secondary Magnetite (Mag II)								
Mg	2892.58	3779.86	3624.1	3764.42	3469.47	3157.43	3275.62	3176.47	3603.38
Al	20.53	145.61	74.8	264.26	187.67	146.38	151.84	159.89	26.97
Si	1226.99	1563.33	1848.95	1581.44	1570.78	1364.15	1724.34	1480.57	1700.07
Ca									
Sc				0.188			0.208		
Ti	116.32	181.9	94.8	294.62	476.59	409.41	410.83	320.06	5.69
V	10.89	8.82	2.8	44.85	51.42	58.11	79.38	29.94	0.44
Cr	0.46	0.66	0.59	2.64	1.02	0.8	0.51		0.96
Mn	6456.06	6380.59	4887.43	7269.23	6889.66	6745.85	7163.42	6426.35	6809.13
Fe	766468.4	766468.4	766468.4	766468.4	766468.4	766468.5	766468.5	766468.4	766468.4
Co									
Ni	1.89								
Cu								0.21	
Zn	99.32	145.69	105.95	151.03	145.78	127.73	131.24	121.93	132.51
Ga	0.727	1.033	0.729	0.993	0.849	0.693	0.795	0.8	0.946
Ge	0.46		0.58	0.6	0.58	0.73	0.91	0.71	0.7
As	0.49	0.54	0.55	0.53	1.58	0.5	0.53	1.7	1.23
Y								0.0089	
Zr		0.0085	0.0071	0.0038	0.0398			0.0238	0.002
Nb	0.0022		0.0409		0.0177		0.0203	0.0058	0.105
Mo		0.128	0.05	0.141		0.081	0.087		0.075
Sn	5.52	6.34	5.74	7.7	7.86	7.26	8.6	7.88	6.08
Hf					0.0029				
Ta		0.00093	0.0031		0.004				0.0045
W		0.0045	0.053	0.01	0.0194	0.034	0.151	0.056	0.123
Pb		0.065	0.793		0.067			2.02	0.153
Th			0.0058						0.0016
U			0.0114		0.0197		0.0141	0.0403	0.077

Sample	004.12.3b									
Analysis	10	11	12	13	14	15	16	17	18	19
Element (ppm)	Secondary Magnetite (Mag II)									
Mg	3149.13	4040.27	3398.43	3666.74	2370.3	4145.98	4156.61	3651.22	3618.16	3146.91
Al	73.75	49.48	77.72	139.09	11.04	214.33	225.07	266.39	85.86	110.42
Si	1512.71	1569.96	1708.12	1652.67	1466.8	1758.82	1728.44	1834.28	1630.2	1573.33
Ca		3455.52								
Sc							0.194			
Ti	17.89	21.6	22.84	52.85	17.53	49.93	43.98	52.79	34.36	17.15
V	2.71	5.74	1.67	9.49	11	8.77	2.91	5.34	4.98	1.015
Cr	0.37	0.75	0.76	0.7	0.98	0.88		0.62	0.73	0.59
Mn	6145.58	6856.38	6990.8	6686.25	7858.2	6895.8	7616.2	6554.17	6472.97	5978.88
Fe	766468.5	766468.4	766468.5	766468.5	766468.5	766468.5	766468.5	766468.5	766468.5	766468.6
Co										
Ni				0.83					0.93	
Cu					0.099			108.85		
Zn	143.18	120.4	140.48	163.18	94.94	154.2	164.85	257.11	158.98	144.31
Ga	0.812	0.935	1.191	0.927	0.868	1.133	1.165	1.083	1.243	0.802
Ge	0.33	0.67	0.37	0.68	0.43	1.22	0.68		0.82	0.38
As	0.61	1.52	0.72	0.5	1.15	0.29	0.48	3.32	0.47	0.48
Y	0.0019	0.0186			0.0036				0.0037	
Zr	0.0056	0.0163			0.0106			0.0048	0.0024	
Nb		0.028	0.0259	0.0131	0.0311			0.0082	0.0014	
Mo		0.107		0.068		0.099			0.163	0.115
Sn	7.48	6.21	6.55	7.81	5.27	7.25	6.89	6.62	6.18	6.33
Hf										
Ta			0.0012					0.0053		
W		0.043	0.0119	0.053	0.0046	0.005		0.025		
Pb		0.135			0.254			7.43		
Th		0.0026		0.0016						
U		0.032	0.0061	0.0055	0.0536			0.0014		

Appendix F-2.2. – LA-ICP-MS ray results of outcrop samples of magnetite fom Montemor-o-Novo iron mines – Monges Mine. (the unfilled spaces in the following tables correspond to values below the limits of detection of the equipment).

Sample	MNG 2.1								
Analysis	1	2	3	4	5	6	7	8	9
Element (ppm)	Leached Primary Magnetite (Leached Mag II)								
Mg	499.91	983.3	522.08	716.42	864.9	474.76	484.26	487.7	579.31
Al	372.41	342.29	450.82	416.79	358.1	374.62	506.83	520.01	591.37
Si	2237.41	2714.96	2450.83	2734.49	2856.62	2163.7	2302.27	2569.19	2595.76
Ca									
Sc	0.263	0.304	0.166		0.361	0.206	0.259	0.236	0.3
Ti	116.21	102.1	91.37	116.05	114.57	110.92	102.2	110.99	110.46
V	15.36	13.92	15.44	15.81	15.36	16.57	23.55	24.22	25.09
Cr	6.66	2.13	7.27	3.18	1.81	1.9	3.66	0.74	14.33
Mn	838.49	783.49	739.4	806.46	687.72	780.2	842.01	886.55	906.48
Fe	758655.4	758655.44	758655.44	758655.5	758655.5	758655.5	758655.4	758655.5	758655.5
Co	0.768	0.791	0.759	0.823	0.714	0.76	0.799	0.774	1.083
Ni					0.69				
Cu									0.164
Zn	59.52	55.57	55.44	58.17	57.89	58.9	54.02	64.06	61.58
Ga	4.72	4.28	3.8	4.89	4.07	4.85	4.48	4.76	5.18
Ge	1.04	0.84	1.14	0.38	0.94	0.62	1.41	0.98	1.57
As		1.44		1.17	0.96		0.26		0.3
Y	0.00078	0.061	0.0025	0.0411	0.0223			0.0047	0.0146
Zr		0.06	0.015	0.0146	0.0127			0.0172	0.133
Nb	0.0036	0.342	0.0678	0.255	0.191	0.0252	0.0249	0.0066	0.0203
Mo	0.171	0.12	0.133	0.145	0.08	0.087	0.145	0.214	0.114
Sn	12.82	11.22	9.54	13.24	10.37	11.45	10.79	11.2	13.72
Hf		0.0027		0.0092					0.003
Ta		0.0266	0.0123	0.0188	0.0165		0.0029		0.00089
W				0.0042		0.0026			
Pb				0.181	0.098				
Th							0.0157		
U		0.07	0.0059	0.0468	0.0385	0.00074	0.0008	0.0022	0.0049

Sample	MNG 2.1								
Analysis	10	11	12	13	14	15	16	17	18
Element (ppm)	Leached Primary Magnetite (Leached Mag II)								
Mg	843.76	632.3	620.02	593.02	626.42	939.95	806.56	590.62	528.14
Al	420.69	611.58	591.69	516.57	567.29	389.48	387.23	639.04	572.88
Si	3094.83	2955.98	2731.84	2533	2534.67	3377.13	1556.54	2336.72	1816.33
Ca									
Sc	0.248	0.329	0.288	0.311	0.165	0.281	0.249	0.169	0.227
Ti	115.38	111.78	119.42	126.27	130.57	121.15	123.37	118.82	100.44
V	18.14	34.22	35.04	24.24	30.71	17.44	19.23	36.18	35.41
Cr	0.69		26.09	2.31	31.26	2.79	1.34	26.62	1.03
Mn	733.2	930.24	1067.09	975.31	953.93	810.78	817.44	947.4	907.41
Fe	758655.4	758655.5	758655.5	758655.4	758655.5	758655.4	758655.5	758655.5	758655.5
Co	0.668	0.892	0.818	0.88	0.983	0.739	0.82	0.973	0.798
Ni		1.14							
Cu			0.083		0.083				
Zn	54.32	62.84	69.32	69.13	71.2	59.74	59.89	63.82	61.54
Ga	4.27	5.02	5.22	5.52	4.72	4.91	5.12	4.68	4.28
Ge	0.99	1.7	2.91	1.68	1.7	0.9	1.01	2.36	2.54
As	0.79		0.3		0.36	1.8	0.81	0.3	0.27
Y	0.0439	0.0019		0.0139		0.122	0.076	0.0491	0.092
Zr	1.15		0.0053			0.393	0.216	0.126	0.182
Nb	0.323	0.034	0.0051	0.0376	0.0226	0.337	0.196	0.09	0.0271
Mo	0.158	0.095	0.191	0.061	0.137	0.088	0.17	0.153	0.059
Sn	11.95	10.99	13.8	12.25	12.12	12.78	11.81	13.41	11.7
Hf	0.031		0.0052	0.0032	0.0029	0.0136	0.0115	0.0059	0.0066
Ta	0.0149	0.0135	0.00076	0.0037		0.023	0.0142		0.0051
W	0.076		0.029	0.252	0.012	0.71	0.004	0.105	
Pb						1.29		8.71	0.09
Th						0.0011			
U	0.108			0.0064	0.0023	0.102	0.0426	0.0201	0.0168

Sample	MNG 2.1								
Analysis	19	20	21	22	23	24	25	26	27
Element (ppm)	Leached Primary Magnetite (Leached Mag II)								
Mg	650.8	1096.44	608.98	1149.63	425.03	1059	808.93	1456.19	407.41
Al	637.3	367.92	198.99	350.19	254.1	620.05	267.23	391.55	280.63
Si	2239.41	3140.27	2454.6	3250.97	2087.02	2201.6	2766.31	3979.58	2773.4
Ca									
Sc	0.488	0.278	0.238	0.191	0.144	0.311	0.27	0.306	0.183
Ti	113.28	119.25	123.19	132.53	124.63	100.16	130.97	131.01	135.31
V	32.53	15.46	11.41	17.77	14.76	24.07	13.81	15.18	17.51
Cr	91.95	2.17		0.47	0.73	23.22	1.47	1.16	1.58
Mn	1063.88	677.04	550.4	769.07	627.81	812.4	634.45	825.49	617.94
Fe	758655.5	758655.5	758655.5	758655.5	758655.5	758655.5	758655.5	758655.4	758655.5
Co	0.842	0.755	0.695	0.73	0.573	0.762	0.601	0.872	0.813
Ni	1.27							0.9	
Cu		0.061							
Zn	76.18	54.05	50.08	59.83	50.43	56.17	56.7	63.25	61.4
Ga	4.98	4.49	4.13	4.53	4.2	4.73	4.18	4.65	4.85
Ge	1.6	0.71	0.38	0.56	0.59	1.9	0.42	0.54	0.58
As	0.29	1.38	0.7	0.87		0.73	0.88	2.15	
Y	0.0034	0.148	0.0099	0.082	0.0186	0.0179	0.0318	0.073	0.0063
Zr		3.76	0.0014	0.093	0.059		0.0074	0.0059	
Nb	0.0507	0.425	0.095	0.257	0.071	0.105	0.221	0.515	0.074
Mo	0.23	0.202	0.163	0.261	0.16	0.11	0.192	0.121	0.138
Sn	12.11	10.73	10.36	13.16	11.11	12.01	12.04	11.21	13.44
Hf		0.133			0.0024	0.0124	0.0107	0.0057	
Ta	0.0027	0.0325	0.0123	0.0226	0.0097	0.0064	0.028	0.0385	
W		0.122		0.187	0.0033	0.026	0.034	0.0079	0.26
Pb				0.7	0.073				0.094
Th						0.0024			
U	0.0361	0.184	0.0167	0.091	0.0477	0.0211	0.0299	0.101	0.02

Sample	MNG 1.2								
Analysis	1	2	3	4	5	6	7	8	9
Element (ppm)	Leached Primary Magnetite (Leached Mag II)								
Mg	2231.01	827.23	1108.79	836.43	3300.5	817.07	823.65	1700.66	1748.71
Al	420.63	451.91	443.19	480.65	595.19	489.08	517.98	596.73	555.7
Si	4465.95	2553.69	2915.03	3000.7	7124.02	3012.54	2823.34	4223.49	3556.06
Ca									
Sc			0.245	0.168		0.149	0.303		
Ti	83.32	79.45	80.26	77.69	79.88	77.49	80.22	88.69	65.76
V	16.55	17.46	15.51	15.79	17.14	15.2	16.56	18.77	14.63
Cr	18.48	0.65		0.44	4.5	0.62			0.57
Mn	1939.52	2154.66	1961.91	2139.79	1930.02	2067.58	2141.05	2192.39	2108.94
Fe	763319.4	763319.4	763319.3	763319.4	763319.3	763319.3	763319.4	763319.4	763319.3
Co	0.714	0.674	0.504	0.502	0.537	0.495	0.545	0.603	0.434
Ni								0.77	
Cu							0.084		
Zn	84.52	83.69	70.54	70.29	76.07	67.79	72.15	78.55	69.07
Ga	3.99	4.53	3.87	4.43	4.15	4.31	4.06	4.4	4.42
Ge	1.48	1.19	0.77	0.92	1.64	0.88	1.13	0.94	0.79
As	2.01	0.39	0.75	0.29	3.57	0.215	0.31	1.6	1.47
Y	0.223	0.0022	0.0049		0.252	0.0026		0.05	0.086
Zr	7.62	0.0029	0.0071		0.08	0.203		0.0122	
Nb	0.0616	0.0093	0.0131	0.0065	0.119	0.0088	0.0023	0.0224	0.062
Mo	0.12	0.135	0.137	0.067	0.11	0.14	0.125	0.15	0.136
Sn	14.47	13.65	12.51	12.67	13.52	13.15	11.55	13.2	9.83
Hf	0.124	0.0021			0.0244	0.0047			
Ta	0.0086	0.00123	0.0024	0.0031	0.0262			0.0059	
W	0.0069	0.0029	0.017	0.009		0.0022		0.0163	
Pb			0.095		0.082			0.063	
Th			0.0016		0.0029				
U	0.66		0.0041	0.0078	0.129	0.0257		0.0258	0.037

Sample	MNG 1.2								
Analysis	10	11	12	13	14	15	16	17	18
Element (ppm)	Leached Primary Magnetite (Leached Mag II)								
Mg	1498.13	1329.3	2035.5	1154.56	2172.92	1268.31	2152.5	890.07	1533.29
Al	644.02	300.67	340.14	472.53	666.1	569.29	292.36	331.55	295.46
Si	3994.45	3927.55	6234.24	3282.48	5457.2	3467.06	4939.35	3066.98	4451.44
Ca									
Sc		0.198	0.214	0.211			0.154	0.249	
Ti	84.81	78.84	93.36	76.76	94.14	84.25	81.81	75.98	84.81
V	18.53	15.98	17.1	15.73	19.44	17.37	16.03	14.68	16.72
Cr		0.65	0.5		5.28				
Mn	2475.55	1672.25	1838.66	1844.05	2253.59	2038.28	1634.61	1834.44	1556.74
Fe	763319.4	763319.3	763319.4	763319.4	763319.4	763319.4	763319.3	763319.3	763319.4
Co	0.634	0.523	0.612	0.46	0.556	0.573	0.519	0.502	0.629
Ni	2.7								
Cu		0.077							
Zn	78.48	71.39	74.31	65.55	72.06	85.66	63.51	74.53	68.15
Ga	4.74	3.89	4.37	3.66	4.35	3.89	3.62	4.1	4.02
Ge	1.28	1.28	1.34	1.01	2.01	1.3	1.54	1.17	1.6
As	1.73	1.67	1.86	0.67	1.84	0.94	1.76	0.45	0.92
Y	0.0398	0.074	0.144	0.0129	0.0417	0.0129	0.103	0.0177	0.04
Zr	0.0105	0.0072	0.0106	0.0136	0.041		0.0256	0.0015	0.0068
Nb	0.0333	0.0282	0.079	0.0129	0.065	0.0215	0.08	0.0143	0.0292
Mo	0.245	0.1	0.197	0.103	0.057	0.038	0.153	0.112	0.14
Sn	15.35	12.13	13.05	10.76	13.82	12.2	13.14	12.1	11.57
Hf					0.0032		0.0071		0.0019
Ta	0.0022	0.00075	0.0083			0.0081	0.0035	0.00064	0.0062
W	0.0157	0.0108	0.0198	0.0032	0.022	0.023	0.029	0.0061	0.0216
Pb	0.071			0.066			0.073	0.058	
Th									
U	0.021	0.0259	0.082	0.011	0.057	0.01	0.048	0.0044	0.0147

Sample	MNG 1.2								
Analysis	19	20	21	22	23	24	25	26	27
Element (ppm)	Leached Primary Magnetite (Leached Mag II)								
Mg	1014.75	969.15	1252.18	739.81	1442.74	634.67	2253.66	1323.3	693.49
Al	266.05	250.56	360.41	231.37	319.87	414.64	630.57	575.32	220.96
Si	3407.18	3229.89	3885.65	2109.33	3624.68	2634.85	5030.64	4015.72	3445.29
Ca									
Sc			0.169	0.156			0.198		
Ti	77.85	90.32	81.07	64.33	77.55	73.42	78.97	82.98	83.57
V	14.48	16.1	16.62	12.85	14.11	15.25	18.22	17.7	15.12
Cr	0.77	0.48	0.64	0.59	26.87	0.51	0.53		1.02
Mn	1567.3	1788.65	1968.52	1438.72	1867.7	1644.24	1868.64	1944.87	1746.15
Fe	763319.3	763319.4	763319.4	763319.3	763319.4	763319.4	763319.3	763319.4	763319.4
Co	0.572	0.545	0.593	0.44	0.496	0.389	0.551	0.582	0.573
Ni									
Cu									
Zn	63.62	83.49	78.95	57.23	65.29	65.92	66.78	80.58	72.17
Ga	3.81	4.64	4.57	4.03	3.6	3.82	3.86	4.39	4.1
Ge	0.94	1.18	1.3	1.08	1.14	1.04	1.77	1.32	0.62
As	0.68	0.52	1.08	0.33	2.19		1.84	1.37	0.42
Y	0.0241	0.014	0.041	0.0158	0.115		0.076	0.0188	
Zr			0.0049		0.0135		0.0293	0.0201	
Nb	0.0561	0.0241	0.039	0.0162	0.0541	0.00075	0.078	0.0231	0.0145
Mo	0.103	0.092	0.107	0.159	0.088	0.141	0.148	0.175	0.135
Sn	10.29	12.52	12.83	9.74	11.33	10.1	11.45	12.24	12.89
Hf			0.0047			0.0167	0.009		
Ta	0.007	0.0058			0.0028	0.00053	0.0112	0.007	0.079
W	0.077	0.0226		0.0109	0.0161	0.0026	0.0125	0.0085	
Pb		10.3							1.41
Th			0.0018						
U	0.0342	0.0076	0.0112	0.0068	0.136	0.0333	0.057	0.022	0.0066

Sample	MNG 1.2								
Analysis	29	29	30	31	32	33	34	35	36
Element (ppm)	Leached Primary Magnetite (Leached Mag II)								
Mg	1533.66	696.26	1648.78	1864.18	551.28	1879.44	734.25	1996.26	1237.03
Al	274.02	400.65	453	508.65	270.51	434.91	313.65	376.04	414.03
Si	4972.57	1675.51	3774.04	4507.93	2137.97	4791.84	2869.44	5885.28	3837.34
Ca									
Sc	0.209		0.171			0.167	0.288	0.319	0.25
Ti	91.35	79.51	76.82	84.99	63.33	78.84	71.85	84.71	74.53
V	16.62	16.21	16.51	16.23	12.75	15.35	14.08	15.89	16.48
Cr	0.57	0.56		0.74	0.6	21.52	0.36		5.29
Mn	1757.11	1755.56	1658.3	1704.68	1446.8	1699.73	1705.71	1903.65	1737.43
Fe	763319.4	763319.4	763319.4	763319.4	763319.4	763319.4	763319.4	763319.4	763319.4
Co	0.621	0.464	0.548	0.648	0.482	0.514	0.521	0.595	0.545
Ni		0.82						1.01	
Cu									
Zn	73.33	68.89	66.1	76.51	58.32	77.33	76.9	80	73.24
Ga	4.21	3.71	4	3.83	3.43	3.78	3.78	5.06	4.16
Ge	1.22	1.03	1.35	1.57	0.94	1.07	0.88	1.3	1.58
As	1.62	0.246	2.29	2.46		2.55	0.44	1.94	1.69
Y	0.089		0.111	0.172	0.0026	0.143	0.0059	0.102	0.045
Zr	0.0258		0.0346	0.058		0.04		0.0301	0.0131
Nb	0.091	0.0076	0.095	0.104	0.0023	0.113	0.0053	0.069	0.095
Mo	0.165	0.135	0.091	0.062	0.128	0.045	0.115	0.137	0.147
Sn	12.26	13.13	11.65	11.92	9.02	12.16	13.16	14.05	12.7
Hf			0.0063	0.0045	0.0037	0.0088	0.0064		
Ta	0.0056		0.012	0.017		0.0101		0.0071	0.0035
W	0.0155	0.0026	0.0204	0.0221			0.065	0.021	0.408
Pb								0.135	
Th								0.0018	
U	0.064	0.0022	0.073	0.073	0.0015	0.106	0.0034	0.056	0.062

Sample	MNG 1.2								
Analysis	37	38	39	40	41	42	43	44	45
Element (ppm)	Leached Primary Magnetite (Leached Mag II)								
Mg	1977.71	1765.5	1629.02	1128.83	2045.67	1365.72	4001.36	847.31	858.14
Al	390.1	377.46	304.59	247.17	418.71	515.96	535.23	514.86	511.07
Si	4939.46	4334.31	4709.41	3987.1	6032.38	4411.59	5163.38	3334.61	3579.71
Ca							81.14		
Sc	0.187							0.221	0.318
Ti	78.13	65.67	81.3	90.66	91.39	88.17	96.32	86.97	81.89
V	15.98	13.15	14.21	13.34	16.77	17.06	17.02	15.64	14.38
Cr	0.45	1.16			1.93	0.71	5.91	0.44	0.6
Mn	1799.94	1536.85	1572.86	1632.29	1817.58	1997.43	2331.35	2356.86	1794.01
Fe	763319.4	763319.4	763319.4	763319.4	763319.4	763319.4	763319.4	763319.4	763319.4
Co	0.615	0.439	0.631	0.394	0.584	0.638	0.694	0.636	0.487
Ni								0.69	
Cu						0.106	0.093		
Zn	79.98	62.58	81.71	67.65	76.88	78.73	99.61	77.99	61.55
Ga	4.1	3.19	4.37	3.97	3.89	4.5	4.44	4.27	3.43
Ge	1.47	1.3	0.8	0.44	1.2	0.96	0.81	1.08	0.73
As	1.97	2.53	1.8	0.94	2.84	0.75	2.41		0.36
Y	0.127	0.119	0.115	0.061	0.206	0.0537	0.196		0.01
Zr	0.0249	0.0244	0.0238	0.0097	0.049	0.0159	0.033		0.9
Nb	0.164	0.148	0.083	0.0341	0.078	0.0279	0.112		0.013
Mo	0.131	0.067	0.207	0.08	0.096	0.191	0.11	0.204	0.161
Sn	14.28	9.26	12.62	12.5	14.17	13.14	12.73	12.47	10.64
Hf	0.0117		0.0031			0.0045			0.0024
Ta	0.0185	0.007	0.009		0.0051	0.0026	0.003		0.00137
W	0.0082		0.0128	0.0144	0.016		0.05		
Pb				0.059	0.065	0.29	0.76		
Th									
U	0.058	0.17	0.0377	0.0123	0.071	0.0178	0.051		0.0153

Sample	MNG 1.2								
Analysis	46	47	48	49	50	51	52	53	54
Element (ppm)	Leached Primary Magnetite (Leached Mag II)								
Mg	743.66	1651.49	959.48	957.4	1167.3	1130.25	745.52	881.77	941.95
Al	480.43	448.23	497.48	435.04	443.2	542.46	404.61	501.74	505.3
Si	5386.22	5067.99	4071.87	3588.76	4100.34	4230.18	3073.59	3631.05	3673.82
Ca		33.32			51.68				
Sc	0.14				0.183		0.138	0.179	0.304
Ti	99.55	81.69	81.66	80.14	81.54	80.65	74.85	86.11	83.61
V	15.64	15.44	14.65	15.38	15.44	16.25	14.87	15.5	16.22
Cr	0.45	0.5	0.65	15.8	0.56	0.65	0.71		0.83
Mn	2022.29	1797.72	1953.73	1769.93	1786.91	1847.02	1683.57	1730.7	2154.71
Fe	763319.4	763319.4	763319.4	763319.4	763319.4	763319.4	763319.4	763319.4	763319.4
Co	0.51	0.487	0.578	0.439	0.576	0.592	0.516	0.624	0.592
Ni									0.8
Cu	0.065								
Zn	78.26	66.6	82.16	79.43	74.11	73.19	74.42	74.43	73.63
Ga	4.77	3.95	4.17	4.16	4.11	3.95	4.15	4.76	4.1
Ge	2.58	1.12	1.11	1.06	1.07	1.01	0.78	0.99	1.53
As		1.31	0.26	1.11	0.66	0.97		0.23	0.29
Y		0.123	0.0092	0.0484	0.0265	0.0212			0.0046
Zr		0.0282		0.0103	0.0114				
Nb		0.0489	0.0028	0.0242	0.0175	0.0123		0.0172	0.0092
Mo	0.2	0.146	0.142	0.073	0.14	0.205	0.097	0.111	0.112
Sn	11.96	10.96	13.23	10.97	12.29	12.03	12.84	11.39	12.97
Hf	0.007		0.0033		0.002		0.0038	0.0026	0.0022
Ta		0.0052		0.0041	0.0023	0.006			0.00063
W	0.0065	0.026	0.0092	0.0029		0.0088			0.0031
Pb		0.077							
Th									
U		0.0319		0.0223	0.0064	0.0075			0.0148

Sample	MNG 1.2								
Analysis	55	56	57	58	59	60	61	62	63
Element (ppm)	Leached Primary Magnetite (Leached Mag II)								
Mg	1430.53	2252.28	1122.85	868.01	664.97	919.92	1642.49	896.27	784.23
Al	480.47	546.93	464.69	408.54	388.21	374.32	447.36	451.55	440.5
Si	4138.08	5721.89	3993.91	3228.37	3070.11	3524.41	4435.18	2807.06	3331.85
Ca								39.34	
Sc		0.214						0.219	
Ti	78.75	82.96	81.28	82.59	86.63	88.6	83.14	77.26	80.17
V	14.79	17.02	16.5	13.33	14.16	15.1	15.9	16.02	15.1
Cr	0.7	1.07		0.82	0.44	1.02	0.67	5.41	
Mn	1982.95	2123.57	2052.83	1829.32	1697.25	2180.61	1783.9	1881.74	1933.08
Fe	763319.4	763319.5	763319.4	763319.4	763319.4	763319.4	763319.4	763319.4	763319.4
Co	0.69	0.677	0.613	0.598	0.478	0.571	0.574	0.591	0.541
Ni									
Cu							0.067		
Zn	64.31	83.77	81.9	74.3	63.54	84.62	69.33	65.91	74.72
Ga	4.15	4.28	4.54	3.8	3.83	4.79	3.93	3.7	3.97
Ge	0.52	1.47	0.84	0.62	0.73	0.89	1.29	1.54	1.27
As	1.08	3.03	0.62	0.25		0.37	1.56	0.245	
Y	0.0351	0.263			0.0035	0.00094	0.113	0.003	
Zr	0.0234	0.08		0.005	0.0016		0.0433	0.0046	0.0031
Nb	0.0393	0.145	0.0348	0.0029	0.0019	0.0124	0.065	0.0062	0.00091
Mo	0.111	0.085	0.167	0.138	0.051	0.072	0.113	0.12	0.136
Sn	11.73	13.63	13.28	12.82	10.58	11.5	11.59	10.57	11.15
Hf		0.0086		0.0047		0.0054			0.0022
Ta	0.0019	0.0149	0.0032	0.00067	0.00065		0.0119	0.00121	
W		0.03	0.0031		0.0117	0.0075	0.0026		
Pb							0.78		
Th							0.0015		
U	0.0147	0.112	0.0062	0.0019		0.0042	0.051		

Sample	MNG 1.2							
Analysis	64	65	66	67	68	69	70	71
Element (ppm)	Leached Primary Magnetite (Leached Mag II)							
Mg	726.59	1304.31	1645.68	1864.22	652.14	3032.86	2677.64	1545.6
Al	399.5	503.76	512.33	405.06	320.39	549.1	534.43	502.44
Si	3209.66	4028.36	4443.67	5157.41	2887.23	6820.49	6129.97	4422.22
Ca								
Sc		0.197		0.3	0.236			0.141
Ti	81.64	83.91	90.76	76.51	69.41	81.44	80.18	96.01
V	14.57	15.38	17.8	13.66	12.81	15.44	16.58	16.38
Cr	0.38	0.69		3.96	0.72		8.95	
Mn	1743.08	1921.77	1831.91	1615.67	1629.9	1932.86	1944.84	1921.8
Fe	763319.4	763319.4	763319.4	763319.5	763319.5	763319.5	763319.5	763319.5
Co	0.432	0.588	0.464	0.577	0.432	0.566	0.635	0.625
Ni								
Cu								
Zn	70.29	79.02	73.82	71.05	64.63	78.77	73.85	73.46
Ga	3.96	4.54	4.22	3.68	3.68	4.1	4.12	4.34
Ge	0.75	1.06	1.35	0.4	0.82	1.1	1.38	0.47
As		0.3	0.92	2.01		2.96	2.1	0.95
Y	0.0022	0.0284	0.084	0.165	0.00134	0.247	0.17	0.0496
Zr		0.0113	0.0215	0.0275		0.049	0.048	0.0148
Nb	0.0034	0.0142	0.0316	0.065	0.0016	0.124	0.097	0.0373
Mo	0.158	0.142	0.24	0.164	0.189	0.127	0.144	0.133
Sn	10.8	12.64	12.29	11.37	10.88	13.04	12.83	12
Hf				0.0116		0.0086		
Ta		0.081		0.0062		0.0128	0.0092	0.0068
W		0.0094		0.0186		0.0239	0.0198	0.0291
Pb								
Th			0.0016					
U	0.00063	0.0071	0.0091	0.042		0.106	0.07	0.0134

Sample	MNG 1.1								
Analysis	1	2	3	4	5	6	7	8	9
Element (ppm)	Leached Primary Magnetite (Leached Mag II)								
Mg	863	1452.51	880.75	494.08	1280.3	618.09	500.07	525.18	548.36
Al	331.91	427.51	347.41	246.31	352.01	262.25	191.55	362.09	314.4
Si	3301.18	4314.91	3415.01	3165.16	3937.47	3516.05	3120.48	3248.86	2706.75
Ca									
Sc	0.108	0.12	0.147	0.209	0.186			0.155	0.168
Ti	67.21	60.06	57.91	62.04	59.97	69.17	65.99	58.41	58.43
V	13.56	13.51	13.09	11.8	12.18	12.67	12.69	13.24	13.14
Cr		0.51	0.35	0.56	0.73	0.74	1.04	0.57	0.59
Mn	1100.49	1188.3	1026.85	964.72	1086.11	1023.52	1114.57	1152.06	1053.88
Fe	701989.7	701989.8	701989.8	701989.7	701989.7	701989.7	701989.8	701989.7	701989.6
Co	0.574	0.478	0.551	0.419	0.445	0.486	0.453	0.451	0.464
Ni				0.47					
Cu									
Zn	67.19	67.5	62.71	57.78	63.97	63.79	66.12	65.76	59.24
Ga	3.86	3.8	3.5	3.24	3.58	3.67	4.31	3.39	3.84
Ge	1.43	1.56	0.98	0.69	1.31	1.06	0.46	1.09	1.02
As	0.57	1.63	0.71	0.222	0.9	0.45	0.253	0.261	0.316
Y	0.0225	0.0596	0.0111		0.0475	0.0112			
Zr	0.004	0.0182	0.005		0.0191			0.0012	0.0027
Nb	0.0296	0.0734	0.0238	0.0118	0.0462	0.0249	0.0061	0.00139	0.0086
Mo	0.076	0.168	0.208	0.112	0.072	0.172	0.076	0.099	0.09
Sn	12.54	11.2	10.55	11	10.89	11.23	12.07	11.82	11.27
Hf		0.0016		0.0022			0.0029		0.0019
Ta	0.00079	0.0055		0.0019	0.007			0.00192	0.0022
W	0.0038		0.0063	0.003	0.0084	0.0041			
Pb	0.115	0.149		0.036				0.157	
Th									
U	0.012	0.0365	0.0082	0.0113	0.0129	0.0024	0.00116	0.0027	0.0015

Sample	MNG 1.1								
Analysis	10	11	12	13	14	15	16	17	18
Element (ppm)	Leached Primary Magnetite (Leached Mag II)								
Mg	529.45	551.8	604.63	693.99	987.57	1124.37	1297.06	574.15	850.12
Al	289.42	286.91	245.75	257.61	248.96	326.37	354.58	270.56	186.05
Si	2969.9	2898.54	3324.54	2883.8	3758.42	3883.53	4445.49	3590.18	3158.26
Ca									
Sc			0.137	0.175					0.133
Ti	64.7	63.12	73.13	59.35	68.55	59.12	66.26	69.71	63.19
V	13.53	13.04	13.67	12.09	13.57	12.22	14.65	12.59	11.41
Cr	0.57	0.76	0.61	0.5	0.45			0.33	17.01
Mn	1069.49	1031.56	1116.64	1027.51	1181.59	1041.68	1221.39	1071.75	999.59
Fe	701989.6	701989.6	701989.6	701989.6	701989.6	701989.6	701989.6	701989.6	701989.6
Co	0.449	0.48	0.446	0.446	0.55	0.541	0.588	0.486	0.424
Ni			0.65						
Cu	0.33								
Zn	64.07	67.6	70.54	59.38	70.83	61.57	72.34	65.16	81.88
Ga	3.62	3.65	4.5	3.7	3.7	3.69	3.88	3.69	3.7
Ge	1.18	1	1.5	0.5	1.16	0.78	1.33		0.61
As	0.193		0.44		0.81	0.73	1.3	0.202	1.18
Y		0.0018		0.0059	0.0457	0.0103	0.0594		0.083
Zr					0.014				0.0082
Nb	0.0079	0.009	0.0276	0.0083	0.028	0.0195	0.0632	0.0095	0.0352
Mo	0.089	0.067		0.063	0.047	0.065	0.113	0.136	0.067
Sn	11.91	11.17	14.17	10.19	12.68	12.74	12.58	11.69	12.03
Hf					0.0024				0.0028
Ta	0.0035	0.00069	0.0024	0.0057	0.0034		0.0072		0.0024
W			0.063	0.0109	0.0132	0.0038	0.0172	0.0039	0.0116
Pb			0.088					0.041	
Th							0.00069		
U	0.0021	0.0058	0.023	0.0016	0.0095	0.0065	0.0333	0.0079	0.0156

Sample	MNG 1.1											
Analysis	19	20	21	22	23	24	25	26	27	28	29	30
Element (ppm)	Leached Primary Magnetite (Leached Mag II)											
Mg	699.15	390.88	469.83	658.84	976.66	1185.39	411.82	1144.12	548.75	754.52	1070.32	655.26
Al	156.24	140.11	200.48	274.07	292	335.21	169.9	257.91	239.49	240.86	277.01	261.47
Si	3318.48	2796.17	2727.48	3395.2	3911.82	4001.37	2554.93	3714.5	3087.45	3559.19	3573.49	3998.46
Ca												
Sc	0.186	0.15	0.197	0.171	0.17	0.245		0.137	0.202		0.115	0.193
Ti	68.47	59.54	56.29	74.03	63.75	73.78	50.86	63.11	62.05	64.5	57.71	71.21
V	12.77	10.97	11.2	16.33	13.24	13.78	9.6	12.1	12.61	12.87	11.07	13.21
Cr	0.87	0.66	0.63	0.8	0.78	0.83	0.54	1.11	0.7	1.09	10.51	1.09
Mn	1021.24	931.82	989.84	1211.83	1037.18	1166.43	867.21	1133.27	1075.37	1052.17	925.97	1164.72
Fe	701989.6	701989.6	701989.6	701989.6	701989.6	701989.6	701989.6	701989.6	701989.6	701989.5	701989.6	701989.6
Co	0.466	0.325	0.426	0.503	0.432	0.494	0.337	0.386	0.393	0.477	0.484	0.503
Ni				0.89								
Cu						0.35						
Zn	52.82	50.36	54.93	74.04	59.67	71.64	49.6	66.37	58.47	62.8	55.34	64.19
Ga	3.77	3.76	3.11	3.66	3.55	4	2.99	3.46	3.45	3.87	3.24	4.11
Ge	0.9	0.86	0.79	1.27	1.11	1.18	0.71	0.78	0.73	0.61	0.81	0.67
As	0.56		0.224		1.04	1		1.49	0.151	0.52	0.7	0.244
Y	0.0058		0.0034	0.0078	0.0673	0.069	0.003	0.103	0.00159	0.0073	0.0307	
Zr	0.0085		0.0017	0.0051	0.0077	0.0122	0.0017	0.0327		0.0028	0.0031	
Nb	0.0185	0.0055	0.0029	0.0044	0.0279	0.0279	0.0063	0.0343	0.0083		0.0308	0.0197
Mo	0.185	0.129		0.083	0.079	0.098	0.074	0.102	0.085	0.123	0.18	0.173
Sn	10.36	10.2	10.57	12.72	11.47	11.51	9.71	11.62	10.14	11.81	9.64	12.4
Hf	0.0039		0.0023		0.0018			0.0037			0.0065	
Ta				0.003	0.002			0.0075	0.00122	0.0022		0.0029
W	0.0107				0.0097	0.029		0.0224	0.0058	0.0107		0.0056
Pb	0.039			0.063						0.034		
Th												
U	0.0015			0.0028	0.0209	0.0277	0.00046	0.0295	0.0045	0.0077	0.0077	0.0016

Sample	MNG 2.2								
Analysis	1	2	3	4	5	6	7	8	9
Element (ppm)	Leached Primary Magnetite (Leached Mag II)								
Mg	783.24	798.32	716.99	411.13	271.62	351.57	453.71	394.99	576.51
Al	285.43	256.69	276.47	291.28	160.67	175.76	188.07	245.5	127.06
Si	3310.62	4328.77	3865.48	3195.33	2713.01	3158.48	3683.45	3666.26	4303.11
Ca									
Sc	0.15	0.213	0.291			0.235	0.252	0.186	0.171
Ti	116.72	130.81	112.86	115.88	96.22	110.72	122.29	116.86	121.35
V	15	14.94	13.02	13.62	11	12.74	14.12	13.77	13.36
Cr	1.01	2.13	0.48	5.04	0.34			3.04	4.99
Mn	724.38	639.56	629.71	719.29	396.76	473.74	576.9	615.17	389.73
Fe	702144.9	702144.9	702144.9	702144.9	702144.9	702144.9	702144.9	702144.9	702144.9
Co	0.709	0.806	0.622	0.719	0.435	0.463	0.672	0.591	0.498
Ni								0.7	
Cu									
Zn	52.74	54.42	48.9	51.11	38.75	40.25	52.02	48.7	43.45
Ga	4.34	4.58	4.3	4.18	3.77	3.39	4.29	4.21	4.09
Ge	0.83	1.07	0.86	0.81	0.48	0.69	0.4	0.9	0.57
As	0.6	0.89	0.89				0.38		0.74
Y	0.0169	0.0294	0.031		0.00128		0.0035		0.026
Zr	0.0037			0.0023	0.0025		0.0081		0.0073
Nb	0.166	0.224	0.332	0.00131	0.0178	0.049	0.0449		0.151
Mo	0.171	0.155	0.129	0.068	0.041	0.122	0.164	0.09	0.087
Sn	10.51	11.32	10.41	10.6	7.82	9.46	9.73	11.12	9.55
Hf	0.0018	0.0043	0.0038						
Ta	0.0189	0.0202	0.0108	0.0023	0.0026		0.0118		0.0138
W	0.0249	0.025	0.879		0.025		0.0138		0.048
Pb			0.184						
Th									0.0014
U	0.0187	0.0295	0.0542		0.0058	0.0063	0.002		0.039

Sample	MNG 2.2								
Analysis	10	11	12	13	14	15	16	17	18
Element (ppm)	Leached Primary Magnetite (Leached Mag II)								
Mg	251.16	383.94	468.36	363.14	474.08	321.79	513.09	363.27	487.58
Al	85.08	197.9	368.27	299.55	291.9	103.41	147.33	291.09	271.25
Si	2699.98	3306.97	3568.97	3269.18	3707.76	3643.92	4220	3230.49	4052.66
Ca								73.37	
Sc			0.116			0.119	0.226	0.196	0.211
Ti	89.38	124.47	109.64	103.2	107.63	107.09	117.73	122.6	119.71
V	11.08	12.81	15.48	13.34	14.1	12.27	12.84	14.11	14.8
Cr	0.28		0.65	4.48	0.97	0.38	0.66	1.23	
Mn	320.74	529.23	702.94	625.23	623.51	360.83	428.59	559.44	625.17
Fe	702144.9	702144.9	702144.9	702144.9	702144.9	702144.9	702144.9	702144.9	702144.9
Co	0.441	0.672	0.681	0.611	0.708	0.487	0.611	0.597	0.594
Ni					0.49				
Cu									
Zn	34.88	55.07	55.32	42.21	46.88	37.13	42.4	46.11	52.41
Ga	3.27	4.01	4.14	3.56	4.09	3.55	3.85	4.09	4.35
Ge	0.51	0.62	1.01	0.54	0.46	0.32	0.43	0.84	0.68
As		0.155	0.167		0.308	0.133	0.29		0.174
Y	0.0045		0.0072	0.00081	0.00097	0.0022	0.0221	0.0406	0.0081
Zr	0.0018	0.0049	0.12		0.0038	0.0014	0.0059	0.344	0.048
Nb	0.079	0.076	0.038	0.00092	0.089	0.0508	0.158	0.211	0.112
Mo	0.077	0.138	0.13	0.121	0.155	0.132	0.063	0.105	0.154
Sn	7.54	10.94	9.43	8.69	10.3	8.38	10.48	9.76	10.44
Hf						0.002			0.0025
Ta	0.0094	0.0069	0.0051		0.0254	0.0075	0.0235	0.0072	0.0114
W	0.0035	0.053	0.0063				0.0115	0.253	
Pb			0.084					0.177	0.048
Th			0.0018						
U	0.0163	0.0097	0.0109		0.0054	0.0106	0.0265	0.043	0.016

Sample	MNG 2.2										
Analysis	19	20	21	22	23	24	25	26	27	28	29
Element (ppm)	Leached Primary Magnetite (Leached Mag II)										
Mg	526.56	578.83	312.57	551.74	485.63	508.74	384.5	515.16	378.83	482.6	350.28
Al	235.82	178.13	205.3	281.43	439.5	439.42	208.7	390.42	251.78	380.26	285.09
Si	3098.48	4188.98	3499.38	3653.01	3496.69	3738.71	3162.37	3448.52	3637.35	3629.29	3027.84
Ca											
Sc	0.161	0.28	0.155	0.204	0.302	0.269	0.179	0.169	0.403		0.143
Ti	101.63	115.48	109.26	121.67	109.17	108.24	101.23	101.54	123.4	120.03	107.49
V	12.02	12.65	12.23	13.09	18.51	19.76	11.03	16.63	15.15	18.04	15.99
Cr	0.72	2.15	3.27	0.93	17.23	2.31		46.41	6.33	3.61	1.27
Mn	535.39	527.27	529.59	596.94	776.67	767.13	542.32	666.92	593.7	758.97	637.45
Fe	702144.9	702144.9	702144.9	702144.9	702144.9	702144.9	702144.9	702144.9	702144.9	702144.9	702144.9
Co	0.608	0.553	0.525	0.68	0.768	0.755	0.552	0.691	0.627	0.727	0.659
Ni								0.66			
Cu			0.5					0.38			
Zn	42.31	44.47	43.79	45.65	51.56	52.64	46.9	52.51	53.62	50.92	53.31
Ga	3.91	4.16	4.09	4.78	4.02	4.09	3.62	3.96	4.32	4.11	3.67
Ge	0.6	0.51	1.02	0.56	0.82	1.62		0.99	0.53	0.93	0.97
As	0.572	0.418		0.214		0.25		0.234		0.149	
Y	0.0099	0.0022	0.0022	0.0044		0.0022	0.00087	0.0095	0.0023		0.0025
Zr	0.0042	0.0014			0.0013	0.0044		0.0025			
Nb	0.139	0.25		0.139	0.0151	0.0584	0.0576	0.0123	0.0035	0.00099	0.0092
Mo	0.068	0.131	0.126	0.183		0.12	0.139	0.115	0.169	0.101	0.177
Sn	8.57	9.31	9.54	11.67	10.42	10.81	9.93	10.33	10.14	10.3	9.63
Hf		0.002		0.0024				0.0034	0.0021		0.0033
Ta	0.0098	0.0423	0.0017	0.0131	0.0021		0.0081	0.0039	0.00118	0.00134	
W	0.0187	0.0251		0.0034	0.0025					0.0033	
Pb			0.042			0.054	0.058		0.031		
Th											
U	0.0244	0.0191		0.0155		0.0097	0.0029	0.0069			

Appendix F-2.3. – LA-ICP-MS ray results of outcrop samples of magnetite fom Montemor-o-Novo iron mines – Serrinha Mine (the unfilled spaces in the following tables correspond to values below the limits of detection of the equipment).

Sample	SER 1.1								
Analysis	1	2	3	4	5	6	7	8	9
Element (ppm)	Primary Magnetite (Mag I)								
Mg	3230.51	2719.72	3767.14	5351.13	4427.49	4013.59	6533.72	5451.92	7236.1
Al	716.69	574.43	651.6	616.74	565.6	587.98	611.92	696.47	625.3
Si	4451.46	3679.02	3751.47	6440.76	4517.95	3858.98	7211.94	5958	6800.88
Ca									
Sc	0.124	0.126		0.128				0.219	
Ti	28.74	25.65	26.95	28.81	25.36	28.41	29.17	33.8	32.09
V	1.61	1.611	1.8	1.95	1.98	1.61	2.4	3.14	4.07
Cr	1.94	0.72	4.59	1.18		0.41	0.53	0.84	0.85
Mn	10285.49	9981.33	10468.92	10577.18	10955.5	11202.44	12340.2	11424.42	11721.09
Fe	692506.3	692506.3	692506.3	692506.3	692506.3	692506.3	692506.3	692506.3	692506.3
Co	0.533	0.481	0.489	0.437	0.532	0.578	0.589	0.451	0.521
Ni	1.28			0.99	0.96			0.85	0.94
Cu					0.33				
Zn	42.13	33.37	39.98	40	39.1	39.03	47.16	42.3	40.37
Ga	0.65	0.435	0.597	0.598	0.543	0.506	0.738	0.389	0.504
Ge	0.77	0.51		0.43	0.63	0.54	0.38	0.61	0.89
As	0.293	0.238	0.489			1.16	0.57	0.82	0.47
Y	0.0121	0.0141	0.0103	0.072	0.0286	0.0429	0.0483	0.0238	0.0322
Zr	1.51	1.47	1.42	1.96	1.357	1.76	1.92	2.05	1.74
Nb	0.0215	0.0302	0.0257	0.055	0.0224	0.042	0.059	0.077	0.0366
Mo	0.832	0.793	0.67	0.48	0.465	0.865	0.62	0.67	0.216
Sn	15.92	13.82	18.27	16.53	17.3	15.23	17.7	17.31	16.3
Hf	0.07	0.054	0.0568	0.06	0.036	0.041	0.028	0.032	0.062
Ta	0.0015	0.0051	0.0062	0.0043	0.0094	0.007	0.0121	0.0091	0.0034
W	0.162	0.39	0.168	0.656	0.567	0.363	0.884	0.619	0.498
Pb	0.036	0.177	0.578			0.219		0.177	
Th	0.0061	0.0147	0.0099	0.028	0.013	0.096	0.0224	0.0158	0.0031
U	0.0072	0.0168	0.0164	0.0266	0.0294	0.178	0.0508	0.042	0.0255

Sample	SER 1.1								
Analysis	10	11	12	13	14	15	16	17	18
Element (ppm)	Primary Magnetite (Mag I)								
Mg	10230.74	4674.89	3269.6	3268.37	3319.04	2845.31	3097.09	3071.54	3554.75
Al	651.35	559.43	590.26	585.24	633.81	477.31	553.01	654.78	662.66
Si	8761.66	5887.38	3559.66	4237.1	4121.36	2915.47	3437.49	4409.78	4273.27
Ca							98.34		
Sc	0.141	0.168	0.206	0.125	0.155	0.132		0.109	
Ti	32.08	27.63	30.33	31.59	29.34	22.94	24.95	30.91	29.91
V	3.61	3.97	3.75	2.99	5.44	1.27	1.78	1.92	1.447
Cr		0.77	0.42	0.51	0.45	0.31	0.37	0.62	0.59
Mn	12263.87	10931.8	10835.66	9762.14	10467.88	8396.39	9562.89	10804.39	10917.9
Fe	692506.3	692506.3	692506.3	692506.3	692506.3	692506.3	692506.3	692506.3	692506.3
Co	0.534	0.507	0.539	0.593	0.558	0.503	0.451	0.529	0.433
Ni	0.71	0.93	0.71			0.79	1.11		
Cu									
Zn	40.24	40.11	39	39	43.34	32.09	36.64	48.52	43.35
Ga	0.51	0.511	0.451	0.654	0.674	0.456	0.444	0.658	0.483
Ge	0.65	0.74	0.56	0.7	0.73	0.36	0.52	0.5	0.45
As	0.183	0.417	0.58		0.269		0.197		
Y	0.0252	0.062	0.00084	0.0103	0.0078		0.0073	0.0024	
Zr	1.768	2.24	1.334	1.216	1.587	1.29	1.581	1.419	1.8
Nb	0.0337	0.0695	0.021	0.0244	0.0264	0.0272	0.0326	0.0261	0.0329
Mo	0.559	0.285	0.685	0.85	0.692	0.573	0.764	0.97	1.01
Sn	17.47	15.71	15.63	14.93	17.1	13.18	16.31	16.71	18.34
Hf	0.036	0.054	0.044	0.04	0.04	0.057	0.0461	0.048	0.062
Ta	0.0045	0.006	0.0064	0.0014	0.0043	0.0064	0.0048	0.0059	0.0077
W	0.586	1.01	0.143	0.288	0.125	0.136	0.317	0.054	0.063
Pb	0.054			0.911			0.16		
Th	0.0208	0.0283	0.0019	0.0139	0.0129		0.0107		
U	0.0309	0.0604	0.005	0.0061	0.0061		0.013	0.0019	

Sample	SER 1.1				
Analysis	19	20	21	22	23
Element (ppm)	Primary Magnetite (Mag I)				
Mg	3403.44	3316.13	3122.75	3474.07	4682.78
Al	609.59	676.83	689.56	620.14	634.81
Si	3917.65	4275.42	3801.12	4553.04	6739.63
Ca					
Sc	0.134				0.186
Ti	26.23	32.58	38.92	34.3	39.82
V	0.987	2.11	2.71	1.62	1.73
Cr		5.36			0.34
Mn	10295.76	9701.23	12322.3	10593.28	10919.74
Fe	692506.3	692506.3	692506.3	692506.3	692506.3
Co	0.467	0.439	0.594	0.515	0.507
Ni	0.56	0.3	1.42		
Cu					
Zn	38.29	41.46	51.24	45.85	41.01
Ga	0.533	0.434	0.735	0.572	0.591
Ge	0.46	0.44			0.49
As	0.221	0.31	0.58	0.253	0.305
Y	0.00053	0.0028	0.0604	0.0029	0.0594
Zr	1.695	1.179	1.95	1.433	1.85
Nb	0.0413	0.0095	0.0551	0.0256	0.0235
Mo	0.976	0.94	1.07	0.89	0.688
Sn	17.52	14.84	19.53	15.59	16.56
Hf	0.035	0.036	0.084	0.072	0.047
Ta	0.0052	0.0039	0.0088	0.0089	0.0142
W	0.171	0.097	0.539	0.199	0.585
Pb		0.047	0.444		0.047
Th	0.0006	0.0047	0.0457	0.0055	0.071
U		0.0097	0.133	0.0091	0.0477

Sample	SER 1.2								
Analysis	1	2	3	4	5	6	7	8	9
Element (ppm)	Primary Magnetite (Mag I)								
Mg	4549.58	4233.08	3954.21	4389.3	4644.44	4577.9	4607.44	4060.54	4471.43
Al	1069.22	931	896.57	1109.67	974.27	970.31	991.5	852.85	973.65
Si	2367.97	2926.98	2924.92	2869.51	3055.1	2825.7	2935.99	3122.93	3188.07
Ca						110.28			
Sc	0.141	0.105	0.088		0.099	0.189	0.108	0.249	0.136
Ti	138.88	117.38	117.47	128.53	147.37	154.25	160.3	132.28	137.2
V	28.17	20.95	21.33	27.41	31.13	31.9	30.89	23.9	32.22
Cr	14.96	2.43	3.95	2.45	13.77	7.08	5.99	6.69	1.24
Mn	11640.59	10162.79	10201.19	10568.92	11413.1	12285.67	12176.59	9904.3	11760.73
Fe	765651.2	765651.2	765651.3	765651.2	765651.2	765651.2	765651.2	765651.3	765651.2
Co	0.588	0.49	0.519	0.429	0.505	0.545	0.551	0.495	0.559
Ni	3.37	1.31	1.21	1.8	1.74	1.64	0.83	0.83	1.79
Cu					0.102				
Zn	50.51	49.28	42.54	42.75	47.26	49.3	59.4	45.9	65.3
Ga	0.942	0.867	0.742	0.812	1.011	0.996	0.88	0.818	0.885
Ge	0.29	0.65	0.378	0.3	0.5	0.435	0.82	0.25	0.54
As	0.39	0.241	6.39	0.53	0.35	1.46	0.445	5.82	0.29
Y		0.0064	0.0092	0.0094	0.0165	0.0106		0.0071	0.008
Zr	1.09	0.852	0.903	1.015	1.11	1.051	1.38	0.852	1.27
Nb	0.0231	0.034	0.03	0.026	0.0307	0.0216	0.0388	0.0292	0.0523
Mo	1.05	0.98	0.887	1.1	0.762	1.19	1.1	0.82	1.16
Sn	19.23	16.14	15.62	17.89	20.18	18.32	18.98	16.45	18.67
Hf	0.05	0.0328	0.029	0.0388	0.043	0.0262	0.04	0.0332	0.0339
Ta	0.0021	0.0027	0.006	0.0052	0.0066	0.0042	0.0051	0.0035	0.0047
W	0.105	0.21	0.128	0.339	0.218	0.317	0.436	0.318	0.257
Pb		0.095	94.53	0.059	0.101	5.51	0.406	0.06	
Th	0.0025	0.0068	0.0186		0.0064	0.0036		0.0196	0.0047
U	0.0025	0.0117	0.0277	0.0028	0.0049	0.005		0.0134	0.0136

Sample	SER 1.2								
Analysis	10	11	12	13	14	15	16	17	18
Element (ppm)	Primary Magnetite (Mag I)								
Mg	4581.02	4221.26	4414.21	4335.89	3929.42	3581.53	3581.02	4505.81	5293.18
Al	961.97	742.85	764.47	706.07	638.53	676.33	578.04	638.36	661.9
Si	3197.99	3117.67	11437.63		3050.03	3150.85	2347.67	2974.62	4626.09
Ca		52.4		379.52					
Sc			0.217		0.183				
Ti	127.25	134.18	139.15	86.65	69.21	122.16	107	79.55	85.18
V	17.97	15.18	12.91	5.14	3.15	9.74	10.91	5.02	6.14
Cr	8.4	10.25	2.99		0.34	4.74	2.25	1.26	0.99
Mn	12387.98	12162.83	13662.27	12421.19	11623.76	11756.3	11334.74	12334.92	12458.5
Fe	765651.2	765651.2	765651.2	765651.1	765651.2	765651.2	765651.3	765651.2	765651.2
Co	0.633	0.495	0.507	0.575	0.483	0.572	0.482	0.53	0.63
Ni	1.84	1.38	1.7	1.17	1.04		1.54	1.08	1.04
Cu						0.1		0.185	76.37
Zn	49.37	59.32	66.1	60.37	55.08	46.64	43.8	48.24	53.24
Ga	0.886	0.54	0.562	0.499	0.42	0.526	0.494	0.633	0.509
Ge	0.45	0.93	0.83	0.56	0.56	0.53	0.26	0.45	0.26
As	6.95	0.66	7.03	3.52	21.08	0.42	0.266	21.67	10.76
Y	0.0085	0.00083		0.081	0.0337		0.0052	0.0313	0.0268
Zr	0.937	0.965	0.8	1.09	1.11	0.768	0.908	1.13	0.919
Nb	0.02	0.0259	0.0126	0.0472	0.0611	0.0123	0.0219	0.0411	0.0283
Mo	0.88	0.82	1.01	1.35	0.95	1.15	0.9	1.12	0.93
Sn	19.02	23.27	18.89	19.02	16.74	21.23	17.12	19.09	19.99
Hf	0.036	0.0186	0.038	0.024	0.035	0.05	0.0202	0.0388	0.0235
Ta	0.007	0.0042	0.0044	0.0017	0.0106	0.0047		0.0042	0.003
W	0.272	0.148	0.104	0.491	0.96	0.091	1.33	0.8	0.88
Pb	0.143		0.089	1.72	0.421		0.072	0.472	0.135
Th	0.0261	0.0029	0.003	0.0458	0.158			0.149	0.0502
U	0.0298	0.006	0.0444	0.177	0.131		0.0025	0.217	0.218

Appendix F-2.4. – LA-ICP-MS ray results of outcrop samples of magnetite fom Montemor-o-Novo iron mines – Vale da Arca Mine (the unfilled spaces in the following tables correspond to values below the limits of detection of the equipment).

Sample	SER 1.2			
Analysis	19	20	21	22
Element (ppm)	Primary Magnetite (Mag I)			
Mg	4568.64	3588.05	6795.56	8294.45
Al	710.5	629.97	724.59	743.74
Si	3284.12	2783.04	3789.49	6214.45
Ca	161.57	66.33	161.81	110.97
Sc	0.157	0.098		
Ti	51.93	56.07	57.36	77.1
V	2.33	3.39	2.42	5.06
Cr		0.64	1.01	0.98
Mn	12424.78	10108.79	14430.19	13104.41
Fe	765651.1	765651.2	765651.2	765651.2
Co	0.772	0.512	0.618	0.547
Ni		1.36	1.64	1.1
Cu				0.073
Zn	59.11	44.22	55.06	60.1
Ga	0.608	0.471	0.437	0.804
Ge	0.46	0.36	0.28	0.69
As	78.52	14.71	1.48	53.91
Y	0.0351	0.0133	0.0312	0.078
Zr	0.969	0.829	0.99	1.41
Nb	0.0543	0.023	0.0314	0.0598
Mo	0.83	0.82	0.98	1.15
Sn	20.47	15.72	22.05	18.63
Hf	0.0163	0.039	0.084	0.0241
Ta		0.00087	0.0037	
W	1.2	0.395	0.98	1.19
Pb	0.668	0.475	0.266	0.627
Th	0.055	0.0326	0.0165	0.103
U	0.091	0.064	0.0034	0.243

Sample	MV3								
Analysis	1	2	3	4	5	6	7	8	9
Element (ppm)	Primary Magnetite (Mag I)								
Mg	1639.57	2154.45	2192.18	2558.64	1273.27	1931.73	2301.81	2025.89	2287.35
Al	63.06	59.74	89.84	155.27	20.55	21.79	17.93	21.73	20.18
Si	1064.52	2118.62	2662.78	3124.99	1064.38	1379.72	1440.46	1363.69	1439.9
Ca			101.39	287.08			211.92		
Sc									
Ti	34.73	137.06	164.36	192.99	114.68	161.26	137.08	130.72	122.26
V	21.87	145.34	139.72	159	108.67	165.18	141.92	123.99	125.92
Cr		1.18	1.12				0.66		0.58
Mn	6686.18	6873.67	6924.3	7074.5	5953.76	8135.66	7572.99	6771.11	7171.15
Fe	765744.5	765744.6	765744.4	765744.5	765744.5	765744.5	765744.5	765744.5	765744.5
Co									
Ni	4.82	17.28	2.34	2.79	33.69	10.54	8.58	8.51	8.36
Cu		0.183							0.128
Zn	79.99	113.74	105.06	126.41	89.12	131.98	129.16	105.1	106.34
Ga	3.49	3.88	3.86	4.39	2.64	3.85	3.02	2.97	2.78
Ge	0.57	1.78	1.97	1.95	0.86	0.81	0.78	0.48	1
As	2.92	1.65	4.61	5.8	0.5	0.88	0.61	0.71	0.62
Y	0.0099	0.099	0.268	0.45			0.0149	0.0361	0.0096
Zr		0.136	0.138	0.273		0.0032	0.0103	0.0171	0.0072
Nb		0.0719	0.11	0.164			0.0108	0.0127	0.0057
Mo		0.15		0.058	0.074			0.099	0.093
Sn	1.95	5.77	6.14	10.46	3.5	4.42	4.31	3.48	3.77
Hf				0.0085					
Ta		0.0018	0.0077	0.0159	0.0025			0.0027	
W		0.039	0.251	0.297	0.0024		0.009	0.0402	0.0164
Pb			0.115	0.243		0.088			
Th		0.0028	0.0203	0.0338	0.0023		0.023	0.0021	0.0045
U	0.0035	0.0528	0.072	0.096	0.0017		0.031	0.0139	0.0097

Sample	MV3		
Analysis	10	11	12
Element (ppm)	Primary Magnetite (Mag I)		
Mg	2752.69	3060.44	2876.8
Al	100.02	95.64	139.88
Si	2704.7	2758.17	3089.49
Ca	160.87	148.54	347.67
Sc			
Ti	163.16	154.93	196.32
V	149.23	139.26	164.51
Cr	1	0.88	
Mn	7582.42	8402.91	7852.48
Fe	765744.5	765744.5	765744.5
Co			0.052
Ni	47.2	36.48	9.53
Cu			
Zn	111.95	102.68	109.71
Ga	3.68	3.49	3.59
Ge	1.4	2.01	2
As	4.21	3.89	8.43
Y	0.306	0.278	0.433
Zr	0.22	0.247	0.405
Nb	0.131	0.108	0.227
Mo	0.081		0.08
Sn	7.2	6.78	9.19
Hf			0.0132
Ta	0.0047	0.01	0.0195
W	0.238	0.124	0.296
Pb	0.082	0.089	0.185
Th	0.0245	0.0157	0.092
U	0.065	0.0506	0.258

Appendix F-3.

Complete results of the LA-ICP-MS analysis of magnetite from the Alvito deposit

Sample	AL 6.1								
Analysis	1	2	3	4	5	6	7	8	9
Element (ppm)									
Mg	4760.35	4955.68	4997.61	4777.07	5149.93	4570.69	5014.98	5118.94	4486.31
Al	8401.12	8571.4	9158.33	8215.58	8735.55	7502.1	8223.51	8106.4	6674.55
Si	3429.49	3588.4	3932.2	3594.84	3616.35	3661.92	3733.52	3779.92	3185.18
Ca	b.d.l.	b.d.l.	b.d.l.	b.d.l.	b.d.l.	284.6	b.d.l.	b.d.l.	b.d.l.
Sc	0.689	0.648	0.543	0.457	0.653	0.574	0.506	0.568	0.318
Ti	1122.11	1203.63	1130.69	1078.11	1122.37	899.08	996.99	990.98	803.74
V	109.68	116.45	112.86	109.36	117.44	101.58	107.9	93.15	73.19
Cr	6.75	12.18	15.23	1.35	3.23	3.5	3.1	0.88	0.9
Mn	1837.44	1759.86	1817.33	2135.13	1534.92	1538.67	1879.16	2166.49	1787.23
Fe	758033.9	758033.9	758033.8	758033.9	758033.9	758033.9	758033.9	758033.9	758033.9
Co	57.67	55.04	58.5	64.23	58.53	53.03	64.02	79.16	64.76
Ni	55.97	58.21	70.47	66.45	72.22	58.6	60.98	69.58	56.49
Cu	b.d.l.	b.d.l.	1.38	b.d.l.	b.d.l.	b.d.l.	b.d.l.	b.d.l.	b.d.l.
Zn	534.97	547.42	615.27	608.39	558.23	530.64	559.6	684.75	511.61
Ga	60.12	61.16	64.88	62.26	62.5	72.24	64.38	62.05	55.96
Ge	1.41	2.35	2.5	1.86	2.45	1.46	2.06	1.82	1.6
As	0.244	<0.239	0.26	0.236	<0.21	0.48	0.33	0.29	0.32
Y	b.d.l.	0.0031	b.d.l.	b.d.l.	0.0027	0.0672		0.0027	0.0098
Zr	12.02	11.96	12.34	14.75	12.2	13.26	10.11	12.8	14.18
Nb	8.05	8.32	8.04	8.52	8.48	7.63	7.39	8.36	7.31
Mo	2.34	2.71	3.22	2.86	2.69	2.37	3.24	2.62	2.48
Sn	25.75	25.81	32.57	29.54	28.12	24.04	29.44	28.84	25.15
Hf	0.274	0.298	0.308	0.273	0.274	0.262	0.365	0.221	0.231
Ta	0.199	0.223	0.197	0.202	0.2	0.164	0.145	0.184	0.145
W	0.0271	0.0169	0.022	0.0243	0.0153	0.069	0.033	0.0166	0.0121
Pb	b.d.l.	12.67	b.d.l.	0.034	b.d.l.	0.036	b.d.l.	b.d.l.	b.d.l.
Th	b.d.l.	b.d.l.	b.d.l.	0.0057	b.d.l.	0.049	b.d.l.	0.0093	0.0148
U	b.d.l.	0.00068	0.0047	b.d.l.	b.d.l.	0.0013	b.d.l.	0.0278	0.0245

Sample	AL 6.1								
Analysis	10	11	12	13	14	15	16	17	18
Element (ppm)									
Mg	5354.82	5305.89	4710.63	4806.4	5325.86	5150.82	4571.41	6102.99	4228.9
Al	8059.98	9200.7	8565.84	8612.77	9149.34	8719.76	8157.21	8771.62	7342.54
Si	3739.86	3880.02	3707.54	3575.54	3724.78	3638.97	3317.78	4988.23	3238.22
Ca	b.d.l.	b.d.l.	105.31	b.d.l.	b.d.l.	b.d.l.	b.d.l.	b.d.l.	b.d.l.
Sc	0.631	0.555	0.663	0.453	0.64	0.57	0.608	0.559	0.516
Ti	963.59	1091.88	1143.96	1162.96	1187.83	1195.19	1157.32	1188.21	948.12
V	87.09	107.4	105.4	109.45	113.49	95.43	85.17	102.69	92.01
Cr	b.d.l.	7.81	3.69	10.63	8.7	13.39	17.97	45.1	8.04
Mn	2210.13	2197.93	1956.29	1715.51	1766.26	1949.92	2217.75	1951.01	1402.9
Fe	758033.9	758033.8	758033.9	758033.8	758033.8	758033.8	758033.9	758033.8	758033.8
Co	75.82	82.44	71.53	54.25	58.02	73.51	73.44	68.42	48.61
Ni	67.15	68.51	60.97	50	67.5	69.47	65.41	68.27	58.01
Cu	b.d.l.	b.d.l.	b.d.l.	b.d.l.	0.41	b.d.l.	b.d.l.	b.d.l.	0.4
Zn	619.18	622.83	581.16	582.46	623.27	601.94	611.46	606.47	646.93
Ga	63.31	64.82	61.57	61.7	86.68	63.67	65.97	74.51	58.16
Ge	1.71	2.64	1.64	1.74	1.72	1.5	1.54	2.29	1.65
As	0.36	0.51	<0.189	0.59	0.25	0.32	0.33	0.48	0.17
Y	0.0033	b.d.l.	0.0255	b.d.l.	0.008	0.0038	b.d.l.	0.0651	0.00099
Zr	12.41	14.55	12.23	14.52	15.23	11.46	13.14	15.91	10.54
Nb	8.64	9.23	8.48	8.61	9.33	8.64	7.97	9.06	7.34
Mo	2.91	3.03	2.6	3.23	2.57	3.14	2.64	2.92	2.16
Sn	31.04	34.21	28.18	29.43	28.76	27.74	26.4	29.59	24.49
Hf	0.239	0.329	0.326	0.418	0.371	0.255	0.32	0.277	0.23
Ta	0.208	0.191	0.23	0.186	0.186	0.256	0.199	0.241	0.209
W	b.d.l.	0.0084	0.036	0.034	0.0099	0.0211	0.035	0.041	0.0074
Pb	b.d.l.	b.d.l.	b.d.l.	b.d.l.	b.d.l.	0.455	b.d.l.	0.153	b.d.l.
Th	0.0023	0.0047	0.0201	0.0024	0.0028	0.004	0.003	0.074	0.001
U	0.0188	0.0194	0.0046	b.d.l.	b.d.l.	0.001	0.0071	0.082	b.d.l.

Sample	AL 6.1		AL 6.2						
Analysis	19	20	1	2	3	4	5	6	7
Element (ppm)									
Mg	4537.15	5161.08	3583.27	2965.79	3102.27	3588.62	3669.49	4361.54	4090.07
Al	7943.27	8398.39	5030.38	6267.76	6108.54	7264.82	6765.45	7776.12	7261.95
Si	3479.75	3438.99	3194.97	3208.27	2625.74	3420.76	3840.76	4286.43	4025.2
Ca	b.d.l.	b.d.l.	b.d.l.	b.d.l.	b.d.l.	b.d.l.	b.d.l.	b.d.l.	b.d.l.
Sc	0.512	0.386	0.381	0.54	0.659	0.682	0.802	0.846	0.746
Ti	991.48	1037.59	430.58	514.65	510.18	494.93	484.75	554.54	525.38
V	94.94	100.2	48.32	63.19	60.13	63.37	61.49	68.6	69.16
Cr	5.37	6.51	0.68	1.18	1.01	0.45	3.23	0.7	b.d.l.
Mn	2026.11	1954.71	1287.38	1650.72	1673.04	1651.5	1328.61	1755.73	1800.95
Fe	758033.8	758033.8	758029.3	758029.3	758029.3	758029.3	758029.3	758029.3	758029.3
Co	65.65	64.01	57.7	68.62	68	64.29	46.67	68.18	60.74
Ni	61.95	62.58	70.09	100.87	85.88	74	70.41	82.62	69.44
Cu	b.d.l.	b.d.l.	0.19	b.d.l.	b.d.l.	b.d.l.	b.d.l.	b.d.l.	0.119
Zn	546.75	604.53	508.95	538.46	538.89	537.39	522.82	508.32	515.77
Ga	63.07	63.8	33.54	47.38	40.62	41.49	40.51	42.91	38.5
Ge	1.68	1.69	1.88	1.9	2.09	1.41	1.12	1.62	1.41
As	0.338	0.28	0.82	0.72	0.63	0.587	0.575	0.47	0.58
Y	0.0062	0.0071	0.0153	0.0102	0.0034	0.0073	b.d.l.	0.0086	0.003
Zr	12.33	14.26	2.86	6.2	5.37	9.79	10.46	13.2	13.43
Nb	7.91	8.46	3.42	5.25	6.14	6.13	5.73	7.31	7.12
Mo	2.71	2.99	1.66	2.35	2.72	2.91	2.72	3.05	2.43
Sn	26.81	29.61	21.31	27.93	24.84	22.83	20.52	24.72	22.25
Hf	0.295	0.243	0.18	0.322	0.223	0.298	0.34	0.332	0.355
Ta	0.185	0.191	0.15	0.194	0.195	0.171	0.177	0.232	0.199
W	0.022	0.034	0.024	0.0146	0.0166	0.0149	0.0139	0.0303	0.02
Pb	0.073	0.049	0.171	0.095	0.506	0.152	0.064	4.78	0.15
Th	0.0037	0.0205	0.0084	0.009	b.d.l.	0.0119	0.00138	0.0182	0.00139
U	0.0143	0.0074	0.0094	0.015	0.0039	0.0115	0.0014	0.0073	b.d.l.

Sample	AL 6.2								
Analysis	8	9	10	11	12	13	14	15	16
Element (ppm)									
Mg	7009.01	4344.89	4206.28	3091.37	3893.79	3500.27	2569.87	65.7	4211.51
Al	8342.07	7518.17	6972.32	6537.21	7054.52	5937.1	5253.71	6.07	7321.66
Si	6324.12	3596.68	3726.46	3803.78	3157.11	3094.44	2822.17	3543.73	3679.25
Ca	74.54	b.d.l.	b.d.l.	b.d.l.	b.d.l.	b.d.l.	b.d.l.	b.d.l.	b.d.l.
Sc	0.852	0.848	0.748	0.63	0.734	0.688	0.485	b.d.l.	1.101
Ti	559.03	524.34	457.88	471.17	500.12	408.74	391.56	0.28	465.63
V	71.33	71.84	62.53	61.91	62.08	52.26	50.95	1	55.04
Cr	b.d.l.	b.d.l.	0.38	2.91	0.66	0.83	1.02	b.d.l.	2.21
Mn	2114.9	2076.76	1832.71	1146.05	1890.62	1165.39	1138.46	1211.41	1310.67
Fe	758029.3	758029.3	758029.3	758029.3	758029.3	758029.3	758029.3	758029.3	758029.3
Co	73.26	69.8	61.17	46.48	60.04	39.64	38.85	6.19	48.63
Ni	89.2	86.34	75.76	68.16	67.52	51.27	48.18	17.87	70.13
Cu	b.d.l.	0.144	0.094	b.d.l.	25.87	0.123	0.164	860.59	0.188
Zn	559.51	579.56	518.58	486.6	490.02	416.95	382.26	19.6	481.43
Ga	44.37	40.94	38.93	38.3	39.07	40.54	32.57	b.d.l.	37.29
Ge	1.6	1.88	1.39	1.11	1.66	1.34	1.09	b.d.l.	1.28
As	0.603	0.77	0.66	0.506	0.9	0.551	0.43	0.69	0.57
Y	0.0781	0.0054	0.0067	0.0129	0.0607	b.d.l.	0.0026	0.0023	0.0034
Zr	16.18	13.01	12.04	7.21	14.91	11.4	7.18	0.0023	17.3
Nb	8.61	7.65	6.62	5.83	6.13	5.86	5.46	b.d.l.	8.22
Mo	2.62	2.85	2.45	2.29	2.32	7.93	2.22	0.625	2.77
Sn	29.91	25.26	24.11	20.55	26.93	16.63	17.56	0.107	22.33
Hf	0.424	0.33	0.402	0.233	0.41	0.307	0.218	b.d.l.	0.419
Ta	0.253	0.209	0.214	0.182	0.202	0.177	0.18	b.d.l.	0.219
W	0.0227	0.0392	0.045	0.0292	0.026	0.0136	0.037	b.d.l.	0.0373
Pb	0.15	0.355	0.093	0.084	0.126	13.3	0.051	3.04	0.155
Th	0.0736	0.00061	0.00138	0.0057	b.d.l.	b.d.l.	b.d.l.	b.d.l.	0.0044
U	0.0198	0.00124	0.0042	0.0033	0.0219	b.d.l.	b.d.l.	b.d.l.	b.d.l.

Sample	AL 6.2								
Analysis	17	18	19	20	21	22	23	24	25
Element (ppm)									
Mg	4318.94	5280.38	3952.77	4639.17	5098.37	5170.77	5661.9	4761.7	3767.39
Al	7386.8	7830.07	6248.61	7153.96	7171.25	6814.11	8178.18	7354.62	5774.28
Si	3985.95	4145.97	3548.3	3776.74	3438.07	3596.36	3922.01	3807.52	3171.36
Ca	b.d.l.	b.d.l.	b.d.l.	b.d.l.	b.d.l.	b.d.l.	b.d.l.	b.d.l.	b.d.l.
Sc	0.993	0.895	0.821	0.89	1.002	0.984	1.008	0.926	0.842
Ti	475.32	476.44	405.82	451.59	440.08	427.97	503.85	461.08	370.52
V	55.02	63.47	51.83	54	55.93	49.62	63.19	54.48	45.26
Cr	1.43	0.55	0.7	1.53	1.52	0.76	b.d.l.	0.63	b.d.l.
Mn	1477.07	2277.32	1722.79	1938.94	1931.02	2013.83	2390.33	1967.8	1568.95
Fe	758029.3	758029.3	758029.3	758029.2	758029.3	758029.2	758029.3	758029.3	758029.3
Co	53.95	77.16	63.02	71.2	67.57	69.82	80.48	72.35	54.43
Ni	71.86	91.94	76.12	76.4	84.96	78.65	100.3	88.42	66.27
Cu	11.12	0.108	0.302	0.1	0.094	b.d.l.	b.d.l.	0.293	b.d.l.
Zn	489.08	592.86	499.72	515.47	571.21	517.78	732.9	560.43	459.99
Ga	41.52	44.52	39.98	41.32	39.9	40.8	46.94	41.73	36.49
Ge	1.35	1.65	1.04	1.65	1.26	1.62	1.86	1.83	1.31
As	0.63	0.48	0.556	0.586	0.36	0.509	0.66	0.64	0.31
Y	0.00125	0.0112	0.0204	0.0048	0.0109	0.0042	0.0066	0.0064	0.0049
Zr	18.19	17.13	12.22	14.19	14.52	15.03	19.11	17.14	13.93
Nb	8.15	9.13	6.91	7.36	7.12	7.34	9.02	8.33	6.68
Mo	2.53	2.79	2.7	2.94	3.02	1.83	2.4	2.07	1.9
Sn	22.27	28.16	22.1	25.3	25.76	26.35	32.23	25.85	21.15
Hf	0.383	0.387	0.306	0.317	0.345	0.344	0.446	0.354	0.306
Ta	0.213	0.226	0.182	0.18	0.205	0.182	0.234	0.219	0.163
W	0.0206	0.0311	0.0377	0.035	0.0271	0.051	0.044	0.0216	0.0239
Pb	2.31	0.758	0.088	b.d.l.	0.098	0.072	0.131	0.083	b.d.l.
Th	b.d.l.	0.00115	0.00052	0.00061	b.d.l.	b.d.l.	b.d.l.	b.d.l.	0.00055
U	0.0014	0.024	0.017	0.0043	0.0045	0.0091	0.0067	0.0128	0.0107

Sample	AL 6.2								
Analysis	26	27	28	29	30	31	32	33	34
Element (ppm)									
Mg	4264.36	5379.79	5140.91	4521.71	5178.36	4233.79	4346.86	4414.15	4884.03
Al	6618.45	7925.47	7585.96	7059.74	8091.51	5350.43	6819.49	7155.55	7422.62
Si	3519.42	4185.99	4020.82	4019.28	4358.42	3963.05	3816.95	3867.33	4018.09
Ca	b.d.l.	b.d.l.	b.d.l.	56.69	b.d.l.	b.d.l.	b.d.l.	b.d.l.	b.d.l.
Sc	0.829	1.013	0.971	0.733	0.885	0.745	0.807	0.828	0.889
Ti	393.44	470.27	479.91	439.18	515.01	389.89	428.96	472.87	502.14
V	48.93	53.7	57.87	55.22	61.11	61.63	72.07	75.82	82.67
Cr	b.d.l.	b.d.l.	0.8	0.46	0.31	2.49		0.69	0.48
Mn	1838.86	2108.91	2101.88	2116.57	2042.82	1991.93	1922.17	2124.07	2262.1
Fe	758029.3	758029.3	758029.3	758029.3	758029.3	758029.3	758029.3	758029.2	758029.2
Co	60.75	76.3	76.76	71.79	78.74	67.56	66.23	70.07	77.8
Ni	73.55	88.7	88.43	80.71	84.69	79.8	79.29	88.11	97.87
Cu	b.d.l.	b.d.l.	b.d.l.	0.074	b.d.l.	b.d.l.	b.d.l.	b.d.l.	b.d.l.
Zn	508.81	581.93	566.93	549.03	563.99	535.22	520.27	585.19	594.08
Ga	37.3	46.46	44.8	40.37	40.38	37.37	41.67	41.83	44.65
Ge	1.14	2.1	2.06	1.43	1.34	1.43	1.46	1.67	1.89
As	0.556	0.54	0.68	0.54	0.55	0.88	0.332	0.44	0.58
Y	0.0142	0.0238	0.0048	0.0149	0.0116	0.0052	0.0024	0.0021	0.0025
Zr	12.99	17.82	14.72	14.88	17.63	8.42	11.2	14.73	13.67
Nb	6.26	8.28	8.39	7.61	8.86	6.55	7.34	7.48	7.08
Mo	2.42	1.8	2.1	2.37	2.73	2.91	2.34	2.06	2.64
Sn	26.66	30.94	27.66	25.45	27.8	23.02	24.41	25.73	32.3
Hf	0.312	0.422	0.423	0.387	0.342	0.292	0.389	0.342	0.376
Ta	0.18	0.241	0.238	0.205	0.246	0.186	0.208	0.202	0.202
W	0.0344	0.041	0.039	0.0303	0.043	0.04	0.0177	0.029	0.039
Pb		0.074	b.d.l.	0.166	0.127	0.06	0.071	0.091	0.09
Th	0.00059	0.0014	b.d.l.	b.d.l.	0.002	0.0242	0.0016	b.d.l.	b.d.l.
U	0.0236	0.0029	b.d.l.	0.0028	0.0111	0.0021	0.00083	b.d.l.	0.0018

Sample	AL 8								
Analysis	1	2	3	4	5	6	7	8	9
Element (ppm)									
Mg	1868.91	2227.45	2254.48	2287.8	1807.33	1746.46	2137.36	2340.08	2185.14
Al	10412.17	12260.13	13424.02	12857.55	11514.9	11073.15	12380.1	13134.44	12508.84
Si	2879.81	4131.9	5573.67	5000.85	4583.85	5052.44	5051.45	5423.1	4951.03
Ca	b.d.l.	b.d.l.	b.d.l.	b.d.l.	b.d.l.	b.d.l.	b.d.l.	b.d.l.	b.d.l.
Sc	b.d.l.	b.d.l.	b.d.l.	0.213	0.159	b.d.l.	b.d.l.	b.d.l.	0.174
Ti	1681.27	1547.73	1768.91	1720.69	1547.81	1705.74	1650.37	1680.01	1657.54
V	107.64	96.26	108.26	103.13	89.7	104.08	92.77	98.09	97.76
Cr	18.67	18.09	22	18.81	10.62	9.29	10.67	9.83	19.94
Mn	2061.97	2205.64	2324.43	2325.19	2024.38	2244.32	2148.87	2383.66	2044.93
Fe	751286.6	751286.6	751286.6	751286.6	751286.6	751286.6	751286.6	751286.6	751286.6
Co	91.64	96.15	95.6	88.05	82.06	95.72	92.96	95.6	98.82
Ni	9.5	10.04	8.69	10.35	24.19	8.33	9	9.1	8.11
Cu	0.111	b.d.l.	b.d.l.	b.d.l.	3.66	0.724	b.d.l.	b.d.l.	b.d.l.
Zn	416.4	384.41	406.16	446.21	387.99	407.66	367.65	355.51	375.74
Ga	39.63	40.28	43.85	42.72	39.87	37.78	39.06	42.61	43.17
Ge	1.07	0.45	0.89	0.65	0.49	0.82	0.66	0.73	0.57
As	b.d.l.	0.301	0.314	0.409	0.344	0.371	0.422	0.319	0.476
Y	0.0115	0.0039	0.0041	0.0039	0.00248	b.d.l.	b.d.l.	b.d.l.	0.0057
Zr	2.3	2.02	2.27	2.33	2.04	2.19	2.24	2.31	2.35
Nb	11.75	11.55	13	11.75	10.18	11.8	11.02	12.92	12.82
Mo	1.92	1.57	2.19	1.52	1.22	1.51	1.33	1.47	1.29
Sn	16.6	14.5	17.37	17.3	14.69	16.27	16.01	17.05	16.94
Hf	0.145	0.109	0.151	0.162	0.095	0.128	0.141	0.149	0.14
Ta	0.592	0.578	0.723	0.708	0.618	0.63	0.689	0.739	0.68
W	0.0105	0.009	0.0042	0.0231	0.587	0.0062	0.0202	0.0144	0.0058
Pb	0.119	b.d.l.	544.13	0.61	44.83	0.183	97.46	0.172	14.2
Th	0.0054	b.d.l.	0.00124	0.0043	0.006	0.0133	b.d.l.	0.00066	0.0045
U	0.0161	0.0072	0.0032	0.0078	0.0036	0.101	0.0161	0.0317	0.0184

Sample	AL 8								
Analysis	10	11	12	13	14	15	16	17	18
Element (ppm)									
Mg	1832.83	2276.63	2184.04	2238.83	2124.89	2392.37	2052.01	1660.88	1211.68
Al	9615.67	12853.72	12416.66	12964.08	11798.37	13287.65	11642.72	11207.93	11566.02
Si	5476.19	5670.13	4835.84	5521.49	5096.89	5706.91	5009.71	4632.95	5821.13
Ca	b.d.l.	b.d.l.	b.d.l.	b.d.l.	b.d.l.	b.d.l.	b.d.l.	37.65	b.d.l.
Sc	b.d.l.	0.309	0.149	0.165	0.199	b.d.l.	0.235	0.251	b.d.l.
Ti	1561.96	1826.23	1707.32	1845.19	1675.39	1899.39	1695.33	1583.43	1551.53
V	87.14	82.26	86.33	96.25	86.16	93.28	80.39	86.39	63.78
Cr	4.55	3.13	13.08	21.03	11.79	7.04	7.21	10.58	0.5
Mn	1954.43	2295.59	2114.03	2217.56	2072.77	2335.4	2014.57	2027.78	2124.95
Fe	751286.6	751286.6	751286.6	751286.6	751286.6	751286.6	751286.6	751286.6	751286.6
Co	91.87	108.29	93.24	94.89	94.55	103.35	92.83	89.82	69.49
Ni	6.67	8.32	8.1	7.63	8.4	10.55	10.11	10.61	8.29
Cu	0.084	b.d.l.	b.d.l.	b.d.l.	b.d.l.	b.d.l.	b.d.l.	b.d.l.	b.d.l.
Zn	361.47	349.14	471.94	411.9	369.46	432.49	356.66	379.85	444.28
Ga	37.09	41.01	38.45	39.55	36.55	42.72	38.46	36.12	36.36
Ge	0.51	0.64	1.05	1.21	0.79	0.73	0.41	0.42	0.72
As	0.27	0.349	0.243	0.54	0.285	0.393	b.d.l.	0.21	b.d.l.
Y	0.012	b.d.l.	0.102	b.d.l.	b.d.l.	0.00152	0.00064	0.0024	0.00153
Zr	2.08	2.49	2.42	2.61	2.34	2.74	2.4	2.12	1.53
Nb	11.92	12.67	11.7	11.39	11.28	13.61	12.61	12.4	9.99
Mo	1.56	0.607	1.04	1.38	0.93	0.71	0.572	1.12	2.86
Sn	17.58	16.96	16.47	16.76	16.04	18.77	17	15.89	17
Hf	0.118	0.181	0.176	0.157	0.138	0.166	0.154	0.122	0.117
Ta	0.565	0.759	0.736	0.753	0.746	0.739	0.691	0.595	0.591
W	0.0138	0.0123	0.0229	0.0128	0.0067	0.0062	0.0105	0.0059	0.0021
Pb	0.129	179.62	0.339	0.19	b.d.l.	b.d.l.	0.109	0.113	b.d.l.
Th	0.071	0.00052	0.003	0.0133	0.0053	b.d.l.	0.0039	0.0047	b.d.l.
U	0.0165	0.0032	0.0024	0.003	0.0021	0.00064	b.d.l.	0.0083	0.00064

Sample	AL 8								
Analysis	19	20	21	22	23	24	25	26	27
Element (ppm)									
Mg	1637.63	1682.34	2049.75	2682.11	2422.19	1708.39	1211.57	1804.65	2077.09
Al	13453.56	11142.11	12415.64	15859.81	14325.03	11071.37	11355.78	12497.41	13730.25
Si	5225.8	4738.71	5456.02	5449.14	5116.61	5543.62	5545.18	5712.58	4554.18
Ca	b.d.l.	b.d.l.	b.d.l.	b.d.l.	b.d.l.	b.d.l.	b.d.l.	b.d.l.	b.d.l.
Sc	b.d.l.	0.194	0.188	b.d.l.	b.d.l.	0.195	b.d.l.	0.182	b.d.l.
Ti	1510.49	1601.05	1653.69	1766.49	1602.81	1623.77	1596.03	1853.11	1499.65
V	77.97	103.61	115.44	92.08	91.81	102.34	89.91	99.88	88.86
Cr	6.95	12.47	19.74	8.61	11.04	13.39	3.07	6.23	4.59
Mn	2374.22	1896	2143.65	2511.09	2449.69	2145.35	2079.93	2205.88	2299.82
Fe	751286.6	751286.6	751286.6	751286.6	751286.6	751286.6	751286.6	751286.6	751286.6
Co	78.29	74.68	90.89	98.93	99.19	83.7	80.83	75.81	95.92
Ni	8.85	9.25	11.54	9.52	10.35	11.11	8.8	8.43	9.05
Cu	b.d.l.	b.d.l.	b.d.l.	b.d.l.	b.d.l.	b.d.l.	b.d.l.	b.d.l.	b.d.l.
Zn	365.48	356.35	411.71	431.7	433.64	393.6	419.56	459.51	335.16
Ga	37.32	37.69	42.15	42.6	38.68	40.66	41.02	40.32	42.06
Ge	0.59	0.54	0.66	0.79	1.47	0.63	0.66	0.71	0.52
As	0.175	0.266	b.d.l.	0.203	0.291	0.37	0.221	0.36	0.166
Y	b.d.l.	0.0067	0.0066	0.0025	0.00067	0.007	0.009	0.022	
Zr	1.96	2.19	2.47	2.54	2.56	2.21	1.93	2.44	1.91
Nb	10.43	10.44	11.21	12.19	11.75	10.71	10.61	12.95	9.19
Mo	2.73	1.61	1.51	1.09	1.18	1.79	2.69	2.12	1.51
Sn	17.47	16.68	18.09	19.16	17.91	15.73	19.09	17.59	16.56
Hf	0.116	0.125	0.201	0.172	0.13	0.188	0.136	0.178	0.112
Ta	0.675	0.55	0.74	0.88	0.85	0.592	0.635	0.69	0.627
W	0.0035	0.002	0.0104	b.d.l.	b.d.l.	b.d.l.	0.0123	0.0112	0.0095
Pb	0.16	0.135	46.91	b.d.l.	0.137	13.05	b.d.l.	0.141	0.254
Th	b.d.l.	b.d.l.	0.00123	0.002	b.d.l.	0.0042	0.0045	0.0188	0.0014
U	0.0065	0.0035	0.0026	0.0011	b.d.l.	0.0089	0.0142	0.0301	0.0022

Sample	AL 8				AL 10				
Analysis	28	29	30	31	1	2	3	4	5
Element (ppm)									
Mg	1976.97	1301.41	1347.46	1173.54	6529.01	5051.82	5200.22	5236.78	4818.33
Al	12946.39	9029.4	8500.36	7928.08	10905.51	7928.96	10427.86	10722.97	8905.81
Si	5331.26	5345.69	4837.88	5013.06	2118.87	2962.26	3031.78	2480.18	2067.77
Ca	b.d.l.	b.d.l.	b.d.l.	b.d.l.	b.d.l.	67.97	b.d.l.	95.08	b.d.l.
Sc	b.d.l.	0.19	b.d.l.	0.185	2.99	1.65	3.2	3.18	3.01
Ti	1484.7	1550.74	1419.52	1498.31	6156.39	6176.97	5112.57	6106.58	4420.8
V	82.47	78.57	75.74	74.64	119.8	128.16	95.16	102.3	76.74
Cr	6.57	9.37	2.4	1.1	290.64	73.65	198.97	213.69	219.6
Mn	2686.39	2178.01	2089.46	2143.52	3134.79	2717.67	3110.78	2734.32	2570.13
Fe	751286.6	751286.6	751286.6	751286.6	749655.6	749655.6	749655.6	749655.6	749655.6
Co	93.95	85.47	92	92.46	41.35	38.82	56.72	66.69	69.3
Ni	10.64	8.77	7.97	8.96	67.35	44.09	46.16	49.66	37.39
Cu	b.d.l.	b.d.l.	b.d.l.	b.d.l.	0.75	0.135	0.23	0.152	b.d.l.
Zn	336.8	383.08	352.57	383.51	908.11	904.94	806.71	808.32	687.95
Ga	39.34	37.46	36.13	35.24	31.62	23.47	28.08	28.99	24.51
Ge	0.48	0.56	0.57	0.69	0.53	0.95	0.99	0.84	0.69
As	0.301	0.371	0.224	0.201	0.66	2.08	3.51	b.d.l.	0.328
Y	0.00074	b.d.l.	0.0027	0.0076	0.0329	0.0167	0.0136	0.0074	0.0086
Zr	2.31	2.1	1.85	1.96	2.81	1.522	3.85	3.43	4.52
Nb	10.71	10.32	9.72	10.41	4.2	3.58	3.54	3.87	2.95
Mo	1.17	1.84	2.03	1.9	3.09	2.8	2.74	2.91	2.11
Sn	16.31	15.09	14.4	13.85	43.59	46.06	36.49	40.78	31.73
Hf	0.138	0.071	0.108	0.059	0.756	0.539	0.686	0.688	0.689
Ta	0.73	0.485	0.559	0.439	0.237	0.244	0.252	0.229	0.232
W	0.009	0.0026	b.d.l.	b.d.l.	1.14	0.8	0.162	0.099	0.0391
Pb	0.147	12.99	0.108	1.1	1.41	1.015	2.81	1.35	0.31
Th	b.d.l.	0.00076	b.d.l.	0.00092	0.0045	0.245	0.0025	0.00047	0.00128
U	0.00093	0.0032	0.0052	0.058	0.0322	0.0135	0.0133	0.00145	0.0168

Sample	AL 10								
Analysis	6	7	8	9	10	11	12	13	14
Element (ppm)									
Mg	4407.18	5419.32	5497.14	15244.57	4791.96	4382.95	4521.56	5710.5	5120.59
Al	9115.1	10897.58	11205.77	8191.88	9610.06	8398.31	8868.95	10998.69	11322.76
Si	2298.65	3507.26	2564.78	2229.87	2235.56	2589.64	2505.99	2631.98	2426.82
Ca	b.d.l.	b.d.l.	b.d.l.	b.d.l.	b.d.l.	b.d.l.	b.d.l.	b.d.l.	b.d.l.
Sc	2.44	3.22	3.07	3.59	3.03	2.62	2.47	3.27	3.36
Ti	5059.23	5872.6	5443.91	5461.9	4820.52	4013.04	5691.28	5296.94	5173.1
V	91.63	111.42	101.84	110.77	89.16	78.71	105.28	92.53	102.66
Cr	91.23	143.96	191.22	127.5	126.93	104.1	98.78	77.49	125.03
Mn	2442.86	3045.58	3145.75	4501	2547.6	3008.63	2687.77	3144.29	3277.81
Fe	749655.6	749655.6	749655.6	749655.8	749655.7	749655.7	749655.7	749655.7	749655.8
Co	49.76	76.37	98.42	104.01	67.82	94.1	71.62	95.78	94.91
Ni	46.14	59.68	51.93	55.23	41.46	48	49.32	49.63	45.56
Cu	0.171	0.118	b.d.l.	3.87	b.d.l.	b.d.l.	b.d.l.	b.d.l.	b.d.l.
Zn	837.03	841.36	655.54	675.17	764.57	791.61	688.18	806.98	720.23
Ga	25.16	33.81	30.2	28.54	26.83	24.16	27.31	31	32.24
Ge	0.8	1.04	0.88	1.06	0.64	0.65	0.77	0.5	0.95
As	0.7	2.56	0.34	7.12	0.255	0.48	0.43	0.31	b.d.l.
Y	0.0096	0.0094	b.d.l.	0.0269	b.d.l.	0.0043	0.0252	0.0179	0.00136
Zr	2.72	4.06	5.04	4.8	5.08	4.16	4.45	4.95	5.49
Nb	3.05	3.78	3.35	3.47	3.28	3.28	3.2	3.92	3.56
Mo	3.01	2.79	2.61	3.19	2.42	2.8	2.48	2.13	2.46
Sn	38.71	39.24	39.15	38.61	32.94	37.94	36	36.92	34.83
Hf	0.525	0.727	0.586	0.649	0.673	0.538	0.679	0.712	0.729
Ta	0.235	0.246	0.247	0.327	0.219	0.211	0.202	0.238	0.226
W	0.151	0.268	0.056	1.76	0.0507	0.0333	0.164	0.133	0.048
Pb	0.466	710.15	b.d.l.	5.46	0.17	0.176	b.d.l.	0.523	0.29
Th	0.0052	0.0053	0.0022	0.0128	0.00209	0.0047	0.0027	0.0062	0.0023
U	0.0112	0.0096	0.0045	0.0349	0.0069	0.0194	0.0466	0.028	0.0041

Sample	AL 10								
Analysis	15	16	17	18	19	20	21	22	23
Element (ppm)									
Mg	4448.47	4662.58	4490.77	4510.31	3973.16	3741.73	6214.52	6375.08	4418.73
Al	8317.63	10472.54	10488.15	10016.64	9242.11	9253.69	11148.2	10940.64	9139.18
Si	1855.39	2223.07	2558.3	2937.4	2390.16	2181.57	2506.86	3255.12	3484.58
Ca	112.72	b.d.l.	b.d.l.	b.d.l.	b.d.l.	b.d.l.	b.d.l.	51.43	b.d.l.
Sc	2.53	2.27	2.92	2.99	2.68	2.77	2.91	2.59	2.7
Ti	4708.17	6127.36	4600.5	6187.86	4608.65	4297.28	4197.79	4173.49	3850.84
V	88.92	120.53	92.64	96.57	91.98	81.36	59.66	73.29	63.58
Cr	147.11	331.64	146.96	177.55	105.66	74.84	359.17	338.41	20.12
Mn	2783.01	2675.19	2847.99	2668.83	2411.74	2484.85	2690.83	2735.82	2354.42
Fe	749655.6	749655.7	749655.7	749655.8	749655.8	749655.8	749655.7	749655.8	749655.7
Co	91.18	50.16	93.71	104.43	92.89	91.68	92.8	97.45	76.26
Ni	45.08	58.64	41.23	50.9	42.96	39.64	43.98	46.22	42.18
Cu	b.d.l.	0.148	b.d.l.	0.179	0.207	b.d.l.	0.143	b.d.l.	0.112
Zn	763.61	1085.13	775.23	842.62	1045.82	836.07	852.16	839.91	748.3
Ga	25.52	24.53	28.58	25.84	25.2	24.39	27.86	30.56	24.17
Ge	0.83	0.95	1.01	0.96	0.61	0.85	0.95	0.59	0.35
As	0.27	0.8	0.41	0.36	1.45	b.d.l.	0.22	0.26	0.55
Y	0.0207	b.d.l.	0.0037	0.0047	0.0171	0.0083	0.0177	0.0073	0.016
Zr	4.43	3.73	4.26	3.99	3.7	4.97	4.03	4.7	3.96
Nb	3.59	3.64	3.71	3.74	3.09	3.29	2.44	3.3	2.8
Mo	2.23	3	2.8	2.52	2.32	2.34	2.73	3.1	2.69
Sn	32.76	37.45	35.11	32.73	33.02	30.55	28.47	32.8	31.25
Hf	0.456	0.674	0.55	0.541	0.479	0.588	0.542	0.651	0.571
Ta	0.214	0.248	0.229	0.238	0.208	0.211	0.181	0.219	0.17
W	0.376	0.0248	0.114	0.175	0.157	0.0283	0.111	0.115	0.029
Pb	1.52	b.d.l.	0.23	0.238	0.914	0.094	0.155	1.013	0.097
Th	0.0305	0.004	0.004	b.d.l.	0.0103	0.0077	0.019	0.0089	b.d.l.
U	0.0285	0.0111	0.0048	0.0114	0.0168	0.012	0.0255	0.0105	0.0099

Sample	AL 10								
Analysis	24	25	26	27	28	29	30	31	32
Element (ppm)									
Mg	5525.98	4870.95	5490.55	5356.49	7366.15	5070.02	5766.27	5862.28	4953.01
Al	10788.51	8989.7	10242.15	9703.35	11840.23	10421.05	11450.45	10755.76	8687.37
Si	2815.51	2512.96	2837.04	2874.92	3952.54	3299.34	4024.04	2812.04	2436
Ca	b.d.l.	b.d.l.	b.d.l.	b.d.l.	b.d.l.	b.d.l.	b.d.l.	36.88	b.d.l.
Sc	2.95	2.28	2.81	3.23	3.95	3.14	3.52	3.16	2.68
Ti	4518.59	3512.09	4417.7	3914.04	4945.52	4283.42	4609.09	4378.86	3730.55
V	68.96	57.45	66.77	63.45	80.76	63.28	66.52	71.64	54.77
Cr	261.66	238.89	210.09	321	349.98	200.75	278.22	50.97	0.61
Mn	2880.68	2560.91	2815.32	2899.03	3566.04	2762.27	2863.19	2902.26	2674.97
Fe	749655.7	749655.7	749655.7	749655.7	749655.7	749655.7	749655.8	749655.7	749655.8
Co	92.22	80.91	94.82	84.37	117.1	90.85	93.28	93.48	95.08
Ni	47.3	42.47	51.21	44.64	59.08	40.68	49.81	46.23	43.81
Cu	b.d.l.	b.d.l.	b.d.l.	0.439	b.d.l.	b.d.l.	0.088	b.d.l.	b.d.l.
Zn	749.51	588.84	932.81	720.42	869.16	677.85	730.77	687.91	643.17
Ga	25.66	23.26	26.38	27	33.1	23.82	27.61	26.67	26.56
Ge	0.59	0.72	0.65	0.68	1.04	0.53	0.53	1.01	0.77
As	0.281	0.377	b.d.l.	0.43	0.37	0.177	0.45	0.33	0.231
Y	0.0136	0.0114	0.0023	0.0199	0.0214	0.0056	0.0128	0.0056	0.0063
Zr	4.51	3.82	4.3	4.3	5.7	4.47	5.41	5.42	5.04
Nb	3.12	2.88	3.78	3.56	4.34	3.42	3.88	3.65	3.24
Mo	2.75	2.61	2.8	2.74	2.91	2.66	2.97	2.85	2.46
Sn	33.65	32.27	35.11	30.92	39.11	31	32.94	33.82	30.3
Hf	0.639	0.466	0.591	0.568	0.497	0.586	0.75	0.727	0.674
Ta	0.226	0.187	0.22	0.194	0.274	0.215	0.225	0.27	0.22
W	0.306	0.133	0.029	0.127	0.267	0.08	0.121	0.071	0.089
Pb	0.309	0.132	0.093	1.015	0.294	b.d.l.	0.13	24.34	0.124
Th	0.00101	0.00066	b.d.l.	0.0192	0.0037	0.0062	0.0039	0.00086	0.00213
U	0.0129	0.0152	0.00075	0.0262	0.0136	0.0079	0.0083	0.0144	0.0058

Sample	AL 10								
Analysis	33	34	35	36	37	38	39	40	41
Element (ppm)									
Mg	5042.75	7324.07	6587.43	5884.35	5172.93	6186.81	6388.95	6078.89	4912.92
Al	8552.36	12296.42	11385.66	11542.16	8644.83	10576.23	9719.43	11398.9	9420.15
Si	2441.49	3735.44	3401.5	3506.55	2945.55	2869.09	3449.13	3299.79	2846.39
Ca	b.d.l.	b.d.l.	b.d.l.	b.d.l.	b.d.l.	b.d.l.	b.d.l.	b.d.l.	b.d.l.
Sc	2.55	3.36	3.42	2.99	3.04	2.93	2.76	2.93	2.29
Ti	3456.58	4970.71	4487.4	4460.26	3635.22	4319.23	4282.27	4393.61	3706.24
V	49.18	73.39	65.81	58.51	52.59	56.93	63.23	59.24	50.61
Cr	0.72	0.82	0.95	0.92	2.98	0.62	0.76	0.87	1.35
Mn	2680.38	3023.6	2948.98	3059.05	2687.83	2792.3	3306.64	2810.61	2501.24
Fe	749655.7	749655.7	749655.7	749655.8	749655.7	749655.8	749655.7	749655.7	749655.7
Co	83.27	112.02	97.93	103.76	72.67	98.42	95.9	104.8	81.07
Ni	38.44	56.89	44.47	42.63	41.29	47.13	54.27	47.06	41.08
Cu	0.109	b.d.l.	b.d.l.	b.d.l.	b.d.l.	b.d.l.	b.d.l.	b.d.l.	b.d.l.
Zn	698.53	904.28	740.65	736.97	583.56	714.84	757.18	768.78	617.31
Ga	22.96	31.2	27.3	27.06	22.8	24.25	26.59	25.79	21.91
Ge	0.84	0.87	0.97	0.98	0.68	0.86	0.91	0.75	0.61
As	0.229	0.26	0.314	0.27	0.314	0.332	0.41	0.43	0.336
Y	0.0052	0.0145	0.0026	0.0061	0.0136	0.0091	0.0161	0.0099	0.0121
Zr	5.05	6.42	5.58	5.76	4.49	5.17	6.05	5.58	5.12
Nb	2.91	4.02	3.87	3.69	3.11	3.24	4.02	3.38	3
Mo	2.01	2.44	2.45	2.45	2.11	2.34	2.58	2.31	1.99
Sn	30.39	33.55	36.54	35.64	28.69	31.21	35.95	35.67	28.85
Hf	0.617	0.948	0.79	0.804	0.682	0.782	0.867	0.88	0.764
Ta	0.223	0.302	0.243	0.195	0.198	0.22	0.296	0.21	0.237
W	0.061	0.156	0.101	0.14	0.127	0.07	0.105	0.124	0.07
Pb	0.093	0.135	0.195	265.3	0.168	0.313	0.124	1.51	0.13
Th	0.0019	0.0048	0.0051	0.0807	0.0076	b.d.l.	0.0025	0.0042	0.0203
U	0.0148	0.0159	0.00067	0.0202	0.0111	0.0229	0.0178	0.0097	0.0231

Sample	AL 10				AL 19				
Analysis	42	43	44	45	1	2	3	4	5
Element (ppm)									
Mg	4663.26	4404.56	5548.56	7089.3	1950.55	1662.59	1649.98	2053.67	1497.27
Al	9442.13	8732.13	10196.24	11384.93	14806.44	11350.27	9959.13	16280.62	12860.71
Si	2952.04	2271.8	2563.88	3105.01	4273.24	4667.85	6422.62	4265.63	2597.41
Ca	b.d.l.	b.d.l.	b.d.l.	b.d.l.	774.32	1634.84	1938.43	1894.84	542.61
Sc	2.61	1.99	2.42	3.02	b.d.l.	b.d.l.	b.d.l.	b.d.l.	b.d.l.
Ti	4254.2	3886.47	4428.11	4753.59	1081.41	1012.92	978.67	1130.35	914.96
V	75.91	72.68	72.91	84.51	25.74	21.93	19.97	23.95	21.38
Cr	184.14	145.44	133.07	176.82	0.87	46.4	1.71	1.55	2.89
Mn	2777.57	2251.44	2876.03	3480.54	1600.42	1407.11	1544.22	1951.1	1528.65
Fe	749655.7	749655.7	749655.7	749655.7	749654.3	749654.2	749654.3	749654.3	749654.3
Co	89.53	71.63	86.93	96.62	135.01	112.94	103.98	136	118.9
Ni	47.77	40.83	44.3	46.92	5.03	3.53	2.46	4.66	5.35
Cu	0.324	b.d.l.	0.162	0.176	0.369	b.d.l.	0.82	0.138	b.d.l.
Zn	748.89	537.97	736.96	821.86	251.31	286.18	217.26	262.59	305.59
Ga	25.45	23.74	23.31	26.54	44.32	42.34	38.15	44.25	38.6
Ge	0.53	0.55	0.87	0.75	1.68	1.75	0.94	1.52	1.99
As	0.26	0.325	0.236	0.28	2	1.06	1.46	b.d.l.	0.47
Y	0.0093	0.0149	0.0196	0.0305	0.941	3.63	1.186	1.528	0.311
Zr	3.71	3.31	3.32	4.11	8.29	10.68	8.43	11.94	10.3
Nb	3.06	2.82	2.93	3.54	19.95	16.43	18.84	19.05	18.37
Mo	2.69	1.81	2.25	2.06	3.75	3.04	3.47	3.41	3.17
Sn	31.96	25.72	32.56	38.79	20.44	18.38	16.67	17.5	17.93
Hf	0.36	0.463	0.485	0.544	0.403	0.385	0.338	0.429	0.378
Ta	0.18	0.171	0.204	0.241	2.31	1.898	2.23	2.29	2.06
W	0.077	0.132	0.223	0.462	0.177	0.079	0.139	0.196	0.103
Pb	0.114	134.11	0.327	0.279	0.987	0.363	1.14		0.104
Th	0.0066	0.0231	0.0159	0.0607	0.119	0.105	0.09	0.098	0.0469
U	0.0079	0.0486	0.0396	0.065	0.565	0.359	1.172	0.22	0.0515

Sample	AL 19								
Analysis	6	7	8	9	10	11	12	13	14
Element (ppm)									
Mg	1862.24	1150.1	1401.79	2146.19	1374.84	2545.82	1348.98	1183.2	1228.49
Al	14453.95	13147.34	14364.98	14504.34	13903.36	13898.27	14856.27	12995.52	12840.83
Si	3817.91	4005.64	1653.45	4412.46	1700.74	3838.82	2033.31	2026.24	1747.01
Ca	1188.91	b.d.l.	b.d.l.	1634.29	b.d.l.	638.12	b.d.l.	b.d.l.	b.d.l.
Sc	b.d.l.	b.d.l.	b.d.l.	0.34	b.d.l.	b.d.l.	0.227	b.d.l.	b.d.l.
Ti	966.39	998.09	1104.81	1161.62	969.92	947.85	963.9	834.91	873.9
V	25.3	23.43	26.33	31.29	23.61	23.81	22.79	20.72	21.44
Cr	3.02	1.05	b.d.l.	2.26	1.76	4.77	1.78	2.25	0.95
Mn	1794.74	1012.44	1704.72	1902.04	1859.14	1544.05	1629.43	1510.52	1642.97
Fe	749654.2	749654.2	749654.2	749654.3	749654.3	749654.3	749654.2	749654.3	749654.2
Co	132.89	94.52	129.23	138.74	132.46	122.6	123.4	115.63	127.21
Ni	2.81	4.51	3.73	4.53	4.11	3.66	3.81	3.45	3.57
Cu	b.d.l.	b.d.l.	b.d.l.	0.315	b.d.l.	b.d.l.	b.d.l.	b.d.l.	b.d.l.
Zn	243.5	106.63	278.58	266.86	245.41	251.67	277.54	205.19	221.75
Ga	43.22	36.24	44.97	48.02	44.49	44.26	43.55	44.6	41.79
Ge	3.36	1.93	1.71	2.49	1.4	1.7	1.92	1.74	1.62
As	b.d.l.	0.36	0.55	1.54	0.93	0.51	0.54	0.56	0.4
Y	0.718	0.0441	0.0061	1.043	0.0104	0.442	0.0334	0.0695	b.d.l.
Zr	10.42	10.7	11.67	14.02	12.1	10.56	12.82	10.43	11.1
Nb	18.3	17.37	19.38	20.38	17.87	17.03	18.66	15.34	16.67
Mo	3.95	4.01	3.96	4.49	3.56	4.45	3.45	3	3.41
Sn	18.54	16.57	21.74	21.93	19.71	16.72	23.31	17.28	20.6
Hf	0.271	0.234	0.377	0.379	0.46	0.277	0.323	0.374	0.388
Ta	1.93	1.827	2.27	2.26	2.22	2.05	1.941	1.918	1.945
W	0.156	0.063	0.039	0.098	0.099	0.086	0.206	0.274	0.057
Pb	0.34	0.188	b.d.l.	0.138	b.d.l.	0.151	b.d.l.	0.138	b.d.l.
Th	0.063	0.0041	0.0041	0.084	b.d.l.	0.075	0.011	0.0428	b.d.l.
U	0.173	0.054	0.0468	0.089	0.057	0.075	0.072	0.0514	0.0243

Sample	AL 19								
Analysis	15	16	17	18	19	20	21	22	23
Element (ppm)									
Mg	1460.77	1183.68	1859.36	1074.02	1206.81	1460.92	846.55	970.56	1174.41
Al	10398.84	11605.65	12871.83	12121.26	12207.08	10488.54	10260.35	9731.28	9697.99
Si	3758.71	1570.11	3314.37	1679.42	1792.72	4232.9	1848.78	1764.79	2702.09
Ca	1333.7	b.d.l.	995.94	b.d.l.	b.d.l.	1458.23	b.d.l.	b.d.l.	431.91
Sc	0.315	0.276	b.d.l.	0.278	b.d.l.	b.d.l.	b.d.l.	0.259	b.d.l.
Ti	820.62	800.26	888.22	930.92	956.92	1461.11	1412.73	1191.6	1148.22
V	19.81	20.92	24.19	21.07	24.62	31.14	31.02	34.36	34.85
Cr	5.81	1.05	3.83	7.14	1.47	1.21	b.d.l.	b.d.l.	2.05
Mn	1467.32	1681.33	1765.39	1633.94	1718.31	1790.02	1569.96	1513.57	1460.86
Fe	749654.3	749654.3	749654.3	749654.2	749654.3	749654.2	749654.2	749654.2	749654.1
Co	115.57	134.24	128.88	121.61	112.33	156.72	128.5	114.13	116.84
Ni	4.82	3.84	3.94	3.83	4.4	5.43	3.57	5.7	3.96
Cu	b.d.l.	b.d.l.	b.d.l.	b.d.l.	b.d.l.	b.d.l.	b.d.l.	b.d.l.	b.d.l.
Zn	237.88	254.28	262.28	237.52	220.11	290.84	245.12	244.68	239.34
Ga	40.49	42.77	43.88	41.78	42.43	45.98	43.14	40.78	42.89
Ge	1.37	1.75	1.58	1.31	1.34	1.68	1.83	1.47	2.15
As	1.11	0.84	0.44	0.43	b.d.l.	0.91	0.74	0.71	0.61
Y	1.091	b.d.l.	0.509	0.0042	0.0331	1.211	0.0126	0.0063	0.486
Zr	10.04	10.91	9.72	10.26	9.76	16.69	14.26	12.77	12.98
Nb	17.5	17.86	18.9	14.5	15.32	22.45	18.91	18.88	19.23
Mo	2.9	3.03	3.16	3.1	3.41	3.65	3.82	3.44	3.94
Sn	17.68	18.12	17.13	17.56	17.05	22.27	20.39	17.41	18
Hf	0.316	0.369	0.252	0.314	0.392	0.607	0.457	0.526	0.537
Ta	2.13	1.942	2.09	1.877	1.95	2.75	2.34	2.25	2.32
W	0.099	0.026	0.172	0.068	0.068	0.098	0.064	0.058	0.064
Pb	b.d.l.	b.d.l.	0.136	b.d.l.	b.d.l.	b.d.l.	b.d.l.	b.d.l.	b.d.l.
Th	0.101	0.0014	0.092	b.d.l.	0.012	0.034	0.00091	b.d.l.	0.0101
U	0.123	0.0527	0.166	0.0366	0.0457	0.14	0.0487	0.0109	0.044

Sample	AL 19					
Analysis	24	25	26	27	28	29
Element (ppm)						
Mg	957.15	1528.22	1260.46	886.58	1050.06	676.1
Al	10444.2	9455.03	9200.04	10029.01	9520.68	8351.83
Si	1892.4	3421.34	2337.16	2263.99	2230.79	1981.41
Ca	b.d.l.	1097.82	396.75	113.79	296.08	b.d.l.
Sc	0.274	0.292	b.d.l.	b.d.l.	b.d.l.	b.d.l.
Ti	1106.52	766.41	677.01	606.58	610.59	1187.72
V	33.08	27.31	25.82	21.14	20.04	41.07
Cr	0.57	0.73	28.91	b.d.l.	0.64	5.85
Mn	1659.48	1500.68	1409.45	1559.45	1393.99	1385.05
Fe	749654.1	749654.1	749654.1	749654.2	749654.2	749654.1
Co	126.24	113.87	110.71	145.25	103.98	115.07
Ni	3.66	4.1	3.52	2.94	4.39	4.72
Cu	b.d.l.	b.d.l.	b.d.l.	b.d.l.	b.d.l.	b.d.l.
Zn	240.58	248.14	232.26	248.23	243.33	218.14
Ga	44.26	45.83	39.34	44.17	39.31	39.16
Ge	1.61	1.67	1.93	2.68	1.65	1.66
As	b.d.l.	1.28	0.66	0.68	b.d.l.	0.49
Y	0.0142	0.859	2.05	0.302	0.295	0.0187
Zr	16.72	13.61	11.95	13.07	11.66	11.42
Nb	19.93	19.92	18.35	18.84	16.12	17.35
Mo	3.91	3.81	3.53	3.57	3.14	3.55
Sn	18.68	18.21	17.91	20.42	18.93	17.45
Hf	0.426	0.53	0.409	0.479	0.419	0.407
Ta	2.32	2.1	2.04	2.35	1.92	2.09
W	0.073	0.212	0.123	0.089	0.126	0.052
Pb	b.d.l.	b.d.l.	b.d.l.	0.208	b.d.l.	b.d.l.
Th	b.d.l.	0.0486	0.0218	0.0049	0.0032	b.d.l.
U	0.0203	0.074	0.0593	0.238	0.0408	0.0159

Appendix F-4.

Complete results of the LA-ICP-MS analysis of magnetite from the Azenhas and Orada deposits

Appendix F-4.1. – LA-ICP-MS ray results of outcrop samples of magnetite from the Azenhas deposit

Sample	AZ 4.2.2								
Analysis	1	2	3	4	5	6	7	8	9
Element (ppm)									
Mg	81.32	97.71	121.16	67.3	72.7	74.01	81.35	103.43	81.98
Al	819.1	866.66	1007.72	734.24	709.5	736.88	761.17	829.06	862.65
Si	2471.27	2531.89	3273.42	2675.04	3070.67	3642.83	2758.78	2411.07	4156.77
Ca	b.d.l.	b.d.l.	b.d.l.	200.36	b.d.l.	b.d.l.	b.d.l.	b.d.l.	b.d.l.
Sc	b.d.l.	b.d.l.	b.d.l.	b.d.l.	b.d.l.	b.d.l.	b.d.l.	b.d.l.	b.d.l.
Ti	1008.58	1018.08	1017.23	853.8	850.66	906.18	807.94	777.51	958.21
V	155.51	153.52	152.83	141.63	137.48	146.98	130.28	122.42	158.97
Cr	b.d.l.	0.43	0.47	0.36	b.d.l.	0.62	0.36	0.34	0.33
Mn	446.48	561.96	531.45	404.21	380.93	372.78	490.56	482.57	423.51
Fe	772211.9	772212	772211.9	772212	772212	772212	772211.9	772211.9	772211.9
Co	4.4	4.8	4.83	4.97	4.12	3.97	4.12	4.03	4.29
Ni	6.47	7.26	7.93	5.49	8.45	8.34	7.75	7.74	6.19
Cu	b.d.l.	0.067	b.d.l.	b.d.l.	b.d.l.	b.d.l.	b.d.l.	b.d.l.	0.067
Zn	169.29	193.18	233.27	122.8	124.52	128.47	176.95	211.85	137.29
Ga	20.15	19.42	20.21	18.98	16.14	18.14	19.49	18.55	18.69
Ge	0.66	0.32	0.24	0.35	0.213	0.388	0.301	0.292	0.54
As	0.4	0.43	0.7	0.74	0.5	0.64	0.57	0.478	0.46
Y	b.d.l.	b.d.l.	b.d.l.	b.d.l.	b.d.l.	0.00049	0.00063	0.00051	0.0015
Zr	b.d.l.	b.d.l.	0.0084	b.d.l.	b.d.l.	b.d.l.	0.0025	b.d.l.	0.0046
Nb	b.d.l.	b.d.l.	0.0041	0.0016	0.00074	0.00115	b.d.l.	0.0018	b.d.l.
Mo	0.34	2.05	0.94	0.61	0.228	0.31	0.247	3.1	0.439
Sn	0.734	0.949	1.062	0.651	0.648	0.626	0.739	0.91	0.797
Hf	b.d.l.	b.d.l.	b.d.l.	b.d.l.	b.d.l.	b.d.l.	0.0054	0.0015	b.d.l.
Ta	b.d.l.	b.d.l.	b.d.l.	0.0011	b.d.l.	0.00081	b.d.l.	b.d.l.	b.d.l.
W	b.d.l.	0.179	0.04	0.436	b.d.l.	b.d.l.	b.d.l.	0.915	b.d.l.
Pb	b.d.l.	0.076	b.d.l.	0.061	b.d.l.	0.058	b.d.l.	0.088	0.103
Th	b.d.l.	0.0034	0.0046	0.0044	0.0021	b.d.l.	b.d.l.	b.d.l.	0.0083
U	b.d.l.	0.0017	b.d.l.	b.d.l.	b.d.l.	0.00111	0.00071	0.00115	b.d.l.

Sample	AZ 4.2.2								
Analysis	10	11	12	13	14	15	16	17	18
Element (ppm)									
Mg	117.13	137.91	106.99	103.64	112	98.55	94.09	109.28	50.69
Al	904.6	972.03	835.96	1026.07	932.61	931.22	981.82	919.64	632.71
Si	2979.85	3207.38	2628.24	3978.6	3140.82	3517.12	4959.92	3619.74	4331.09
Ca	b.d.l.	b.d.l.	74.34	b.d.l.	b.d.l.	b.d.l.	34.67	b.d.l.	b.d.l.
Sc	b.d.l.	b.d.l.	b.d.l.	b.d.l.	b.d.l.	b.d.l.	b.d.l.	b.d.l.	b.d.l.
Ti	845.81	921.03	818.44	1118.53	963.21	1141.36	1147.16	901.22	919.24
V	141	134.46	112.66	160.98	143.39	168.81	163.53	138.97	162.11
Cr	b.d.l.	0.42	0.39	0.47	b.d.l.	0.55	b.d.l.	0.34	0.74
Mn	536.85	658.01	480.44	656.83	655.02	560.31	436.26	576.94	298.68
Fe	772212	772212	772211.9	772212	772212	772212	772212	772211.9	772212
Co	4.67	4.83	3.95	5.09	4.78	5.24	4.75	4.63	4.18
Ni	7.54	9.21	8.52	10.43	11.23	12.1	10.97	8.93	5.53
Cu	b.d.l.	b.d.l.	b.d.l.	0.059	b.d.l.	b.d.l.	b.d.l.	b.d.l.	b.d.l.
Zn	244.43	265.44	177.31	210.4	295.41	207.61	171.72	247.84	68.98
Ga	18.91	19.8	17.55	23.12	20.48	23.73	19.61	20.33	18.37
Ge	b.d.l.	0.284	0.248	0.26	0.21	b.d.l.	0.54	0.32	0.37
As	0.46	0.66	0.53	0.57	0.54	0.6	0.19	0.296	0.38
Y	0.0031	b.d.l.	0.0035	b.d.l.	0.0046	b.d.l.	b.d.l.	0.0044	b.d.l.
Zr	b.d.l.	0.008	b.d.l.	b.d.l.	b.d.l.	0.0015	b.d.l.	b.d.l.	b.d.l.
Nb	0.003	b.d.l.	b.d.l.	0.0017	0.0107	b.d.l.	b.d.l.	0.00128	b.d.l.
Mo	16.13	4.24	4.22	13.92	60.65	0.566	1.01	19.03	3.1
Sn	0.89	1.138	0.898	1.26	1.07	1.21	0.863	1.023	0.482
Hf	0.003	0.0044	0.0046	0.0042	b.d.l.	b.d.l.	b.d.l.	0.0031	b.d.l.
Ta	0.003	b.d.l.	b.d.l.	b.d.l.	b.d.l.	0.0024	b.d.l.	b.d.l.	b.d.l.
W	8.49	2.58	1.07	5.7	13.99	b.d.l.	b.d.l.	4.05	1.54
Pb	0.057	0.1	0.165	296.54	0.087	0.07	b.d.l.	0.072	b.d.l.
Th	0.0114	0.0017	0.0053	b.d.l.	0.0201	0.00081	0.002	0.0036	b.d.l.
U	0.0053	0.00116	0.0072	0.0017	0.0167	0.0017	b.d.l.	b.d.l.	0.00074

Sample	AZ 4.2.2								
Analysis	19	20	21	22	23	24	25	26	27
Element (ppm)									
Mg	75.02	79.5	52.66	54.83	67.4	48.55	54.81	67.96	69.81
Al	728.67	811.8	579.31	730.37	717.46	525.98	630.84	709.77	749.7
Si	3929.66	3159.21	3040.86	4346.81	3976.67	3319.35	3554.88	3922.04	2967.53
Ca	b.d.l.	b.d.l.	32.69	b.d.l.	b.d.l.	b.d.l.	b.d.l.	b.d.l.	b.d.l.
Sc	b.d.l.	b.d.l.	b.d.l.	b.d.l.	b.d.l.	b.d.l.	b.d.l.	b.d.l.	b.d.l.
Ti	809.87	760.89	781.34	772.2	907.94	774.38	825.63	839.13	853.28
V	147.4	142.84	119.53	137.23	155.46	134.27	140.91	144.8	143.73
Cr	0.5	0.45	0.28	0.75	0.29	b.d.l.	b.d.l.	0.58	0.68
Mn	387.8	426.26	312.75	274.85	353.51	280.99	313.31	405.83	379.16
Fe	772212	772211.9	772211.9	772211.9	772211.9	772211.9	772211.9	772211.9	772211.9
Co	3.89	4.33	3.85	3.66	4.27	4.28	3.81	3.95	4.39
Ni	6.05	8.16	5.91	5.89	6.95	5.88	5.44	5.23	8.26
Cu	b.d.l.	b.d.l.	b.d.l.	b.d.l.	b.d.l.	b.d.l.	b.d.l.	b.d.l.	b.d.l.
Zn	102.62	149.74	92.41	72.18	105.43	89.9	89.18	98.24	132.71
Ga	20.14	20.33	15.36	17.94	19.35	17.26	17.34	17.63	19.23
Ge	0.47	b.d.l.	b.d.l.	0.22	0.57	0.396	0.408	0.55	0.44
As	0.6	0.31	0.445	0.73	0.44	0.72	0.49	0.62	0.83
Y	b.d.l.	b.d.l.	b.d.l.	0.0032	0.0076	0.0098	0.0083	0.0039	0.0137
Zr	b.d.l.	b.d.l.	b.d.l.	b.d.l.	0.0033	0.0094	b.d.l.	0.0056	0.0028
Nb	b.d.l.	0.00056	b.d.l.	0.0021	b.d.l.	0.006	0.0026	0.0068	0.0024
Mo	0.474	0.398	0.186	12.25	47.49	104.62	52.21	13.67	94.05
Sn	0.504	0.758	0.382	0.489	0.481	0.428	0.494	0.533	0.61
Hf	b.d.l.	b.d.l.	b.d.l.	b.d.l.	b.d.l.	b.d.l.	0.0021	b.d.l.	0.0058
Ta	b.d.l.	0.00039	b.d.l.	b.d.l.	b.d.l.	0.00042	b.d.l.	b.d.l.	0.00056
W	b.d.l.	b.d.l.	0.0021	5.93	8.27	28.54	11.81	3.61	13.1
Pb	0.064	b.d.l.	b.d.l.	353.43	0.08	0.099	583.46	0.3	349.3
Th	0.00062	b.d.l.	0.00057	0.005	0.0142	0.11	0.0119	0.0042	0.0379
U	b.d.l.	b.d.l.	b.d.l.	0.0226	0.003	0.0115	0.0118	0.0022	0.0031

Sample	AZ 4.2.2				AZ 4.3				
Analysis	28	29	30	31	1	2	3	4	5
Element (ppm)									
Mg	76.12	226.32	56.42	65.85	83.53	200.5	113.78	94.47	72.53
Al	818.31	1055.77	620.38	878.85	1162.23	845.14	998.72	837.84	926.43
Si	3843.02	4532.92	3763.66	4460.02	3932.74	4768.8	5637.91	4169.95	4743.61
Ca	90.67	42.38	b.d.l.	b.d.l.	b.d.l.	b.d.l.	97.61	52.42	115.17
Sc	b.d.l.	b.d.l.	b.d.l.	b.d.l.	0.15	b.d.l.	0.165	b.d.l.	b.d.l.
Ti	838.29	750.23	797.23	1015.55	891.51	671.18	796.86	651.55	792.6
V	138.31	140.78	148.44	156.66	132.42	109.09	130.64	118.56	120.83
Cr	0.38	0.42	0.43	0.99	b.d.l.	0.34	b.d.l.	0.4	0.44
Mn	392.04	312.54	332.97	303.44	1020.02	800.87	962.59	945.28	940.41
Fe	772211.9	772211.9	772211.9	772211.9	772211.7	772211.7	772211.7	772211.7	772211.7
Co	4.88	3.58	4.09	5.1	7.37	5.18	5.82	5.36	6.11
Ni	8.81	5.43	6.11	7.96	17.53	10.27	14.21	11.88	16.02
Cu	b.d.l.	b.d.l.	b.d.l.	b.d.l.	b.d.l.	b.d.l.	b.d.l.	b.d.l.	b.d.l.
Zn	137.02	101.59	91.98	101.69	301.78	178.66	265.05	246.91	241.82
Ga	20.9	19.37	20.41	16.93	12.73	12.24	12.95	13.25	12.36
Ge	0.38	0.41	0.51	0.74	0.373	0.175	0.48	b.d.l.	b.d.l.
As	0.6	0.57	0.77	0.59	0.289	0.279	0.252	0.337	b.d.l.
Y	0.0052	0.0049	0.0007	0.0016	0.00042	b.d.l.	0.0074	0.0369	b.d.l.
Zr	0.003	0.005	b.d.l.	b.d.l.	0.0017	b.d.l.	0.0215	0.036	0.0016
Nb	0.0026	b.d.l.	0.0016	b.d.l.	0.0043	0.0052	0.0413	0.0283	0.0045
Mo	11.88	0.213	32.29	5.52	4.39	0.563	35.38	5.55	0.633
Sn	0.719	0.416	0.341	0.411	0.798	0.788	0.98	0.775	0.915
Hf	b.d.l.	b.d.l.	0.002	0.009	b.d.l.	b.d.l.	0.0101	b.d.l.	b.d.l.
Ta	0.0206	b.d.l.	b.d.l.	b.d.l.	0.00148	0.093	0.0227	0.0033	b.d.l.
W	3.7	0.005	8.95	2.34	0.872	0.0017	5.35	1.49	0.1
Pb	0.134	b.d.l.	0.116	0.176	b.d.l.	0.115	1.52	0.111	0.108
Th	0.0292	b.d.l.	0.0137	0.0104	0.0026	0.142	0.0411	0.0238	0.0024
U	0.0166	0.0082	0.00078	0.057	0.0043	b.d.l.	0.0412	0.0291	0.0025

Sample	AZ 4.3								
Analysis	6	7	8	9	10	11	12	13	14
Element (ppm)									
Mg	79.42	3195.36	522.36	81.75	541.21	158.34	97.05	104.94	705.77
Al	896.35	9568.12	2199.95	976.81	1671.46	1305.55	736.48	1090.52	2614.61
Si	3866.18	16551.66	5568.13	4718.09	5814.41	5354.13	3168.35	5660.81	8173.65
Ca	b.d.l.	251.24	58.07	b.d.l.	191.95	b.d.l.	57.78	b.d.l.	b.d.l.
Sc	b.d.l.	b.d.l.	b.d.l.	0.127	b.d.l.	b.d.l.	b.d.l.	0.171	b.d.l.
Ti	701.93	745.42	679.13	920.3	976.91	1051.04	805.62	1104.62	1386.21
V	104.86	136.55	111.92	116.72	117.05	128.86	101.23	135.49	129.62
Cr	0.43	0.52	0.37	1.24	0.52	0.42	0.312	b.d.l.	0.49
Mn	924.63	1135.55	873.67	918.31	688.33	825.94	682.36	865.1	918.88
Fe	772211.7	772211.7	772211.7	772211.7	772211.7	772211.7	772211.6	772211.6	772211.8
Co	5.31	4.42	5.43	5.67	5.29	6.42	4.63	7.27	6.2
Ni	13.43	10.47	13.86	14.15	8.31	12.3	9.81	18.51	16.14
Cu	b.d.l.	b.d.l.	b.d.l.	b.d.l.	b.d.l.	b.d.l.	b.d.l.	b.d.l.	b.d.l.
Zn	238.47	162.13	250.42	213.97	122.09	236.27	221.6	268.13	273.03
Ga	11.45	16.1	13.06	13.74	11.97	11.8	9.76	13.53	14.57
Ge	b.d.l.	0.333	b.d.l.	0.376	0.438	b.d.l.	0.33	b.d.l.	b.d.l.
As	4.83	b.d.l.	0.276	0.35	b.d.l.	0.235	0.182	0.322	0.329
Y	b.d.l.	0.183	0.0116	b.d.l.	0.0327	0.0048	0.0185	0.0083	0.0232
Zr	0.0682	0.149	0.0065	0.0026	0.024	0.0099	0.025	0.024	0.0166
Nb	0.178	0.0075	0.007	0.0064	0.0572	0.0062	0.0106	0.0421	0.0206
Mo	0.585	2.92	2.79	0.715	0.409	14.4	44.66	23.02	8.13
Sn	0.921	0.6	0.872	1.022	0.414	0.887	0.957	1.71	0.737
Hf	b.d.l.	0.0015	b.d.l.	b.d.l.	0.0043	b.d.l.	0.0079	b.d.l.	0.0296
Ta	b.d.l.	b.d.l.	0.00033	b.d.l.	0.0105	b.d.l.	0.00178	0.0536	0.0196
W	0.127	0.056	0.73	0.117	0.2	4.3	28.2	4.02	5.75
Pb	1248.47	0.228	0.445	b.d.l.	0.106	0.269	0.138	159.03	0.452
Th	0.0074	0.0232	0.303	0.0037	0.0491	0.0296	0.0345	0.0393	0.06
U	0.0029	0.102	0.0223	0.0071	0.124	0.0689	0.0056	0.321	0.23

Sample	AZ 4.3				AZ 7.4				
Analysis	15	16	17	18	1	2	3	4	5
Element (ppm)									
Mg	398.57	90.45	80.17	602.81	18241.56	4466.58	7545.76	13139.17	8192.49
Al	10704.13	1194.7	980.44	2778.56	7059.03	1437.24	1793.89	4473.04	3091.37
Si	27240.1	4922.88	5414.99	8268.73	10241.63	4360.39	5842.95	9641.5	7003.49
Ca	436.71	b.d.l.	b.d.l.	56.6	4321.64	2636.67	1791.76	103.39	b.d.l.
Sc	b.d.l.	b.d.l.	b.d.l.	b.d.l.	0.59	0.482	0.518	0.82	0.525
Ti	961.06	1074.23	937.73	1210.23	2985.03	2978.87	1810.29	3154.88	2493.1
V	138.42	134.87	126.93	128.32	158.28	117.81	97.22	158.66	95.64
Cr	b.d.l.	b.d.l.	0.5	b.d.l.	21.61	16.34	10.64	9.16	34.45
Mn	990.36	1106.84	949.27	1055.28	5553.19	5553.87	3926.12	5887.8	4643.06
Fe	772211.8	772211.7	772211.8	772211.8	749180.7	749180.8	749180.8	749180.8	749180.8
Co	6.17	6.55	6.2	7.77	49.69	56.21	34.06	51.84	41.24
Ni	12.95	13.65	10.99	16.35	33.07	23.15	19.87	23.19	18.14
Cu	b.d.l.	b.d.l.	b.d.l.	0.829	b.d.l.	0.389	b.d.l.	b.d.l.	b.d.l.
Zn	268.51	272.07	219.16	241.03	652.7	666.12	475.1	659.44	542.13
Ga	14.36	15.53	13.09	13.77	7.53	6.29	6.64	8.42	6.24
Ge	0.29	b.d.l.	0.287	b.d.l.	0.89	0.6	0.79	1.18	0.81
As	0.425	0.314	0.303	0.235	3.07	1.97	2.58	3.03	5.86
Y	0.0276	0.00082	0.0095	0.0229	0.57	0.277	0.498	0.313	0.342
Zr	0.0536	b.d.l.	0.128	0.0314	0.689	0.432	1.79	0.506	0.893
Nb	0.0444	0.0085	0.0037	0.0147	0.831	0.862	1.68	1.129	1.59
Mo	24.79	1	0.153	1.08	0.19	0.149	0.121	0.138	0.094
Sn	0.838	1.23	0.566	0.941	11.13	11.76	7.59	11.9	8.39
Hf	b.d.l.	b.d.l.	b.d.l.	0.0033	0.019	0.045	0.077	0.029	0.03
Ta	0.007	0.0057	0.0004	0.00046	0.1	0.059	0.156	0.074	0.121
W	4.2	0.037	0.0038	0.18	0.464	0.533	1.8	0.655	1
Pb	6.02	0.14	b.d.l.	2.25	1.95	5.39	2.88	1.26	6.27
Th	0.0157	0.0139	0.00056	0.0142	0.315	0.151	0.675	0.393	0.454
U	0.0424	0.0448	0.0029	0.0615	0.559	0.32	1.83	0.698	1.053

Sample	AZ 7.4								
Analysis	6	7	8	9	10	11	12	13	14
Element (ppm)									
Mg	30772.91	8424.9	9575.21	3880.3	14445.26	9484.99	6410.12	9074.16	8342.35
Al	9585.04	2511.93	2584.96	535.26	4053.07	2061.35	1388.67	2044.11	3445.61
Si	25887.66	6881.95	5879.12	3737.28	10848.82	5791.03	3856.61	6729.48	6763.93
Ca	417.98	76.18	b.d.l.	127.58	372.17	763.18	451.66	4238.17	41.69
Sc	1.1	0.58	0.561	0.613	0.43	0.501	0.473	1.04	0.53
Ti	2415.4	3290.05	1868.24	1728.17	1506.18	1689.18	2020.82	2406.95	1863.04
V	124.67	131.71	105.68	112.35	67.49	93.33	103.23	152.94	101.74
Cr	10.08	49.87	10.21	0.87	13.28	12.36	8.81	25.25	9.9
Mn	5566.25	4899.23	3898.08	4687.4	3787.49	4586.42	4759.07	6109.59	5729.35
Fe	749180.8	749180.8	749180.8	749180.8	749180.8	749180.7	749180.7	749180.8	749180.8
Co	74.49	62.83	35.16	45.89	28.2	39.55	39.96	46.71	40.29
Ni	27.57	22.22	15.27	25.09	19.82	20.19	14.42	24.1	18.54
Cu	0.45	0.303	0.198	3.5	b.d.l.	0.94	1.02	1.31	0.636
Zn	658.26	627.47	383.24	637.04	518.96	325.32	158.51	447.34	295.05
Ga	7.16	7.48	3.88	6.01	4.97	4.67	4.52	5	4.81
Ge	1.26	b.d.l.	0.72	0.55	0.38	0.56	0.32	0.71	0.77
As	5.42	4.3	4.68	2.23	2.64	3.02	2.96	5.67	1.6
Y	0.778	0.224	0.309	0.191	0.578	0.305	2.61	2.08	0.181
Zr	1.6	0.437	0.485	0.415	49.99	0.803	86	2.21	0.695
Nb	2.35	1.83	1.097	1.001	0.601	1.118	2.64	2.64	0.995
Mo	0.087	0.234	0.119	0.214	0.076	0.156	0.14	0.282	0.107
Sn	13.5	11.69	8.56	7.85	8.18	9.65	7.04	9.7	7.71
Hf	0.075	0.074	0.008	0.0132	1.31	0.0328	3.65	0.098	0.0386
Ta	0.254	0.093	0.102	0.0922	0.066	0.0949	0.231	0.375	0.0962
W	1.12	1.02	0.395	0.532	0.437	1.44	0.832	1.68	0.412
Pb	5.44	8.97	3.78	4.03	3.89	3.17	139.25	6.27	148.15
Th	0.815	0.287	0.279	0.177	0.383	0.246	0.843	1.6	0.158
U	2.64	0.58	0.776	0.456	0.769	0.669	2.98	3.28	0.414

Sample	AZ 8.1								
Analysis	1	2	3	4	5	6	7	8	9
Element (ppm)									
Mg	15650.3	6402.6	5173.69	6425.28	5252.18	7408.85	24962.46	8474.56	6270.9
Al	4760.04	887.64	701.67	824.93	280.33	995.06	8511.04	2445.2	717.27
Si	9325.85	2170.8	724.45	2135.19	1267.75	2339.69	15232.31	3513.14	1531.94
Ca	b.d.l.	169.25	b.d.l.	b.d.l.	b.d.l.	b.d.l.	b.d.l.	170.02	b.d.l.
Sc	b.d.l.	b.d.l.	b.d.l.	b.d.l.	b.d.l.	b.d.l.	b.d.l.	b.d.l.	b.d.l.
Ti	1729.87	2275.34	1911.83	2075.35	1892.73	2087.46	1641.72	1917.78	2116.67
V	137.13	158.94	143.11	149.48	139.91	166.56	148.74	149.21	170.32
Cr	1.47	3.91	2.83	b.d.l.	3.7	1.23	1.4	3.35	2.9
Mn	4147.64	5654.48	4700.35	4623.75	4094.4	4972.2	4392.08	4935.51	5318.8
Fe	761049.8	761049.8	761049.8	761049.8	761049.8	761049.8	761049.8	761049.8	761049.8
Co	57.49	63	51.75	60.58	63.41	82.68	58.72	59.99	66.59
Ni	12.64	13.17	13.67	11.99	15.19	12.43	14.13	12.95	15.05
Cu	b.d.l.	b.d.l.	b.d.l.	0.41	b.d.l.	0.65	b.d.l.	b.d.l.	b.d.l.
Zn	732.72	1051.24	876.73	859.09	771.92	885.99	851.09	852.42	874.65
Ga	19.34	22.31	24.22	20.96	17.23	22.78	22.85	20.6	23.22
Ge	0.8	1.05	1.27	1.4	0.48	0.72	0.85	0.72	1.41
As	1.55	1.14	b.d.l.	0.8	0.58	2.16	2.22	0.81	b.d.l.
Y	0.0237	0.117	0.0175	b.d.l.	b.d.l.	0.0117	0.0355	0.0095	0.0181
Zr	0.092	0.431	0.196	0.134	0.158	b.d.l.	0.13	0.047	0.064
Nb	0.054	0.317	0.311	0.0515	0.099	0.0265	0.0313	0.0337	0.023
Mo	0.28	0.215	b.d.l.	b.d.l.	0.185	0.259	0.39	0.292	0.288
Sn	8.92	10.96	10.15	10.18	8.4	10.53	8.87	9.64	9.75
Hf	0.018	0.041	b.d.l.	b.d.l.	0.02	0.032	0.028	0.0111	0.0197
Ta	0.0026	0.0192	0.0242	0.0062	0.0059	0.007	0.0062	0.0053	0.0057
W	0.024	0.485	b.d.l.	0.044	0.354	0.021	b.d.l.	0.0074	0.048
Pb	0.471	1.06	b.d.l.	0.564	0.255	0.203	0.74	0.228	0.127
Th	0.0041	0.141	b.d.l.	0.0024	0.071	0.0036	0.181	b.d.l.	0.0292
U	0.0181	0.587	0.102	0.0345	0.091	0.012	0.527	b.d.l.	5.37

Sample	AZ 8.1	
Analysis	1	2
Element (ppm)		
Mg	7404.54	6596.36
Al	1127.64	1887.78
Si	2592.23	2761.96
Ca	565.78	123.91
Sc	0.47	b.d.l.
Ti	2000.46	1634.95
V	174.06	132.11
Cr	3.58	b.d.l.
Mn	5225.84	4058.16
Fe	761049.8	761049.8
Co	66.06	54.65
Ni	12.95	10.16
Cu	b.d.l.	1.01
Zn	1052.2	800.1
Ga	21.98	19.57
Ge	1.24	0.71
As	3.7	11.42
Y	0.075	0.0253
Zr	0.171	0.196
Nb	0.161	0.061
Mo	0.29	0.124
Sn	10.49	9.08
Hf	0.049	b.d.l.
Ta	0.0081	b.d.l.
W	0.272	0.041
Pb	0.83	0.171
Th	0.08	b.d.l.
U	0.108	0.0049

Appendix F-4.2. – LA-ICP-MS ray results of outcrop samples of magnetite from the Orada deposit (the unfilled spaces in the following tables correspond to values below the limits of detection of the equipment).

Sample	ORA 2								
Analysis	1	2	3	4	5	6	7	8	9
Element (ppm)									
Mg	2692.39	2271.2	3359.22	2443.29	2882.86	2323.61	2050.53	2394.36	2139.88
Al	3577	1615.62	2405.71	2468.53	3268.65	1919.89	2494.33	2219.9	1500.57
Si	3416.74	3829.1	5258.45	4480.42	4661.62	3623.17	3950.34	3650.19	5276.82
Ca		96.1	209.39	136.94	207.96				
Sc	0.205	0.166	0.259	0.171	0.243		0.166	0.221	0.271
Ti	149.47	149.6	148.5	169.54	158.23	133.91	143.04	152.96	154.56
V	45.1	43.45	45.21	47.98	46.86	45.47	45.89	48.87	52.66
Cr	0.71	0.92	3.79	1.63	4.09	1.79	0.79	4.79	3.58
Mn	531.48	414.36	510.07	648.95	526.08	482.09	475.97	484.41	491.85
Fe	723598.8	723598.8	723598.8	723598.8	723598.7	723598.7	723598.6	723598.6	723598.7
Co	29.8	27.51	27.76	30.55	29.44	32.92	27.06	28.5	28.68
Ni	26.88	26.91	25.28	25.47	23.62	27.21	24.49	26.23	26.4
Cu	0.28		0.77		0.34	0.48			
Zn	89.61	61.01	74.87	71.9	84.28	74.84	57.04	69.1	76.58
Ga	9.22	6.85	8.97	8.19	8.81	10.01	7.93	7.66	7.82
Ge	0.95	0.96	0.62	1.04	0.63	1.61	0.68	1.14	1.2
As	0.4	0.46	1.04	0.87	0.75	0.21	0.188	0.42	
Y	0.0076	0.0269	0.0567	0.0079	0.162	0.0013	0.00079	0.0068	0.0281
Zr	2.29	1.94	1.9	2.24	2.99	1.67	1.77	2.69	2.01
Nb	0.392	0.237	0.51	0.206	0.587	0.18	0.218	0.338	0.344
Mo	3.2	2.87	2.99	3.19	3.14	2.84	3.23	3.24	2.85
Sn	12.32	10.85	13.07	11.78	12.18	12.26	10.72	14.48	13.5
Hf	0.085	0.061	0.063	0.08	0.084	0.035	0.042	0.117	0.122
Ta	0.0069	0.0043	0.0052		0.0072	0.001	0.0037	0.0081	0.0041
W	0.0459	0.131	0.274	0.148	0.189	0.03	0.0029	0.028	0.034
Pb	10.57	0.398	1.45	0.501	0.547		0.064	0.751	0.113
Th	0.0082	0.0091	0.117	0.0016	0.0375	0.0121	0.004	0.0317	0.127
U	0.0079	0.0051	0.0237	0.005	0.074	0.0069	0.0016	0.0356	0.052

Sample	ORA 2								
Analysis	1	2	3	4	5	6	7	8	9
Element (ppm)									
Mg	2535.86	2542.7	2234.01	1895.07	1916.11	2421.3	2044.64	2194.44	2909.27
Al	2675.9	3225.89	2878.54	1451.8	1651.43	2761.96	2527.71	3094.96	3921.39
Si	4279.61	4760.54	4010.98	4231.64	2851.16	4858.53	4092.93	4505.65	4428.75
Ca						94.57	67.03		
Sc	0.137	0.178	0.138	0.204		0.189	0.188	0.1	0.194
Ti	150.02	161.82	139.65	140.76	119.28	141.5	141.38	150.41	147.19
V	47.07	47.89	39.61	43.3	30.74	41.94	40.6	43.74	46.76
Cr	1.1	1.51	0.71	1.58	0.98	1.07	2.51	1.47	0.81
Mn	505.4	569.32	484.98	459.48	360.93	524.5	493.67	518.93	549.59
Fe	723598.6	723598.6	723598.6	723598.7	723598.6	723598.7	723598.6	723598.7	723598.6
Co	29.66	29.3	30.88	29.92	20.04	28.74	26.47	30.24	30.27
Ni	26.43	25.52	23.7	25.23	16.75	23.23	23.38	23.68	29.34
Cu									
Zn	70.77	73.32	63.14	61.8	56.83	73.68	64.9	79.97	72.5
Ga	8.98	9.97	8.5	8.52	5.57	7.91	8.04	8.39	8.79
Ge	1.08	1.19	0.86	1.08	0.39	1.08	0.79	1.45	1.12
As	0.33	0.2		0.19	0.25	0.42	0.63	0.22	
Y	0.0105		0.0074	0.0025	0.0049	0.0535	0.0047	0.0065	
Zr	1.74	2.03	1.89	2.06	1.26	2.51	2.2	2.71	3.24
Nb	0.252	0.283	0.214	0.209	0.118	0.272	0.375	0.363	0.42
Mo	3.09	3.44	3.17	3.15	2.49	3.54	3.13	3.17	3.3
Sn	12.6	12.46	11.46	12.83	8.41	12.03	10.91	11.91	13.41
Hf	0.0395	0.064	0.084	0.084	0.033	0.082	0.09	0.075	0.091
Ta	0.0044	0.0017	0.0028	0.0051	0.0037		0.0063	0.0058	0.0071
W	0.0135	0.0125	0.031	0.0061	0.045	0.111	0.098	0.028	0.0308
Pb	0.119	0.046	0.045	0.076	0.078	0.406	0.173	0.378	0.047
Th	0.0057	0.0012		0.0093	0.0025	0.0191	0.0035	0.0187	0.00096
U	0.0039	0.0024		0.0165		0.0184	0.0109	0.0407	0.0029

Sample	ORA 2								
Analysis	1	2	3	4	5	6	7	8	9
Element (ppm)									
Mg	2526.91	2581.04	3153.21	2554.53	2556.6	3616.13	4915.11	3555.78	2622.03
Al	2984.6	3169.95	2920.75	2081.53	2272.13	2423.78	2326.58	3956.65	2744.69
Si	4821.75	4303.19	4782.5	4610.94	5113.24	5661.47	7441.73	5988.61	4191.06
Ca			72.1		203.12	53.98		2143.14	
Sc	0.221	0.13	0.127	0.127	0.146	0.129	0.293	0.215	0.205
Ti	142.14	128.19	156.87	138.46	132.57	139.08	146.25	147.03	136.75
V	42.81	41.12	51.07	41.77	43.14	41.86	44.12	43.23	41.09
Cr	1.24	1.01	0.91	2.7	1.86	0.75	1.44	7.95	1.8
Mn	520.4	497.28	534.01	476.18	474.24	490.93	509.42	544.67	476.46
Fe	723598.7	723598.6	723598.7	723598.7	723598.6	723598.7	723598.6	723598.6	723598.6
Co	28.82	28.16	31.17	28.83	27.88	28.84	30.94	30.68	26.99
Ni	22.77	21.54	25.16	23.14	23.42	21.59	24.19	28.36	19.72
Cu				0.57	0.39				
Zn	61.17	78.49	59.43	53.06	48.07	50.43	46.69	86.02	60.41
Ga	8.16	8.15	8.86	7.81	7.6	8.15	8.89	8.95	8.12
Ge	0.89	1.09	1.01	0.97	0.96	1.02	1.01	0.75	0.98
As	0.24	0.4	0.68	0.29	0.178	0.41		0.147	0.35
Y	0.0183	0.0129	0.0195	0.0401	0.0488	0.0749	0.14	0.0469	
Zr	3.54	2.71	2.56	2.7	3.71	2.59	3.9	2.76	2.37
Nb	0.553	0.375	0.422	0.489	0.794	0.787	1.006	0.753	0.34
Mo	3.83	2.99	3.29	3.12	2.47	3.39	2.46	3.07	3.3
Sn	12.24	10.95	12.69	11.5	11.76	11.73	12.08	12.82	10.49
Hf	0.098	0.066	0.078	0.072	0.099	0.075	0.082	0.089	0.053
Ta	0.0113	0.01	0.006	0.0049	0.0079	0.0124	0.0096	0.0093	0.0024
W	0.032	0.043	0.133	0.041	0.08	0.156	0.077	0.069	0.035
Pb	0.091	0.131	0.335	0.55	0.116	0.061	0.068	0.4	0.514
Th	0.074	0.0111	0.0477	0.107	0.229	0.13	0.237	0.0327	0.0089
U	0.0496	0.0176	0.0237	0.05	0.118	0.0625	0.142	0.0312	0.0141

Sample	ORA 2								
Analysis	1	2	3	4	5	6	7	8	
Element (ppm)									
Mg	2421.15	2537.12	3132.3	2439.2	2689.84	2073.31	2132.51	2152.64	
Al	3865.46	3749.81	3488	3097.94	3463.86	2783.53	3085.03	2964.92	
Si	4703.41	4902.28	4963.9	4454.87	4877.99	5522.66	5253.82	4406.07	
Ca			174.6		121.34				
Sc	0.184	0.208	0.148	0.186	0.222	0.217	0.16	0.103	
Ti	134.25	146.31	141.94	133.64	141.14	150.13	152.88	125.59	
V	42.89	44.2	45.33	45.85	44.5	44.39	45.4	40.35	
Cr	0.85	2.57	3.95	0.89	1.41	1.34	0.32	0.45	
Mn	543.57	549.73	564.47	490.52	488.21	416.4	414.21	393.5	
Fe	723598.6	723598.6	723598.6	723598.6	723598.5	723598.6	723598.5	723598.6	
Co	28.73	29.24	33.9	27.1	28.38	31.53	29.44	25.67	
Ni	23.92	24.18	22.57	24.69	26.37	23.72	26.49	22.27	
Cu	0.25				0.27				
Zn	85.46	100.21	76.01	63.53	84.51	57.73	63.02	58.15	
Ga	8.71	8.32	8.83	8.68	8.67	8.15	9.84	7.29	
Ge	0.8	0.72	1.34	1.29	0.71	0.38	0.6	0.89	
As	0.206	0.33	0.47	0.195	0.53	0.116	0.32		
Y	0.0058	0.0156	0.09	0.0057	0.0138	0.0277	0.011		
Zr	3.29	2.84	4.11	2.7	2.17	1.47	1.5	1.23	
Nb	0.521	0.491	0.552	0.334	0.429	0.265	0.34	0.316	
Mo	3.1	3.57	3.01	3.24	3.27	2.39	2.29	1.97	
Sn	11.5	11.75	14.32	12.63	12.11	12.46	11.92	11.78	
Hf	0.082	0.066	0.051	0.069	0.048	0.068	0.06	0.063	
Ta	0.0052	0.011	0.0045		0.0104	0.0015	0.0048	0.009	
W	0.038	0.0113	0.035		0.093	0.018	0.0066	0.0132	
Pb	0.322	0.178	0.88	0.048	0.466	0.24	0.065		
Th	0.0106	0.0084	0.049	0.0087	0.0139	0.006	0.0119	0.0018	
U	0.0348	0.0086	0.076	0.0069	0.0055	0.002	0.0038		